HYDROACOUSTIC MODELLING AND NUMERICAL SIMULATION OF UNSTEADY OPERATION OF HYDROELECTRIC SYSTEMS

THÈSE N^{O} 3751 (2007)

PRÉSENTÉE LE 23 MARS 2007

À LA FACULTÉ SCIENCES ET TECHNIQUES DE L'INGÉNIEUR

Laboratoire de machines hydrauliques

SECTION DE GÉNIE MÉCANIQUE

ÉCOLE POLYTECHNIQUE FÉDÉRALE DE LAUSANNE

POUR L'OBTENTION DU GRADE DE DOCTEUR ÈS SCIENCES

PAR

Christophe NICOLET

Ingénieur mécanicien diplômé EPF
de nationalité suisse et orginaire de Cottens (FR)

acceptée sur proposition du jury:

Prof. P. Xirouchakis, président du jury
Prof. F. Avellan, Prof. J.-J. Simond, directeurs de thèse
Dr E. Bollaert, rapporteur
Dr J. Koutnik, rapporteur
Prof. Y. Tsujimoto, rapporteur

ÉCOLE POLYTECHNIQUE
FÉDÉRALE DE LAUSANNE

Lausanne, EPFL
2007

”On se lasse de tout, excepté d’apprendre.”

Virgile

Remerciements

Il me tient à coeur, ici au début de ce document, de remercier toutes les personnes qui ont contribués de près ou de loin à la réalisation de ce travail de thèse.

Ce travail n'aurait pas été possible sans le soutien financier des fonds de recherche de la CTI, et du PSEL, ainsi que celui des exploitants EOS, BKW, EEF, SIG, EDF, de Electricité Suisse, mais également de celui des constructeurs VOITH-Siemens et ALSTOM.

Je commence par exprimer tout ma gratitude à mes deux directeurs de thèse, le Professeur François Avellan, directeur du Laboratoire de Machines Hydrauliques, et le Professeur Jean-Jacques Simond, directeur du Laboratoire de Machines Electriques, pour m'avoir proposé et encouragé à me lancer dans cette enrichissante aventure qu'est le travail de thèse. Durant cette période, j'ai beaucoup apprécié la liberté de manoeuvre et la confiance dont j'ai pu bénéficier ainsi que de l'atmosphère stimulante et dynamique qu'ils ont créé et maintenu au cours du projet.

Mes remerciements vont également aux membres du jury, Professeur Paul Xirouchakis, Président du Jury, Dr. Erik Bollaert de l'EPFL, Dr. Jiri Koutnik de VOITH-Siemens et Professeur Yoshinobu Tsujimoto de l'Université de Osaka, pour le temps consacré à lecture de ce manuscrit ainsi que pour toutes les remarques et discussions constructives lors de la défense privée.

Je souhaite également remercier les différents responsables du LMH, le Professeur Jean-Louis Kueny, pour sa bonne humeur et son enthousiasme, Jean Prénat pour ses encouragements, et le Dr. Mohammed Farhat pour son aide lors de la réalisation des mesures.

Dans le cadre des projets industriels auxquels j'ai pu participer, j'ai beaucoup apprécié la collaboration avec le Dr. Jean-Jacques Hérou et Mme Nadine Pajean-Wassong de EDF, le Dr. Johann Gülich de Sulzer Pumps, et de M. Jordi Rossell de Meditecnic. Je remercie tout particulièrement le Dr. Jiri Koutnik et ses collègues de VOITH-Siemens avec qui ca a vraiment été un plaisir de collaborer.

Je souhaite remercier le personnel du groupe GEM, et du BE, pour leur aide lors de la réalisation d'essais, de dessins, pour leurs divers coups de mains et aussi pour l'ambiance de travail agréable à laquelle ils contribuent : merci à Pierre Barmaverain, Philippe Faucherre, Alain Renaud, Pierre Dutoit, Henri-Pascal Mombelli, Georges Crittin et à Philippe Cerrutti. Toutes les expériences et autres manips n'auraient bien sûr pas été possibles sans le soutien de l'équipe de l'atelier, coordonnée par Louis Bezençon, que je remercie aussi pour ses bons tuyaux oenologiques, Jean-Daniel Niederhauser, Raymond Fazan, Maxime Raton, Jérôme Gruaz et Christian Sierro. Je tiens aussi bien sûr à remercier Isabelle Stoudmann, Maria Anitua, Anne Ecabert et Shadije Avdulahi pour leur aide au quotidien et leur contribution à l'atmosphère du laboratoire.

Je souhaite bien sûr remercier mes compagnons de l'aventure SIMSEN, je pense en particulier à Philippe Allenbach pour toutes les heures passées à debugger le programme, heureusement parfois récompensées par une mousse salvatrice, mais aussi pour son enthousiasme dans le projet. Je remercie également le Dr. Alain Spain, père de SIMSEN, qui a su me faire profiter de son expérience et qui a toujours été disponible pour nous apporter son aide. Je remercie le Dr. Mai Tuxuan pour ses explications sur les machines électriques et bien d'autres domaines, sans oublier le Dr. Basile Kawkabani, Stefan Keller, et Antoine Béguin avec qui la collaboration a été agréable.

Je souhaite remercier les étudiants qui ont contribué à ce travail au travers de leur travaux de diplômes, merci à Bob Greiveldinger, pour son aide pour la modélisation des réseaux, à Nicolas Ruchonnet, pour son aide dans les développements rotor-stator, Yves Vaillant pour son aide avec la Kaplan, et Cécile Picollet pour son aide dans les manipulations de caractéristiques.

Une mention toute spéciale à mon Silverback de compagnon d'infortune dans cette aventure que représente une thèse, le regretté Dr. Alexandre Perrig, qui m'aura toujours impressionné par sa rigueur avec lui-même, mais aussi par ses capacités rédactionnelles dont il n'a jamais hésité à me faire profiter, et avec qui les discussions scientifiques et gastronomiques ont été très sympathiques. Merci pour la superbe ambiance tant au travail que lors d'excursions valaisannes, gruyèriennes ou même népalaises!

Je ne saurais oublier tous mes collègues et amis, anciens ou actuels, du laboratoire avec qui les jeudis de l'angoisse et les terrasses de St-Sulpices resteront d'excellents moments, comme dirait un certain Bob, c'était YES PUR, donc un grand merci à Tino, Youss, Sonia, Lluis, Silvia, Philippe, Ali, Olivier Braun, Nicolas, Fred, Javi, Stefan, Cécile, Pierre, Faiçal, Bernd, Pierre-Yves, Lavinia, Gabi, Georgetta et Monica, mais aussi Jorge, Gino, Couty, Alex, Sebastiano, et scusi à tous ceux que j'aurais pu oublier...

Je remercie également mes amis et mes colocs avec qui j'ai pu partagé cette aventure Lausannoise, merci à Win, Val, Guillaume, Ivano, Eric, Brigitte, Orane, Oli, Andréanne, Lio, Nat, Reynald, Arrigo, Eli, Zoé, Christine, et tous les autres.

Enfin, je tiens à remercier du fond du coeur mes parents Mutti et Padré et ma soeur Anne, qui m'ont toujours encouragés et m'ont soutenu tout au long de mon parcours !

Résumé

La production hydroélectrique représentait en 1999 le 19% de la production mondiale d'électricité et il est à prévoir qu'elle aie une forte augmentation d'ici à 2030. Les turbines Francis ont un rôle majeur à jouer dans cette production de par leur gamme étendue d'application. La dérégulation du marché de l'électricité conduit à une exploitation des turbines hors de leurs conditions optimales de fonctionnement et engendre des séquences d'arrêts et de démarrages fréquentes. De ce fait, les turbines Francis sont sujettes à des sollicitations relatives à des phénomènes transitoires et périodiques dont la nature propagative est prépondérante. Ce travail est une contribution à la modélisation hydroacoustique des centrales hydroélectriques équipées de turbines Francis.

La première partie de ce travail présente la modélisation du comportement dynamique et l'étude des phénomènes transitoires survenant dans les centrales hydroélectriques. Ainsi, un modèle monodimensionnel d'une conduite est établi à partir des équations fondamentales de conservation de la quantité de mouvement et de continuité. L'utilisation de schémas numériques appropriés permet de représenter une conduite par un circuit électrique équivalent en T. La précision de ce modèle numérique est évaluée dans le domaine fréquentiel par comparaison à une solution analytique.

Cette approche de modélisation est ensuite étendue à d'autres composants hydrauliques tels que : vanne, cheminée d'équilibre, réservoir d'air, développement de cavitation, etc. Ensuite, la modélisation des turbines Francis, Pelton et Kaplan est présentée. Cette modélisation est basée sur l'utilisation de caractéristiques statiques des machines hydrauliques. Les modèles des composants hydrauliques ont été implémentés dans un logiciel de simulation d'installation électrique nommé SIMSEN. Après la validation des modèles des composants hydrauliques, une étude des régimes transitoires dans les centrales hydroélectriques est réalisée. Il est montré en particulier, que la modélisation seule de la partie hydraulique ou électrique de la centrale est suffisante pour le dimensionnement de l'installation, alors que l'optimisation des régulateurs de vitesse des turbines requiert une modélisation de la centrale dans son ensemble.

La deuxième partie de ce travail porte sur la modélisation et l'analyse de phénomènes de résonance ou d'instabilité survenant dans les centrales hydrauliques équipées de turbines Francis. La revue des sources d'excitations inhérentes à l'exploitation des turbines Francis indique que les fluctuations de pression dues au diffuseur et aux effets rotor-stator sont prépondérantes. Etant donné que la modélisation des fluctuations de pression dans le diffuseur survenant à charge partielle est bien établie, l'accent est mis sur la modélisation des phénomènes tels que les fluctuations de pression de haut de charge partielle, de rotor-stator ainsi que sur les instabilités de fortes charges.

Trois études hydroacoustiques sont réalisées. D'abord, les phénomènes de fluctuations de haut de charge partielle identifiés expérimentalement sur un stand d'essai sont étudiés au sens de simulations hydroacoustiques et de visualisations par caméra rapide. La résonance du stand d'essai induite part l'excitation associée à la torche de cavitation est confirmée par le modèle hydroacoustique alors que le mouvement de la torche sur elle-même est identifié à partir les visualisations. Une description des mécanismes d'excitation possibles est proposée. Ensuite, une étude des oscillations de pressions et de puissance survenues sur une installation de pompage-turbinage de 4 × 400 MW en régime de forte charge est réalisée. La modélisation de l'installation dans son ensemble, qui prend en compte le circuit hydraulique, les inerties en rotation et les installations électriques, fournit l'explication du phénomène ainsi que ses conditions d'apparitions. Un modèle non-linéaire de la torche de forte charge est établi et validé qualitativement. Finalement, les interactions rotor-stator sont étudiées dans le cas d'un modèle réduit de pompe-turbine installé sur stand d'essai. Une approche originale basée sur la distribution de l'écoulement entre les parties fixes et les parties tournantes de la turbine est utilisée pour la modélisation de ce phénomène. Le modèle permet de reproduire correctement les caractéristiques rotor-stator dans le jeu entre parties fixes et tournantes; il permet aussi la prédiction d'ondes stationnaires dans la bâche spirale et le système d'adduction.

La modélisation monodimensionnelle proposée dans ce travail permet la simulation, l'analyse et l'optimisation du comportement dynamique d'une centrale hydroélectrique. Cette approche a prouvé sa capacité à simuler correctement à la fois les régimes transitoires et périodiques auxquels les turbines Francis sont soumises durant leur exploitation. Ce type d'étude peut être entrepris lors des phases d'avant-projets déjà, de sorte à pouvoir choisir les solutions les plus appropriées pour la sécurité de l'installation et l'optimisation de ses performances dynamiques.

Mots clefs: Systèmes hydrauliques, turbine Francis, phénomènes transitoires, modélisation hydroacoustique, comportement dynamique, analogie électrique.

Abstract

Hydropower represented in 1999 19% of the world electricity production and the absolute production is expected to grow considerably during the next 30 years. Francis turbines play a major role in the hydroelectric production due to their extended range of application. Due to the deregulated energy market, hydroelectric power plants are increasingly subjecting to off design operation, start-up and shutdown and new control strategies. Consequently, the operation of Francis turbine power plants leads to transients phenomena, risk of resonance or instabilities. The understanding of these propagation phenomena is therefore paramount. This work is a contribution to the hydroacoustic modelling of Francis turbine power plants for the investigation of the aforementioned problematic.

The first part of the document presents the modelling of the dynamic behavior and the transient analysis of hydroelectric power plants. Therefore, the one-dimensional model of an elementary pipe is derived from the governing equations, *i.e.* momentum and continuity equations. The use of appropriate numerical schemes leads to a discrete model of the pipe consisting of a T-shaped equivalent electrical circuit. The accuracy in the frequency domain of the discrete model of the pipe is determined by comparison with the analytical solution of the governing equations.

The modelling approach is extended to hydraulic components such as valve, surge tanks, surge shaft, air vessels, cavitation development, etc. Then, the modelling of the Francis, Pelton and Kaplan turbines for transient analysis purposes is presented. This modelling is based on the use of the static characteristic of the turbines. The hydraulic components models are implemented in the EPFL software SIMSEN developed for the simulation of electrical installations. After validation of the hydraulic models, transient phenomena in hydroelectric power plants are investigated. It appears that standard separate studies of either the hydraulic or of the electrical part are valid only for design purposes, while full hydroelectric models are necessary for the optimization of turbine speed governors.

The second part of the document deals with the modelling and analysis of possible resonance or operating instabilities in Francis turbine power plants. The review of the excitation sources inherent to Francis turbine operations indicates that the draft tube and the rotor-stator interaction pressure fluctuations are of the major concern. As the modelling of part load pressure fluctuations induced by the cavitating vortex rope that develops in the draft tube at low frequencies is well established, the focus is put on higher frequency phenomena such as higher part load pressure fluctuations and rotor-stator interactions or full load instabilities.

Three hydroacoustic investigations are performed. (i) Pressure fluctuations identified experimentally at higher part load on a reduced scale model Francis turbine are investigated by means of hydroacoustic simulations and high speed flow visualizations. The resonance of the test rig due to the vortex rope excitation is pointed out by the simulation while the special motion and shape of the cavitating vortex rope at the resonance frequency is highlighted by the visualization. A description of the possible excitation mechanisms is proposed. (ii) A pressure and power surge measured on a 4 × 400 MW pumped-storage plant operating at full load is investigated. The modelling of the entire system, including the hydraulic circuit, the rotating inertias and the electrical installation provides an explanation of the phenomenon and the related conditions of apparition. A non-linear model of the full load vortex rope is established and qualitatively validated. (iii) The rotor-stator interactions (RSI) are studied in the case of a reduced scale pump-turbine model. An original modelling approach of this phenomenon based on the flow distribution between the stationnary and the rotating part is presented. The model provides the RSI pressure fluctuation patterns in the vaneless gap and enables to predict standing waves in the spiral case and adduction pipe.

The proposed one-dimensional modelling approach enables the simulation, analysis and optimization of the dynamic behavior of hydroelectric power plants. The approach has proven its capability of simulating properly both transient and periodic phenomena. Such investigations can be undertaken at early stages of a project to assess the possible dynamic problems and to select appropriate solutions ensuring the safest and optimal operation of the facility.

Keywords: Hydraulic systems, Francis turbine, transient simulation, hydroacoustic modelling, dynamic behavior, electrical analogy.

Contents

Notations

Nomenclature

Latin characters

a	Wave speed $a = \sqrt{E/\rho}$ (for infinite fluid)	[m/s]
dx	Spatial discretization step	[m]
dt	Temporal discretization step	[s]
f	Frequency $f = 1/T$	[Hz]
g	Terrestrial acceleration $g \simeq 9.81$ m/s^2	[m/s^2]
h	Piezometric head $h = z + p/(\rho g)$	[m/s^2]
l_c	Characteristic length	[m]
n	Polytropic coefficient	[-]
n	Rotational frequency	[Hz]
p	Static pressure	[Pa]
$\tilde{p}$	Fluctuating pressure	[Pa]
t	Time	[s]
x	Abscissa	[m]
y	Guide vane opening (GVO)	[-]
z	Elevation	[m]
A	Pipe area	[m^2]
C	Absolute flow velocity	[m/s]
D	Diameter	[m]
E	Massic energy $E = gH = p/\rho + gz + C^2/2$	[J/Kg]
E	Bulk modulus	[Pa]
E_c	Young modulus	[Pa]
E_r	Massic energy loss	[J/kg]
H	Head	[m]
K	Local loss coefficient	[-]
N	Rotational speed	[rpm]
R	Radius $R = D/2$	[m]
T	Torque	[Nm]

T	Period	[s]
U	Peripheral velocity	[m/s]
V	Volume	[m^3]
$\underline{Z}$	Complex acoustic impedance $\underline{Z} = \underline{h}/\underline{Q}$	[m/s^2]
Z	Acoustic impedance	[m/s^2]

Greek symbols

α	Flow angle	[rad]
β	Blade angle	[rad]
γ	Wave number $\gamma = 2\pi/\lambda = \omega/a$	[1/m]
$\underline{\gamma}$	Complex wave number	[1/m]
θ	Polar abscissa of turbine characteristic $\theta = (Q/Q_{BEP})/(N/N_{BEP})$	[-]
κ	Adiabatic coefficient	[-]
λ	Wave length $\lambda = a/f$	[m]
λ	Local loss coefficient	[-]
μ	Fluid dynamic viscosity	[Pa s]
ν	Fluid kinematic viscosity $\nu = \mu/\rho$	[m^2/s]
ρ	Density	[kg/m^3]
σ	Stress	[Pa]
τ	Shear stress	[Pa]
ϕ	Phase	[rad]
χ	Mass flow gain factor $\chi = -\partial V/\partial Q$	[s]
ω	Pulsation $\omega = 2\pi f$	[rad/s]

Non-dimensional values in turbomachinery

Fr	Froude number $Fr = C_\infty/\sqrt{gl_c}$	[-]
Re	Reynolds number $Re = C_\infty l_c/\nu$	[-]
St	Strouhal number $St = C_\infty/fl_c$	[-]
η	Efficiency $\eta = T\omega/(\rho QE)$	[-]
ν	Specific speed $\nu = \varphi^{1/2}/\psi^{3/4}$	[-]
σ	Thoma number $\sigma = (p_\infty - p_v)/(\frac{1}{2}\rho C_\infty^2)$	[-]
φ	Flow coefficient $\varphi = Q/(\pi\omega R^3)$	[-]
ψ	Energy coefficient $\psi = 2E/(\omega^2 R^2)$	[-]
$NPSE$	Net Positive Suction Energy $NPSE = \sigma E$	[J/Kg]

Hydroacoustic equivalent scheme

R	Hydraulic resistance $R = \lambda dx\lvert\overline{Q}\rvert/(2gDA^2)$	$[\mathrm{s/m^2}]$
R_d	Diaphragm hydraulic resistance $R = K\lvert\overline{Q}\rvert/(2gA^2)$	$[\mathrm{s/m^2}]$
R_{ve}	Viscoelastic resistance $R_{ve} = \mu/(\rho gAdx)$	$[\mathrm{s/m^2}]$
L	Hydraulic inductance $L = dx/(gA)$	$[s^2/m^2]$
L	General hydraulic inductance $L = \int dx/(gA(x))$	$[s^2/m^2]$
C	Hydraulic capacitance $C = dxgA/a^2$	$[\mathrm{m^2}]$
C	Cavitation capacitance $C = -\partial V/\partial h = V/(nh)$	$[\mathrm{m^2}]$

Turbine location and section definition

I	Reference section high pressure side; inlet spiral casing
3	Stay vanes
2	Guide vanes
1	Runner blade high pressure side edge
i	Runner blade interior streamline (shroud)
e	Runner blade exterior streamline (hub)
$\overline{1}$	Runner blade low pressure side edge
$\overline{2}$	Draft tube inlet
$\overline{I}$	Reference section low pressure side; outlet draft tube

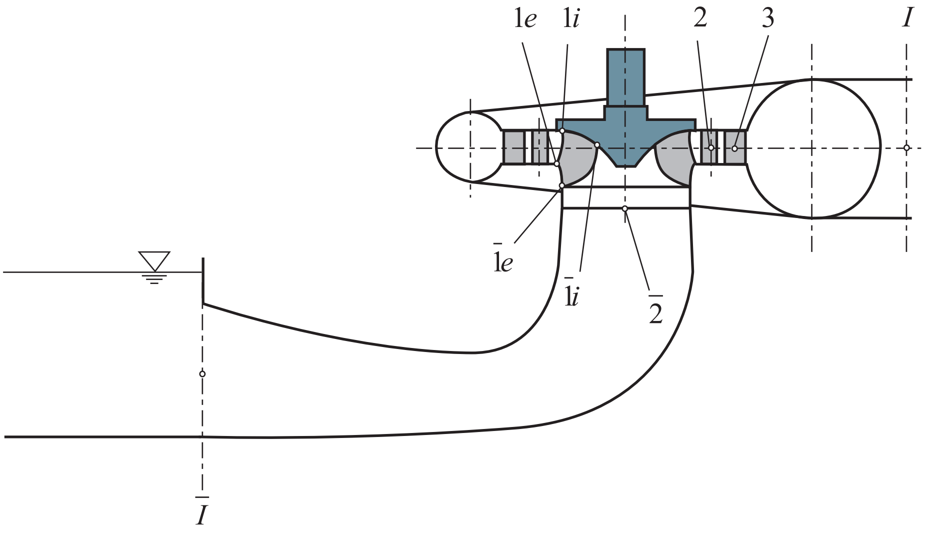

Subscript

BEP	Best efficiency point
n	Nominal operating point
i	Incident
r	Reflected
t	Transmitted

Introduction

Chapter 1

Introduction

1.1 Hydropower: Facts and Issues

The demand for electricity is constantly increasing because of the demographic growth and social level increase of developing countries. Worldwide projections for the period 2003-2030 predict that the electricity consumption will more than double from 14'781 TWh/year to 30'116 TWh/year [50]. Figure 1.1 shows the evolution of the sources of electricity generation from 2003 until 2030. To cope with this need, a gain in efficiency in all domains, *i.e.* production, transport, consumption, but also an increase of renewable energies capacity are required in order to refrain the development of solutions generating greenhouse gases. The development of the related infrastructure and technologies minimizing social and environmental impacts represents a huge challenge for mankind.

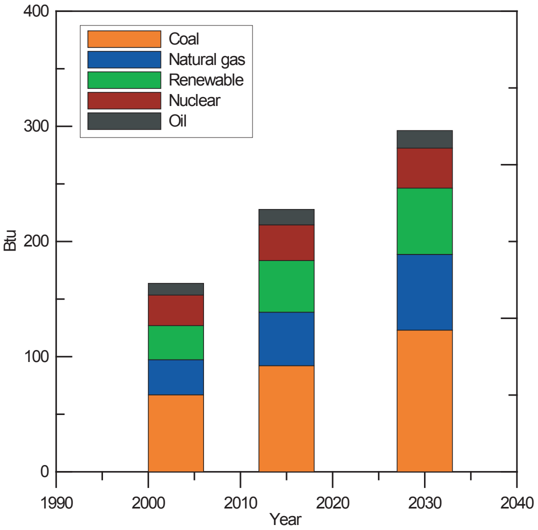

Figure 1.1: Projection of the electricity generation by fuel type for 2003, 2015 and 2030 in Btu (British thermal units) [50].

The contribution of renewable energy in the future is expected to grow mainly due to the increase of large hydropower capability. In 1999, the hydropower production covered

19% of the world electricity needs with a total installed capacity estimated around 692 GW [156], [144], [78]. The geographical distribution of the total production capacity is illustrated in figure 1.2 with about 31% of the installed capacity in Europe, 25% in Asia, 23% in North America, 15% in South America and the remaining 6% are shared between Africa, Oceania and the Middle East. However, the 2'633 TWh of hydroelectricity produced in 1999 represents only 33.2% of the economically exploitable resources and 18.3% of the technically exploitable capability. Therefore, hydropower has still a high potential for growth in the 21^{st} century. As illustrated in figure 1.3, the regions with the highest potential are Asia, Africa, South America but also in Europe. In addition, hydropower presents the advantage of avoiding emissions of gases in spite of others environmental impacts on the fauna, flora and sediments. The social impact are on the one hand detrimental because of the population displacements and land transformation but on the other hand positive as hydropower offers the possibility to mitigate flood, enabling better fluvial navigation and irrigation and providing employment. Moreover, the drawbacks related to hydropower production can be mitigated by taking appropriate counter measures at the early stages of the projects.

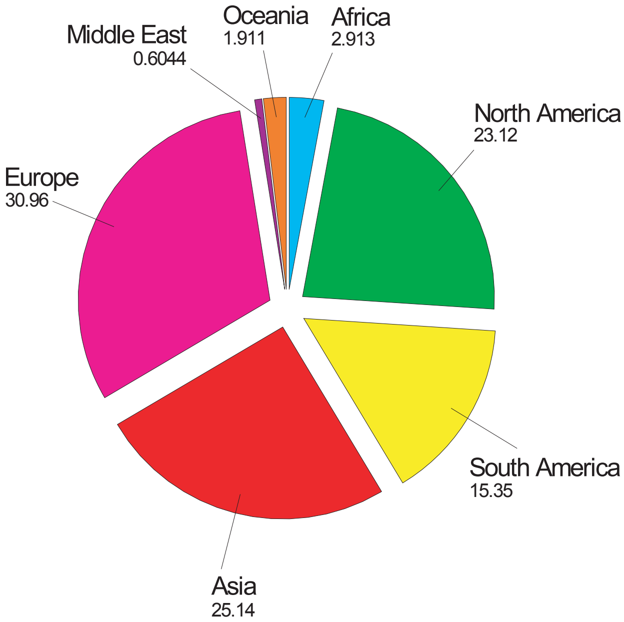

Figure 1.2: Distribution of hydropower capacity (for the year 1999); 100% being 692 GW [144].

1.2 The Increase of Hydropower Production

1.2.1 Increase of the Capacity

As illustrated in figure 1.1, the contribution of hydropower is expected to grow considerably in the next 30 years, and 553 GW of renewable production capability increase are predicted, corresponding to an annual rate of 1.9% [156]. Regarding the development of the hydroelectric production, it can be decomposed in 4 main areas:

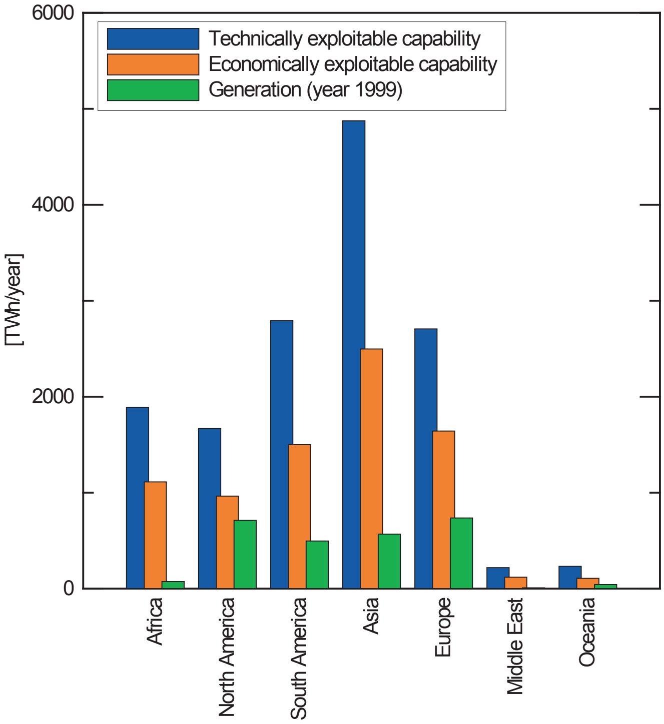

Figure 1.3: Distribution of the hydropower technically and economically exploitable capability and generation (for the year 1999) [144].

- **exploitation of new hydropower resources:** the main contribution is expected to come from the completion of hydro facilities in Asia and particularly in China;
- **refurbishment of existing power plants:** a gain of efficiency of old electromechanical equipment can represent a significant increase of the production capacity. It is mainly the case in Europe and North America for 50 years old facilities;
- **rehabilitation of old power plants:** older facilities in Europe and North America are subject to full re-equipment considering also new civil work in order to increase drastically the capacity of a power plant;
- **small hydro:** is related to developing countries where electrification of rural area can be achieved through small-hydro with reduced environmental impacts.

1.2.2 Over-Equipment for Improving Network Stability

Another aspect of development of the hydroelectric market is the increasing need for power plants able to stabilize the global power network by allowing quick set point changes in terms of both active and reactive power in generating and in motor mode. Indeed, the increase of renewable energy source contribution such as wind power, whose availability cannot be ensured, will represent a source of disturbances for power networks that are nowadays considered to be stable. For example in Europe, where thermal power plants still represent the major contribution, the impact of sudden changes of wind production cannot be counter-balanced by thermal power plants but goes to hydropower. Therefore, there is a need for the development of pump-storage capability in order to be able not only to change the set point, but also to store exceeding produced energy. Actually, pump-storage power plants are the only high capacity solution for storing energy and balancing with nuclear broad band production at various time scales, *i.e.* daily as well as seasonally. Another side effect of a deregulated energy market is the gain of interest for peak production requiring availability of high production capability.

New technologies like variable speed solutions also provide an additional degree of freedom for reducing time response of power plants and offering flexibility to the power management. Variable speed solutions enable taking advantage of flywheel effects of hydrogenerators for fast loading or unloading of units and spinning reserve [92].

1.2.3 The Hydropower Challenge

Modern hydropower has to face new challenges related to completely different exploitation strategies leading to an increase of the solicitation of the entire machine. Thus, hydraulic machines are increasingly subject to off-design operation, startup and shutdown sequences, quick set point changes, etc. To be competitive on the energy market, the specific power and efficiency of hydro units, which are already high, are constantly increased in order to meet economical issues but lead to higher loading of the structure of the turbines.

Consequently, manufacturers, consultants and electric utilities of hydro power plants need integrating new technologies and methodologies for improving dynamic performances, ensuring the safety and increasing the competitiveness of hydroelectric power plants. This requires developing appropriate experimental and numerical tools and methods for a better understanding and thus a more accurate prediction of the micro and macro-scale behavior of hydroelectric power plants.

1.3 Francis Turbine in the Context of Hydropower

The hydraulic power P_h results from the product of the mass flow $\dot{M} = \rho \cdot Q$ and of the specific energy $E = g \cdot H$ and is therefore given by:

$$P_h = \rho \cdot Q \cdot E \tag{1.1}$$

The role of a hydraulic turbine is to convert the hydraulic power into mechanical power $P_m = T \cdot \omega$ with the highest hydraulic efficiency η_h which is given for a turbine by:

$$\eta_h = \frac{P_m}{P_h} = \frac{T \cdot \omega}{\rho \cdot Q \cdot E} \tag{1.2}$$

According to the hydrology and the exploitation strategy of a given hydraulic project, a goal discharge Q_{plant} and a goal specific energy E_{plant} are determined for the site. Then, depending on the number of machines and the selection of the synchronous rotational speed $N = (f_{network} \cdot 60)/(pairepoles)$, the type of turbine can be chosen between the "standard" hydraulic turbines which are: (i) Pelton turbines, (ii) Francis turbines, (iii) Kaplan turbines, (iv) bulbe turbine, (v) or propellers.

Figure 1.4 shows the domain of application of the different types of turbines as function of the nominal net head H_n and the nominal discharge Q of the machine. Typically, for high head, medium head and low head, Pelton, Francis and Kaplan turbines are respectively chosen. However, for the intermediate range of head, 2 types of turbines are in competition. Then, the final selection of a type of turbine results from an iteration process aiming to maximize the produced energy on a standard year of exploitation taking into account maintenance, civil work and flexibility of operation issues. Because of its wide application range, the Francis turbine is often selected. Table 1.1 summarizes the worldwide percentage sales of turbines of each type for the period 1997-2001. It arises that 56% of the turbines are of the Francis type with an additional 5% of pump-turbines.

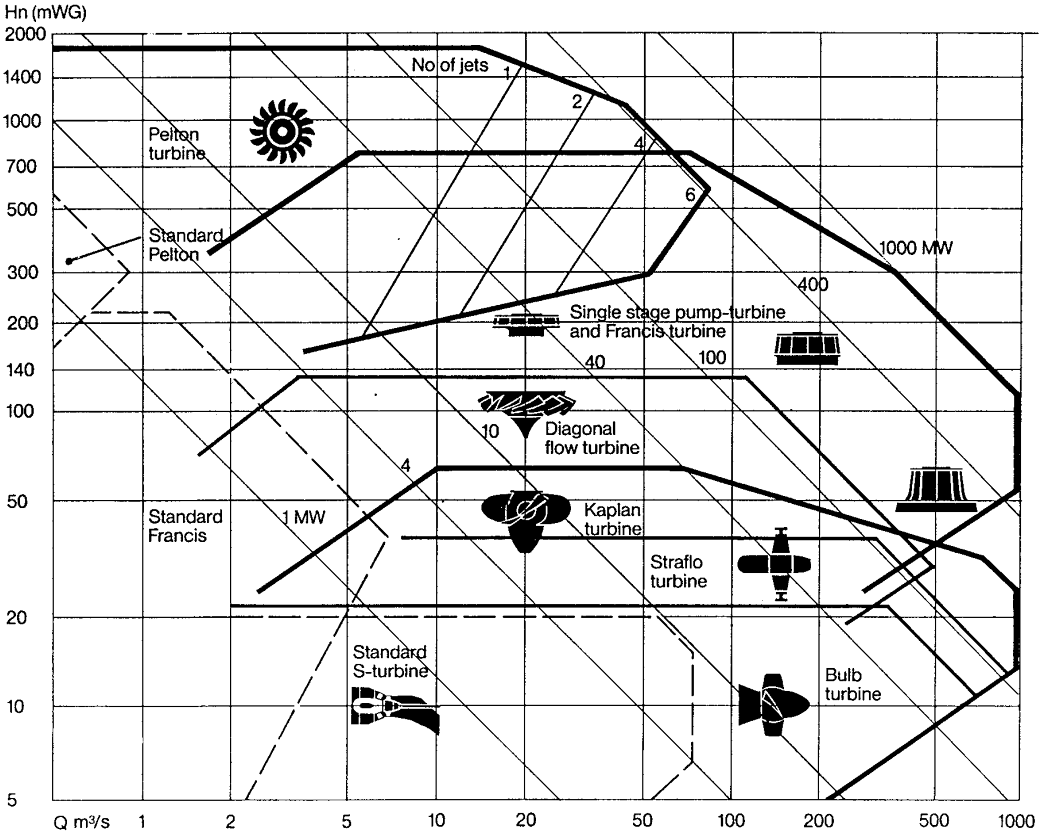

Figure 1.4: Turbine application range [56].

Table 1.1: Distribution of sales of the different types of turbines during the period 1997 to 2001 [124].

Francis %	Pelton %	Kaplan %	Bulbes %	Pump-turbines %
56	15	15	9	5

Once the nominal discharge Q_n, specific energy E_n and rotational pulsation ω_n are known, the specific speed of the machine can be determined as follows:

$$\nu = \omega \cdot \frac{(Q_n/\pi)^{1/2}}{(2 \cdot E_n)^{3/4}} \tag{1.3}$$

All turbines having the same specific speed are geometrically similar.

1.3.1 The Francis Turbine

General

The francis turbine is made of 5 main components as illustrated by figure 1.5:

- **the spiral case:** converts axial momentum into angular momentum and distributes uniformly the flow into the stay vanes;
- **the stay vanes:** are fixed blades having the structural role to close the force loop of the pressurized spiral case ;
- **the guide vanes:** are mobile blades allowing controlling the flow rate through the turbine;
- **the runner:** converts the angular momentum of the flow into mechanical momentum by deviating the flow from the inlet to the outlet so that the flow has no more angular momentum at the outlet, the reaction force acting on the blade inducing the mechanical torque;
- **the diffuser or draft tube:** has the role to convert the kinetic energy of the flow into potential energy and therefore enables increasing the efficiency of the turbine by reducing the pressure level at the runner outlet.

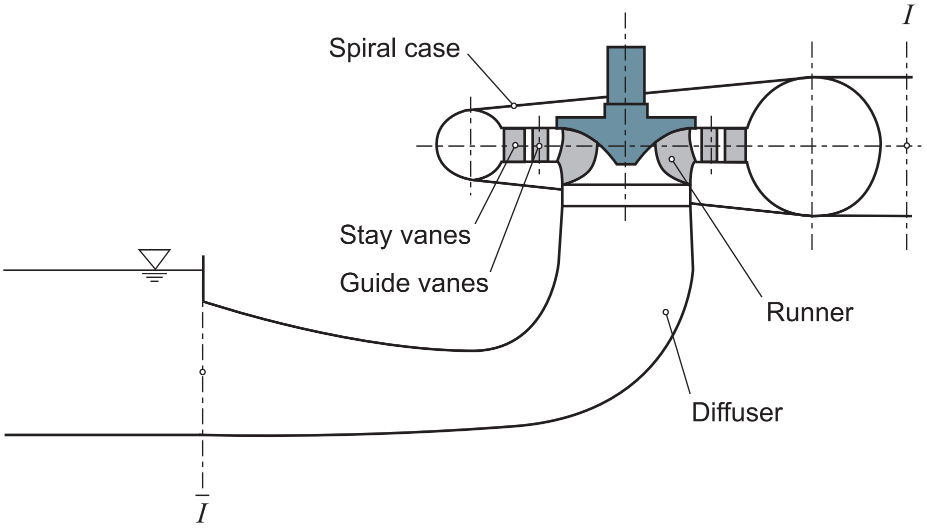

Figure 1.5: Components of a Francis turbine.

Figure 1.6 shows an example of turbine prototype and figure 1.7 shows typical geometries of Francis turbine runner for different specific speed ν.

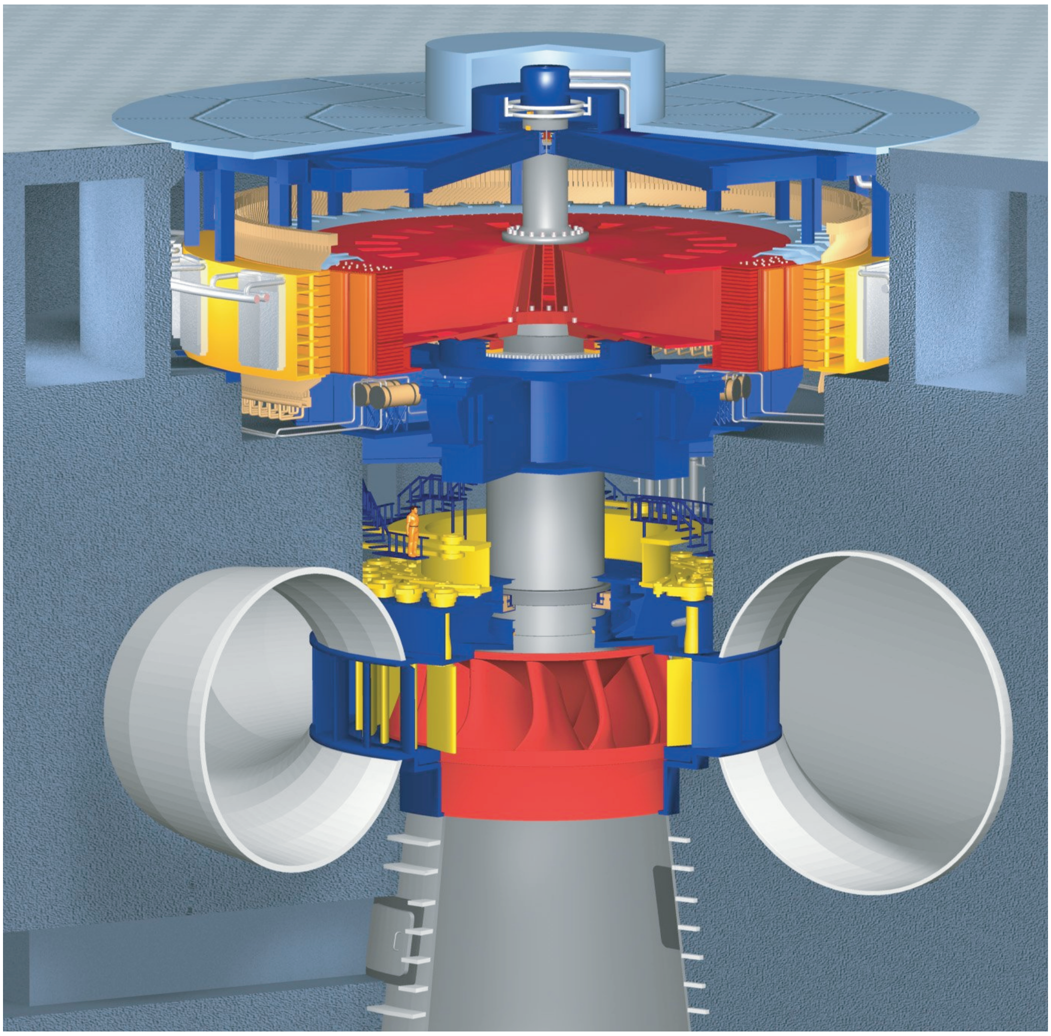

Figure 1.6: Example of prototype turbine; Three Gorges (Sanxia) 26 × 700 MW (Courtesy of Voith-Siemens Hydro).

Velocity Triangles

The absolute velocity $\overrightarrow{C}$ at any point of the turbine can be decomposed as the sum of the peripheral velocity of the turbine $\overrightarrow{U}$ and of the relative velocity $\overrightarrow{W}$ and is therefore given by:

$$\overrightarrow{C} = \overrightarrow{U} + \overrightarrow{W} \tag{1.4}$$

The velocity triangle at the inlet and outlet of a Francis turbine runner for the optimum operating conditions is illustrated in figure 1.8. The relative velocity $\overrightarrow{W}$ is perfectly adapted at both leading edge and trailing edge of the blade profile while the absolute velocity at the outlet $\overrightarrow{C}_{\bar{1}}$, is usually almost axial. The influence of the discharge on the velocity triangle at the runner outlet is illustrated in figure 1.9. It can be seen that for discharge below the optimum discharge, the flow at the runner outlet is animated with

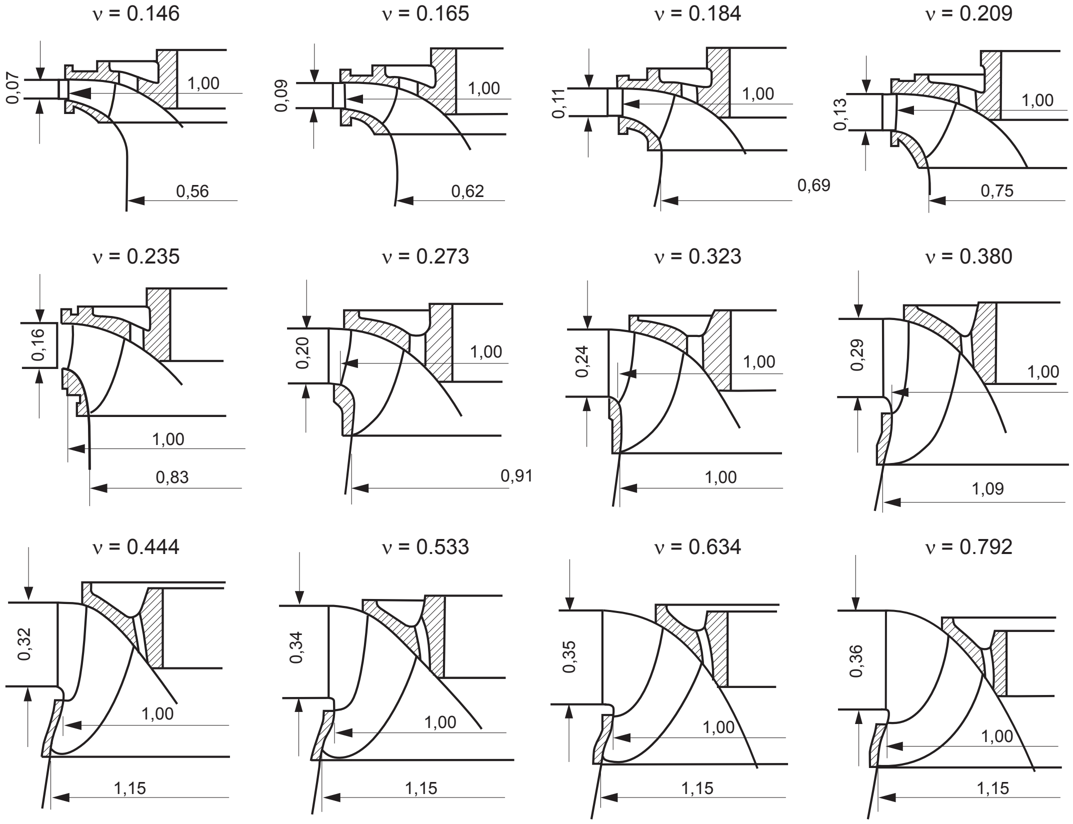

Figure 1.7: Francis turbine runner geometry as function of the specific speed ν [10].

a positive absolute circumferential velocity $\overrightarrow{C}_{u\bar{1}}$, while it is negative for discharge above optimum discharge.

The energy of the flow is converted into mechanical torque along the runner blade. This transformation can be expressed by the momentum of angular momentum conservation equation:

$$\frac{d}{dt}(\overrightarrow{r} \times m \cdot \overrightarrow{C}) = \overrightarrow{T} \tag{1.5}$$

Where m is the mass of the fluid particle, $\overrightarrow{r}$ is the radius and $\overrightarrow{T}$ is the mechanical torque. The balance of the momentum of angular momentum between runner inlet (1) and the runner outlet ($\bar{1}$) leads to the well known Euler's equation. The transformed energy, E_t, is given by:

$$\overrightarrow{E}_t = \overrightarrow{U}_1 \cdot \overrightarrow{C}_1 - \overrightarrow{U}_{\bar{1}} \cdot \overrightarrow{C}_{\bar{1}} \tag{1.6}$$

The scalar value of the transformed energy is given by:

$$E_t = U_1 \cdot C_{u1} - U_{\bar{1}} \cdot C_{u\bar{1}} \tag{1.7}$$

The transformed energy, is by definition given by:

$$E_t = \frac{T \cdot \omega}{\rho \cdot Q} \tag{1.8}$$

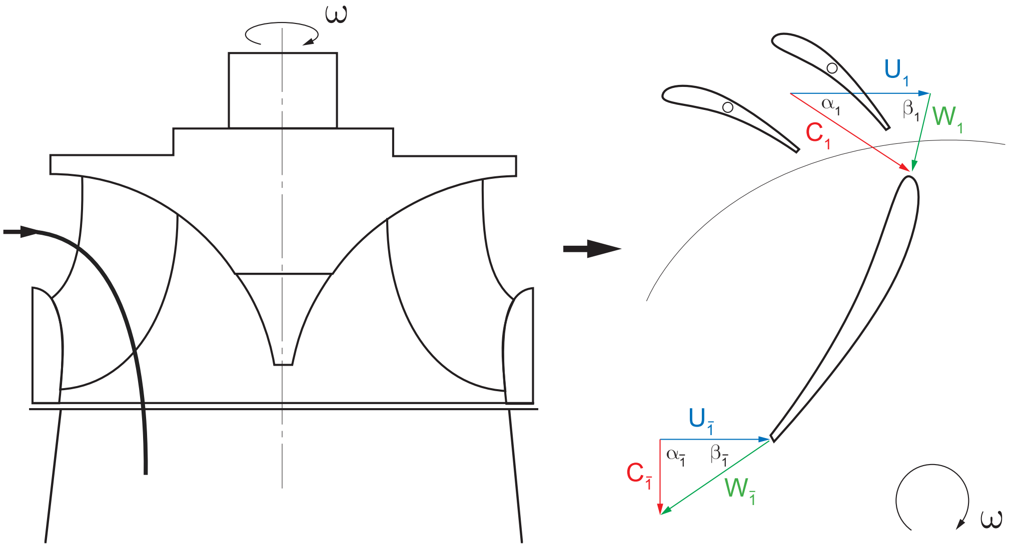

Figure 1.8: Velocity triangles at inlet and outlet of the runner blade.

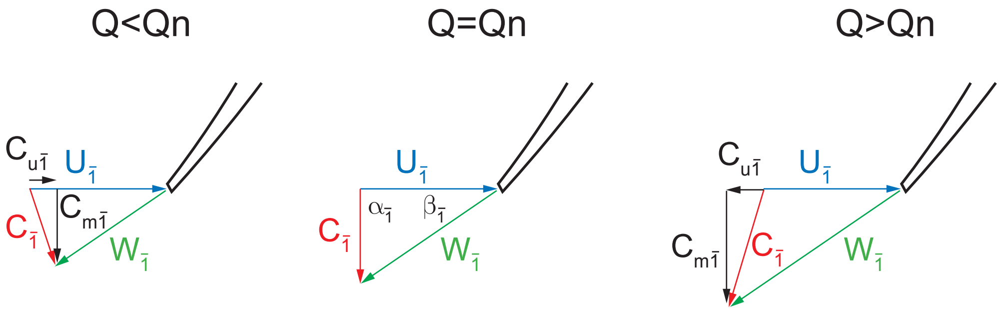

Figure 1.9: Influence of the discharge on the circumferential component of the absolute velocity.

And consequently it yields to:

$$\eta_h = \frac{E_t}{E} \tag{1.9}$$

The analysis of equation 1.7 shows that the energy transferred from the fluid to the runner depends on the change of circumferential velocity C_u through the runner, *i.e.* the deviation of the flow induced by the blades. It points out that it is interesting to minimize the outlet C_u in order to reduces losses by residual kinetic energy.

Turbine Performances

The evaluation of the performances of a turbine on its whole operating range requires, according to equation 1.2, measuring the discharge Q, the specific energy E, the rotational speed N and the mechanical torque T for different guide vanes openings. The representation of the efficiency as function of the operating conditions $[Q, E, N, T]$ requires to suppress one operating parameter to enable a 3 dimensional representation. For performances purposes, it is convenient to use dimensionless coefficients where the rotational speed N is eliminated, leading to the expression of 2 coefficients:

- the discharge coefficient: $\varphi = \frac{Q}{\pi \cdot \omega \cdot R_{\bar{1}e}^3}$;
- the energy coefficient: $\psi = \frac{2 \cdot E}{\omega^2 \cdot R_{\bar{1}e}^2}$

According to these definitions, the specific speed becomes:

$$\nu = \frac{\varphi^{1/2}}{\psi^{3/4}} \tag{1.10}$$

Then, for a given turbine, the hydraulic efficiency η_h can be evaluated on the complete operating range of the turbine and represented as a function of the discharge and energy coefficients: $\eta_h = \eta_h(\varphi, \psi)$, providing the efficiency hill chart of the machine. However, it is convenient to rate the 2 coefficients by their values at the Best Efficiency Point of the machine (BEP), *i.e.* $\eta_h = \eta_h(\varphi/\varphi_{BEP}, \psi/\psi_{BEP})$ as illustrated in figure 1.10.

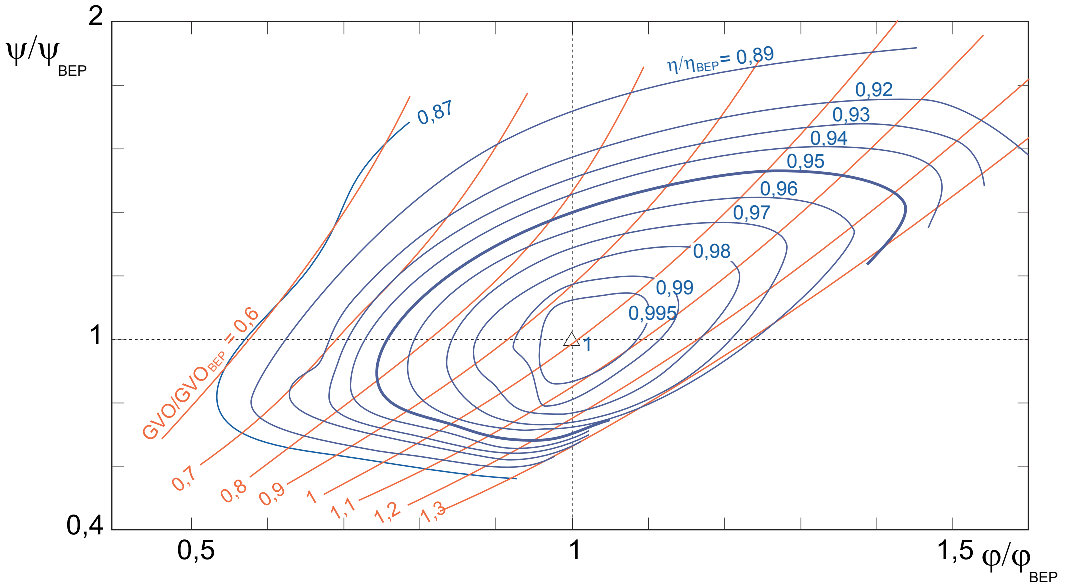

Figure 1.10: Efficiency hill diagram of a Francis turbine [56].

Cavitation

The velocity magnitudes in a turbine are very high and can easily reach 40 m/s. According to Bernoulli's law, low pressure arise in areas of high velocities. Then, depending on the local mean static pressure, the water can vaporize if the pressure drops below the vaporization pressure p_v. This phenomenon, referred as cavitation, corresponds to vaporization at constant temperature due to pressure decrease. Consequently, the cavitation is most likely to appear in the low pressure sides of a hydraulic machine. To qualify the pressure level inside the turbine, the Net Positive Suction Energy (NPSE) is introduced and refers to the downstream conditions of the turbine ($\bar{I}$) as follows:

$$NPSE = \frac{p_{\bar{I}}}{\rho} + g \cdot (Z_{\bar{I}} - Z_{ref}) + \frac{1}{2} \cdot C_{\bar{I}}^2 - \frac{p_v}{\rho} \tag{1.11}$$

Where p_v is the vaporization pressure and Z_{ref} is a reference elevation, for example the center line of the guide vanes.

The dimensionless cavitation number also known as the Thoma number is then introduced:

$$\sigma = \frac{NPSE}{E} \tag{1.12}$$

Low cavitation numbers indicate high risks of cavitation. The undesirable effects of cavitation are the risk of erosion, noise and mechanical vibrations but also flow distortions and efficiency drop [56].

At off design operating conditions, the outlet velocity triangles features a circumferential velocity component. At part load operation, the swirl flow induced in the draft tube may lead to flow instabilities resulting in the apparition of a helicoidal vortex precessing in the draft tube with a frequency of about 0.2 to 0.4 times the rotational frequency n [108], [79]. This vortex, called the "vortex rope", is visible if the tailrace water level is sufficiently low, *i.e.* for a low cavitation number. Depending on the cavitation number and the rotational speed, a pressure surge may occurs, resulting into unacceptable pressure and output power fluctuations amplitudes due to resonance between pressure excitation induced by the vortex rope and the natural frequency of the hydraulic circuit [109].

1.3.2 Operating Stability of Francis Turbine Units

Scale Model Testing

Scale model testing offers the opportunity to evaluate the performances of a hydraulic turbine in the phase of the design of a project. Homologous reduced-scale model of the hydraulic turbine comprising the spiral case, distributor, runner and draft tube are tested on a test rig [26]. The flow similitude is ensured by having the model geometry similar to that of the prototype. The similitude of the velocity triangles at the runner inlet and outlet is ensured by the identical φ and ψ conditions [72]. From the scale model tests, the following investigations can be undertaken: (i) efficiency hill chart measurement, (ii) cavitation inception/influence, (iii) pressure fluctuations measurement, (iv) axial thrust measurements, (v) test of mitigating counter-measures, and so on.

Typical observations of cavitation on a reduced-scale model are presented in figure 1.11 for the whole operating range of a Francis turbine. The following types of cavitation and related influences are identified:

- (1) and (2) inlet edge cavitation types that occurs at low and large energy coefficient ψ: may present a risk of erosion [89];

- (3) interblade cavitation vortices: can induce high cycle fatigue breaks [47], [100];
- (5) part load vortex rope: can be associated with pressure source excitation that may lead to resonance with the hydraulic system [40];
- (6) full load vortex rope: can lead to self-excited pressure fluctuations [85], [97];
- (7) outlet edge bubble cavitation: can lead to erosion of cavitation [73].

Regarding the operating stability of Francis turbine prototype, the pressure fluctuations measurements are of major concerns. The pressure fluctuations measured at different draft tube wall locations during the model tests can be presented in a waterfall diagram as a function of the rated frequency and of the rated discharge as illustrated in figure 1.12. This diagram highlights pressure amplitudes of 3 different types:

- (2) part load pressure fluctuations;
- (3) upper part load pressure fluctuations;
- (5) full load pressure fluctuations.

No pressure pulsations are measured close to the best efficiency operating point (4) in figure 1.11 where the velocity triangle at the outlet leads to almost purely axial flow.

Part Load Draft Tube Vortex Rope

Francis turbine power plants operating at part load may present instabilities in terms of pressure, discharge, rotational speed and torque. These phenomena are strongly linked to the swirl flow structure at the runner outlet inducing a vortex core precession in the draft tube [108]. This leads to hydrodynamic instabilities [79]. The decrease of the tailrace pressure level makes the vortex core visible as a gaseous vortex rope. The volume of the gaseous vortex rope is dependent on the cavitation number σ and affects the parameters characterizing the hydroacoustic behavior of the entire power plant. As a result, eigen frequencies of the hydraulic system decrease with the cavitation number. Interaction between excitation sources like vortex rope precession and system eigen frequencies may result in resonance effect and induce a so called draft tube surge and electrical power swing [58]. Consequences on pressure fluctuations and power oscillations were observed in the framework of many prototypes projects [126], [31], [52], [151], [58], [83] and [93].

Full Load Draft Tube Vortex Rope

Full load operation of Francis turbine creates a circumferential component of the outflow velocity inducing a swirl flow rotating in the opposite direction of the runner. For some operating points, the resulting axisymmetric vortex rope developing in the draft tube is known to start breathing [81]. These specific operating conditions may lead on prototype to severe self excited pressure fluctuations [85], [97], [93].

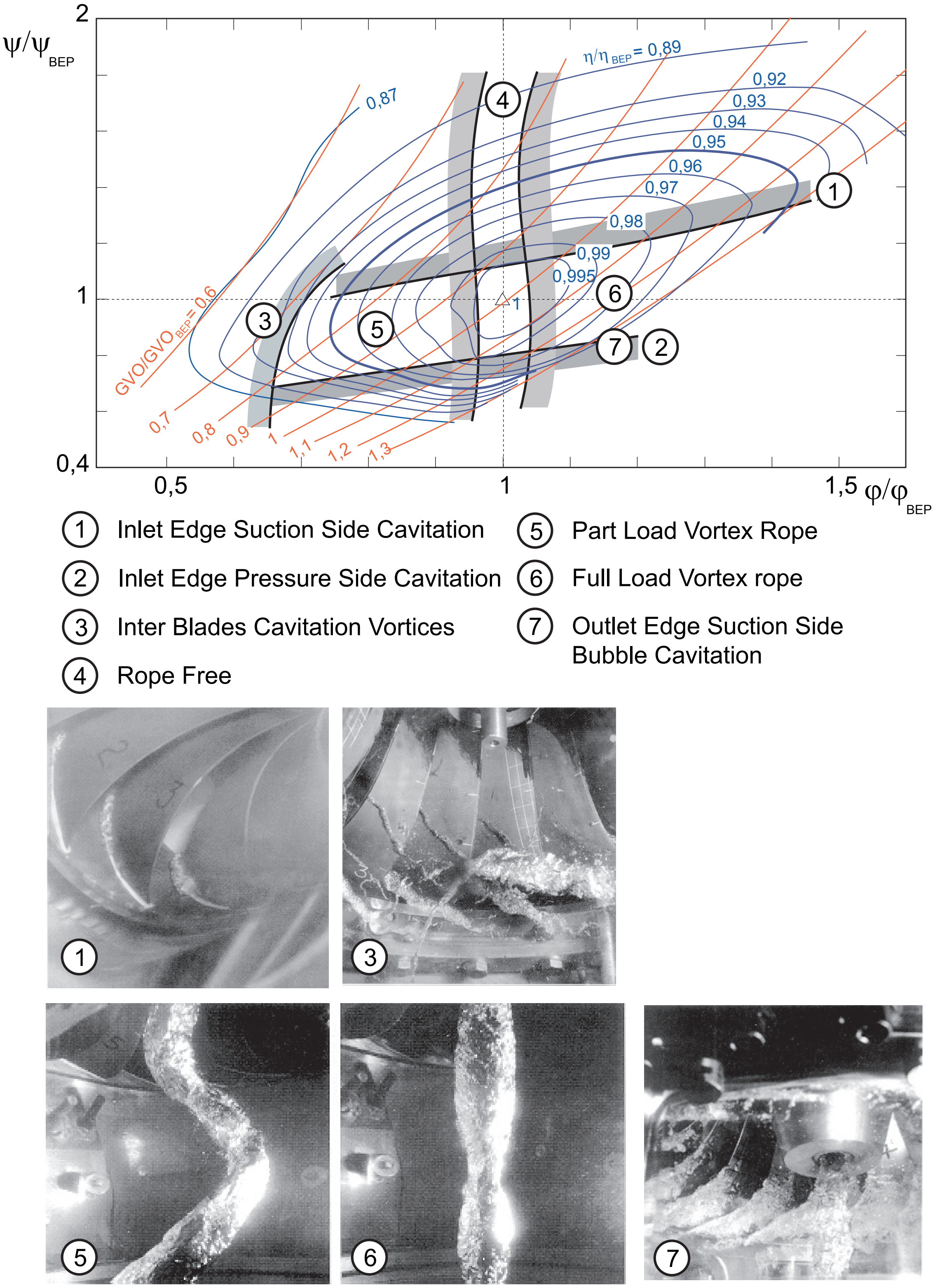

Figure 1.11: Typical cavitation regimes in the Francis turbine [56].

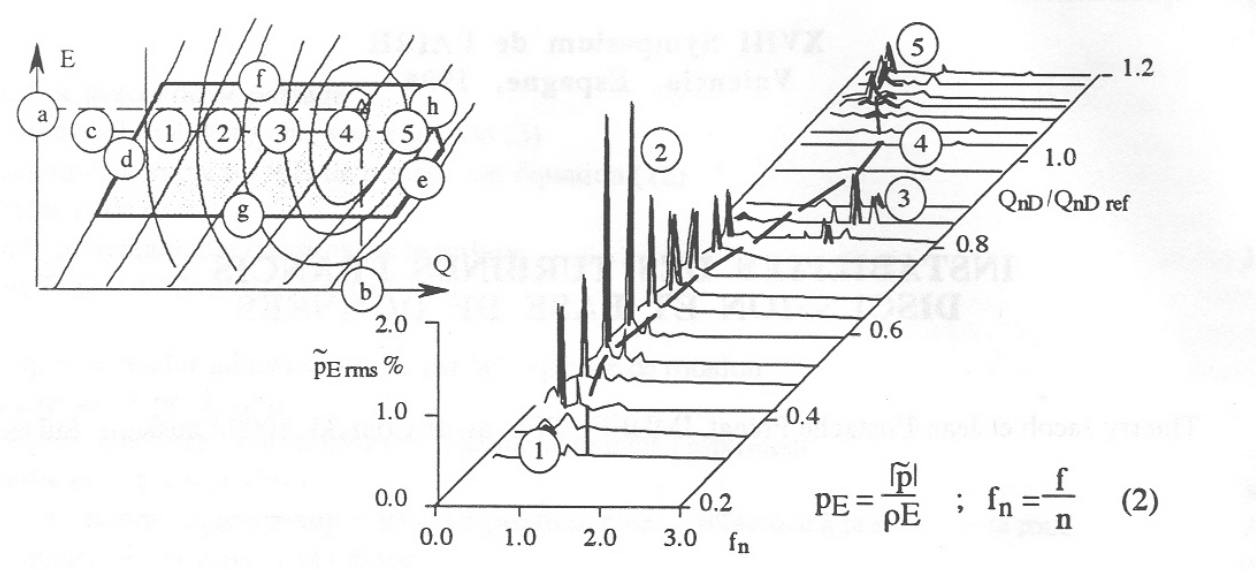

Figure 1.12: Waterfall diagram of pressure pulsations at the turbine draft tube cone at constant ψ [81].

Rotor-Stator Interactions

Interactions between rotating parts and stationary parts of a Francis turbine result in pressure fluctuations that propagate in the entire machine [37]. The combination of these pressure waves may result in resonance effects and induces unacceptable pressure fluctuations jeopardizing the safety of the whole power plant [70], [113], [57] and [42].

Mitigation Measures

The mitigation of resonance problems requires acting either on the excitation source or on the system parameters in order to detune the excitation from the systems eigen frequencies. The main solutions to achieve the mitigation are:

- **draft tube fins**, used to induce swirl flow distortions and then modify pressure source frequencies or amplitudes [64], [15];
- **cylinder in the draft tube** or **extensions of the runner cone**, also used to induce swirl flow distortions and then modify the pressure source frequencies or amplitudes [64];
- **air injection**, to modify the hydroacoustic parameters of the turbine in order to detune the systems eigen frequencies from the excitation sources[64], [119], [118];
- **mechanical dampers** act like Frahm dampers in order to absorb energy of resonance [4], [117];
- **active control of the pressure fluctuations**, using a complex control strategy based on a rotating valve or a mechanical piston in order to inject pressure fluctuations in the draft tube with the same amplitude as the source but in phase opposition [21], [19];

- **water jet control** located in the center of the runner cone to modify the swirl momentum ratio and eliminate pressure source [140].

However, the success of one of the above mitigating solutions is never ensured and often has detrimental effects on the turbine efficiency. In addition, some of them are technically complex solutions and difficult to set up.

Regarding the full load surge, injection of air appeared to be successful in some cases [97], [8]. Use of fins is also sometimes beneficial.

The resonances resulting from rotor-stator problems can usually be solved by modifying the rotor-stator arrangement, *i.e.* the number of guide vanes or runner blades. It is also possible to mitigate pressure excitations by changing the rotor-stator interface geometry by increasing the guide vane-runner blade gap, or using blades with skew angles. If resonance occurs with specific mechanical parts of the turbine, their structural characteristics can be modified in order to change their eigen frequencies, and again detune the resonance.

1.3.3 Transient Behavior of Francis Turbine Units

General

In the deregulated electricity market, hydropower plants are more and more solicited in order to adapt the production to the demand in energy. Consequently, the power plants are victim of their availability and are subject to an increasing number of startup and shutdown sequences. During operation, short-circuits resulting from the failure of power lines may trigger an emergency shutdown of the power plant. In addition, hydropower plants are constantly modernized to increase their flexibility by taking advantage of new control strategies or installing new technologies such as variable speed solutions. Such events are parts of the today's normal operation of hydropower plants whose solicitations changes according to technologies and energy market issues.

Transients: the Safety Issues

Transient phenomena result from a change in the operating conditions of a system. In the case of hydroelectric power plants, transient phenomena can be caused by: (i) unit shutdown or startup, (ii) change in operating set point, (iii) load rejection or acceptance, (iv) emergency shutdown and (v) electrical faults such as earth fault, short-circuit, out of phase synchronization, and so on.

All the above listed events induce changes of discharge, pressure, rotational speed, voltage, current and so on in the entire power plant. The impacts of these changes on the safety of the power plants should be assessed at the early stage of any hydroelectric project in order to be able to select the critical dimensions of the system with appropriate margins. Therefore transient analysis should be performed accounting for the entire system; *i.e.* the whole adduction system, the hydraulic machines, the mechanical inertias, the electrical machines, the controllers, the emergency systems, etc, as illustrated in figure 1.13. The transient analysis aims to determine: the pipe wall thickness, the surge tank diameters, the coupling shaft diameters, appropriate emergency procedure, control parameters, conductors diameters, etc.

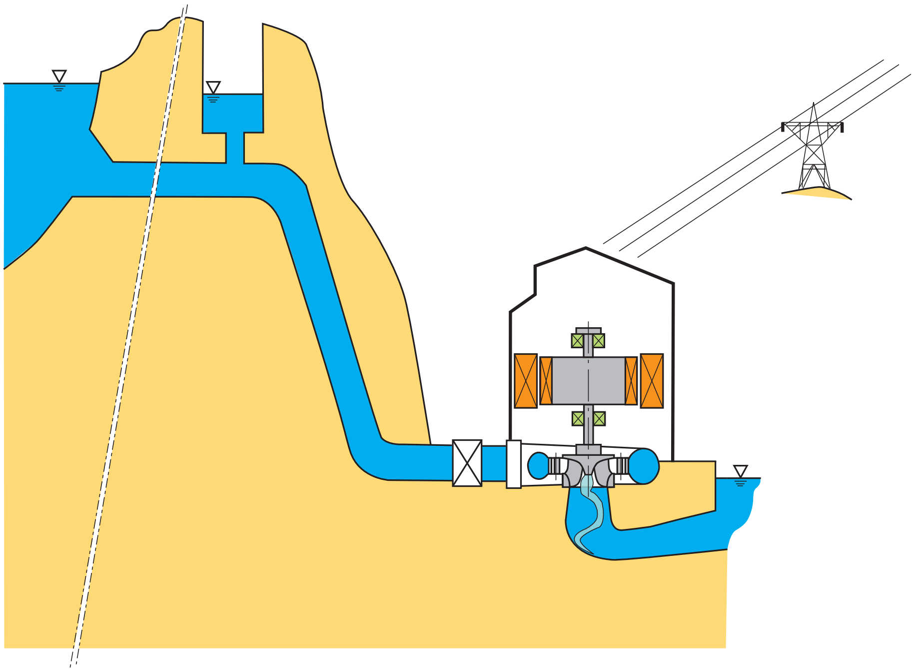

Figure 1.13: Layout of Francis power plant.

Improving the Stability of Power Network

Due to their flexibility of exploitation, hydroelectric power plants have an important role to play in stabilizing electrical power networks. This is the case not only in Europe, because of the decentralization of the production and the use of renewable energies whose availability cannot be influenced, but also in emerging countries where the networks are poorly interconnected and distances between electricity producers and consumers are large.

Thus, the controllers and governors parameters should be optimized according to operating conditions that the power plants will face. Typically, 3 production modes are distinguished:

- interconnected production: the power plant is connected to a very large power grid;
- islanded production: the power plant is connected to a weak power grid typically smaller than 10 GW;
- isolated production: the power plant is producing energy only for the subsidiaries and local loads.

The regulation of a hydropower plant is achieved using at least 2 and sometimes 3 regulators:

- the turbine speed governor: has usually both speed and power set points and acts on the guide vane opening of the Francis turbine;
- the generator voltage regulator has a line voltage set point and acts on the excitation voltage of the rotor;

- the Power System Stabilizer (PSS) acts also on the excitation voltage but has the rotational speed and power as set points.

In addition, for variable speed solutions, a supervisor governor is necessary to select appropriate rotational speed set points and enabling rotational speed changes. The determination of the parameters sets of these regulators represents a challenging task that should account for the system layout and exploitation conditions.

In the control strategy of power networks, 3 different levels are distinguished: the primary, secondary and tertiary levels. The related regulation times and devices are summarized in table 1.2.

Table 1.2: Regulation levels [48].

Level	Governors	Regulation time
Primary	- turbine speed governor - generator voltage regulator	10 - 20 sec.
Secondary	- frequency/power regulation - energy transfer regulation	20 - 120 sec.
Tertiary	- power production dispatching	1 - 15 min.

1.4 The Role of Numerical Simulation in Improving Hydropower Operation

As illustrated in the previous sections, the design, operation and regulation of hydroelectric power plant require the ability to predict the dynamic behavior of the power plant taking into account various aspects of the exploitation of the installation. Therefore, mathematical models able to represent the dynamic behavior of hydropower plants with high fidelity are necessary. The complexity of the model used for the simulation should be adapted according to the issues.

Since most of the aforementioned issues regard optimization or parametrization, small computation times are required. In addition, many of the investigations require a **multi-physics** model of the power plant, comprising: (i) the entire hydraulic circuit, (ii) the mechanical inertias, (iii) the electrical installation, and (iv) the regulation systems.

For these applications, one-dimensional models offer the best compromise in terms of computational effort and accuracy. As propagation phenomena globally dominate in the dynamic behavior of the entire hydraulic circuit, hydroacoustic models are the most appropriate.

1.5 Description of the Present Work

1.5.1 Problematic

Hydropower, and more precisely Francis turbines are paramount in the context of electricity production. During the exploitation of Francis turbine power plants, the installation is subject to transients phenomena and to a risk of resonance or instabilities. The prediction of these phenomena is crucial for ensuring the safety of the power plant and of the population. Numerical simulation of the dynamic behavior of the whole installation enables these predictions. However, classical approaches features 2 main drawbacks:

- the focus of the modelling is usually put either on the hydraulic or on the electrical side, using too much simplified models for the other side;
- most of the stability/resonance analysis are based on linearized models, however accurate prediction of amplitudes requires taking into account system non-linearities.

The strong interaction between hydraulic and electrical parts of an installation is evidenced in the table of influence of figure 1.14. In this figure, the complexity of the modelling of any part of the installation required for a given issue is indicated. It can be seen that, if for classical design purposes, separated investigations are sufficient, coupled investigations are necessary for a complete quantification of the phenomena related to control optimization, resonance and instability risk assessment.

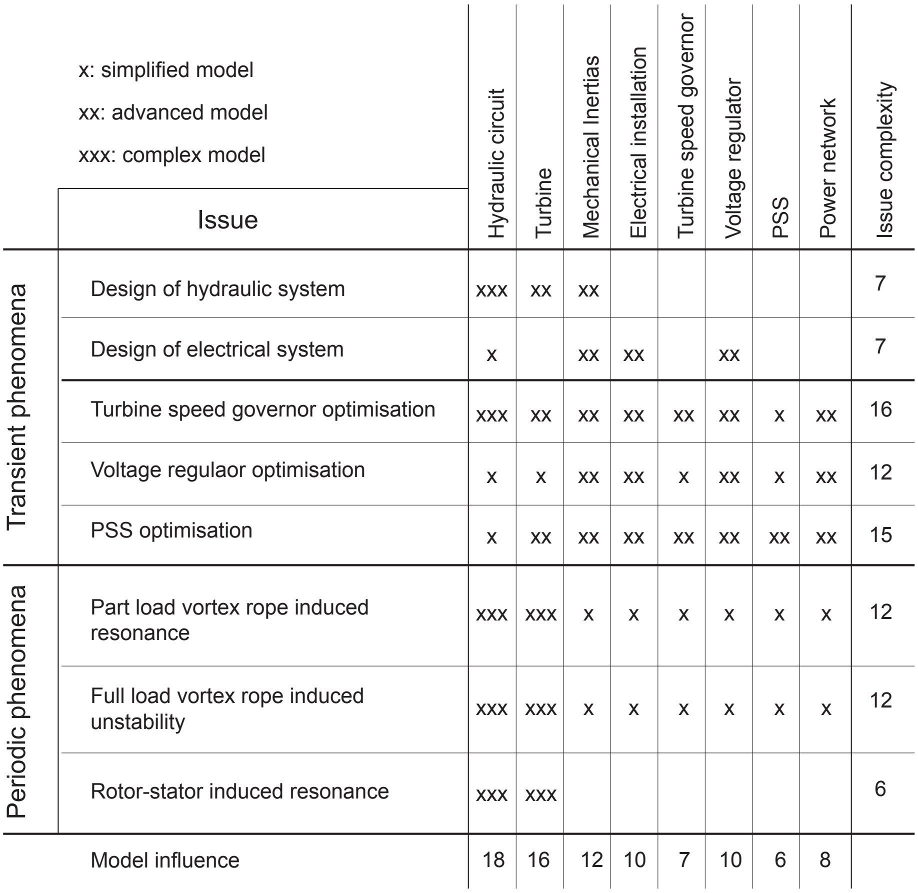

x: simplified model
xx: advanced model
xxx: complex model

	Issue	Hydraulic circuit	Turbine	Mechanical Inertias	Electrical installation	Turbine speed governor	Voltage regulator	PSS	Power network	Issue complexity
Transient phenomena	Design of hydraulic system	xxx	xx	xx						7
	Design of electrical system	x		xx	xx		xx			7
	Turbine speed governor optimisation	xxx	xx	xx	xx	xx	xx	x	xx	16
	Voltage regulaor optimisation	x	x	xx	xx	x	xx	x	xx	12
	PSS optimisation	x	xx	xx	xx	xx	xx	xx	xx	15
Periodic phenomena	Part load vortex rope induced resonance	xxx	xxx	x	x	x	x	x	x	12
	Full load vortex rope induced unstability	xxx	xxx	x	x	x	x	x	x	12
	Rotor-stator induced resonance	xxx	xxx							6
	Model influence	18	16	12	10	7	10	6	8	

Figure 1.14: Table of influence of the installation components versus issues.

Classical modelling approaches are sufficient when safety margins is large and when exploitation configurations are simple. However, economical issues tend to increase specific power and to lead to completely different exploitation strategies, thus requiring appropriate simulation tools. These tools should enable multi-physics approaches and encompass the system non-linearities to improve the accuracy of the prediction of the solicitations undergone by the facility.

1.5.2 Methodology

The proposed approach is based on the development of an appropriate tool for the simulation of the dynamic behavior of an entire hydropower plant and on the improvement of models for resonance and instability phenomena assessment. Thus, the present work can be decomposed as follows:

- (1) setup of the models of hydraulic components for the simulation of their dynamic behavior;
- (2) validation of the proposed models;
- (3) implementation of the models in an existing software application developed for the simulation of the dynamic behavior of electrical installations;
- (4) investigation of the hydroelectric transients;
- (5) development and validation of new models of Francis turbine for the simulation of vortex rope induced resonance or instabilities and for rotor-stator resonance;
- (6) development/proposition of system parameters and source excitations identification methods.

1.5.3 Structure of the Document

This document splits in two main parts. The first part is devoted to the establishment of hydroacoustic models of hydraulic components, their validation and the simulation of hydroelectric transients. The second part focuses on the modelling of possible resonance and instabilities in hydroelectric power plants.

Part I: Hydroacoustic Modelling of Hydraulic Circuits

The fundamental equations used for the hydroacoustic modelling are introduced in chapter 2. In chapter 3, the different solution methods applicable to the set of equation derived in chapter 2 are presented and compared. The use of the solution methods is illustrated in chapter 4 by their application for the characterization of the hydroacoustic behavior of a hydraulic pipe. The modelling approach selected is extended to other standard hydraulic components in chapter 5. Quasi-static models of hydraulic turbines are also presented. An analytical analysis of the simple hydraulic systems based on equivalent models developed previously are presented in chapter 6. Such methods provide some stability criteria of the hydraulic installation for classical transients problems.

In chapter 7, after the validation of the hydraulic components models, hydroelectric transients are investigated. Consequences of classical electrical faults on hydraulic installations are studied and the stability of turbine speed governor of a simplified hydroelectric power plant is assessed. The stability of turbine speed governor is then investigated for a realistic case of hydroelectric power plant operating in an islanded power network.

Part II: Hydroacoustic Modelling of Pressure Fluctuations in Francis Turbine

Chapter 8 is a literature review of the possible problems of pressure pulsations in Francis turbine and their possible interactions with the circuits. Existing models of vortex rope and and rotor-stator interactions are presented. Chapter 9 focuses on a peculiar problem often encountered on scale model but never on prototype: the upper part load pressure pulsations. The problem is investigated experimentally and numerically for a given operating point. Then, the results of flow visualizations and the influence of the operating parameters are presented.

The modelling of full load pressure pulsations induced by the vortex rope is illustrated in chapter 10 by an investigation of an over-load surge event occurring on a prototype. The modelling of the phenomenon is presented. The hydroacoustic rotor-stator interactions are simulated for the case of a scale model of pump-turbine in chapter 11. A new modelling approach is proposed. The problematic of the transposition from model tests to prototype is presented in chapter 12 and proposition of a methodology for the resonance risk assessment is made.

Part I

Hydroacoustic Modelling of Hydraulic Circuits

Chapter 2

Fundamental Equations

2.1 General

A mathematical model based on mass and momentum conservation can properly describe the dynamic behavior of a pipe filled with water. Hydraulic installations feature longitudinal dimensions greater than transversal dimensions, thus justifying a one-dimensional approach based on the following assumption:

- the flow is normal to the cross-sections A;
- the pressure p, the flow velocity C and the density ρ are uniform in a cross-section A.

2.2 Momentum Equation

The momentum equation is applied to the control volume, dashed-line in figure 2.1, of length dx. The momentum equation expresses the balance of the forces acting on this fluid volume, the momentum flux through the surfaces and the rate of change of the momentum in the volume itself. The integral form of the momentum equation applied to a volume of fluid is given by:

$$\int_V \frac{\partial}{\partial t}\left(\rho \cdot \overrightarrow{C} \cdot \overrightarrow{n}\right) dV + \int_{\partial V} \rho \overrightarrow{C} \cdot \left(\overrightarrow{C} - \overrightarrow{u}\right) \cdot \overrightarrow{n} \, dA = \Sigma \overrightarrow{F} \tag{2.1}$$

The momentum equation along the x-axis neglecting axial displacement of the pipe u, and considering gravity, pressure and friction forces is expressed as:

$$\rho A dx \frac{DC}{Dt} = pA - [pA + \frac{\partial (pA)}{\partial x} dx] + (p + \frac{\partial p}{\partial x}\frac{dx}{2})\frac{\partial A}{\partial x} dx - \tau_o \pi D dx - \rho g A dx \sin(\alpha) \tag{2.2}$$

With:
A : pipe cross-section $[m^2]$;
ρ : density $[Kg/m^3]$;
C : flow velocity $[m/s]$;
τ : shear stress $[N/m^2]$;

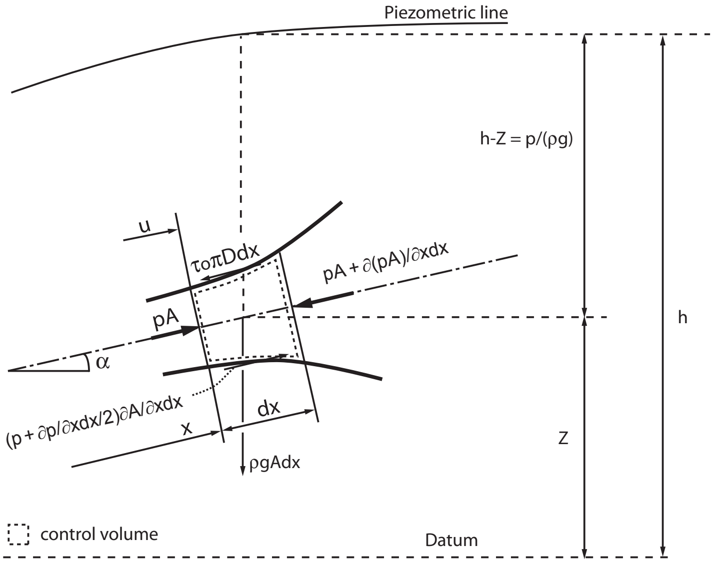

Figure 2.1: Momentum equation applied to the control volume of length dx.

D : pipe diameter $[m]$.

Rearranging equation 2.2 and neglecting the second order terms dx^2, yields to :

$$A\frac{\partial p}{\partial x} + \tau_o \pi D + \rho g A \sin(\alpha) + \rho A \frac{DC}{Dt} = 0 \tag{2.3}$$

According to Darcy-Weisbach [138], the friction coefficient can be written as:

$$\tau_o = \frac{\rho \lambda C^2}{8} \tag{2.4}$$

The particular derivative is given by:

$$\frac{DC}{Dt} = \frac{\partial C}{\partial t} + C\frac{\partial C}{\partial x} \tag{2.5}$$

Combining equations 2.3, 2.4 and 2.5, gives:

$$\frac{1}{\rho}\frac{\partial p}{\partial x} + \frac{\partial C}{\partial t} + C\frac{\partial C}{\partial x} + g\sin(\alpha) + \frac{\lambda C|C|}{2D} = 0 \tag{2.6}$$

The absolute value of the velocity ensures always dissipative term.

2.3 Continuity Equation

The mass balance in the control volume of length dx, in figure 2.2, can be expressed as follow:

$$\frac{dM}{dt} = \frac{\partial}{\partial t}\int_{V} \rho dV + \int_{\partial V} \rho \cdot \left(\overrightarrow{C} - \overrightarrow{u}\right) \cdot \overrightarrow{n} \cdot dA = 0 \tag{2.7}$$

Developing all the terms and neglecting the axial displacement of the pipe u, yields to:

$$\frac{\partial(\rho A dx)}{\partial t} = \rho AC - \left[\rho AC + \frac{\partial(\rho AC)}{\partial x}dx\right] \tag{2.8}$$

Then:

$$\frac{\partial(\rho A)}{\partial t} = -\frac{\partial(\rho AC)}{\partial x} \tag{2.9}$$

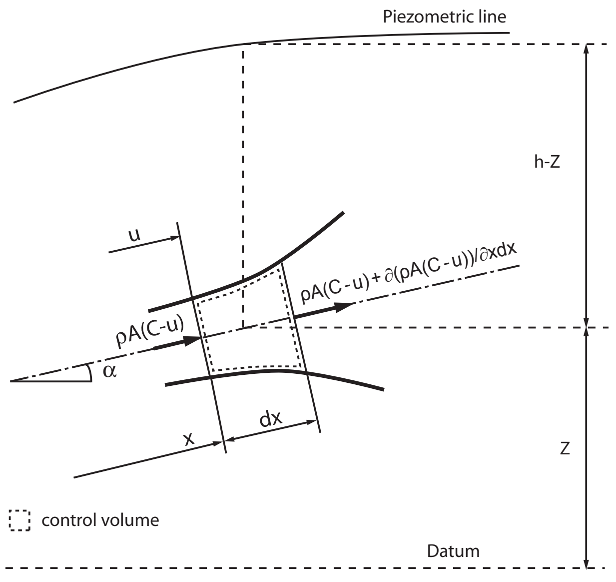

Figure 2.2: Continuity equation applied to pipe control volume of length dx.

Expressing the partial derivative gives:

$$\frac{1}{\rho}\frac{\partial \rho}{\partial x} + \frac{1}{A}\frac{\partial A}{\partial x} + \frac{1}{C}\frac{\partial C}{\partial x} + \frac{1}{\rho C}\frac{\partial \rho}{\partial t} + \frac{1}{AC}\frac{\partial A}{\partial t} = 0 \tag{2.10}$$

Introducing:

$$\frac{D\rho}{Dt} = \frac{\partial \rho}{\partial t} + C\frac{\partial \rho}{\partial x} \quad and \quad \frac{DA}{Dt} = \frac{\partial A}{\partial t} + C\frac{\partial A}{\partial x} \tag{2.11}$$

Equation 2.10 becomes:

$$\frac{1}{\rho}\frac{D\rho}{Dt} + \frac{1}{A}\frac{DA}{Dt} + \frac{\partial C}{\partial x} = 0 \tag{2.12}$$

Assuming barotropic behavior of the fluid, *i.e.* $\rho = \rho(p)$, and introducing the fluid bulk modulus E_{water} yields to:

$$dp = E_{water}\frac{d\rho}{\rho} \tag{2.13}$$

Then:

$$\frac{1}{\rho}\frac{d\rho}{dt} = \frac{1}{E_{water}}\frac{dp}{dt} \tag{2.14}$$

The traction strain of the pipe wall can be expressed as follows:

$$\sigma = E_c\frac{dR}{R} \tag{2.15}$$

With the change of pipe cross section:

$$\frac{dA}{dt} = 2\pi R\frac{dR}{dt} = \frac{2\pi R^2}{E_c}\frac{d\sigma}{dt} \tag{2.16}$$

The strain in the pipe wall is deduced from figure 2.3:

$$\sigma = \frac{pD}{2e} \quad \text{gives} \quad \frac{d\sigma}{dt} = \frac{D}{2e}\frac{dp}{dt} \tag{2.17}$$

With:

e = pipe wall thickness [m]

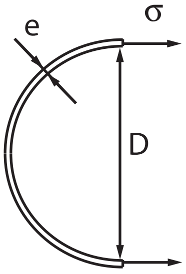

Figure 2.3: Traction stress in pipe wall due to pressure.

Finally :

$$\frac{1}{A}\frac{dA}{dt} = \frac{D}{eE_c}\frac{dp}{dt} \tag{2.18}$$

Combining equations 2.13 and 2.18 with equation 2.12 yields to :

$$\rho a^2\frac{\partial C}{\partial x} + \frac{dp}{dt} = 0 \tag{2.19}$$

Where the wave speed is given by :

$$a^2 = \frac{1}{\rho\left(\frac{1}{E_{water}} + \frac{D}{eE_c}\right)} \tag{2.20}$$

Knowing $p = p(x,t)$ gives:

$$\rho a^2\frac{\partial C}{\partial x} + \frac{\partial p}{\partial t} + C\frac{\partial p}{\partial x} = 0 \tag{2.21}$$

2.4 Simplified Equations

The mathematical model of the dynamic behavior of an elementary pipe of length dx consists of 2 equations: the conservation of both mass and momentum.

$$\begin{cases} \frac{1}{\rho}\frac{\partial p}{\partial x} + \frac{\partial C}{\partial t} + C\frac{\partial C}{\partial x} + g\sin(\alpha) + \frac{\lambda C\left|C\right|}{2D} = 0 \\ \rho a^2 \frac{\partial C}{\partial x} + \frac{\partial p}{\partial t} + C\frac{\partial p}{\partial x} = 0 \end{cases} \tag{2.22}$$

In hydraulics, it is useful to use the discharge Q and the piezometric head h as state variables instead of the flow velocity C and pressure p. The discharge and the piezometric head are defined as:

$$h = Z + \frac{p}{\rho g} \tag{2.23}$$

$$Q = C \cdot A \tag{2.24}$$

With Z the elevation $[m]$. The piezometric head is the pressure given in meters of water column, mWC, above a given datum. Injecting equations 2.23 and 2.24 in equation 2.22, assuming no vertical displacements of the pipe $\partial z/\partial t \cong 0$ and noticing that $\partial z/\partial x = sin(\alpha)$, gives:

$$\begin{cases} \frac{\partial h}{\partial x} + \frac{1}{gA}\left[\frac{\partial Q}{\partial t} + C\frac{\partial Q}{\partial x}\right] + \frac{\lambda Q\left|Q\right|}{2gDA^2} = 0 \\ \left[\frac{\partial h}{\partial t} + C\frac{\partial h}{\partial x}\right] + \frac{a^2}{gA}\frac{\partial Q}{\partial x} = 0 \end{cases} \tag{2.25}$$

Hydroacoustic phenomena are characterized by a high wave speed $a(a = 1430\ m/s$ at $20^{\circ}C)$ and low flow velocities $(C = 10\ m/s)$, thus the convective terms $C\partial/\partial x$ related to the transport phenomena can be neglected with respect to the propagative terms $\partial/\partial t$. This simplification leads to the following set of of partial derivative equations:

$$\begin{cases} \frac{\partial h}{\partial x} + \frac{1}{gA}\frac{\partial Q}{\partial t} + \frac{\lambda Q\left|Q\right|}{2gDA^2} = 0 \\ \frac{\partial h}{\partial t} + \frac{a^2}{gA}\frac{\partial Q}{\partial x} = 0 \end{cases} \tag{2.26}$$

2.5 Resolution Methods

The system of equations 2.26 can be rewritten in matrix form:

$$\begin{bmatrix} \frac{\partial Q}{\partial t} \\ \frac{\partial h}{\partial t} \end{bmatrix} + \underbrace{\begin{bmatrix} 0 & gA \\ \frac{a^2}{gA} & 0 \end{bmatrix}}_{[A]} \cdot \begin{bmatrix} \frac{\partial Q}{\partial x} \\ \frac{\partial h}{\partial x} \end{bmatrix} = \begin{bmatrix} -\frac{\lambda Q|Q|}{2DA} \\ 0 \end{bmatrix} \tag{2.27}$$

The eigen values of this set of equations are the roots of the following characteristic equation:

$$\det\left([A] - \delta[I]\right) = 0 \tag{2.28}$$

The equation system 2.27 has the 2 following distinct roots:

$$\delta = \pm a \tag{2.29}$$

Since the eigen values of the equation system 2.27 are real, it corresponds to a system of hyperbolic partial differential equations. This type of equation is related to propagative problems that can be solved with various methods:

- arithmetic method of Allievi (1925) [2];
- graphical method of Schnyder-Bergeron (1950) [14];
- method of characteristics (MOC) [138], [141], [36];
- transfer matrix method [138], [55];
- impedance method [138].

All these methods enable analyzing the dynamic behavior of hydraulic system.

Chapter 3

Resolution Methods of the Set of Hyperbolic Partial Differential Equations

3.1 Electrical Analogy

The solution of a system of hyperbolic partial differential equations such as the set of equations 2.26, was at first inspired by the methods developed in the field of telecommunication [116], [87]. The resolution of the propagation of electrical waves in conductors is based on an equivalent scheme representation providing a high level of abstraction and having a rigorous formalism. The study of electrical wave propagation in conductors leads to the establishment of the set of equations expressed as follows, referred to as the telegraphist's equation:

$$\begin{cases} \dfrac{\partial U}{\partial x} + L'_e \dfrac{\partial i}{\partial t} + R'_e i \; = 0 \\ \dfrac{\partial U}{\partial t} + \dfrac{1}{C'_e} \dfrac{\partial i}{\partial x} = 0 \end{cases} \tag{3.1}$$

Where:
i: electrical current $[A]$
U : electrical potential $[V]$
R'_e : lineic electrical resistance $[\Omega/m]$
L'_e : lineic electrical inductance $[H/m]$
C'_e : lineic electrical capacitance $[F/m]$

The analogy between equation set 2.26 modelling the propagation of pressure waves in hydraulic systems and the equation set 3.1 modelling the propagation of voltage waves in conductors allows identifying a lineic hydraulic resistance R', a lineic hydraulic inductance L' and a lineic hydraulic inductance C'. The equation set 2.26 can be rewritten as:

$$\begin{cases} \dfrac{\partial h}{\partial x} + L' \dfrac{\partial Q}{\partial t} + R'(Q)Q = 0 \\ \dfrac{\partial h}{\partial t} + \dfrac{1}{C'} \dfrac{\partial Q}{\partial x} = 0 \end{cases} \tag{3.2}$$

Where the lineic hydroacoustic parameters are defined as:

- lineic hydroacoustic capacitance $C' = \frac{g \cdot A}{a^2}[m]$;
- lineic hydroacoustic inductance $L' = \frac{1}{g \cdot A}[s^2/m^3]$;
- lineic hydroacoustic resistance $R' = \frac{\lambda \cdot |\bar{Q}|}{2 \cdot g \cdot D \cdot A^2}[s/m^3]$.

Hydraulic and electrical systems are both characterized by an extensive state variable, *i.e.* discharge Q and current i, and by a potential state variable, *i.e.* piezometric head h and voltage U. The electrical analogy permits to apply the mathematical formalism developed initially for electrical purposes to hydroacoustic problems and to use powerful concepts such as equivalent scheme, impedance or transfer matrix. Two modelling approaches of hydraulic system are distinguished:

- to consider the system as a system with distributed parameters, or as a continuous system;
- to consider the system as a system with lumped parameters, or as a discrete system.

Analytical solutions can be derived for continuous systems, but require the linearization of the system and thus restricts the study to small perturbations. Analytical solutions are not possible for discrete systems of large dimension and thus numerical methods should be used, but enables to take into account system non-linearities. Nevertheless, this modelling approach introduces approximation errors that have to be quantified.

3.2 Resolution of the Set of Hyperbolic Partial Differential Equations for Continuous System

Pressure wave propagation in hydraulic systems can be modelled using continuity and momentum equations. The resulting set of hyperbolic partial differential equations can be written as:

$$\begin{cases} \dfrac{\partial h}{\partial x} + L' \cdot \dfrac{\partial Q}{\partial t} + R' \cdot Q = 0 \\ \dfrac{\partial h}{\partial t} + \dfrac{1}{C'} \cdot \dfrac{\partial Q}{\partial x} = 0 \end{cases} \tag{3.3}$$

The set of equations 3.3 can be rewritten using the separation of variables method assuming a sinusoidal variation of the piezometric head $h(x,t)$ and of the discharge $Q(x,t)$ defined as complex function:

$$\begin{cases} \underline{h}(x,t) = \underline{h}(x) \cdot e^{\underline{s}t} \\ \underline{Q}(x,t) = \underline{Q}(x) \cdot e^{\underline{s}t} \end{cases} \tag{3.4}$$

Where the constant $\underline{s}$ is the complex frequency also referred to as Laplace variable. The complex frequency is composed of an imaginary part and of a real part:

$$\underline{s} = \sigma + j \cdot \omega \tag{3.5}$$

For simplicity, the complex frequency $\underline{s}$ is written as s in the next section of this document. The set of equations 3.3 is rewritten as follows:

$$\begin{cases} \dfrac{\partial^2 \underline{h}}{\partial x^2} = \underline{\gamma}^2 \cdot \underline{h}(x) \\ \dfrac{\partial^2 \underline{Q}}{\partial x^2} = \underline{\gamma}^2 \cdot \underline{Q}(x) \end{cases} \tag{3.6}$$

Where $\underline{\gamma}$ is the complex wave number:

$$\underline{\gamma}^2 = C' \cdot s \cdot (L' \cdot s + R') \tag{3.7}$$

3.2.1 Resolution of the Wave Equation: Exact Solution

Equation 3.3 admits as a particular solution for the piezometric head:

$$\underline{h}(x,t) = e^{st} \cdot (C_1 \cdot e^{-\underline{\gamma} \cdot x} + C_2 \cdot e^{\underline{\gamma} \cdot x}) \tag{3.8}$$

The constants C_1 and C_2 are to be determined from the boundary conditions. Thus equation 3.6 for the piezometric head admits as solution both a progressive wave $\underline{h}_p(x)$ and a retrograde wave $\underline{h}_r(x)$, defined from the boundary condition at $x = 0$:

$$\underline{h}_p(x) = \underline{h}_p(0) \cdot e^{-\underline{\gamma} \cdot x} \tag{3.9}$$

$$\underline{h}_r(x) = \underline{h}_r(0) \cdot e^{\underline{\gamma} \cdot x} \tag{3.10}$$

Rewriting the equations set 3.3 assuming a sinusoidal evolution of the piezometric head and of the discharge yields to:

$$-\frac{\partial \underline{h}}{\partial x} = (L' \cdot s + R') \cdot \underline{Q} \tag{3.11}$$

$$-\frac{\partial \underline{Q}}{\partial x} = C' \cdot s \cdot \underline{h} \tag{3.12}$$

Equations 3.11 and 3.12 provide the solution of the discharge equation of equation 3.3 admitting as solution a progressive discharge wave $\underline{Q}_p(x)$ and a retrograde discharge wave $\underline{Q}_r(x)$ expressed as:

$$\underline{Q}_p(x) = -\frac{1}{(L' \cdot s + R')} \cdot \frac{\partial \underline{h}_p(x)}{\partial x} = -\frac{(-\underline{\gamma})}{(L' \cdot s + R')} \cdot \underline{h}_p(x) = \frac{\underline{h}_p(x)}{\underline{Z}_c} \tag{3.13}$$

$$\underline{Q}_r(x) = -\frac{1}{(L' \cdot s + R')} \cdot \frac{\partial \underline{h}_r(x)}{\partial x} = -\frac{\underline{\gamma}}{(L' \cdot s + R')} \cdot \underline{h}_r(x) = -\frac{\underline{h}_r(x)}{\underline{Z}_c} \tag{3.14}$$

The ratio between the piezometric head and the discharge variations is the characteristic impedance of the pipe $\underline{Z}_c$ defined as:

$$\underline{Z}_c = \sqrt{\frac{(L' \cdot s + R')}{C' \cdot s}} \tag{3.15}$$

The solution to the equation system 3.6 is the sum of the progressive and the retrograde waves yielding to:

$$\underline{h}(x) = \underline{h}_p(x) + \underline{h}_r(x) \tag{3.16}$$

$$\underline{Q}(x) = \frac{\underline{h}_p(x) + \underline{h}_r(x)}{\underline{Z}_c} \tag{3.17}$$

Combining equations 3.9 and 3.10 with the equations 3.16 and 3.17 established for $x = 0$, gives:

$$\underline{h}_p(x) = \frac{\underline{h}(0) + \underline{Z}_c \cdot \underline{Q}(0)}{2} \cdot e^{-\underline{\gamma} \cdot x} \tag{3.18}$$

$$\underline{h}_r(x) = \frac{\underline{h}(0) - \underline{Z}_c \cdot \underline{Q}(0)}{2} \cdot e^{-\underline{\gamma} \cdot x} \tag{3.19}$$

The constants $\underline{C}_1$ and $\underline{C}_2$ are derived from equation 3.8:

$$\underline{C}_1 = \frac{\underline{h}(0) + \underline{Z}_c \cdot \underline{Q}(0)}{2} \tag{3.20}$$

$$\underline{C}_2 = \frac{\underline{h}(0) - \underline{Z}_c \cdot \underline{Q}(0)}{2} \tag{3.21}$$

Reformulating the equations 3.16 and 3.17 with equations 3.18 and 3.19, gives:

$$\begin{cases} \underline{h}(x) = \underline{h}(0) \cdot \cosh(\underline{\gamma} \cdot x) - \underline{Z}_c \cdot \underline{Q}(0) \cdot \sinh(\underline{\gamma} \cdot x) \\ \underline{Q}(x) = -\dfrac{\underline{h}(0)}{\underline{Z}_c} \cdot \sinh(\underline{\gamma} \cdot x) + \underline{Q}(0) \cdot \cosh(\underline{\gamma} \cdot x) \end{cases} \tag{3.22}$$

For a pipe of length l in matrix notation:

$$\begin{bmatrix} \underline{h}(l) \\ \underline{Q}(l) \end{bmatrix} = \begin{bmatrix} \cosh(\underline{\gamma} \cdot l) & -\underline{Z}_c \cdot \sinh(\underline{\gamma} \cdot l) \\ -\frac{1}{\underline{Z}_c} \cdot \sinh(\underline{\gamma} \cdot l) & \cosh(\underline{\gamma} \cdot l) \end{bmatrix} \cdot \begin{bmatrix} \underline{h}(0) \\ \underline{Q}(0) \end{bmatrix} \tag{3.23}$$

The transfer matrix offers the possibility to determine the fluctuations of piezometric head and discharge at the end of a pipe resulting from the excitation at the other end. For a system made of pipes in series, it is possible to compute the global transfer matrix of the system by performing the matricial product of the transfer matrices of all the pipes in series:

$$[\underline{M}_{tot}] = \prod_{1 \leq k \leq n} [\underline{M}_i] \tag{3.24}$$

3.2.2 Resolution of the Wave Equation: Conservative Form

Neglecting dissipation, ($R' = 0$) the complex number of waves of equation 3.7 becomes:

$$\gamma = s \cdot \sqrt{C' \cdot L'} = s \cdot \sqrt{\frac{g \cdot A}{a^2} \cdot \frac{1}{g \cdot A}} = \frac{\omega}{a} \tag{3.25}$$

Similarly, the characteristic complex impedance $\underline{Z}_c$ of equation 3.15 becomes a scalar value:

$$Z_c = \sqrt{\frac{L'}{C'}} = \frac{a}{g \cdot A} \tag{3.26}$$

Without damping, the complex frequency s is simplified as $s = j\omega$. In addition, noticing that $\cosh(\alpha) = \cos(j \cdot \alpha)$ and $\sinh(\alpha) = -j \cdot \sin(j \cdot \alpha)$, the transfer matrix of equation 3.23 for a frictionless pipe becomes:

$$\begin{bmatrix} \underline{h}(l) \\ \underline{Q}(l) \end{bmatrix} = \begin{bmatrix} \cos(\frac{\omega \cdot l}{a}) & -j \cdot Z_c \cdot \sinh(\frac{\omega \cdot l}{a}) \\ -j \cdot \frac{1}{Z_c} \cdot \sinh(\frac{\omega \cdot l}{a}) & \cosh(\frac{\omega \cdot l}{a}) \end{bmatrix} \cdot \begin{bmatrix} \underline{h}(0) \\ \underline{Q}(0) \end{bmatrix} \tag{3.27}$$

3.2.3 Solution of d'Alembert of the Wave Equation

The spatial partial derivative of the piezometric head combined with the equation of discharge of the equation system 3.3 gives:

$$\frac{\partial^2 Q}{\partial x^2} = C' \cdot L' \cdot \frac{\partial^2 Q}{\partial t^2} + C' \cdot R' \cdot \frac{\partial Q}{\partial t} \tag{3.28}$$

The time partial derivative of the piezometric head combined with the equation of discharge of the equation system 3.3 gives:

$$\frac{\partial^2 h}{\partial x^2} = C' \cdot L' \cdot \frac{\partial^2 h}{\partial t^2} + C' \cdot R' \cdot \frac{\partial h}{\partial t} \tag{3.29}$$

The above system expressed for a frictionless system, *i.e.* $R' = 0$, yields to the wave equation:

$$\begin{cases} \dfrac{\partial^2 Q}{\partial t^2} = a^2 \cdot \dfrac{\partial^2 Q}{\partial x^2} \\ \dfrac{\partial^2 h}{\partial t^2} = a^2 \cdot \dfrac{\partial^2 h}{\partial x^2} \end{cases} \tag{3.30}$$

D'Alembert has derived the general solution of this set of equations for the piezometric head back in 1747:

$$h(x,t) = F_p(a \cdot t - x) + G_r(a \cdot t + x) = F_p(t - x/a) + G_r(t + x/a) \tag{3.31}$$

The function $F_p(t - x/a)$ is a progressive wave whose shape is fixed, and is propagating at the wave speed a towards positive x values and $G_r(t + x/a)$ is a retrograde wave propagating at the same wave speed towards negative x values.

Wave Reflection at an Open End

The open end of a pipe located at $x = 0$ implies no piezometric head fluctuations, thus:

$$\begin{aligned} h(x,t) &= F_p(a \cdot t - x) + G_r(a \cdot t + x) \\ 0 &= F_p(a \cdot t - 0) + G_r(a \cdot t + 0) \\ &\Rightarrow F_p(a \cdot t) = -G_r(a \cdot t) \end{aligned} \tag{3.32}$$

A progressive wave reflected at an open end becomes a retrograde wave with the same shape but opposite sign as presented in figure 3.1.

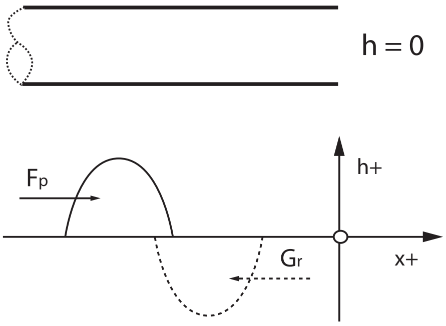

Figure 3.1: Reflection of a progressive wave at an open end of a pipe.

Wave Reflection at a Dead End

The dead end of a pipe located at $x = 0$ implies no discharge fluctuations. Thus, expressing the piezometric head fluctuation for the same location using the equation 3.11, yields to:

$$-\frac{\partial h}{\partial x} = (L' \cdot s + R') \cdot Q = (L' \cdot s + 0) \cdot 0 \tag{3.33}$$

Considering a purely real piezometric head gives:

$$\begin{aligned} h(x,t) &= F_p(a \cdot t - x) + G_r(a \cdot t + x) \\ -\frac{\partial h}{\partial x} &= -F_p(a \cdot t) + G_r(a \cdot t) \\ &\Rightarrow F_p(a \cdot t) = G_r(a \cdot t) \end{aligned} \tag{3.34}$$

A progressive wave reflected at a dead end becomes a retrograde wave with same shape and same sign as presented in figure 3.2.

Wave Reflection at a Junction

A progressive wave propagating in a pipe with change of hydroacoustic parameters in the longitudinal axis is subject to wave reflection. A change of hydroacoustic nature can

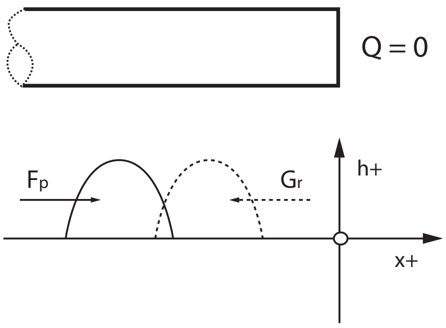

Figure 3.2: Reflection of a progressive wave at a dead end of a pipe.

be understood as a change of the complex characteristic impedance of the pipe $\underline{Z}_c$, see equation 3.15. The characteristic impedance $\underline{Z}_c$ depends mainly on 2 parameters: the pipe diameter D and the pipe wave speed a. One considers a junction located at $x = 0$ between 2 pipes characterized by the complex characteristic impedances $\underline{Z}_{c1}$ and $\underline{Z}_{c2}$ as illustrated by figure 3.3. The impedance at a location x defines the ratio between the complex piezometric head $\underline{\mathrm{h}}$ and the complex discharge $\underline{\mathrm{Q}}$ and is therefore given by:

$$\underline{Z}(x) = \frac{\underline{h}(x)}{\underline{Q}(x)} \tag{3.35}$$

Expressing the impedance of the second pipe using the sum of incident and reflected waves of pipe 1, and introducing equations 3.13 and 3.14 gives:

$$\underline{Z}_{c2} = \frac{\underline{h}_t}{\underline{Q}_t} = \frac{\underline{h}_i + \underline{h}_r}{\underline{Q}_i + \underline{Q}_r} = \frac{\underline{h}_i + \underline{h}_r}{\frac{1}{\underline{Z}_{c1}} \cdot (\underline{h}_i - \underline{h}_r)} \tag{3.36}$$

As the reflected wave is retrograde, its sign is negative, after rearranging it becomes:

$$\underline{Z}_{c2} = \underline{Z}_{c1} \cdot \frac{\underline{h}_i + \underline{h}_r}{\underline{h}_i - \underline{h}_r} \tag{3.37}$$

From equation 3.37, one can express the ratio between the incident and the reflected waves as:

$$\frac{\underline{h}_r}{\underline{h}_i} = \frac{\underline{Z}_{c2} - \underline{Z}_{c1}}{\underline{Z}_{c2} + \underline{Z}_{c1}} \tag{3.38}$$

In addition, the piezometric head at the junction is identical for both pipes, thus:

$$\underline{h}_i + \underline{h}_r = \underline{h}_t \tag{3.39}$$

The ratio between the incident and transmitted waves for the piezometric head is therefore given by:

$$\frac{\underline{h}_t}{\underline{h}_i} = \frac{2 \cdot \underline{Z}_{c2}}{\underline{Z}_{c2} + \underline{Z}_{c1}} \tag{3.40}$$

For the cases of open and dead end pipes, one get:

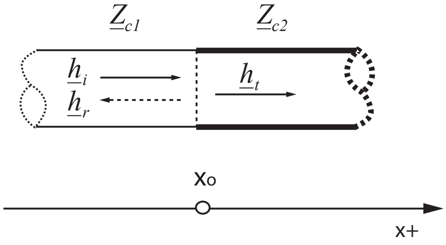

Figure 3.3: Wave reflection of incident wave i at a junction of 2 pipes having different characteristic impedance $\underline{Z}_{c1}$ amd $\underline{Z}_{c2}$.

- open end: $\underline{h}(x_o) = 0 : \underline{Z}_{c2} = 0 \Rightarrow \frac{\underline{h}_r}{\underline{h}_i} = \frac{0-\underline{Z}_{c1}}{0+\underline{Z}_{c1}} = -1$
- dead end: $\underline{Q}(x_o) = 0 : \underline{Z}_{c2} \approx \infty \Rightarrow \frac{\underline{h}_r}{\underline{h}_i} = \frac{\infty-\underline{Z}_{c1}}{\infty+\underline{Z}_{c1}} \approx 1$

Rearranging equation 3.36 with respect to the discharge gives:

$$\frac{\underline{Q}_r}{\underline{Q}_i} = \frac{\underline{Z}_{c1} - \underline{Z}_{c2}}{\underline{Z}_{c1} + \underline{Z}_{c2}} \tag{3.41}$$

In addition the discharge at the junction is identical for both pipes, thus:

$$\underline{Q}_i + \underline{Q}_r = \underline{Q}_t \tag{3.42}$$

Then the ratio between the incident and the transmitted wave is given by:

$$\frac{\underline{Q}_t}{\underline{Q}_i} = \frac{2 \cdot \underline{Z}_{c1}}{\underline{Z}_{c1} + \underline{Z}_{c2}} \tag{3.43}$$

Thus, for a dead or open end pipe, one obtains:

- open end: $\underline{h}(x_o) = 0 : \underline{Z}_{c2} = 0 \Rightarrow \frac{\underline{Q}_r}{\underline{Q}_i} = \frac{\underline{Z}_{c1}-0}{\underline{Z}_{c1}+0} = 1$
- dead end: $\underline{Q}(x_o) = 0 : \underline{Z}_{c2} \approx \infty \Rightarrow \frac{\underline{Q}_r}{\underline{Q}_i} = \frac{\underline{Z}_{c1}-\infty}{\underline{Z}_{c1}+\infty} \approx -1$

These results agree well with the previous results obtained from d'Alembert equation.

Paradox of the Wave Reflection Consecutive to a Waterhammer

The case of a pressure wave induced by the sudden closure of a valve downstream of a pipe, as presented in figure 3.4, inducing a waterhammer in the pipe can be first analyzed using the d'Alembert solution. It is important to notice that the solution of the pressure wave given by equation 3.31 for a given time t and a given location x, is the sum of **all** the incident, transmitted and reflected waves.

The pressure wave of amplitude Δh generated by the downstream valve closure is reflected by the upstream tank with a negative sign because of the open end boundary condition. In turn the piezometric head in the pipe is the sum of the incident and the reflected waves as the amplitude of both waves is identical and therefore, their sum is zero. As a result, when the reflected wave reaches the downstream valve, the piezometric head in the pipe recovers its initial value, *i.e.* h_o. At this moment, the reflected wave is reflected again with the same sign, as the closed valve represents a dead end boundary condition. The sum of the 3 waves propagating in the pipe, 1 incident wave with positive amplitude Δh and 2 reflected waves with negative amplitudes $-\Delta h$ gives a piezometric head below h_o equal to $h = h_o - \Delta h$.

The paradox lies to the fact that observing the time evolution of the piezometric head in the pipe gives the impression that the incident wave is reflected at the downstream valve with the same sign, which is not the case. If the piezometric head recovers the value h_o, this is because the sum of incident and reflected wave is zero. Similarly, the reflection at the downstream valve gives the impression that the wave is reflected with opposite sign which is again not the case. If the piezometric head reaches values below h_o, this is because the sum of the 3 waves is smaller than h_o.

This example demonstrates that even for a simple case, made of one pipe, it is not easy to predict the time evolution of the piezometric head h because it results from the summation of all the wave propagating in the pipe. Therefore, it becomes very difficult to predict accurately the piezometric head time evolution with d'Alembert solution in complex cases made of several pipes, connections and junctions. Only numerical solution of momentum and mass conservation equation can describe the phenomenon with sufficient accuracy.

3.2.4 Hydroacoustic Impedance Method

The complex characteristic impedance of equation 3.15, characterizes the hydroacoustic system in which the pressure/discharge waves are propagating. It is function of the local parameters of the pipe such as $(D, a$ and $\lambda)$ which are constant along the x abscissa [138].

The complex characteristic impedance defines the ratio between the piezometric head phasor and the discharge phasor at a given location of the pipe for progressive or retrograde waves only and only if this system is reflectionless. One can notice that if this system is frictionless, then the discharge and piezometric head phasors are in phase. In a system with reflections, the characteristic impedance does not define the ratio between piezometric head and discharge anymore. It is then necessary to evaluate the *specific hydroacoustic impedance* $\underline{Z}_a$ which is a function of the location x and of the boundary conditions of the system. The specific hydroacoustic impedance can be defined from equation 3.22 as follows:

$$\underline{Z}_a(x) = \frac{\underline{h}(x)}{\underline{Q}(x)} = \frac{\cosh(\underline{\gamma} \cdot x) \cdot \underline{h}(0) - \underline{Z}_c \cdot \sinh(\underline{\gamma} \cdot x) \cdot \underline{Q}(0)}{-\frac{1}{\underline{Z}_c} \sinh(\underline{\gamma} \cdot x) \cdot \underline{h}(0) + \cosh(\underline{\gamma} \cdot x) \cdot \underline{Q}(0)} \tag{3.44}$$

Expressing the specific impedance $\underline{Z}_a(l)$ for $x = l$ from the specific impedance $\underline{Z}_a(0)$ at $x = 0$ provides:

$$\underline{Z}_a(l) = \frac{\underline{Z}_a(0) - \underline{Z}_c \cdot \tanh(\underline{\gamma} \cdot l)}{1 - \frac{\underline{Z}_a(0)}{\underline{Z}_c} \cdot \tanh(\underline{\gamma} \cdot l)} \tag{3.45}$$

Using known boundary conditions such as $\underline{Z}_a(0) = 0$ (open end) or $\underline{Z}_a(0) = \infty$ (dead end) it is possible to determine the specific impedance for any location x. It is then

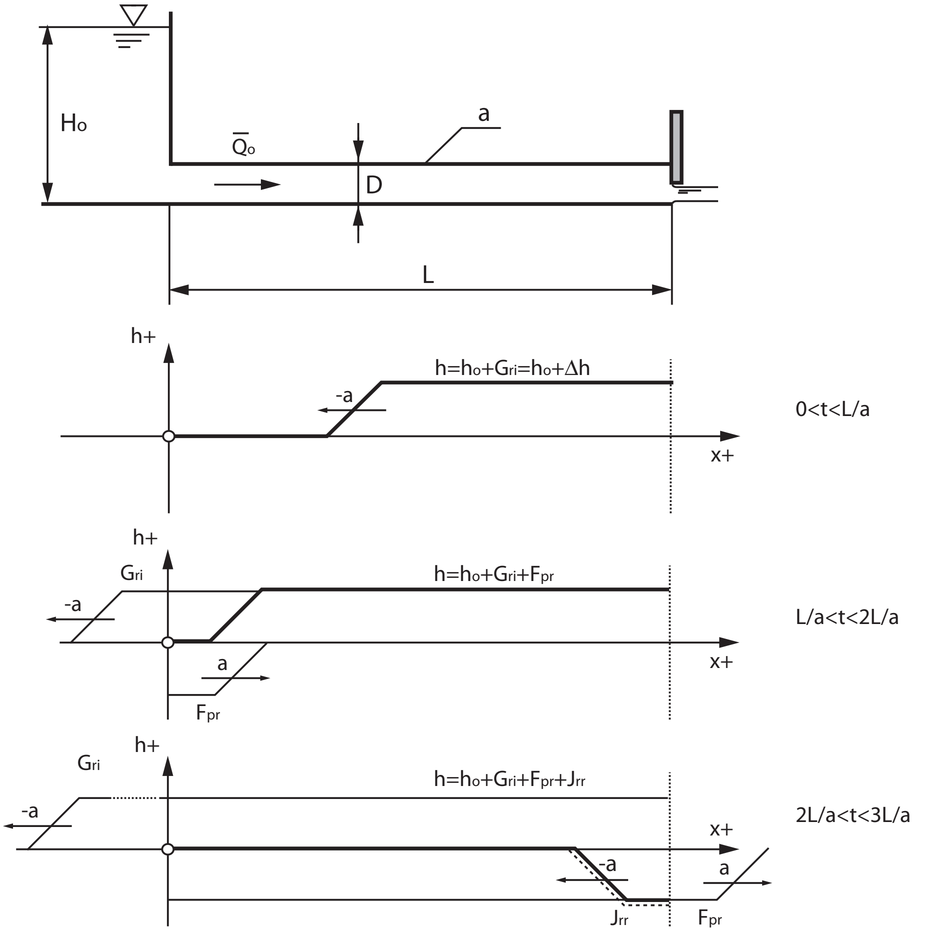

Figure 3.4: Time evolution of the piezometric head h resulting from the closure of the downstream valve inducing waterhammer.

possible to determine the specific impedance of one end of a system, by combining the impedance of all hydraulic components starting from the other end where the impedance is known. It is also possible to determine the specific impedance at $x = 0$ from the specific impedance at $x = l$ giving:

$$\underline{Z}_a(0) = \frac{\underline{Z}_a(l) + \underline{Z}_c \cdot \tanh(\underline{\gamma} \cdot l)}{1 + \frac{\underline{Z}_a(l)}{\underline{Z}_c} \cdot \tanh(\underline{\gamma} \cdot l)} \tag{3.46}$$

For infinite pipe, one get:

- $\underline{Z}_a(0) = \underline{Z}_c$
- $\underline{Z}_a(\infty) = \underline{Z}_c$

An ambiguity appears related to the fact that the specific impedance of a given system can be determined either from $x = 0$ to $x = l$, or from $x = l$ to $x = 0$, and these two impedance are usually different. It means that the problem to be solved, is to find the complex frequency s *i.e.* fulfilling both boundary conditions. This problem corresponds to the search of the natural frequencies of the system; *i.e.* the free oscillations analysis, see the next section. For simplicity, the specific impedance will be denoted impedance in the following sections of the document.

3.2.5 Free Oscillation Analysis: Continuous System

The study of the free oscillations regime of a hydraulic facility can be treated for a continuous system through 2 methods: (i) the transfer matrix method and (ii) the impedance method. These calculation methods are described below.

Free Oscillation Analysis: Transfer Matrix Method

Using the transfer matrix of each hydraulic component, it is possible to combine them to set up the global matrix of the system including the boundary conditions leading to the following equation:

$$[\underline{G}] \cdot \overrightarrow{x} = \overrightarrow{0} \tag{3.47}$$

Where the complex matrix $[\underline{G}]$ is the global matrix of the system, and $\overrightarrow{x}$ is the state vector. Obtaining a non trivial solution of equation 3.47 requires the determinant of matrix $[\underline{G}]$ to be equal to zero:

$$\det([\underline{G}]) = 0 \tag{3.48}$$

Equation 3.48 is the characteristic equation of the system whose k complex roots $s_k = \sigma_k + j \cdot \omega_k$ are the complex eigen values and $\overrightarrow{x}_k$ the eigen vectors. The free oscillation regime of the system is then given by:

$$\overrightarrow{x}(t) = \overrightarrow{x}_1 \cdot e^{s_1 \cdot t} + \overrightarrow{x}_2 \cdot e^{s_2 \cdot t} + \overrightarrow{x}_3 \cdot e^{s_3 \cdot t} + \dots \tag{3.49}$$

Free Oscillation Analysis: Impedance Method

Combining the n impedances of each element constituting the system allows determining the global impedance of the system at one end:

$$\underline{Z}_{atot}(x_n) = \frac{\underline{Z}_a(x_{n-1}) - \underline{Z}_{cn} \cdot \tanh(\underline{\gamma}_n \cdot (x_n - x_{n-1}))}{1 - \frac{\underline{Z}_a(x_{n_1})}{\underline{Z}_{cn}} \cdot \tanh(\underline{\gamma} \cdot (x_n - x_{n-1}))} \tag{3.50}$$

If the boundary condition at this end is known, the problem to be solved boils down to find the k complex frequencies $s_k = \sigma_k + j \cdot \omega_k$ satisfying the following equation :

$$\underline{Z}_{atot}(x_{end}, s_k) = \underline{Z}_{end} \tag{3.51}$$

Once the complex frequencies, *i.e.* the eigen frequencies, are known, the corresponding eigen modes can be determined using equations 3.22.

3.3 Resolution of the Set of Hyperbolic Partial Differential Equation for Discrete System

The hyperbolic partial differential equation set 3.3, can be solved numerically leading to the modelling as a discrete system. The state variables, *i.e.* the piezometric head h and the discharge Q, cannot be determined for any x or t, but are known only for given locations and given times according to the numerical scheme used to solve equation set 3.3.

3.3.1 Numerical Resolution of the Hyperbolic Partial Differential Equation set

The numerical integration in space and in time of equation set 3.3 requires appropriate discretization. Regarding the spatial discretization, the centered scheme illustrated in figure 3.5 can be used.

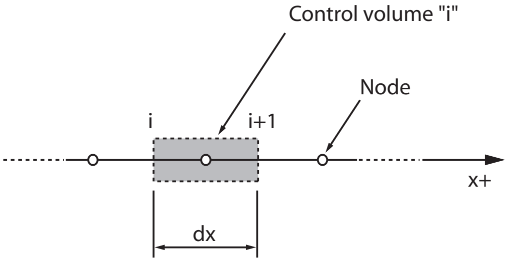

Figure 3.5: Control volume i having center node at i+1/2.

Using the scheme centered at location $i + 1/2$ of the figure 3.5, one gets the following expression for the piezometric head and discharge space partial derivatives:

$$\frac{\partial h}{\partial x}|_{i+1/2} = \frac{h_{i+1} - h_i}{dx} \tag{3.52}$$

$$\frac{\partial Q}{\partial x}|_{i+1/2} = \frac{Q_{i+1} - Q_i}{dx} \tag{3.53}$$

Considering the above numerical scheme and using the total differential in equation set 3.3 expressed for a location $i + 1/2$ gives:

$$\begin{cases} \frac{dh_{i+1/2}}{dt} + \frac{1}{C'} \cdot \frac{Q_{i+1} - Q_i}{dx} = 0 \\ \frac{h_{i+1} - h_i}{dx} + L' \cdot \frac{dQ_{i+1/2}}{dt} + R' \cdot Q_{i+1/2} = 0 \end{cases} \tag{3.54}$$

In order to ensure stability of the computation, a numerical scheme of Lax, based on the mean value of the discharge, is used:

$$Q_{i+1/2} = \frac{Q_{i+1} + Q_i}{2} \tag{3.55}$$

Equations set 3.54 becomes:

$$\begin{cases} C' \cdot dx \dfrac{dh_{i+1/2}}{dt} = Q_i - Q_{i+1} \\ \underbrace{h_{i+1} + \dfrac{L' \cdot dx}{2} \cdot \dfrac{dQ_{i+1}}{dt} + \dfrac{R' \cdot dx}{2} \cdot Q_{i+1}}_{h_{i+1/2}} = \underbrace{h_i - \left(\dfrac{L' \cdot dx}{2} \cdot \dfrac{dQ_i}{dt} + \dfrac{R' \cdot dx}{2} \cdot Q_i \right)}_{h_{i+1/2}} \end{cases} \tag{3.56}$$

Noticing that the second part of the equation corresponds to the piezometric head for the location $i + 1/2$, the system can be expressed under implicit matrix form:

$$\begin{bmatrix} C & 0 & 0 \\ 0 & L/2 & 0 \\ 0 & 0 & L/2 \end{bmatrix} \cdot \frac{d}{dt} \cdot \begin{bmatrix} h_{i+1/2} \\ Q_i \\ Q_{i+1} \end{bmatrix} + \begin{bmatrix} 0 & -1 & 1 \\ 1 & R/2 & 0 \\ -1 & 0 & R/2 \end{bmatrix} \cdot \begin{bmatrix} h_{i+1/2} \\ Q_i \\ Q_{i+1} \end{bmatrix} = \begin{bmatrix} 0 \\ h_i \\ -h_{i+1} \end{bmatrix} \tag{3.57}$$

Set of equations 3.57 is written using the hydroacoustic parameters obtained for a length dx given by:

$$\begin{cases} R = R' \cdot dx \\ L = L' \cdot dx \\ C = C' \cdot dx \end{cases} \tag{3.58}$$

The compact expression of equation set 3.57 is given by:

$$[A] \cdot \frac{d\overrightarrow{x}}{dt} + [B] \cdot \overrightarrow{x} = \overrightarrow{C} \tag{3.59}$$

Set of equations 3.57 can be integrated numerically using classical methods such as Euler, Runge-Kutta, etc. Courant-Friederichs-Lewy have demonstrated that there exists a numerical stability criteria known as the "CFL" criteria linking the space and time discretization, respectively dx and dt through the wave speed a [38]. This criteria ensures the causality of the system because the information cannot transit faster than the wave speed. The CLF criteria is given by:

$$dt < \frac{dx}{a} \tag{3.60}$$

The equation set 3.57 features the following state variables:

- piezometric head in the middle of the element i: $h_{i+1/2}$
- discharge at the inlet of the elements i: Q_i
- discharge at the outlet of the elements i: Q_{i+1}

The system has the following boundary conditions:

- piezometric head at the inlet of the elements i: h_i
- piezometric head at the outlet of the elements i: h_{i+1}

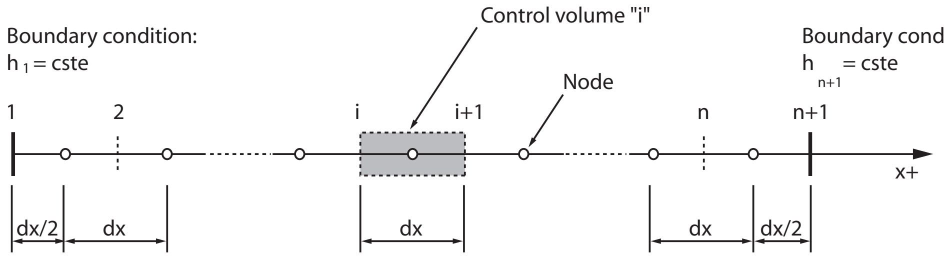

Figure 3.6: Spatial discretization of a pipe of length l.

Equation set 3.57 corresponds to the equation describing the dynamic behavior of a pipe of length dx. A pipe is modelled by n pipes of length dx and $dx = L/n$. The corresponding spatial discretization is presented in figure 3.6.

For a pipe of length l, the boundary conditions are the piezometric head at both ends of the pipe, whereas momentum equations can be merged 2 by 2, introducing the piezometric head at each node $i + 1/2$. The matrices $[A]$ and $[B]$ of equations set 3.57 becomes for a pipe of length l:

$$[A] = \begin{bmatrix} C & & & & {\scriptstyle (n)} & & & & & {\scriptstyle (2n+1)} \\ & C & & & & & & & & \\ & & \ddots & & & & & 0 & & \\ & & & C & & & & & & \\ {\scriptstyle (n)} & & & & C & & & & & \\ & & & & & L/2 & & & & \\ & & & & & & L & & & \\ & & 0 & & & & & \ddots & & \\ & & & & & & & & L & \\ {\scriptstyle (2n+1)} & & & & & & & & & L/2 \end{bmatrix} \tag{3.61}$$

And:

$$[B] = \begin{bmatrix} & & & & {\scriptstyle (n)} & -1 & 1 & & & {\scriptstyle (2n+1)} \\ & & & & & & -1 & 1 & & \\ & & 0 & & & & & \ddots & & \\ & & & & & & & -1 & 1 & \\ {\scriptstyle (n)} & & & & & & & & -1 & 1 \\ 1 & & & & & R/2 & & & & \\ -1 & 1 & & & & & R & & & \\ & & \ddots & & & & & \ddots & & \\ & & & -1 & 1 & & & & R & \\ {\scriptstyle (2n+1)} & & & & -1 & & & & & R/2 \end{bmatrix} \tag{3.62}$$

One can notice that the equation set has the dimension $(2n + 1) \cdot (2n + 1)$ and the state vector comprises n piezometric heads along the pipe for the nodes $1 + 1/2$ to $n + 1/2$ and $n + 1$ discharges at both end of n pipes of length dx.

The state vector of dimension $(2n+1)\cdot 1$ is given by:

$$\overrightarrow{x} = \begin{bmatrix} h_{1+1/2} & h_{2+1/2} & \ldots & h_{n+1/2} & Q_1 & Q_2 & \ldots & Q_{n+1} \end{bmatrix}^T \tag{3.63}$$

The boundary conditions vector of dimension $(2n+1)\cdot 1$ is given by:

$$\overrightarrow{C} = \begin{bmatrix} 0 & \ldots & 0 & h_1 & 0 & \ldots & 0 & -h_{n+1} \end{bmatrix}^T \tag{3.64}$$

It is also important to notice that the matrix $[B(Q_i)]$ is function of the discharge and introduces a non-linear behavior. For the numerical integration of this set of equation, all the discharge Q_i in matrix $[B(Q_i)]$ are retrieved from the previous time step.

3.3.2 Equivalent Scheme Representation

Set of equation 3.57 corresponds to the equations of an equivalent scheme which is a T-shaped "quadripol" as presented in figure 3.7 [135].

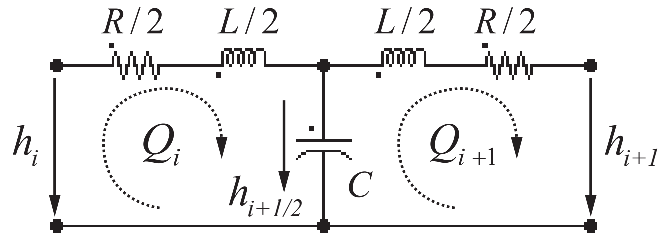

Figure 3.7: Equivalent scheme of a pipe of length dx.

This equivalent scheme is the model of a pipe with length dx where the hydroacoustic parameters are defined as follows:

- hydroacoustic capacitance $C = \frac{dx\cdot g\cdot A}{a^2}$ $[m^2]$, related to storage effect due to pressure increase and is therefore function of the wave speed ; in the wave speed equation 2.20, the term ρ/E_{water} account for water compressibility storage and the term $D/(eE_c)$ account for pipe wall deflection storage;
- hydroacoustic inductance $L = \frac{dx}{g\cdot A}$ $[s^2/m^2]$, related to inertia effect of the water;
- hydroacoustic resistance $R = \frac{\lambda\cdot dx\cdot|\bar{Q}|}{2\cdot g\cdot D\cdot A^2}$ $[s/m^2]$, related to the head losses through the pipe.

Qualitative Analysis of the Equivalent Scheme

The equivalent scheme can be analyzed qualitatively for both steady state and transient conditions. First, for the steady state conditions the inductances and capacitances do not play any role: only the resistance causes head losses along the x coordinates according to the length of the pipe. The discharge in both loops are identical: $Q_i = Q_{i+1}$ and the head losses correspond to the piezometric head difference between the inlet and the outlet. The steady state conditions lead to the following equation:

$$\begin{aligned} h_i - h_{i+1/2} &= \frac{R}{2} \cdot Q_i \\ h_{i+1/2} - h_{i+1} &= \frac{R}{2} \cdot Q_{i+1} \end{aligned} \tag{3.65}$$

The sum of the two above equations gives:

$$h_i - h_{i+1} = R \cdot Q_i \tag{3.66}$$

During transients, assuming a sudden increase of the downstream head h_{i+1} gives the following equation for the second loop of the equivalent scheme:

$$h_{i+1/2} - h_{i+1} - \frac{R}{2} \cdot Q_{i+1} = \frac{L}{2} \cdot \frac{dQ_{i+1}}{dt} \tag{3.67}$$

For an increase of the downstream piezometric head h_{i+1}, the inequality is obtained:

$$h_{i+1/2} - h_{i+1} - \frac{R}{2} \cdot Q_{i+1} < 0 \rightarrow \frac{dQ_{i+1}}{dt} < 0 \tag{3.68}$$

The increase of the downstream piezometric head induces the decrease of the discharge in the second loop, and as a result, the piezometric head in the middle of the pipe increases because the discharge in the first loop has not changed after an infinitesimal time interval:

$$C \cdot \frac{dh_{i+1/2}}{dt} = Q_i - Q_{i+1} \rightarrow \frac{dh_{i+1/2}}{dt} > 0 \tag{3.69}$$

This qualitative explanation describes how the equivalent scheme of a pipe represents the propagation of pressure waves in a pipe when the downstream pressure increases suddenly.

Generalized Representation of a Pipe

The implicit system of equation 3.57 can be derived directly from the equivalent scheme of the pipe of figure 3.7 using Kirchhoff's law. The same approach can be used to model a pipe of length l made of n pipes of length dx as presented in figure 3.6. Kirchhoff's law applied to this system leads to equation 3.57.

It can be noticed that the piezometric heads are determined for the node $i + 1/2$ and the discharges are determined for the loops i as indicated in figure 3.8. The corresponding equivalent scheme is presented in figure 3.9 where n equivalent schemes are concatenated together.

The 3-step modelling procedure is summarized in figure 3.10: (i) a mathematical model of the physical system is established, providing a set of hyperbolic partial differential equations; (ii) a numerical integration scheme in space provides the structure of the equivalent scheme that can be generalized, meaning that the set of total partial derivative equations can be obtained directly from the equivalent scheme using Kirchhoff's law; (iii) the set of total derivative equations is integrated numerically using standard algorithm such as Runge-Kutta.

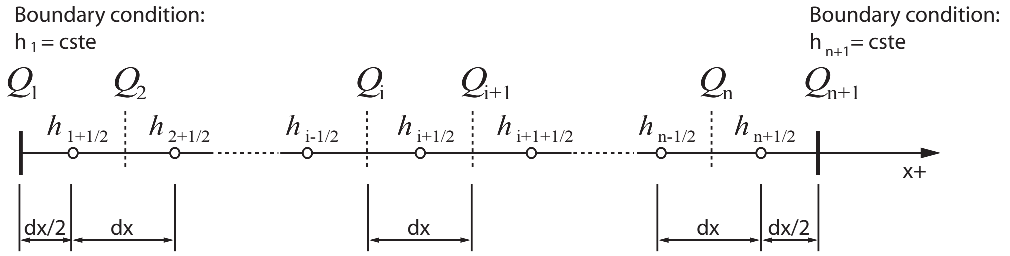

Figure 3.8: State variable location definition.

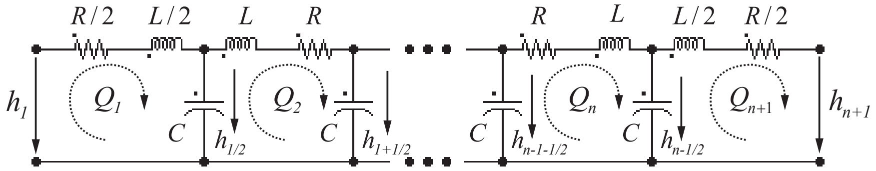

Figure 3.9: Equivalent scheme of the system of figure 3.8.

3.3.3 Free Oscillation Analysis: Discrete System

The free oscillation analysis of a hydraulic facility can be performed from its equivalent circuit with 2 different approaches: (i) solving the eigen value/vectors problem, directly from the total differential equation set 3.59; (ii) performing a numerical calculation of the system impedance, and searching for the complex frequencies satisfying all the boundary conditions.

Eigen Values/Vectors Problem

The free oscillation analysis of a discrete system modelled by n elements corresponds to the problem of the determination of the eigen values/vectors of the system of partial differential equations 3.59 using Kirchhoff's law:

$$[A] \cdot \frac{d\overrightarrow{x}}{dt} + [B] \cdot \overrightarrow{x} = \overrightarrow{0} \tag{3.70}$$

Introducing Laplace operator $s = \sigma + j \cdot \omega$ yields to:

$$[A] \cdot s \cdot \overrightarrow{x} + [B] \cdot \overrightarrow{x} = \overrightarrow{0} \tag{3.71}$$

Rearranging equation 3.71 gives a system of dimension $(2n+1) \times (2n+1)$:

$$\big([I] \cdot s + [A]^{-1}[B]\big) \cdot \overrightarrow{x} = \overrightarrow{0} \tag{3.72}$$

Where $[I]$ is the identity matrix. To ensure a non-trivial solution, the determinant of the global matrix of the system must be zero:

$$\det \big([I] \cdot s + [A]^{-1}[B]\big) = 0 \tag{3.73}$$

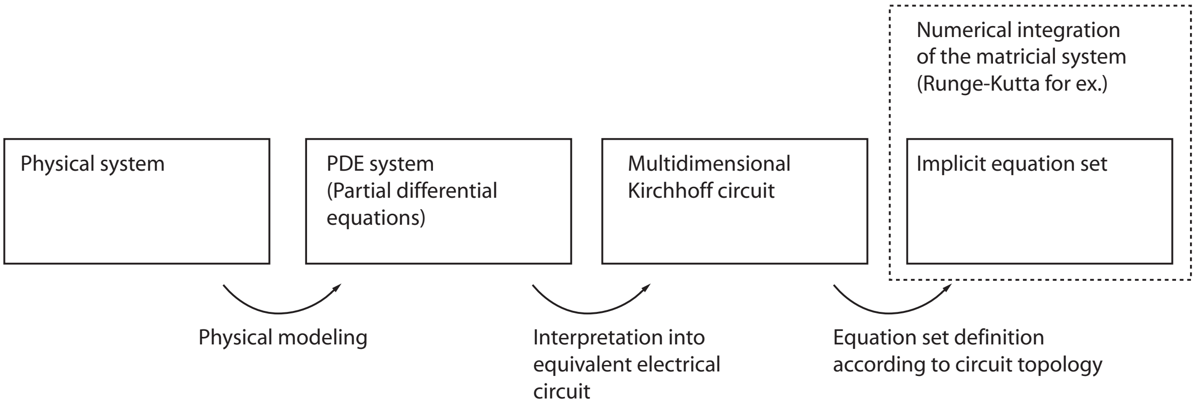

Figure 3.10: Global discrete modelling approach.

This equation is the characteristic equation of the system whose $(2n+1)$ roots comprising a null root and n double complex roots $s_n = \sigma_n \pm j \cdot \omega_n$ are the eigen values of the system with the corresponding eigen vectors $\overrightarrow{x}_n$. The free oscillation regime of this system is then given by:

$$\overrightarrow{x}(t) = \overrightarrow{x}_1 \cdot e^{s_1 \cdot t} + \overrightarrow{x}_2 \cdot e^{s_2 \cdot t} + \ldots + \overrightarrow{x}_n \cdot e^{s_n \cdot t} \tag{3.74}$$

It can be noticed that the real part of the eigen values σ_n are the damping coefficients; negative values correspond to damped modes. Stability of the system is ensured only if all the damping coefficient of the system are negative. This stability criteria is represented graphically in the complex plane where the shadow area in figure 3.11 is the stable domain.

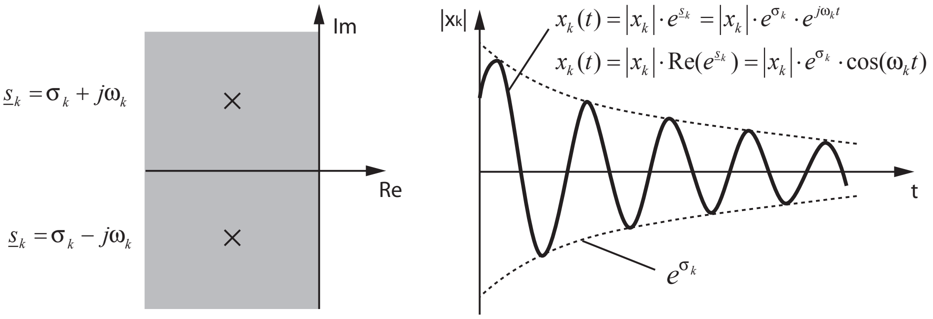

Figure 3.11: Complex eigen values with complex conjugates.

Discrete Impedance Method

This method is similar to the impedance method applied to a continuous system except the fact that the impedance is calculated from the equivalent scheme [20]. The impedance is calculated starting from one end where the boundary condition are known, for example an open end or a dead end, and then calculated until another end. The calculation is done by successive series and parallel equivalent computation of the branches of the system. The first loop of a pipe with a load impedance $\underline{Z}_{load}$ at the end is presented in figure 3.12.

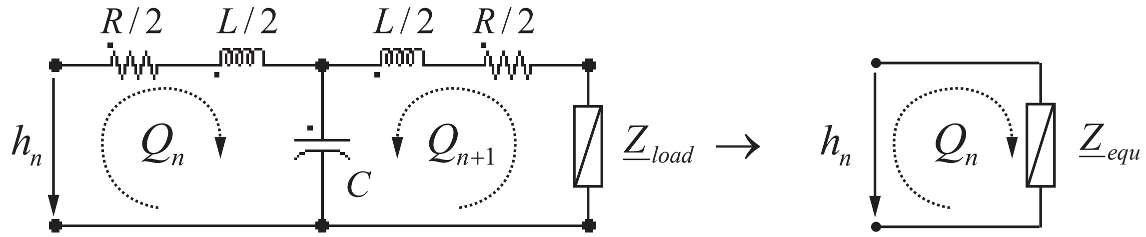

Figure 3.12: Equivalent impedance of the last loop of a pipe with load impedance Z_{load} .

The equivalent impedance of figure 3.12 can be expressed as follows:

$$\underline{Z}_{equ} = (L/2 \cdot s + R/2) + \frac{(L/2 \cdot s + R/2 + \underline{Z}_{load}) \cdot \frac{1}{C \cdot s}}{(L/2 \cdot s + R/2 + \underline{Z}_{load}) + \frac{1}{C \cdot s}} \tag{3.75}$$

If the pipe is modelled by n elements, the equivalent impedance is calculated recursively considering as load impedance $\underline{Z}_{load}$ for the loop $n-1$, the equivalent impedance $\underline{Z}_{equ}$ of the loop n, given by :

$$\underline{Z}_{equ_i} = (L/2 \cdot s + R/2) + \frac{\left(L/2 \cdot s + R/2 + \underline{Z}_{equ_{i+1}}\right) \cdot \frac{1}{C \cdot s}}{\left(L/2 \cdot s + R/2 + \underline{Z}_{equ_{i+1}}\right) + \frac{1}{C \cdot s}} \tag{3.76}$$

The computation is done for a given complex frequency. The problem to be solved is therefore to find the complex frequency satisfying all the boundary conditions. This leads to a minimization calculation based, for example, on Newton-Raphson's algorithm. It is convenient to use a first guess obtained from frictionless system whose complex roots become:

$$s = j \cdot \omega$$

This approach allows computing the impedance of the system at one end for a given range of pulsation ω and identifying which are satisfying the boundary conditions. The typical boundary conditions are:

- open end: $|\underline{Z}_x(j\omega)| = 0$
- dead end: $|\underline{Z}_x(j\omega)| = \infty$

The pulsations obtained from frictionless conditions are an excellent guess for the research of the eigen values $s_k = \sigma_k + j \cdot \omega_k$ of the dissipative system as the damping affects only slightly the eigen pulsation of a system. Once the eigen frequencies are known, the impedance can be computed along the system for the eigen value of interest indicating the location of minima and maxima of the discharge and the head.

3.4 Comparison of Continuous and Discrete Simulation Model

3.4.1 Truncation Error

The spatial discretization of the partial derivative introduces truncation errors as the Taylor development of a value u is given for a progressive scheme by:

$$u_{i+1} \simeq u_i + \left(\frac{\partial u}{\partial x}\right)_i \cdot \Delta x + \left(\frac{\partial^2 u}{\partial x^2}\right)_i \cdot \frac{(\Delta x)^2}{2} + \left(\frac{\partial^3 u}{\partial x^3}\right)_i \cdot \frac{(\Delta x)^3}{6} + \dots \tag{3.77}$$

After rearrangement, the approximation of the partial derivative of u at the location i is given by:

$$\left(\frac{\partial u}{\partial x}\right)_i \simeq \frac{u_{i+1} - u_i}{\Delta x} + O(\Delta x) \tag{3.78}$$

A progressive or backward finite difference scheme leads to a truncation error $O(\Delta x)$ of first order (Δx). A centered scheme leads to a truncation error of second order $O(\Delta x^2)$. In order to assess this truncation error, the transfer matrix of a pipe is computed using the discrete model and compared with the exact solution obtained for a continuous system and taken as reference value. Finally, the error is quantified in the frequency domain. This quantification is done for 3 numerical finite difference schemes: (i) the "progressive" scheme, (ii) the "backward" scheme and (iii) the "centered" scheme. This comparison permits to establish a *confidence threshold*.

Centered Scheme

The finite difference scheme developed above leads to an equivalent scheme, see figure 3.13, whose set of ordinary differential equations can be derived directly from Kirchhoff's law.

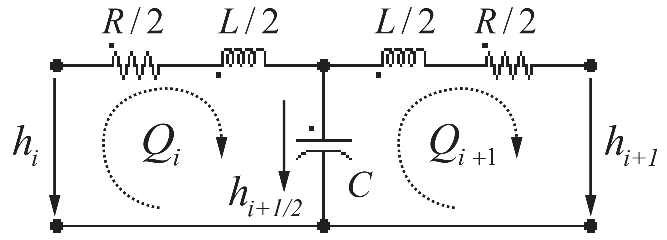

Figure 3.13: Centered equivalent scheme of a pipe of length dx.

The corresponding set of equations is given by:

$$\begin{cases} h_i = \frac{L}{2} \cdot \frac{dQ_i}{dt} + \frac{R}{2} \cdot Q_i + h_{i+1/2} \\ C \cdot \frac{dh_{i+1/2}}{dt} = Q_i - Q_{i+1} \\ h_{i+1/2} = \frac{L}{2} \cdot \frac{dQ_{i+1}}{dt} + \frac{R}{2} \cdot Q_{i+1} + h_{i+1} \end{cases} \tag{3.79}$$

Combining equations 3.79 yields to the transfer matrix of the equivalent circuit of figure 3.13 :

$$\begin{bmatrix} \underline{h}_i \\ \underline{Q}_i \end{bmatrix} = \begin{bmatrix} \left(\frac{\underline{\gamma}_x^2}{2} + 1\right) & \left(\frac{\underline{\gamma}_x^2}{2 \cdot C \cdot s} \cdot \left[1 + \left[\frac{\underline{\gamma}_x^2}{2} + 1\right]\right]\right) \\ C \cdot s & \left(\frac{\underline{\gamma}_x^2}{2} + 1\right) \end{bmatrix} \cdot \begin{bmatrix} \underline{h}_{i+1} \\ \underline{Q}_{i+1} \end{bmatrix} \tag{3.80}$$

Where: $\underline{\gamma}_x = \underline{\gamma} \cdot dx$.

Backward Scheme

Conserving the RL terms of the branch of the equivalent scheme of a pipe while moving the capacitance upstream leads to the equivalent scheme of figure 3.14. This equivalent scheme is based on backward numerical scheme without Lax scheme.

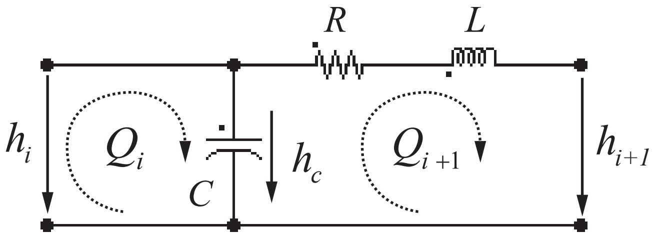

Figure 3.14: Backward equivalent scheme of a pipe of length dx.

The corresponding set of equations is given by:

$$\begin{cases} h_i = h_{i+1/2} \\ C \cdot \frac{dh_{i+1/2}}{dt} = Q_i - Q_{i+1} \\ h_{i+1/2} = L \cdot \frac{dQ_{i+1}}{dt} + R \cdot Q_{i+1} + h_{i+1} \end{cases} \tag{3.81}$$

Combining equations 3.81 yields to the transfer matrix of the equivalent circuit of figure 3.14:

$$\begin{bmatrix} \underline{h}_i \\ \underline{Q}_i \end{bmatrix} = \begin{bmatrix} 1 & \frac{\underline{\gamma}_x^2}{C \cdot s} \\ C \cdot s & \left(\underline{\gamma}_x^2 + 1\right) \end{bmatrix} \cdot \begin{bmatrix} \underline{h}_{i+1} \\ \underline{Q}_{i+1} \end{bmatrix} \tag{3.82}$$

Progressive Scheme

As it is done for the backward scheme, RL terms are conserved, but the capacitance is moved downstream. This leads to the equivalent scheme of figure 3.15, corresponding to a progressive numerical scheme without Lax scheme.

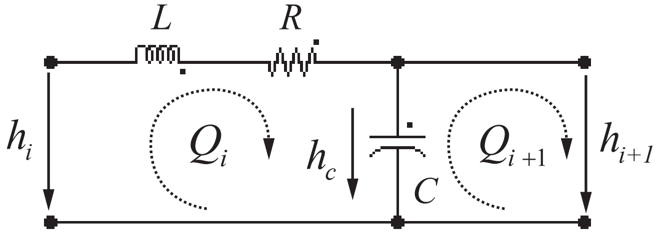

Figure 3.15: Progressive equivalent scheme of a pipe of length dx.

The corresponding set of equations is given by:

$$\begin{cases} h_i = \dfrac{L}{2} \cdot \dfrac{dQ_i}{dt} + \dfrac{R}{2} \cdot Q_i + h_{i+1/2} \\ C \cdot \dfrac{dh_{i+1/2}}{dt} = Q_i - Q_{i+1} \\ h_{i+1/2} = h_{i+1} \end{cases} \tag{3.83}$$

Combining the above equations 3.83, yields to the transfer matrix of the equivalent circuit of figure 3.15:

$$\begin{bmatrix} \underline{h}_i \\ \underline{Q}_i \end{bmatrix} = \begin{bmatrix} \left(\underline{\gamma}_x^2 + 1\right) & \frac{\underline{\gamma}_x^2}{C \cdot s} \\ C \cdot s & 1 \end{bmatrix} \cdot \begin{bmatrix} \underline{h}_{i+1} \\ \underline{Q}_{i+1} \end{bmatrix} \tag{3.84}$$

3.4.2 Comparison of Hydroacoustic Models

The transfer matrix of the following 4 models are compared: (i) the continuous hyperbolic model, (ii) the discrete centered model, (iii) the discrete backward model, and (iv) the discrete progressive model. The transfer matrix and the equivalent scheme of these models are summarized in figure 3.1.

Table 3.1: Comparison of the transfer matrix of 4 models of a pipe of length dx.

Model	Equivalent scheme	Transfer matrix
Continuous hyperbolic	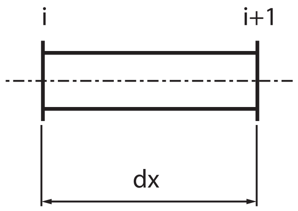	$\begin{bmatrix} \underline{h}(dx) \\ \underline{Q}(dx) \end{bmatrix} = [M] \cdot \begin{bmatrix} \underline{h}(0) \\ \underline{Q}(0) \end{bmatrix}$ $[M] = \begin{bmatrix} \cosh(\underline{\gamma} \cdot dx) & -\underline{Z}_c \cdot \sinh(\underline{\gamma} \cdot dx) \\ -\frac{1}{\underline{Z}_c} \cdot \sinh(\underline{\gamma} \cdot dx) & \cosh(\underline{\gamma} \cdot dx) \end{bmatrix}$
Discrete centered	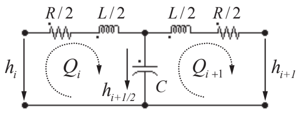	$\begin{bmatrix} \underline{h}_i \\ \underline{Q}_i \end{bmatrix} = [M] \cdot \begin{bmatrix} \underline{h}_{i+1} \\ \underline{Q}_{i+1} \end{bmatrix}$ $[M] = \begin{bmatrix} \left(\frac{\underline{\gamma}_x^2}{2} + 1\right) & \left(\frac{\underline{\gamma}_x^2}{2 \cdot C \cdot s} \cdot \left[1 + \left[\frac{\underline{\gamma}_x^2}{2} + 1\right]\right]\right) \\ C \cdot s & \left(\frac{\underline{\gamma}_x^2}{2} + 1\right) \end{bmatrix}$
Discrete backward	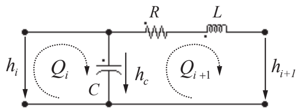	$\begin{bmatrix} \underline{h}_i \\ \underline{Q}_i \end{bmatrix} = \begin{bmatrix} 1 & \frac{\underline{\gamma}_x^2}{C \cdot s} \\ C \cdot s & \left(\underline{\gamma}_x^2 + 1\right) \end{bmatrix} \cdot \begin{bmatrix} \underline{h}_{i+1} \\ \underline{Q}_{i+1} \end{bmatrix}$
Discrete progressive	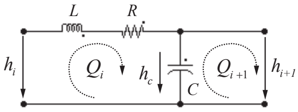	$\begin{bmatrix} \underline{h}_i \\ \underline{Q}_i \end{bmatrix} = \begin{bmatrix} \left(\underline{\gamma}_x^2 + 1\right) & \frac{\underline{\gamma}_x^2}{C \cdot s} \\ C \cdot s & 1 \end{bmatrix} \cdot \begin{bmatrix} \underline{h}_{i+1} \\ \underline{Q}_{i+1} \end{bmatrix}$

Assuming frictionless regime, the transfer matrix of equation 3.27 becomes for a length dx:

$$\begin{bmatrix} \underline{h}(dx) \\ \underline{Q}(dx) \end{bmatrix} = \begin{bmatrix} \cos(\frac{\omega \cdot dx}{a}) & -j \cdot Z_c \cdot \sinh(\frac{\omega \cdot dx}{a}) \\ -j \cdot \frac{1}{Z_c} \cdot \sinh(\frac{\omega \cdot dx}{a}) & \cosh(\frac{\omega \cdot dx}{a}) \end{bmatrix} \cdot \begin{bmatrix} \underline{h}(0) \\ \underline{Q}(0) \end{bmatrix} \tag{3.85}$$

Introducing the wave length λ:

$$\lambda = \frac{a}{f} = \frac{2 \cdot \pi \cdot a}{\omega}, \tag{3.86}$$

the attribute of the trigonometric functions of 3.85 is given by:

$$\frac{\omega \cdot dx}{a} = 2 \cdot \pi \cdot \frac{dx}{\lambda} \tag{3.87}$$

The key parameter for a study in the frequency domain is the ratio:

$$\frac{dx}{\lambda} \tag{3.88}$$

It is necessary that the wavelength of the phenomenon of interest is at least 10 times larger than the length of the elements modelling the pipe [79]. The amplitude of the 4 terms of the matrix transfer are computed for a pipe characterized by $\lambda/dx = 10$ and presented in figure 3.16. The boundary conditions of the pipe is set as open end for $x = 0$. The 4 terms of the transfer matrix are defined as follows:

$$\begin{bmatrix} \underline{h}(dx) \\ \underline{Q}(dx) \end{bmatrix} = \begin{bmatrix} \underline{M}_{11} & \underline{M}_{12} \\ \underline{M}_{21} & \underline{M}_{22} \end{bmatrix} \cdot \begin{bmatrix} \underline{h}(0) \\ \underline{Q}(0) \end{bmatrix} \tag{3.89}$$

The impedance of the pipe of length dx is evaluated starting from the open end $x = 0$ until the end of the pipe $x = dx$ using one element for the modelling of the pipe. The resulting impedance amplitude are represented in figure 3.17. The impedance of the pipe with open end is given by:

$$\underline{Z}(dx) = \frac{\underline{M}_{12}(dx)}{\underline{M}_{22}(dx)} \tag{3.90}$$

3.4.3 Frequency Confidence Threshold of the Model

The amplitude of the impedance can be used to compare the accuracy of the 3 discrete models, the continuous hyperbolic model being taken as reference. The error of the impedance amplitude is represented for the 3 discrete models as a function of the rated wavelength λ/dx in figure 3.18. The error is provided in table 3.2 for $\lambda/dx = 10$ and $\lambda/dx = 20$.

The numerical scheme of the centered model is of the second order while the numerical scheme of both the backward and the progressive scheme are of the first order. As a result, the centered scheme features an error less than 3% for $\lambda = 10 \cdot dx$ and even less than 1% for $\lambda = 20 \cdot dx$. This means that 20 nodes are required to model properly a standing wave of one wavelength with less than 1% of error. The 4 terms of the transfer matrix

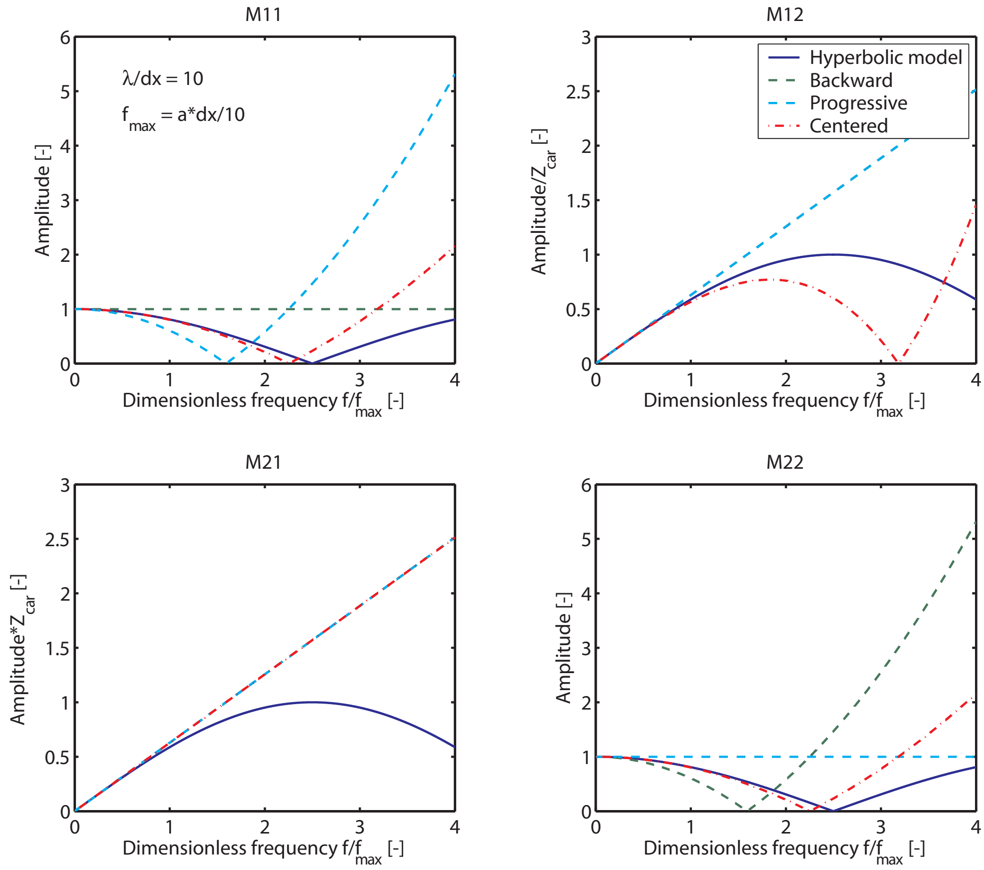

Figure 3.16: Comparison of the amplitude of the 4 terms of the transfer matrix of the 4 models.

of the centered scheme presented in figure 3.16 show good agreement with the hyperbolic solution up to $f = f_{max}$ corresponding to $\lambda = 10 \cdot dx$. Whereas for both first order scheme the accuracy is much worst due to the non symmetry of the models. Thus, the models behave differently if they are considered from one side or the other. The increase of spatial resolution presents the drawback of increasing the size of the equation system to be solved and reducing the integration time step. It is therefore very important to have criteria to define the appropriate discretization offering a good balance between accuracy and computational time.

To summarize, the spatial discretization of a hydraulic system should be defined prior

Error	Centered scheme [%] $(\lvert Z\rvert - \lvert Z_{ref}\rvert)/\lvert Z_{ref}\rvert$	Backward scheme [%] $(\lvert Z\rvert - \lvert Z_{ref}\rvert)/\lvert Z_{ref}\rvert$	Progressive scheme [%] $(\lvert Z\rvert - \lvert Z_{ref}\rvert)/\lvert Z_{ref}\rvert$
$\lambda = 10 \cdot dx$	2.9	13.5	42.9
$\lambda = 20 \cdot dx$	0.8	3.3	7.3

Table 3.2: Error on the impedance amplitude obtained for a pipe of length dx with the 3 discrete models as a function of the rated wavelength λ/dx.

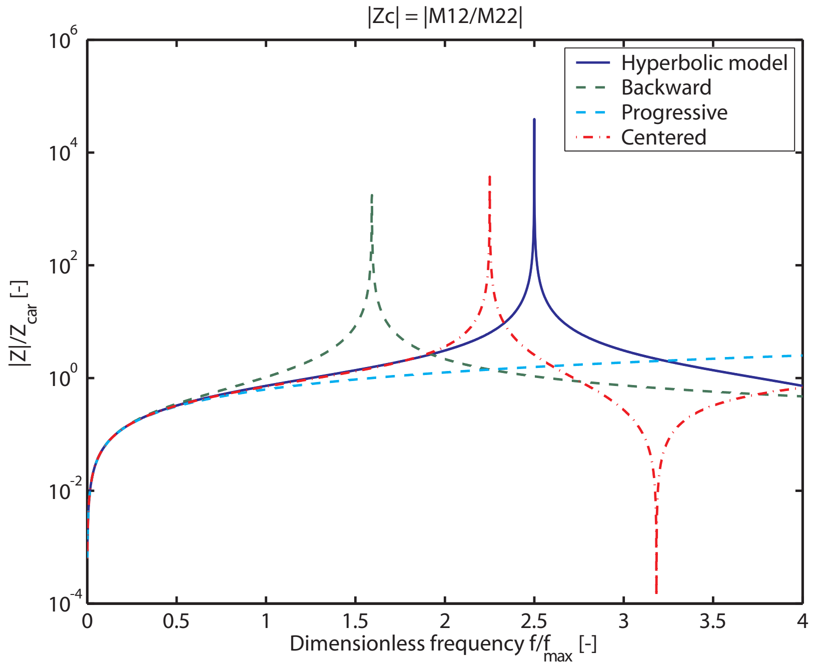

Figure 3.17: Comparison of the magnitude of the impedance $\underline{Z}_{x=dx}$ of the 4 terms of the transfer matrix obtained for the 4 models.

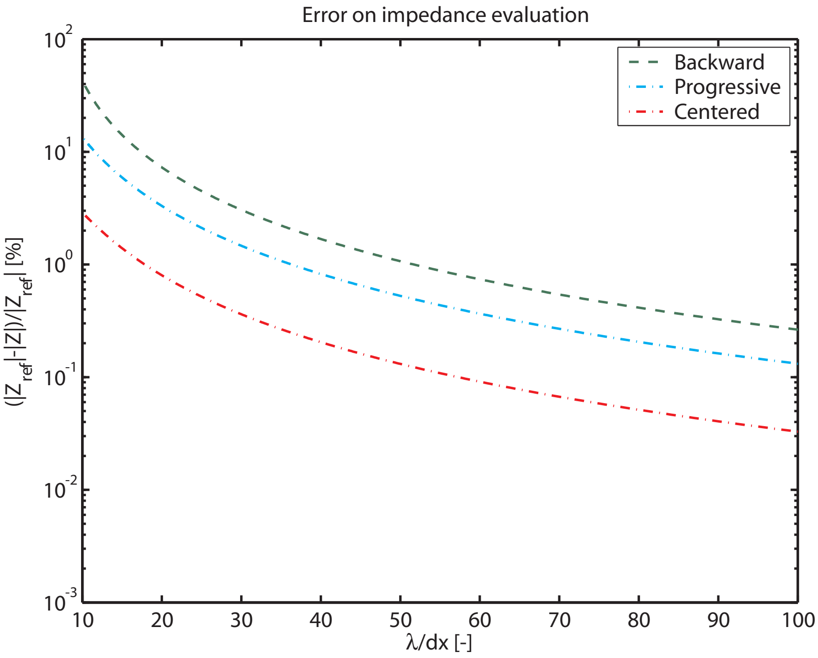

Figure 3.18: Comparison of the error on the impedance amplitude of the 3 discrete models regarding the continuous model.

to the simulation and setup according to the frequency of interest $f_{interest}$ and the wave speed a of the pipe with the following resolution:

$$\begin{aligned} dx &= \frac{a}{10 \cdot f_{interest}} \rightarrow error < 3\%; \\ dx &= \frac{a}{20 \cdot f_{interest}} \rightarrow error < 1\%. \end{aligned} \tag{3.91}$$

3.5 Summary of the Approach

Figure 3.19 is a synoptic representation of the analysis of the dynamic behavior of a hydraulic circuit by solving equation 2.26. Two general approaches are considered: (i) a continuous model with analytical resolution and (ii) a discrete model with numerical resolution.

The approach based on a continuous system has the advantage of providing the exact solution of the set of hyperbolic partial differential equations. The resolution in the frequency domain is rather convenient, however the resolution in time domain is complex because it requires to perform an inverse Fourrier transform. Moreover, the determination of the natural frequencies of the system requires an iterative algorithm.

The discrete approach presents numerical modelling errors that can be evaluated with equation 3.91 in order to use an appropriate spatial discretization ensuring reasonable accuracy at the frequency of interest while minimizing computation time.

Furthermore, the approach based on equivalent schemes is an intuitive way to represent and understand the dynamic behavior of hydraulic systems and helps for the elaboration of advanced models.

Moreover, once the ordinary equation set is established for a given topology, matrix mathematical operators can be used for the study in the frequency domain (eigen value/vector problem) and in the time domain (simulation of the dynamic behavior of the system considering all the system non-linearities).

Overall, the discrete approach offers many advantages in spite of the errors introduced by the numerical scheme. Such approach appears to be the most suitable for analyzing in detail the dynamic behavior of hydraulic circuits.

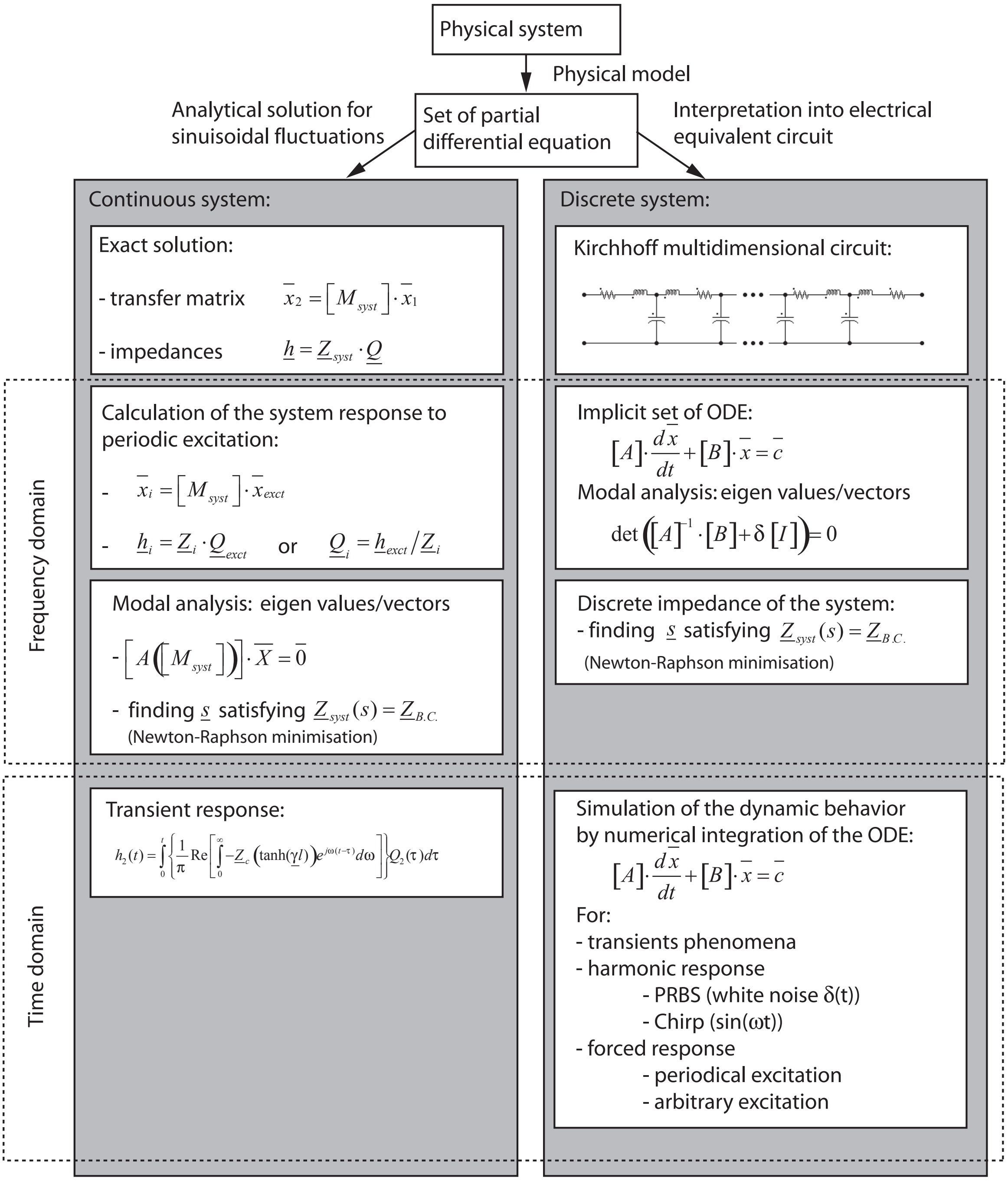

Figure 3.19: Summary of the methods for analyzing dynamic behavior of a pipe.

Chapter 4

Hydroacoustic Characterization of a Pipe

4.1 Case Study Definition: Pipe with Constant Parameters

To illustrate the hydroacoustic modelling methods presented in chapter 3, the case of a single pipe of figure 4.1 is investigated. The pipe is fed by an upstream reservoir and the discharge through the pipe is controlled by a downstream valve. The main characteristics of the problem are summarized in table 4.1.

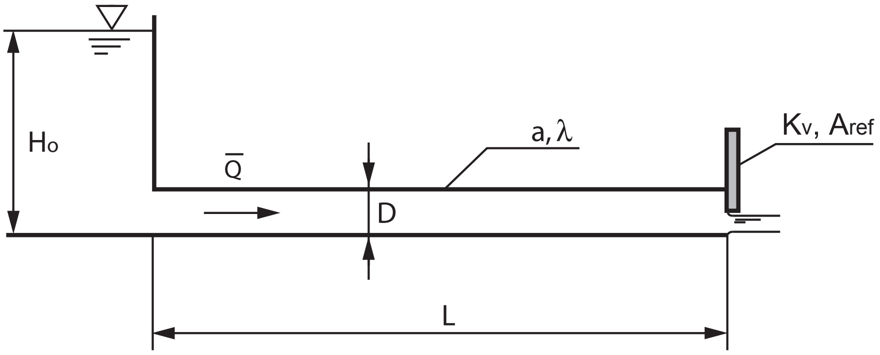

Figure 4.1: Case study of a pipe of length L.

Table 4.1: Parameters of the hydraulic system of figure 4.1.

L $[m]$	D $[m]$	a $[m/s]$	λ $[-]$	Q_o $[m^3/s]$	$f_o = a/(4L)$ $[Hz]$
600	0.5	1200	0.02	0.5	0.5

In order to characterize the hydroacoustic behavior of the above hydraulic installation, both frequency domain and time domain analysis are performed. The frequency domain analysis consists of: (i) a free oscillation analysis, (ii) a forced response, (iii) an impedance calculation of the system. The time domain analysis consists of: (i) the determination of the maximum amplitude of the waterhammer overpressure, (ii) the graphical resolution of the waterhammer problem by the method of the characteristics, (iii) the numerical resolution of the waterhammer problem.

4.2 Frequency Domain Analysis

The hydraulic system of interest includes a valve characterized by a energetic loss coefficient K_v and a reference cross section A_{ref}. The head losses through the valve for a given discharge are given by:

$$H_r = \frac{K_v}{2 \cdot g \cdot A_{ref}^2} Q^2 = R_v \cdot Q \tag{4.1}$$

The valve resistance is given by:

$$R_v = \frac{K_v}{2 \cdot g \cdot A_{ref}^2} \left|\overline{Q}\right| [s/m2] \tag{4.2}$$

The valve impedance $\underline{Z}_v$ can be obtained by linearizing the energetic loss for a mean discharge $\overline{Q}$:

$$dH_r = \frac{K_v}{2 \cdot g \cdot A_{ref}^2} dQ^2 = \frac{K_v}{2 \cdot g \cdot A_{ref}^2} 2 \cdot \overline{Q} \cdot dQ \tag{4.3}$$

The valve impedance is given by:

$$\underline{Z}_v = \frac{\underline{H}(j\omega)}{\underline{Q}(j\omega)} = R_v \cong \frac{dH_r}{dQ} = \frac{K_v}{2 \cdot g \cdot A_{ref}^2} 2 \cdot \overline{Q} \tag{4.4}$$

For a given valve stroke position, the energetic losses can be expressed by:

$$\frac{H_{ro}}{Q_o^2} = \frac{K_v}{2 \cdot g \cdot A_{ref}^2} \tag{4.5}$$

The impedance is finally expressed as function of the nominal values:

$$\underline{Z}_v \cong \frac{K_v}{2 \cdot g \cdot A_{ref}^2} 2 \cdot \overline{Q} = \frac{2 \cdot H_{ro}}{\overline{Q}_o} \tag{4.6}$$

4.2.1 Free Oscillation Analysis

Continuous System

The analytical expression of the eigen frequencies of the system can be determined using the characteristic impedance of the system, equation 3.45. The eigen values of the system are the complex frequencies s satisfying the following boundary conditions:

- for x=0 ; $\underline{Z}_a(0) = 0$;

- for x = L ; $\underline{Z}_a(L) = \underline{Z}_v$.

Introducing the above boundary conditions in equation 3.45 yields to:

$$\underline{Z}_v \cdot \cosh(\underline{\gamma \cdot l}) + \underline{Z}_C \cdot \sinh(\underline{\gamma \cdot l}) = 0 \tag{4.7}$$

The exponential expression of the hyperbolic functions gives:

$$e^{2\cdot\underline{\gamma}\cdot l}\left(\underline{Z}_C + \underline{Z}_v\right) + \left(\underline{Z}_v - \underline{Z}_C\right) = 0 \tag{4.8}$$

Thus:

$$2 \cdot \underline{\gamma} \cdot l = \ln\left((-1)^k \frac{\underline{Z}_C - \underline{Z}_v}{\underline{Z}_C + \underline{Z}_v}\right) + i \cdot (k \cdot \pi) \tag{4.9}$$

Assuming a frictionless pipe gives $\underline{\gamma} = s/a$, $\underline{Z}_C = Z_C = a/(gA)$; and noticing that $\underline{Z}_v = Z_v$, enables the separation of the imaginary and the real part of equation 4.9:

$$\omega = \frac{k \cdot \pi \cdot a}{2 \cdot l} \quad ; k = 1, 2, 3, ... \tag{4.10}$$

And:

$$\sigma = \frac{a}{2 \cdot l} \ln\left((-1)^k \frac{Z_C - Z_v}{Z_C + Z_v}\right) \tag{4.11}$$

As the attribute of logarithm functions must be positive, 2 cases are identified for real positive values of Zc and Zv:

- $Z_v > Z_C$: $\sigma = \frac{a}{2\cdot l} \ln\left(\frac{\underline{Z}_v - \underline{Z}_C}{\underline{Z}_C + \underline{Z}_v}\right)$ and $\omega = \frac{k\cdot\pi\cdot a}{2\cdot l} \quad ; k = 1, 3, 5, ...$ (4.12)

- $Z_v < Z_C$: $\sigma = \frac{a}{2\cdot l} \ln\left(\frac{\underline{Z}_C - \underline{Z}_v}{\underline{Z}_C + \underline{Z}_v}\right)$ and $\omega = \frac{k\cdot\pi\cdot a}{2\cdot l} \quad ; k = 2, 4, 6, ...$ (4.13)

The following conclusion can be drawn:

- if $Z_v > Z_C$, the eigen mode are the odd harmonics; the valve behaves as a dead end;
- si $Z_v < Z_C$, the eigen mode are the even harmonics; the valve behaves as an open end;

Discrete System

For the hydraulic system of figure 4.1 the eigen frequencies and corresponding mode shapes are determined from equation 2.28 for the 2 following boundary conditions:

- 2 open ends ($K_v = 0$) ;
- 1 open and 1 dead end ($K_v = \infty$).

The 3 first eigen modes of the pipe are determined for both above boundary conditions with a model of the pipe made of $n = 100$ elements and are presented in table 4.2. It can be noticed that eigen frequencies computed with the discrete model present good agreement with the eigen frequencies obtained with the continuous model given by equations 4.12 and 4.13.

Table 4.2: Three first eigen mode shape determined with the discrete model with $n = 100$ elements for open/open and open/dead boundary conditions.

 	
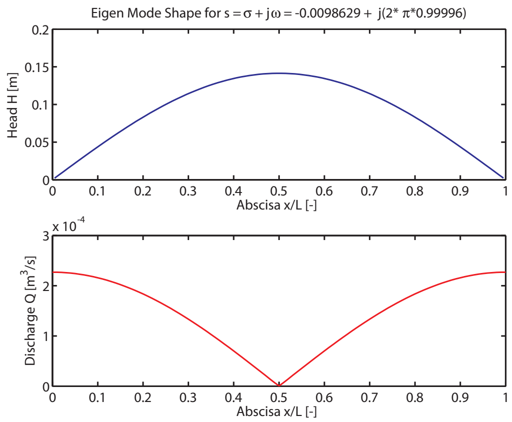 Eigen Mode Shape for s = σ + jω = -0.0098629 + j(2* π*0.99996) 	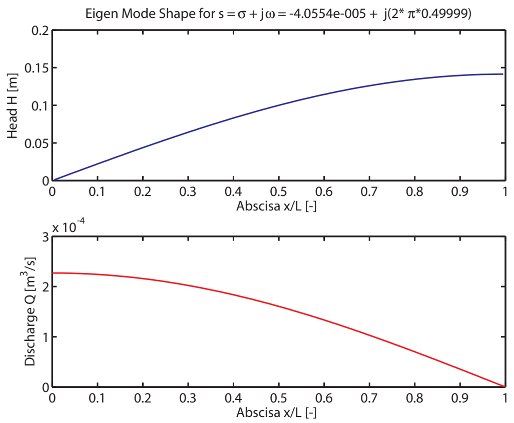 Eigen Mode Shape for s = σ + jω = -4.0554e-005 + j(2* π*0.49999)
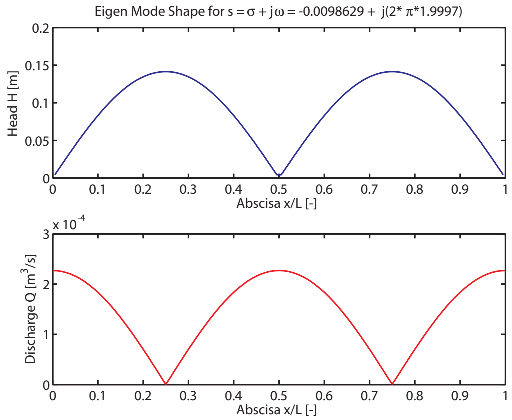 Eigen Mode Shape for s = σ + jω = -0.0098629 + j(2* π*1.9997) 	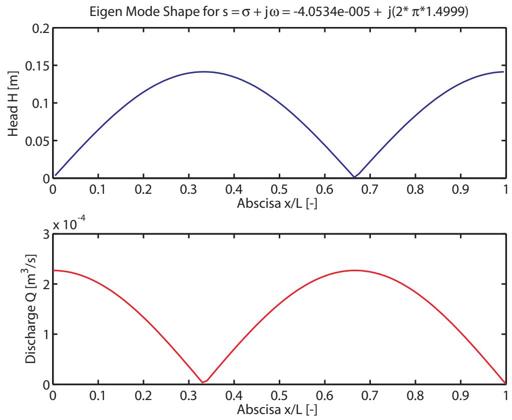 Eigen Mode Shape for s = σ + jω = -4.0534e-005 + j(2* π*1.4999)
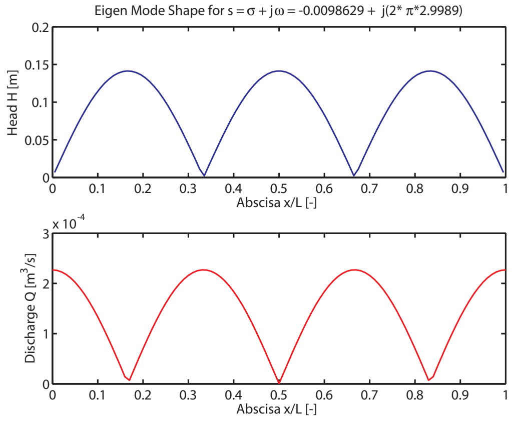 Eigen Mode Shape for s = σ + jω = -0.0098629 + j(2* π*2.9989) 	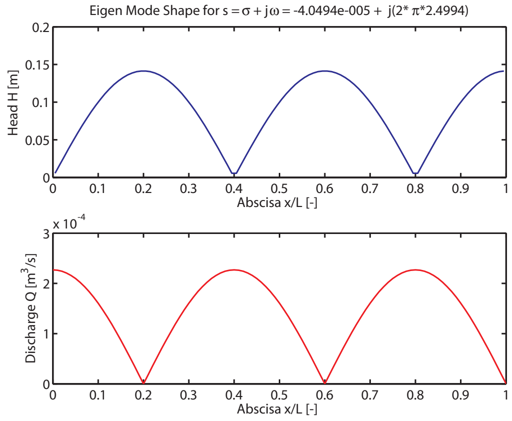 Eigen Mode Shape for s = σ + jω = -4.0494e-005 + j(2* π*2.4994)

Influence of the Number of Elements Modelling the Pipe

Increasing the number of elements n modelling the pipe enables improving the accuracy of the value of the eigen frequencies of the pipe. The evolution of the first eigen frequency f_o of figure 4.1 is reported in figure 4.2 as a function of the number of elements n considering open/dead boundary conditions. It can be seen that a good accuracy on the determination of the first eigen frequency of the pipe is reached from $n = 10$ elements, with an error equal to 0.1%.

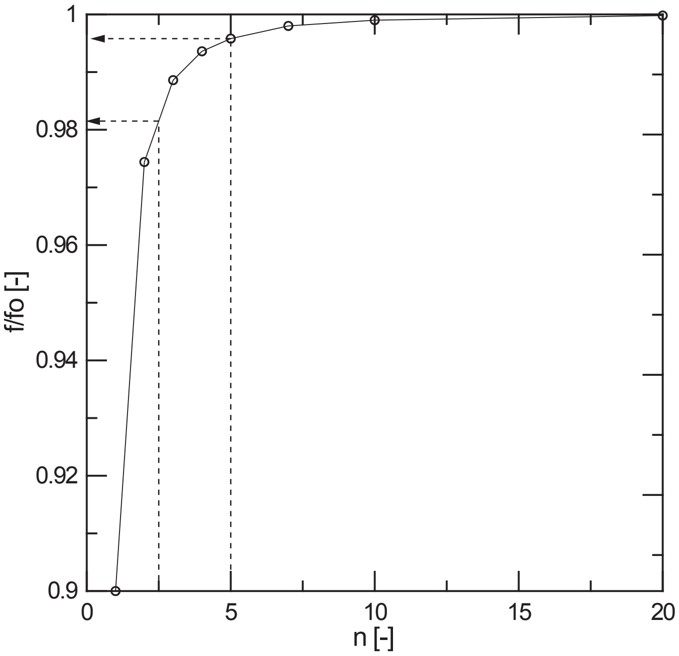

Figure 4.2: First natural frequency f_o as function of the number of elements n modelling the pipe.

The confidence threshold is connected to the number of elements as follow:

$$\frac{\lambda}{dx} = \frac{a}{f \cdot dx} = \frac{a \cdot n}{f \cdot L} \tag{4.14}$$

Therefore:

$$n = \frac{\lambda}{dx} \cdot \frac{f \cdot L}{a} \tag{4.15}$$

For the confidence threshold previously determined the following values are obtained:

- confidence threshold of 3 % : $n = \frac{\lambda}{dx} \cdot \frac{f \cdot L}{a} = 10 \cdot \frac{0.5 \cdot 600}{1200} = 2.5$; from figure 4.2 → 1.85% < 3% ok!;

- confidence threshold of 1 % : $n = \frac{\lambda}{dx} \cdot \frac{f \cdot L}{a} = 20 \cdot \frac{0.5 \cdot 600}{1200} = 5$; from figure 4.2 → 0.42% < 1% ok!.

The above results show good agreement with the confidence threshold.

4.2.2 Forced Response Analysis

The eigen frequencies of the system, see figure 4.1, can be also determined from a time domain simulation with a frequency domain analysis. Therefore, a simulation model made of the upstream reservoir, a pressure source excitation $H(t)$, the studied pipe and the downstream valve is set up. The time domain simulation is performed considering a Pseudo Random Binary Sequence, PRBS, pressure source excitation. The pressure source is in series, and therefore corresponds to a difference of pressure specified between 2 elements (and not the pressure at a given node).

A PRBS signal is a random sequence of number of value 0 or 1. Such a signal is a good approximation of white noise excitation as the energy of the signal is distributed almost uniformly in the frequency domain. The amplitude spectra of a PRBS signal with period $dT = 0.01s$ is presented in figure 4.4 and the corresponding energy spectra of the signal are presented in figure 4.5. This PRBS signal is obtained using a shift register as illustrated by figure 4.6. The energy spectra shows that the energy of the signal is distributed uniformly in the range 0 to 50 Hz.

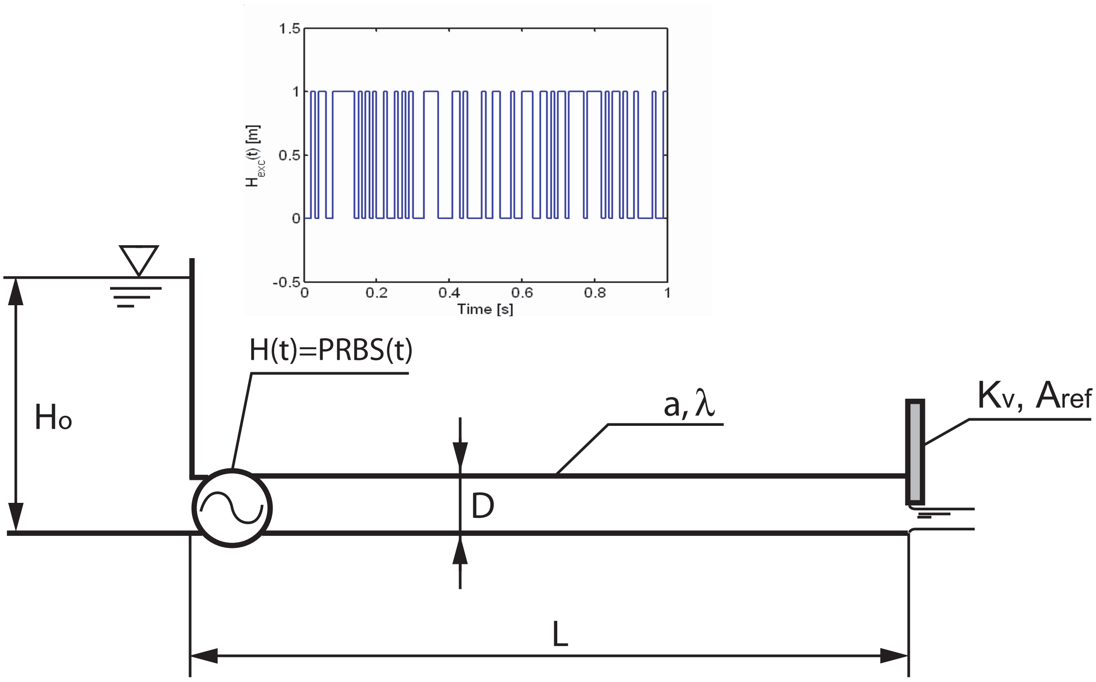

Figure 4.3: Case study including pressure source excitation for forced response analysis.

The simulation of the dynamic behavior of the case study with the pipe modelled by $n = 100$ elements under PRBS pressure source excitation provides the pressure and discharge fluctuations in the time domain. The waterfall diagram representation of the pressure fluctuations reveals the eigen mode and frequencies of the system. The downstream valve opening is selected ranging from open end until dead end conditions, and is characterized using the linearized impedance Z_v. The resulting waterfall diagrams are presented as a function of the rated valve impedance Z_v/Z_c in table 4.3; where Z_c is the

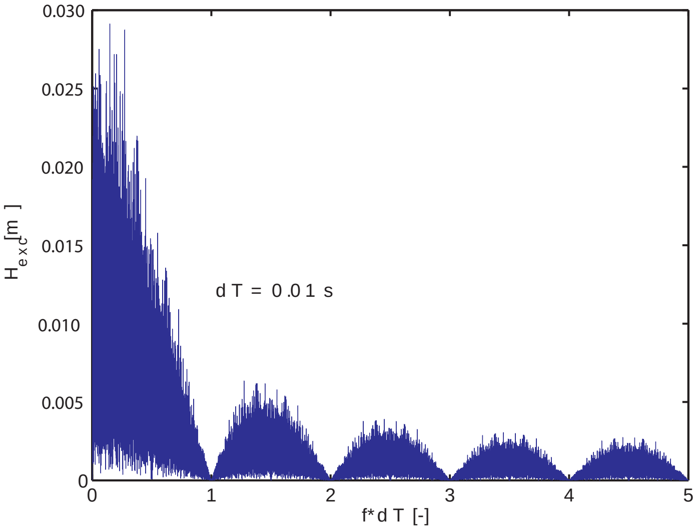

Figure 4.4: Amplitude spectra of a PRBS signal for period $dT = 0.01s$.

characteristic impedance of the pipe. As expected, the resulting eigen modes fulfil the specified boundary conditions.

When $Z_v/Z_c < 1$, according to equation 4.12 the eigen frequencies obtained are given by:

$$f_k = k\frac{a}{2 \cdot L} \quad ; \; k = 1, 2, 3, ... \tag{4.16}$$

When $Z_v/Z_C > 1$, according to equation 4.13 the eigen frequencies are given by:

$$f_k = (2 \cdot k - 1)\frac{a}{4 \cdot L} \quad ; \; k = 1, 2, 3, ... \tag{4.17}$$

When $Z_v/Z_C = 1$, the boundary condition is "anechoic", and there is no wave reflection downstream the pipe and no piping mode shape can be excited. To summarize:

- $f_k = k\frac{a}{2 \cdot L} \quad ; \; k = 1, 2, 3, ...$ for $Z_v/Z_C < 1$, it is an open end;

$$\tag{4.18}$$

- $f_k = (2 \cdot k - 1)\frac{a}{4 \cdot L} \quad ; \; k = 1, 2, 3, ...$ for $Z_v/Z_C > 1$, it is a dead end.

$$\tag{4.19}$$

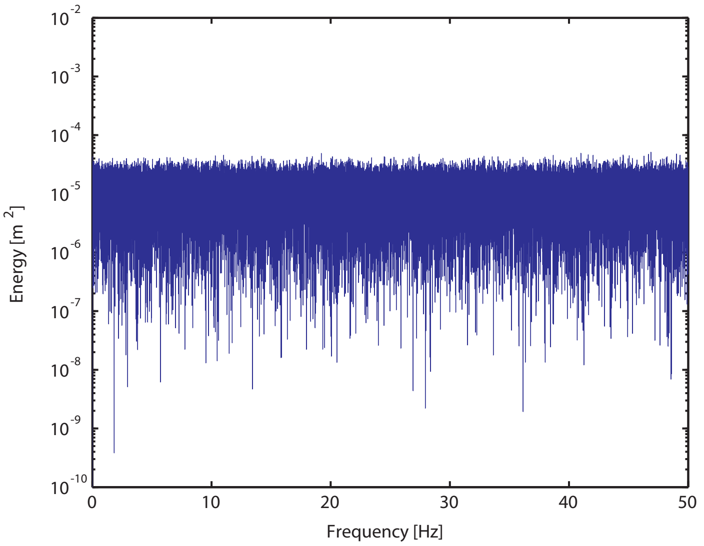

Figure 4.5: Energy spectra of a PRBS signal for period $dT = 0.01s$.

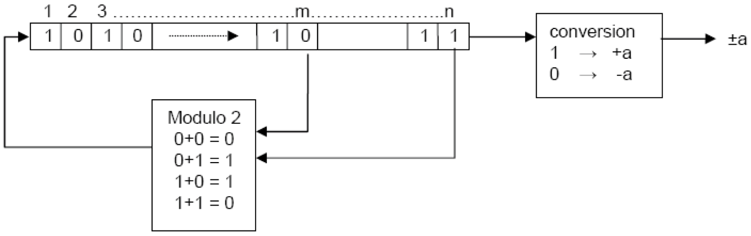

Figure 4.6: Shift register algorithm for generation of PRBS signal.

Table 4.3: Waterfall diagram obtained from PRBS excitation of the pipe with downstream valve.

$Z_v/Z_C = 0$ 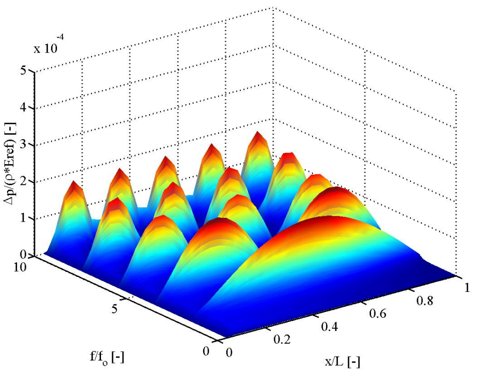	$Z_v/Z_C = 0.96$ 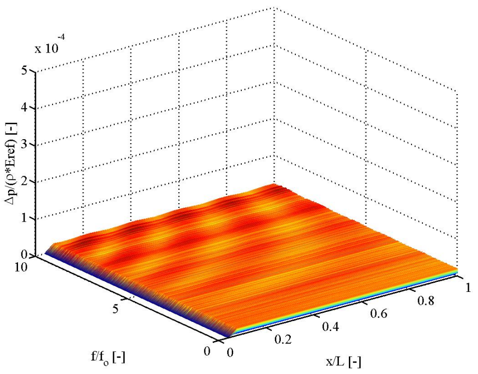
$Z_v/Z_C = 0.04$ 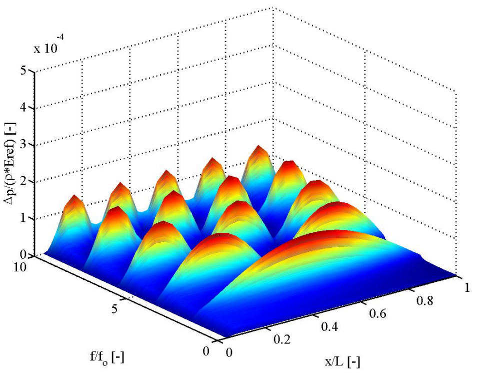	$Z_v/Z_C = 3.13$ 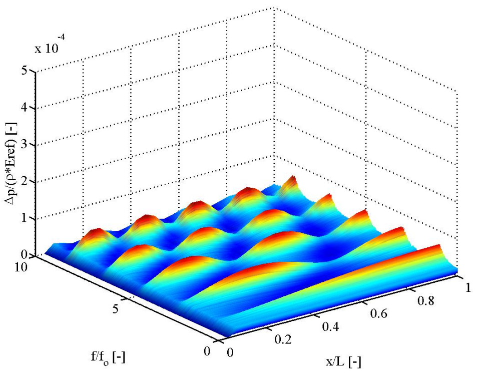
$Z_v/Z_C = 0.25$ 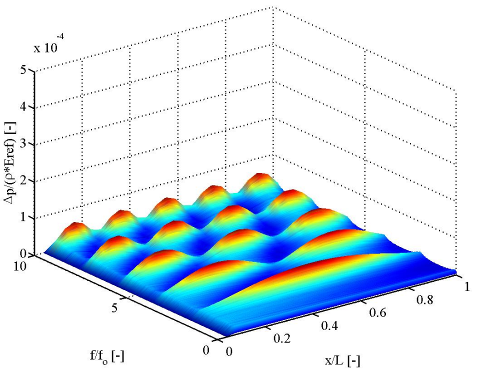	$Z_v/Z_C = 10.1$ 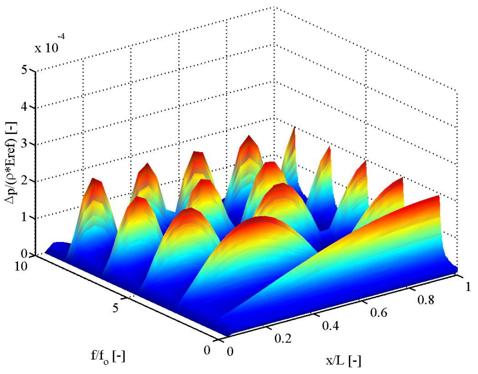

4.2.3 System Impedance

The impedance of the hydraulic system of figure 4.1 can also be calculated using equation 3.76. The impedance of this system $\underline{Z} = \underline{Z}(x, f)$, is calculated assuming an upstream tank impedance $Z = 0$. The magnitude of the impedance divided by the characteristic impedance of the pipe Z_c is represented as a 3D plot function of the rated frequency f/f_o and rated location x/L, see figure 4.7. This impedance reveals 2 pieces of information:

- the impedance downstream the pipe, $|\underline{Z}(x = L, f)|$, providing the determination of the eigen frequencies f_k;
- the longitudinal impedance, $|\underline{Z}(x, f = f_k)|$, providing the location of pressure/discharge minima and maxima.

The downstream impedance corresponds to the front face of the 3D impedance while the longitudinal impedance is a cut at an eigen frequency $f = f_k$. The downstream impedance is extracted from figure 4.7 and presented in figure 4.8.

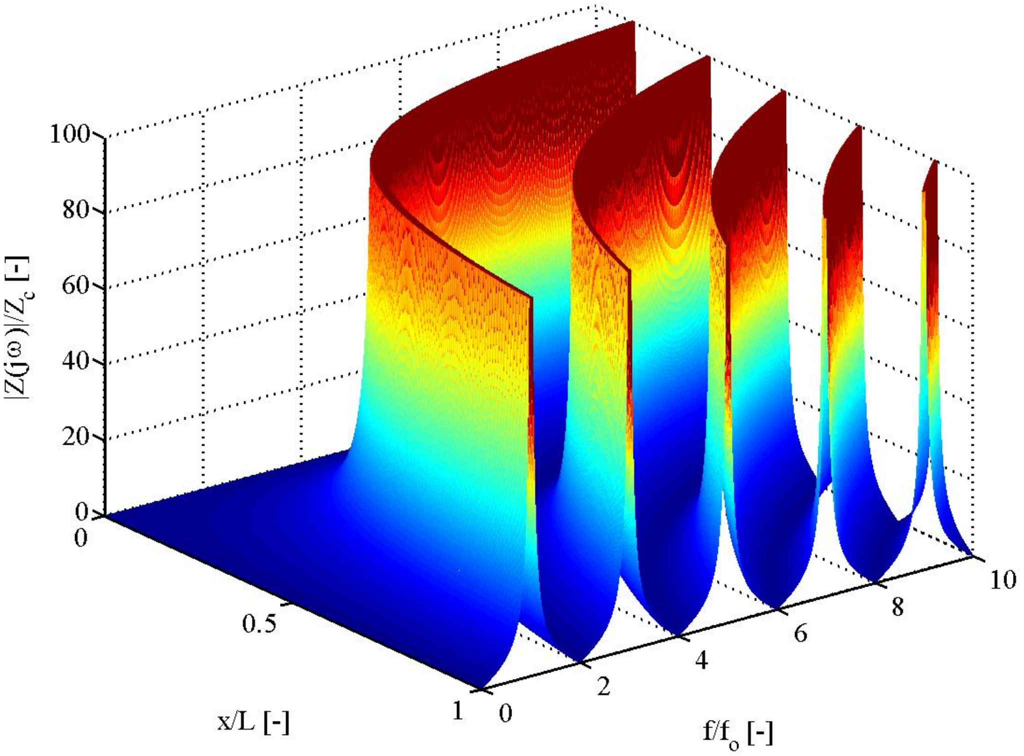

Figure 4.7: Three dimensional representation of the magnitude of the impedance of the pipe.

As the downstream conditions are supposed to be known, it is possible to identify the eigen frequencies of the whole system. The odd modes, $f/f_o = 1, 3, 5, etc$, correspond to the dead end condition $|\underline{Z}(x = L, f)| = \infty$, while the even modes $f/f_o = 2, 4, 6, etc$ correspond to the open end condition $|\underline{Z}(x = L, f)| = 0$. The longitudinal impedance

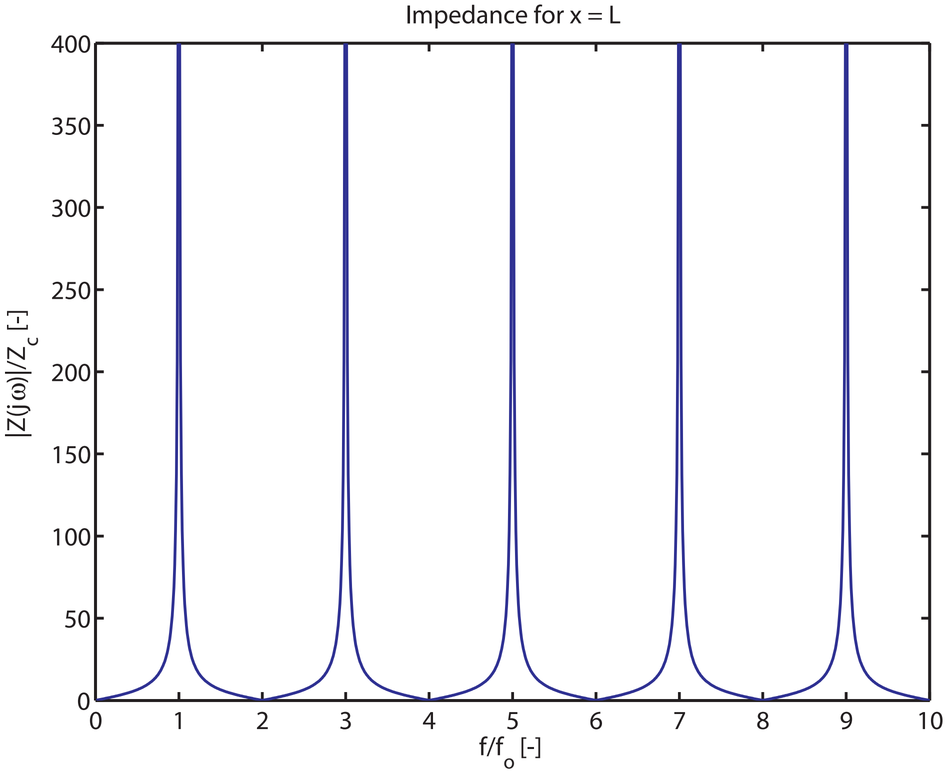

Figure 4.8: Downstream impedance of the pipe.

extracted for the first 4 eigen frequencies identified from figure 4.8 are presented in table 4.4. The minima and maxima of pressure and discharge locations are determined knowing that:

- for $\underline{Z}_x(f_k) = \underline{H}(j\omega)/\underline{Q}(j\omega) = 0$ are the minima of pressure and maxima of discharge;
- for $\underline{Z}_x(f_k) = \underline{H}(j\omega)/\underline{Q}(j\omega) = \infty$ are the maxima of pressure and minima of discharge.

The locations of pressure and discharge minima and maxima present good agreement with the results of table 4.2.

Table 4.4: Longitudinal impedance of the pipe for the different eigen frequencies $f/f_o = 1, 2, 3$ and 4.

$f/f_o = 1$	$f/f_o = 2$
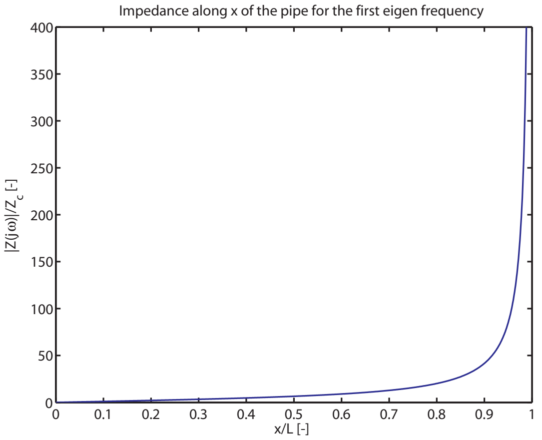	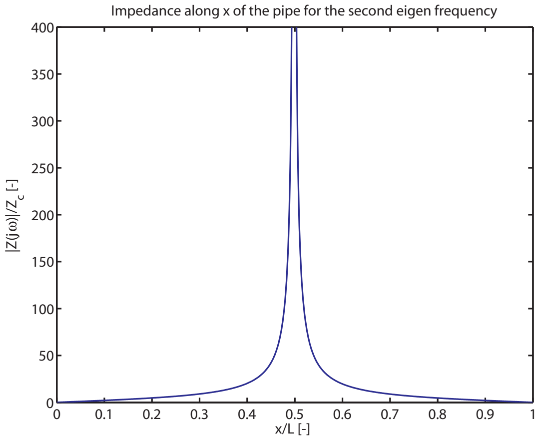
$f/f_o = 3$	$f/f_o = 4$
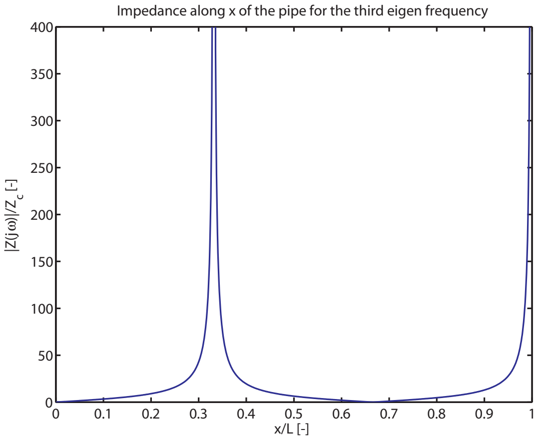	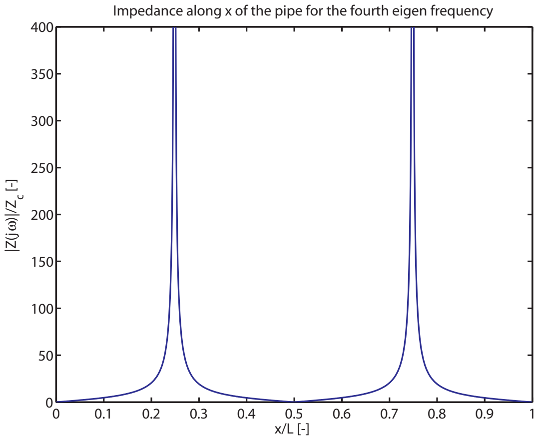

4.3 Transient Behavior Simulation

Waterhammer are produced by sudden closure of valves in piping systems. In this section, the waterhammer problem is treated for the case study of figure 4.1 via 3 different time domain approaches: (i) analytical determination of the overpressure, (ii) graphical resolution, and (iii) numerical simulation.

4.3.1 Determination of the Maximum Amplitude of Waterhammer Overpressure

Applying mass and momentum conservation law to the volume of control $V3$ of figure 4.9 leads to the determination of the overpressure due to the valve closure.

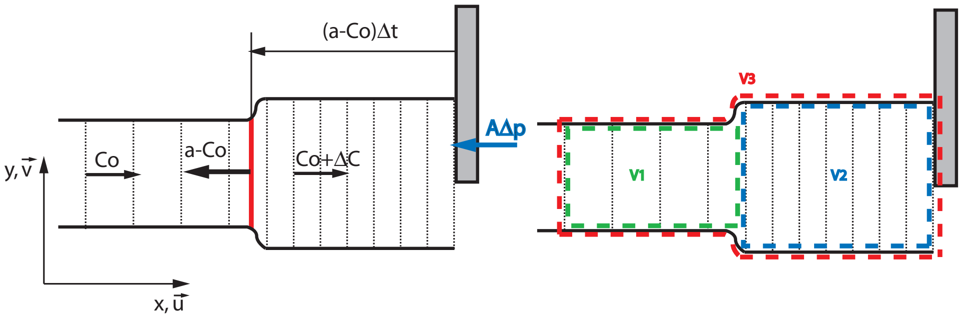

Figure 4.9: Control volume definition at the end of the pipe.

The momentum conservation equation applied to the control volume $V3$ is expressed as:

$$\int_{V3} \frac{\partial}{\partial t}\left(\rho \cdot \vec{C} \cdot \vec{n}\right) dV + \int_{\partial V3} \rho \vec{C} \cdot \left(\vec{C} \cdot \vec{n}\right) dA = \Sigma F_x \tag{4.20}$$

The momentum change in the control volume $V3$ can be decomposed in momentum change in the volumes $V1$ and $V2$:

$$\int_{V3} \frac{\partial}{\partial t}\left(\rho \cdot \vec{C} \cdot \vec{n}\right) dV = \int_{V1} \frac{\partial}{\partial t}\left(\rho \cdot \vec{C} \cdot \vec{n}\right) dV + \int_{V2} \frac{\partial}{\partial t}\left(\rho \cdot \vec{C} \cdot \vec{n}\right) dV \tag{4.21}$$

There is no momentum variation in the volume $V1$ while momentum change in volume $V2$ for a time interval Δt is given by:

$$\int_{V3} \frac{\partial}{\partial t}\left(\rho \cdot \vec{C} \cdot \vec{n}\right) dV = 0 + A(a - C_o)\Delta t \frac{[(\rho + \Delta\rho) \cdot (C_o + \Delta C) - \rho \cdot C_o]}{\Delta t} \tag{4.22}$$

The momentum balance on the surfaces of the volume $V3$ gives:

$$\int_{\partial V3} \rho \vec{C} \cdot \left(\vec{C} \cdot \vec{n}\right) dA = (\rho + \Delta\rho)\left(C_o + \Delta C\right)^2 \cdot A - \rho \cdot A \cdot C_o^2 \tag{4.23}$$

Introducing equations 4.22 and 4.23 in equation 4.20 and expressing the force resulting from the pressure balance yields to:

$$A(a-C_o)\Delta t\frac{[(\rho+\Delta\rho)\cdot(C_o+\Delta C)-\rho\cdot C_o]}{\Delta t}+(\rho+\Delta\rho)\left(C_o+\Delta C\right)^2\cdot A-\rho\cdot A\cdot C_o^2=(p_2-p_1)A \tag{4.24}$$

The mass conservation equation for the same volume $V3$ can be written as:

$$\frac{dM}{dt}=\frac{\partial}{\partial t}\int\limits_{V3}\rho dV+\int\limits_{\partial V3}\rho\cdot\overrightarrow{C}\cdot\overrightarrow{n}\cdot dA=0 \tag{4.25}$$

For a time interval Δt, one gets:

$$A\left(a-C_o\right)\Delta t\frac{[(\rho+\Delta\rho)-\rho]}{\Delta t}-A\left[\rho C_o-(\rho+\Delta\rho)\cdot(C_o+\Delta C)\right]=0 \tag{4.26}$$

Combining equations 4.24 and 4.26 leads to an expression for the overpressure as a function of the velocity change:

$$\Delta p=-\rho A\Delta C \tag{4.27}$$

The overpressure expressed in water column:

$$\Delta H=-\frac{a\cdot\Delta C}{g} \tag{4.28}$$

For a total closure of the valve: $\Delta C=-Co$, leading to the maximum overpressure given by:

$$H_{\max}=\frac{a\cdot C_o}{g} \tag{4.29}$$

4.3.2 Graphical Method of Characteristics (MOC)

The hyperbolic partial differential equations 2.26 can be solved using the method of characteristics [14]. The set of differential equations to be solved is given by:

$$\begin{aligned}L_1&=\frac{\partial Q}{\partial t}+gA\frac{\partial h}{\partial x}+\frac{\lambda Q\left|Q\right|}{2DA^2}=0\\L_2&=gA\frac{\partial h}{\partial t}+a^2\frac{\partial Q}{\partial x}=0\end{aligned} \tag{4.30}$$

The linear combination of the 2 equations above gives:

$$L_1+\mu L_2=0 \tag{4.31}$$

Combining equations 4.30 and 4.31 yields to:

$$\left(\frac{\partial Q}{\partial t}+\mu a^2\frac{\partial Q}{\partial x}\right)+\mu gA\left(\frac{\partial h}{\partial t}+\frac{1}{\mu}\frac{\partial h}{\partial x}\right)+\frac{\lambda Q\left|Q\right|}{2DA^2}=0 \tag{4.32}$$

The piezometric head and discharge are both functions of the location x and the time t, thus:

$$\frac{dh}{dt}=\frac{\partial h}{\partial x}\frac{dx}{dt}+\frac{\partial h}{\partial t} \quad ; \quad \frac{dQ}{dt}=\frac{\partial Q}{\partial x}\frac{dx}{dt}+\frac{\partial Q}{\partial t} \tag{4.33}$$

Identification between equations 4.33 and 4.32 leads to:

$$\frac{dx}{dt}=\frac{1}{\mu}=\mu a^2 \tag{4.34}$$

One obtains:

$$\frac{dQ}{dt}+\mu gA\frac{dh}{dt}+\frac{\lambda Q\left|Q\right|}{2DA^2}=0 \tag{4.35}$$

With:

$$\mu=\pm\frac{1}{a} \tag{4.36}$$

Finally, the following set of equations is obtained:

$$\begin{cases}\dfrac{dQ}{dt}+\dfrac{gA}{a}\dfrac{dh}{dt}+\dfrac{\lambda Q\left|Q\right|}{2DA^2}=0\\ \dfrac{dx}{dt}=a\end{cases} \tag{4.37}$$

$$\begin{cases}\dfrac{dQ}{dt}-\dfrac{gA}{a}\dfrac{dh}{dt}+\dfrac{\lambda Q\left|Q\right|}{2DA^2}=0\\ \dfrac{dx}{dt}=-a\end{cases} \tag{4.38}$$

The above equation sets 4.37 and 4.38 consists of a "compatibility" equation, which is only a function of the time derivative and a characteristic equation given by $dx/dt=\pm a$. To summarize, the linear combination of equations 4.30 leads to the more convenient compatibility equations, but their validity is restricted along the characteristic lines.

For graphical resolution purposes, the equation sets 4.37 and 4.38 are expressed in terms of finite differences while head losses are assumed to be concentrated at one pipe end, yielding to:

$$\begin{cases}\dfrac{\Delta h}{\Delta Q}=-\dfrac{a}{gA}\\ \dfrac{\Delta x}{\Delta t}=a\end{cases} \tag{4.39}$$

$$\begin{cases}\dfrac{\Delta h}{\Delta Q}=+\dfrac{a}{gA}\\ \dfrac{\Delta x}{\Delta t}=-a\end{cases} \tag{4.40}$$

The equation sets 4.39 and 4.40 define straight lines in the diagram $[Q, h]$ with the slopes $\pm a/(gA)$ with respective straight lines in the diagram $[x, t]$ with slopes $\pm a$. Figures 4.10 and 4.11 presents the graphical resolution in both diagram $[x, t]$ and $[Q, h]$ of a waterhammer resulting from a valve closure with $t_{closure} = 4L/a$. The resolution is based on the survey of 2 observers leaving at same time locations A and B, respectively the reservoir and the valve. The 2 observers travel with the wave speed velocity a along the characteristic lines $dx/dt = +/-a$ in the diagram $[Q, h]$, see figure 4.11 left, going forth and back from the valve characteristic $H_v(K_v(t_i))$ and reservoir characteristic $H_o - H_r$. The combination of the journey of the 2 observers in terms of location and time in both diagrams $[x, t]$ and $[Q, h]$, provides the time evolution of the head and the discharge at the valve and reservoir. In addition, the $[Q, h]$ diagram provides the maximum amplitude of the pressure $H_{max} = a \cdot C_o/g$ from the characteristic line starting from the steady state operation $A(t1)$ to the vertical abscissa H. From this characteristic line, it can be stated that:

$$t_{closure} < 2L/a \rightarrow \Delta H = \Delta H_{\max} \tag{4.41}$$

It leads to the expression of the critical closure time of the valve given by:

$$t_{crit} = \frac{2L}{a} \tag{4.42}$$

Finally, it can be noticed that:

- valves closing faster than the critical time t_{crit}, induces the maximum overpressure H_{max};
- valves closing slower than the critical time $t_{crit} = 2(L/a)$ leads to amplitudes below H_{max}.

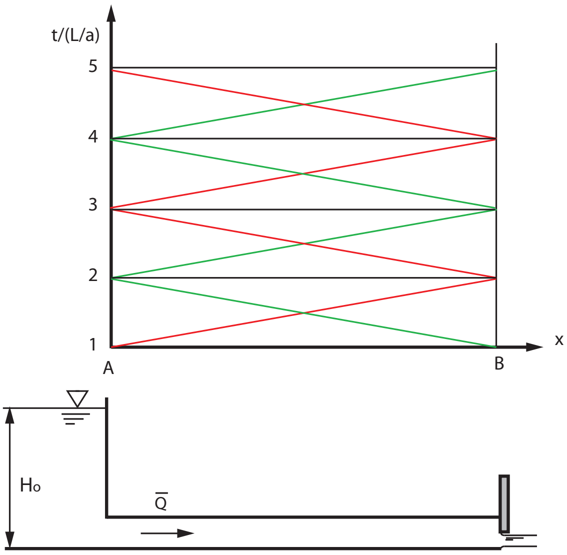

Figure 4.10: Diagram $[x, t]$ for the graphical resolution by the method of the characteristic

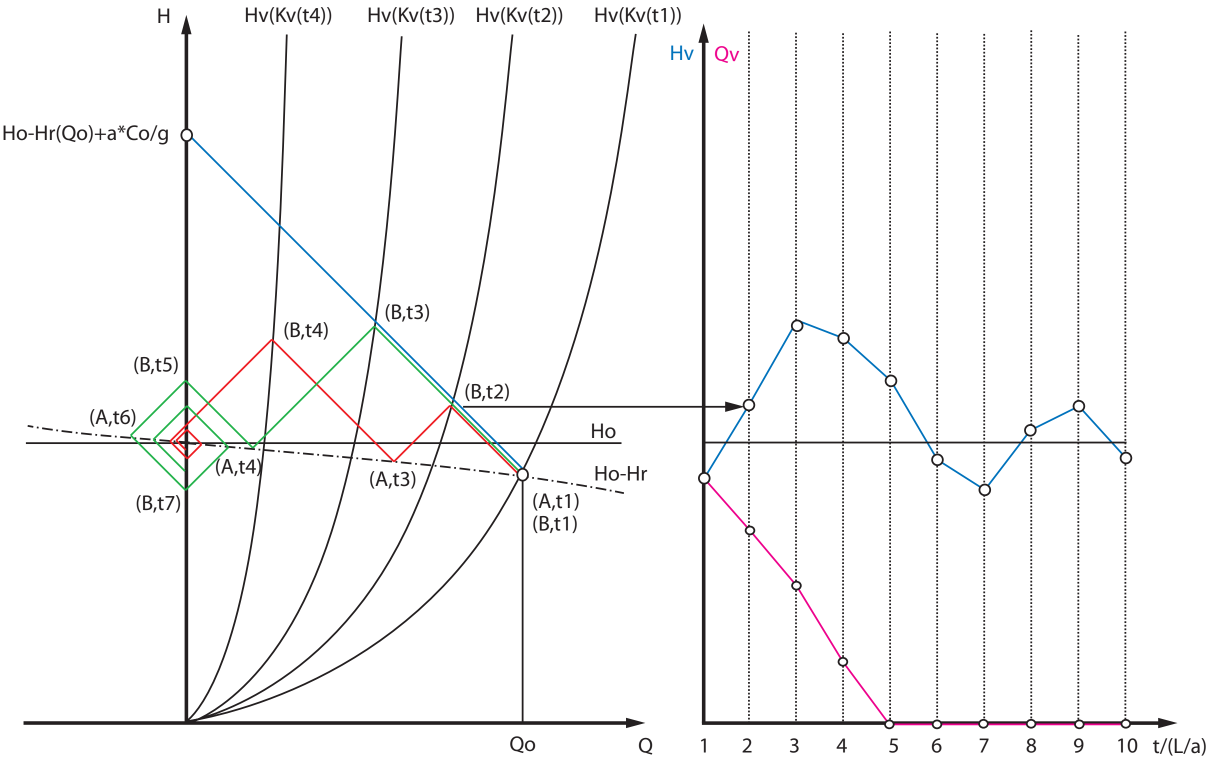

Figure 4.11: Diagram $[Q, h]$ for the graphical resolution by the method of the characteristic and resulting time evolution of the discharge and the pressure.

4.3.3 Numerical Simulation of Waterhammer

The equivalent scheme of the system presented in figure 4.1 is presented in figure 4.12. The equivalent scheme is made of a pressure source Ho, a series of n T-shaped equivalent schemes of elements of length dx and a variable resistance modelling the downstream valve.

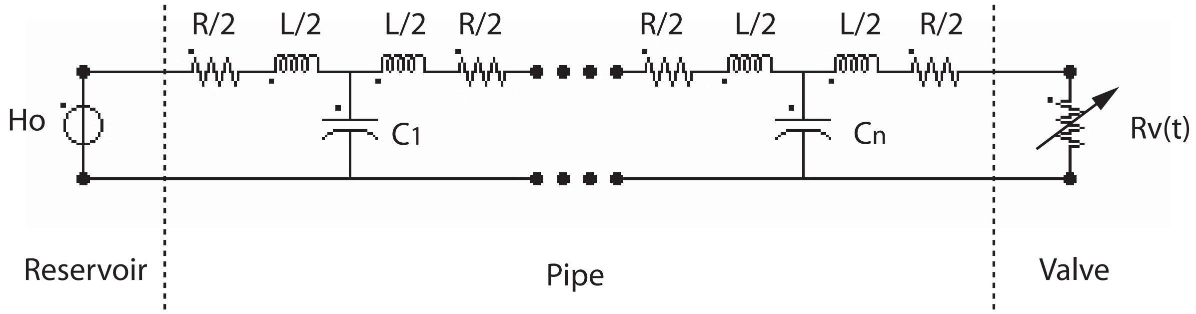

Figure 4.12: Equivalent scheme of the case study.

The downstream valve is closed according to:

$$y_1 = 1 - \left(\frac{t - T_{start}}{T_{closure}}\right)^{0.75} \tag{4.43}$$

With:
T_{start}: time at the start of the closure $[s]$
T_{close} : valve closure time $[s]$

The valve loss coefficient is defined as follows:

$$K_v(t) = \frac{K_{vo}}{y_1(t)^2} \tag{4.44}$$

Applying Kirchhoff's law to the equivalent scheme of figure 4.12 leads to a set of ordinary differential equations given by:

$$[A] \cdot \frac{d\overline{x}}{dt} + [B] \cdot \overline{x} = \overline{C} \tag{4.45}$$

This system is solved by using the 4^{th} order explicit Runge-Kutta method. The simulation parameters are summarized in table 4.5.

Table 4.5: Simulation parameters

$n[-]$	$dt[s]$	$T_{close}[s]$
50	0.005	2.1

The critical time of the valve closure for the case study is $t_{crit} = 2L/a = 1$ s. As a result, the amplitude of the waterhammer overpressure with a valve closing time of 2.1 s is below the maximum overpressure H_{max}. The time evolution of the head at the valve, H_v, of the discharge at the valve, Q_v and of the discharge at the reservoir, Q_b, are represented in figure 4.13. It can be noticed that the discharge at the valve decreases until zero within the valve closure time inducing an overpressure at the valve of amplitude $0.8 \cdot Ho$. The maximum overpressure occurs at the instant $T_{start} + 2L/a$.

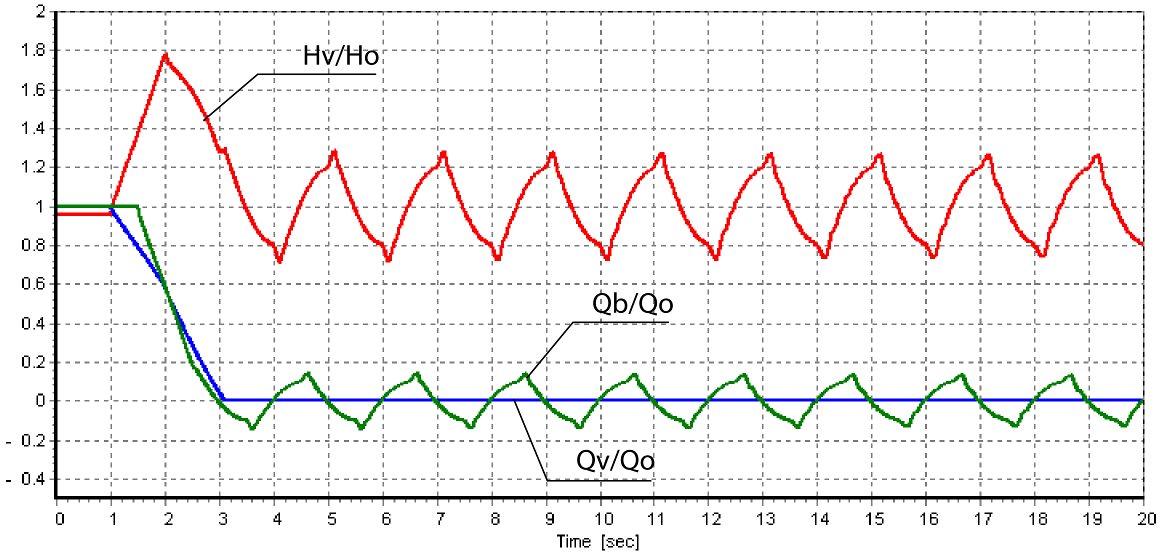

Figure 4.13: Time evolution in rated values of the head at the valve H_v/Ho, the discharge at the valve Q_v/Qo and of the discharge at the reservoir Q_b/Qo resulting from a valve closure in $2.1s$, *i.e.* $4.2L/a$.

The simulation results obtained with the equivalent scheme are compared with the simulation results obtained by MOC solved using a finite difference method. The comparison of the simulation results is presented for the head at the valve and the discharge at the reservoir in table 4.14. The results obtained with the equivalent scheme show good agreements with the ones obtained with MOC.

The results of the simulation of the valve closure in 0.2s $(0.1 \cdot t_{crit})$ are presented in figure 4.15. The maximum amplitude of $H_v/Ho = 3$ is reached after the full valve closure for $t = 0.2s$. The time evolution of the pressure exhibits square shape with period $T = 4L/a$.

The piezometric line along the pipe is represented in figure 4.16 for 8 different times extending from $t_o + T/8$ to $t_o + T$ with $T = 4L/a$. This representation evidences the pressure wave propagation and also shows the steep slope of the pressure wave propagating in the pipe for a valve closure time below the critical time t_{crit}. The pipe experiences successively overpressure and underpressure phases lasting each $2L/a$. The 4 phases are summarized in figure 4.17.

Figure 4.15 depicts numerical instabilities visible on the head signal and on the discharge signal at the valve. The longer the simulation, the higher the numerical instabilities. These simulation errors are amplified at each wave reflection owing to the fact that the model of the pipe is of the second order in the middle of the pipe but only of the first order at the end. Furthermore, the quicker the valve closure, the higher the amplitude

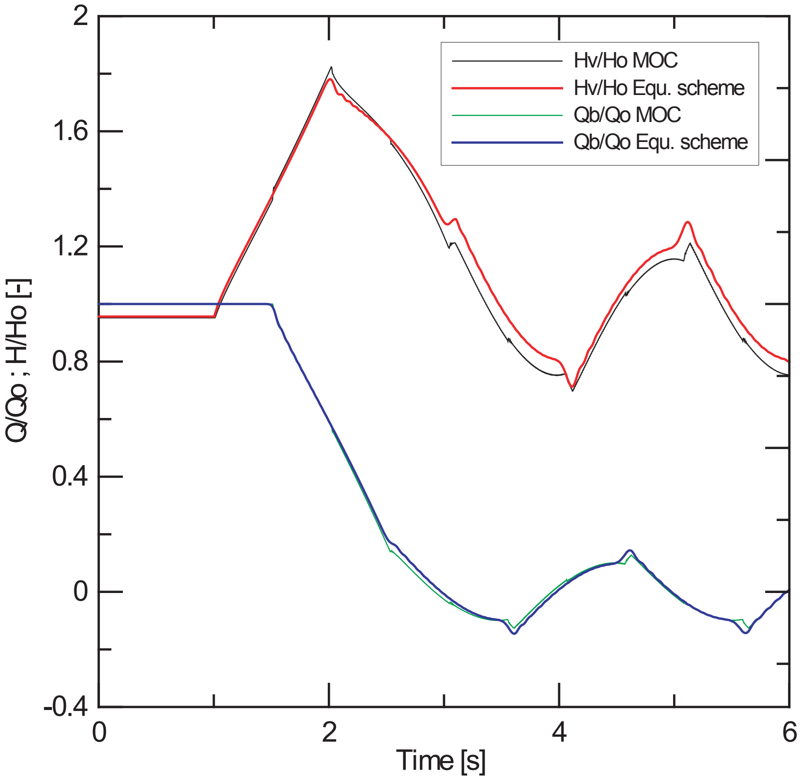

Figure 4.14: Comparison of the time evolution of the pressure at the valve (left) and discharge at the reservoir (right) obtained with equivalent scheme and method of characteristic (MOC).

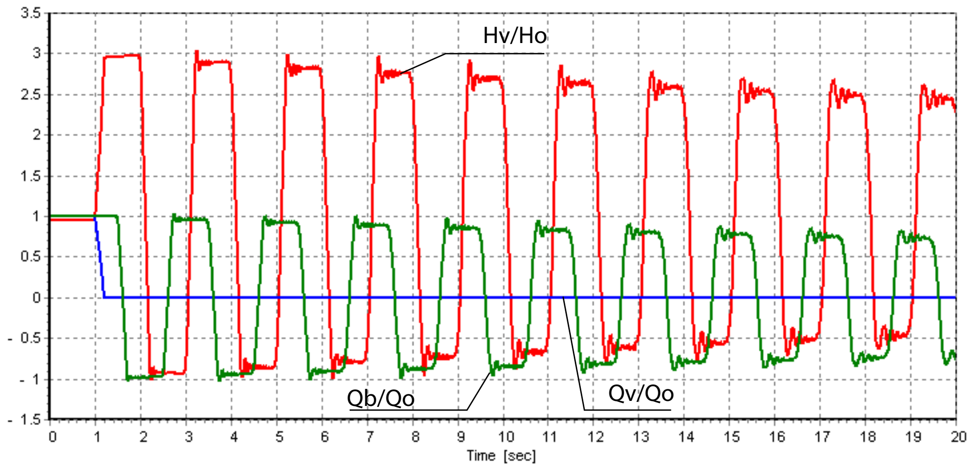

Figure 4.15: Time evolution of the rated head at the valve H_v/Ho, of the rated discharge at the valve Q_v/Qo and of the rated discharge at the reservoir Q_b/Qo resulting from valve closure in $0.2s$, $(0.4 \cdot L/a)$.

of the numerical instabilities because the frequency content of the pressure wave shape becomes higher and thus requires a higher number of elements to properly model the phenomenon. Figure 4.18 shows how numerical instabilities can be reduced by increasing the number of elements n from 10 to 100. This means that for simulating an instantaneous valve closure, an infinite number of elements would be required and therefore, infinitely small time steps. The influence of the integration method on the numerical instabilities is discussed in appendix A.

For the real cases encountered in the operation of hydropower plants, instantaneous valve closures are not supposed to be experienced. Indeed, designing the pipe walls with a thickness capable of supporting the maximum amplitudes of waterhammer overpressure or underpressure is not possible for economical reasons. Thus, the appropriate spatial discretization must be a compromise between computational time and simulation accuracy.

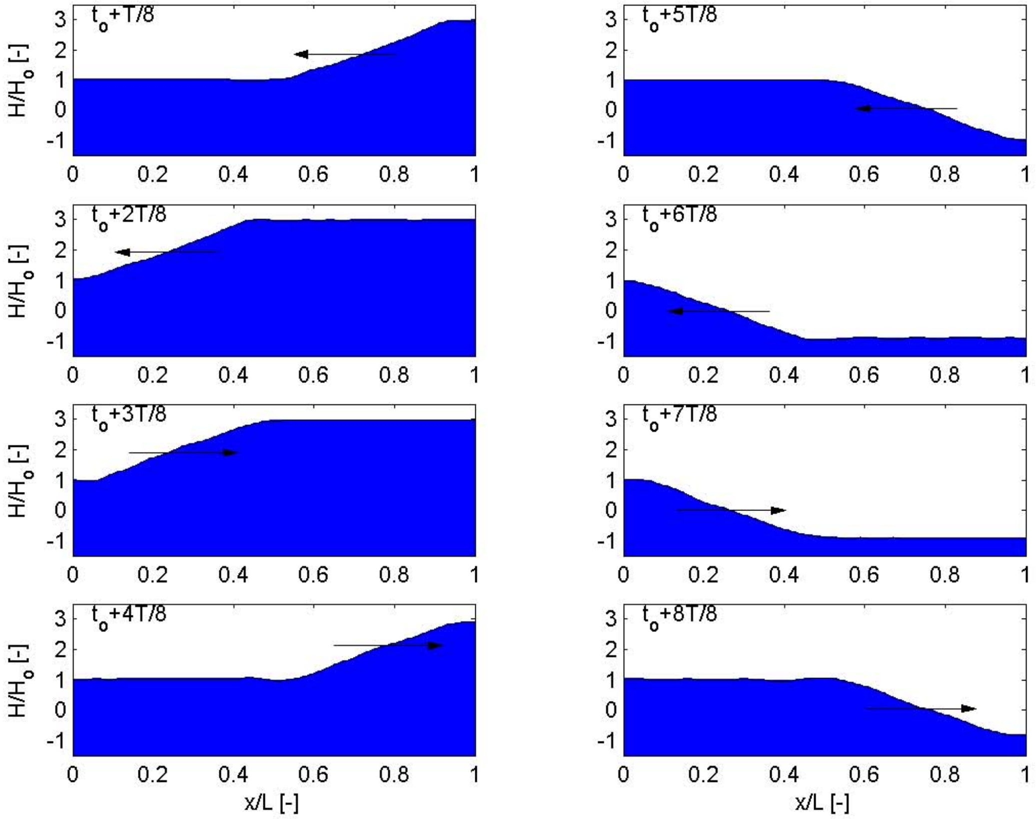

Figure 4.16: Piezometric line along the piping for different time ($T = 4L/a$).

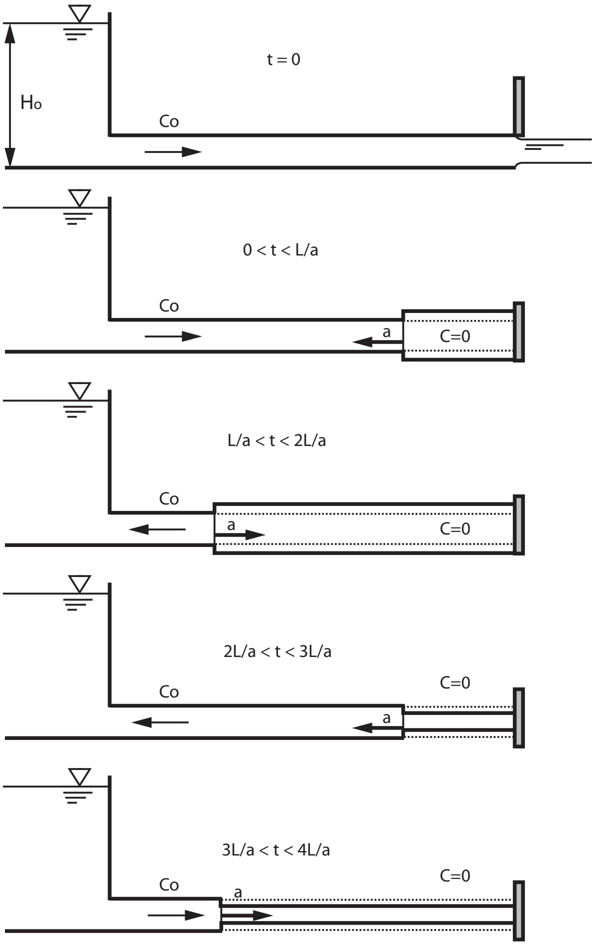

Figure 4.17: Definition of the 4 phases of the waterhammer.

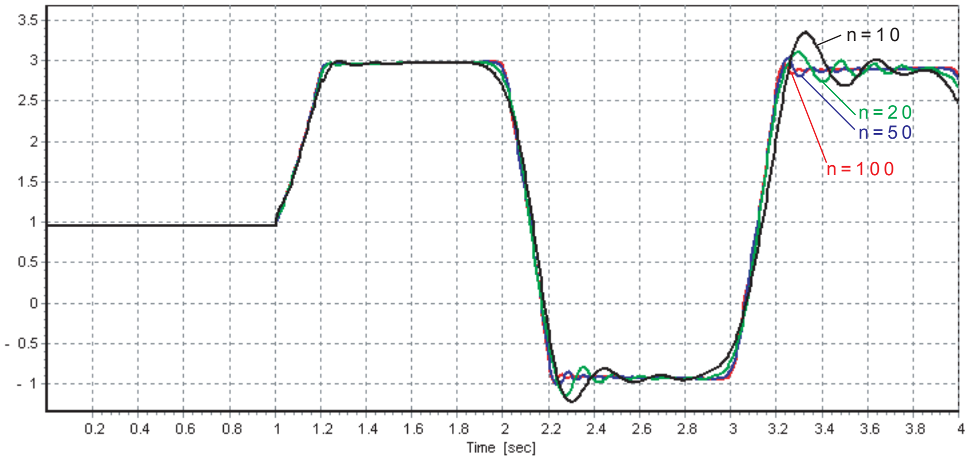

Figure 4.18: Comparison of the time evolution of the head at the valve for different spatial discretizations of the pipe.

Chapter 5

Modelling of Hydraulic Components

5.1 Circuit Components Modelling

The hydraulic circuits of hydroelectric power plants are made of several components that have to be included to model its dynamic behavior. The modelling of the following components are presented: (i) elastic or viscoelastic pipe, (ii) valve, (iii) surge tank, (iv) surge shaft, (v) air vessel, (vi) cavitating flow.

5.1.1 Pipe

The pipe model is the key component of the hydroacoustic modelling. In most of industrial applications pipes are made of metallic materials with elastic behavior. However, recent developments in the domain of polymer materials has brought a wide range of new materials to hydraulic installations. PVC for industrial applications and fiber glass for prototyping are 2 examples of polymers that are commonly used in the construction of hydraulic circuits.

Many polymers materials exhibit a viscoelastic behavior that induces additional damping in the systems that has to be properly taken into account especially for stability analysis purposes. Therefore, the model of the pipe presented in chapter 3 is extended for taking into account possible viscoelastic effects of the pipe wall material. The concept of viscoelastic behavior is also extended to the fluid.

Elastic Pipe

The model of the pipe derived from the momentum and mass equations leads to the representation of pipe of length dx by an equivalent electrical circuit made of 2 resistances, 2 inductances and one capacitance as presented in figure 5.1.

This modelling approach can be extended to a full length pipe by considering n equivalents schemes in series as shown in figure 5.2.

Viscoelastic Pipe

Viscoelastic materials present dynamic behavior as stress σ in the material is not only proportional to the rated deformation $\varepsilon = dl/l$ but is also function of the rate of defor-

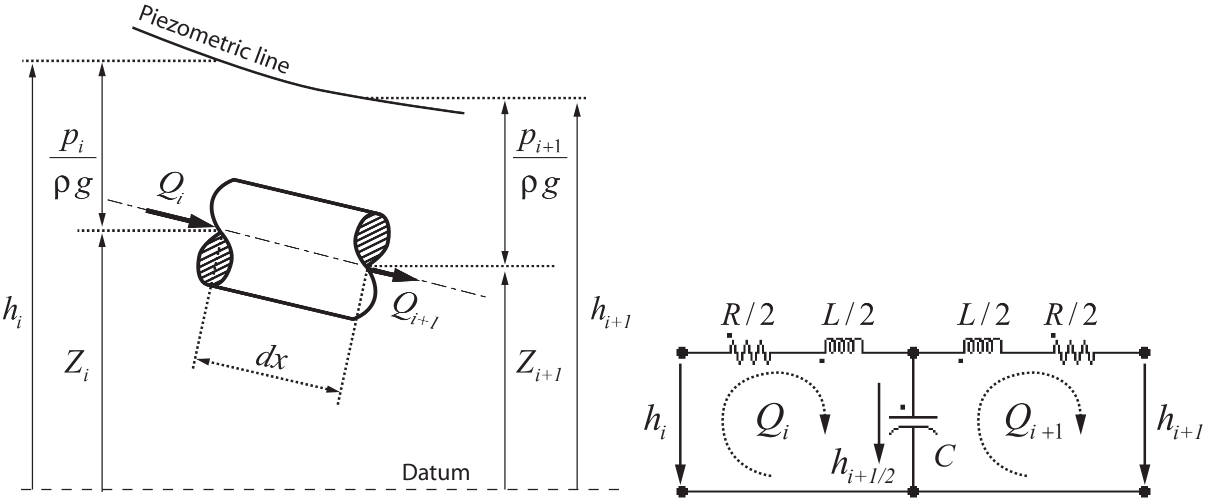

Figure 5.1: Modelling of a pipe of length dx (left), with the corresponding equivalent scheme (right).

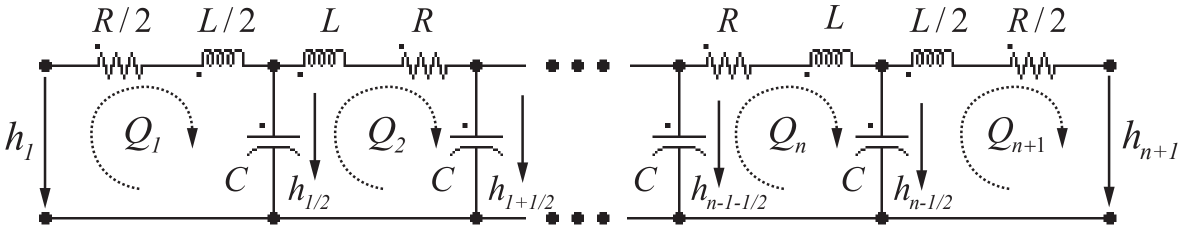

Figure 5.2: Full length pipe model made by n elements.

mation $d\varepsilon/dt$. Figure 5.3 shows typical time evolution of the stress as a function of the rated deformation for viscoelastic materials.

The modelling of the viscoelastic behavior can be achieved using rheologic models made of springs and dashpots. Maxwell's, Kelvin-Voigt's and Standard models are 3 common rheologic models presented in table 5.1 with their equivalent electrical schemes. Theses models are elementary models from which more advanced models can be derived.

Without loss of generality, a viscoelastic pipe accounting for both pipe material and water viscoelasticity can be modelled by 2 Kelvin-Voigt models as presented in figure 5.4. Therefore, considering first the pipe wall material viscoelastic behavior and assuming a pipe perimeter deflection $\varepsilon = dD/D$ due to pressure increase leads to:

$$\sigma = E_{pipe} \cdot \varepsilon + \mu_{pipe} \cdot \frac{d\varepsilon}{dt} = E_{pipe} \cdot \frac{dD}{D} + \mu_{pipe} \cdot \frac{1}{D} \cdot \frac{d(dD)}{dt} \tag{5.1}$$

The total derivative of the volume of the pipe V of length dx is given by:

$$dV = d(\pi D^2/4) \cdot dx = \frac{\pi \cdot D}{2} dD \tag{5.2}$$

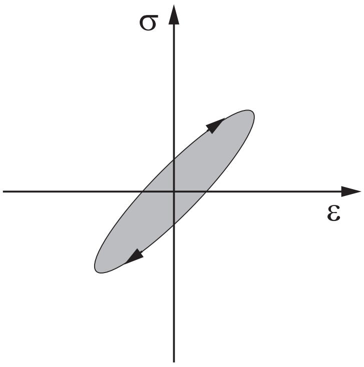

Figure 5.3: Stress as function of the deformation for a viscoelastic material.

Table 5.1: Rheologic models of viscoelastic materials and their equivalent scheme.

Model	Rheologic model	Equivalent scheme	Equations
Maxwell	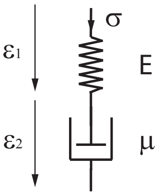	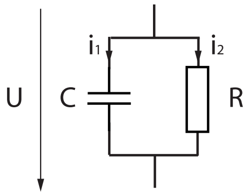	$\sigma = \varepsilon_1 \cdot E = \mu \cdot \frac{d\varepsilon_2}{dt}$ $U = \frac{1}{C}\int i_1 \cdot dt = R \cdot i_2$
Kelvin-Voigt	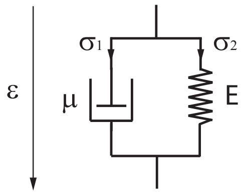	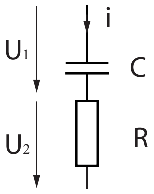	$\sigma = \sigma_1 + \sigma_2 = \varepsilon \cdot E + \mu \cdot \frac{d\varepsilon}{dt}$ $U = U_1 + U_2 = \frac{1}{C}\int i \cdot dt + R \cdot i$
Standard	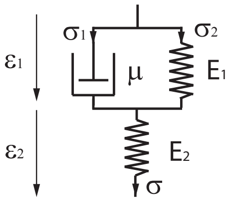	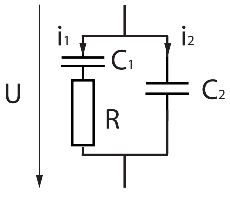	$\sigma = \varepsilon_2 \cdot E_2 = \varepsilon_1 \cdot E_1 + \mu \cdot \frac{d\varepsilon_1}{dt}$ $\varepsilon = \varepsilon_1 + \varepsilon_2$ $U = \frac{1}{C_2}\int i_2 \cdot dt$ $U = \frac{1}{C_1}\int i_1 \cdot dt + R \cdot i_1$ $i = i_1 + i_2$

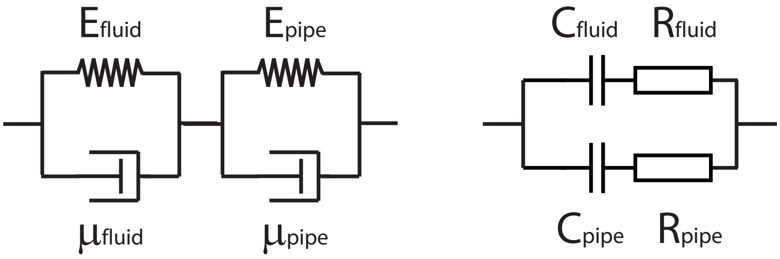

Figure 5.4: Rheologic (left) and equivalent (right) models of a viscoelastic pipe with contribution of water and and pipe material viscoelastic behavior.

Introducing the piezometric head, $h = p/(\rho g) + z$, in equation 2.18, and neglecting vertical displacement of the pipe ($dz/dt = 0$), gives:

$$\frac{d\sigma}{dt} = \frac{D\rho g}{2e} \cdot \frac{dh}{dt} \tag{5.3}$$

Combining equations 5.1, 5.2 and 5.3 and introducing the stored discharge $Q_p = dV/dt$ leads to:

$$\frac{dh}{dt} = \frac{E_{pipe}e}{AD\rho gdx} \cdot Q_p + \frac{\mu_{pipe}e}{AD\rho gdx} \cdot \frac{dQ_p}{dt} \tag{5.4}$$

By integrating equation 5.4, one gets Kelvin-Voigt's equation of the pipe wall material:

$$h = \frac{1}{C_{pipe}} \int Q_p \cdot dt + R_{pipe} \cdot Q_p \tag{5.5}$$

Where the viscoelastic resistance R_{pipe} and capacitance C_{pipe} of a pipe of length dx are given by:

$$R_{pipe} = \frac{\mu_{pipe}e}{AD\rho gdx} \quad ; \quad C_{pipe} = \frac{AD\rho gdx}{E_{pipe}e} \tag{5.6}$$

Then, considering the fluid compressibility from equation 2.14 and the second viscosity μ_{fluid} leads to:

$$\frac{dp}{dt} = \frac{E_{fluid}}{\rho} \cdot \frac{d\rho}{dt} + \frac{\mu_{fluid}}{\rho} \cdot \frac{d^2\rho}{dt^2} \tag{5.7}$$

Reintroducing the piezometric head $h = p/(\rho g) + z$ and the stored discharge due to fluid compressibility $Q_f = -\frac{V}{\rho} \cdot d\rho/dt$ gives:

$$\frac{dh}{dt} = \frac{E_{fluid}}{A\rho gdx} \cdot Q_f + \frac{\mu_{fluid}}{A\rho gdx} \cdot \frac{dQ_f}{dt} \tag{5.8}$$

By integration of equation 5.8, one gets Kelvin-Voigt's equation of the pipe fluid:

$$h = \frac{1}{C_{fluid}} \int Q_f \cdot dt + R_{fluid} \cdot Q_f \tag{5.9}$$

Where the viscoelastic resistance R_{fluid} and capacitance C_{fluid} of a pipe of length dx are given by:

$$R_{fluid} = \frac{\mu_{fluid}}{A\rho g dx} \quad ; \quad C_{fluid} = \frac{A\rho g dx}{E_{fluid}} \tag{5.10}$$

It can be noticed that:

- both viscoelastic resistances are proportional to the invert of the length of the pipe dx;
- the viscoelastic losses are proportional to the discharge and **not** to the square of the discharge.

It can be also noticed that, if, in the model of the pipe of figure 5.4, the 2 viscoelastic resistances of the fluid and of the wall material are neglected, the 2 capacitances in parallel are equivalent to the capacitance of the elastic pipe:

$$C_{equ} = C_{pipe} + C_{fluid} = A\rho g dx \left[\frac{D}{E_{pipe}e} + \frac{1}{E_{fluid}}\right] = \frac{gAdx}{a^2} \tag{5.11}$$

In the same way, if compressibility effects are neglected, the 2 viscoelastic resistances in parallel can be expressed as:

$$R_{equ} = \frac{1}{\frac{1}{R_{pipe}} + \frac{1}{R_{fluid}}} = \frac{1}{A\rho g dx} \cdot \frac{1}{\frac{D}{\mu_{pipe}e} + \frac{1}{\mu_{fluid}}} = \frac{\mu_{equ}}{A\rho g dx} \tag{5.12}$$

From the strict modelling point of view, a viscoelastic pipe is modelled by considering the equivalent scheme of figure 5.4 made of 2 Kelvin-Voigt models for both the pipe material and the fluid instead of the single capacitance of the elastic pipe model of table 5.1 (right). From the practical point of view, the determination of either the second viscosity of the fluid or the viscosity of the pipe material is very difficult to perform with good accuracy. However, experiments described by Haban *et al.* [66] have provided data for a pipe filled with water. In this case, the equivalent viscosity is determined rather than the fluid viscosity as in the experiment both viscosity contributions can not be dissociated. As a result, it is very convenient to use a model made only of one Kelvin-Voigt model of the whole pipe and accounting for both the fluid and the pipe material. In this model the capacitance is calculated according to equation 5.11 and the viscoelastic resistance R_{ve} is calculated according to equation 5.12. The resulting model is presented in figure 5.5.

5.1.2 Valve

A valve induces head losses in hydraulic systems which are function of the valve obturator position s. The head losses through a valve are given by:

$$H_v = \frac{K_v(s)}{2gA_{ref}^2} \cdot Q_i^2 \tag{5.13}$$

With K_v the valve head loss coefficient. Therefore the valve corresponds to a variable resistance function of the obturator position. The valve hydraulic resistance is given by:

$$R_v(s) = \frac{K_v(s)}{2gA_{ref}^2} \cdot |Q_i| \tag{5.14}$$

The valve equivalent scheme is presented in figure 5.6.

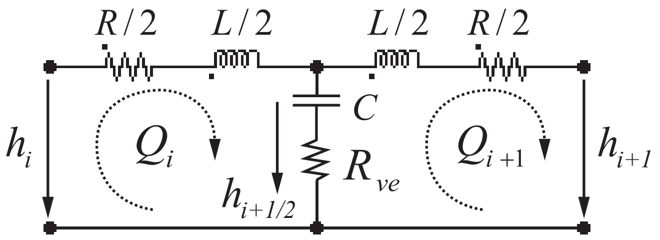

Figure 5.5: Equivalent scheme of a viscoelastic pipe of length dx.

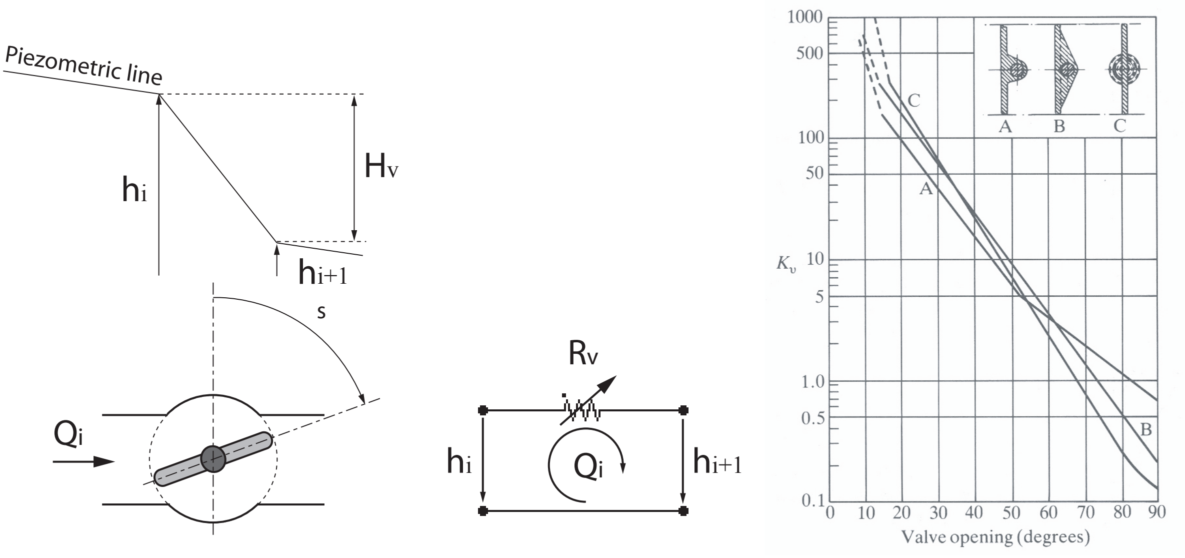

Figure 5.6: Valve modelling with the example of a butterfly valve characteristic [105].

5.1.3 Surge Tank

The surge tank is a protection device against waterhammer effect behaving as a free surface for wave reflection but where the water level is function of the discharge time history. Surge tanks sometimes feature a cross section being function of the elevation z. The volume of the surge tank is therefore expressed as the integral of the cross section $A(Z)$ along the elevation Z and is given by:

$$V_{ST} = \int A(z)dz \tag{5.15}$$

The time derivative of the surge tank volume is:

$$\frac{dV_{ST}}{dt} = A(z) \cdot \frac{dz}{dt} \tag{5.16}$$

Noticing that the volume variation of the water in the surge tank is equivalent to the stored discharge $Q_c = dV_{ST}/dt$ and introducing the piezometric head h_c leads to:

$$A(z) \cdot \frac{dh_c}{dt} = Qc \tag{5.17}$$

Equation 5.17 evidences the capacitive behavior of the surge tank whose capacitance is directly the surge tank cross section:

$$C_{ST} = A(z) \tag{5.18}$$

The flow incoming and leaving the surge tank is subject to sudden cross section changes and therefore energetic losses. It is common to have a diaphragm at the surge tank inlet in order to increase the damping of water level oscillations. The head losses through the diaphragm or the sudden change of cross section are given by:

$$H_d = \frac{K_d}{2gA_{ref}^2} \cdot Q_c^2 \tag{5.19}$$

With K_d, the diaphragm head loss coefficient $[-]$. The corresponding hydraulic resistance is given by:

$$R_d(Q_c) = \frac{K_d(Q_c)}{2gA_{ref}^2} \cdot |Q_c| \tag{5.20}$$

The head at the T-junction H_{ST} is given by:

$$H_{ST} = h_c + R_d(Q_c) \cdot Q_c \tag{5.21}$$

It can be noticed that the diaphragm loss coefficient K_d is usually function of the discharge amplitude and direction: $K_d = K_d(Q_c)$. The equivalent scheme of the surge tank is made of a resistance and a capacitance in series as presented in figure 5.7. The discharge incoming into the surge tank Q_c is equal to the difference of the discharges at the T-junction and is given by:

$$Q_c = Q_i - Q_{i+1} \tag{5.22}$$

5.1.4 Surge Shaft

Surge shafts are surge tanks with small cross sections. If the surge tank inductance effects can be neglected as the inductance is inversely proportional to the cross section $L = l/(gA)$, it is not anymore the case for the surge shaft. The inductance related to the water inside the surge shaft is given by integrating the inductance along elevation axis z and is given by:

$$L_{SS} = \int_{z_{min}}^{h_c} \frac{dz}{g \cdot A(z)} = \frac{h_c - z_{min}}{g \cdot \overline{A}} \tag{5.23}$$

The capacitance and resistance of the surge shaft have the same expression as that of the surge tank and are given by:

$$R_d(Q_c) = \frac{K_d(Q_c)}{2gA_{ref}^2} \cdot |Q_c| \quad \text{and} \quad C_{SS} = A(z) \tag{5.24}$$

The head at the T-junction H_{SS} is then given by:

$$H_{SS} = h_c + R_d(Q_c) \cdot Q_c + L_{SS} \cdot \frac{dQ_c}{dt} \tag{5.25}$$

The resulting surge shaft equivalent scheme is presented in figure 5.8.

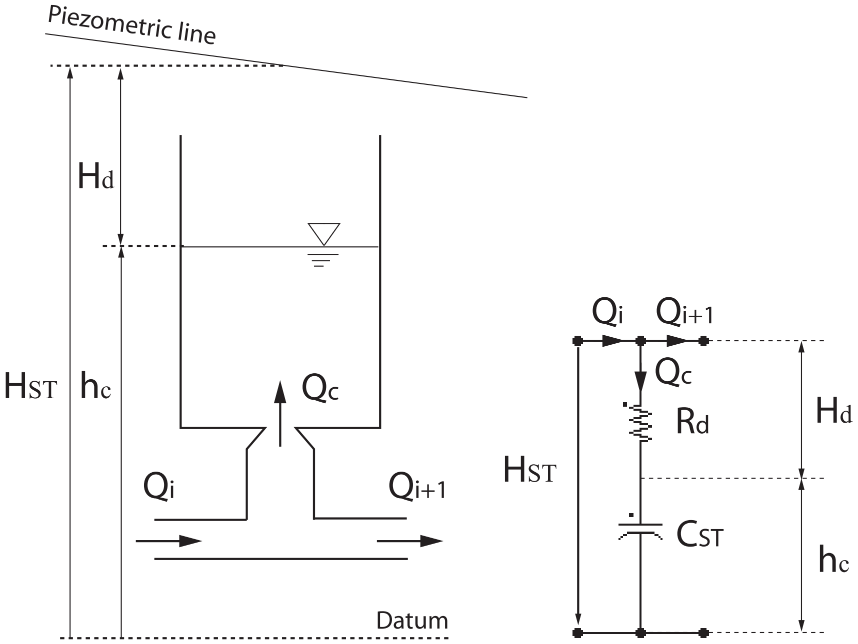

Figure 5.7: Surge tank model.

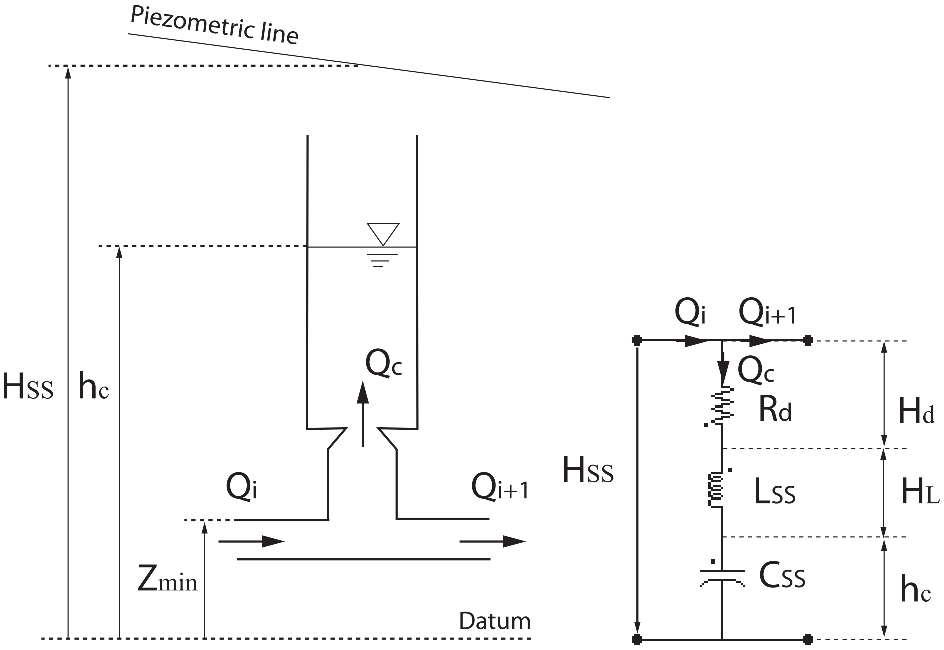

Figure 5.8: Surge shaft model.

5.1.5 Air Vessel

Air vessels are used for mitigating pressure fluctuations induced in hydraulic systems by pumps, vortex shedding, valves openning/closure, etc. The water level h_c changes in the vessel lead to capacitive behavior. The stored discharge Q_c and the cross section are linked as follows:

$$A(z) \cdot \frac{dh_c}{dt} = Qc \tag{5.26}$$

The capacitance is given by:

$$C_{AV} = A(z) \tag{5.27}$$

The gas volume is varying due to water level changes. Assuming a polytropic transformation of the gas leads to:

$$h_g \cdot V_g^n = cste \tag{5.28}$$

The total derivative of equation 5.28 gives:

$$h_g \cdot n \cdot V_g^{n-1} \cdot dV_g + V_g^n \cdot dh_g = 0 \tag{5.29}$$

After rearrangement, and introducing the stored discharge Q_c yields to:

$$\frac{V_g}{h_g \cdot n} \cdot \frac{dh_g}{dt} = -\frac{dV_g}{dt} = Q_c \tag{5.30}$$

Equation 5.30 evidences the non-linear capacitive behavior of the gas volume for which the capacitance is given by:

$$C_{AV}(V_g, h_g) = \frac{V_g}{h_g \cdot n} \tag{5.31}$$

The head at the junction H_{AV} is then given by:

$$H_{AV} = h_c + h_g \tag{5.32}$$

The equivalent scheme of the air vessel is therefore made of 2 capacitances in series as presented in figure 5.8.

5.1.6 Cavitating Flow

The development of cavitation in fluid flows is known to be a source of instabilities for the whole hydraulic system. It was found that cavitation does not only represent a passive additional compliance to the flow [27] but can play a crucial role of self excitation source like of the famous POGO effect in propulsion systems of aerospace aircrafts [128]. The stability of such system was studied using an one-dimensional approach to model the cavitation development with lumped elements. The volume of a cavitation development is function of the head and discharge, therefore the total derivative of the volume is given by:

$$V(Q,h)_{i+1} \Rightarrow dV = \frac{\partial V}{\partial h_{i+1}} \cdot dh_{i+1} + \frac{\partial V}{\partial Q_{i+1}} \cdot dQ_{i+1} \tag{5.33}$$

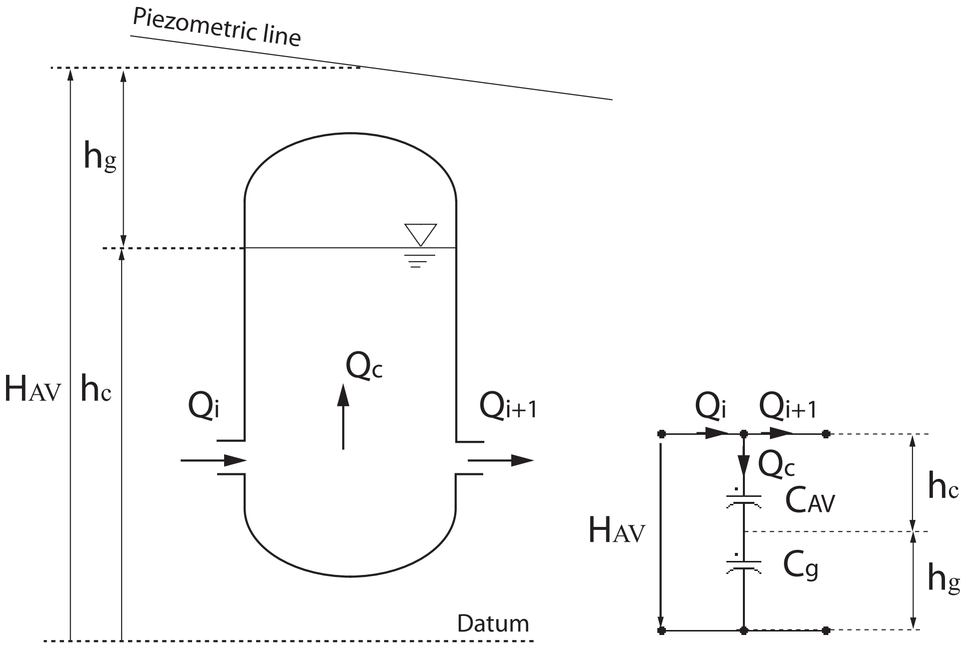

Figure 5.9: Air vessel model.

Time variation is given by:

$$\frac{dV}{dt} = \frac{\partial V}{\partial h_{i+1}} \cdot \frac{dh_{i+1}}{dt} + \frac{\partial V}{\partial Q_{i+1}} \cdot \frac{dQ_{i+1}}{dt} \tag{5.34}$$

Defining:

- the cavity compliance $C = -\frac{\partial V}{\partial h}$;
- the mass flow gain factor $\chi = -\frac{\partial V}{\partial Q_{i+1}}$.

yields to:

$$Q_i - Q_{i+1} = Q_c = C \cdot \frac{dh_{i+1}}{dt} + \chi \cdot \frac{dQ_{i+1}}{dt} \tag{5.35}$$

In addition, no losses or inertia effects are considered, and leads to:

$$h_i = h_{i+1} \tag{5.36}$$

Cavitation development can be modelled using equations 5.35 and 5.36. The resulting equivalent scheme of the cavitation development is made of 1 capacitance as presented in figure 5.10. The representation of the mass flow gain factor is difficult as it is kind of mutual inductance effect and it is represented in figure 5.10 only by the χ value referring to the discharge Q_{i+1}

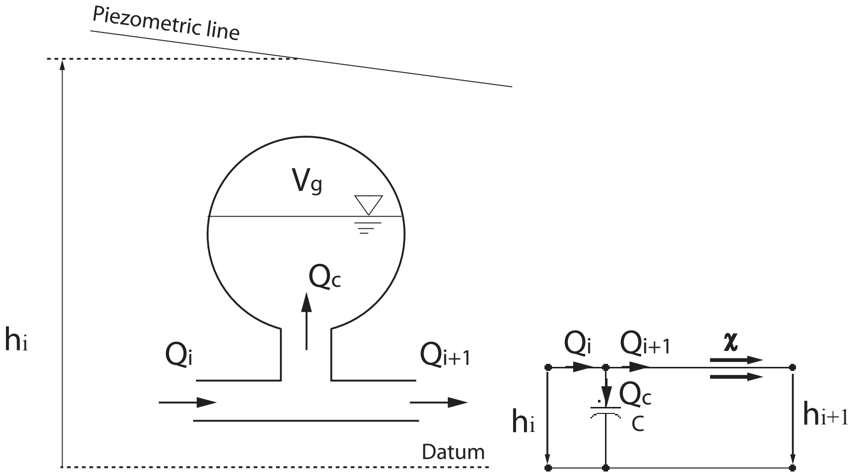

Figure 5.10: Cavitating flow model.

5.2 Quasi Static Modelling of Hydraulic Machines

5.2.1 General

There are 3 different types of hydraulic machines that are commonly used in the context of hydroelectric power production: (i) the Francis turbine, or pump-turbine, (ii) the Pelton turbine and (iii) the Kaplan turbine.

For safety purposes, the transient behavior of the entire hydraulic system comprising the turbine must be undertaken with appropriate turbine models. However, during the exploitation, these hydraulic machines are subject to off design operations where 3D complex flow structures such as flow separations, secondary flows, reverse flows, vortices, cavitation development arise. Mathematical modelling of such flows leads to Computational Fluid Dynamic codes, which are nowadays far from being able to provide the transient turbine parameters at a reasonable computational time with sufficient accuracy for all the flow regimes experienced during transients. Therefore, experimental data are required for the modelling of the dynamic behavior of turbines and pump-turbines. It is assumed that the transient behavior of the hydraulic machines can be accurately simulated by considering that the machines are experiencing a succession of different steady state operating points and therefore, can be modelled using the static characteristic of the machine [90]. These models are called "quasi-static" models.

An operating point of a hydraulic machine is characterized by 5 quantities: the specific energy E, the discharge Q, the rotational speed N, the torque T, and the guide vane opening y. Therefore, the graphical representation of a turbine characteristic requires the elimination of one of these quantities by the use of the hydraulic machines similitude laws. For efficiency purposes, where the rotational speed can be considered to be constant, it is convenient to use the dimensionless representation with φ , ψ and τ. For transients analysis, it is more convenient to use dimensional factors where the specific energy E is eliminated. These factors are given by:

$$N_{11} = \frac{N \cdot D_{ref}}{\sqrt{(E/g)}} \quad ; \quad Q_{11} = \frac{Q}{D_{ref}^2 \cdot \sqrt{(E/g)}} \quad ; \quad T_{11} = \frac{T}{D_{ref}^3 \cdot E/g} \tag{5.37}$$

The modelling of hydraulic turbines based on the quasi-static approach is described below.

5.2.2 Francis Pump-Turbine

Francis pump-turbines are reaction turbines, *i.e.* they convert both kinetic and potential energy of the fluid into mechanical work. The Francis turbine features fixed blades and therefore the discharge through the turbine is controlled by the distributor. Figure 5.11 presents a vertical cutting plan of a Francis turbine.

Figure 5.12 presents a 4 quadrants characteristic of a Francis pump-turbine having a specific speed of $\nu = 0.217$. The discharge and torque factors are represented as a function of the speed factor with the guide vane opening y as parameter; all values are rated by the best efficiency point (BEP) value.

Some of the curves $Q_{11} = Q_{11}(N_{11})$ of the pump-turbine characteristics of figure 5.12 exhibit a typical pump-turbine "S" shape between the 1^{st} and the 4^{th} quadrants leading to numerical troubles for the interpolation of the Q_{11} values in the surface characteristics

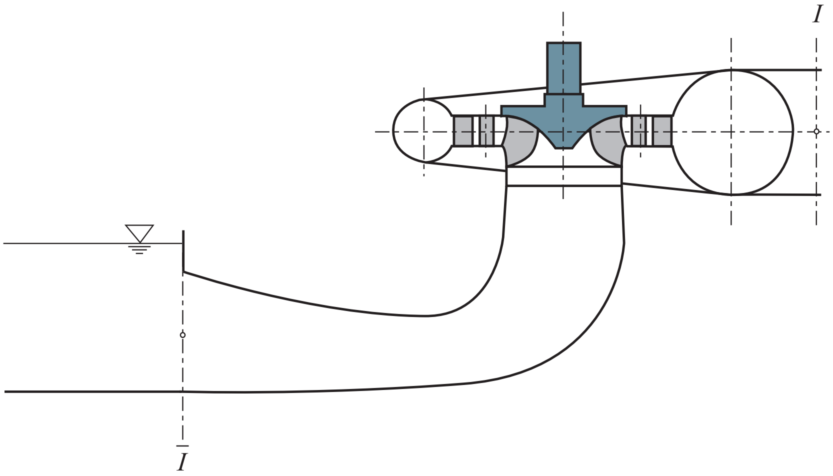

Figure 5.11: Francis turbine cutting plan.

as illustrated in figure 5.13. This problem has been successfully solved by Marchal *et al.* [101] who used a polar representation of the turbine characteristics. The polar coordinates are defined in the plane $N_{11} - Q_{11}$. Accordingly the polar angle θ is given by:

$$\theta = \operatorname{atan}\left(\frac{Q_{11}/Q_{11BEP}}{N_{11}/N_{11BEP}}\right) \tag{5.38}$$

After simplification:

$$\theta = \operatorname{atan}\left(\frac{Q/Q_{BEP}}{N/N_{BEP}}\right) \tag{5.39}$$

The radial coordinate of the polar representation is defined as:

$$r(\theta)^2 = \left(Q_{11}/Q_{11BEP}\right)^2 + \left(N_{11}/N_{11BEP}\right)^2 \tag{5.40}$$

Lets introduce the new parameter $W_H(\theta)$:

$$W_H(\theta) = \frac{1}{r(\theta)^2} \tag{5.41}$$

After rearranging the terms:

$$W_H(\theta) = \frac{H/H_{BEP}}{\left(Q/Q_{BEP}\right)^2 + \left(N/N_{BEP}\right)^2} \tag{5.42}$$

A new parameter $W_B(\theta)$ is introduced for the torque and is given by:

$$W_B(\theta) = W_H(\theta) \cdot \frac{T_{11}}{T_{11BEP}} = \frac{T/T_{BEP}}{\left(Q/Q_{BEP}\right)^2 + \left(N/N_{BEP}\right)^2} \tag{5.43}$$

The polar representation of the turbine characteristics of figure 5.12 is presented in figure 5.14. This representation has the advantage of preserving the similitude law. However, numerical troubles appears for closed guide vanes where there is no discharge and

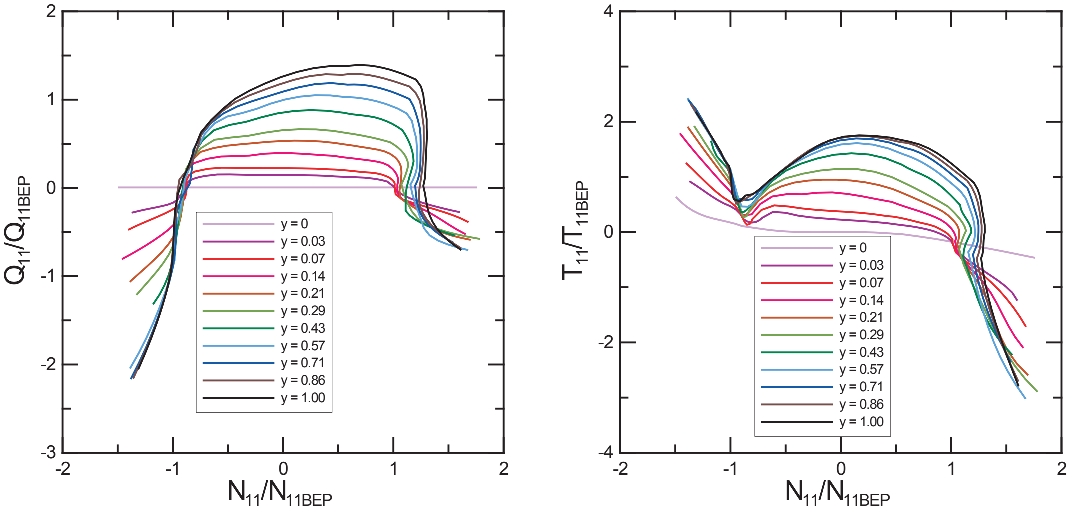

Figure 5.12: 4 quadrants characteristics of a turbine with specific speed $\nu = 0.217$.

therefore the abscissa θ is equal either to 0 or to π. This problem can be overcome by introducing a small leakage discharge for closed guide vanes.

From the modelling point of view, the turbine behaves essentially as a pressure source converting hydraulic energy into mechanical work. Inertia effects of the water in the turbine can be taken into account through the equivalent inductance of the turbine that can be determined by a curvilinear integration from turbine inlet I to turbine outlet $\overline{I}$ as follows:

$$L_t = \int_I^{\overline{I}} \frac{dx}{g \cdot A(x)} = \frac{l_{equ}}{g \cdot \overline{A}} \tag{5.44}$$

The full closure of the guide vanes of the turbine must ensure no discharge through the turbine. This can be only achieved, from the simulation point of view, with a resistance. This resistance is effective only for small discharge, below 5% of the nominal value. The resulting equivalent scheme of the Francis pump-turbine is made of an inductance, a resistance and a pressure source in series as presented in figure 5.15. The pressure source of the model is directly driven from the turbine characteristic $W_H(y, \theta(Q, N))$ function of the guide vane opening y, the rotational speed N and the discharge Q. The rotational speed evolution is obtained using the momentum equation applied to the rotational inertias and given by:

$$J \cdot \frac{d\omega}{dt} = \sum T_{ext} = T_{turb} - T_{elect} \tag{5.45}$$

Where:

- J: total inertia of the rotating parts $[kgm^2]$
- ω: rotational pulsation $[rd/s]$
- T_{turb}: mechanical torque of the turbine $[Nm]$

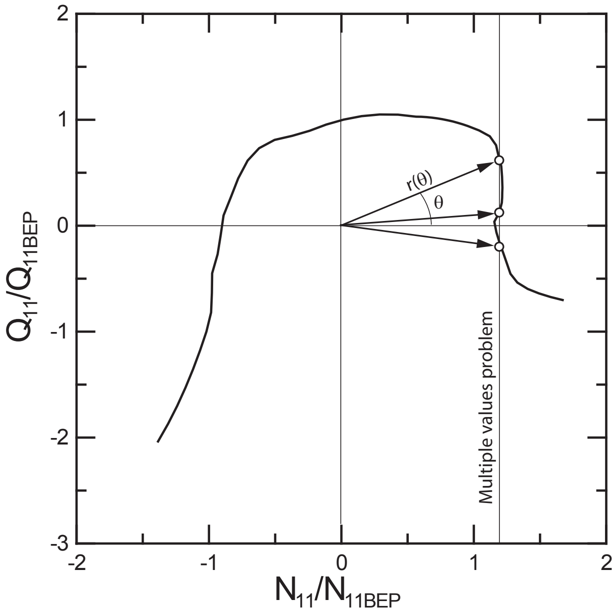

Figure 5.13: Multiple value problem due to "S" shape of the characteristics and definition of the polar representation.

- T_{elect}: electromagnetic torque of the generator $[Nm]$

The mechanical torque of the pump-turbine is obtained from the torque characteristic $W_B(y, \theta(Q, N))$ also function of the guide vane opening y, the rotational speed N and the discharge Q.

It is possible to improve the model of the turbine by considering the dynamic behavior of the spiral case and of the diffuser of the turbine that can be both modelled as straight pipes. Doing so, the compressibility and inertias effects of the water in spiral case and diffuser are also taken into account. Such model has been successfully validated by Bolleter in the case of a pump [23]. Such an approach is suitable for transients purposes. However, the modelling of more complex phenomena occurring in the hydraulic machine itself requires even more detailed modelling.

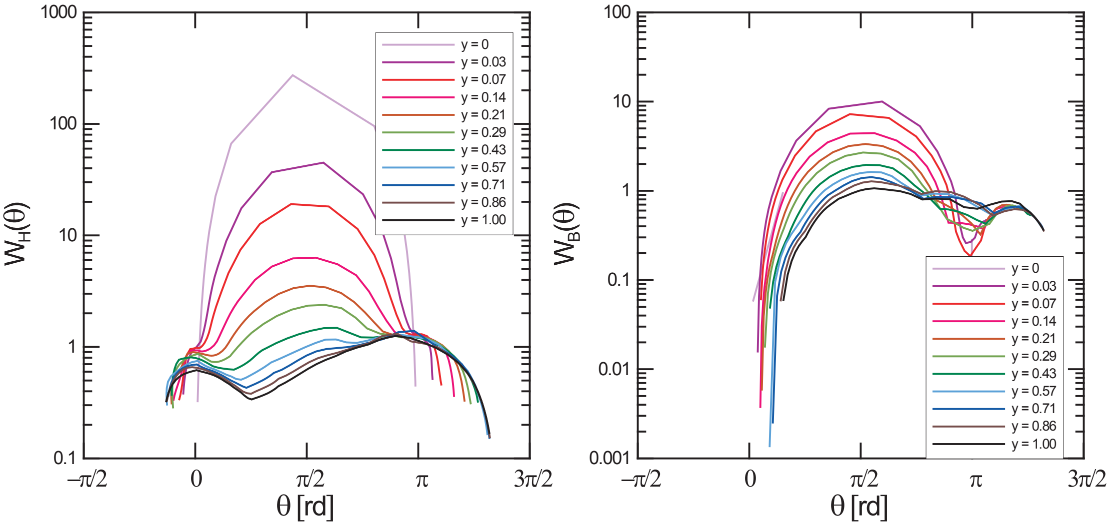

Figure 5.14: Polar representation of the pump-turbine characteristics of figure 5.12.

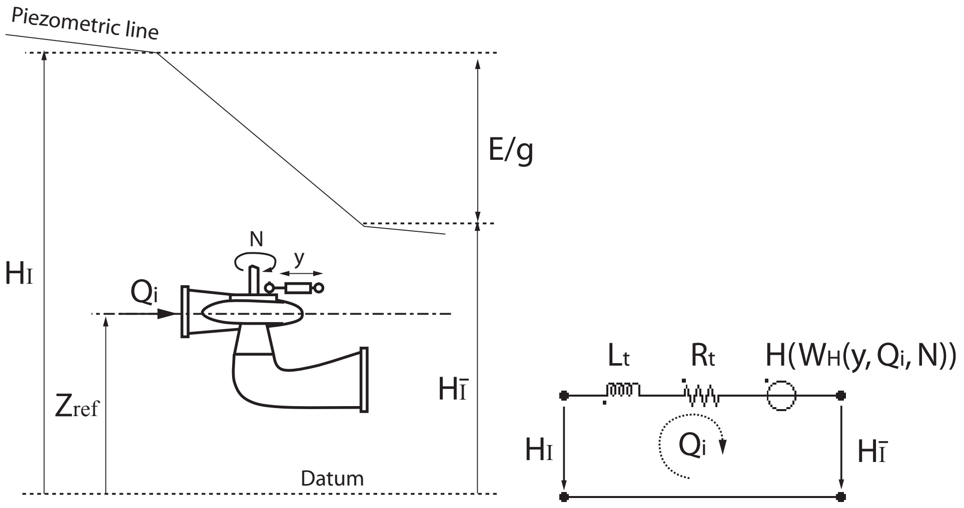

Figure 5.15: Francis turbine model.

5.2.3 Pelton Turbine

Single Injector Modelling

Pelton turbines are impulse turbines; *i.e.* the conversion of the kinetic energy of the flow into mechanical work is performed at the atmospheric pressure. The discharge of each injector is controlled by a nozzle leading to a free water jet. The jet interacts with the turbine buckets deviating the jet so that the outflow has almost no kinetic energy.

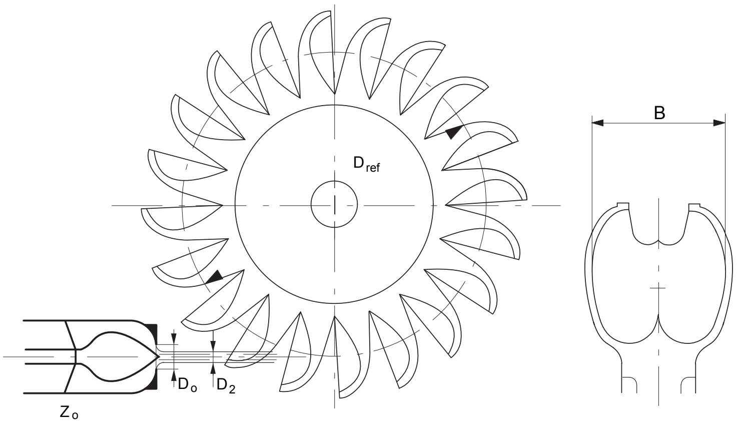

Figure 5.16: Pelton turbine.

The Pelton turbine is modelled by N_{inj} times a single injector turbine characteristic. As a result, the Pelton turbine is viewed from the hydraulic circuit only as N_{inj} valves in parallel. The equivalent circuit modelling the Pelton turbine corresponds to an equivalent resistance of all injectors single resistance, as illustrated in figure 5.17 and given by:

$$R_t = \frac{1}{\sum\limits_{i=1}^{N_{inj}} \frac{1}{R_{inj_i}}} \tag{5.46}$$

The single injector resistance is calculated from the characteristic of the turbine $Q_{11} = Q_{11}(y_{inj})$, see figure 5.18, and is given by:

$$R_{inj} = \frac{|Q_{inj}|}{Q_{11}^2(y_{inj}) \cdot D_{ref}^4} \tag{5.47}$$

The mechanical torque of the machine is calculated as the sum of the contribution of the torque of each single injector as follows:

$$T = K_t \cdot \sum_{i=1}^{N_{inj}} T_{11}(N_{11}, y_{inj_i}) \cdot D_{ref}^3 \cdot H \tag{5.48}$$

Where K_t is a torque coefficient that accounts for the unsteadiness of the torque during operation.

This modelling neglects both the influence on the efficiency of the multi-injectors operation and the dynamic behavior of the piping of the flow repartitor. However, with this

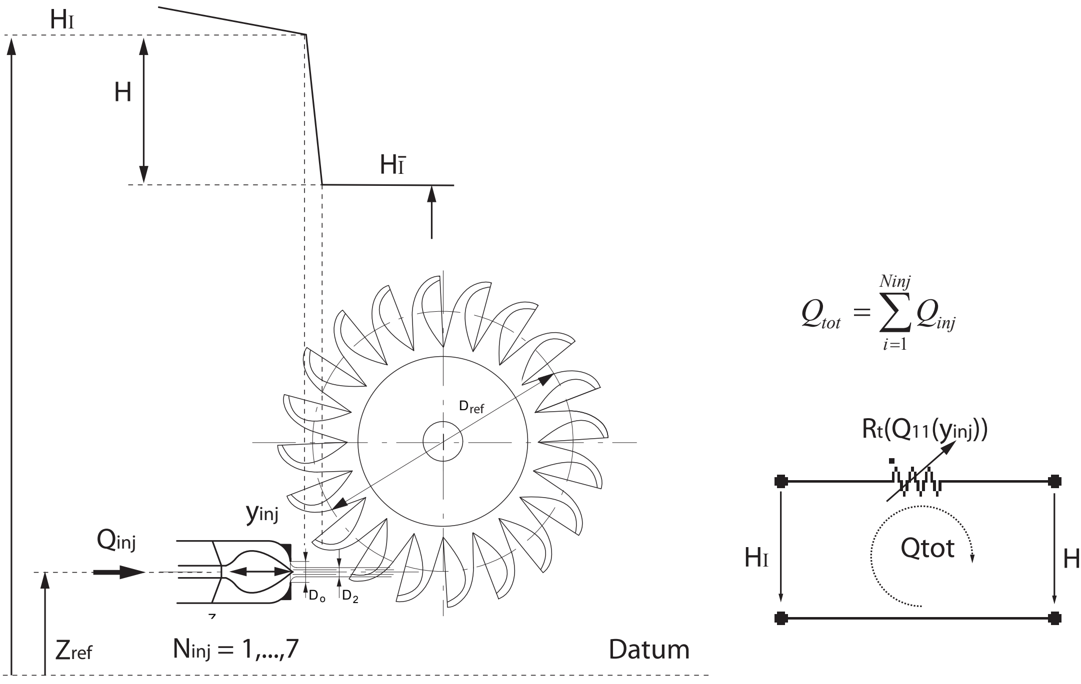

Figure 5.17: Pelton turbine model.

model, injectors can be put in operation or shut off using the same turbine characteristic. As the main purpose of such model is to perform transient simulations and not performing energy production optimization, the single injector model is the most suitable.

Deflector Modelling

Pelton installations usually feature very long penstocks. As a consequence, the piping critical valve closure time are very long and usually in contradiction with flywheel time constants of the rotating parts. Specific protection devices have been developed, consisting of deflectors cutting or deviating the jet between the injector and the turbine runner, see figure 5.19. Such system can be activated within a very short time, $1-3$ seconds, and inducing a quick drop to zero of the mechanical torque, providing time for a slow closure of the injectors in order to minimize the waterhammer effects in the piping.

As it exists several different types of deflectors, it is suitable to use a general method for its modelling allowing to take into account any kind of deflectors. Therefore, a deflector coefficient is introduced and is given by the ratio between the discharge that effectively reaches the turbine and the discharge of the injector and is given for the i^{th} injector by:

$$K_{def\_i} = \frac{Q_{runner\_i}}{Q_{injector\_i}} \tag{5.49}$$

An "equivalent" nozzle stroke $y_{def}(t)$ corresponding to the discharge of the deflector times this deflector coefficient is determined from the nozzle characteristic $y(Q_{11})$. Finally the torque of the turbine is determined not from the nozzle position but from the equivalent nozzle position y_{def}. In this modelling the deflector function K_{def} has to be known. The algorithm for the consideration of the deflector is illustrated in figure 5.20.

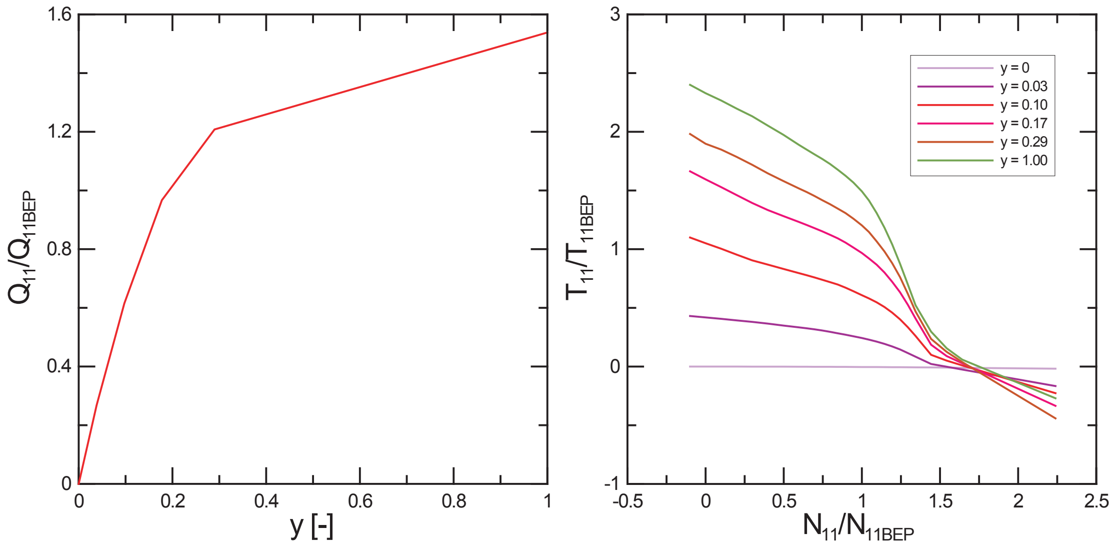

Figure 5.18: Single injector Pelton turbine characteristic.

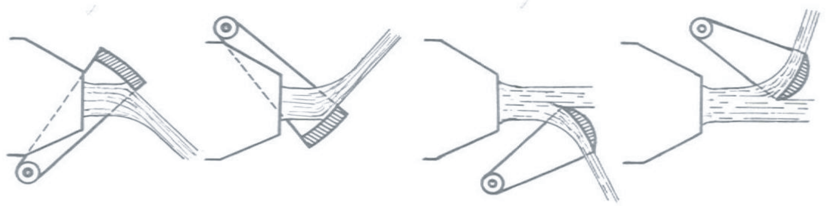

Figure 5.19: Different types of deflectors, deviating jet (left) and cutting jet (right) [127].

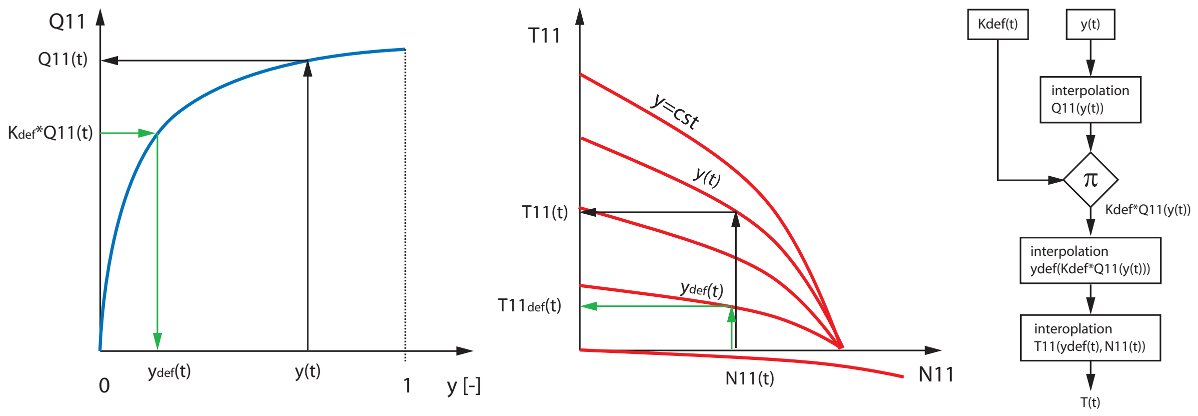

Figure 5.20: Consideration of the deflector in the torque calculation.

5.2.4 Kaplan Turbine

Kaplan turbines are reaction turbines, converting both kinetic and potential energy into mechanical work. Because Kaplan turbines are subject to high relative variations of the available energy $\Delta E/E$, they feature a double control system comprising the distributor and mobile blades in order to ensure high efficiency on the whole operating range, see figure 5.21. As a consequence, the characteristics of the Kaplan turbine has an extra parameter, compared to Francis turbines, *i.e.* the blade pitch angle β. Thus, the turbine characteristics is made of a family of characteristics defined for different blade angles. Figure 5.23 presents 2 characteristics for 2 different blade angles.

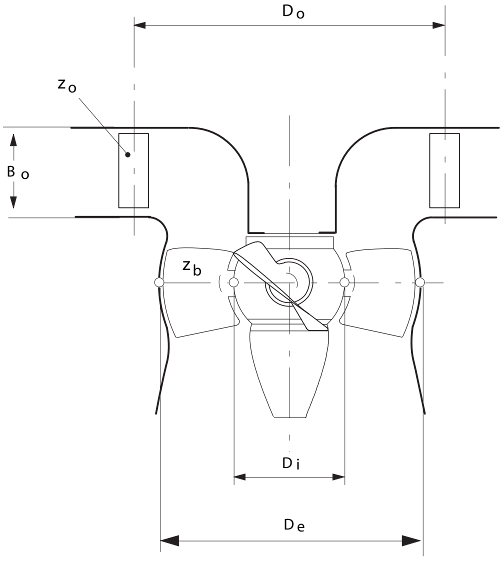

Figure 5.21: Kaplan turbine.

The model of the Kaplan turbine is also based on the polar representation of Suter, as for the Francis turbine model, but the $W_H(\theta, \beta)$ and $W_B(\theta, \beta)$ values are interpolated linearly between 2 blades angles as illustrated in figure 5.23 [69]. The linear interpolation is given by:

$$W_{H,B}(\theta, \beta) = \frac{W_{H,B}(\theta, \beta_2) - W_{H,B}(\theta, \beta_1)}{\beta_2 - \beta_1} \cdot (\beta - \beta_1) \tag{5.50}$$

Linear interpolation is preferred to higher order interpolation as it requires only 2 values for the calculations of the interpolated value, and therefore overlapping of only 2 characteristics is necessary. Indeed, experimental data are not always available on the same range for all tested blade angles, especially in the polar reference frame.

The equivalent scheme of the Kaplan turbine is identical to the Francis turbine model except the fact that the head of the turbine is also function of the blade angle β. Figure 5.24 presents the equivalent model of the Kaplan turbine made of an inductance, a resistance, and a source.

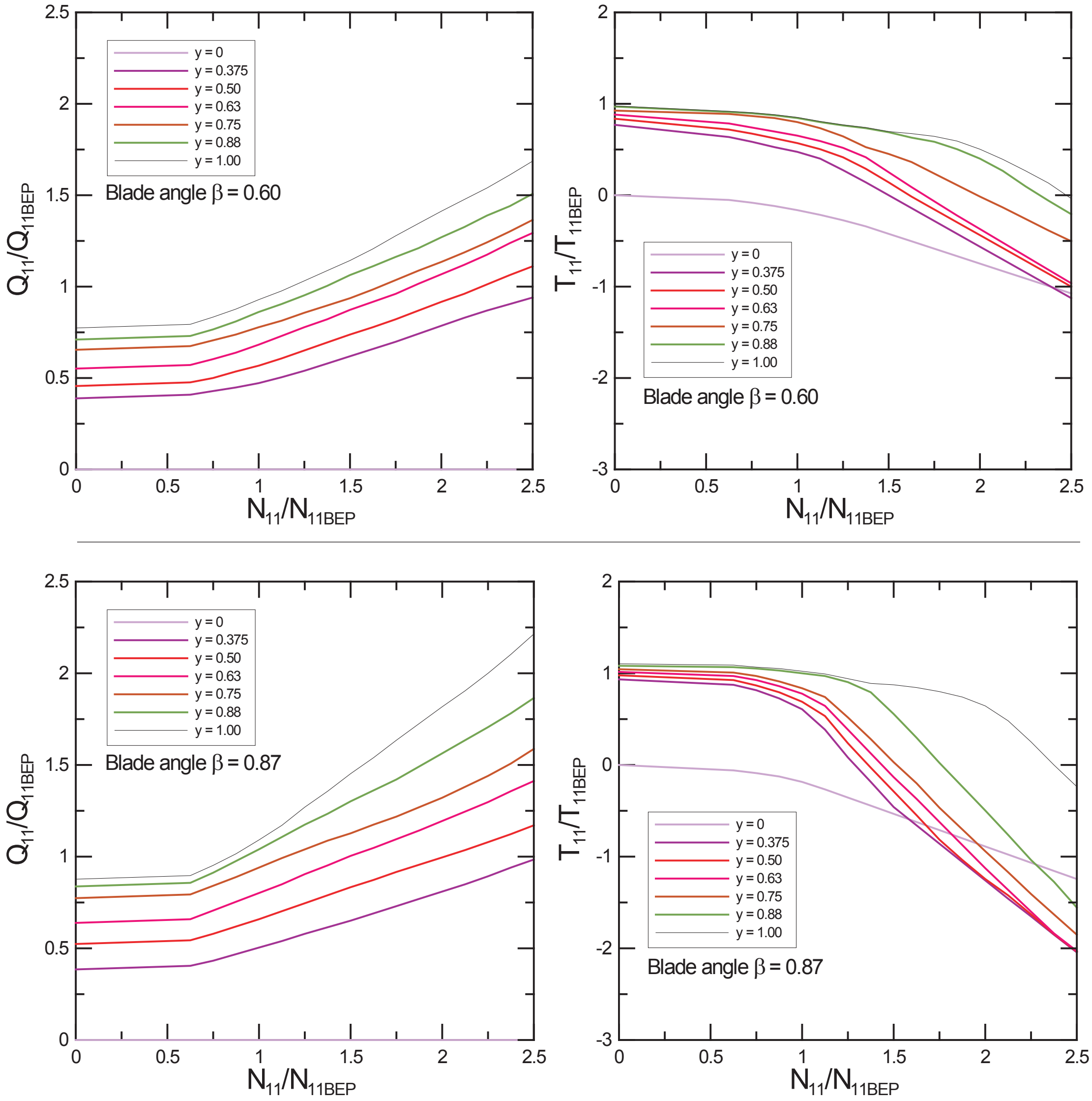

Figure 5.22: Kaplan turbine characteristic for 2 blades angles; $\beta = 0.60$ (top) and $\beta = 0.87$ (bottom).

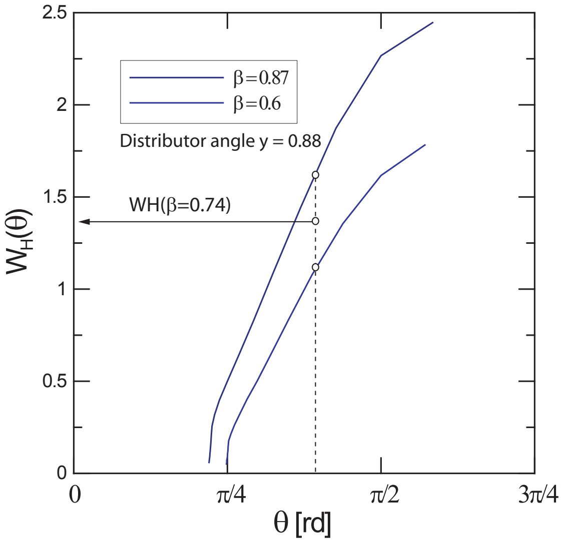

Figure 5.23: Linear interpolation of W_H between 2 different blade angles β for given guide vane opening y.

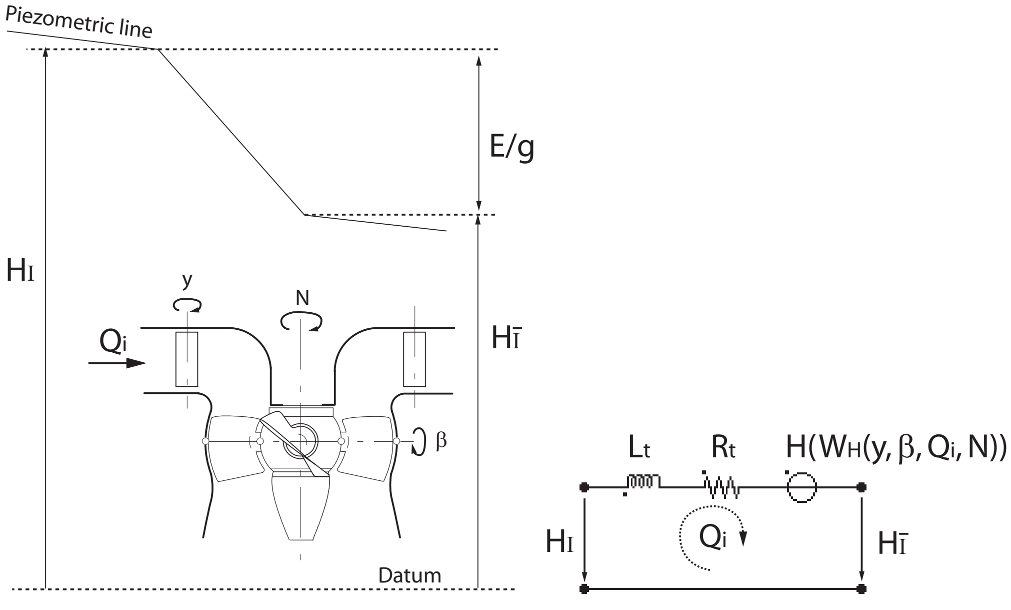

Figure 5.24: Kaplan turbine equivalent scheme.

5.3 Hydraulic Models Implementation in SIMSEN

5.3.1 General

Once the models of the main hydraulic components constituting the hydroelectric power plants are established, it is important to implement them in a software enabling a fast modelling of the system, robust and efficient time domain integration and results analysis in order to perform systematic analysis and optimization of the system. The Laboratory of Electrical Machines (LME) of the EPFL has developed a simulation software for the analysis of electrical power networks and adjustable speed drives called SIMSEN [130]. This software enables the time domain simulation of the dynamic behavior of an electrical installation featuring an arbitrary topology including the electrical machines, the mechanical inertias and the control devices.

The modelling of the hydraulic components with electrical equivalents offers the possibility to implement them in SIMSEN in an easy way as it is based on the same syntax and conventions. Thus, all the hydraulic components models described above have been implemented in SIMSEN with the following advantages:

- treating systems with arbitrary topology;
- modelling hydroelectric systems comprising hydraulic circuit, electrical installations, mechanical inertias and control devices;
- ensuring to properly take into account the interaction between all components of the installation as there is only one set of differential equations to be solved within the same integration time step.

However, there is a drawback resulting from the last point. Electrical systems feature time constants of about $\tau_{elec} = 0.001s$ while hydraulic system features time constants of about $\tau = 0.1s$, *i.e.* 100 times larger.

5.3.2 The Simulation Software SIMSEN

Structure of SIMSEN

The SIMSEN software enables to set up the simulation model of a system according to its own topology using electrical, mechanical and control modules through a Graphical User Interface (GUI). Once all the parameters of each components are defined, the software builds up a global system matrix using Kirchhoff's laws of the following form:

$$[A] \cdot \frac{d\overrightarrow{x}}{dt} + [B] \cdot \overrightarrow{x} = \overrightarrow{C} \tag{5.51}$$

With:

- $[A]$, $[B]$: system global matrix;
- $\overrightarrow{x}$: state vector;
- $\overrightarrow{C}$: boundary conditions vector.

Equation system 5.51 is solved in SIMSEN with the procedure of Runge-Kutta 4^{th} order taking into account all the non-linearities of the system as every parameter of each component can be parameterized using external functions. Finally, all the simulation results are stored in text files.

Electrotechnic Modules

SIMSEN offers a wide range of electrotechnic modules comprising:

- **electrical machines:** synchronous machine, induction, permanent magnet and DC motors;
- **mechanical inertias:** rotor, stator, shaft stiffness and damping, clutch, gear-box;
- **three-phase elements:** voltage supply, transmission lines, circuit breaker, transformers, loads;
- **semi-conductors:** diode, thyristor, thyristor GTO, IGTB;
- **single-phase elements:** voltage supply, resistance, inductance, capacitance, circuit breaker, linked inductor, transformer;
- **analog functions:** program, s-transfer function, regulators, points/grid functions, external DLL;
- **digital functions:** limiter, pulse, generator, z-transfer function, hysteresis, sample.

The above list is non-exhaustive. These modules have been successfully validated by comparison with experimental data [131] as illustrated by the example presented in figure 5.25. This example is the simulation of a load acceptance of an asynchronous machine with a frequency converter of the Three-level Voltage Source Inverter (VSI) type. Figure 5.26 presents the comparison of the simulated and experimental results witnessing the good agreement.

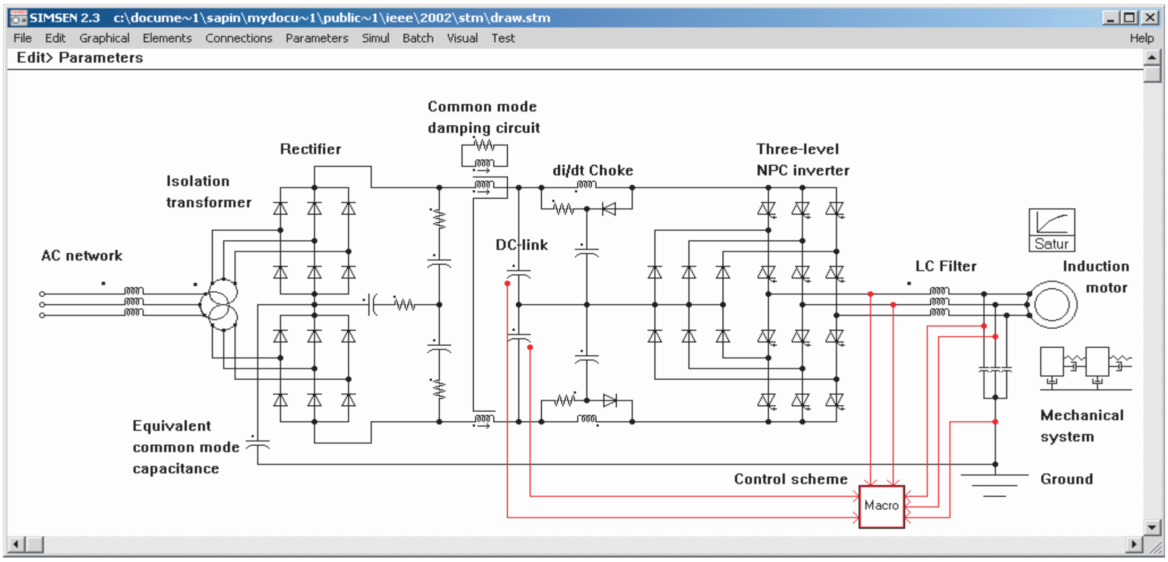

Figure 5.25: Three-level Voltage Source Inverter (VSI) simulation example.

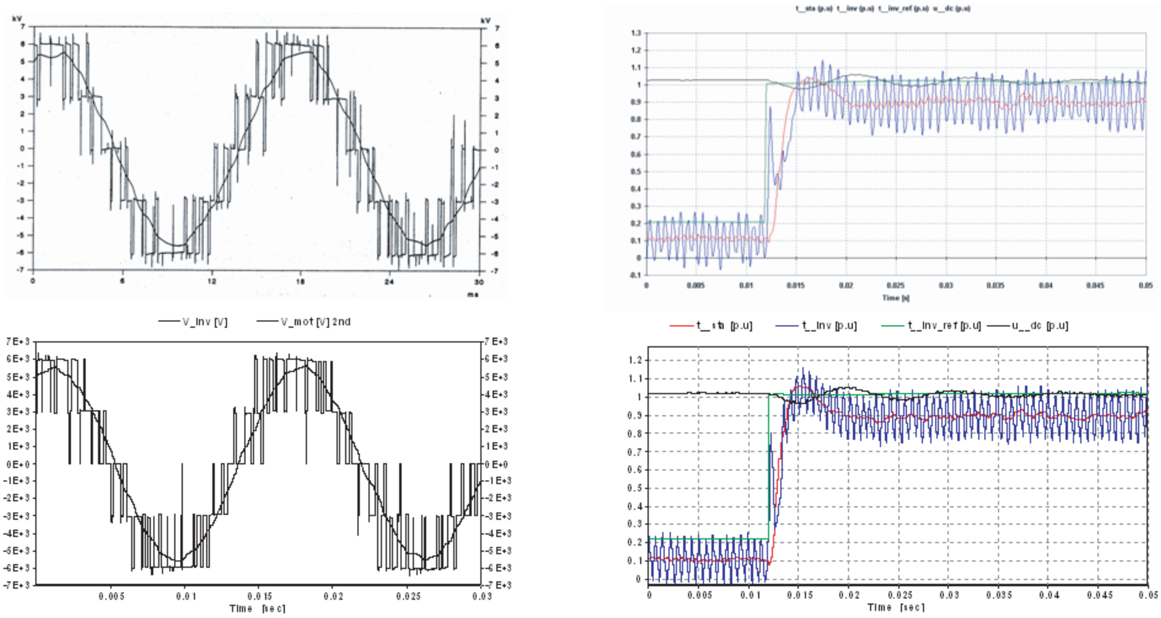

Figure 5.26: Comparison between simulation (bottom) and measurements (top) of voltages (left) and torques (right) resulting from load acceptance of the system of figure 5.25 [131].

Synchronous Machine Modelling

Synchronous machines are playing an important role in hydropower plants. Hydrogenerators feature salient poles with laminated rotor (see figure 5.27 (a)) with strong geometric anisotropy and therefore their modelling is decomposed in 2 axis, the direct axis *d* and the quadrature axis *q*; as illustrated in figure 5.27 (b). Using Park's transformation, it is possible to represent the synchronous machine as 2 equivalent schemes in the direct and quadrature axis [32], see 5.27 (c). The equivalent scheme of the synchronous machine leads to a set of 5 first order differential equations with 5 currents as state variables and 5 voltages as boundary conditions and the rotor position as parameter. Introducing the momentum equation applied to the rotating inertias including the electromagnetic torque obtained from the current and flux, gives a system of 7 equations and 7 unknowns. The equivalent scheme parameters, state variables and boundary conditions of this set of equations are given in table 5.2 defined according to the scheme of figure 5.27 (c).

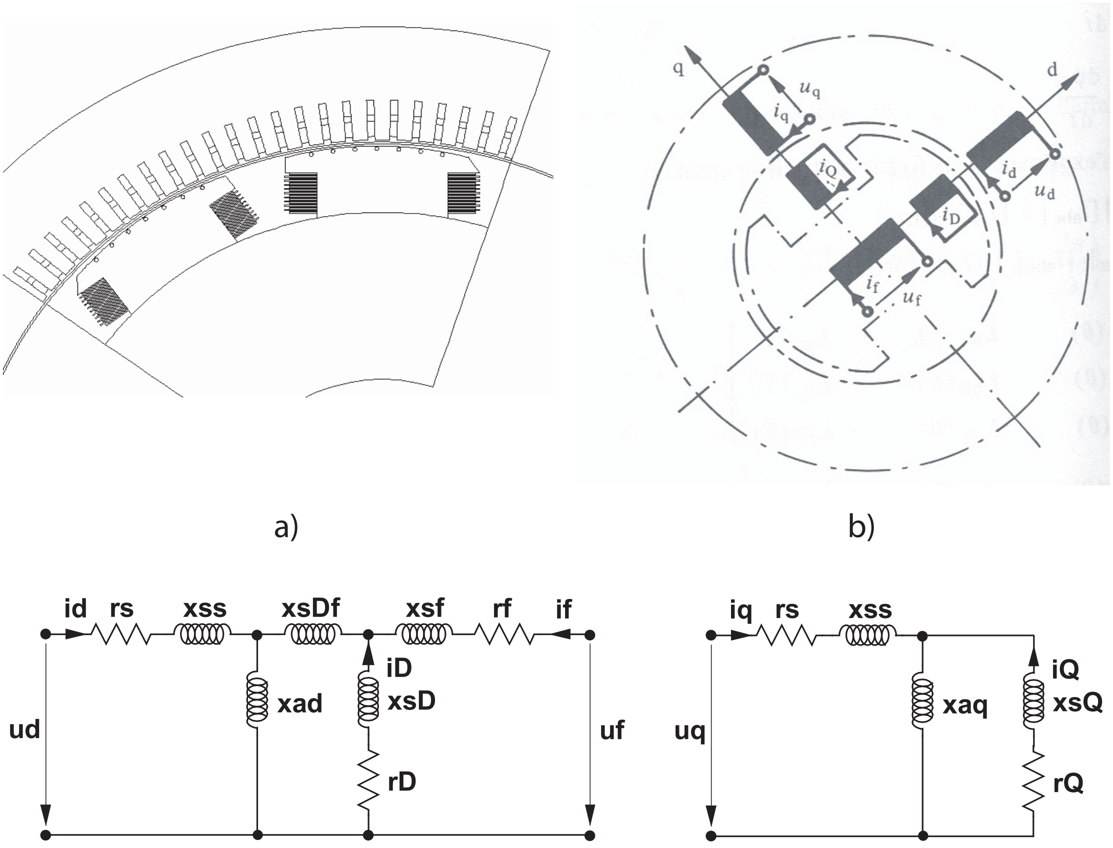

a) b)

c)

Figure 5.27: Modelling of a synchronous machine with decomposition in the direct and quadrature axis; a) geometry of salient pole [123], b) direct and quadrature axis [35], c) equivalent schemes [32].

Table 5.2: Synchronous machine equivalent scheme parameters, state variables and boundary conditions.

Parameters	**Units**	**Description**
r_s, X_{xs}	[p.u.]	statoric resistance and leakage inductance
X_{ad}	[p.u.]	inductance of principal field in axis d
X_{sDf}	[p.u.]	exclusive mutual inductance between dampers of d axis and excitation
r_f, X_{sf}	[p.u.]	excitation resistance and leakage inductance
r_D, X_{sD}	[p.u.]	damper circuit resistance and leakage inductance in axis d
X_{aq}	[p.u.]	principal field inductance in axis q
r_{Q1}, X_{sQ1}	[p.u.]	resistance and leakage inductance of the damper circuit in axis q
p	[-]	number of pair poles
State variables	**Units**	**Description**
i_d,i_q	[p.u.]	statoric phase in axis d and q
i_D	[p.u.]	damper circuit current in axis d
i_f	[p.u.]	excitation current
i_{Q1}	[p.u.]	damper circuit current in axis q
θ_m	[rd]	angular position of the rotor
$\omega_m = d\theta_m/dt$	[rd]	angular pulsation of the rotor
Boundary conditions	**Units**	**Description**
u_d,u_q	[p.u.]	statoric voltages in axis d and q
$u_D \equiv 0$	[p.u.]	damper circuit voltage in axis d
u_f	[p.u.]	excitation voltage
$u_Q \equiv 0$	[p.u.]	damper circuit voltage in axis q

Initial Conditions Determinations

The determination of the initial conditions of an electrical simulation should be achieved according to the boundary conditions prior to a time domain simulation. This initial conditions problem is solved for electrical systems in SIMSEN by performing a load flow calculation where 2 situations can be treated:

- the loads parameters are specified and the excitation voltage of the synchronous machines are adapted to match the demand of active and reactive power, see figure 5.28 (top);

- the active and reactive power of the synchronous machines are specified and the loads parameters are adapted to match the production, see figure 5.28 (bottom).

In both cases, the load flow calculation is achieved in SIMSEN using Newton-Raphson's algorithm.

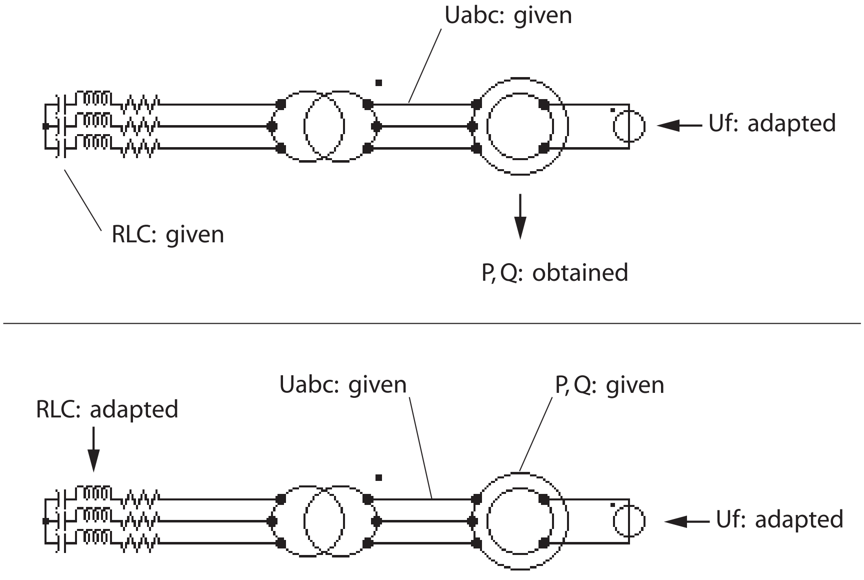

Figure 5.28: Load flow scenarios according to available data; excitation voltage adapted to the demand (top) or load parameters adapted to the production (bottom).

5.3.3 Extension to Hydraulic Systems: SIMSEN-Hydro

Hydraulic Modules

A hydraulic extension comprising all the hydraulic models presented above and called SIMSEN-Hydro, has been implemented in SIMSEN. These hydraulic models are summarized in figure 5.29 for the hydraulic circuit components and in figure 5.31 for the hydraulic turbines.

Turbine Characteristics Interpolation

The modelling of the turbines is based on their characteristics curves. Therefore it is necessary to perform interpolation of the $W_{H,B}$ values for the given abscissa y and θ. The interpolation method implemented in SIMSEN-Hydro is based on a Delaunay triangulation in the plane $y - \theta$. To each vertex of the triangle is associated the corresponding $W_{H,B}$ values. Then, a "planar" interpolation is performed from the equation of the plan in three dimensions. This method ensures the continuity of order 0 on the whole turbine characteristic. The representation of the $2D$ triangulation and the resulting 3D surface of the pump-turbine characteristic of figure 5.14 are presented in figure 5.31.

Initial Conditions Determination

Similarly to electrical systems, initial conditions of a hydraulic system simulation should be determined according to the system boundary conditions prior to perform time domain simulation. In SIMSEN-Hydro, the initial condition procedure is not achieved by Newton-Raphson algorithm but by performing a "fast" simulation of the transient behavior of the system leading to steady state conditions. However, to speed up the stabilization of the

Description	Scheme	Equivalent scheme
Elastic pipe		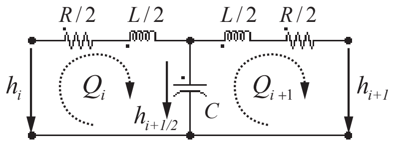
Viscoelastic pipe		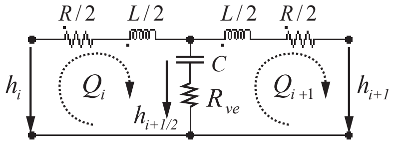
Valve	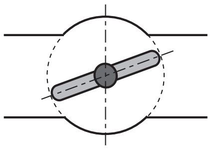	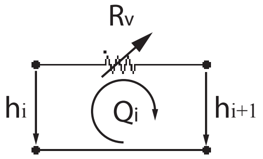
Surge tank	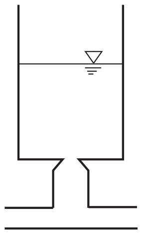	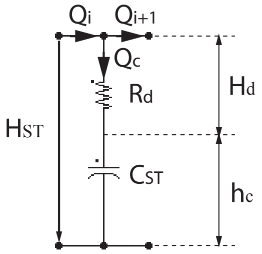
Surge shaft	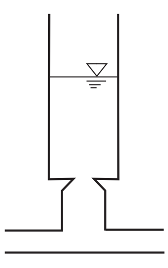	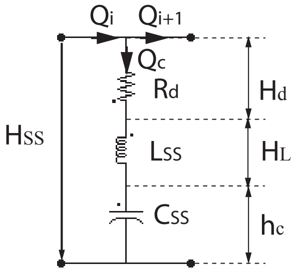
Air vessel	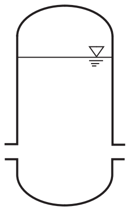	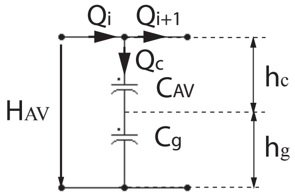
Cavitating flow	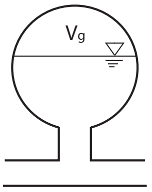	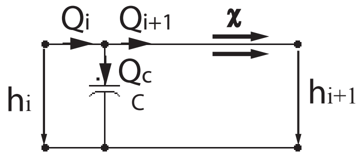

Figure 5.29: Summary of the models of the hydraulic circuit components.

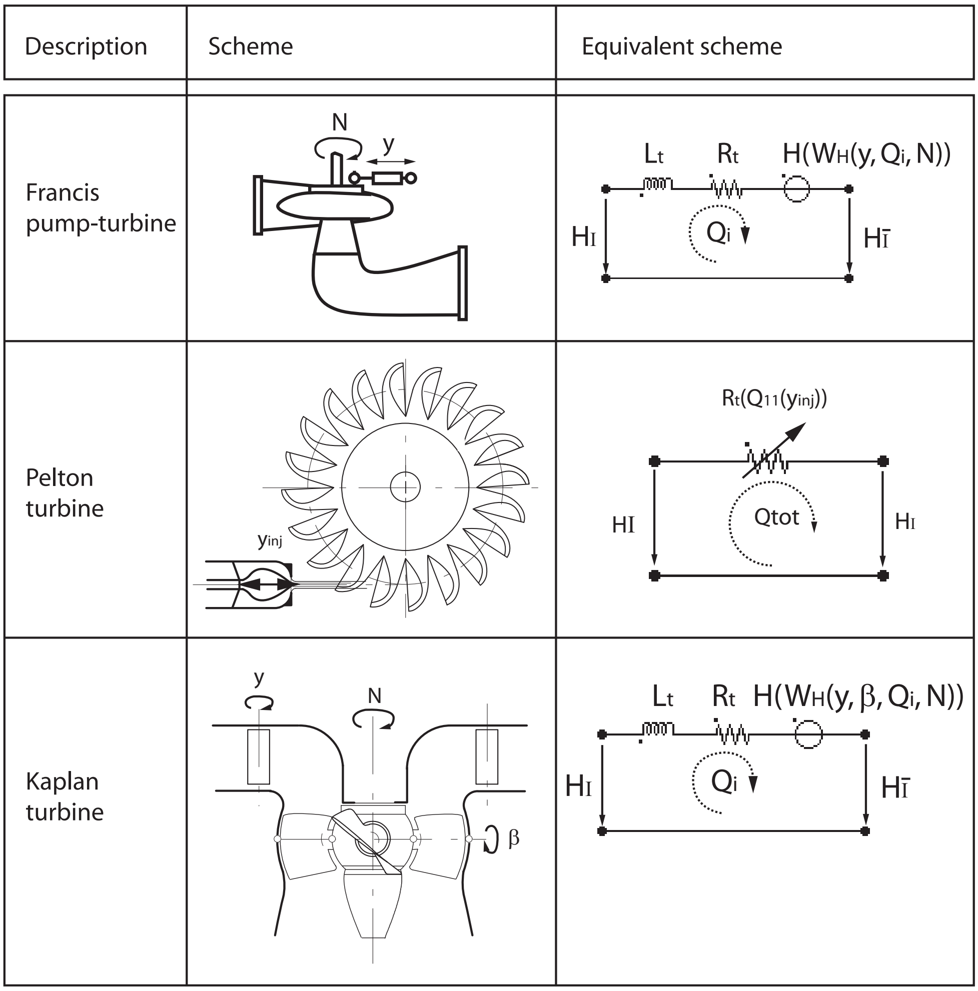

Figure 5.30: Summary of the models of the hydraulic turbines.

system, the system parameters are optimized. Basically, 3 optimizations are undertaken:

- an additional damping is introduced;
- large capacitances leading to high period oscillations are reduced;
- turbine characteristics are bounded in order to avoid errors due the search of a point outside the turbine characteristic.

The additional damping is introduced by setting the viscoelastic resistance of the pipes according to the system limit time constants. The time constant of the RC elements in series in the T-branch of the pipe model is given by:

$$\tau_{RC} = R_{ve} \cdot C \tag{5.52}$$

The value of the viscoelastic resistance can therefore be determined with respect to the integration time step to avoid numerical integration troubles by setting the integration

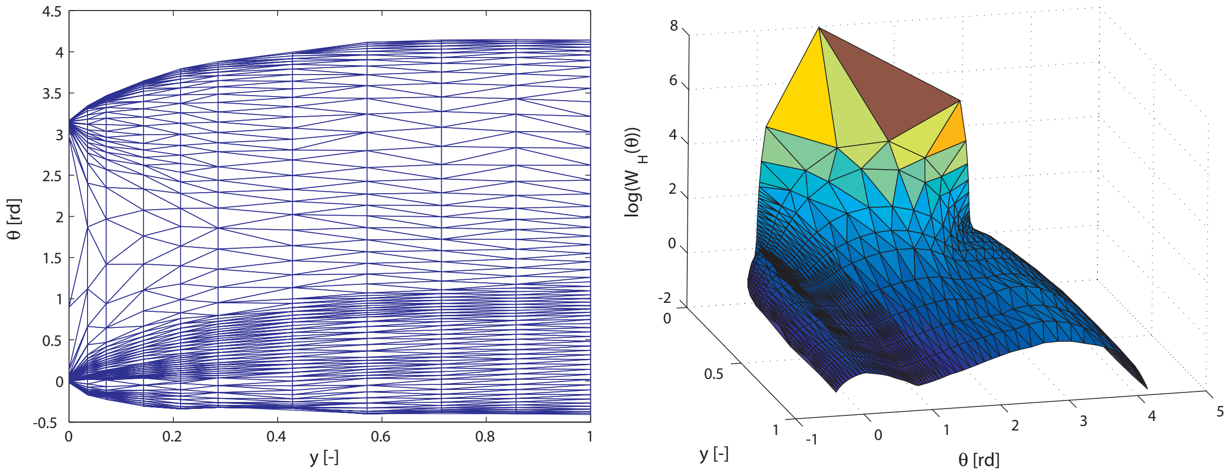

Figure 5.31: Delaunay triangulation of the pump-turbine characteristic of the figure 5.14; $2D$ (left) and $3D$ (right).

time step dt equal to the RC time constant divided by two leading to:

$$\tau_{RC} = R_{ve} \cdot C > 2 \cdot dt \tag{5.53}$$

Hence:

$$R_{ve} = \frac{2 \cdot dt}{C} \tag{5.54}$$

Regarding the initial condition determination, there are 2 possible scenarios:

- the pump-turbine is in generating mode: the water levels of the reservoirs, the mechanical torque and the rotational speed of the pump-turbine are specified and the corresponding guide vanes opening is determined;
- the pump-turbine is in pumping mode: the water levels of the reservoirs, the rotational speed and the guide vanes opening of the pump-turbine are specified and the resulting mechanical power is determined.

The 2 above scenarios are illustrated in figure 5.32.

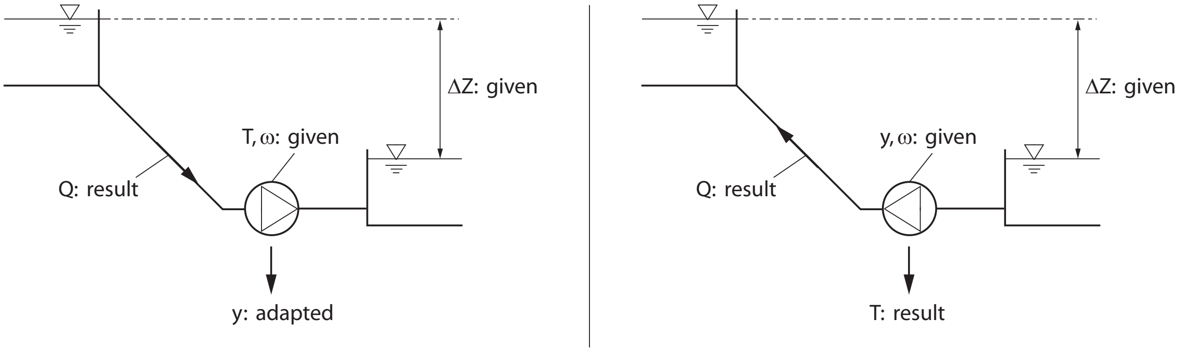

Figure 5.32: Hydraulic load flow scenarios for generating mode (left) and pumping mode (right).

Chapter 6

Analytical Analysis of Simplified Hydraulic Systems

6.1 General

The modelling by electrical equivalent enables to set up simplified models of hydraulic installation to study their global dynamic behavior. The simplified models are preferably of a low order to obtain the analytical solutions of the related differential equation set. Such solutions provide the main dynamic quantities of the system in terms of eigen frequencies and damping [1], [3], [34].

6.2 Mass Oscillations Problems

In the following sections, the eigen frequency related to mass oscillation problems is analyzed for various types of tanks, *i.e.* (i) a surge tank, (ii) a surge shaft and (iii) an air vessel.

6.2.1 System with Surge Tank

The dynamic behavior of the hydraulic circuit shown by figure 6.1 (left) comprising an upstream reservoir, a gallery, a surge tank and a penstock with a downstream valve is investigated. Focusing only on low frequencies permits to neglect the compressibility of both pipes. Thus the equivalent circuit of this system is made of a pressure source H_o, the gallery inductance L_G and resistance R_G, the surge tank capacitance C_{ST} and the diaphragm resistance R_d, the penstock inductance L_P and resistance R_P and the valve resistance R_v as presented in figure 6.1 (right).

The consequence of a sudden closure of the valve is analyzed assuming an initial steady state condition with constant valve opening. Closing the valve yields to open the right hand loop of the equivalent scheme related to Q_2. The differential equations written using Kirchhoff's law applied to the left hand loop leads to:

$$\begin{cases} H_o = L_G \cdot \dfrac{dQ_1}{dt} + (R_d + R_G) \cdot Q_1 + h_{ST} \\ C_{ST} \cdot \dfrac{dh_{ST}}{dt} = Q_1 \end{cases} \tag{6.1}$$

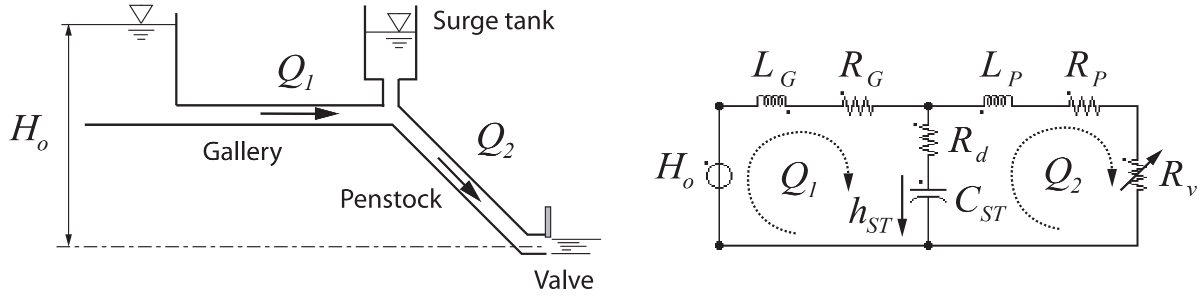

Figure 6.1: Hydraulic circuit with surge tank.

Combining the 2 above equations leads to the following characteristic equation:

$$\frac{d^2h_{ST}}{dt^2}+\underbrace{\frac{R_d+R_G}{L_G}}_{2\cdot\mu}\cdot\frac{dh_{ST}}{dt}+\underbrace{\frac{1}{C_{ST}\cdot L_G}}_{\omega_o^2}\cdot h_{ST}=0 \tag{6.2}$$

The general solution of the above equation is given by:

$$h_{ST}(t)=h_{STo}\cdot e^{-\mu\cdot t}\cdot sin(\omega_1\cdot t) \tag{6.3}$$

With:

$$\omega_1=\omega_o\cdot\sqrt{1-\zeta^2}\quad;\quad\zeta=\frac{\mu}{\omega_o} \tag{6.4}$$

The natural frequency of the frictionless system is given by:

$$\omega_o=\frac{1}{\sqrt{(C_{ST}\cdot L_G)}} \tag{6.5}$$

The related period is then given by:

$$T_o=2\cdot\pi\cdot\sqrt{\left(\frac{l_G\cdot A_{ST}}{g\cdot A_G}\right)} \tag{6.6}$$

Where:

- l_G: length of the gallery $[m]$
- A_{ST}: surge tank cross section $[m^2]$
- A_G: gallery cross section $[m^2]$

The period T_o is usually very low as the surge tank cross section and the gallery length are large and the gallery cross section is small. This period is called the mass oscillation period related the oscillation of the discharge in the gallery between the reservoir and the surge tank.

The amplitude of the water level oscillations in the surge tank, assuming a constant surge tank cross section and a frictionless system, is obtained considering a solution of type $h_{ST}(t) = h_{STo} \cdot sin(\omega_o \cdot t + \phi)$ whose first derivative introduced in equation 6.1 gives the oscillation amplitude:

$$h_{STo} = \frac{Q_{1o}}{C_{ST}} \cdot \frac{1}{\omega_o} = C_{1o} \cdot \sqrt{\frac{l_G \cdot A_G}{g \cdot A_{ST}}} \tag{6.7}$$

Where $C_{1o} = \frac{Q_{1o}}{A_G}$ is the initial flow velocity in the gallery.

6.2.2 System with Surge Shaft

The dynamic behavior of the hydraulic circuit presented by figure 6.2 (top) comprising an upstream reservoir, a first part of gallery, an upstream valve, a surge shaft, a second part of gallery, a surge tank and a penstock with a downstream valve is investigated. Focusing again only on low frequencies, the compressibility of the pipes are neglected. The system is considered frictionless. Thus the equivalent circuit of this system is made of a pressure source H_o, the first gallery inductance L_{Go}, the valve resistance R_{v1}, the surge shaft capacitance C_{SS} and inductance L_{SS}, the second gallery inductance L_{G1}, the surge tank capacitance C_{ST}, the penstock inductance L_P and the downstream valve resistance R_{v2} as presented in figure 6.2 (bottom).

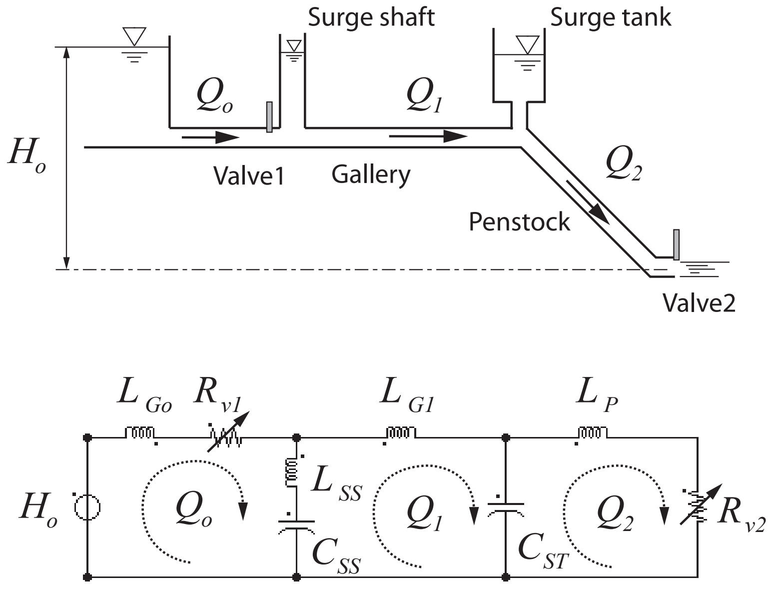

Figure 6.2: Hydraulic circuit with surge tank and surge shaft.

The consequence of a sudden closure of both valves is analyzed assuming an initial steady state condition with constant valves openings. Closing valves 1 and 2 yields to open loops related to Q_o and Q_2. The differential equations written using Kirchhoff's law applied to the loop related to Q_1 leads to:

$$\begin{cases} (L_{G1} + L_{SS}) \cdot \dfrac{dQ_1}{dt} + h_{ST} - h_{SS} = 0 \\ C_{ST} \cdot \dfrac{dh_{ST}}{dt} = Q_1 \\ C_{SS} \cdot \dfrac{dh_{SS}}{dt} = -Q_1 \end{cases} \tag{6.8}$$

Combining the 3 above equations leads to the following characteristic equation:

$$\frac{d^2Q_1}{dt^2} + \underbrace{\left(\frac{1}{C_{ST}} + \frac{1}{C_{SS}}\right) \cdot \frac{1}{L_{SS} + L_{G1}}}_{\omega_o^2} Q_1 = 0 \tag{6.9}$$

The natural frequency of the frictionless system is given by:

$$\omega_o^2 = \frac{\frac{1}{C_{SS}} + \frac{1}{C_{ST}}}{L_{SS} + L_{ST}} \tag{6.10}$$

The corresponding mass oscillation period is given by:

$$T = 2 \cdot \pi \cdot \sqrt{\frac{\frac{l_{SS}}{g \cdot A_{SS}} + \frac{l_{G1}}{g \cdot A_{G1}}}{\frac{1}{A_{SS}} + \frac{1}{A_{ST}}}} \tag{6.11}$$

Once the 2 valves are closed the system constituted of the surge shaft, the gallery and the surge tank undergo mass oscillations. The mass of water oscillates between the surge shaft and the surge tank with amplitudes driven by the tanks cross sections. It can be seen that the inertia of the water in the surge shaft may strongly influence the oscillation period depending on the inductance ratio between the surge shaft and the gallery.

6.2.3 System with Air Vessel

The dynamic behavior of the hydraulic circuit presented by figure 6.3 (left) comprising an upstream reservoir, a gallery, an air vessel and a penstock with a downstream valve is investigated. Focusing only on low frequencies permits to neglect the compressibility of both pipes. The system is considered frictionless. Thus, the equivalent circuit of this system is made of a pressure source H_o, the gallery inductance L_G, the 2 air vessel capacitances C_{AV} and C_g, the penstock inductance L_P and the valve resistance R_v as presented in figure 6.3 (right).

The consequence of a sudden closure of the valve is analyzed assuming an initial steady state condition with constant valve opening. Closing the downstream valve yields to open loop related to Q_2. The differential equations written using Kirchhoff's law applied to the first loop leads to:

$$\begin{cases} L_G \cdot \dfrac{dQ_1}{dt} + h_{AV} + h_g = H_o \\ C_{AV} \cdot \dfrac{dh_{AV}}{dt} = Q_1 \\ C_g \cdot \dfrac{dh_g}{dt} = Q_1 \end{cases} \tag{6.12}$$

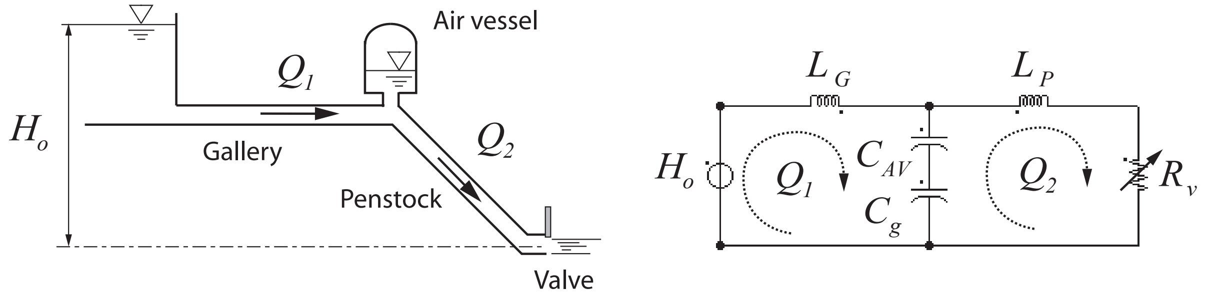

Figure 6.3: Hydraulic circuit with air vessel.

Combining the 3 above equations leads to the following characteristic equation:

$$\frac{d^2Q_1}{dt^2} + \underbrace{\left(\frac{1}{C_{AV}} + \frac{1}{C_g}\right) \cdot \frac{1}{L_G}}_{\omega_o^2} Q_1 = 0 \tag{6.13}$$

The natural frequency of the frictionless system is given by:

$$\omega_o^2 = \frac{\frac{1}{C_{AV}} + \frac{1}{C_g}}{L_G} \tag{6.14}$$

The corresponding mass oscillation period is given by:

$$T = 2 \cdot \pi \cdot \sqrt{\frac{\frac{l_G}{g \cdot A_G}}{\frac{1}{A_{AV}} + \frac{1}{\left(\frac{V_g}{H_g \cdot n}\right)}}} \tag{6.15}$$

Comparing the mass oscillation period obtained for a system with air vessel with the period obtained for a system with a surge tank, given by equation 6.5, it can be noticed that:

- if the gas volume tends to infinity, the period of the system with air vessel corresponds to the period of the system with a surge tank;
- if the volume of gas becomes small, the mass oscillation period decreases;
- for small gas volume and high oscillation amplitudes, the system becomes strongly non-linear as the air vessel capacitance is function of the gas volume and pressure.

To illustrate the influence of the gas volume on the mass oscillation period and time evolution, the simulation of the sudden closure of the downstream valve is performed for 3 different gas volumes. The dimensions of the hydraulic circuit are summarized in table 6.1. The time domain evolution of the gas piezometric head h_g, the water level in the air vessel h_{AV} and the total piezometric head $h = h_g + h_{AV}$ are represented in dimensionless values in figure 6.4. The above 3 statements are clearly confirmed by the simulations. Especially the non-linear behavior induced by the gas volume is clearly pointed out for the simulation results with $V_g = 50\ m^3$.

Table 6.1: Parameters of the hydraulic installation with air vessel of figure 6.3.

Gallery	**Air vessel**	**Penstock**	**Nominal values**
$l = 1100\ m$ $a = 1100\ m/s$ $D = 3.57\ m$	$A = 38.48\ m^2$ $h_{go} = 100\ m$ $h_{AVo} = 598\ m$	$l = 1100\ m$ $a = 1100\ m/s$ $D = 2.52\ m$	$H_o = 700\ m$ $Q_{1o} = 30.9\ m$

6.3 Stability of Hydraulic Circuit

In the following sections, stability criteria are determined for the following installations: (i) power plant with regulated turbine and surge tank; (ii) piping with cavitation development; (iii) piping with valve leakage; (iv) pumping system; and (v) pump-turbine power plant.

6.3.1 Mass Oscillation Stability: Thoma Cross Section Criteria

A hydraulic circuit comprising an upstream reservoir, a gallery, a surge tank, a penstock connected to a turbine driven by a speed controller is subject to system instabilities. Therefore the stability limit of the system must be determined. The system and the corresponding equivalent scheme are presented in figure 6.5. For the purpose of the present investigation, the dynamic behavior of the penstock and the diaphragm losses are neglected and the perturbation are considered small so that the turbine efficiency can be assumed to be constant.

The differential equation related to the loop of discharge Q_1 is given by:

$$\begin{cases} L_G \cdot \dfrac{dQ_1}{dt} + R_G \cdot Q_1 + h_{ST} = H_o \\ C_{ST} \cdot \dfrac{dh_{ST}}{dt} = Q_{ST} \end{cases} \tag{6.16}$$

The continuity equation gives:

$$Q_{ST} = Q_1 - Q_2 \tag{6.17}$$

From the second loop, it can be stated that the piezometric head of the surge tank corresponds to the turbine head H_t which is equal to the initial head H_{to} plus a perturbation z and is therefore given by:

$$h_{ST} = H_t = H_{to} + z \tag{6.18}$$

The similitude of the turbine efficiency gives:

$$Q_2 \cdot H_t = Q_{2o} \cdot H_{to} \tag{6.19}$$

Then the discharge of the turbine can be expressed with equation 6.18 and then expressed with the limited development $(1/(1+x) = 1 - x + x^2 - x^3 ...)$ leading to:

$$Q_2 = Q_{2o} \cdot \frac{H_{to}}{H_{to} + z} \simeq Q_{2o} \cdot \left(1 - \frac{z}{H_{to}}\right) \tag{6.20}$$

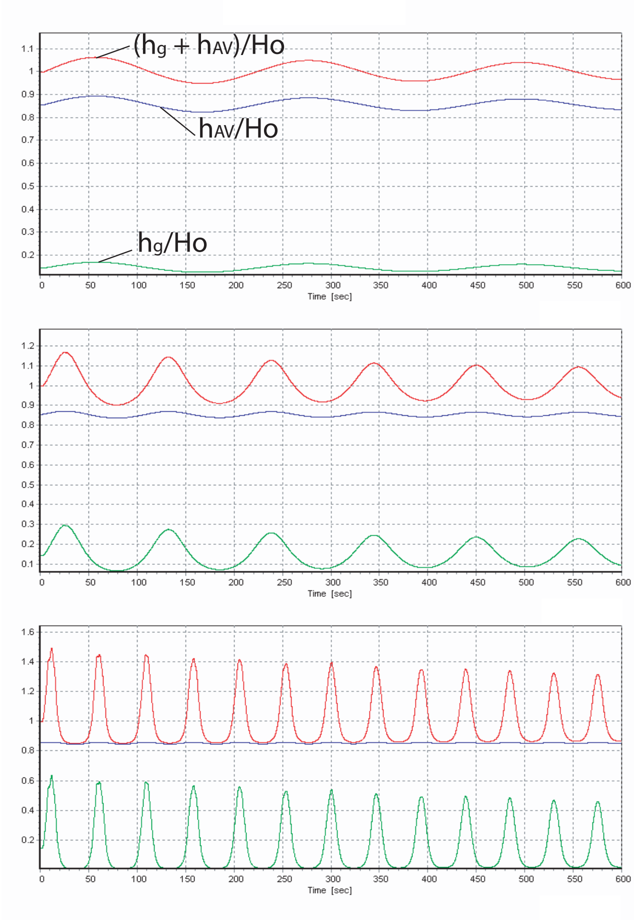

Figure 6.4: Mass oscillations with air vessel of volume: $V_g = 5000\ m^3$ (top), $V_g = 500\ m^3$ (middle), $V_g = 50\ m^3$ (bottom).

Combining equation 6.18 and 6.20 gives:

$$\frac{dQ_2}{dt} = -\frac{Q_{2o}}{H_{to}} \cdot \frac{dh_{ST}}{dt} \tag{6.21}$$

Introducing equations 6.17 and 6.21 in equations 6.16 leads to:

$$L_G \cdot \left[-\frac{Q_{2o}}{H_{to}} \cdot \frac{dh_{ST}}{dt} + C_{ST} \cdot \frac{d^2 h_{ST}}{dt^2} \right] + R_G \cdot Q_1 + h_{ST} = H_o \tag{6.22}$$

The head loss in the gallery is a non-linear term that requires to be developed, and therefore the head losses are expressed as follows:

$$R_G \cdot Q_1 = R'_G \cdot Q_1^2 \tag{6.23}$$

With equation 6.17 and 6.20, the discharge in the gallery gives:

$$Q_1^2 = (Q_{ST} + Q_2)^2 = \left(Q_{ST} + Q_{2o} \cdot \left(1 - \frac{h_{ST}}{H_{to}} \right) \right)^2 \tag{6.24}$$

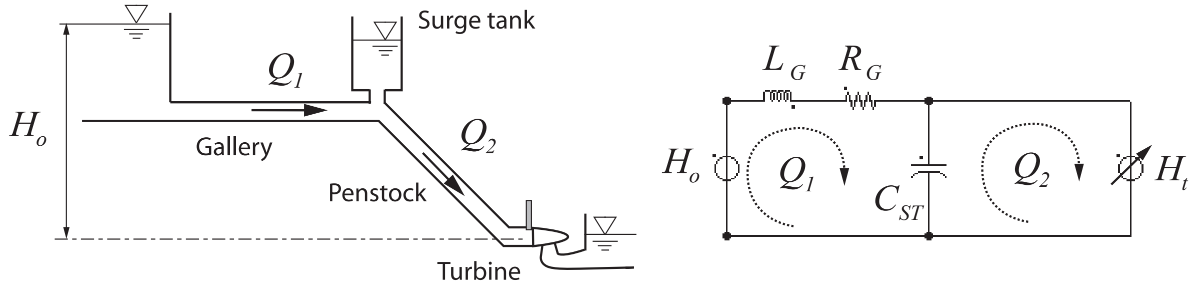

Figure 6.5: Hydraulic system with surge tank and regulated turbine.

Equation 6.24 above can be rearranged in the following form:

$$Q_1^2 = Q_{2o}^2 \cdot \left(1 + \left(\frac{Q_{ST}}{Q_{2o}} - \frac{h_{ST}}{H_{to}}\right)\right)^2 \simeq Q_o^2 \cdot \left(1 + 2 \cdot \left(\frac{Q_{ST}}{Q_{2o}} - \frac{h_{ST}}{H_{to}}\right)\right) \tag{6.25}$$

Introducing equation 6.16, 6.21 and 6.25 in equation 6.22 leads to the characteristic equation:

$$\frac{d^2 h_{ST}}{dt^2} + \underbrace{\left(2 \cdot \frac{R'_G \cdot Q_{2o}}{L_G} - \frac{Q_{2o}}{H_{to} \cdot C_{ST}}\right)}_{2\cdot\mu} \cdot \frac{dh_{ST}}{dt} + \underbrace{\left(1 - 2 \cdot \frac{R'_G \cdot Q_{2o}^2}{H_{to}}\right) \cdot \frac{1}{L_G \cdot C_{ST}}}_{\omega_o^2} \cdot h_{ST} =$$
$$= \frac{H_{to} - R'_G \cdot Q_{2o}^2}{L_G \cdot C_{ST}} \tag{6.26}$$

The stability of the system is ensured when $2 \cdot \mu > 0$, leading to the following stability criteria:

$$C_{ST} > \frac{Q_{2o}}{H_{to}} \cdot \frac{L_G}{2 \cdot R_G} \tag{6.27}$$

After expressing the inductance, resistance and capacitances, the stability criteria gives the **Thoma cross section**:

$$A_{ST} > \frac{Q_{2o}^2}{2 \cdot g} \cdot \frac{l_G}{H_{to} \cdot H_{rGo} \cdot A_G} \tag{6.28}$$

Where H_{rGo} are the head losses in the gallery calculated with the initial discharge Q_{2o}, l_G and A_G are respectively the length and the cross section of the gallery, and H_{to} is the initial head of the turbine.

The Thoma cross section is the surge tank limit cross section below which the system becomes unstable after a perturbation induced by the turbine [145].

6.3.2 Cavitating Flow Stability

Cavitation development was early identified as a source of instabilities in pumping systems and is known as the POGO effect [128]. A theoretical model for the cavitation development was set up by Brennen and Acosta [27]. For simplicity, this model is applied to study the dynamic behavior of the piping system presented figure 6.6 (left) comprising an upstream reservoir, a first pipe, a cavitation development, a second pipe and a downstream reservoir. The 2 pipes of this system being identical, the equivalent model of this system is made of a resistance R and inductance L for the modelling of the pipes, the compressibility of the pipe being neglected, and a capacitance C related to the cavitation compliance. In addition, the model of the cavitation development includes the mass flow gain factor χ referring to the discharge of the second loop. The equivalent scheme of the hydraulic system is presented figure 6.6 (right).

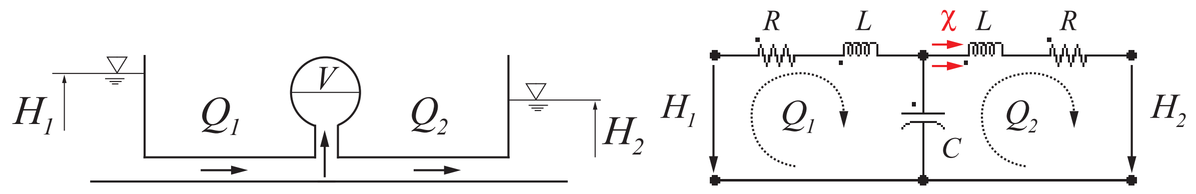

Figure 6.6: Hydraulic circuit with cavitation development in the middle.

The system of differential equations of the equivalent scheme of the hydraulic system is given by:

$$\begin{cases} H_1 = L \cdot \dfrac{dQ_1}{dt} + R \cdot Q_1 + H_c \\ \chi \cdot \dfrac{dQ_2}{dt} + C\dfrac{dH_c}{dt} = Q_1 - Q_2 \\ H_c = L \cdot \dfrac{dQ_2}{dt} + R \cdot Q_2 + H_2 \end{cases} \tag{6.29}$$

The determinant of this set of equations written in matrix form leads to the characteristic equation:

$$\left(\underbrace{\frac{R}{L}}_{1/\tau} + \delta\right)\left(\delta^2 + \underbrace{\left[\frac{R}{L} + \frac{\chi}{L \cdot C}\right]}_{2\cdot\mu} \cdot \delta + \underbrace{\frac{2}{L \cdot C}}_{\omega_o^2}\right) = 0 \tag{6.30}$$

Where δ is the eigen value of the set of equation 6.29. The free motion time constant τ of the fluid in the pipe can be identified in the left hand term of equation 6.30. The frictionless eigen pulsation of the system ω_o and the stability criteria of the system given by $2 \cdot \mu > 0$ are determined from the right hand term. The stability criteria leads to the following criteria:

$$-R < \frac{\chi}{C} \tag{6.31}$$

The above criteria as illustrated in figure 6.7 indicates that the stability of the system depends on both values of the cavitation development, the cavitation compliance C and the cavitation mass flow gain factor χ. The ratio χ/C can be viewed as a damping or amplification factor related to the cavitation development. The system starts to oscillate if this ratio is above the resistance of the system R. As R and C are always positive, it means that only negative values of the mass flow gain factor lead to system instabilities, *i.e.* for positive $\partial V/\partial Q$; when cavitation volume increases with the discharge.

Caution should be payed to the fact that the resistance of the system R is a function of the discharge and thus the criteria of equation 6.31 cannot be applied directly.

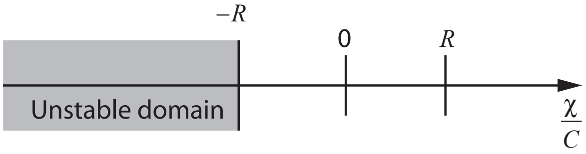

Figure 6.7: Stability domain related to cavitation development.

6.3.3 Valve Leakage Induced Instabilities

Hydraulic circuit comprising an upstream reservoir, a pipe and a downstream valve may present an unstable behavior after perturbations [86], [112]. Such a system can be modelled with a first order equivalent scheme of the pipe made of an inductance L_p and a capacitance C_p while the valve is modelled by a variable resistance R_v as presented in figure 6.8. The corresponding set of differential equations is given by:

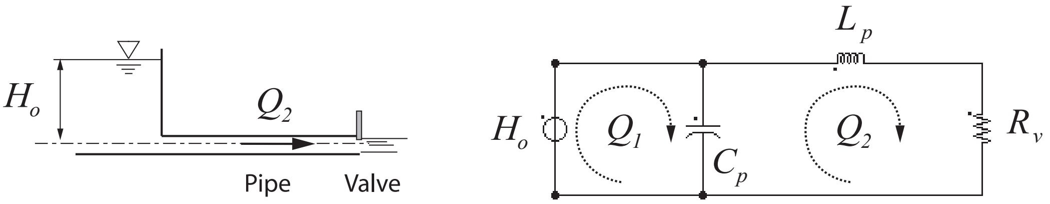

Figure 6.8: Hydraulic circuite with downstream valve.

$$\begin{cases} L_p \cdot \dfrac{dQ_2}{dt} + R_v \cdot Q_2 + h_c = 0 \\ C_p \cdot \dfrac{dh_c}{dt} = Q_1 - Q_2 \end{cases} \tag{6.32}$$

Combining the 2 equations above leads to the following characteristic equation:

$$\frac{d^2Q_2}{dt^2} + \underbrace{\frac{R_v}{L_p}}_{2\cdot\mu} \cdot \frac{dQ_2}{dt} + \underbrace{\frac{1}{C_p \cdot L_p}}_{\omega_o^2} \cdot Q_2 = 0 \tag{6.33}$$

The system remains stable for $2 \cdot \mu > 0$, leading to the following stability criteria:

$$R_v > 0 \tag{6.34}$$

It means that negative slopes of a valve characteristic in the $Q - h$ diagram lead to system instabilities. Such phenomenon can occur for valves whose seals are located on the downstream side of the valve bearing axis. A pressure increase at the valve induces a valve deflection that reduces the leakage discharge because of the reduction of the seals gap. On the contrary, if the seals are located upstream the bearing axis, a pressure increase leads naturally to an increase of the leakage discharge. These 2 situations are illustrated in figure 6.9.

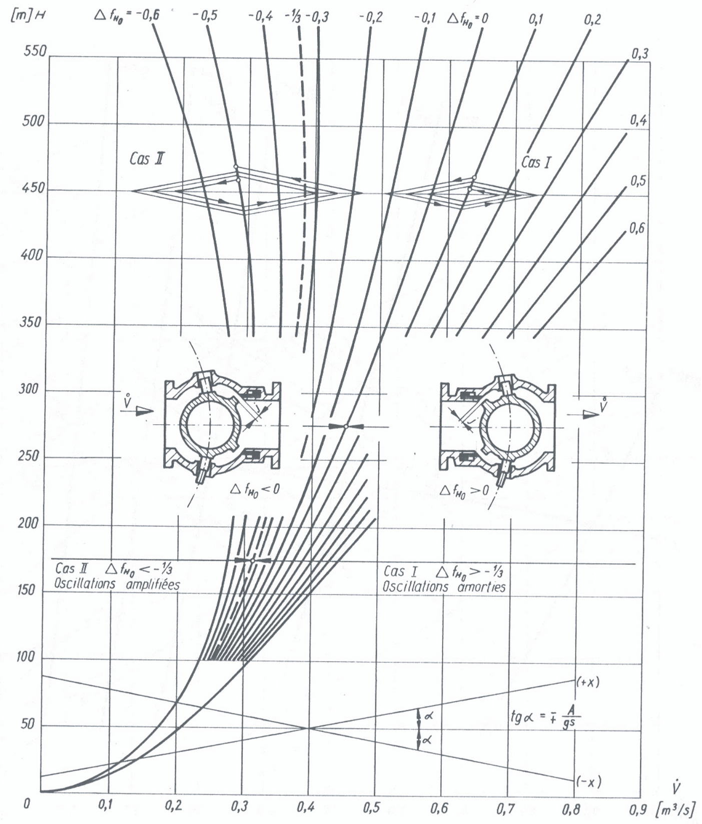

Figure 6.9: Diagram $Q - h$ for a valve with leakage [63].

6.3.4 Pumping System Stability

Pumping systems comprising an air vessel may feature instabilities as reported by Greitzer [65]. Such a system can be simplified for investigation purposes to a system comprising a downstream reservoir, a pump with fixed rotational speed, a pipe, a valve, an air vessel and an upstream reservoir. The equivalent scheme of this system is made of the pump pressure source $H_p(Q)$, the pipe model with the pipe inductance L_p and resistance R_p, while the air vessel is modelled by its capacitance C_{AV} and the valve by its resistance R_v, see figure 6.10. The compliance of the pipe is neglected with respect to the air vessel compliance.

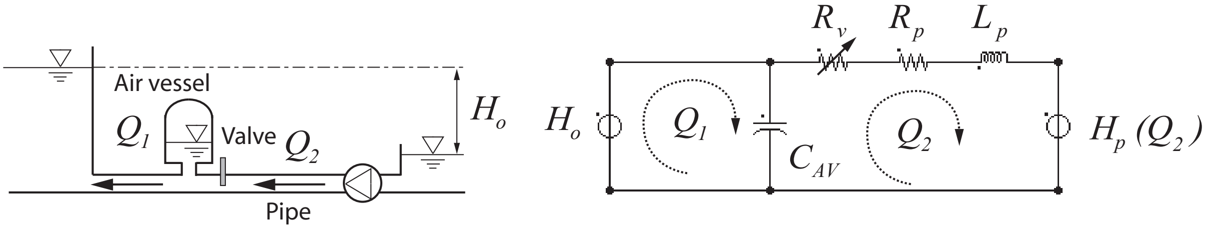

Figure 6.10: Hydraulic circuit with pump.

The corresponding set of differential equations is given by:

$$\begin{cases} L_p \cdot \dfrac{dQ_2}{dt} + R_p \cdot Q_2 + R_v \cdot Q_2 + H_p(Q_2) = h_{AV} \\ C_{AV} \cdot \dfrac{dh_{AV}}{dt} = Q_1 - Q_2 \end{cases} \tag{6.35}$$

The head of the pump can be linearized around the operating point Q_2* of interest as follows:

$$H_p(Q_2) = H_{p*} + \underbrace{\frac{dH}{dQ_2}|_{Q_2*}}_{R_{Q_2*}} \cdot (Q_2 - Q_2*) \tag{6.36}$$

Combining the 2 above equations and assuming that the upstream discharge fluctuations are negligible leads to the following characteristic equation:

$$\frac{d^2Q_2}{dt^2} + \underbrace{\frac{R_v + R_p + R_{Q_2*}}{L_p}}_{2\cdot\mu} \cdot \frac{dQ_2}{dt} - \underbrace{\frac{1}{C_{AV} \cdot L_p}}_{\omega_o^2} \cdot Q_2 = 0 \tag{6.37}$$

The system remains stable for $2 \cdot \mu > 0$, leading to the following stability criteria:

$$R_v + R_p > -\frac{dH}{dQ_2} \tag{6.38}$$

The above stability criteria shows that a negative slope of the characteristic curve of the pump $H_p = H_p(Q)$ considering a negative discharge in pump mode may lead to system instabilities. Then, for system whose slope of energetic losses in the pipe and the valve are higher than the slope of the pump characteristic, the system is stable, as illustrated in figure 6.11 left. But, if the slope of the energetic losses are below the energetic losses, as illustrated in figure 6.11 right, the system is unstable.

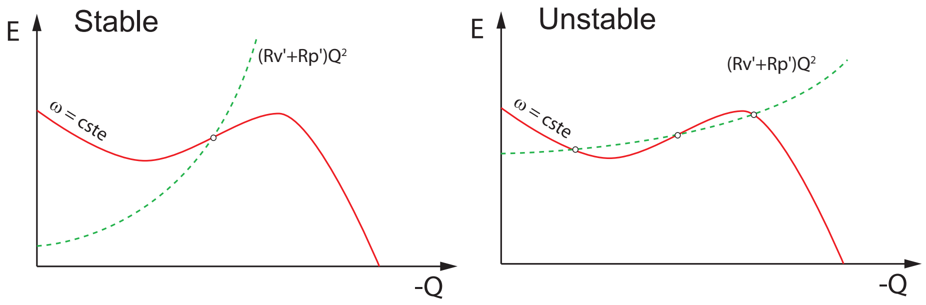

Figure 6.11: Condition of stability of a pumping system.

6.3.5 Pump-Turbine Installation Stability

A hydraulic circuit comprising an upstream reservoir, a pipe and a non-cavitating pump-turbine may exhibit an unstable behavior after perturbations (Greitzer [65], Martin [102], Jacob [79], Huvet [75]). For the stability analysis of such a system, the rotational speed changes of the pump-turbine has to be taken into account (Martin [102], Huvet [75]) and therefore the model should consider both the hydraulic and mechanical properties. The hydraulic part of the system can be modelled with a first order equivalent scheme for the pipe made of a resistance R_p and an inductance L_p, compressibility effects being neglected, while the pump-turbine is modelled by a variable pressure source H_{pt} as presented in figure 6.12. For the mechanical model, the angular momentum law is applied to the inertia J accounting for both the rotor of the generator and the turbine inertia.

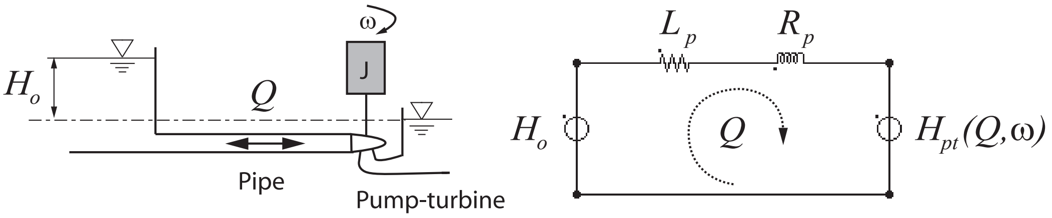

Figure 6.12: Hydraulic circuit with pump-turbine.

The corresponding set of differential equations is given by:

$$\begin{cases} H_o = L_p \cdot \dfrac{dQ}{dt} + R_p \cdot Q + H_{pt} \\ J \cdot \dfrac{d\omega}{dt} = T_{pt} + T_{el} \end{cases} \tag{6.39}$$

Where T_{el} is the electromagnetic torque and T_{pt} is the torque of the pump-turbine. The head and the torque of the pump can be linearized around the operating point $Q*, \omega*$ of interest as follows:

$$\begin{aligned} H_{pt}(Q,\omega) &= H_{pt*} + \underbrace{\frac{dH}{dQ}|_{Q*}}_{R_{Q*}} \cdot (Q - Q*) + \underbrace{\frac{dH}{d\omega}|_{\omega*}}_{R_{\omega*}} \cdot (\omega - \omega_*) \\ T_{pt}(Q,\omega) &= T_{pt*} + \underbrace{\frac{dT}{dQ}|_{Q*}}_{K_{Q*}} \cdot (Q - Q*) + \underbrace{\frac{dT}{d\omega}|_{\omega*}}_{K_{\omega*}} \cdot (\omega - \omega*) \end{aligned} \tag{6.40}$$

Combining equations 6.39 and 6.40 leads to the following matrix equation:

$$\frac{d}{dt} \cdot \begin{bmatrix} Q \\ \omega \end{bmatrix} = \underbrace{\begin{bmatrix} -\frac{R_{Q*}+R}{L_p} & -\frac{R_{\omega*}}{L_p} \\ \frac{k_{Q*}}{J} & \frac{k_{\omega*}}{J} \end{bmatrix}}_{[A]} \cdot \begin{bmatrix} Q \\ \omega \end{bmatrix} + \begin{bmatrix} H * - H_{pt*} + R_{\omega*} \cdot \omega_* + R_{Q*} \cdot Q* \\ T_{pt*} + T_{el} - k_{\omega*} \cdot \omega_* - k_{Q*} \cdot Q* \end{bmatrix} \tag{6.41}$$

The characteristic equation of the system 6.41 is obtained with the determinant $det([A] - [I] \cdot \delta)$, leading to:

$$\delta^2 + \underbrace{\left(\frac{R_{Q*} + R_p}{L_p} - \frac{k_{\omega*}}{J} \right)}_{2 \cdot \mu} \cdot \delta + \underbrace{\frac{k_{Q*} \cdot R_{\omega*}}{J \cdot L_p}}_{\omega_o^2} = 0 \tag{6.42}$$

The system remains stable for $2 \cdot \mu > 0$, leading to the following stability criteria:

$$\frac{R_{Q*} + R_p}{L_p} > \frac{k_{\omega*}}{J} \tag{6.43}$$

Expressing again the local derivative gives:

$$\underbrace{\frac{\frac{dH}{dQ}|_{Q*} + R_p}{L_p}}_{1/\tau_{fQ*}} > \underbrace{\frac{\frac{dT}{d\omega}|_{\omega*}}{J}}_{1/\tau_{m\omega*}} \tag{6.44}$$

In equation 6.44 above, the local fluid time constant τ_{fQ*} evaluated for a given Q_* and the local mechanical time constant $\tau_{m\omega*}$ evaluated for a given ω_* are introduced. The above stability criteria indicates that it is necessary that $\tau_{m\omega*} > \tau_{fQ*}$. The US Bureau of Reclamation even specifies that the stability of the power plant is ensured if $\tau_m > 2 \cdot \tau_f^2$ [98]. Where:

- $\tau_m = \frac{J \cdot \omega_{BEP}}{T_{BEP}}$: is the nominal mechanical time constant $[s]$;
- $\tau_f = \frac{l_p \cdot Q_{BEP}}{g \cdot H_{BEP} \cdot A_p}$: is the nominal fluid time constant $[s]$.

This criteria basically indicates that:

- a low penstock inductance L_p is suitable; *i.e.* a short penstock with large diameter;

- a high mechanical inertia J is suitable; *i.e.* a large diameter of generators rotors;
- the penstock and valves head losses have a positive effect, as it was identified by Dörfler [46];
- negative slope in the $H(Q)$ curves is not suitable; *i.e.* a positive slope in a $H - Q$ curve of a pump when the discharge is considered positive, or in the "S" part of the $Q_{11}(N_{11})$ curve in turbine mode;
- positive slopes of the $T(\omega)$ curves are not suitable.

From the above statements, it can be deduced that the stability criterion is intrinsically fulfilled for low head Francis turbines, but for high head Francis turbines or pump-turbines with a long penstock of small diameter, and low rotating inertia, the situation is more critical. Furthermore, high head pump-turbines are commonly of the low specific speed types and therefore presents "S"-shapes $Q_{11}(n_{11})$ and $T_{11}(n_{11})$ characteristic curves. But Martin [103] has demonstrated that overall, the relevant criteria is the sign of the slope of the $T_{11}(n_{11})$ for $T_{11} = 0$, the runaway condition, which should be negative to ensure stability. Martin has also established the period of the undamped oscillations using linearization of the turbine characteristic curves in order to evaluate the values of the coefficient k_{Q*} and $R_{\omega *}$ of equation 6.42 yielding to ω_o [102]. This method was validated on full scale facilities by Dörfler[46]. The stability criterion of Martin is illustrated in figure 6.13.

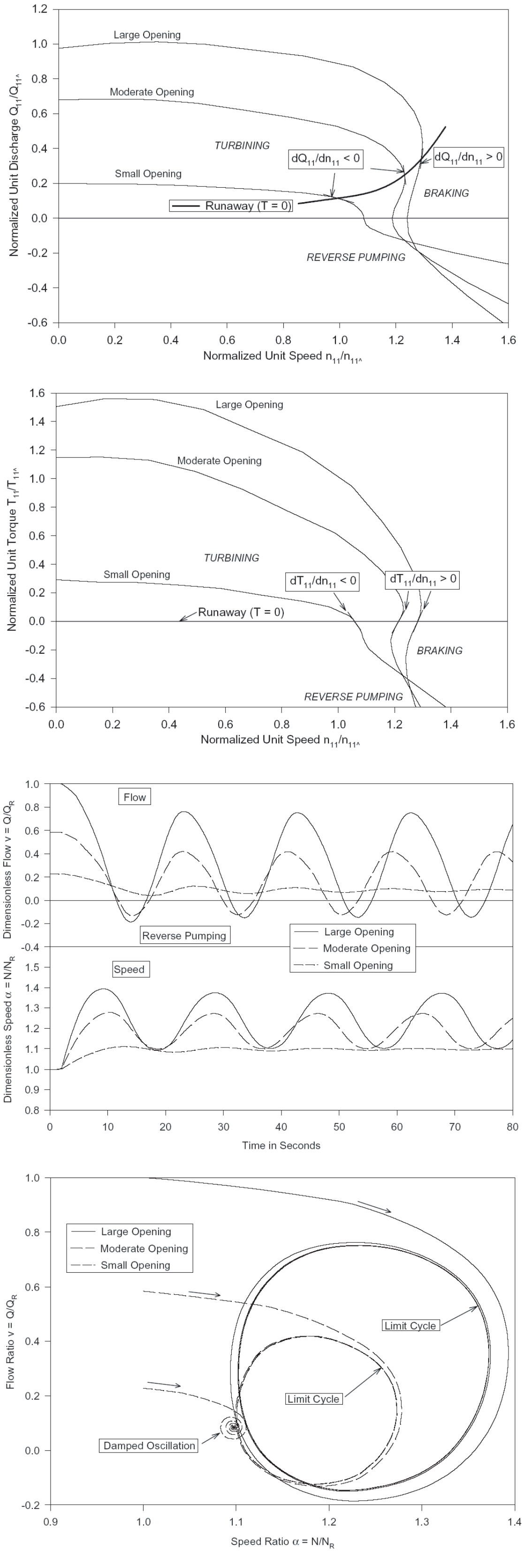

Figure 6.13: Stability analysis in the plane $Q_{11}(n_{11})$ and $T_{11}(n_{11})$ for a low specific speed Francis turbine [103].

Chapter 7

Transient Phenomena in Hydroelectric Power Plants

7.1 General

Once the models and the related equivalent schemes of the hydraulic components are established, transient simulation can be performed to highlight the possible hydroelectric interactions. The following aspects are treated in the following sections:

- validation of the hydraulic modules of SIMSEN-Hydro;
- investigation of the impact of classical hydraulic or electric disturbances on the dynamic behavior of a hydroelectric power plant;
- comparison of the stability of the turbine speed governor using a hydraulic model versus a hydroelectric model in isolated production mode;
- investigation on the turbine speed governor stability in islanded production mode.

7.2 Validation of SIMSEN-Hydro

7.2.1 Case Study Definition

The validation of SIMSEN-Hydro is achieved by simulating the transient behavior of a 1260 MW pumped storage plant resulting from the emergency shutdown in generating and pumping modes and comparing the simulation results with the available data. The hydraulic layout of the pumped storage plant is presented in figure 7.1. A 590 m long penstock is feeding 4 Francis pump-turbines, with 4 downstream surge chambers of variable sections that are all connected to a 304 m long pressurized tailrace water tunnel. The data related to the piping system are presented in table 7.1 and the design values of the pump-turbines are given in table 7.2. The cross sections and elevations of the downstream surge chambers are given in figure 7.2. The loss coefficient of the surge chambers sudden cross section changes is calculated to be $K = 1.5$. The number of nodes used for the modelling of each pipe is calculated in order to fulfill the CFL criterion with the same frequency resolution.

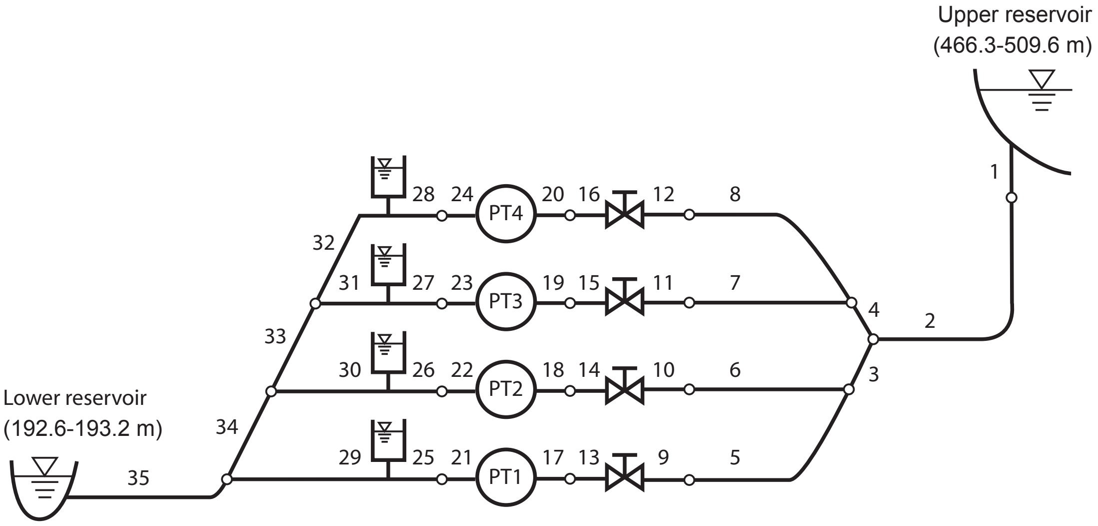

Figure 7.1: Layout and pipe numbering of the pumped storage plant test case.

Table 7.1: Rated values of the pump-turbines of the validation test case.

H_n	Q_n	P_n	N_n	D_{ref}	J_{tot}	ν
$[m]$	$[m^3/s]$	$[MW]$	$[rpm]$	$[m]$	$[kg \cdot m^2]$	$[-]$
305	109	315	300	5.08	$2.77 \cdot 10^6$	0.272

The pump-turbine characteristic of the pumped storage plant are represented in figure 7.3. The modelling of the pump-turbines takes into account kinematic relation between the servomotor stroke and the guide vane opening. The spiral case and draft tube are modelled as pipes of equivalent length and diameter and correspond respectively to pipes N° $17-20$ and N° $21-24$. During the load rejection, the circuit breaker between the generator and the transformer is opened, which leads to an electromagnetic torque equal to zero. Consequently, the electrical installations are assumed to have no significant influence

Table 7.2: Pipes dimensions according to the numbering in figure 7.1.

Pipe	**1**	**2**	**3**	**4**	**5**	**6**	**7**	**8**	**9-12**	**13-16**
$L[m]$	30.48	590.4	29.14	29.14	78.70	72.89	67.06	61.23	24.23	28.96
$D[m]$	13.02	10.67	7.47	7.47	5.33	5.33	5.33	5.33	4.18	3.05
$a[m/s]$	1219	1297	1166	1166	1311	1325	1341	1225	1212	1158
$\lambda[-]$	0.015	0.015	0.015	0.015	0.015	0.015	0.015	0.015	0.015	0.015

Pipe	**17-20**	**21-24**	**25-28**	**29**	**30**	**31**	**32**	**33**	**34**	**35**
$L[m]$	30.48	26.85	60.14	79.49	62.06	38.77	42.67	33.96	33.96	304.8
$D[m]$	2.20	5.015	5.33	5.33	5.33	5.33	5.33	7.47	9.30	10.67
$a[m/s]$	870	1342	1336	1324	1241	1292	1219	1358	1358	1287
$\lambda[-]$	0.015	0.015	0.015	0.015	0.015	0.015	0.015	0.015	0.015	0.015

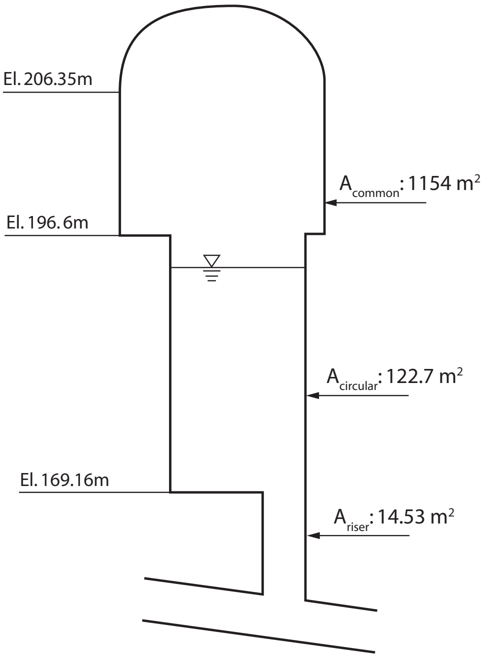

Figure 7.2: Surge chamber cross sections and elevations.

on the transient and are modelled as an external torque acting on the mechanical inertias.

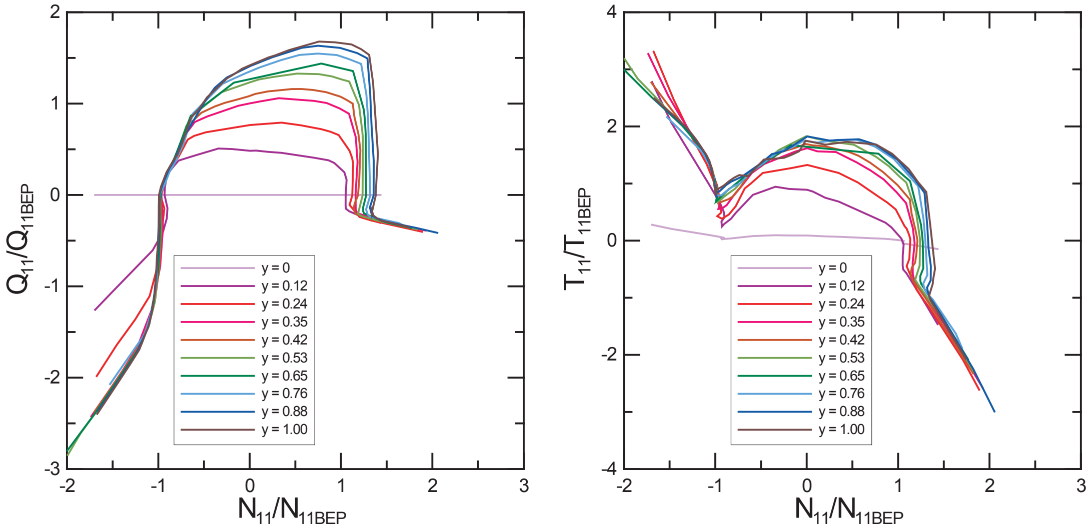

Figure 7.3: Pump-turbine characteristic of the pumped storage plant.

7.2.2 Simulation Results

Transients Simulation Scenarios

Transient tests carried out during commissioning have been performed for different situations of emergency shutdown and load acceptance/rejection. Two transients tests are selected for the validation of the simulation results. Their corresponding sequences are the following:

- emergency generating shutdown test: Units 1, 3 and 4 are set to fully opened guide vanes, y=1, which corresponds to 390 MW under the test head defined by the upstream reservoir level of 489.2 m (1605 ft), Unit 2 being kept in operation. The guide vanes of pump-turbines 1, 3 and 4 are closed within 24 seconds with 2 slopes.

- emergency pumping shutdown test: Units 1, 3 and 4 are set to 65% guide vane opening, best pump efficiency point, under an upstream reservoir water level of 481 m (1578 ft), Unit 2 being at rest with the guide vanes closed. The guide vanes of the pump-turbines 1, 3 and 4 are closed in 16.4 seconds, with two slopes.

The servomotor stroke closing law used for both simulations is based on a closure in 20 seconds from $y = 1$ to $y = 0.08$, and 4 seconds from $y = 0.08$ to $y = 0$.

Simulation Results for Emergency Shutdown in Generating Mode

The results of the simulation of the emergency shutdown of the Units 1, 3 and 4 while Unit 2 is kept at the same operating point, are presented for the pump-turbine 1, for the surge tank of Unit 1, and for the level of the 4 surge tanks, in figure 7.4.

The pump-turbine of Unit 1 is operating at the full guide vane opening, $y = 1$, for 10 s, then the electromagnetic torque is set to zero. As a consequence the rotational speed of the Unit is increasing. To reduce the runaway rotational speed the guide vanes are closed linearly with 2 slopes thus reducing the discharge and therefore the mechanical torque of the pump-turbine. When the torque reaches zero, the maximum over-speed is attained. Then the discharge becomes also negative and the pump-turbine is in the turbine dissipation quadrant. The closure of the guide vanes induces a waterhammer effect in the penstock leading to head fluctuations. The related head fluctuation is quickly damped as the discharge in Unit 2 remains almost constant. When the guide vanes are fully closed, after 24 s, the discharge value is zero, the rotational speed decreases because of the negative value of the torque. The operating points of the pump-turbine during the transient are represented in the $Q_{11}(N_{11})$ and $T_{11}(N_{11})$ plane in figure 7.5. Due to the shutdown of the pump-turbines of Unit 1, 3 and 4, the water level of the surge chambers first decreases according to the downstream mass oscillation period between the tailrace tunnel and the surge chambers. The water level evolution s in the surge chambers are almost simultaneous for Units 1, 3 and 4 while the water level decrease starts later on Unit 2 because the pump-turbine is kept in operation. The influence of the different cross sections is visible on the time evolution of the water level in the surge tank. The mass oscillation period is about $100s$ and is dependant on the water level history as the cross section of the surge chambers is changing during the transient.

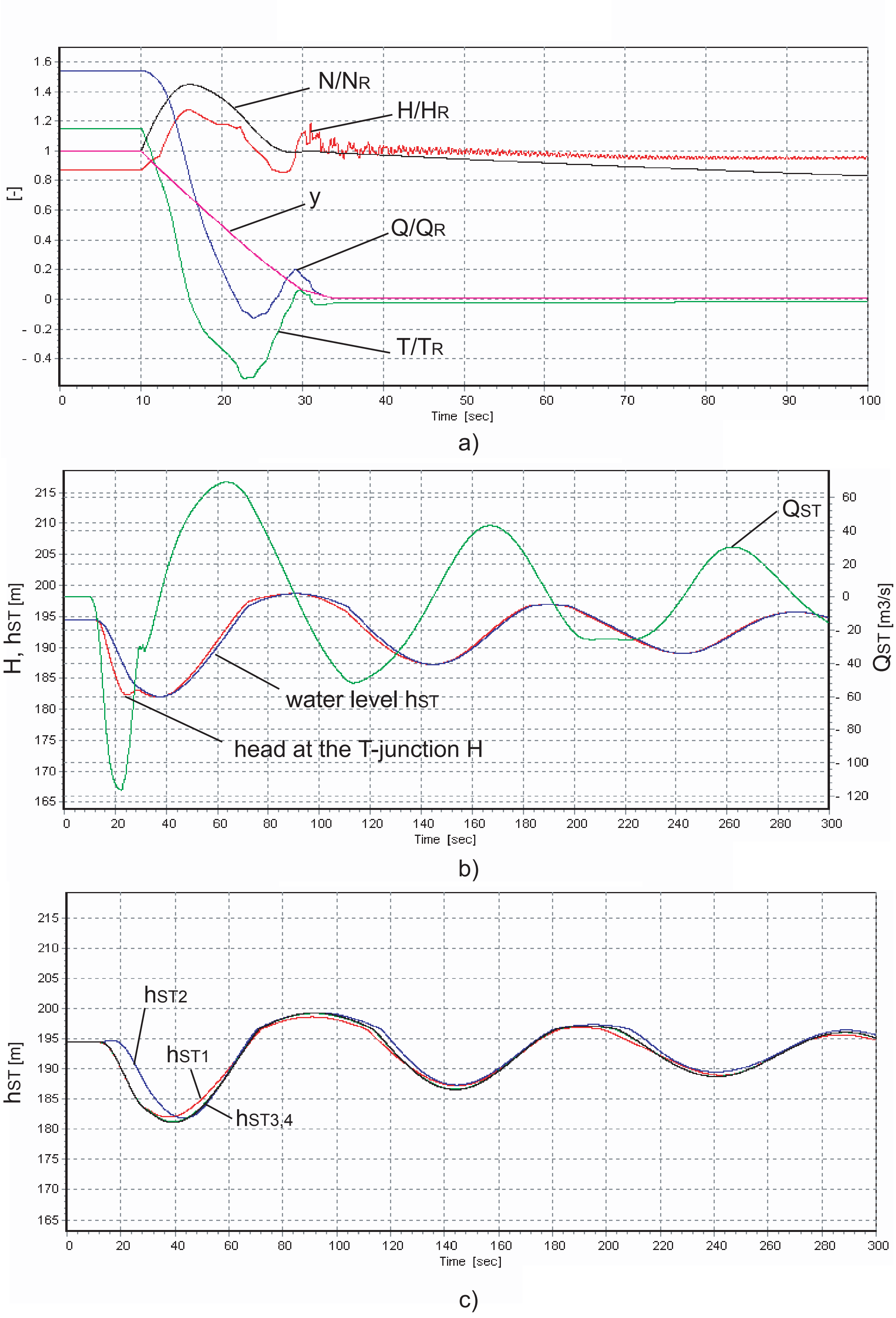

a)

b)

c)

Figure 7.4: Transient behavior of the pumped storage plant resulting from an emergency shutdown in generating mode; transient of the pump-turbine Unit 1 in rated values a), transient of surge chamber of Unit 1 b), transient of the 4 surge tanks c).

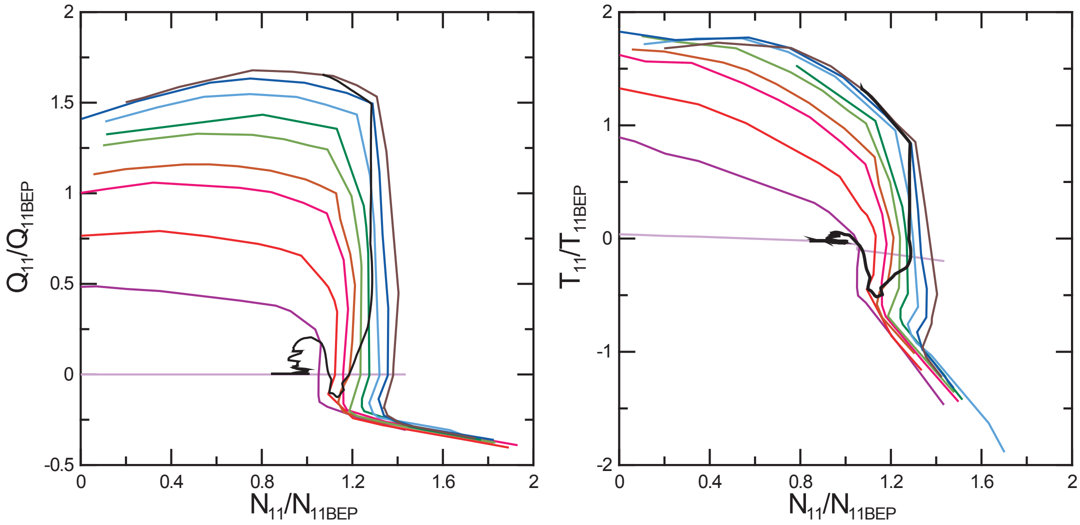

Figure 7.5: Operating point trajectory in the plan $Q_{11}(N_{11})$ and $T_{11}(N_{11})$ during the emergency shutdown in generating mode for Unit 1.

Simulation Results for Emergency Shutdown in Pumping Mode

The simulation results of emergency shutdown of Units 1, 3 and 4 in pumping mode while Unit 2 is at rest are presented in figure 7.6 for pump-turbine 1, surge tank 1 and the 4 surge tanks water levels.

The pump-turbine of Unit 1 is operating at the steady state pump operating point corresponding to $y = 0.65$, negative discharge and negative rotational speed for 10 s. Then the electromagnetic torque is set to zero, inducing the slow down of the rotational speed of the Unit 1, as well as the decrease of the discharge, head and torque. Then the discharge becomes positive and the pump-turbine is operating in the pump dissipation quadrant. Once the guide vanes are fully closed the discharge value is zero and the rotational speed is positive but decreasing. Waterhammer is also induced in the penstock and leads to head fluctuations. Here the amplitudes require more time to damp out as there is no more discharge in the 4 pump-turbines. Here the mass oscillation starts by an increase of the water level in the surge chamber as the initial discharge is negative. The operating points of the pump-turbine during the transient are represented in the $Q_{11}(N_{11})$ and $T_{11}(N_{11})$ plane in figure 7.7.

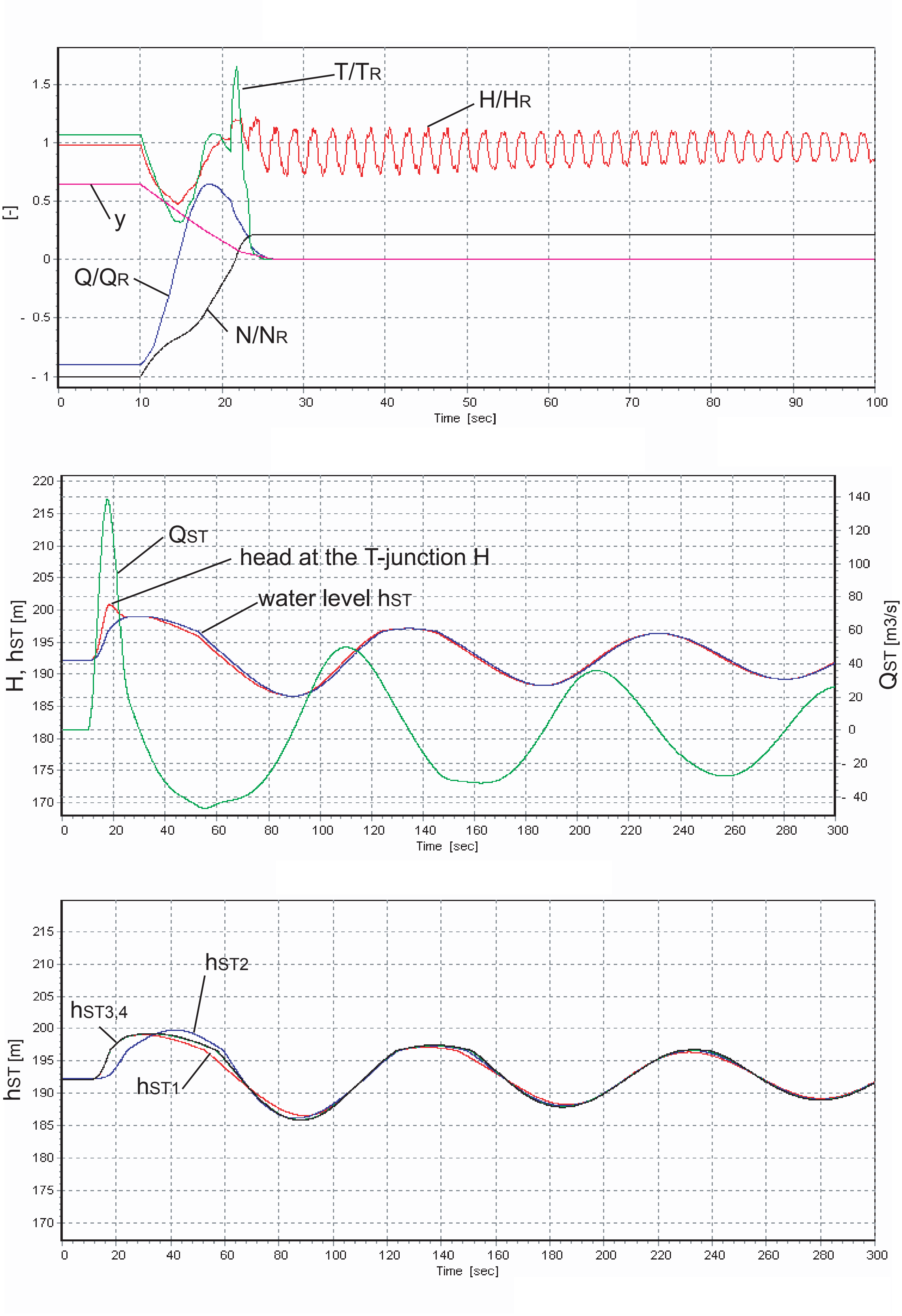

Figure 7.6: Transient behavior of the pumped storage plant resulting from an emergency shutdown in pumping mode; transient of the pump-turbine Unit 1 in rated values a), transient of surge chamber of Unit 1 b), transient of the 4 surge tanks c).

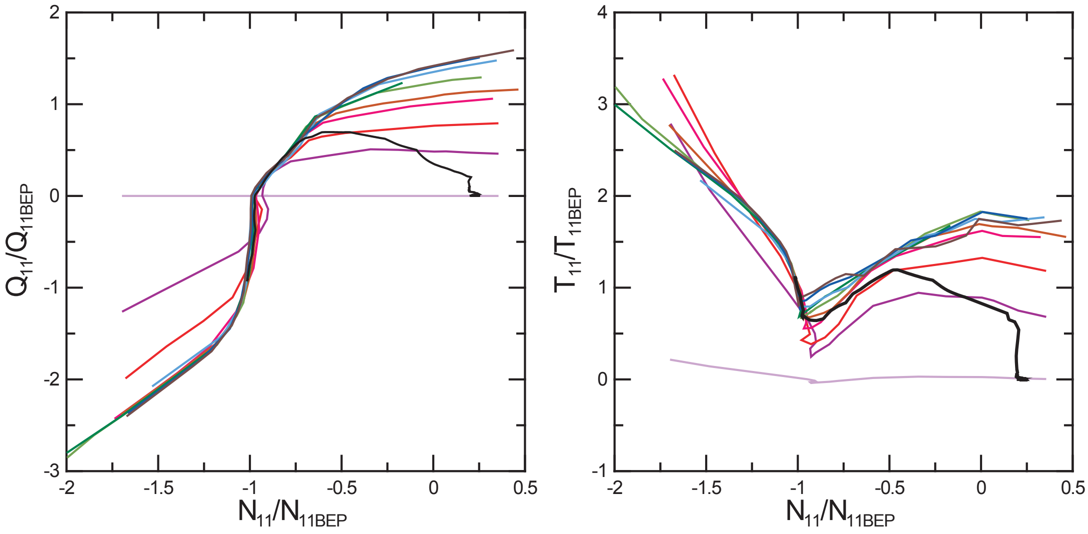

Figure 7.7: Operating point trajectory in the plan $Q_{11}(N_{11})$ and $T_{11}(N_{11})$ during the emergency shutdown in pumping mode for Unit 1.

7.2.3 Validation

During the transients tests carried out at the commissioning of the pumped storage plant, the piezometric head time history was recorded on Unit 1 at the spiral case inlet, at the draft tube man-door, and the surge chamber. The simulation results in generating and pumping mode time evolution are compared for these 3 values and represented in table 7.3.

Table 7.3: Comparison of simulation results with transient tests carried out on Unit 1 during an emergency shutdown in both generating and pumping mode; simulation in light red line and measurements in bold black line.

<table>
<tr><th>Generating Mode</th><th>Pumping Mode</th></tr>
<tr><td>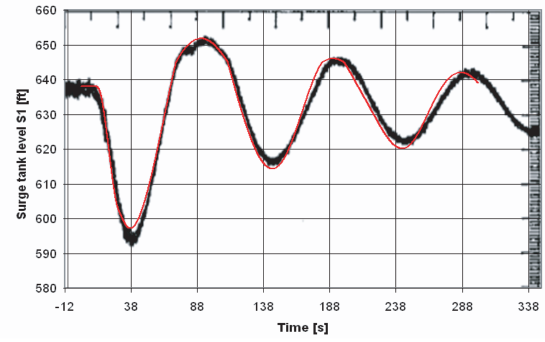
</td><td>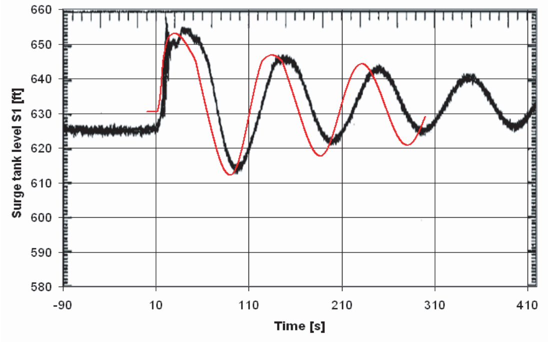
</td></tr>
<tr><td>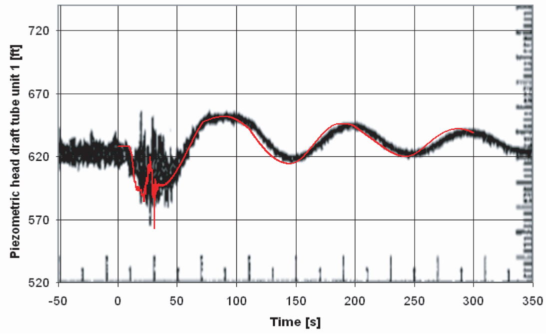
</td><td>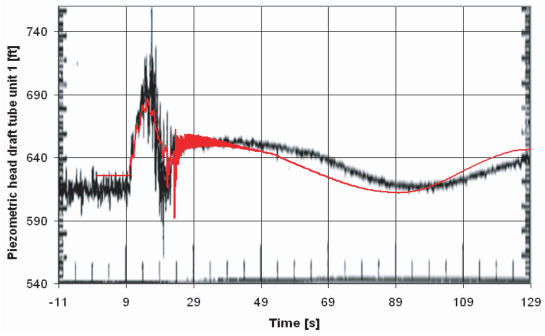
</td></tr>
<tr><td>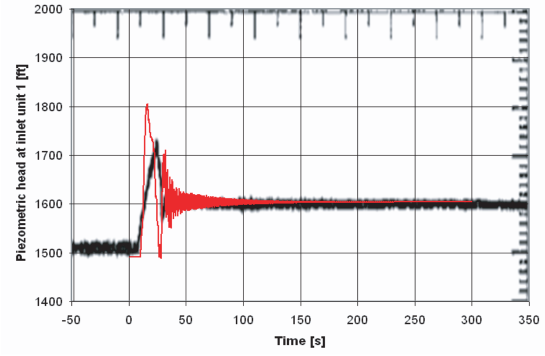
</td><td>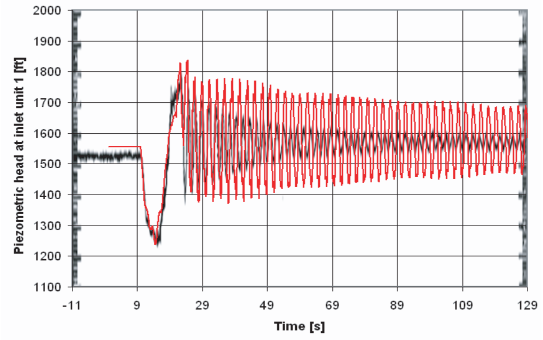
</td></tr>
</table>

By comparing the simulation results with the measurements on site during an emergency shutdown in generating mode it can be noticed that:

- the steady state conditions before the transients presents a very good agreement;

- the amplitudes and time evolution of water level in surge tank 1 and piezometric head in draft tube of unit 1 present also a very good agreement;
- the overpressure amplitude of the piezometric head at the unit 1 inlet presents a discrepancy of 30%, however the time evolution of the piezometric head shows a good agreement.

By comparing the simulation results with the measurements on site during emergency shutdown in pumping mode it can be noticed that:

- the steady state conditions of the simulation presents small discrepancies that can be due to errors on the downstream water level, difference in the friction losses in pumping and generating mode or difference between scale model and prototype characteristics;
- the amplitudes of the piezometric head at the inlet of pump-turbine 1 presents a good agreement;
- the waterhammer at the pump-turbine 1 inlet does not damp out as quickly as the in measurements;
- the time evolution of the water level in the surge tank 1 and the piezometric head in the draft tube of Unit 1 presents a discrepancy on the period of the mass oscillation but the amplitudes fit roughly.

In order to identify the origin of the discrepancies of the surge tank water level time evolution during the emergency shutdown in pumping mode, the steady state discharge obtained by simulation is compared to the discharge measured on site. The comparison of the steady state discharge for generating and pumping mode is presented in table 7.4. The measured values of the discharges are given with a confidence range of ± $8m^3/s$ because of the poor resolution of the graphical representation of the time evolution of the discharge from which the value is deduced.

Table 7.4: Initial steady state conditions of discharge for Unit 1.

Test Case	**Simulation** $Q\ [m^3/s]$	**Measurements** $Q\ [m^3/s]$	**Error** $[-]$
Generating mode	166.8	155.7 ± 8	$+0.07$
Pumping mode	98.1	120 ± 8	-0.18

The comparison of the simulated and measured discharges points out an error on the discharge in generating mode that is in the range of uncertainties of the measured value. However, a difference of about 18% is found on the initial conditions of the discharge in pumping mode. Given small error in generating mode, the error in pumping mode is probably not due to errors on the friction parameters of the hydraulic circuit. The error is probably due to differences of the pump-turbine characteristic between the scale model and the prototype.

Moreover, the mechanical power obtained in generating mode differs between the simulations and the measurements. The measurements report a power of 390 MW for the chosen operating point while the simulation predicts only 362 MW. This corresponds to an efficiency difference between the scale model and the prototype: the prototype efficiency is higher than the scale model efficiency. This fact is commonly admitted.

As the initial discharge in pumping mode is smaller in the simulation compared to the experiments, the amplitudes are also smaller, thus reducing the oscillation period due to the non-linear cross section of the surge chambers. It also explains the difference of the initial conditions of the piezometric head which value would be reduced in the case of a higher discharge and thus would present a better fit with the experiments. Therefore, if the discharge were higher in the simulation, the waterhammer in the spiral case would show higher amplitudes in similar fashion as in generating mode.

The error on the amplitude of the waterhammer is probably also due to differences of the pump-turbine characteristics that strongly influences the overpressure of the emergency shutdown of the pump-turbine. Indeed, as the turbine goes through the "S" shape of the pump-turbine during such a transient, see figures 7.5 and 7.7, the discharge becomes negative during the closure of the guide vanes and therefore induces a higher overpressure than in the case of turbines without "S" shape characteristic.

Despite the differences between the simulation and the experiments found in pumping mode, the models of hydraulic components developed and implemented in SIMSEN-Hydro are satisfactory.

7.2.4 Numerical Instabilities

The simulation of the emergency shutdown resulting from a full load rejection of a pump-turbine shows that the pump-turbine is going through the unstable part of the characteristic, *i.e.* the S-shape. The numerical integration of the differential equation set of the whole system using Runge-Kutta 4th order has proven its robustness, see appendix A. However, when simulating the load rejection, numerical instabilities have been pointed out during the transit through the "S". To overcome this numerical problem, it has been identified that the CFL criteria, equation 3.60, must be fulfilled as follow:

$$\frac{dx}{a \cdot dt} = k \qquad ; \quad k = 1, 2, 3... \tag{7.1}$$

Then, for each pipe, the wave speed has to be adapted in order to satisfy the above criteria. It is acceptable to adapt the wave speed as there are uncertainties on this value because its analytical value presents some dispersion compared to the experimental data due to errors on the wall material properties, dimensions, contact between the pipe and the support or concrete, or air content. A comparison of the simulation results of a load rejection of a pump-turbine with constant guide vane opening y is presented in figure 7.8 for both cases: wave speed adapted or not. It appears, that when the turbine is going through the unstable part of the characteristic, *i.e.* negative torque, the torque and the head start oscillating for the simulation without adaptation of the wave speed, while, the torque and head evolution stay stable over time evolution for the simulation with adaptation of the wave speed.

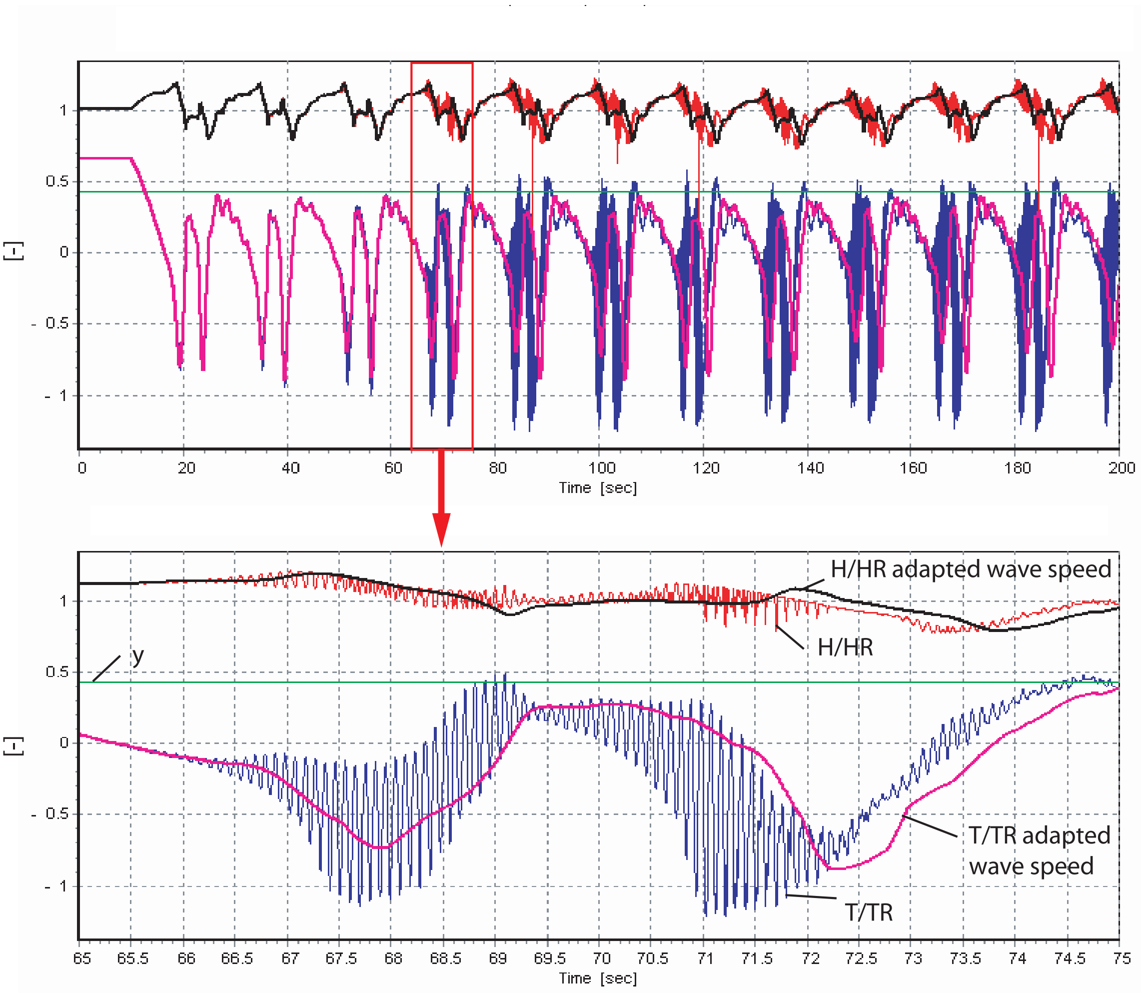

Figure 7.8: Simulation of a full load rejection with constant guide vane opening with and without adaptation of the wave speed.

7.3 Hydroelectric Transients

7.3.1 Case Study Definition

In order to highlight hydroelectric interactions, a hydroelectric power plant comprising both the hydraulic circuit and the electrical installation is modelled. The system investigated comprises an upstream reservoir, a gallery, a surge tank with variable cross section, 2 Francis turbines of 86 MW and 2 generators connected to a 205 kV network, see figure 7.9. The data related to this example are presented in table 7.5. The Francis turbine and the generator are regulated as follows:

- a turbine power or speed governor acting on the guide vane opening of the Francis turbine;
- a voltage regulator acting on the excitation field voltage of the generators.

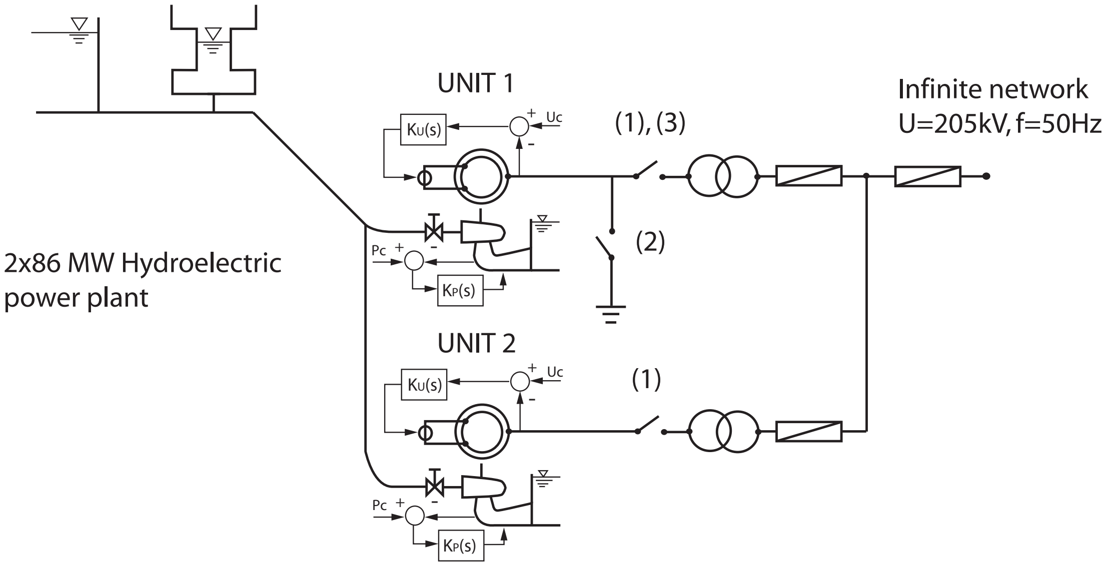

Figure 7.9: Layout of the hydroelectric power plant case study.

To investigate the dynamic behavior of the power plant, 3 simulation models are used: (i) a hydraulic model, (ii) an electric model and (iii) a hydroelectric model. Then, the hydroelectric model simulation results are compared either with the results obtained with the hydraulic model for hydraulic disturbances or with the results obtained with the electric model for electric disturbances. Therefore, 3 standard disturbances are simulated:

- a total load rejection: the 2 circuit breakers between the transformers and the synchronous machines of both Units, see figure 7.9 (1), are opened at $t = 1$ s, while the guide vanes of the 2 Francis turbines are closed linearly in 7 s; hydraulic and hydroelectric models are compared;

Table 7.5: Main dimensions of the power plant.

Reservoir	**Gallery**	**Surge Tank**
$H_o = 85\ m$	$L = 4000\ m$	$A_{ST}(Z_{ST} < 77) = 700\ m^2$
	$D = 10\ m$	$A_{ST}(77 < Z_{ST} < 87) = 400\ m^2$
	$\lambda = 0.02$	$A_{ST}(Z_{ST} > 87) = 700\ m^2$
	$a = 1000\ m/s$	

Penstock	**Turbine**	**Generator**
$L = 125\ m$	$H_n = 82\ m$	$S_n = 98\ MVA$
$D = 5.5\ m$	$Q_n = 114\ m^3/s$	$U_n = 17.5\ kV$
$\lambda = 0.02$	$N_n = 200\ rpm$	$f = 50\ Hz$
$a = 1250\ m/s$	$T_n = 4.11 \cdot 10^6\ Nm$	pair pole = 15
	$J_t = 8.415 \cdot 10^4\ kg \cdot m^2$	$J_g = 1.683 \cdot 10^6\ kg \cdot m^2$
		$K_{shaft} = 1.27 \cdot 10^{10}\ Nm$

- an earth fault: the 3 phases between the synchronous machine and the transformer of Unit 1 are connected to the ground by closing the circuit breaker (2) of figure 7.9, electric and hydroelectric models are compared;
- an out of phase synchronization: the circuit breaker between the transformers and the synchronous machines of Unit 1, see figure 7.9 (3), is closed with an error of synchronization with the infinite network, only the hydroelectric model is used.

7.3.2 Load Rejection

The first investigation deals with the case of a total load rejection where the circuit-breaker between the transformer and the generator is tripped. Simultaneously, the guide vanes of the two Francis turbines are closed linearly in 7 seconds. The evolution of the main variables during the total load rejection is presented in figure 7.10.

At the outset, the electromagnetic torque of the generators drops to zero instantaneously, as a result the rotational speed of the 2 Units increases. The closure of the guide vanes reduces the hydraulic torque, quickly limiting the maximum rotational speed. The guide vanes closure induces a waterhammer effect in the adduction part of the power plant and a mass oscillation between the reservoir and the surge tank.

The comparison between the hydraulic and hydroelectric simulation results are shown in figure 7.11 for the rotational speed and the pressure at the turbine inlet. In the hydraulic model, the electrical installation is modelled by a constant torque dropping to zero instantaneously at $t = 1s$. It can be seen that the 2 simulation results are identical and therefore a hydroelectric model is not required for simulating such transient phenomena.

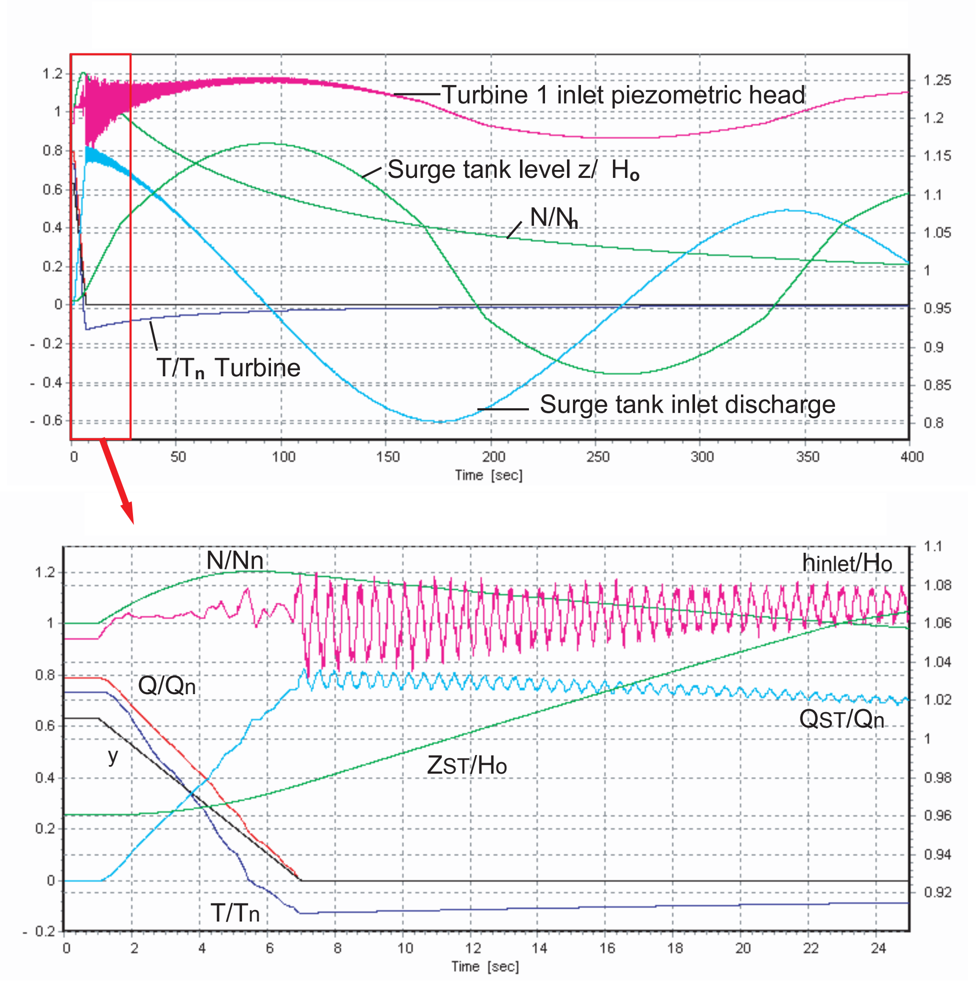

Figure 7.10: Evolution of the turbine 1 and surge tank variables during total load rejection.

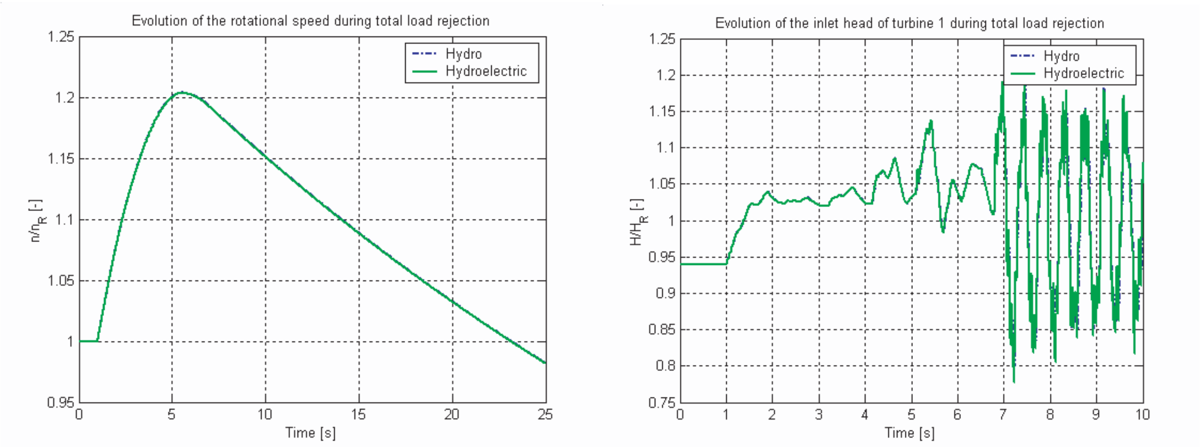

Figure 7.11: Comparison of the evolution of the turbine 1 rotational speed n (left) and inlet piezometric head H (right) obtained with two simulations: simulation with hydraulic model and simulation with the hydroelectric model.

7.3.3 Earth fault

The effect of an earth fault occurring between the generator and the transformer of Unit 1 is evaluated using both the electric and hydroelectric simulation models. Depending on the duration of the fault, the synchronization is maintained or lost after the fault is removed, leading to the critical time t_c. Figure 7.12 presents the comparison of the simulation results obtained using the two models, for a duration inferior and superior to the critical time t_c. It is pointed out that the critical time t_c is underestimated by 2% using the electric model in which the turbine torque is assumed constant. The difference between the 2 simulation results is due to the action of the turbine power regulator that is taken into account by the hydroelectric model. For the simulation, it can be seen that the maximum amplitudes are well predicted by the electric model but the time history is more realistic using the hydroelectric simulation as the influence of the turbine speed governor is properly taken into account. However, its influence on the critical time of the duration of the fault is negligible.

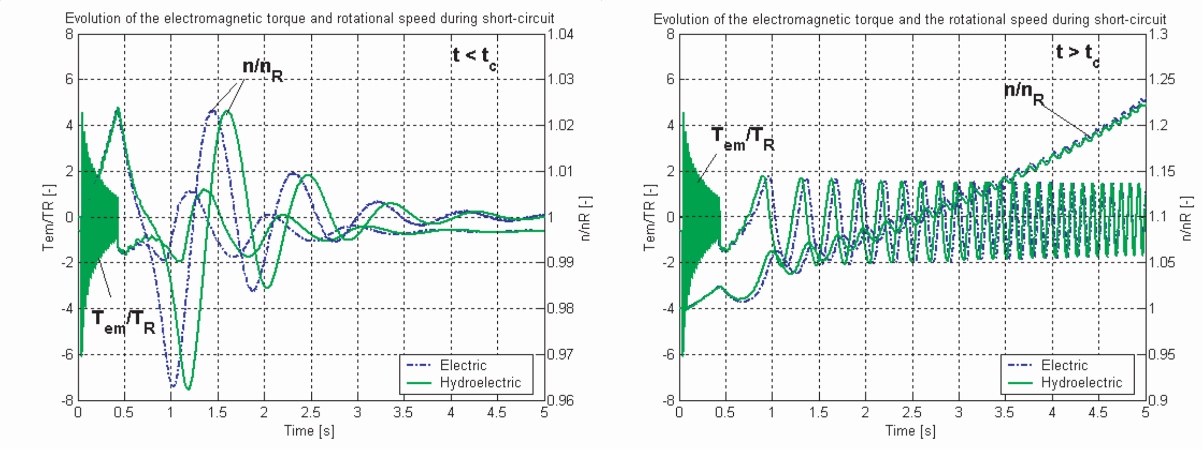

Figure 7.12: Comparison of the effect of an earth fault on Unit 1 with a duration under and over critical time t_c obtained with two simulation models: electric model and the hydroelectric model. On the left the synchronism is kept and on the right it is lost.

7.3.4 Out of Phase Synchronization

Three conditions are required for the success of the synchronization of the generator to the power network during the group start-up: the frequency, the phase and the magnitude have to match the corresponding network conditions before the closure of the circuit-breaker (3). The worst synchronization cases occur when the generator and the network are 120° and 180° out of phase. The simulation results obtained with the hydroelectric model are presented in figure 7.13 for Unit 1, and the impact on Unit 2 is presented in figure 7.14 for the out of phase synchronization of 120°. For these simulations a turbine speed governor is used in state of the turbine power governor.

In the case of a 120° out of phase synchronization, the closure of the circuit-breaker induces a strong transient electromagnetic torque up to 6 *pu* that produces rotational speed variations. This induces a reaction of the turbine speed governor acting on the

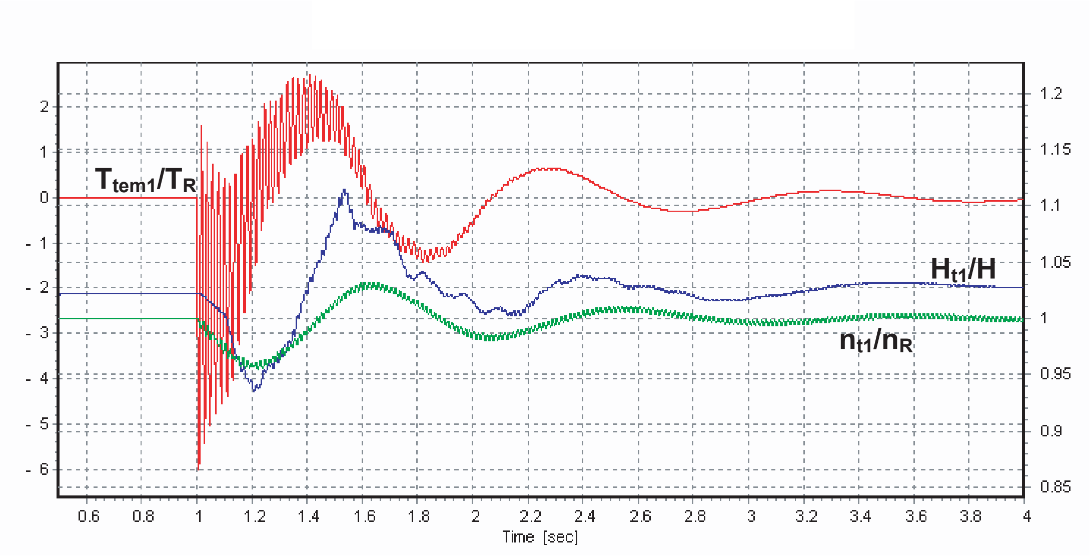

Figure 7.13: Evolution of the electromagnetic torque, the head of the turbine and rotational speed of the group number 1 during synchronization fault of 120° electrical degree.

guide vane opening in order to keep the rotational speed constant. Both effects contribute to the variation of the inlet pressure variations of the Unit 1 turbine. In addition, the first peak of the electromagnetic torque produces free torsional vibrations at 63 Hz of the shaft line constituted of the turbine and the generator inertias linked through the connecting shaft. This dynamic response of the structure is observable on the pressure at the inlet of the turbine of Unit 1 which evidences the coupling between the hydraulic and mechanical parts. It is interesting to notice that Unit 2 is also affected by the fault on Unit 1 through both the piping system and the electrical lines. Thus, the head of the turbine and the current of the stator of the generator of Unit 2 are disturbed by the out of phase synchronization of Unit 1.

The simulation results of the 180° out of phase synchronization are presented for Unit 1 in figure 7.15. It can be noticed that, as expected, this fault produces stronger current variations in the stator than for 120°. The statoric current reaches 8 pu while transient electromagnetic peak is reduced to 4 pu.

The simulation of the out of phase synchronization clearly points out the interaction between the hydraulic and electric parts of the installation due to the link between the 2 Units through the piping and the electrical lines. Such influence can only be analyzed with a hydroelectric simulation model.

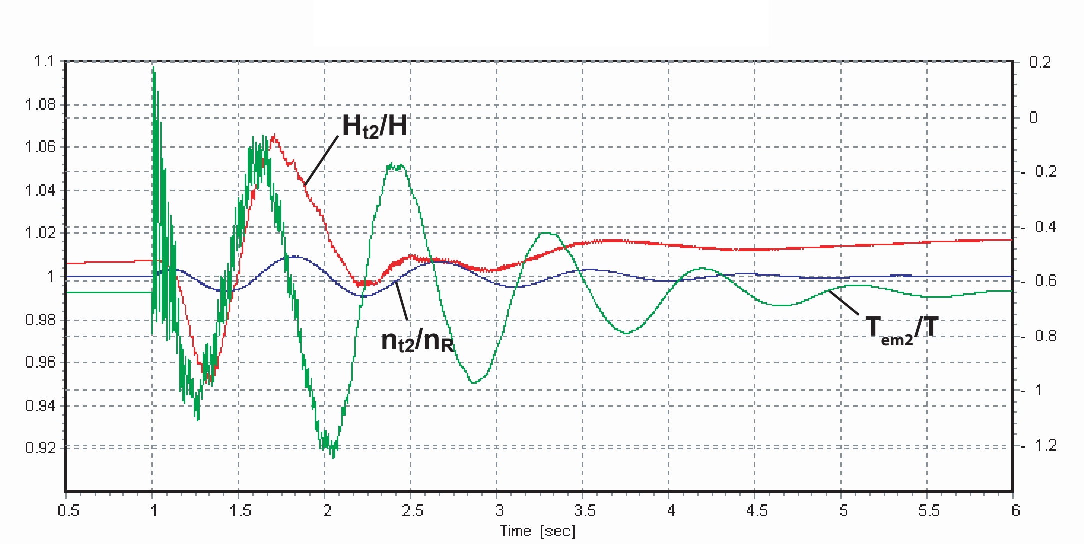

Figure 7.14: Effects of 120° out of phase fault of the Unit 1 on the Unit 2.

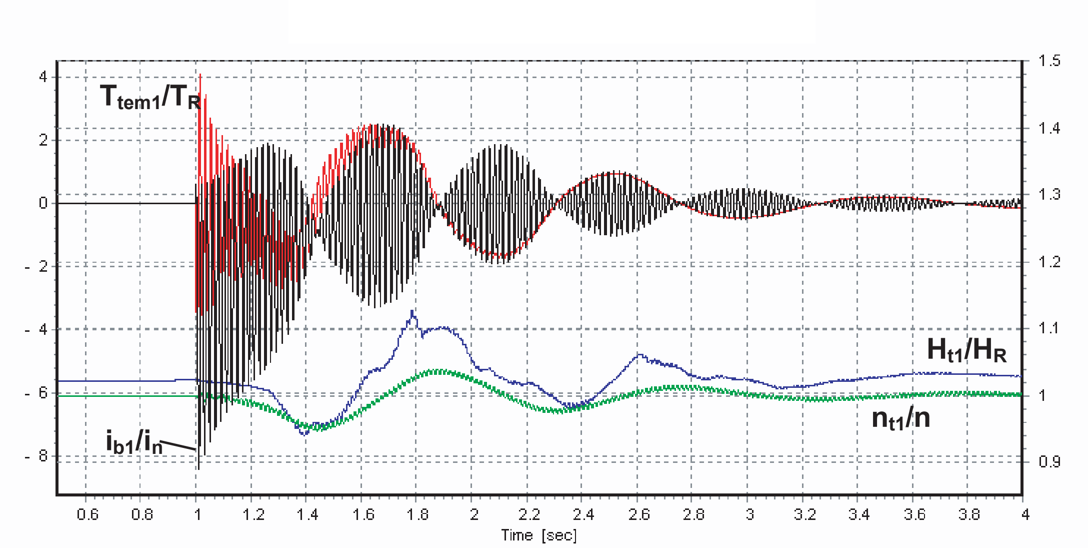

Figure 7.15: Time evolution of the electromagnetic torque, the head of the turbine and rotational speed of Unit 1 due to 180° out of phase synchronization.

7.4 Stability of Turbine Speed Governor

Hydroelectric interactions have been pointed out by simulating classical faults that occur on hydroelectric power plant such as total load rejection, earth fault and out of phase synchronization. The maximum amplitudes of dimensioning values such as current, pressure, and rotational speed, are properly predicted by either a single electric or a single hydraulic model as they mainly depend on short term transients. On the other hand, differences on long terms transients are highlighted. As a consequence, the difference in the dynamic behavior of the single electric or hydraulic model compared to the hydroelectric model becomes more significant when the focus is put on the stability of the turbine speed governor.

This is the reason why the stability of the turbine speed governor during load rejection is investigated using 2 different simulation models: (i) a hydraulic model and (ii) a hydroelectric model. In order to emphasize the possible interactions, the case of an islanded production mode resulting from the disconnection from the infinite electrical grid is simulated using the hydroelectric model.

7.4.1 Case Study Definition

The investigated hydroelectric power plant comprises an upstream reservoir, a 1100 meters long penstock, a 230 MW Francis turbine connected by mechanical inertias to a 250 MVA synchronous generator linked to a 205 kV infinite network through a 17.5/205 kV transformer. A passive RL load is also connected on the high voltage side. The layout of the hydroelectric power plant is presented by figure 7.16. The main dimensions of the power plant are summarized in table 7.6. The installation is driven by a turbine speed governor and a generator voltage regulator, both of the PID type.

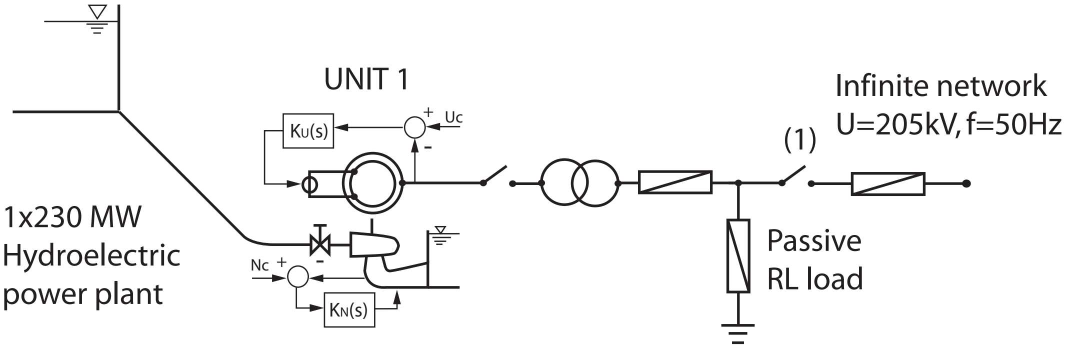

Figure 7.16: Layout of the hydroelectric power plant case study.

The transient behavior investigated is a 25% load rejection simulated as follows:

- (i) hydroelectric model: the infinite power network is disconnected at $t = 10\ s$ by tripping the circuit breaker (1), see figure 7.16. The synchronous generator faces an isolated production mode, *i.e.* connected with only the passive RL load 25% smaller than the original condition;

Table 7.6: Main dimensions of the power plant.

Reservoir	**Penstock**	**Turbine**	**Generator**
$H_o = 315\ m$	$L = 1100\ m$ $D = 5\ m$ $\lambda = 0.02$ $a = 1100\ m/s$	$H_n = 309\ m$ $Q_n = 85.3\ m^3/s$ $N_n = 375\ rpm$ $T_n = 5.85 \cdot 10^6\ Nm$ $J_t = 5 \cdot 10^4\ kg \cdot m^2$	$S_n = 250\ MVA$ $U_n = 17.5\ kV$ $f = 50\ Hz$ pair pole = 8 $J_g = 1 \cdot 10^6\ kg \cdot m^2$ $K_{shaft} = 5 \cdot 10^8\ Nm$

- (ii) hydraulic model: the dynamic behavior of the synchronous generator is modelled by a constant torque dropping by 25% instantaneously at $t = 10s$.

The initial conditions in terms of power distribution are given in table 7.7.

Table 7.7: Initial conditions of power distribution.

Element	**Active Power**	**Reactive Power**
Generator	$P = -200$ MW	$Q = -100$ MVAR
Passive Load	$P = 150$ MW	$Q = 50$ MVAR
Network	$P = 50$ MW	$Q = 50$ MVAR

7.4.2 Simulation Results and Analysis

The simulation results of the 25% load rejection obtained with the hydraulic and the hydroelectric models are presented respectively in figure 7.17 top and bottom. The time evolution of the rated head H/H_n, discharge Q/Q_n, rotational speed N/N_n, torque T/T_n, guide vane opening y and electromagnetic torque T_{el}/T_n are represented. It can be seen that the simulation results obtained using the hydraulic model are fully stable and stable operating conditions are recovered $40s$ after the disturbance. However, using the same turbine speed governor settings with the hydroelectric model leads to a dynamic response at the limit of stability of the system, and after $90s$, the system still not recovers stable operating conditions. This difference is due to the strong influence of the dynamic behavior of the electrical installation in the isolated production mode. This difference is evidenced by the time evolution representation of the rated electromagnetic torque T_{el}/T_n obtained with the hydroelectric model compared with the one obtained with the hydraulic model. This means that **for isolated production modes, the set of parameters of a turbine speed governor cannot be determined with a single hydraulic simulation model.**

In order to analyze the dynamic behavior of both models in more detail, the transfer function of the turbine $G(s)$ is identified by simulation considering the guide vane opening y as input variable and the turbine rotational speed N as output variable. The transfer function of the turbine is expressed in the Laplace domain as follows:

$$G(s) = \frac{N(s)}{Y(s)} \tag{7.2}$$

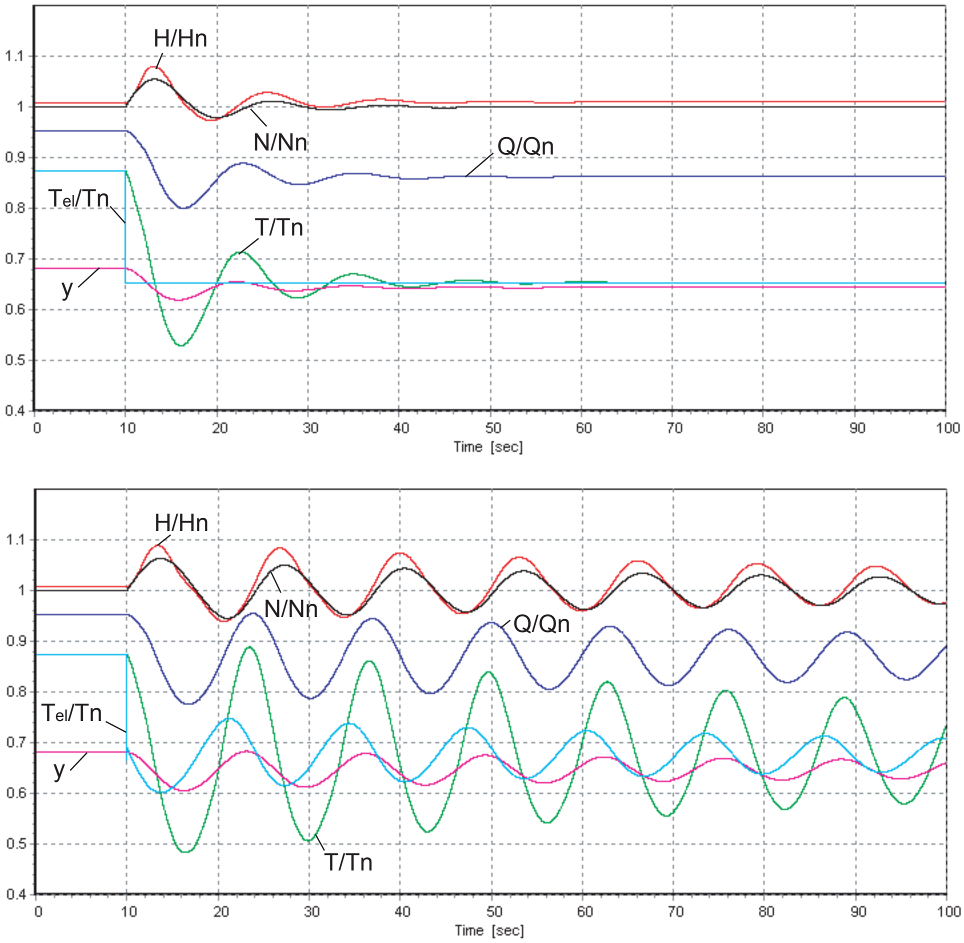

Figure 7.17: Simulation results of the transient of the Francis turbine resulting from a 25% load rejection based on the hydraulic model (top) and the hydroelectric model (bottom).

A PRBS signal of 2% amplitude is superimposed on the mean value of the guide vane opening y for the identification of the transfer function of the turbine. From the time domain simulation, the time history of the rated rotational speed and of the guide vane opening are used for the calculation of the transfer function using the hydraulic and hydroelectric models. The 2 resulting transfer functions are compared in figure 7.18. First, the natural frequencies of the mechanical inertias are visible at 3.5 Hz and 16.3 Hz. The lowest one is an anti-resonance of the generator inertia while the second one is the resonance of the turbine inertia. The odd eigen frequencies of the penstock are also visible for $f = 0.25, 0.75, 1.25$ Hz and so on, corresponding respectively to $f = a/(4l), 3a/(4l), 5a/(4l)$, etc, up to the 20^{th} eigen frequency as the penstock is modelled using 20 nodes.

However, the 2 transfer functions are almost identical except for very low frequencies where the amplitude of the hydroelectric transfer function exhibits much higher amplitudes than the hydraulic transfer function. These high amplitudes result from the dynamics of the electrical installation in the isolated production mode. Because this difference appears at very low frequency, it restricts the performances of the turbine speed governor.

As a consequence, to guarantee the stability in the islanded production mode with the hydroelectric model, the integrator time constant T_i of the PID turbine speed governor is increased to reduce the amplification at low frequencies. The initial integration time constant was $T_i = 3.7\ s$ and is increased to $T_i = 14\ s$ to have an efficient governor; the gain and the derivative time constant remain unchanged ($K_p = 1, T_d = 1.21\ s$). The simulation results of the dynamic behavior of the installation resulting from a 25% load rejection using the hydroelectric model is presented in figure 7.19. It can be seen that, as expected, the system is again fully stable in the isolated production mode.

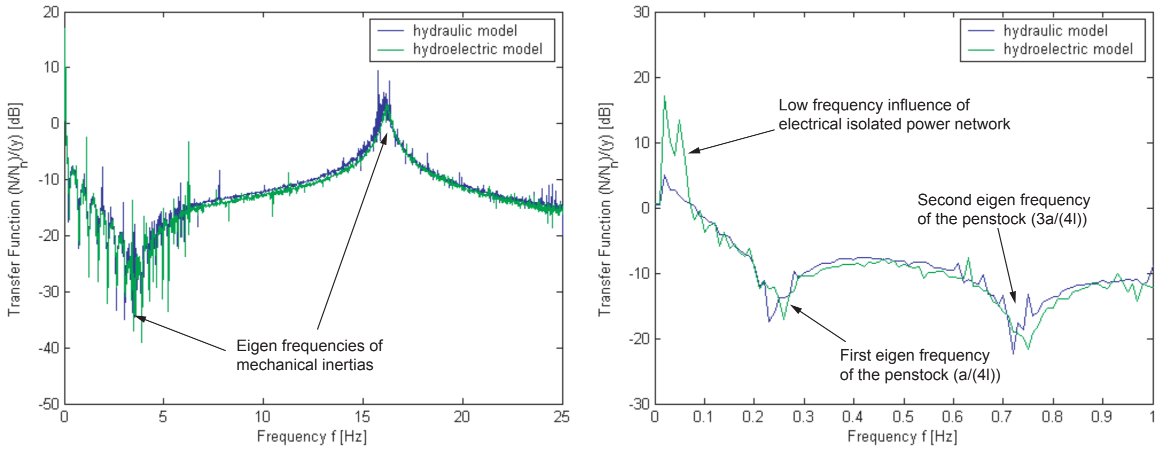

Figure 7.18: Transfer function of the turbine $G(s) = N(s)/Y(s)$ in the range $0 \rightarrow 25Hz$ on the left, and $0 \rightarrow 1Hz$ on the right.

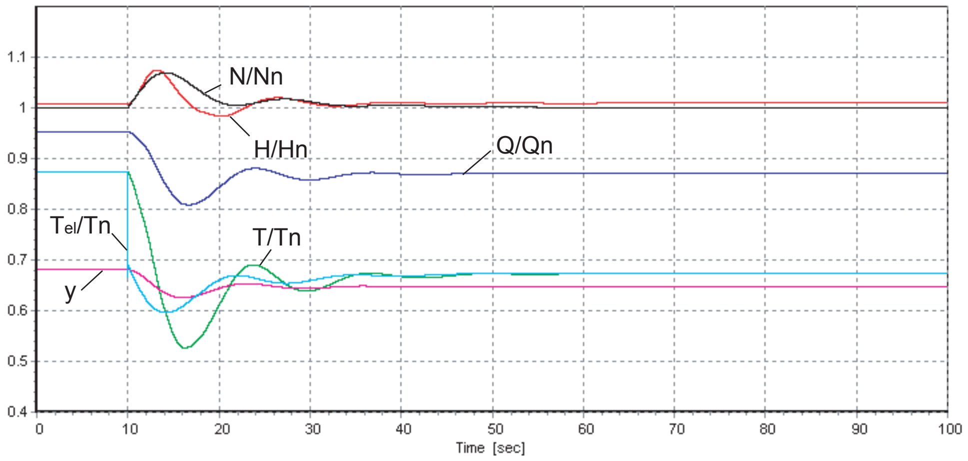

Figure 7.19: Simulation results of the transient of the Francis turbine resulting from a 25% load rejection with the hydroelectric model and the modified integration time constant of the turbine speed governor.

7.5 Hydroelectric Stability in Islanded Production Mode

Islanded power networks feature a small number of power plants and loads leading to high interactions between all the components. Therefore high performance governors must be used for each power unit. It is even more important for hydraulic power plants which dynamic behavior is strongly related to the hydraulic circuit layout. Since every hydraulic power plant is unique, no standard governor setting can be used. Hydraulic power plants featuring a long penstock and a surge tank need to be properly modelled in order to take into account waterhammer, surge tank water level oscillations and the effects of the turbine characteristics. All these phenomena present a non-linear behavior, thus restricting the performance of the turbine speed/power governor. To ensure the stability of the turbine governor, the governor parameters have to be validated by a time domain simulation. The order of the model of the hydraulic installation has to be adapted to the hydraulic layout and the investigated case, as advised by the "working group on prime mover and energy supply models for system dynamic performance studies" [155]. It appears that hydroelectric power plants featuring a surge tank and a long penstock connected to an islanded power network require a high order model. Such an installation is investigated in this section.

7.5.1 Case Study Definition

The investigated test case is an islanded power network comprising:

- a 1 GW hydroelectric power plant with 4 × 250 MW Francis turbines;
- 4 × 1.3 GW thermal power plants;
- 2 passive consumer loads: one 200 MW load that can be tripped and one 2.1 GW to 6 GW whose power is adapted to the network power level considered.

The 5 power plants and the 2 loads are connected through a 400 kV transmission line network as presented by figure 7.20. The case is investigated with a 3-step approach. (i) The modelling of a 1 GW hydroelectric power plant in an islanded power network considering the waterhammer effects, the surge tank water level oscillations and the dynamics due to turbine characteristics is performed. The determination of the governor parameters is based on the identification of the turbine transfer function using a time domain simulation with a PRBS excitation. (ii) A 1.3 GW thermal power plant is modelled using a simplified approach based on the steam flux. (iii) Combining both models, the whole 6.2 GW islanded power network comprising the 4 thermal and the hydraulic power plants is set up. The turbine governor performances are assessed for 5 different hydro to thermal power ratios.

7.5.2 Modelling of the Hydroelectric Power Plant

Hydraulic Power Plant Model

The power plant is made of a $1'515$ meters long gallery, a surge tank with variable section, a $1'388$ meters long penstock and a manifold feeding 4 × 245 MW Francis turbines. The

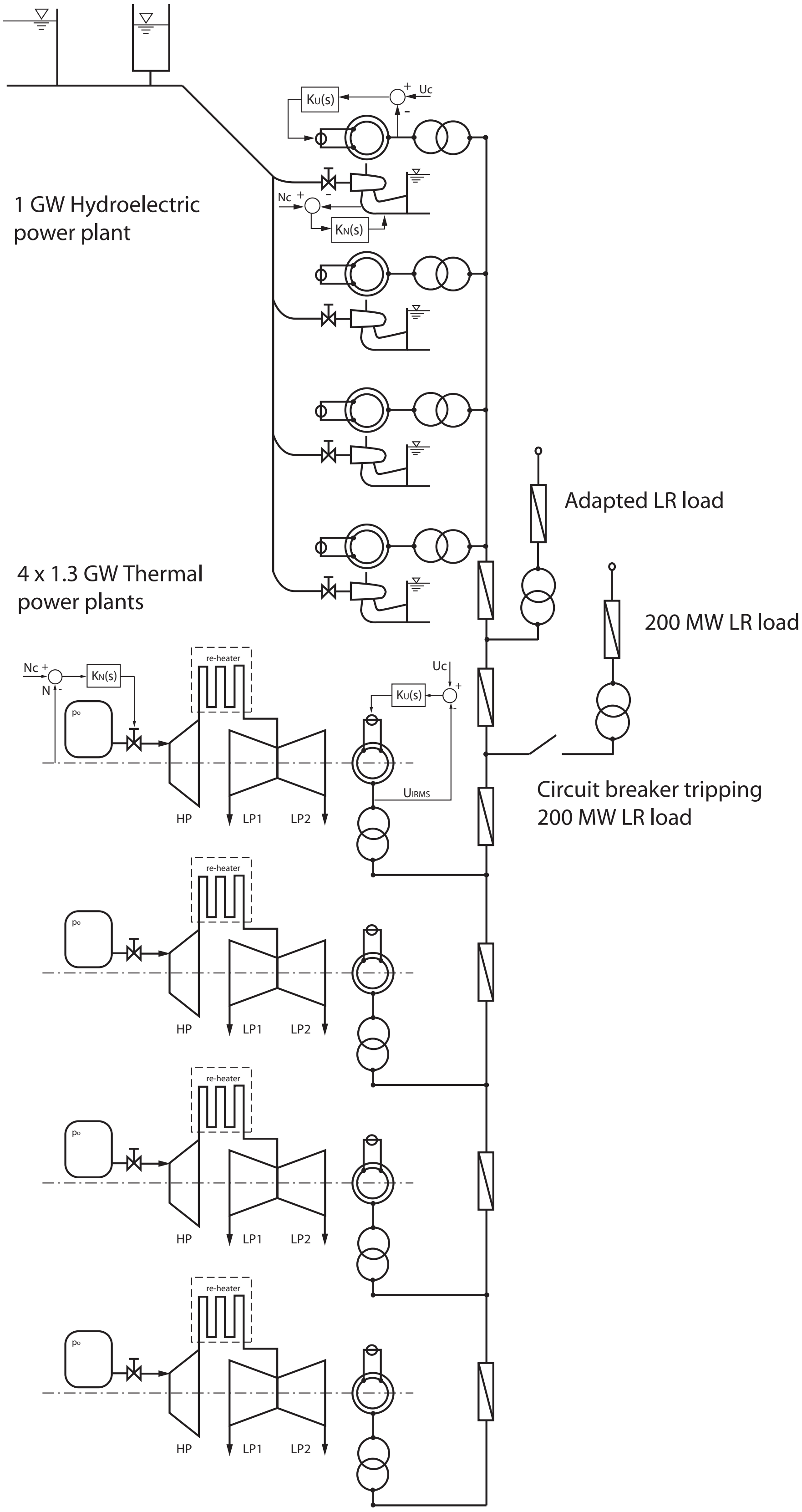

Figure 7.20: Islanded power network structure.

main parameters of the hydraulic circuit are summarized in table 7.8.

Table 7.8: Main dimensions of the hydraulic installation.

Element	Dimensions
Reservoir	$H_o = 364\ m$
Gallery	$L = 1'515\ m$ $D = 8.8\ m$ $a = 1'000\ m/s$
Surge tank	Mid tank section: $A_{ST} = 133\ m^2$
Penstock	$L = 1'388\ m$ $D = 8.8/7.15\ m$ $a = 1'200\ m/s$
Francis turbine	$P_n = 250\ MW$ $N_n = 333.3\ rpm$ $Q_n = 75\ m^3/s$ $H_n = 350\ m$ $\nu = 0.23$ $D_{ref} = 2.82\ m$ $J_t = 1.7 \cdot 10^5\ kg \cdot m^2$
Generator	$S_n = 270\ MVA$ $U_n = 18\ kV$ $f = 50\ Hz$ Pole pairs: $p = 9$ Stator windings: Y $J_G = 1.54 \cdot 10^6\ kg \cdot m^2$
Coupling shaft	$K = 3.62 \cdot 10^8\ Nm/rad$ Viscous damping: $\mu = 6.7 \cdot 10^3\ Nms/rad$

The gallery and the penstock are respectively discretized into 22 and 31 elements. The turbine draft tube is modelled by 2 pipe elements. The Francis turbine characteristics, discharge and torque factors versus the speed factor are presented for different guide vane opening values y, see figure 7.21.

The block diagram of the PID governor of the Francis turbine is presented in figure 7.22. The governor structure includes both speed and power feedbacks. The network frequency feedback is neglected in this study because only islanded and isolated production modes are considered. The servomotor of the guide vanes is modelled using a first order transfer function with a time constant of $\tau_{sv} = 0.1\ s$.

Turbine Governor Parameters Determination

The transfer function of the system to be regulated, $G(s)$, should be determined for setting the parameters of the turbine governor. The system consists of a turbine with the guide vane opening y as input parameter and the rotational speed N as output parameter. The transfer function of the turbine is identified for 4 different power levels: $P/P_n = 0.4, 0.7, 1$

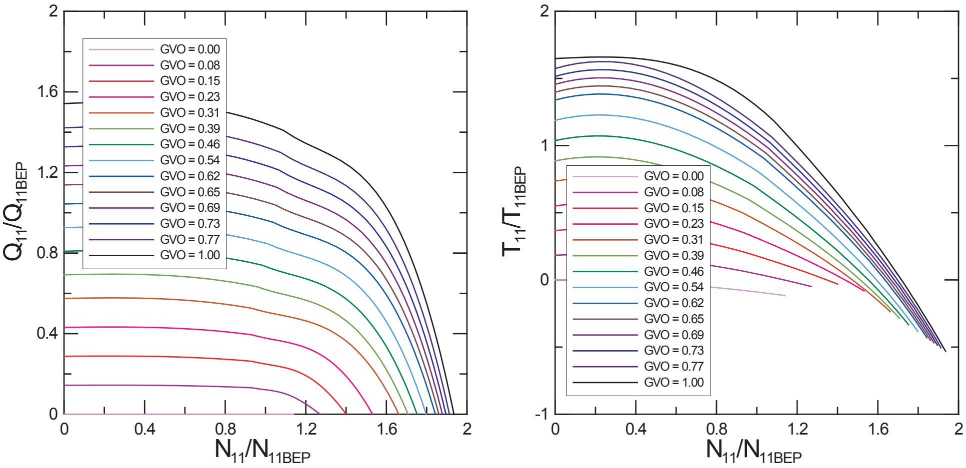

Figure 7.21: Turbine characteristics $Q_{11} = Q_{11}(N_{11})$, left, and $T_{11} = T_{11}(N_{11})$, right, for different GVO opening.

and 1.15 *p.u.*, in order to take into account the influence of the local gradient of the turbine characteristics.

The model of the hydraulic installation set up using SIMSEN-Hydro is of a high order (up to 150 ODE), however the transfer function of the system cannot be directly inferred from them. The transfer function of the turbine including the hydraulic circuit is identified through a time domain simulation considering a white noise excitation. A PRBS signal of 5% amplitude around a mean value of guide vane opening is used as excitation signal, see figure 7.23. The mean value is set in accordance with the turbine power for which the transfer function is identified. The PRBS excitation function [153] is preferred to an indicial response because of its higher frequency content that evidences all natural frequencies of the system. The PRBS signal is obtained using a shift register [60].

The amplitude and phase spectra of the turbine transfer function obtained from the PRBS identification, for $P/P_n = 0.4$ is presented in figure 7.24. The amplitude of the transfer function reveals that the hydraulic system natural frequencies are mainly related to the piping system, the mechanical masses and the surge tank. The first natural frequency of the piping system is $f_o = 0.2\ Hz$ and corresponds to the fourth wavelength free oscillation mode of the penstock given by $f = a/(4l)$. The natural frequencies above correspond to higher mode eigen frequencies of the piping system. The natural frequency of the mechanical masses presents a high amplitude at $f_m = 7.6\ Hz$ and is given by [117]:

$$\omega_{m1,2}^2 = \frac{1}{2} \cdot \left(\Omega_1^2 + \Omega_2^2\right) \pm \sqrt{\left(\frac{\Omega_2^2 - \Omega_1^2}{2}\right)^2 + \Omega_{12}^4} \tag{7.3}$$

Where :

$$\Omega_1^2 = \frac{K_{shaft}}{J_G} \quad ; \quad \Omega_2^2 = \frac{K_{shaft}}{J_T} \quad ; \quad \Omega_{12}^4 = \frac{K_{shaft}^2}{J_G \cdot J_T} \tag{7.4}$$

The anti-resonance of the generator inertia corresponding to Ω_1 is also visible for $f_m = 2.44\ Hz$. The eigen frequency of the mass oscillation between the upstream reservoir and

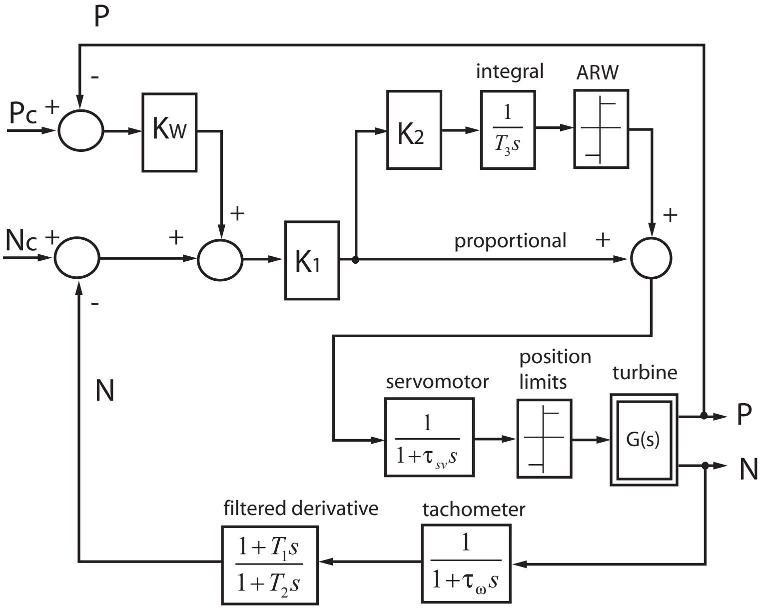

Figure 7.22: Block diagram of the turbine governor.

the surge tank is calculated with equation 6.6 and is equal to $f_{ST} = 0.00866\ Hz$, *i.e.* $T_{ST} = 115.5\ s$. This frequency is visible also as an anti-resonance on the spectrum. The anti-resonance behavior results from the fact that when more power is required, the guide vanes open, resulting in an increase of the discharge coming from the surge tank but reducing its water level, thus the available head at the turbine inlet. As a consequence, the hydraulic power may decrease depending on the governor action. Similarly, the gate opening induces a pressure drop at the turbine inlet resulting from a waterhammer effect leading to a non-minimum phase visible on the lin-lin phase plot. The non-minimum phase corresponds to half a period of the penstock, *i.e.* 2.5 seconds. This non-minimum phase is clearly pointed out in figure 7.25 where the guide vane step responses are simulated for the

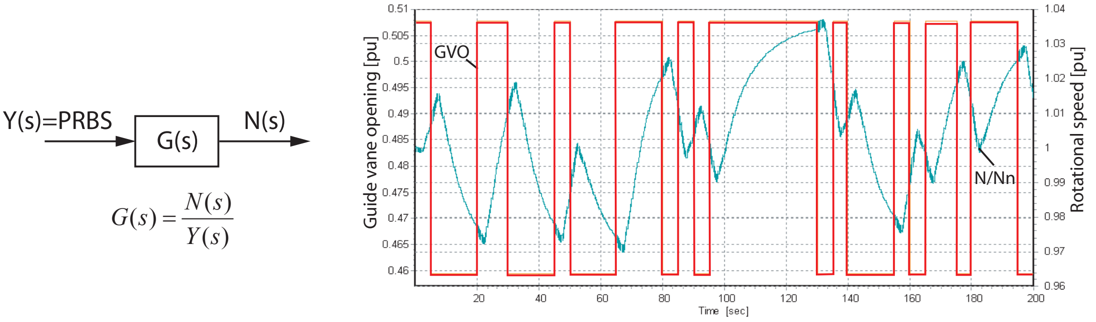

Figure 7.23: Open loop transfer function identification with a PRBS excitation for $P/P_n = 0.4$.

4 different power levels. It can be noticed that even if the guide vanes open, the rotational speed does not increase immediately due to the waterhammer under pressure. It can also be noticed that the higher the power level the higher the non-minimum phase influence. Therefore, this non-minimum phase is strongly restrictive for the governor performance. A large integrator time constant T_i is consequently required to ensure the system stability.

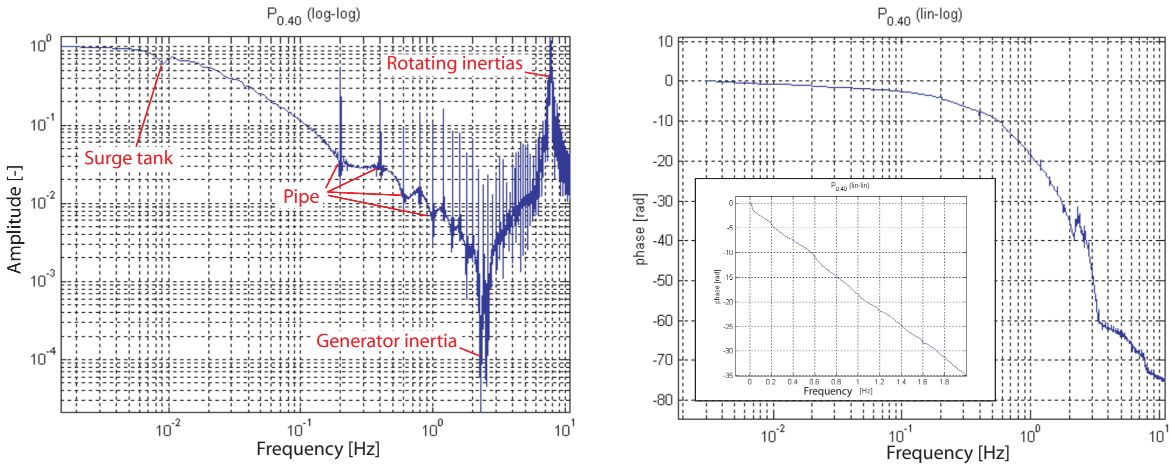

Figure 7.24: Amplitude (left) and phase (right) of the transfer function of the Francis turbine for $P/P_n = 0.4$ including the hydraulic circuit and mechanical inertia.

The transfer function of the turbine is identified for the 4 power levels considered $P/P_n = 0.4, 0.7, 1$ and 1.15 $p.u.$ and are represented in figure 7.26. As the 4 transfer functions are different because of the turbine characteristic, the determination of the PID parameters is based on the most restrictive one, *i.e.* on the most critical behavior of the system. The parameters of the governor are set in order to ensure a phase margin of $60 - 90^\circ$, a gain margin of $6 - 9$ dB, a cut-off frequency of 0.02 Hz to avoid resonance amplification and a slope of -20 dB/decade at the cut-off frequency.

Then, the assessment of the regulator performance is performed by simulating the dynamic behavior of the hydraulic power plant resulting from a successive 6% load rejection and acceptance for $P/P_n = 0.4, 0.7, 1$ and 1.15 $p.u.$. The electromagnetic torque is modelled by an external torque function which does not take into account the dynamic behavior of any electrical installation. The resulting time evolution of the rotational speed N/N_n and guide vane position y are presented in figure 7.27 for $P/P_n = 0.7$ and 1.15 $p.u.$. The speed deviations obtained from the simulation correspond to 1.5% and 4.5% of the nominal speed. For $P/P_n = 0.7$ $p.u.$ the speed is stabilized after 10 seconds while it takes 150 seconds to stabilize the speed for $P/P_n = 1.15$ $p.u.$ The full load appears to be more critical because of the influence of the surge tank. A surge phenomenon occurs between the PID governor and the surge tank. It is clearly visible from the time evolution of the guide vane opening which fluctuates at the mass oscillation period ($T_{ST} = 115$ s). The cross section of the surge tank is far from the Thoma section calculated to be $80m^2$ according to equation 6.28. It appears clearly that this criterion is not sufficient, especially at full load where the turbine efficiency gradient becomes negative ($d\eta/dQ < 0$). The governor parameter values have to be validated by a time dependent simulation to ensure

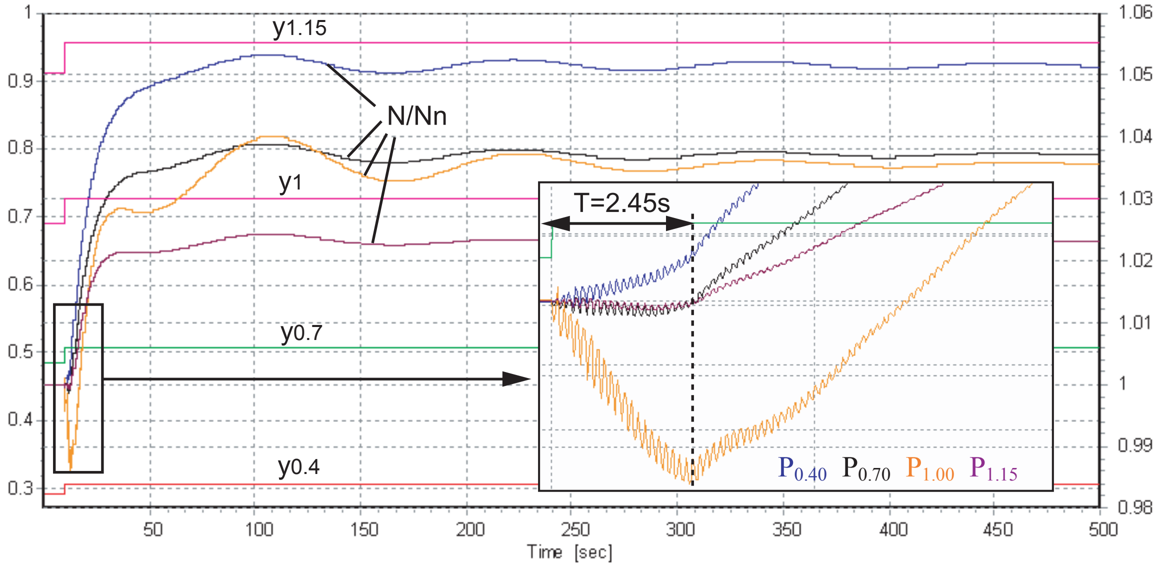

Figure 7.25: Non-minimum phase of the turbines evidenced by rated transient rotational speed N/N_n resulting from a guide vane opening step response for different power levels $P/P_n = 0.4, 0.7, 1, 1.15$.

the stability on the whole operating range, even for large stroke variations of the guide vanes.

7.5.3 Modelling of the Thermal Power Plant

As the turbine governor parameter values are validated only with the hydraulic simulation model, a model of a thermal power plant is set up to investigate the influence of the connection to an islanded power network. The thermal power plant is modelled with a constant pressure tank, the steam generator dynamics being neglected, feeding the High Pressure steam turbine (HP) through a regulating valve. Then the vapor flux transits through a re-heater before feeding 2 Low Pressure (LP) steam turbines as presented in figure 7.28. The model of this thermal power plant is made of a proportional governor with a frequency drop feedback and a speed feedback, a valve model, the model of the HP, LP1 and LP2 steam turbines and the mechanical masses as presented in figure 7.29. The parameter values of the model are given in table 7.9. The model of the steam turbines is made of 3 parallels branches, one for each steam turbine, driven by the valve opening. A time delay of $b = 4$ seconds is considered between the high pressure steam turbines and the low pressure steam turbines to take into account the transit time of the steam through the re-heaters. The 3 turbines are modelled by first order transfer functions with a short time constant for the high pressure and a long time constant for the low pressure steam turbines. The model includes also simplified steam turbine characteristics that are deduced from [17]. The inertia, stiffness and damping of the mechanical shaft are obtained from [62]. The synchronous machine excitation is controlled by an ABB Unitrol

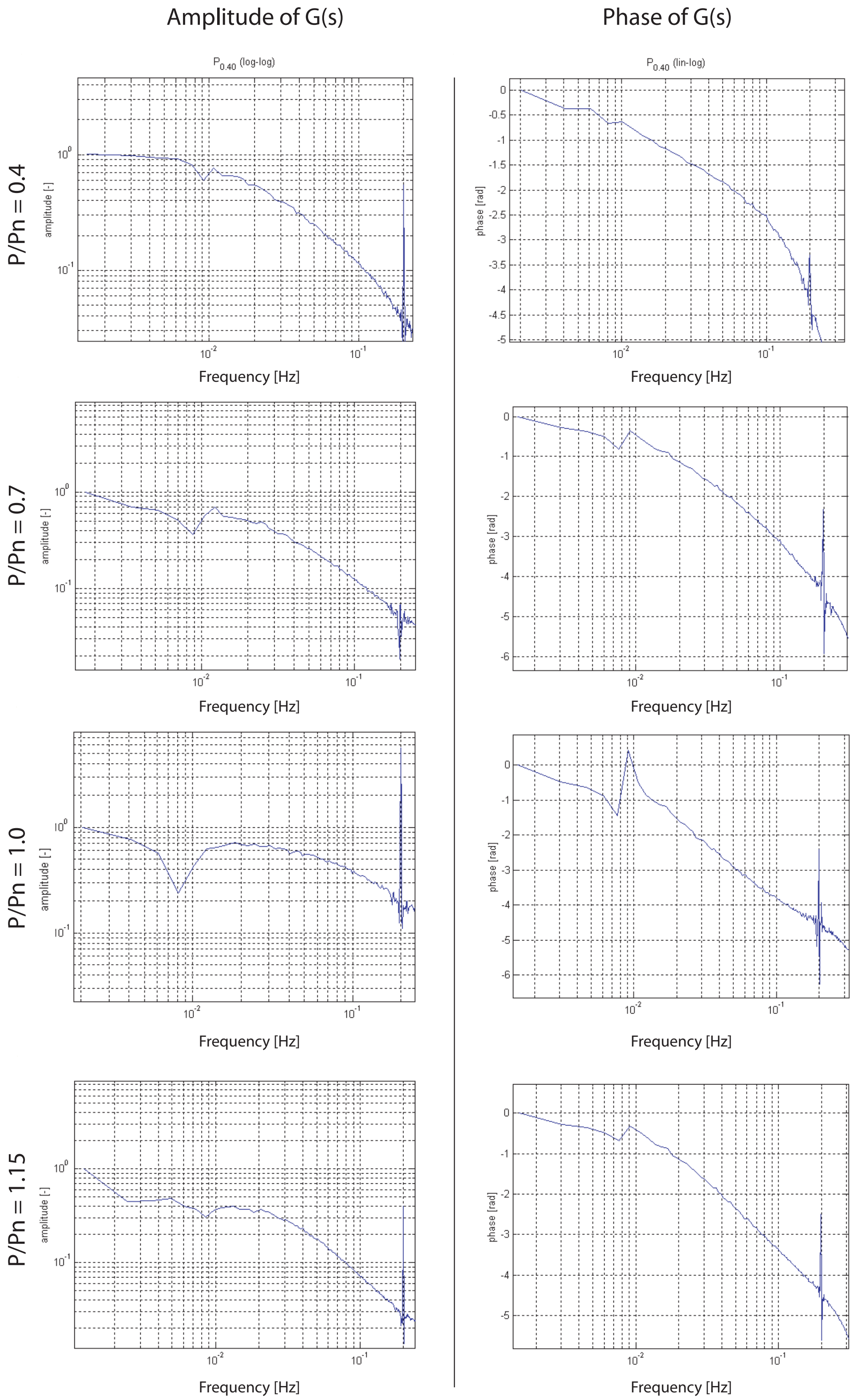

Figure 7.26: Amplitude (left) and phase (right) of the transfer function of the Francis turbine for $P/P_n = 0.4, 0.7, 1$ and 1.15 $p.u.$.

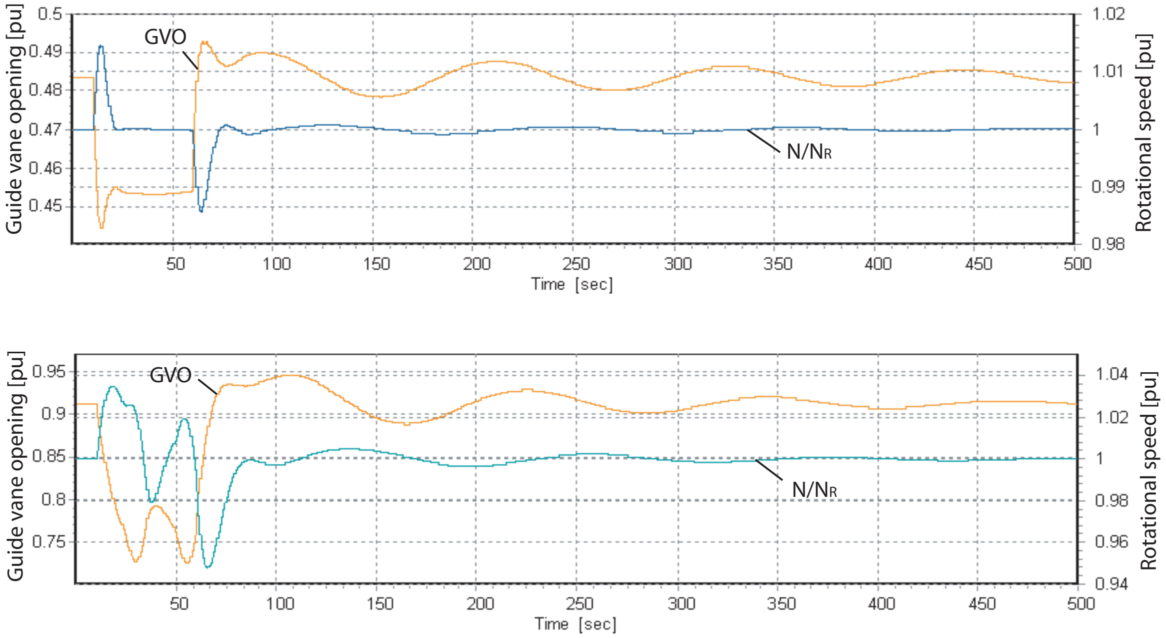

Figure 7.27: Time evolution of rotational speed N/N_n and guide vane opening GVO of the Francis turbine during a 6% load rejection at 0.7 $p.u.$ (top) and 1.15 $p.u.$ (bottom) power level.

voltage regulator. The synchronous machine is connected to a 28.5/400 kV transformer with Yd5 connection. As the synchronous machine is of the solid iron rotor type, its modelling takes into account the damping of the windings, saturation and leakage effects.

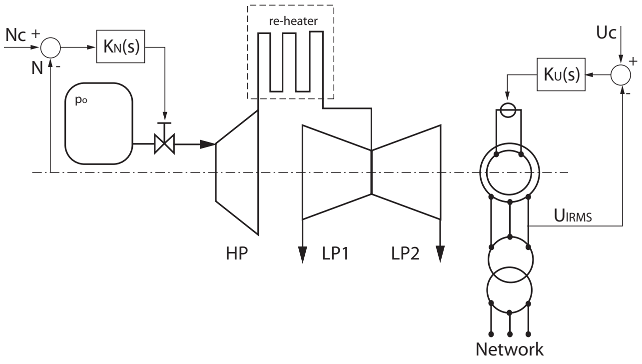

Figure 7.28: Layout of the thermal power plant.

The dynamic response of the thermal power plant is investigated for a 6% load rejection. The time evolution of the rotational speed N/N_R, the electromagnetic torque T_{em}/T_R and the valve opening y_{valve} are represented in $p.u.$ in figure 7.30. The rotational speed recovers stability after 10 seconds, demonstrating the fast dynamic response of the thermal power plant. However, due to the proportional nature of the governor, a static error can be noticed after full stabilization of the system. The pressurized steam reservoir enables the thermal power plant to have short time constant. The static error is not compensated because the steam generator dynamics are neglected. The transient response of this thermal power plant was validated by comparison with measurements on a power plant performed by EDF [39].

Table 7.9: Main dimensions of the thermal power plant.

Element	Dimensions
Steam turbines model	$\tau_{HP} = 0.5\ s$ $\tau_{LP} = 12\ s$ $b = 4\ s$ $K_p = 25$
Mechanical inertias	$J_{HP} = 1.867 \cdot 10^4\ kg \cdot m^2$ $J_{LP1} = 1.907 \cdot 10^5\ kg \cdot m^2$ $J_{LP2} = 2.136 \cdot 10^5\ kg \cdot m^2$ $J_{gen} = 5.223 \cdot 10^4\ kg \cdot m^2$
Mechanical shaft stiffness and damping	$K_1 = 3.614 \cdot 10^8\ Nm/rd$ $K_2 = 8.206 \cdot 10^8\ Nm/rd$ $K_3 = 4.116 \cdot 10^8\ Nm/rd$ $\mu_1 = 6.719 \cdot 10^3\ Nms/rd$ $\mu_2 = 7.06 \cdot 10^3\ Nms/rd$ $\mu_3 = 7.06 \cdot 10^3\ Nms/rd$
Generator	$S_n = 1400\ MVA$ $U_n = 28.5\ kV$ $f = 50\ Hz$ Polepaire: $p = 2$ Stator windings: Y

7.5.4 Simulation of a Load Rejection in Islanded Power Network

To investigate the influence of the power network, a simulation model of an islanded power network is build up. The islanded power network of concern, see figure 7.20, is composed of the hydraulic power plant, 4 thermal power plants and 2 passive consumer loads. The 5 power plants represent all together a 6.2 GW power network. Figure 7.31 presents the topology of this power network where the power plants are connected to 2 passive consumer loads through 400 kV transport lines. The LR parameters of the 2 consumer loads are set in order to absorb the production of all the power plant of the network. One is a 200 MW load and the other one represents the complement to the total power of the islanded power network. In order to investigate the transients due to a load rejection, the 200 MW consumer load is disconnected by tripping the circuit breaker considering the 5 different network power levels given in table 7.10.

For completeness, the electrical installation of the hydroelectric installation is included in the simulation model. The 4 hydrogenerators are 270 MVA synchronous machines and

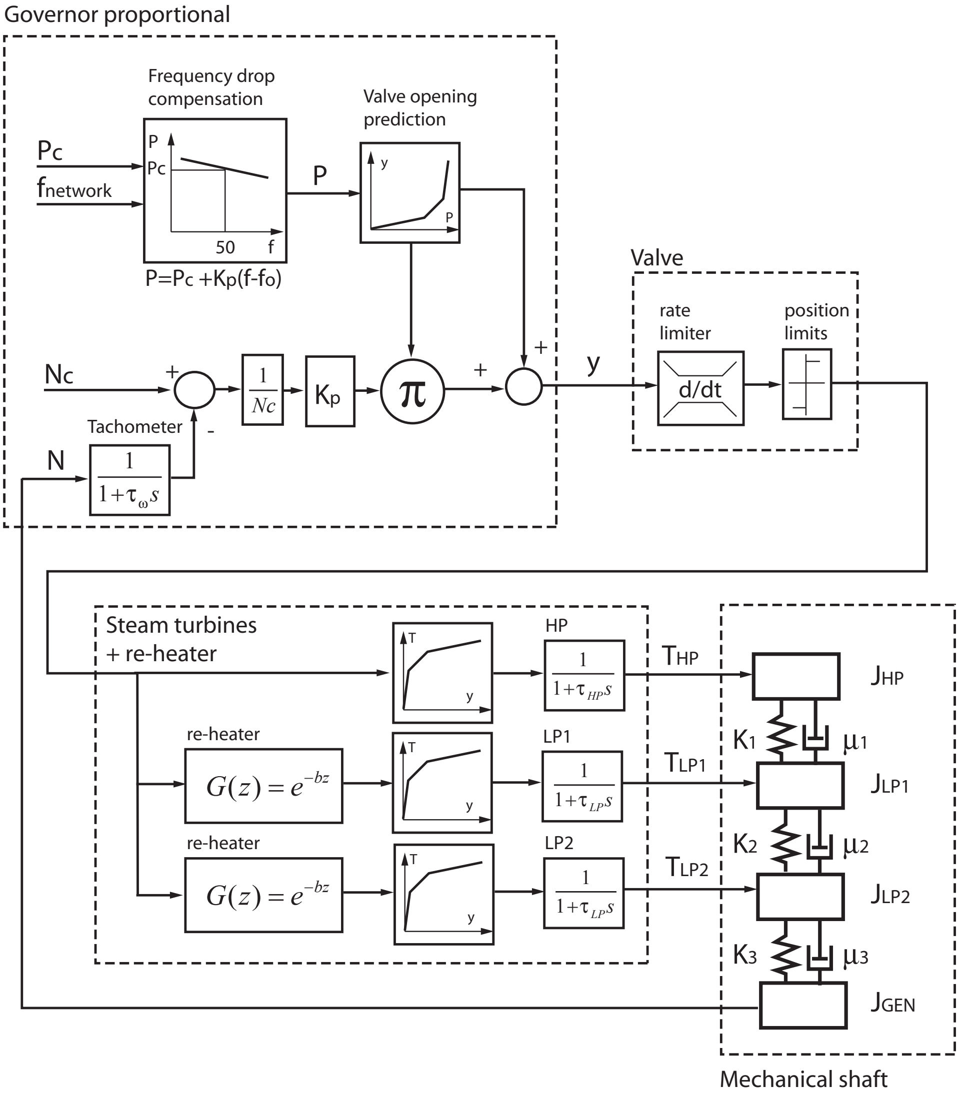

Figure 7.29: Block diagram of the model of the thermal power plant.

Table 7.10: Power distribution.

Hydraulic Power Production P_{hydro}	**Thermal Power Production** P_{TH}	**Power Ratio** P_{Hydro}/P_{tot}
1 GW	1.3 GW	0.43
1 GW	2.6 GW	0.28
1 GW	3.9 GW	0.20
1 GW	5.2 GW	0.16
1 GW	∞	0

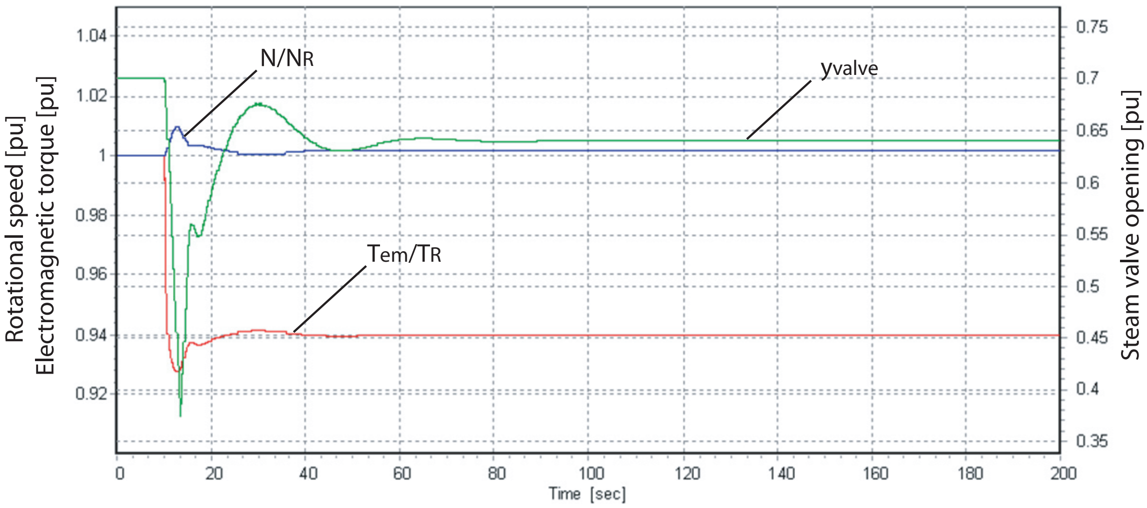

Figure 7.30: Transient response of the 1300 MW thermal power plant resulting from a 6% load rejection.

are connected to the islanded network through 18.5/400 kV Yd5 transformers. The synchronous machine excitations are controlled by ABB Unitrol voltage regulators. The synchronous machines are of the laminated rotor type. The model is considering saturation, leakage and damping effects of windings, allowing taking into account a sub-transient behavior.

The Power System Stabilizers -PSS- of the hydroelectric power plant are not considered in this investigation in order to focus on the performances and stability of the turbine speed governors. The use of PSS would help reducing the speed deviations as demonstrated by Kamwa *et al.* [88] but the influence of such device is out of the scope of the present work.

Frequency Analysis

The transfer function of the turbine connected to the power network is re-identified for 3 different network power levels: $P_{tot} = \infty$, 6.2 and 2.3 GW, the power of the hydraulic power plant being 1 GW. The amplitude spectra of the resulting transfer function are presented in figure 7.32. From the new transfer function an additional natural frequency with high amplitude is pointed out at $1.36Hz$. This corresponds to the synchronous machine's natural frequency depending on the operating point of the generator, voltage regulator and system configuration [91]. The source of this frequency was checked by introducing a sinusoidal excitation added to the wicket gate mean value in open loop conditions.

A high stabilization effect of the power network can be noticed on the amplitude spectrum of the turbine transfer function for low frequencies. The attenuation and the frequency range affected by the network become smaller as the level of the power network decreases. The power network behaves like a high-pass filter. It means that the perturbations of the rotational speed at low frequencies are reduced by the power network "stiffness" and that the higher the power level of a network, the lower the performances of the governor required.

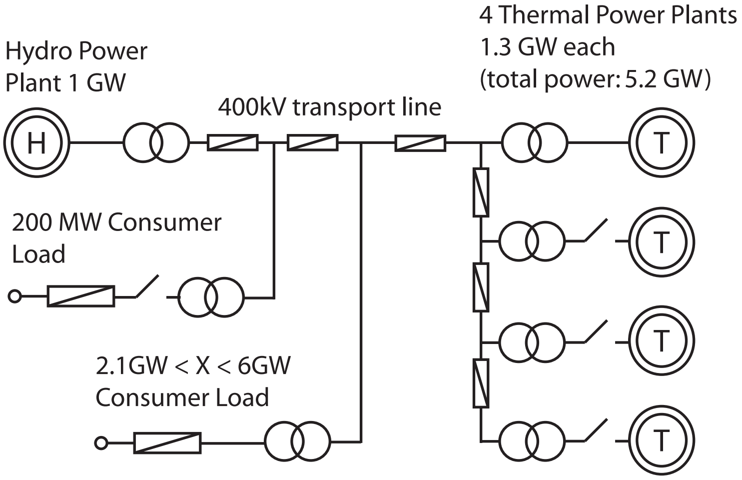

Figure 7.31: Islanded power network.

Transient Analysis

A time domain simulation of the tripping of the 200 MW consumer load is performed without considering the synchronous machine's natural frequency in the turbine speed governor design. The simulation is done for $P_{hydro}/P_{tot} = 0.43, 0.28, 0.20, 0.16, 0$, and the resulting turbine rotational speed evolutions are presented figure in 7.33. As expected, whatever the power level of the network, the turbine's operation is unstable and the rotational speed exhibits a fluctuation at 1.36 Hz. To avoid a resonance between the turbine speed governor and the synchronous machine, the filter time constant of the turbine rotational speed is reduced to $\tau = 0.3\ s$. Consequently, the turbine rotational speed remains stable as presented in figure 7.34. As expected from the turbine transfer function analysis, the islanded network power level has a strong influence on the speed deviation. For infinite power level the tripping of the 200 MW load is almost not perceptible while for a ratio $P_{Hydro}/P_{tot} = 0.43$ the speed deviation reaches 3.5%. The amplitudes of the speed deviation are reported in figure 7.35 as a function of the ratio between the power of the hydraulic part (1 GW here) and the power of the whole network.

7.5.5 Concluding Remarks

This investigation demonstrates the importance of a high order modelling in the case of a hydroelectric power plant featuring a surge tank with a small diameter and a long penstock in islanded power networks. A detailed setup and an analysis procedure necessary to ensure the hydraulic turbine governor stability are presented. The case of a 1 GW hydroelectric power plant connected to a 5.2 GW islanded power network is investigated. The transfer function of the hydraulic turbine is identified using a time domain simulation with a PRBS excitation. This method has the advantage to evidence all the natural frequencies of the hydraulic system. The governor performances are tied to the natural frequencies of the power plant. The analysis of the transfer function of the turbine in different islanded production levels, evidences a stabilization effect below 1 Hz in larger

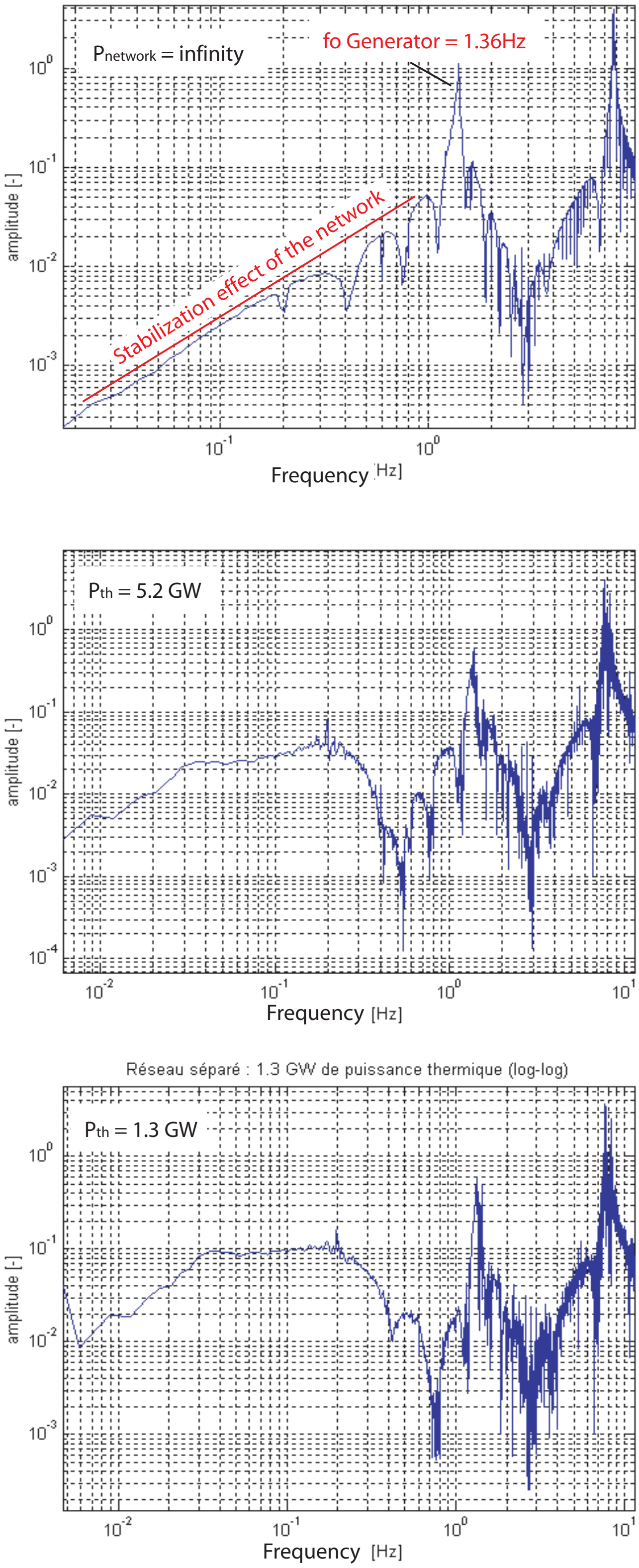

Figure 7.32: Francis turbine transfer function considering connection to an infinite power network (top), 5.2 GW power network (middle) and 1.3 GW power network (bottom).

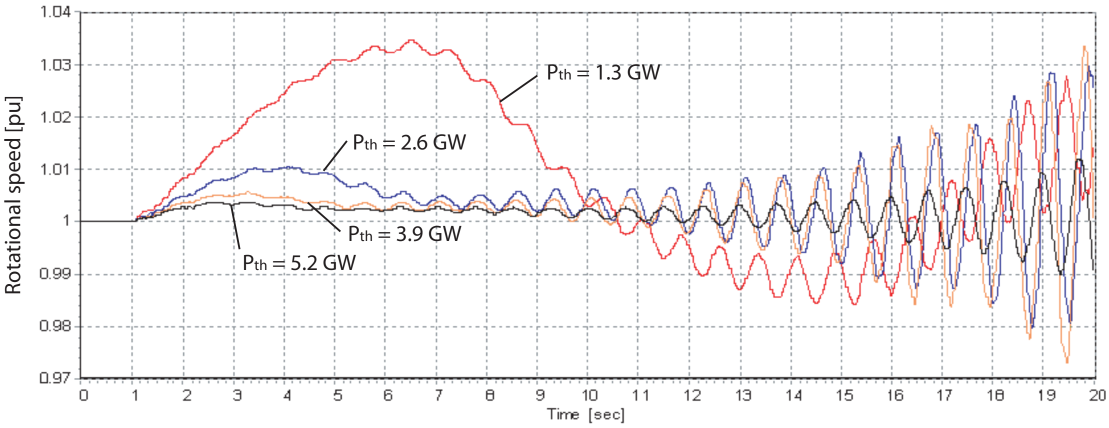

Figure 7.33: Francis turbine rotational speed evolution after 200 MW load tripping for $P_{Hydro}/P_{tot} = 0.43, 0.28, 0.2$ and 0.16 without filter modification.

power networks. In the case of weak power networks, the stability of hydraulic installations with a long penstock featuring natural frequencies in this frequency range can be strongly affected. A study taking all these considerations into account eases the final tuning of governors and hence reduces the commissioning delay.

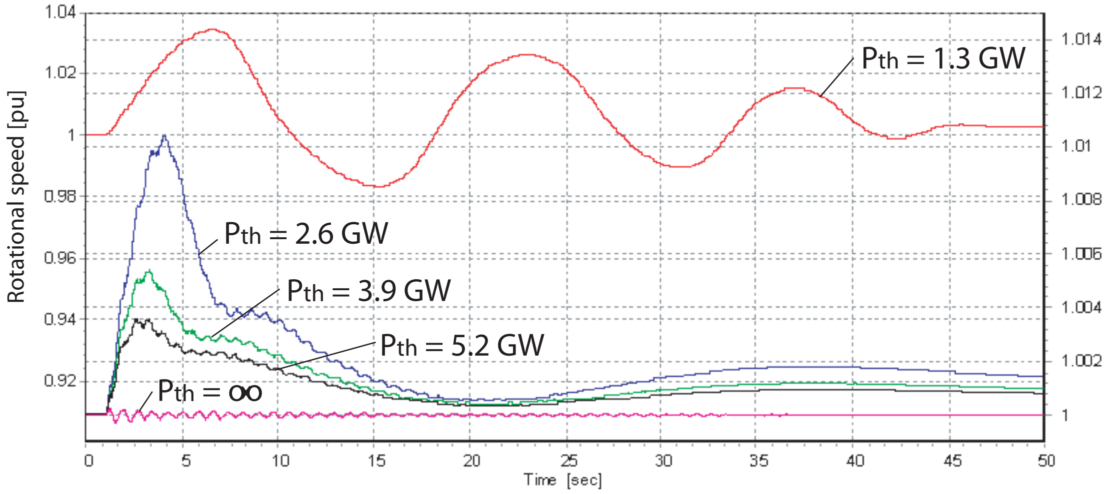

Figure 7.34: Time evolution of the turbine rotational speed resulting from the tripping of a 200 MW load for different thermal power plant levels, with filter modification.

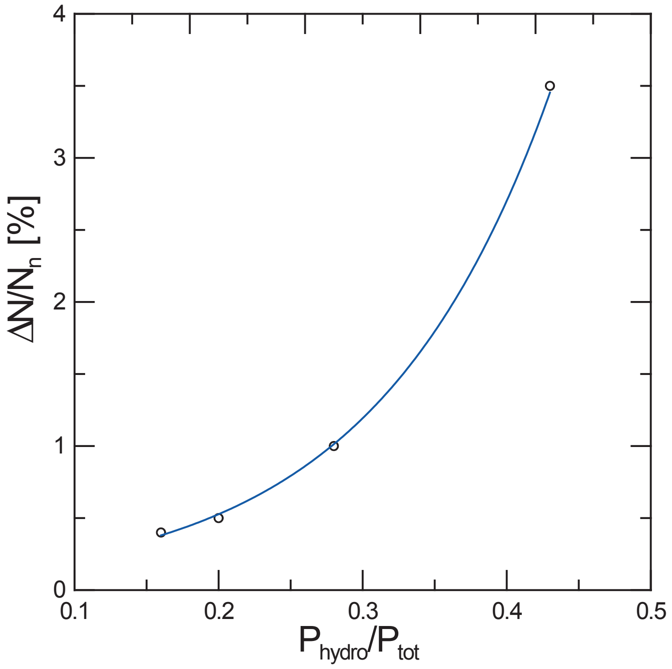

Figure 7.35: Speed deviation due to a 200 MW load tripping as a function of power ratio between the hydraulic power plant and the total power of the islanded power network.

Part II

Modelling of Pressure Fluctuations in Francis Turbines

Chapter 8

Pressure Excitation Sources in Francis Turbines

8.1 General Remarks

Hydraulic installations comprising Francis turbines, pump-turbines or pumps are subject to pressure fluctuations induced by the complex flow developing in the hydraulic machine, which is three dimensional, in rotation, unsteady, and often features cavitation. These pressure fluctuations lead to pressure waves propagating in the entire hydraulic system and their superposition may result in resonance between the pressure excitation source and the hydraulic circuit. Therefore, mathematical models are required to model hydraulic systems and the possible pressure excitation sources in order to assess the risk of resonance and hopefully predict amplitudes of pressure fluctuations for safety guarantee purposes.

In this section, the different types of excitations that may result in hydroacoustic resonance will be described, and existing models are presented.

8.2 Mathematical Models of Excitation

From mathematical point of view, there is distinction between 3 types of excitations can be distinguished: (i) forced excitation, (ii) parametric excitation, (iii) self excitation.

These 3 types of excitation mechanisms are illustrated with basic equivalent electrical circuits. The characteristic equations derived from the circuits point out the nature of the excitation in the following subsections.

Forced Excitation

The figure 8.1 presents the equivalent scheme of a hydraulic system subject to a forced excitation. The system is made up of a pressure excitation source $H(t)$, a resistance R, an inductance L and a capacitance C. The related equation set is given by:

$$\begin{cases} L \cdot \dfrac{dQ}{dt} + R \cdot Q + h_c = H(t) \\ C \cdot \dfrac{dh_c}{dt} = Q \end{cases} \tag{8.1}$$

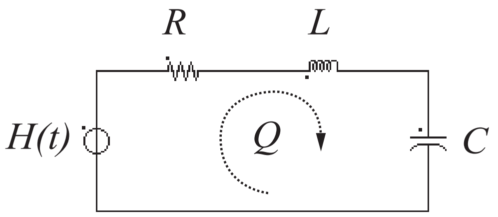

Figure 8.1: System subject to forced pressure excitation $H(t)$.

The characteristic equation of the above system is expressed as follows:

$$\frac{d^2h_c}{dt^2} + \underbrace{\frac{R}{L}}_{2\cdot\mu} \cdot \frac{dh_c}{dt} + \underbrace{\frac{1}{L \cdot C}}_{\omega_o^2} \cdot h_c = 0 \tag{8.2}$$

The harmonic response of the system of figure 8.1 is presented in figure 8.2 for different values of the relative damping $\gamma = R/(2 \cdot L \cdot \omega_o)$. The resonance occuring for $\omega = \omega_0$ is clearly evident and the influence of the relative damping is pointed out.

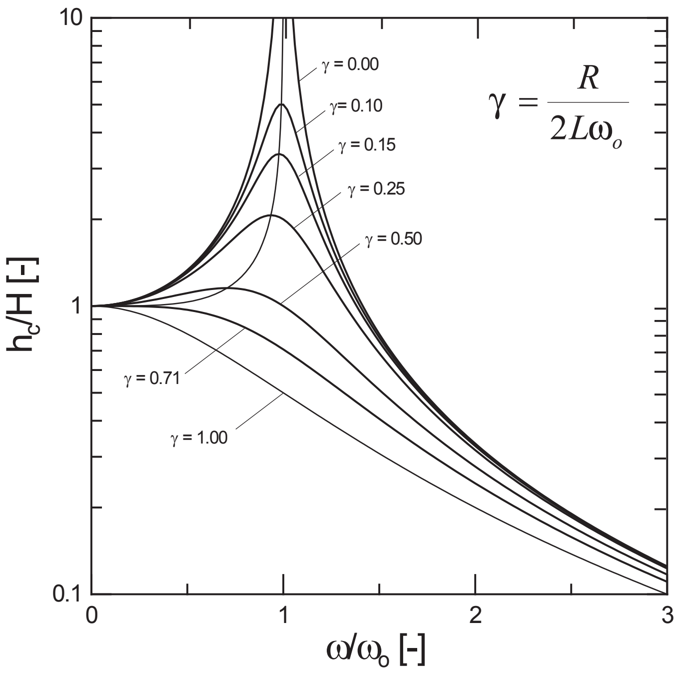

Figure 8.2: Forced response of the system of figure 8.1.

Parametric Excitation

The figure 8.3 presents the equivalent scheme of a hydraulic system subject to parametric excitation. The system is made of a constant pressure source H_o, a resistance R, an inductance L and a time dependant capacitance $C(t)$. The related equation set is given by:

$$\begin{cases} L \cdot \dfrac{dQ}{dt} + R \cdot Q + h_c = H_o \\ C(t) \cdot \dfrac{dh_c}{dt} = Q \end{cases} \tag{8.3}$$

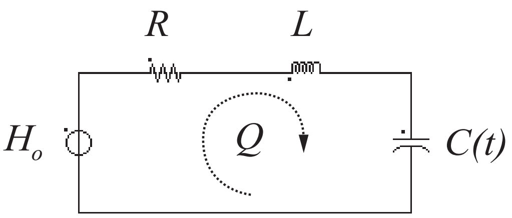

Figure 8.3: System subject to parametric excitation $C(t)$.

The characteristic equation of the above system is expressed as follows:

$$\frac{d^2 h_c}{dt^2} + \underbrace{\frac{R}{L}}_{2\cdot\mu} \cdot \frac{dh_c}{dt} + \underbrace{\frac{1}{L \cdot C(t)}}_{\omega_o^2} \cdot h_c = 0 \tag{8.4}$$

A sinusoidal variation of the capacitance $C = C_o + \Delta C_o \cdot sin(\omega \cdot t + \varphi)$ induces an excitation of the system. Considering this sinusoidal variation and assuming system without losses $R = 0$ leads to the Mathieu equation for which the stability diagram of figure 8.4 shows the unstable domains as function of the rated frequency $(\omega/\omega_o)^2$ and the parametric excitation $\Delta C_o/C_o \cdot (\omega/\omega_o)^2$.

Self Excitation

The figure 8.5 presents the equivalent scheme of a hydraulic system subject to self excitation. The system is made of a constant pressure source H_o, a resistance R, an inductance L, a capacitance C and a mass flow gain factor $\chi(Q)$ function of the discharge. The related equation set is given by:

$$\begin{cases} L \cdot \dfrac{dQ}{dt} + R \cdot Q + h_c = H_o \\ C \cdot \dfrac{dh_c}{dt} + \chi \cdot \dfrac{dQ}{dt} = Q \end{cases} \tag{8.5}$$

The characteristic equation of the above system is expressed as follow:

$$\frac{d^2 h_c}{dt^2} + \underbrace{(1 - \frac{\chi(Q)}{C \cdot R}) \cdot \frac{R}{L}}_{2\cdot\mu} \cdot \frac{dh_c}{dt} + \underbrace{\frac{1}{C \cdot L}}_{\omega_o^2} \cdot h_c = 0 \tag{8.6}$$

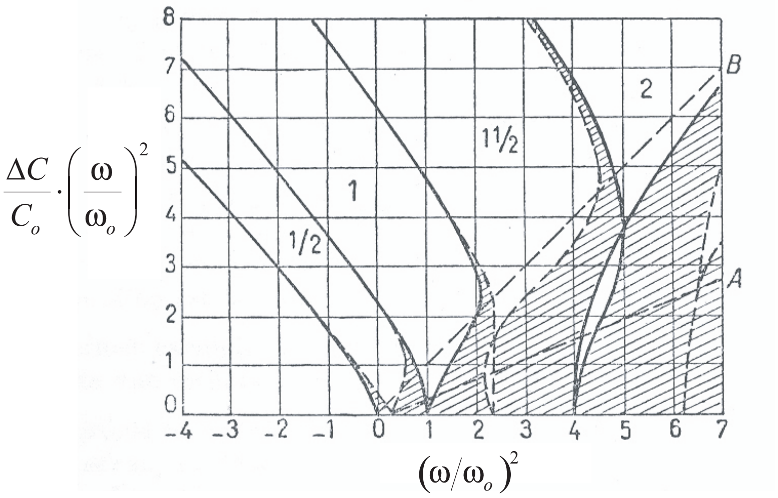

Figure 8.4: Stability diagram of the system of figure 8.3 [70].

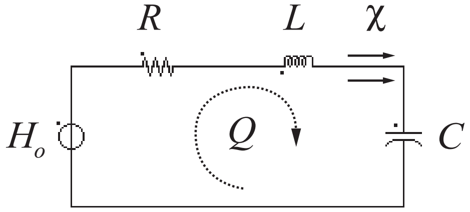

Figure 8.5: System subject to self excitation.

Considering a system for which the mass flow gain factor is a quadratic function of the discharge expressed as $\chi = \chi_o \cdot Q^2$ leads to the Van der Pol equation. The unsteady behavior related to this equation is presented in figure 8.6. Such a system features amplitude amplification for $\chi_o \cdot Q^2/(C \cdot R) < 1$ and amplitude damping for $\chi_o \cdot Q^2/(C \cdot R) > 1$.

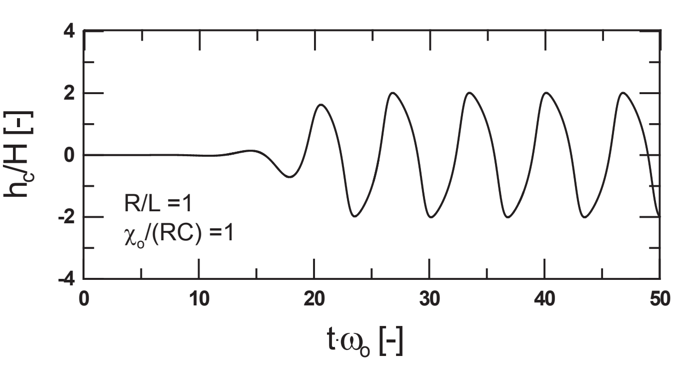

Figure 8.6: Time evolution of h_c of system of figure 8.5 leading to the Van der Pol equation.

The Role of the Type of Excitation

From the modelling point of view, it is important to be able to associate a physical excitation mechanism to a mathematical expression. This enables to clearly identify the key parameters of the system that have to be determined/known for their simulation.

8.3 Excitations Sources in Francis Turbines

The complex flow structure developing in a Francis turbine leads to several types of excitation related to cavitation, vortices (cavitating or not) and rotor-stator interactions. The typical excitations source induced by the flow in a Francis turbine are the following:

- **part load vortex rope excitation:** in the frequency range of $0.2 - 0.4 \cdot n$ [126];
- **upper part load vortex rope excitation:** in the frequency range of $2 - 6 \cdot n$ [44];
- **full load vortex rope excitation:** in the frequency range of $0.1 - 1 \cdot n$ [79];
- **interblade cavitating vortices:** in the frequency range of $8 - 12 \cdot n$ [100];
- **rotor stator excitation:** in the frequency range of $1 - 4 \cdot Z_b \cdot n$ [22];
- **von Karman vortex shedding:** in the Strouhal range of $St = 0.1 - 0.3$ [18];
- **bubble and sheet cavitation:** in the frequency range of $0.5 - 12$ kHz [25].

If all these excitation sources may result in unacceptable solicitations of the turbine structure, only a small part of them is expected to result in strong interaction with the hydraulic system. Indeed, many of these excitations are in a high frequency range with respect to the size of the hydraulic circuit of a power plant. However, some ”high” frequency phenomena can excite an eigen frequency of a scale model test rig, while it does not on the prototype because of the difference of hydroacoustic parameters of both installations. Especially, a given rated frequency on a scale model corresponds usually to a higher rank of system eigen frequency harmonics of the actual power plant, and then benefits from higher damping on the prototype.

Therefore, the excitations of particular interest regarding the risk of hydroacoustic resonance during prototype operation, are the part load, upper part load and full load vortex rope excitations, and the rotor-stator excitations. The risk of resonance with interblade vortices potentially exists, but was never reported on prototype or scale model. However, the related cavitation compliance may play a strong role in the determination of the eigen frequencies of a hydraulic installation.

Consequently, the focus of the hydroacoustic modelling of the present work is put particularly on the vortex rope excitations and the rotor-stator excitations. The basics of the related excitation mechanisms are described in the following sections.

8.4 Vortex Rope Induced Pressure Fluctuations

The cavitating vortex rope developing in the draft tube features different patterns in terms of shape and related pressure pulsation frequencies and amplitudes. The figure 8.7 presents a waterfall diagram of the wall pressure fluctuations as function of the rated frequency and discharge coefficient measured in the draft tube cone of a Francis turbine of specific speed $\nu = 0.22$ for the best efficiency energy coefficient $\psi = \psi_{BEP}$, [79]. From the waterfall diagram it can be seen that the part load and full load pressure fluctuations are paramount.

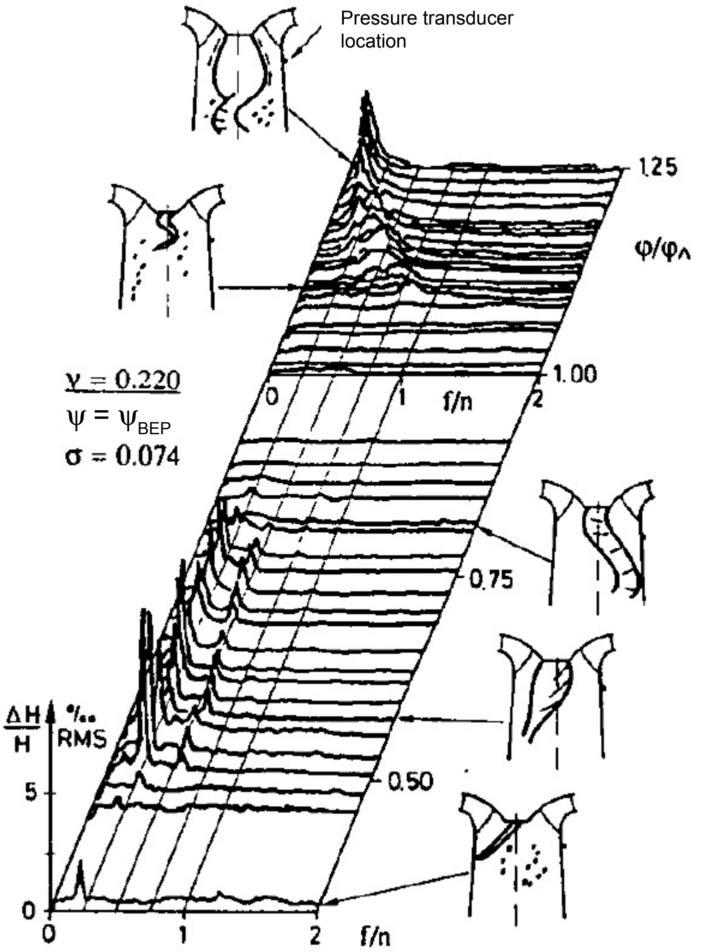

Figure 8.7: Waterfall diagram of pressure excitation and related vortex rope shape [79].

The figure 8.8 [43] presents the typical patterns of the vortex rope with respect to the rated flow. It can be seen that the occurrence of forced excitations are common for part load operation and are occasional for full load operation. Self excitations are occasional at lower part load and full load as it is also mentioned by Jacob [79]. Pressure shocks resulting from the impact of the cavitating vortex rope on the draft tube wall are occasionally expected for a large part of part load and beginning of full load operation. But it is usually at the upper part load that they may feature high amplitudes and are coming with strong noise and mechanical vibrations [44].

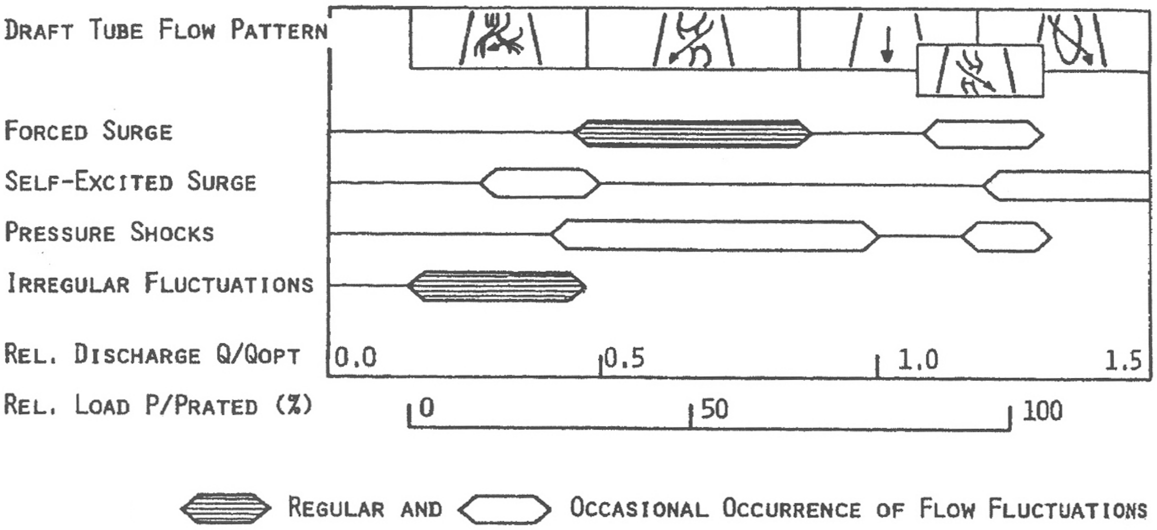

Figure 8.8: Draft tube flow patterns and associated excitations types [43].

8.4.1 Part Load Vortex Rope Pressure Fluctuations

The part load pressure fluctuations induced by the vortex rope are of major concern as they are regularly expected on both scale model and prototype and can feature high amplitudes. Hydroacoustic resonance is expected because these pressure fluctuations are of the forced type. In the following subsections the excitation mechanism associated with the part load vortex rope is presented, then the possible modelling approaches are discussed.

From the Vortex Breakdown to the Draft Tube Surge

The draft tube of a Francis turbine is characterized by the fact that it is divergent, with elbow and is subjected to high swirl momentum induced by the runner at part load. Consequently, the flow extending in the draft tube is fully 3 dimensional, unsteady, may feature separation and cavitation. Therefore, it is suitable to analyze the onset of the cavitating vortex rope step by step.

Initially, the focus was on the identification of the different flow patterns that may result from a swirling flow developing in an axial tube. Swirling flow is defined to result from both axial and vortex motion. Increasing the swirl momentum, the flow starts from purely steady axial flow and suddenly becomes unsteady and features a precessing vortex. Early analytical investigations were able to predict the occurrence of the famous phenomenon known as the vortex breakdown and are expected when reverse flow occurs along the axis, see Benjamin 1962 [12]. Such phenomenon was soon confirmed experimentally by Harvey, 1962 [71], with an apparatus generating an air swirling flow extending in a cone and evidencing the vortex breakdown by smoke injection, see figure 8.9. The precessing motion of the vortex induced by the swirling flow was also evidenced. Using a similar apparatus, Cassidy and Flavey, 1970 [33], have highlighted the dependency of the vortex precession frequency on the ratio between the axial and swirl momentum. Therefore the dimensionless swirl momentum ratio was introduced:

$$MomentumRatio = \frac{\Omega \cdot D_{ref}}{\rho \cdot Q^2} \tag{8.7}$$

Where Ω is the flux of swirl momentum and is given by:

$$\Omega = \int \rho \cdot r \cdot C_u \cdot C_n \cdot dA \tag{8.8}$$

In addition, they have pointed out that wall pressure fluctuations are induced by the helical vortex precessing about the axis of the tube. It was also shown analytically that such precessing flow is capable of sustaining an axisymmetric standing wave, see Benjamin 1967 [13]. The method of swirl momentum was then applied by Uldis and Palde, 1974 [114], to Francis turbine scale models in order to try to predict the surging operating range and the related frequency of pressure fluctuations on the prototype. The method showed that improvement was required, probably because the influence of the cavitation number was not considered.

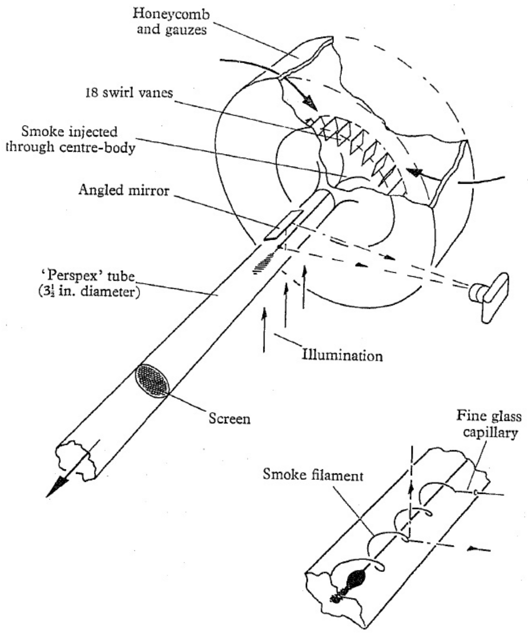

Figure 8.9: Vortex tube developed by Harvey, [71].

Similarly, investigations based on the experience gained on the vortex precession in straight tubes with swirling air were undertaken with water in an elbow draft tube by Nishi, 1980 [109], 1982 [110], 1994 [111], but without runner, see figure 8.10. He pointed out the role of the cavitation number on the amplitudes of the pressure pulsations and on the vortex precession frequency. Particularly, resonance was measured on the test rig and described as the draft tube surge. The resonance depends on the precessing frequency and on the cavitation number, *i.e.* the cavitation volume, see figure 8.12. Furthermore, the pressure pulsations appeared to be constituted of two components: (i) a rotating component related to the distorted convective pressure field in the cross section, and (ii) a synchronous component related to the axisymmetric pressure pulsation associated with swirling flow as described by Benjamin in 1967 [13]. Dörfler [40] showed such decomposition in the draft tube of a Francis turbine. Angelico *et al.*, 1986 [5], demonstrated that using 3 pressure transducers located in a cross section of the draft tube it is possible to determine both the rotating part and the synchronous part of the pressure fluctuations. The pressure fluctuation phasors at the frequency of the vortex rope obtained from 4 different pressure transducers located in the draft tube cone of a Francis turbine scale model are presented in figure 8.13 in the complex plane. It can be noticed that the 4 phasors represent a circle whose radius is the rotating part of the pressure and the position of the circle center is the synchronous part.

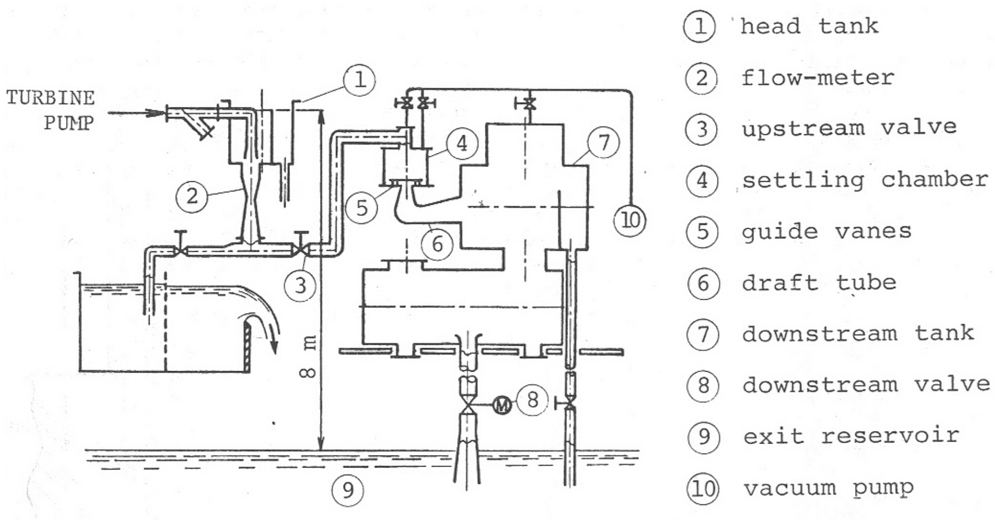

Figure 8.10: Conical elbow draft tube with swirl generator at inlet without runner [108].

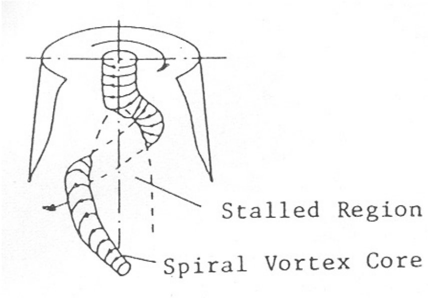

Figure 8.11: Helicoidal vortex rope precessing around a recirculating zone in the conical elbow draft tube with swirl generator at inlet without runner [110].

In parallel many investigations were undertaken on scale model conical elbow draft tubes of Francis turbines under cavitating and non cavitating conditions, see Dériaz 1960 [47], Ulith *et al.* 1974 [149], Henry *et al.* 1981 [74], Muciaccia 1984 [107], Jacob 1996 [81]). Particularly, investigations in the framework of the FLINDT project, FLow INvestigation in Draft Tube, pointed out analytically the unstable nature of the flow in a conical draft

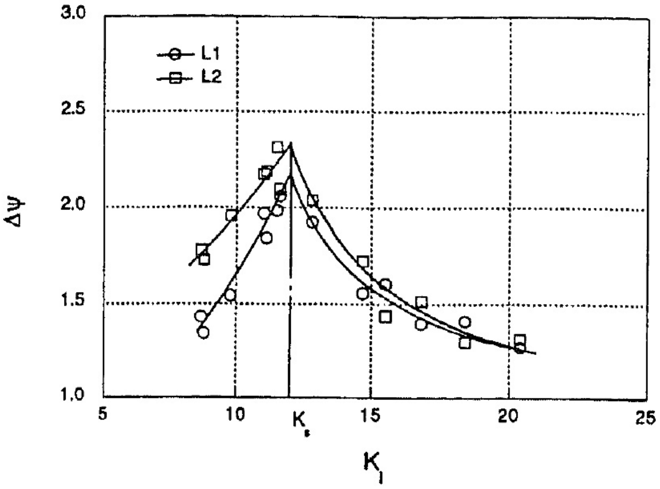

Figure 8.12: Draft tube pressure pulsation as function of the cavitation number [111].

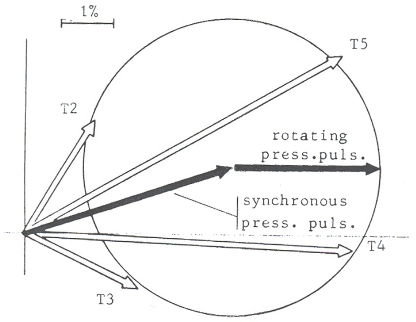

Figure 8.13: Decomposition of draft tube pressure pulsation in rotating and synchronous component [5].

tube, see Avellan 2000 [9] and Resiga *et al.* 2006 [139]. It was shown that the swirling flow can be accurately decomposed in a sum of 3 Batchelor vortices, Batchelor 1967 [11]. The solution of the eigen value problem of the related swirling flow, keeping the discharge flow coefficient as a parameter, shows the unstable nature of the flow for low discharge. Such an approach provides the insights for the optimization of the runner geometry with respect to the stability of the draft tube flow.

Modelling of Part Load Pressure Fluctuations

The understanding of the onset conditions of the vortex breakdown and the related pressure excitation was a helpful approach for developing models of the excitation related to the part load vortex rope and assessing the risk of resonance on the prototype. It was understood early on that a resonance risk evaluation should be conducted directly for the power plant installation itself and cannot be directly transposed from scale model to prototype. Thus the method of transfer matrices was applied by Zielke, 1972 [160], for determining the eigen frequencies of the system. Then in 1980, [159], [158], assuming a stochastic nature of the vortex rope excitation, he predicted pressure amplitudes by correlating the pressure eigen modes shapes of the pumped storage power plant and the power density spectra of the vortex rope excitation. However, doing so, he was neglecting two important facts:

- the pressure fluctuations measured on the test rig is the sum of the pressure excitation and the response of the test rig;
- the compliance of the cavitating vortex rope affects strongly the eigen frequencies of the power plant.

Aware of these drawbacks, Dörfler 1982 [40], set up a procedure for the prediction of the pressure amplitudes of a hydroelectric power plant also using the impedance method. The procedure is based on the identification of the pressure source excitation on the scale model first without cavitation using the synchronous and pulsating separation method. Extracting the synchronous part of the pressure pulsations and using the impedance model of the test rig, he determined iteratively the amplitude of the pressure excitation required to reach the measured amplitudes. Then, he assumed that the excitation source amplitude is identical for cavitating and not cavitating flow, assuming that the swirl momentum induced by the runner is only slightly affected by the cavitation [111]. Consequently, the only difference of pressure fluctuation amplitudes between measurements with and without cavitation is due to the change of the vortex rope compliance C given by:

$$C = \frac{\partial V_{cavitation}}{\partial H} \tag{8.9}$$

Where $V_{cavitation}$ is the volume of the cavitation and H is here the static pressure expressed in $[mWC]$.

This concept of cavitation compliance was successfully introduced by Ghahermani and Rubin, in 1971 and in 1966 [59], [128], for the understanding of the so called POGO effect in the liquid rocket propulsion system. Brennen and Acosta, in 1973 [27], then extended this method by evaluating the cavitation compliance using quasi potential flow applied to a cavitating cascade and investigating the influence of both the cascade geometry and the cavitation number.

Similarly, Dörfler [40] determined the cavitation compliance as function of the cavitation number σ as illustrated in figure 8.14. For transposition purposes, he introduced the following dimensionless compliance:

$$C' = \frac{C \cdot H_{kin}}{D_{ref}^3} \tag{8.10}$$

Where H_{kin} is the kinetic head given by:

$$H_{kin} = \frac{Q^2}{2 \cdot g \cdot A} \tag{8.11}$$

Using this method, he obtained results with very good agreement with the measurements as illustrated in figure 8.15 where pressure and torque fluctuations amplitudes are presented. The torque fluctuations are obtained by linearizing the turbine characteristic, Dörfler 1980 [45]. Later, Tadel and Maria 1986 [142], used the impedance model of Dörfler

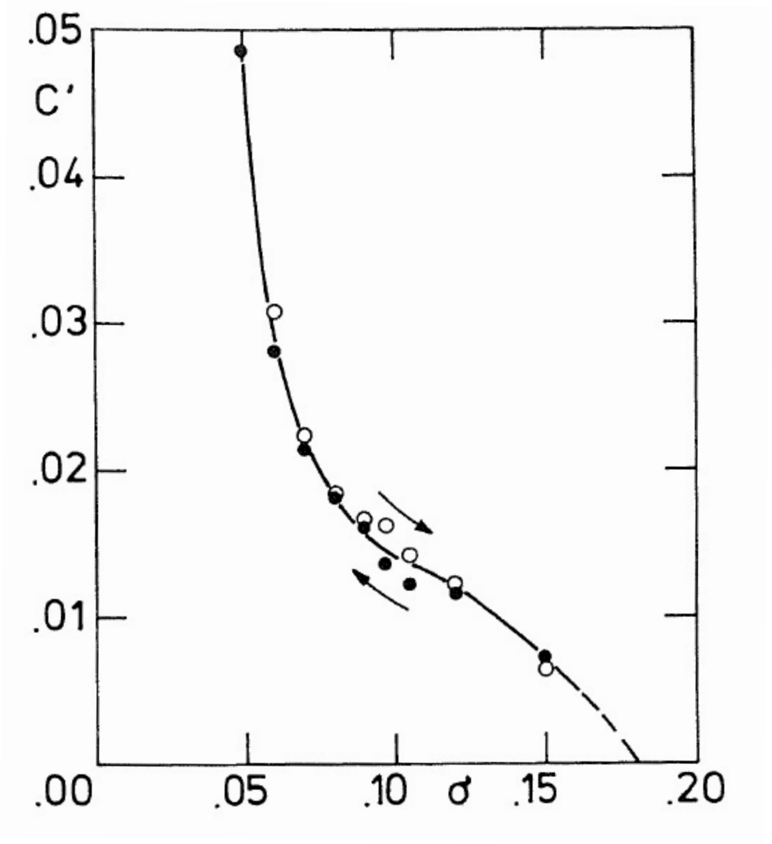

Figure 8.14: Dimensionless cavitation compliance as function of the cavitation number [40].

to show the influence of upstream and downstream arrangement of the power plant on the pressure pulsation amplitudes but also on mechanical torque.

However, the impedance model of Dörfler is based on the modelling of the vortex rope compliance by a single lumped capacitance C. Therefore, this modelling is restricted to "low" frequency phenomena, *i.e.* below 10 Hz, as it was shown by Couston and Philibert [120]. These authors proposed a new matrix model of the entire draft tube including the cavitating vortex rope based on the analytical expression of the vortex rope diameter as function of the curvilinear abscissa. This model presented good agreement with measurements.

The parametric excitation model was used by Koutnik and Pochyly, 2002 [96], for the understanding of atypical pressure fluctuation frequencies measured on pump-turbine power plants. In this modelling, a time dependant solution was necessary to investigate the influence of sinusoidal variation of the cavitation compliance.

Some recent work has been carried out with the aim to couple CFD computations of the vortex rope extending in the draft tube with a hydroacoustic model of the power plant piping for the prediction of resonance by Ruprecht and Helmrich [129]. However, the CFD computation does not take into account the compressibility effect in the draft tube, which is significant as very low wave speed is expected in this component. Consequently it does not represent the hydroacoustic behavior of the draft tube.

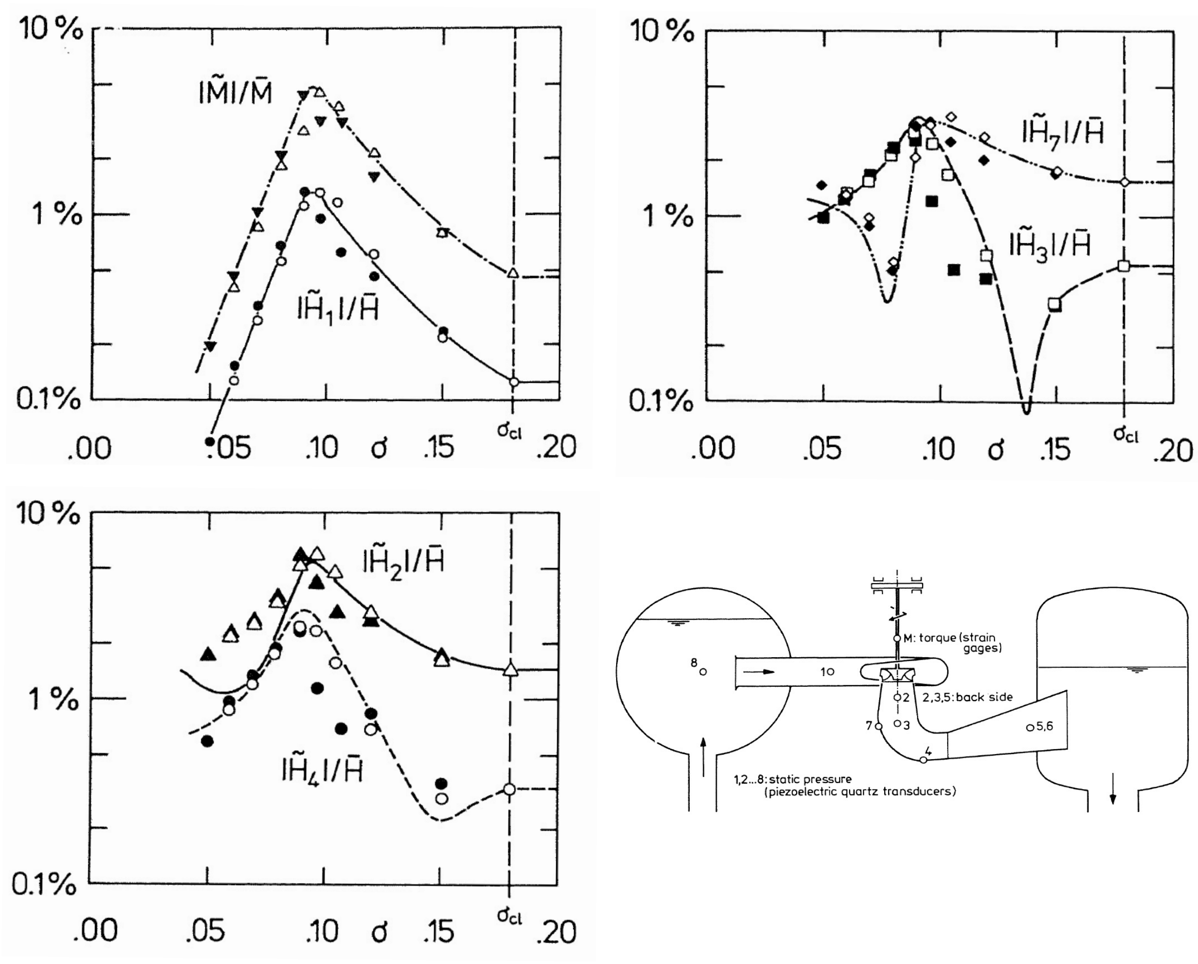

Figure 8.15: Comparison of measurements (dots; black/white decreasing/increasing cavitation number) and model (solid lines) at the vortex rope frequency $f_{rope}/n = 0.224$ [40].

8.4.2 Upper Part Load Vortex Rope Pressure Fluctuations

While the vortex rope precession frequency commonly corresponds to 0.2 to 0.4 times the turbine rotational frequency n, pressure fluctuations may occur in a higher frequency range, $2 \cdot n$ to $4 \cdot n$, for high specific speed turbines at upper part load range as described by Fischer in 1980 [52], Dörfler in 1994 [44] and Jacob in 1996 [81]. Figure 8.16 shows a waterfall diagram where upper part load pressure fluctuations are pointed out at the point number (3). Moreover, a "shock phenomenon" may occur in the same operating range and induces structural vibrations due to vortex rope impacts on the draft tube wall, see Dörfler 1994 [44].

However, from the modelling point of view, no investigations on the upper part load pressure fluctuations are reported in the literature. In addition, it is not very well understood why on the prototype this phenomenon is not present or results in small amplitudes only [52], [44].

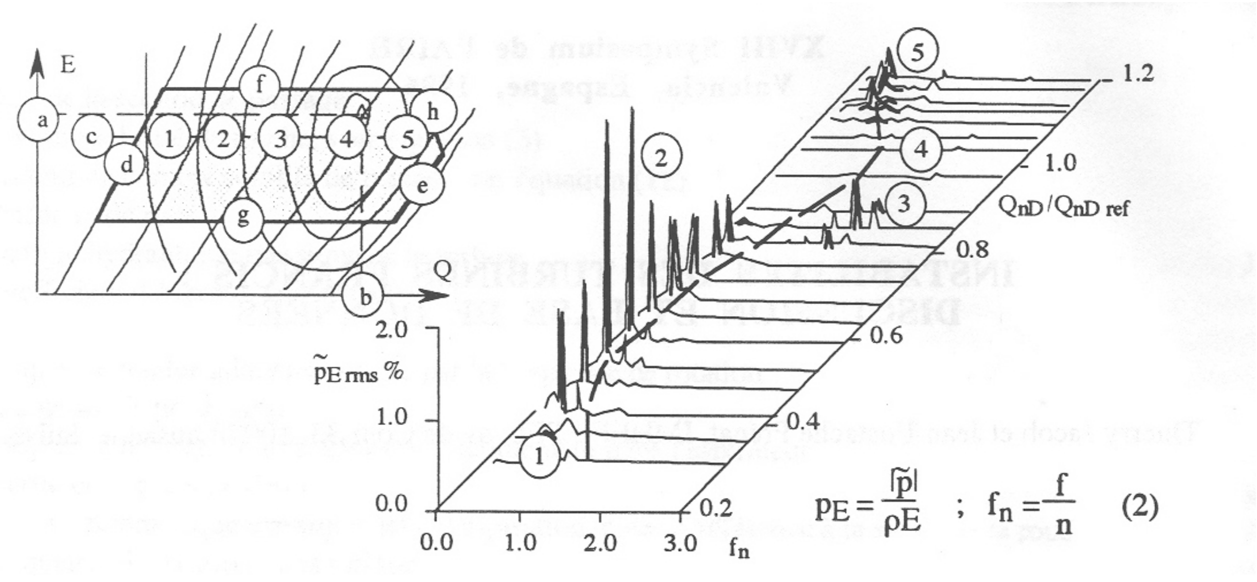

Figure 8.16: Waterfall diagram of pressure pulsations at turbine draft tube cone at constant ψ of a medium head Francis turbine [81].

8.4.3 Full Load Vortex Rope Self Excitation

At full load operating conditions, Francis turbines feature an axisymmetric cavitating vortex rope in the draft tube cone generated by the incoming swirling flow, Jacob [79]. The cavitating rope may under certain conditions act as an energy source, which leads to self-excited pressure oscillations in the whole hydraulic system [84], [79]. These pressure oscillations can jeopardize the safety of mechanical and hydraulic systems on the prototype, see Jacob 1992 [85]. Depending on the turbine relative location in the circuit, the turbine head may oscillate and generate power swings as shown by Koutnik and Pulpitel in 1996 [97], and by Arzola in 2006 [8].

However, contrary to the half-load which are of the forced excitation type, the full-load surge are of the self-excitation type, [79], [97]. Koutnik and Pulpitel [97] have applied the modelling approach developed initially for pump stability analysis based on the use of the cavitation compliance C and of the mass flow gain factor χ, see Brennen and Acosta in 1976 [28] and 1978 [30]. It was shown in section 6.3.2 that negative values of χ may lead to system instabilities. It is well known that the vortex rope cavitating volume increases with the discharge at full load as well as for very low part load. The mass flow gain factor being defined as $\chi = -\partial V/\partial Q$ becomes negative for low part load and full load operation and may lead to self-excited pressure fluctuations as already indicated in the figure 8.8 by Dörfler. Based on the transfer matrix approach and considering both the cavitation compliance C and the mass flow gain factor χ as parameters, Koutnik and Pulpitel [97] derived a stability diagram for the explanation of full load surge occurring on a 4 × 39 MW Francis turbine power plant, see figure 8.17. The successful influence of air injection on pressure fluctuation amplitudes was also qualitatively explained in this investigation. Such analysis is a powerful tool for the qualitative analysis of the dynamic behavior of a hydroelectric power plant. However, the prediction of pressure fluctuation amplitudes requires performing time domain simulation including system non-linearities.

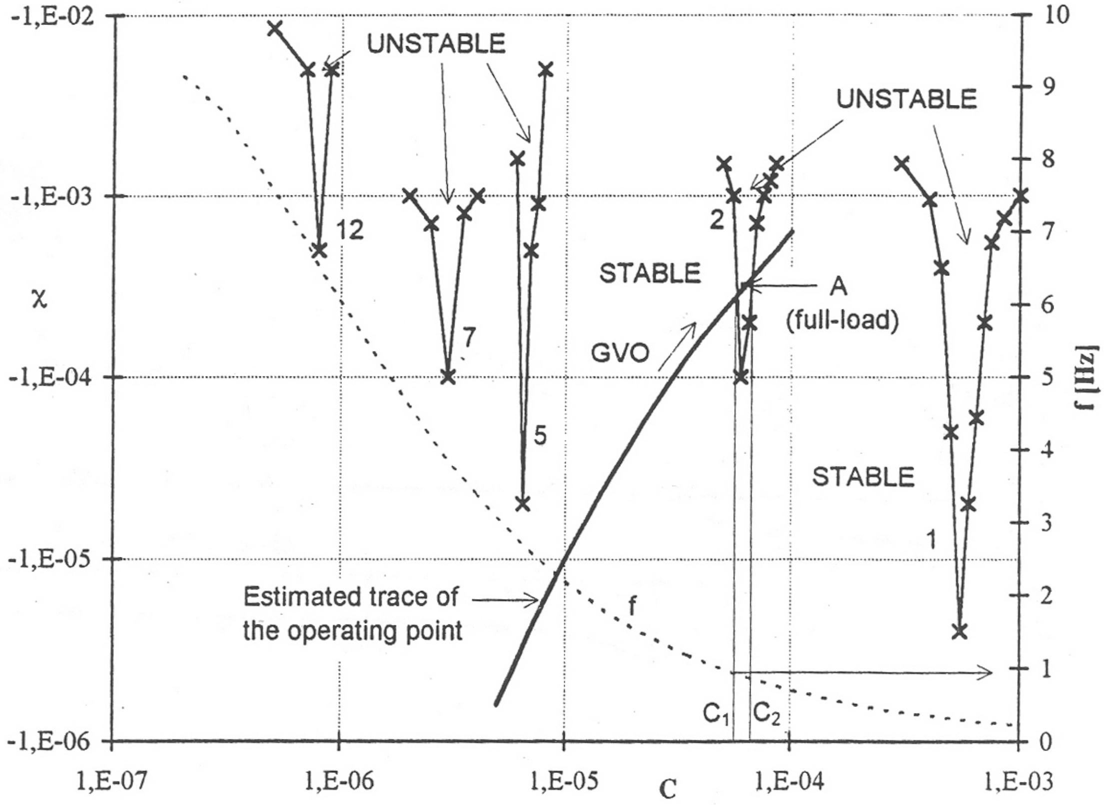

Figure 8.17: Stability diagram of a power plant with respect to the cavitation compliance C and mass flow gain factor χ [97].

A similar approach of cavitation parameter mapping was also successfully applied for the explanation of inducer instabilities by Tsujimoto *et al.* in 1997 [148] and of propeller instabilities in cavitation tunnels by Duttweiler and Brennen in 2002 [49] and by Watanabe and Brennen in 2003 [154].

8.5 Rotor Stator Interactions

Hydraulic pumps, turbines or pump-turbines operating under steady state conditions are subject to pressure fluctuations resulting from the interaction of the rotating parts and the stationary parts of the machine. This Rotor-Stator Interaction, RSI, is the consequence of the interaction between the rotating flow perturbations so-called potential flow perturbations caused by the impeller blades and the flow perturbation caused by the guide vanes. This interaction induces pressure waves propagating in the entire hydraulic machine. As a result the RSI phenomena may cause two different kinds of pressure fluctuations in the machine: (i) diametrical pressure mode rotating in the vaneless gap between the guide vane and the impeller blades as described by Bolleter in 1988 [22] and by Ohura *et al.* in 1990 [113]; (ii) standing waves in the spiral casing as described by Chen in 1961 [37] and by Dörfler in 1984 [42].

The first phenomenon may cause hydromechanics resonance between the rotating diametrical pressure mode and the structure of the impeller, see Tanaka 1994 [143], or of the head cover see Fischer 2004 [53] and Franke 2005 [57], and may induce strong vibrations, noise, fissures or guide vane bearing ruins. The second phenomenon may cause resonance with the power house structure that generates unacceptable vibrations and noise levels, see Ohura 1990 [113]. The standing wave phenomenon may affect also the penstock, Dörfler 1984 [42], Den Hartog 1956 [70], which evidences the potential interaction of the hydraulic machine with the hydraulic circuit.

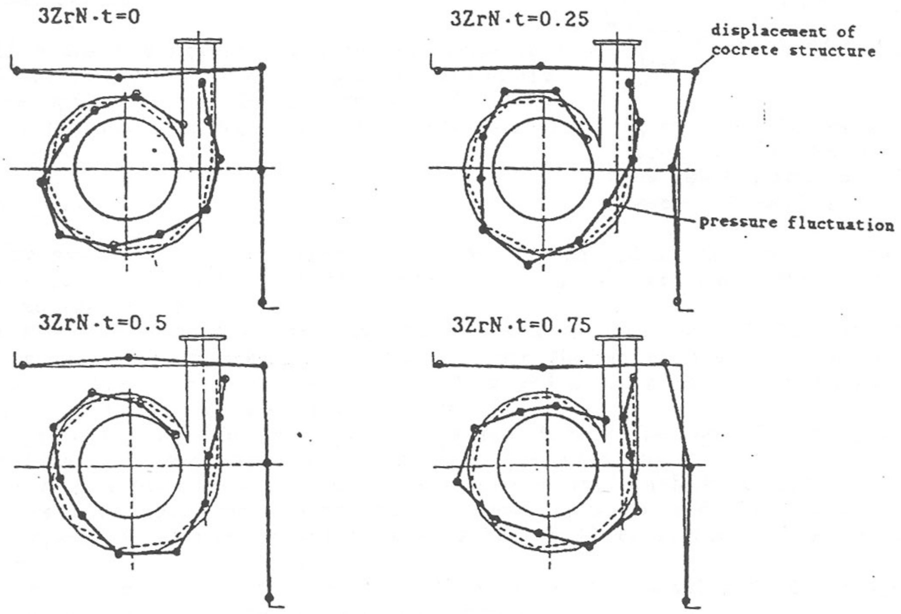

Figure 8.18: Power house structure vibrations measured by Ohura *et al.* [113].

The prediction of such phenomena is a challenging task during the early stage of the design of a reversible pump-turbine unit for a hydroelectric power plant. Some analytical models have been developed by Bolleter in 1988 [22] and Ohura *et al.* in 1990 [113] for the diametrical mode shape and by Chen in 1961 [37] and Dörfler in 1984 [42] for the standing wave to predicts the risk of occurrence of these phenomena. The prediction of the occurrence of the standing wave is based on the analysis of the travelling time of pressure waves propagating in a one-dimensional system modelling the pump-turbine according to its topology. Recently, Haban *et al.* in 2002 [66] have developed more sophisticated one-dimensional models based on the transfer matrix method that have shown their capability of predicting spiral casing standing wave patterns. By the use of such models Francke *et al.* in 2005 [57] have pointed out the link between the standing waves in the spiral casing and the penstock and the diametrical pressure mode rotating in the vaneless gap by performing a forced response analysis in the frequency domain. However this approach requires the identification of the excitation pattern by the method described by Bolleter [22] and Ohura *et al.* [113].

The simulation of the incompressible 3D unsteady flow of a vaneless centrifugal pump performed by Gonzalez *et al.* in 2002 [61] using a commercial CFD tool has shown the capability of CFD to predict accurately the unsteady convective field related to the RSI phenomenon at the blade passing frequency which is dominant close to the nominal operating point. However some discrepancies appeared for off-design operating conditions where hydroacoustic behavior becomes more effective due to a blade-tongue interaction. Such an incompressible code cannot account for the propagating part of the flow which may lead to standing wave phenomena. Therefore the separation of hydraulic and acoustic pressure fluctuations by means of the least-squares residual method developed by Morgenroth in 1998 [106] was used. A model accounting for both the jet-wake pattern of the convective flow and for the blade-tongue interaction has been set up by Parrondo *et al.* in 2002 [115]. Through an experimental identification of the parameters of the acoustic model, a good agreement has been found between the model and the measurements even for off-design operating conditions where the amplitude of the blade-tongue interaction was found to have 10 times the amplitudes of the wake jet part of the flow.

Chapter 9

Upper Part Load Pressure Fluctuations Analysis on a Scale Model

9.1 General Remarks

Upper part load pressure pulsations are commonly reported from scale model tests and are usually attributed to test rig resonance. However, the excitation source mechanism is not well understood. Does the pressure pulsation result from vortex rope pressure source excitation or is it of the self excited nature? What is the role of the shock phenomenon mentioned in chapter 8.4.2 ?

The upper part load pressure fluctuations phenomenon was observed and measured in the framework of the FLINDT project, providing the opportunity to set up a hydroacoustic model of the test rig and to assess resonance conditions of the full hydraulic system. However, the analysis on the FLINDT project is done for only one operating point. Therefore, to clarify some unanswered questions on the role of the cavitation and Froude numbers on the upper part load pressure fluctuations, an experimental investigation is carried out on a similar scale model Francis turbine by performing vortex rope visualizations.

9.2 Modelling of Upper Part Load Pressure Fluctuations

9.2.1 General

In the framework of the FLINDT project [9], wall pressure fluctuation measurements were carried out on the draft tube of a scale model of a medium head Francis turbine of specific speed $\nu = 0.56$ for several operating points by Arpe [6]. For the upper part load under low cavitation number conditions, $\sigma = 0.38$, pressure fluctuations were recorded at a frequency value of about $2.5 \cdot n$. For these operating conditions, structural vibrations of the whole test rig and strong noise were also observed.

This section presents the analysis of the pressure fluctuations measured in the draft tube at part load operation under low cavitation number. First a phase shift analysis is carried out, pointing out a pressure excitation source in the elbow of the draft tube. The wave speed along the draft tube is deduced from this analysis enabling to carry out a hydroacoustic model of the entire test rig using SIMSEN. Then, a free oscillation analysis as well as a forced oscillation analysis are performed in order to explain the pressure fluctuation mechanism.

9.2.2 Experimental Investigation on Francis Scale Model

The experimental investigations are performed on a scale model of a high specific speed Francis turbine, $\nu = 0.56$, see figure 9.1. The draft tube is equipped with 292 pressure taps, distributed in 13 sections. The draft tube is composed of a cone made in plexiglas, an elbow in glass fiber-epoxy resin and a diffuser with a pier made of welded stainless steel plates. A set of 104 miniatures Keller Piezoresistive pressure transducers series 2MI are mounted on the draft tube wall. The transducers range covers 0 to 3 bars to measure low pressures that extend in the whole draft tube. The scale model equipped with the FLINDT draft tube is installed in the test rig PF3 of the EPFL Laboratory for Hydraulic Machines and the tests are carried out according to IEC 60913 standards [77].

To capture phenomena of interest at low flow rate turbine conditions, all pressure signals are acquired simultaneously with a HP-VXI acquisition system using a sampling frequency of 200 Hz and 2^{14} samples. This setup enables recording 430 vortex passages providing a number of segments acceptable for the averaging process.

9.2.3 Phenomenon of Interest

The turbine operating point selected for the investigation at low discharge is given in table 9.1.

Table 9.1: Studied operating point.

Specific speed ν $[-]$	φ/φ_{BEP} $[-]$	ψ/ψ_{BEP} $[-]$	**N** $[rpm]$	**Guide Vane Opening** $[^\circ]$
0.56	0.703	1.06	750	16

The spectral analysis of the pressure fluctuations measured in the cone are presented for different σ values in figure 9.2. Pressure fluctuations between $2 \cdot n$ and $4 \cdot n$ appear for low σ values. The amplitudes decrease and the frequencies increase as σ is increasing as shown in figure 9.3 (right). These fluctuations are apparently modulated by the vortex precession and give pressure fluctuation amplitudes for $f = 2.5 \cdot n$, $2.5 \cdot n \pm f_{rope}$, $2.5 \cdot n \pm 2 \cdot f_{rope}$, etc. During measurements, strong noise and vibration of the draft tube were reported. Concerning the pressure fluctuations at the vortex rope frequency, their amplitudes increase with σ while the vortex rope frequency drops slightly, see figure 9.3 left. Moreover, the amplitude spectra following 4 paths along the draft tube are presented in figure 9.4. It can be noticed that the pressure fluctuations associated with the vortex rope and its harmonics are restricted to the area of the draft tube cone and elbow, sections (1) to (3). While the pressure fluctuations at $2.5 \cdot n$ are present in the entire draft tube.

A maximum of pressure amplitudes is visible at the section (3) and minimum at section (11), the draft tube outlet. The spectra along each path is quite similar. This suggests that it is a one-dimensional pressure fluctuation present in the entire draft tube.

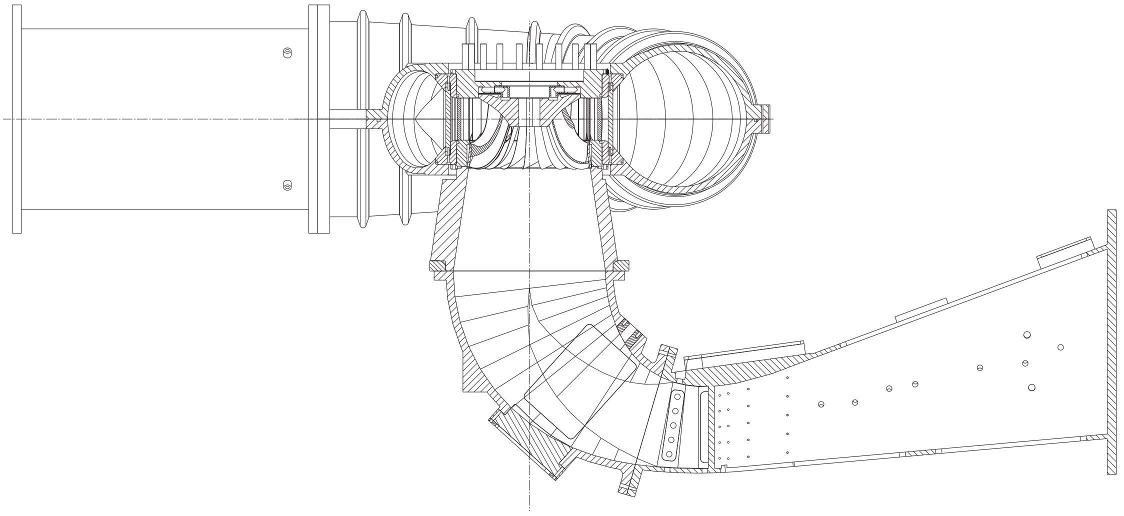

Figure 9.1: FLINDT Francis turbine scale model.

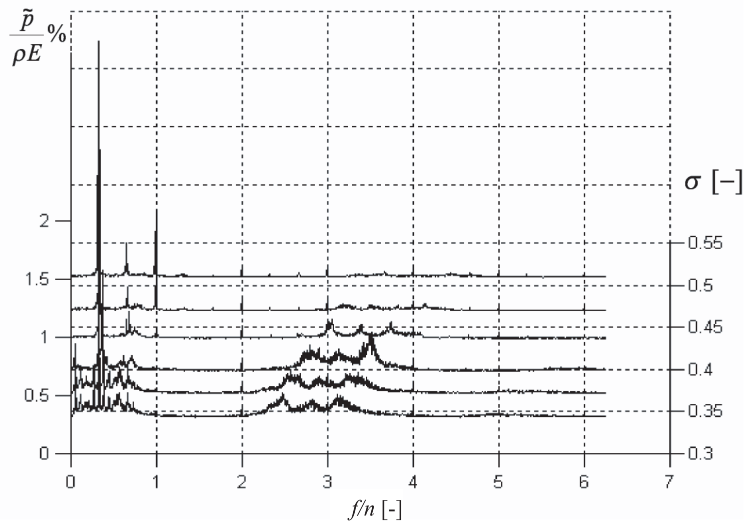

Figure 9.2: Influence of σ on the pressure fluctuations measured in the draft tube cone [6].

The pressure fluctuations spectrum provides the phase angle between two signals at the frequency $2.5 \cdot n$. The phase shift is calculated for every pressure signal with respect to a reference signal in the cone, see Arpe [7]. Those phase shifts are presented in an

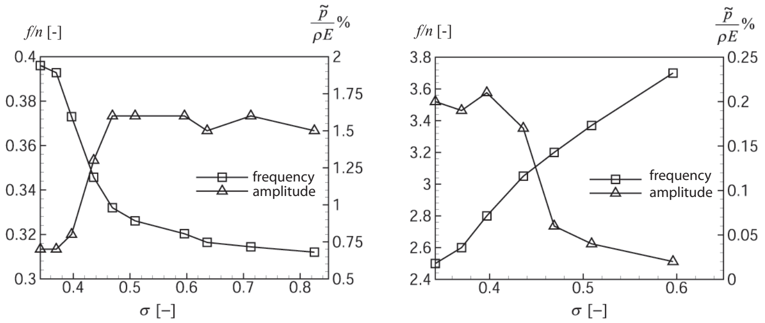

Vortex rope precession

Higher frequency

Figure 9.3: Influence of σ on the frequency and amplitudes of the pressure fluctuations for the vortex rope precession (left) and the higher frequency (right) [6].

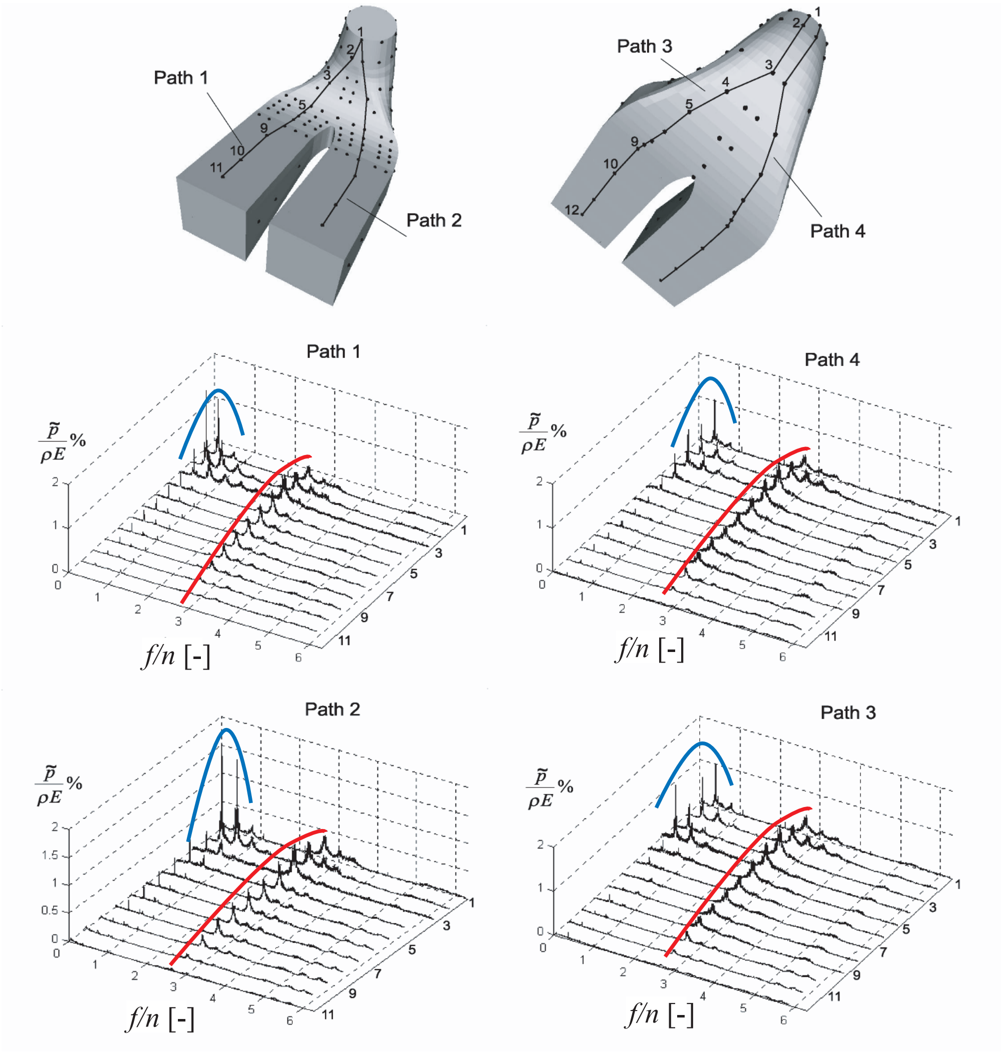

Figure 9.4: Spectra of pressure fluctuations along 4 paths for $\sigma = 0.38$ [6].

unfolded draft tube representation, see figure 9.5 left. It can be observed that in the cone, there is no phase shift between pressure signals recorded in the same section pointing out a synchronous pressure fluctuation. On the other hand, there is a maximum of phase located at the inner part of the elbow. It corresponds to the location where impacts between vortex rope and the wall occur. The phase evolution indicates that pressure waves start from this point towards both upstream and downstream. These results indicate a source of pressure waves as it is illustrated on the 3D phase representation on the draft tube wall in figure 9.5 right.

The calculated phase shifts can be expressed in time for the studied frequency. The resulting wave speed are presented along the 4 paths defined in figure 9.4 in figure 9.6. The wave speed starts from 20 m/s in the cone, increases to about 450 m/s in the elbow and decreases to 200 m/s in the channels. Generally, the acoustic wave speed depends mainly on the diameter of the cross-section, the pipe wall thickness and material and strongly on the vapor content. The low value of the wave speed in the cone is due to the low Young modulus of the plexiglass but mainly due to high vapor content due to the vortex rope. In the elbow, the wave speed increases because of the section stiffness and the decreasing vapor content. The wave speed decreases in the draft tube channels mainly because of the lateral deformations of the rectangular sections of the channels. It can be also noticed that the wave speed is higher in the outer elbow than in the inner elbow because of the difference of travel length.

During experiments, impacts between the vortex rope and the inner part of the elbow wall were noticed. Those impacts are producing strong acoustic noise similar to hammer strike. This shock phenomenon, described by Dörfler [44] and Jacob [81], can be assumed to be a broad band noise source supplying the system with energy distributed on a wide frequency range. This assumption is confirmed by the comparison between pressure fluctuation energy at the pressure source location and at the upper cone part in figure 9.7. One can notice that energy is uniformly distributed for the pressure source with higher amplitudes at the vortex rope precession harmonics. Whereas, at the upper part of the cone, there is energy only at $2.5 \cdot n$, the modulation frequencies, $5 \cdot n$ and the vortex rope precession. This evidences the white noise excitation characteristic of the pressure source.

9.2.4 Hydroacoustic Modelling of the Test Rig

To identify the origin of the pressure fluctuations at the frequency $2.5{\cdot}n$, the hydroacoustic behavior of the entire test rig is investigated. The test rig is simulated using SIMSEN-Hydro including the Francis turbine scale model, the free surface downstream tank, the connecting pipes and the 2 circulating pumps operating in parallel mode, see figure 9.8. The hydroacoustic characteristics of the simulation model are given in table 9.2. The pipes spatial discretization is set according to equation 3.91 to ensure an error below 1% at the frequency of $2.5 \cdot n$.

The wave speed of the pipe L6 is determined experimentally and the same value is also considered for the pipes L1 to L5. The cross section and equivalent length of the circulating pumps are obtained from [22]. The wave speed through the turbine is determined using the phase shift at the frequency $2.5n$ between the turbine intake and the runner outlet pressure transducers. The geometrical dimensions are deduced from the drawings.

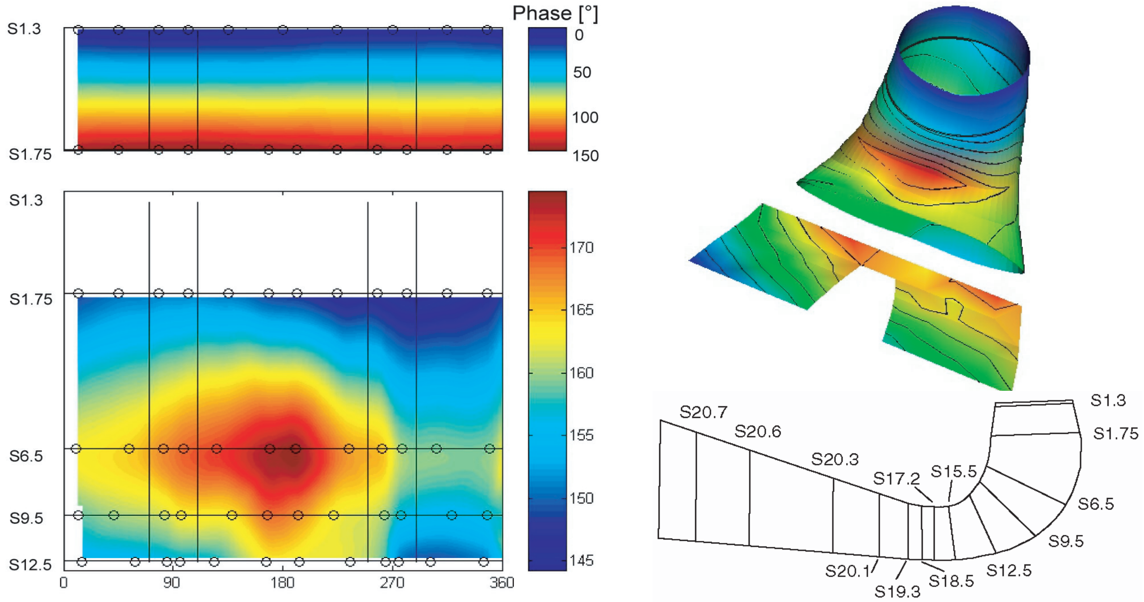

Figure 9.5: Field of the phase shift at the wall of the cone and the elbow at $2.5 \cdot n$; unfolded mapping (left) and 3D distribution (right) [6].

Hydraulic Machines Modelling

The hydroacoustic behavior of a turbine, pump or pump-turbine can be modelled as an equivalent pipe for which the head losses are determined from the slope of the static characteristic of the machine for the operating point of interest, according to Stirnemann [137]. This hydroacoustic model can be improved by considering a pressure source driven by the hydraulic characteristic of the machine instead of a pure resistance, see figure 9.9.

By taking into account the continuous area change of the machine cross section, the

Table 9.2: Dimensions of the equivalent pipe modelling the PF3 test rig.

Pipe	L $[m]$	D_{equ} $[m]$	A_{equ} $[m^2]$	a $[m/s]$
L1	11.53	0.610	0.292	1057
L2	2.55	0.610	0.292	1057
L3	7.09	0.610	0.292	1057
L4	2.30	0.484	0.184	1057
L5	4.03	0.508	0.203	1057
L6	34.27	0.529	0.220	1057
Pumps 1 and 2	2.55	0.270	0.06	850
Spiral + distributor + runner	3.49	0.418	0.137	852

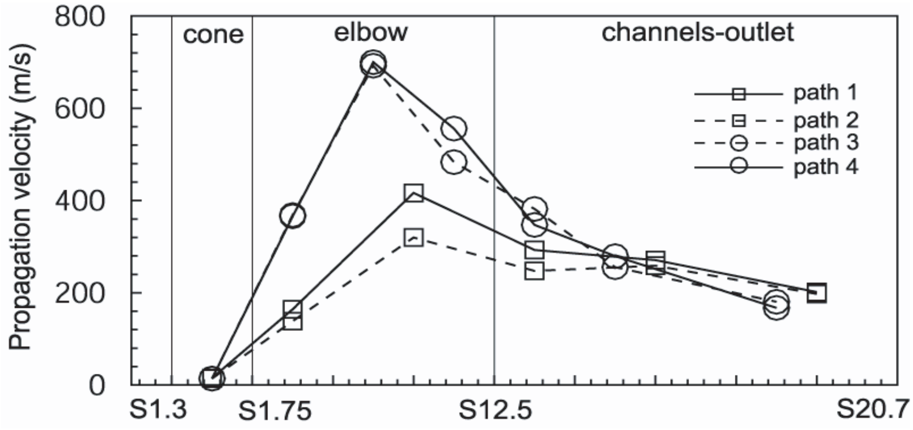

Figure 9.6: Distribution of the wave velocity along the draft tube along 4 different paths [6].

inductance term is evaluated according to:

$$L_{equ} = \int_{I}^{\overline{I}} \frac{dx}{gA(x)} = \frac{l_{tot}}{g\overline{A}} \tag{9.1}$$

Where:

- $\overline{A}$: average area of the pump-turbine cross section $[m^2]$;
- l_{tot}: total length of the pump-turbine in terms of curvilinear abscissa $[m]$.

The capacitance value is a function of the equivalent wave speed in the hydraulic machine. The evaluation of this term requires the knowledge of the bulk modulus of the water, E_w, and the variation of the cross section area under the pressure increase $\Delta A/(A \cdot \Delta P)$. Bolleter [23] performed investigations for a centrifugal pump and determined the RLC terms of the corresponding hydroacoustic model. He demonstrated the good agreement between measurements and the model for the inductance and the resistance terms. However, the model overpredicted the capacitance by twice the measured value. It allows estimating the wave speed for such a pump:

$$a = \frac{a*}{\sqrt{2}} = \frac{1200}{\sqrt{2}} = 850m/s \tag{9.2}$$

Draft Tube Modelling

The hydroacoustic modelling of the draft tube can be achieved using 3 different models:

- a concentrated compliance model;
- a distributed mean compliance model;
- a distributed compliance model.

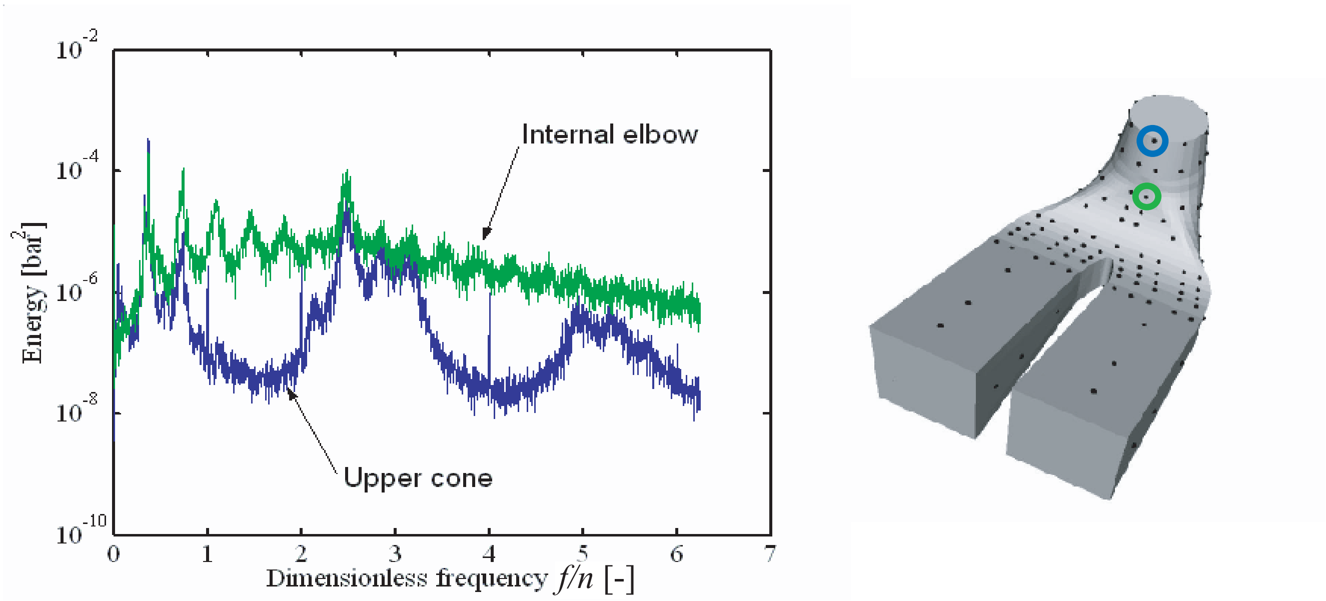

Figure 9.7: Energy spectra of the pressure fluctuation for the upper cone and for the pressure source location.

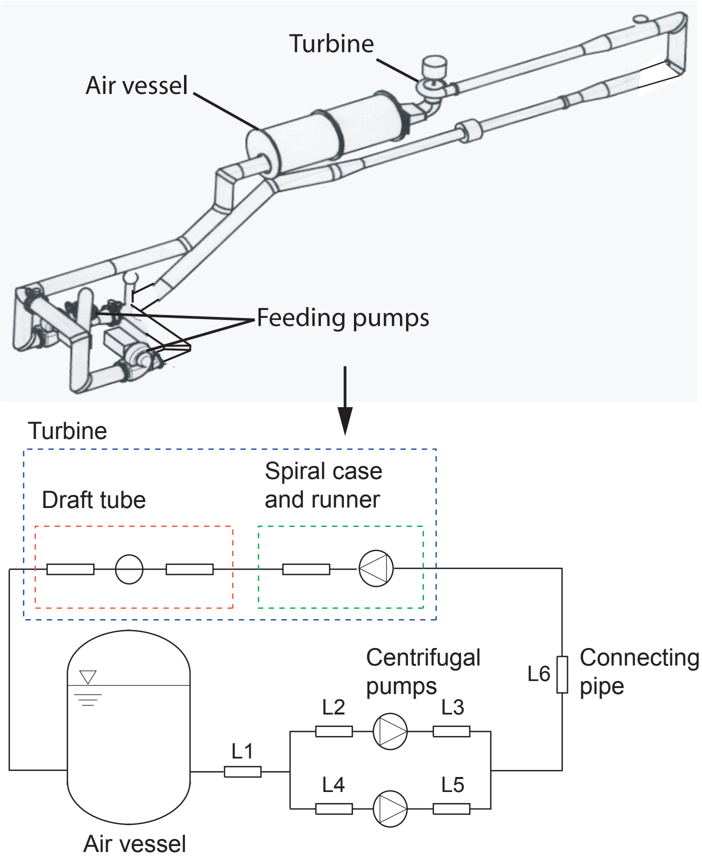

Figure 9.8: Hydroacoustic model of the PF3 test rig.

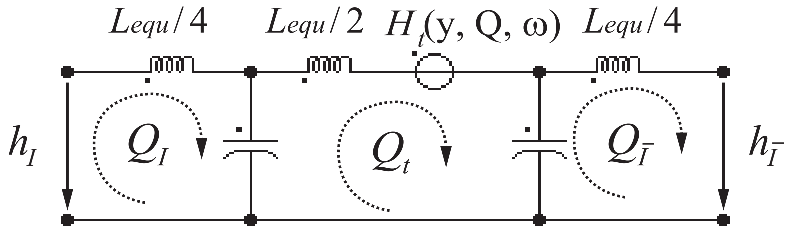

Figure 9.9: Modelling of a hydraulic machine, turbine, pump or pump-turbine.

The 3 models are illustrated in figure 9.10. The concentrated compliance model is made of one pipe with one node, whose *RLC* terms are calculated with the mean hydroacoustic parameters obtained by integration between the inlet and the outlet of the draft tube. The corresponding equivalent scheme is presented in figure 9.11 with the parameters of equation 9.4.

The distributed mean compliance model is made up out of 2 pipes with constant hydroacoustic parameters. The first pipe accounts for the inlet part of the draft tube where the wave speed is increasing and comprises 9 nodes. The second pipe accounts for the second part of the draft tube where the wave speed is decreasing and comprises only 5 nodes. This node repartition results from the fact that high number of nodes are required to model pipes with low wave speed. For both pipes, the hydroacoustic parameters are obtained by integration along the curvilinear abscissa.

The distributed compliance model is made up out of 26 pipes with constant parameters. The values of the parameters are obtained as a function of the curvilinear abscissa as illustrated by the equivalent scheme of figure 9.12 and the related equations 9.5.

The mean wave speed of a part of any of the 2 first models is determined assuming a linear change of the wave speed, and is thus given between the point i and $i+1$ by:

$$\overline{a} = \frac{L}{dt} = \frac{L}{\int_i^{i+1} \frac{dx}{a(x)}} = \frac{a_i - a_{i+1}}{\ln(a_i/a_{i+1})} \tag{9.3}$$

The cross section and wave speed distribution along the curvilinear abscissa obtained for the 3 different models are reported in figure 9.14 respectively left and right. The draft tube wave speed distribution is deduced from figure 9.6.

$$R_d = \frac{\overline{\lambda} \cdot |Q_d| \cdot l_d}{2 \cdot g \cdot \overline{D} \cdot \overline{A}^2} \quad ; \quad L_d = \frac{l_d}{g \cdot \overline{A}} \quad ; \quad C_d = \frac{g \cdot \overline{A} \cdot l_d}{\overline{a}^2} \tag{9.4}$$

$$R(x) = \frac{\lambda(x) \cdot |Q| \cdot dx}{2 \cdot g \cdot D(x) \cdot A(x)^2} \quad ; \quad L(x) = \frac{dx}{g \cdot A(x)} \quad ; \quad C(x) = \frac{g \cdot A(x) \cdot dx}{a(x)^2} \tag{9.5}$$

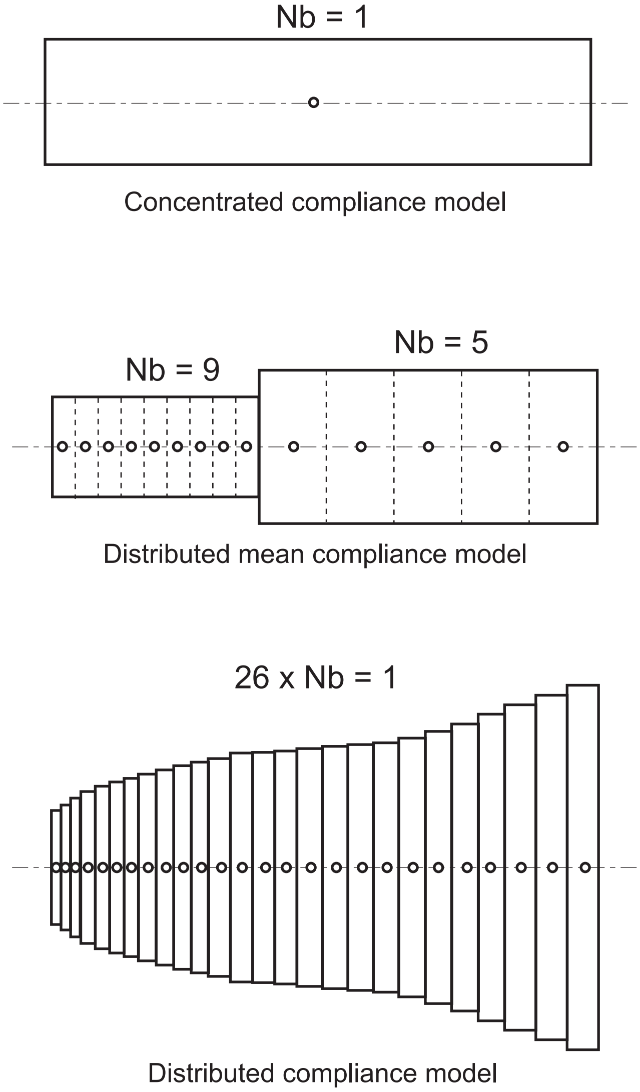

Figure 9.10: 3 possible models of the draft tube.

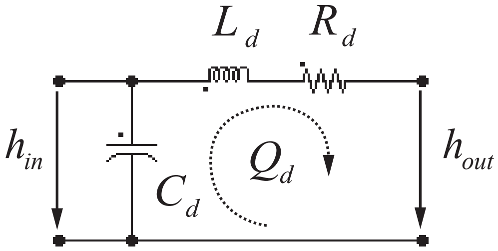

Figure 9.11: First order model of a diffuser with concentrated compliance.

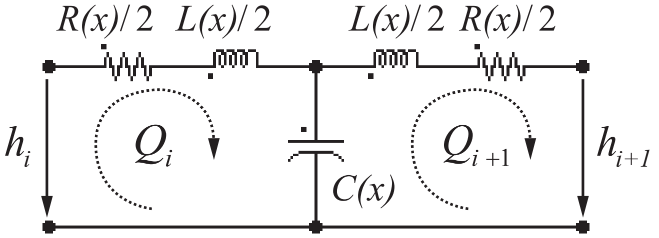

Figure 9.12: Model of an infinitesimal pipe cross section for high order modelling of the pipe with parameters function of the location x.

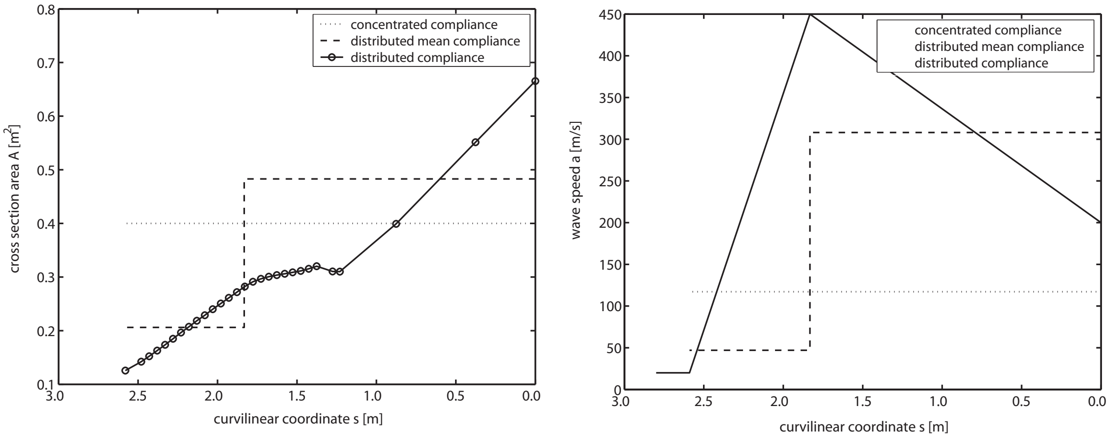

Figure 9.13: Draft tube model parameters: cross section $A(x)$ (left) and wave speed $a(x)$ (right) for the 3 different models of the draft tube.

For comparing the 3 different proposed models, the impedance of the draft tube is evaluated using the discrete impedance calculation of equation 3.76. Starting from impedance equal to 0 at the draft tube outlet, $x = 0$, up to the draft tube inlet (runner outlet) for $x = 2.59\ m$. The magnitude of the 3 impedances obtained for $x = 2.59\ m$ are presented in figure 9.14. As expected, the concentrated compliance model features only one eigen frequency at low frequency about 8 Hz and the frequencies above 16 Hz are all damped. The 2 distributed compliance models exhibits eigen frequencies at least up to 60 Hz. The distributed mean frequency model impedance fits the distributed compliance model rather well until 40 Hz and then high discrepancies appear. These results present good agreements with the transfer matrix model proposed by Philibert and Couston [120]. Although the distributed compliance model is more accurate, it requires more effort to be set up. Therefore, the distributed mean compliance model is a good compromise for investigations until 40 Hz. Therefore the frequency response and the forced oscillation analysis will be performed with distributed compliance and distributed mean compliance models and compared.

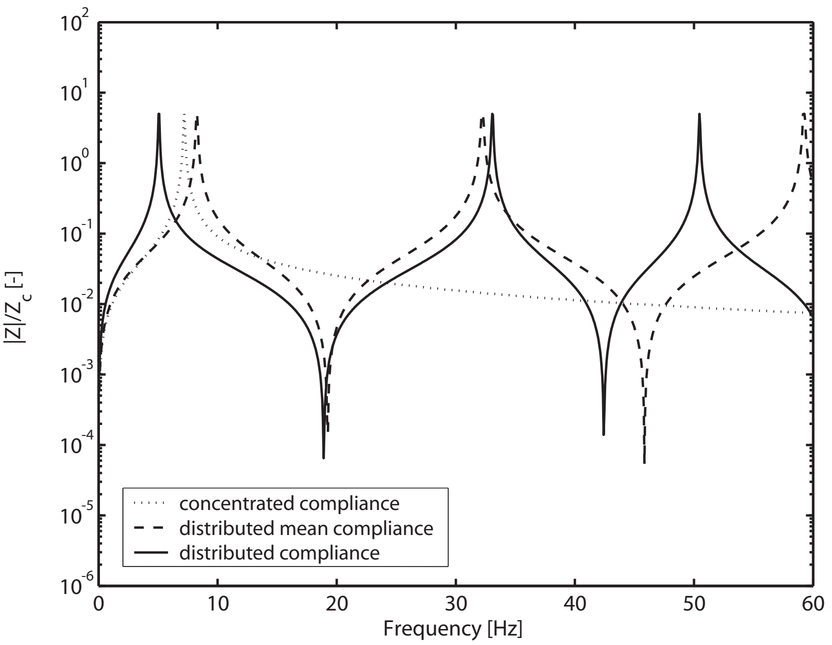

Figure 9.14: Comparison of the draft tube impedance evaluated form draft tube outlet ($x = 0\ m$) until the draft tube inlet ($x = 2.59\ m$) for three models: concentrated compliance (doted line), distributed mean compliance (dashed line) and distributed compliance (solid line).

9.2.5 Frequency Response Analysis of the Test Rig

To determine the eigen frequencies of the entire test rig, a PRBS excitation is imposed at the pressure source location. The spectral analysis of the pressure fluctuations obtained at every spatial node with both the distributed mean compliance and the distributed compliance models, are presented as a waterfall diagram in figure 9.15 respectively left and right. The waterfall diagrams point out the eigen frequencies of the test rig and the related eigen mode shapes. The draft tube extends over on the first 17 nodes for the distributed mean compliance model while it extends over on the first 26 nodes for the distributed compliance model.

In the frequency range 0 to $3 \cdot n$, the system exhibits 12 eigen frequencies with one at $2.46 \cdot n$, which corresponds to the pressure fluctuation peaks measured at $2.5 \cdot n$. The corresponding mode shape exhibits 5 pressure maxima along the test rig. One is located in the draft tube elbow. A simulation of the test rig dynamic behavior using the distibuted mean compliance model and considering a sinusoidal excitation at the frequency of $2.46 \cdot n$ in the draft tube elbow provides the corresponding eigen mode shape, see figure 9.16 left and right. The amplitude of the excitation is optimized to fit the experimental pressure amplitudes in the draft tube elbow, leading to a pressure excitation source amplitude for the frequency $2.46 \cdot n$, equal to 0.5% of the reference energy E_{ref}. The pressure fluctuation profile in the draft tube at the frequency $2.46 \cdot n$ obtained by simulation presents a good agreement with measurements of figure 9.4. Moreover, pressure fluctuations at the turbine intake, element node 17, are found to correspond to a pressure maximum, which is in

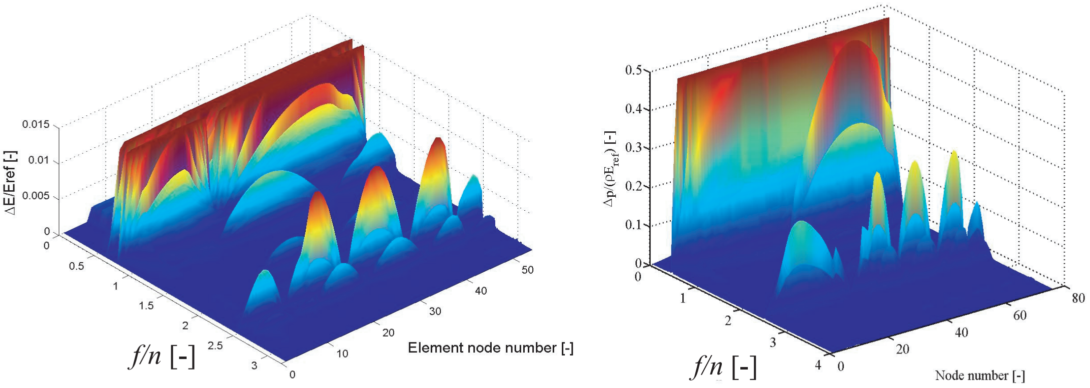

Figure 9.15: Frequency response of the test rig resulting from draft tube PRBS excitation with the distributed mean compliance (left) and distributed compliance model (right).

good agreement with the measurements too. Finally, one can notice the high amplitudes of discharge fluctuations in the draft tube cone, see figure 9.16 left, due to the vortex rope compliance.

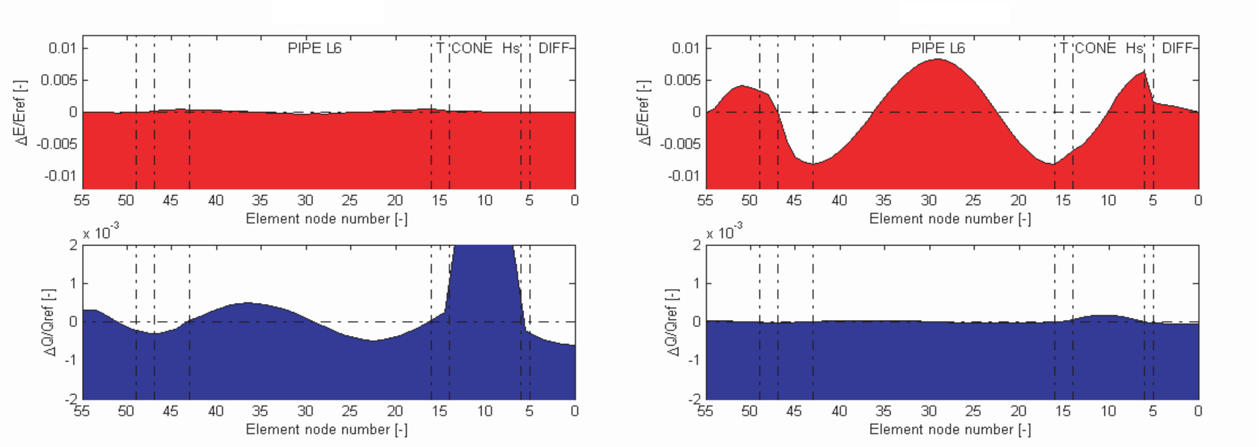

Figure 9.16: Eigen mode shape of the hydraulic system for $f/n = 2.46$ for $t = to$ (left) and for $t = to + T/4$ (right).

9.2.6 Forced Response Analysis of the Test Rig

The pressure excitation source identified experimentally, located in the draft tube elbow, is related to both the shock phenomenon and the vortex rope precession, see figure 9.18. Therefore, a forced excitation analysis simulation is performed, considering both synchronous pressure fluctuations and Dirac impulses at the frequency of the vortex rope. The synchronous excitation is considered for f_{rope} and the corresponding harmonics which are obtained experimentally by a decomposition procedure of the pressure fluctuations under cavitation free operating conditions as prescribed by Dörfler [41]. The pressure excitation source used for the simulation is presented in figure 9.17, and is expressed as follow:

$$\begin{aligned} H_s(t) = H_\delta \cdot \sum_{k=1}^{\infty} \delta(t - k \cdot \frac{1}{f_{rope}}) + H_{syn1} \cdot \sin(2 \cdot \pi \cdot f_{rope} \cdot t + \varphi_1)... \\ +H_{syn2} \cdot \sin(2 \cdot \pi \cdot (2 \cdot f_{rope}) \cdot t + \varphi_2)... \\ +H_{syn3} \cdot \sin(2 \cdot \pi \cdot (3 \cdot f_{rope}) \cdot t + \varphi_3) \end{aligned} \tag{9.6}$$

The amplitude of the Dirac term of the pressure source excitation is obtained by minimization procedure in order to obtain 0.5% of E_{ref} in the spectral decomposition of the excitation signal at the frequency of $2.46 \cdot n$. The amplitude of the Dirac impulses is found to be 5% of E_{ref} and the duration is found to be 1/18 of the vortex rope precession period, *i.e.* $T_{Dirac} = 0.0123\ s$. The pressure source imposed for the simulation is a difference of pressure between two pipes (and not a pressure specified at a node). The resulting pressure fluctuation spectra obtained for every element node are presented as a waterfall diagram, again for both the distributed mean compliance and the distributed compliance models in figure 9.19. One can notice, that even if the test rig presents several eigen frequencies in the frequency range 0 to $10 \cdot n$, the only significant pressure amplitudes correspond to $0.72 \cdot n$, $2.46 \cdot n$, $5 \cdot n$ and $7.5 \cdot n$, and are in good agreement with the measurements.

A comparison between simulation and measurement of pressure fluctuations resulting from forced excitation in the upper part of the cone using the distributed mean compliance model is presented in figure 9.20. The numerical simulations at the upper part of the cone show good agreement with the experimental values for the frequencies of interest, i. e. vortex rope precession and all the harmonics as well as eigen frequencies of the hydraulic system.

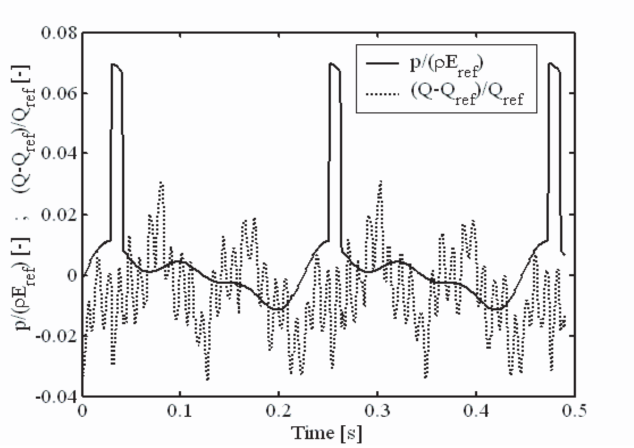

Figure 9.17: Time evolution of the pressure excitation imposed in the draft tube for the forced response analysis according to equation 9.6.

9.2.7 Vortex Rope Diameter Calculation

The evolution of the wave speed obtained experimentally, see figure 9.6, is compared to a theoretical value, that takes into account only pipe wall deformation and water

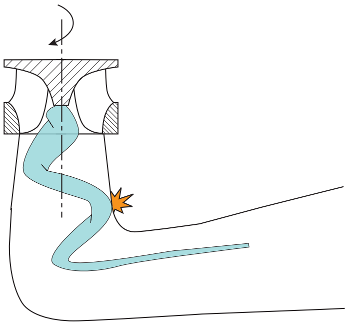

Figure 9.18: Vortex rope shock on the draft tube wall at inner elbow part.

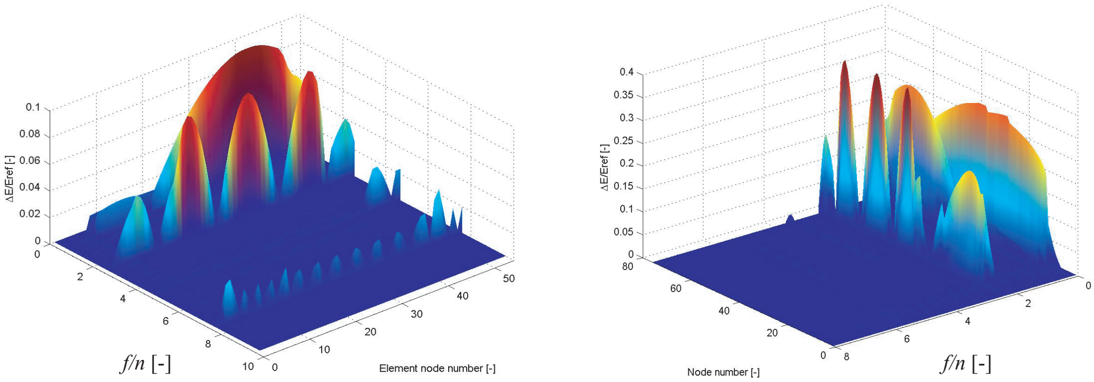

Figure 9.19: Waterfall diagram of pressure fluctuations obtained by forced response of the test rig resulting from draft tube forced excitation with the distributed mean compliance (left) and distributed compliance model (right).

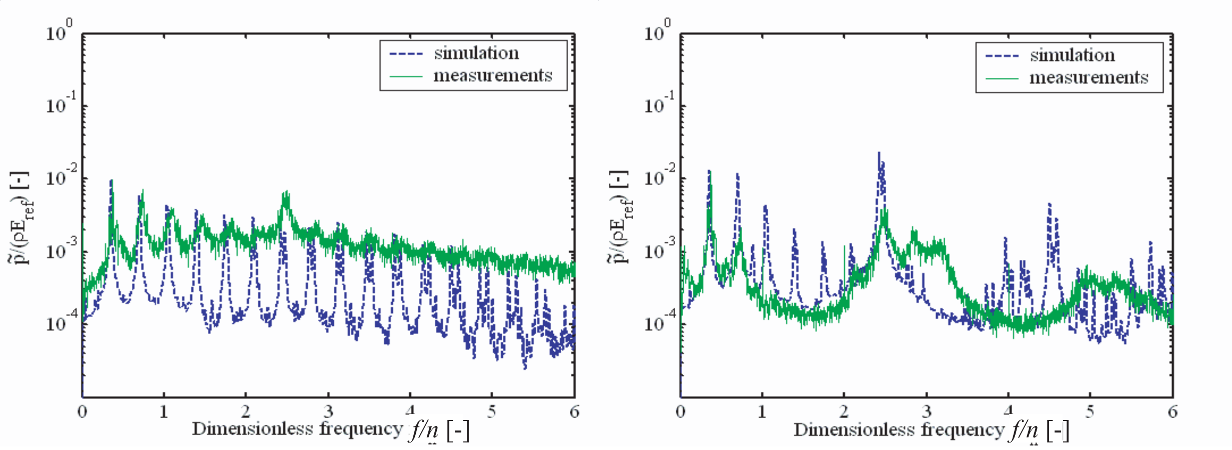

Figure 9.20: Comparison of simulated and measured pressure fluctuations at the pressure source (left) and upper cone (right).

compressibility, see figure 9.22. The wave speed accounting only for wall deformation and water compressibility is much higher than the measured wave speed, the difference between those 2 values being due to the vortex rope compliance. To properly model a draft tube cross section with vortex rope, the capacitive term of the electrical model must include the vortex rope compliance. Figure 9.21 presents the equivalent capacitance C_{equ} corresponding to 2 capacitances: (i) one for the wall deformation and the water compressibility, C_o, and (ii) one for the rope compliance, C_{rope}.

$$C_{equ} = C_o + C_{rope} \tag{9.7}$$

The capacitances are in a parallel scheme because the rope compressibility effects and the pipe wall plus the water compressibility effects are related to the same pressure field. The two discharges related to C_o and C_{rope} correspond to the discharge stored respectively by both effects. Introducing the expression of the capacitance of a pipe in equation 9.7 and assuming a barotrop behavior of the vapor volume gives [24]:

$$\frac{dx \cdot g \cdot A}{a_{equ}^2} = \frac{dx \cdot g \cdot A}{a_o^2} + \frac{V_{rope}}{H_{rope} \cdot \kappa} \tag{9.8}$$

Expressing the volume of vapor yields:

$$\frac{dx \cdot g \cdot A}{a_{equ}^2} = \frac{dx \cdot g \cdot A}{a_o^2} + \frac{dx \cdot A_{rope}}{H_{rope} \cdot \kappa} \tag{9.9}$$

Finally, the ratio between the vortex rope area and the draft tube cross section area is deduced:

$$\frac{A_{rope}}{A} = g \cdot H_{rope} \cdot \kappa \cdot \left(\frac{1}{a_{equ}^2} - \frac{1}{a_o^2} \right) \tag{9.10}$$

Where:

- A_{rope}: is the vortex rope cross section $[m^2]$;
- H_{rope}: is the head of the vapor inside the rope $[m]$; ($H_{rope} = 0.24$ m for T=20°C);
- κ: is the polytropic coefficient ($\kappa = 1.4$ for vapor).

One may notice, that, if the equivalent wave speed in the draft tube a_{equ} corresponds to the theoretical wave speed without vapor a_o, the vortex rope section is zero. Using the estimated and measured wave speeds in the draft tube and the vapor properties at $T = 20^\circ$ C given above, the diameter of the vortex rope is calculated along the draft tube curvilinear abscissa using equation 9.10 and presented in figure 9.22. The value of the rated rope diameter D_{rope}/D is found to be 9% in the cone, which presents good agreement with the rated diameter determined using 3D PIV on the same turbine scale model by Illiescu [76], and also found to be 9% for the same operating conditions. So it means that knowing the rope diameter for a given operating point allows estimating the wave speed in the draft tube cone for cavitating conditions.

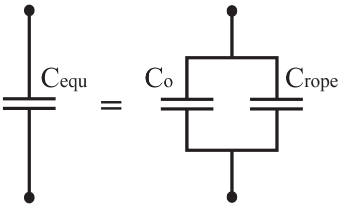

Figure 9.21: Equivalent capacitance accounting for both cavitating vortex rope compliance and pipe compliance.

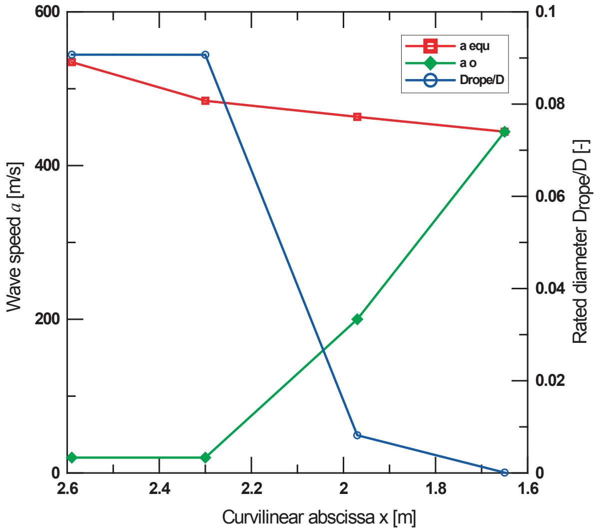

Figure 9.22: Representation of the calculated wave speed without cavitation (a_o), the equivalent wave speed from measurement (a_{equ}) and deduced rated vortex rope diameter (D_{rope}/D) as function of curvilinear abscissa of the draft tube x.

9.2.8 Concluding Remarks on the Modelling of Upper part Load Pressure Fluctuations

This case study presents the analysis of the origin of the pressure fluctuations measured in the elbow draft tube of a Francis turbine scale model for low discharge operation. A component of pressure fluctuation at $2.5 \cdot n$ frequency is identified all along the draft tube walls, the source of those pressure fluctuations being located at the inner part of the draft tube elbow. The energy of the pressure source extends over a wide frequency range and results from the impact of the vortex rope on the draft tube wall at this location. The analysis of the pressure fluctuations phases for the $2.5 \cdot n$ frequency provides a way to determine experimentally the wave speed along the draft tube, which is the key parameter for a numerical simulation of the hydroacoustic behavior of the test rig. The simulation carried out for the full test rig, taking into account piping, circulating pumps and the scale turbine model with the elbow draft tube shows that the $2.5 \cdot n$ frequency value corresponds to an eigen frequency of the system. Therefore, a model of the excitation source is synthesized as a forcing function made of the superposition of the dominant components of the rope precession signal and a series of Dirac pressure impulses at the vortex rope frequency. The forced system response reveals predominant amplitudes at the $2.5 \cdot n$ eigen frequency, in agreement with the excitation mechanism model.

9.3 High Speed Visualization of the Upper Part Load Vortex Rope

9.3.1 General Remarks

In the framework of the FLINDT project, the operating point investigated previously is very particular as it is a case of resonance between the vortex rope and the test rig. Moreover, it was noticed that the 7^{th} harmonic of the vortex rope precession matches an eigen frequency of the test rig under the chosen operating conditions. Unfortunately no investigations on the influence of the rotational speed, *i.e.* the Froude number, or of the cavitation number σ where performed. Thus, new investigations on upper part load pressure fluctuations performed by Koutnik *et al.* in 2006 [94] have pointed out the influence of these 2 parameters noticing that upper part load pressure fluctuations can also occur even if the predominant amplitudes are not found at a frequency being a multiple of the vortex rope precession. Therefore, the origin of these pressure fluctuations cannot only be induced by the shock phenomenon. In addition, the physical modulation process was identified by Koutnik *et al.* [94] to be related to the elliptical shape of the vortex rope cross section observed on test rig at upper part load. The motion of the elliptical vortex rope at upper part load that can be decomposed in precession movement with pulsation ω_{rope} and the self rotation of the rope with pulsation $\omega*$ as it is illustrated in figure 9.23.

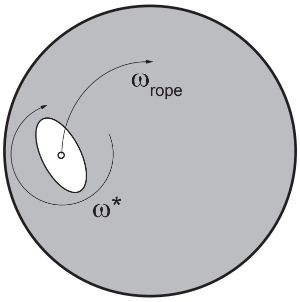

Figure 9.23: Elliptical vortex rope precessing in the draft tube cone at upper part load.

Thus, other investigations have been carried out on a Francis turbine similar to the FLINDT Francis turbine, $\nu = 0.5$ instead of $\nu = 0.56$, to clarify by experiments the role of rotational speed and of the cavitation number on the upper part load vortex rope. The investigations have been undertaken by means of both: (i) vortex rope visualization using high speed camera; (ii) simultaneous pressure fluctuations records.

9.3.2 Case Study Definition

The waterfall diagram of the wall pressure fluctuations measured at the downstream cone of the draft tube of the Francis turbine of $\nu = 0.5$ investigated here is presented in figure 9.24 as function of the discharge coefficient φ/φ_{BEP}. This diagram points out upper part load pressure pulsations in the range of 1 to 3 times the rotational speed for a rated discharge coefficient around 0.8. The operating point of table 9.3 is chosen for investigating: (i) the influence of the cavitation number σ; (ii) the influence of the Froude number Fr.

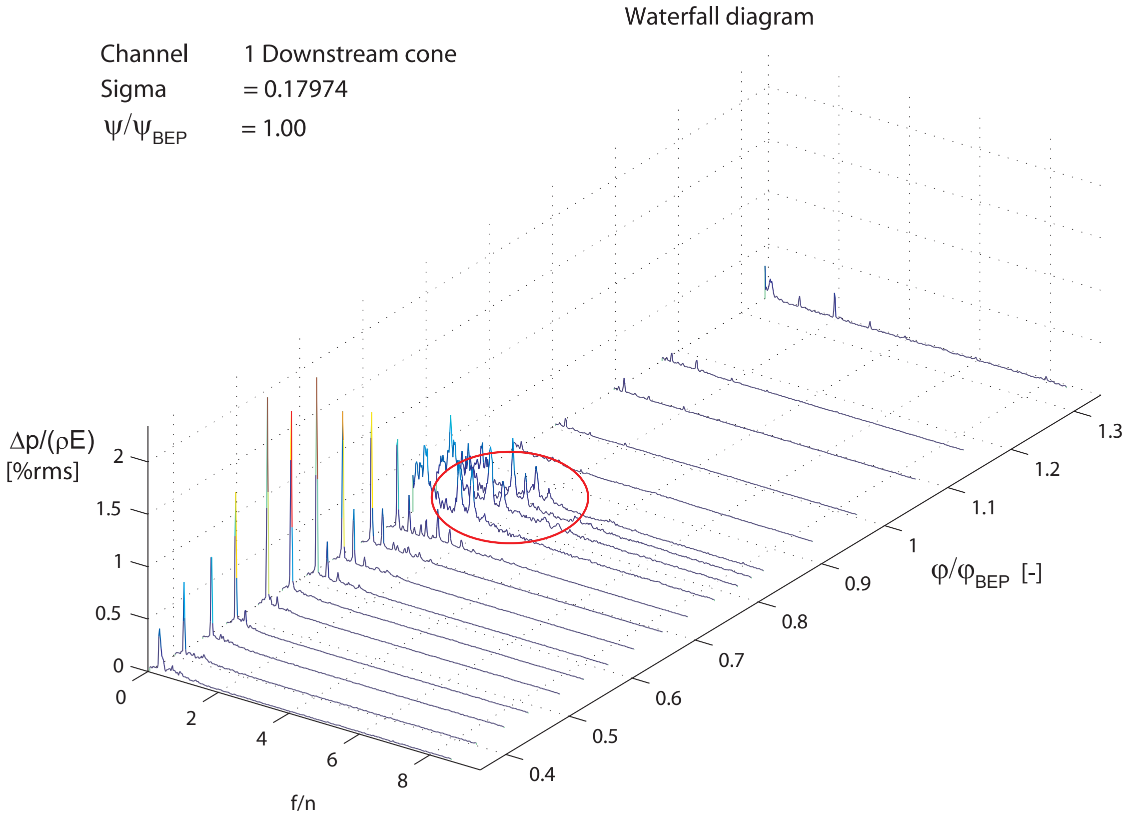

Figure 9.24: Waterfall diagram of the pressure fluctuations measured at the downstream cone of the draft tube for $\psi/\psi_{BEP} = 1$ and $\sigma = 0.18$.

Table 9.3: Parameter of the scale model Francis turbine and investigated operating point.

Specific speed ν $[-]$	φ/φ_{BEP} $[-]$	ψ/ψ_{BEP} $[-]$	**N** $[rpm]$	**Guide Vane Opening** $[^\circ]$
0.50	0.832	1.00	700	21.5°

9.3.3 Experimental Apparatus

To perform the visualization of the vortex rope, a high speed camera Photron is used. The frame rate used for the investigation is 4000 frames/seconds using a diaphragm aperture time of 1/4000 s and a number of 3600 frames per movie. The images are obtained with a resolution of 1024 × 512 pixels. The lighting is ensured by 2 continuous spot lights of 600 W each located at 45° of each side of the high speed camera as illustrated in figure 9.25. The Francis turbine scale model is also equipped with 3 wall Quartz pressure transducers Kistler 701A measuring the unsteady part of the pressure. The synchronization between the pressure acquisition and the image records is ensured by the trigger of the oscilloscope as illustrated in figure 9.26. The oscilloscope LeCroy is also used to store a 1 second time history pressure signal with a sampling rate of 12.5 kHz. In parallel, the pressure is also recorded using an HP 3566A PC Spectrum/Network Analyser system but without synchronization with the camera. These measurements are used for the representation of the waterfall diagram of the pressure fluctuations obtained by the averaging of 8 pressure amplitude spectrums based on a 4 seconds pressure time history with a sampling rate of 256 Hz.

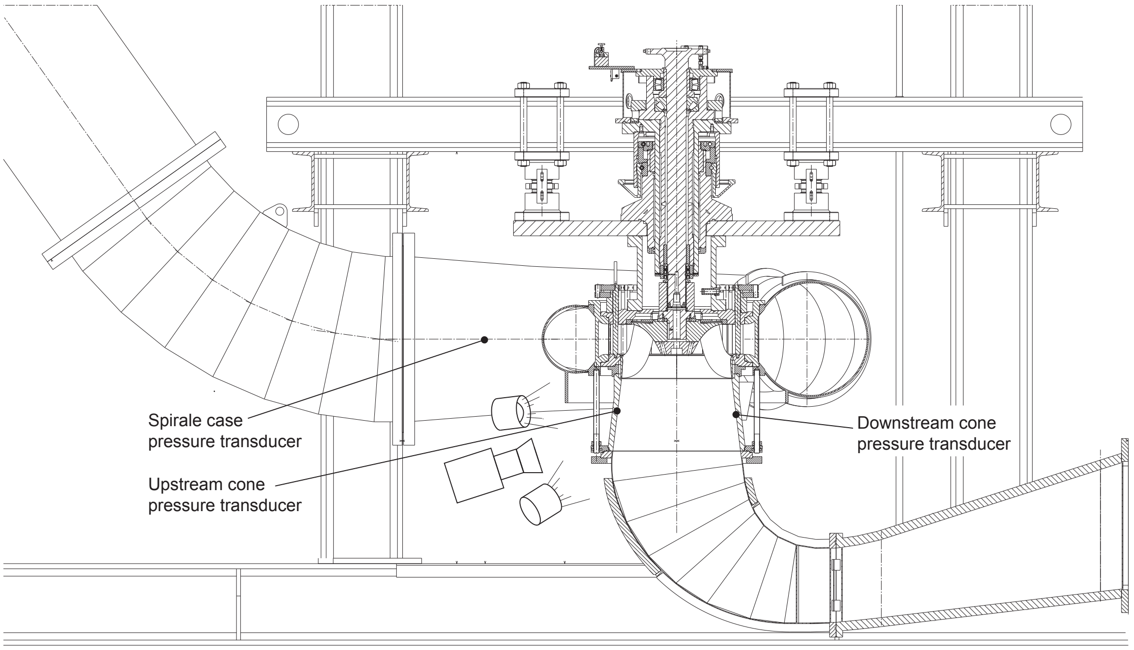

Figure 9.25: Scale model installed on the test rig for high speed camera visualization.

9.3.4 Results

Influence of the Cavitation Number

The operating conditions selected for the investigation of the influence of cavitation correspond to the upper part load pressure fluctuations and are summarized in table 9.3. For this operating condition, 6 different cavitation numbers are tested in the range of $\sigma = 0.1$ to 0.3; the Froude number being kept constant. The operating parameters as well as the observation remarks are reported in the table 9.4. The waterfall diagrams of the pressure fluctuations at the upstream cone, downstream cone and spiral case measured for the tests number 1 to 6 are presented in figure 9.27.

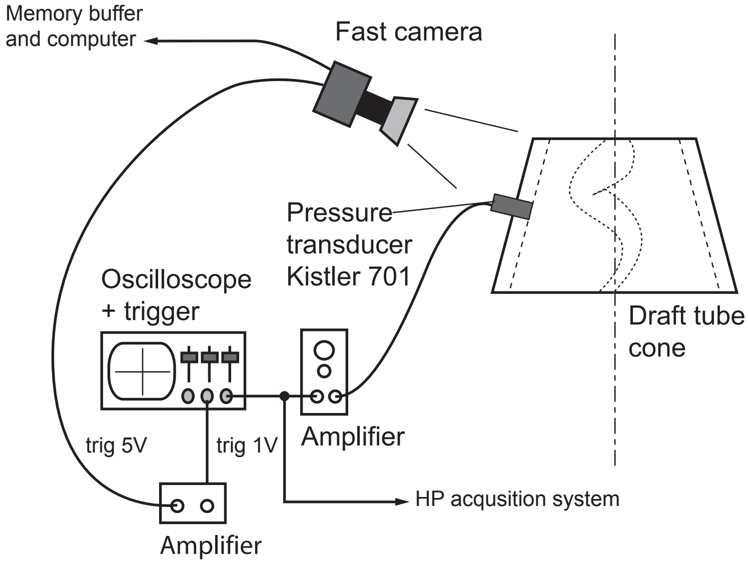

Figure 9.26: Synoptic scheme of the acquisition system.

Similarly to the FLINDT case, the frequency of the pressure fluctuations in the range of 1 to 3 times the rotational speed increases with the cavitation number. The frequencies and amplitudes of these pressure pulsations are reported in figure 9.28. It can be noticed that frequency increases almost linearly with the cavitation while the amplitude of the pressure pulsations rises quickly up to 2.5% of the specific energy E for $\sigma = 0.3$. The amplitudes of pressure pulsations for this cavitation number are similar for the 3 pressure transducers. In addition, strong mechanical vibrations and noise were noticed during the measurements. The shock phenomenon was also strongly present for these operating conditions. This operating point corresponds again to the resonance between the vortex rope and the test rig.

The figure 9.29 depicts the elliptical shape of the vortex rope self rotating at the pulsation ω^* and precessing with a pulsation ω_{rope} for the resonance operating conditions, *i.e.* $\sigma = 0.3$. For the 6 operating points investigated here, the pictures resulting from the movie records of the vortex rope with synchronized pressure records are reported in figures 9.30 to 9.35. For each operating point, 5 successive pictures are extracted from the movie and correspond to one period of the pressure fluctuations of interest $T*$; *i.e.* from $t = to$ to $t = to + T*$. The influence of the pressure on the dimensions of the vortex rope appears clearly, as for $t = to$, when the pressure is high, the vortex rope features small diameter while the diameter is the highest for $t = to + T*/2$ when the pressure is the lower. This pressure dependence is identical for the 6 operating points. It can be noticed that, as expected, the mean diameter of the vortex rope increases as the cavitation number σ decreases. But for small values of cavitation number, the pressure amplitudes becomes smaller, even if locally they can be biggerlarger. This phenomenon can be correlated with the apparition of cavitation at the trailing edge of the runner blades. This cavitation is visible on the pictures but also on the pressure time history where very high frequency is visible, see figures 9.34 and 9.35. So it means that the higher

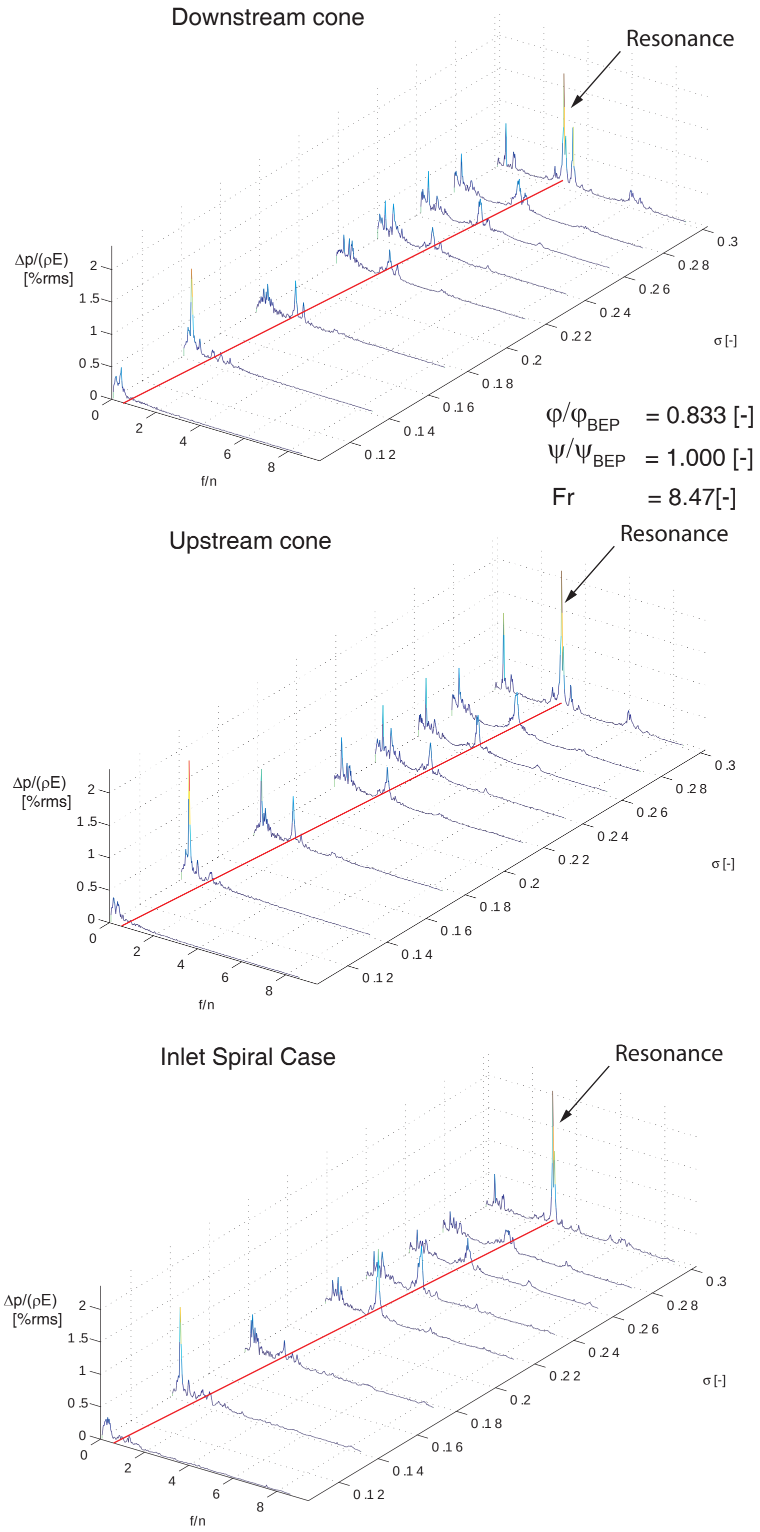

Figure 9.27: Waterfall diagram of the pressure fluctuations measured at the spiral case, upstream and downstream cone as function of the frequency and cavitation number for $\psi/\psi_{BEP} = 1$, $\varphi/\varphi_{BEP} = 0.833$ and $Fr = 8.47$.

Table 9.4: Operating parameters for the influence of the cavitation number.

N°	σ $[-]$	**Froude** $[-]$	**N** $[rpm]$	**Remarks**
1	0.30	8.47	700	Hydroacoustic resonance, strong vortex rope shock on draft tube wall and mechanical vibrations
2	0.26	8.47	700	Random hydroacoustic resonance vortex rope shock on draft tube wall and mechanical vibrations
3	0.22	8.47	700	
4	0.18	8.47	700	
5	0.14	8.47	700	Low inter-blade cavitation development
6	0.10	8.47	700	Strong inter-blade cavitation development

content of cavitation bubbles and development in the runner outlet and draft tube helps to mitigate the pressure pulsations appearing in the range of 1 to 3 times the rotational speed. This result can be therefore also obtained by air injection in the flow. As illustrated in figure 9.36 where the cavitation number is $\sigma = 0.18$ with air injection but the pressure pulsations present in figure 9.33 almost vanished.

The pictures of the vortex rope for the 6 operating points considered, feature the expected elliptical cross section of the vortex rope. When the cavitation number is the lowest, *i.e.* for $\sigma = 0.14$ and 0.1, see figure 9.34 and 9.35, the elliptical cross section is evidenced by 2 vortex ropes rotating in the same directions. The scheme of figure 9.37 depicts the complex structure of the vortex rope which under these conditions presents small vortices attached to the runner nose and rotating on themselves at the pulsation ω_2, while 2 vortex ropes rotating on themselves at a pulsation ω_1 constitute the main body of the rope self rotating at the pulsation $\omega*$ and the rope being animated of the precession pulsation ω_{rope}. By Analyzing the pictures of figures 9.30 to 9.35 it is found in accordance with Koutnik *et al.* [94], that the pulsation of the self rotation of the elliptical vortex rope $\omega*$ is half the pulsation of the measured pressure fluctuations. Therefore, the combination between the rope precession ω_{rope} and the self rotation of the rope ω_1 leads to the modulation process already described by Arpe in 2003 on FLINDT [6]. The elliptical shape of the vortex rope make apparent the non-uniformity of the pressure distribution in the cross section of the cone. Consequently, if the elliptical vortex rope rotates with the pulsation $\omega*$, the associated pressure fluctuation features a pulsation of $\omega = 2 \cdot \omega*$, as illustrated in figure 9.39.

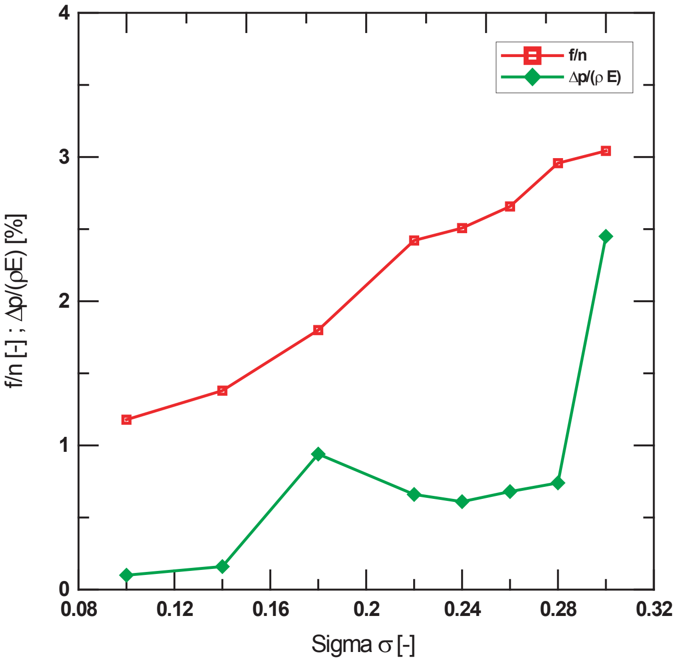

Figure 9.28: Evolution of the frequency and amplitude of the pressure pulsations as function of the cavitation number for $\psi/\psi_{BEP} = 1$, $\varphi/\varphi_{BEP} = 0.833$ and $Fr = 8.47$ at the downstream cone.

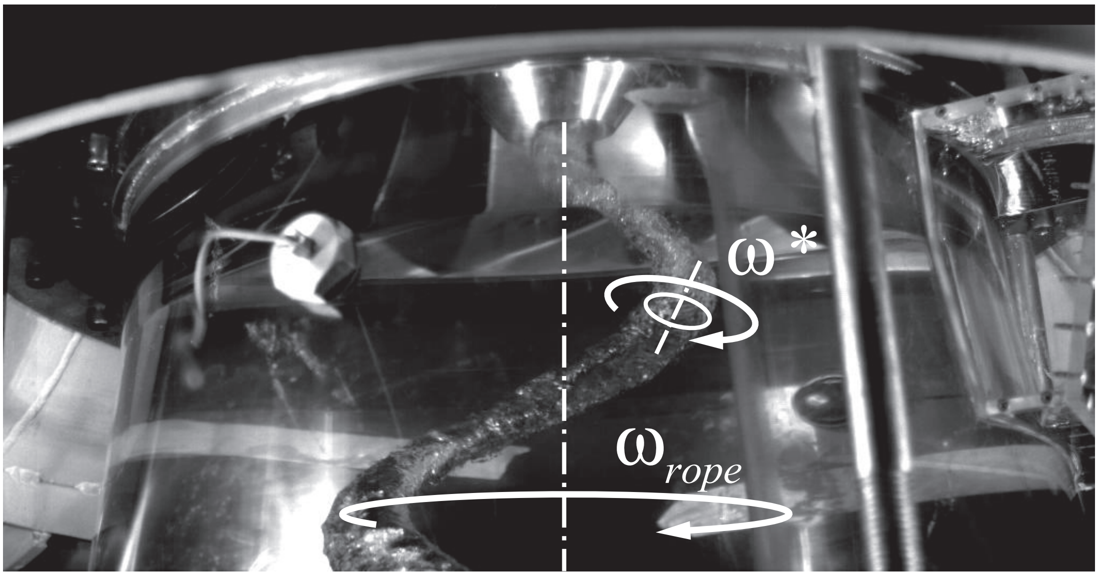

Figure 9.29: Vortex rope precession at ω_{rope} and self rotating at ω^* for operating point N°1: $\sigma = 0.30, Fr = 8.47$.

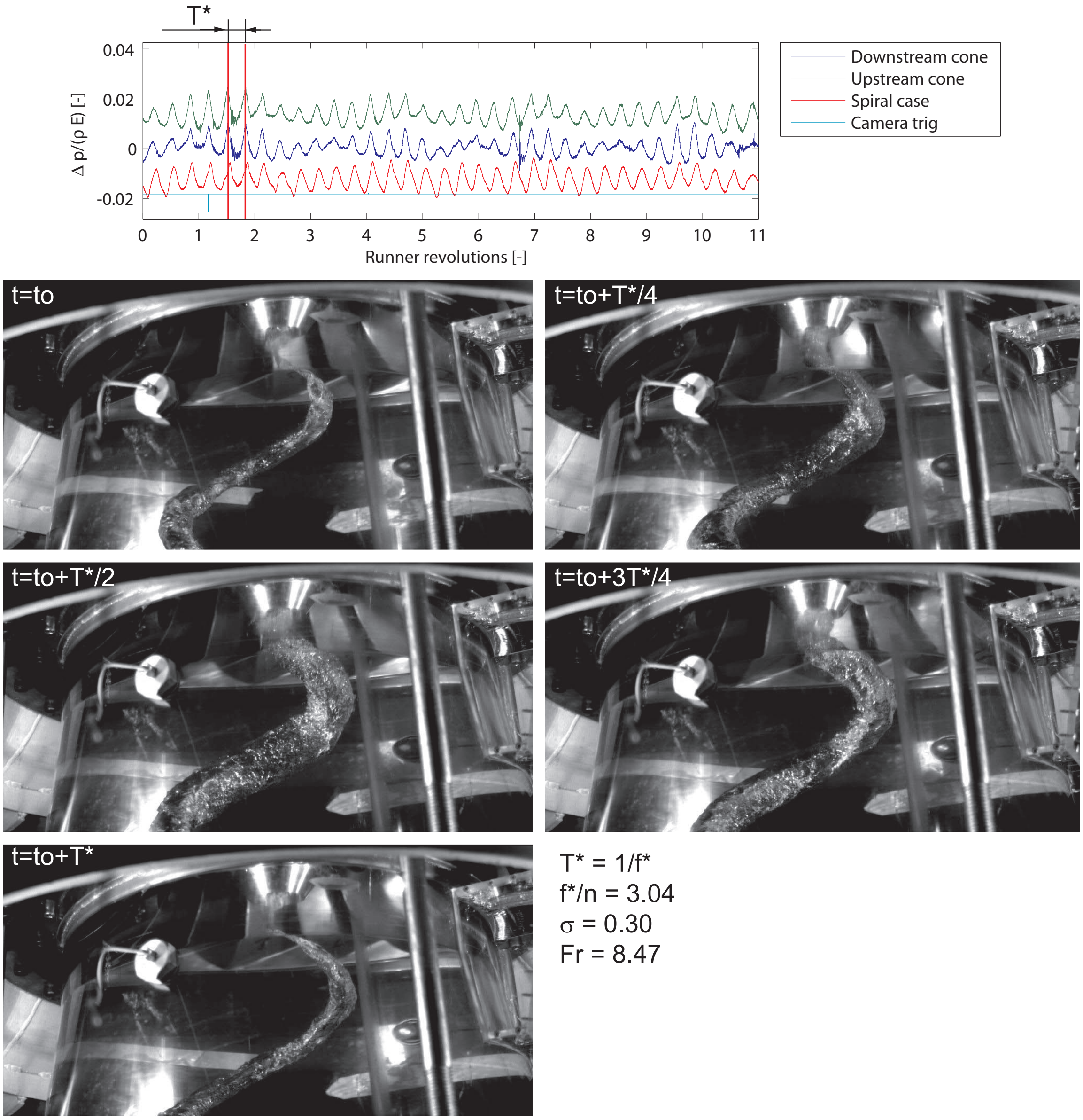

Figure 9.30: Vortex rope development for operating point N°1: $\sigma = 0.30, Fr = 8.47$.

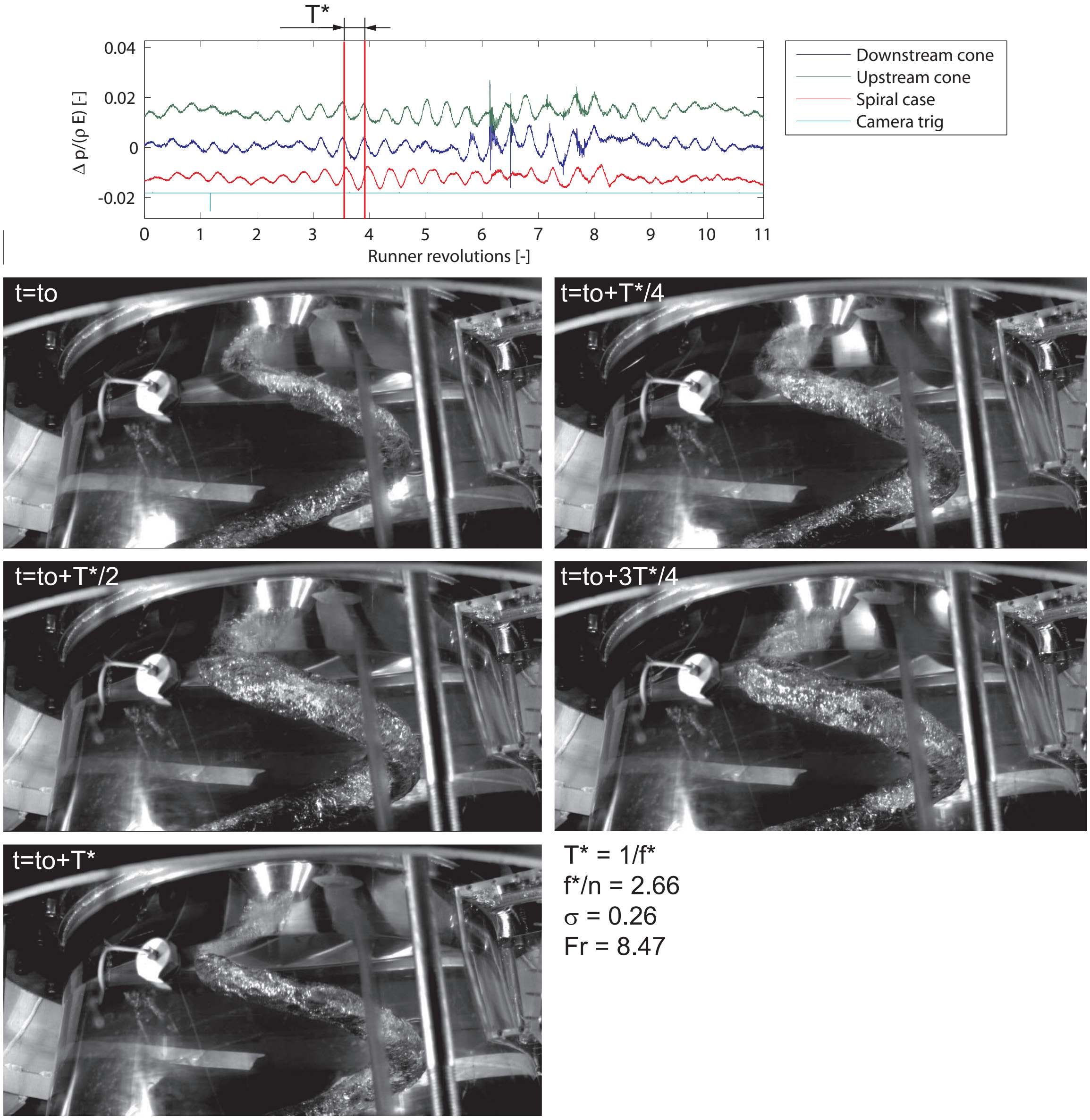

T* = 1/f*
f*/n = 2.66
σ = 0.26
Fr = 8.47

Figure 9.31: Vortex rope development for operating point N°2: $\sigma = 0.26, Fr = 8.47$.

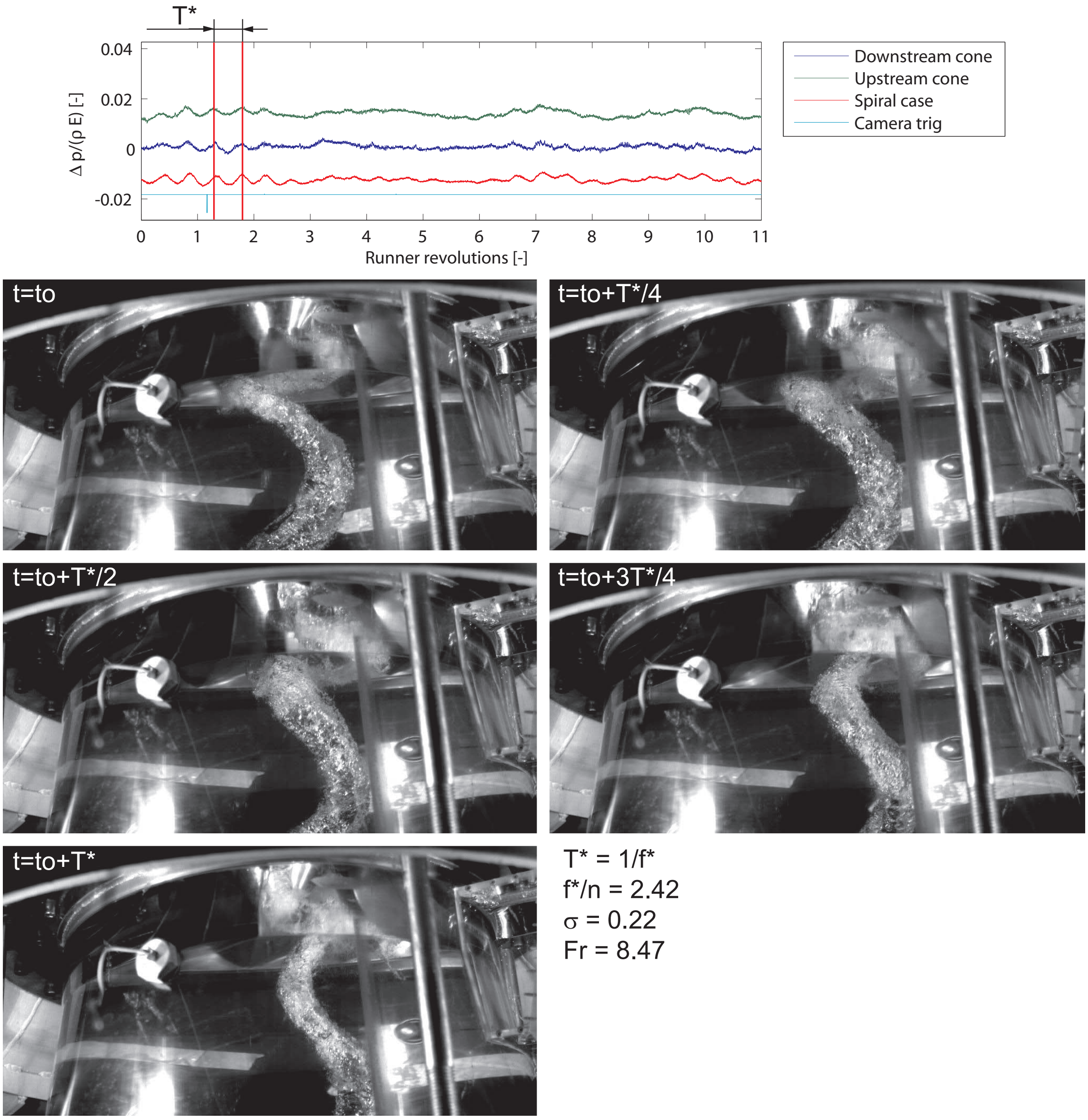

T* = 1/f*
f*/n = 2.42
σ = 0.22
Fr = 8.47

Figure 9.32: Vortex rope development for operating point N°3: $\sigma = 0.22, Fr = 8.47$.

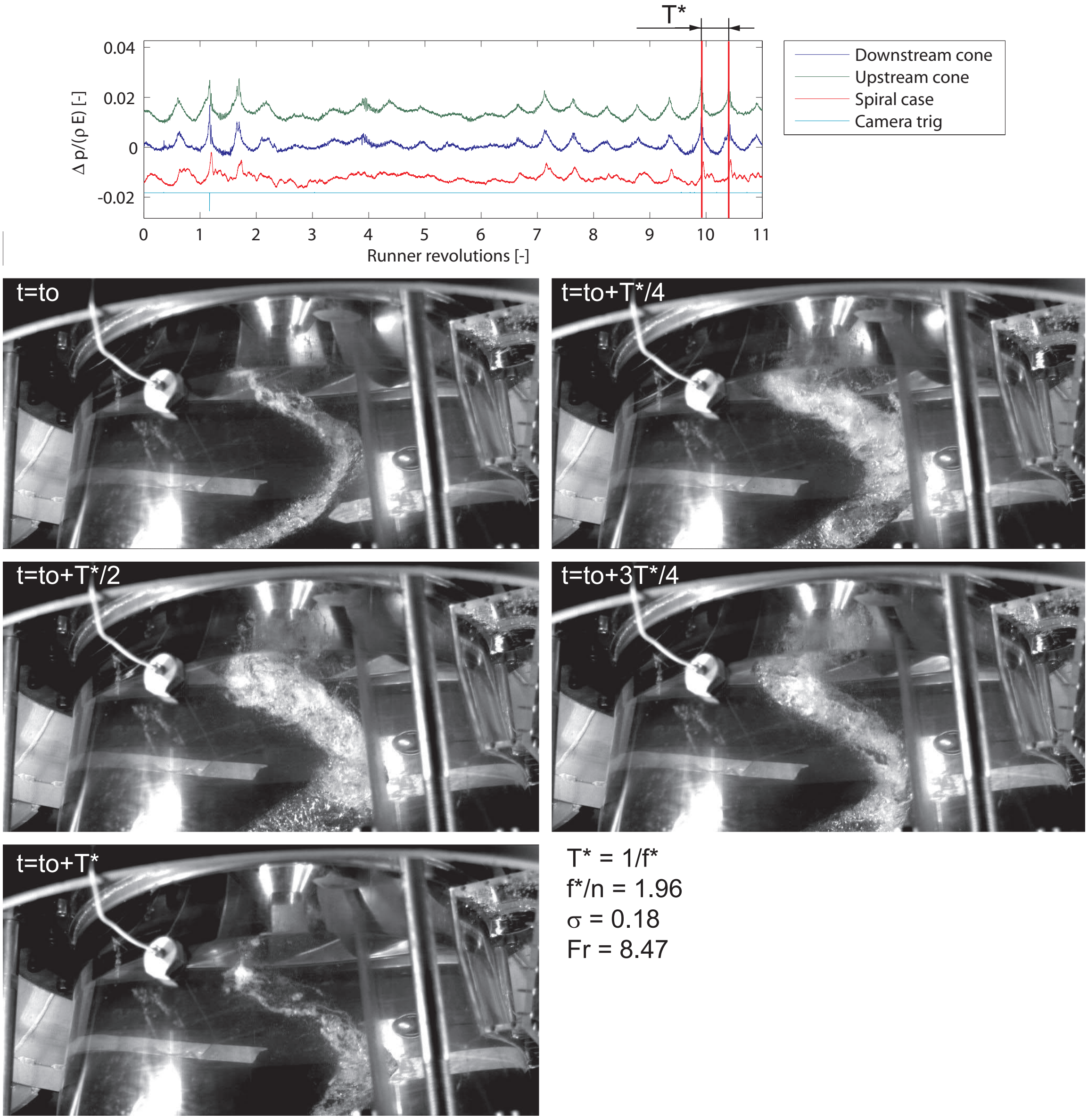

Figure 9.33: Vortex rope development for operating point N°4: $\sigma = 0.18, Fr = 8.47$.

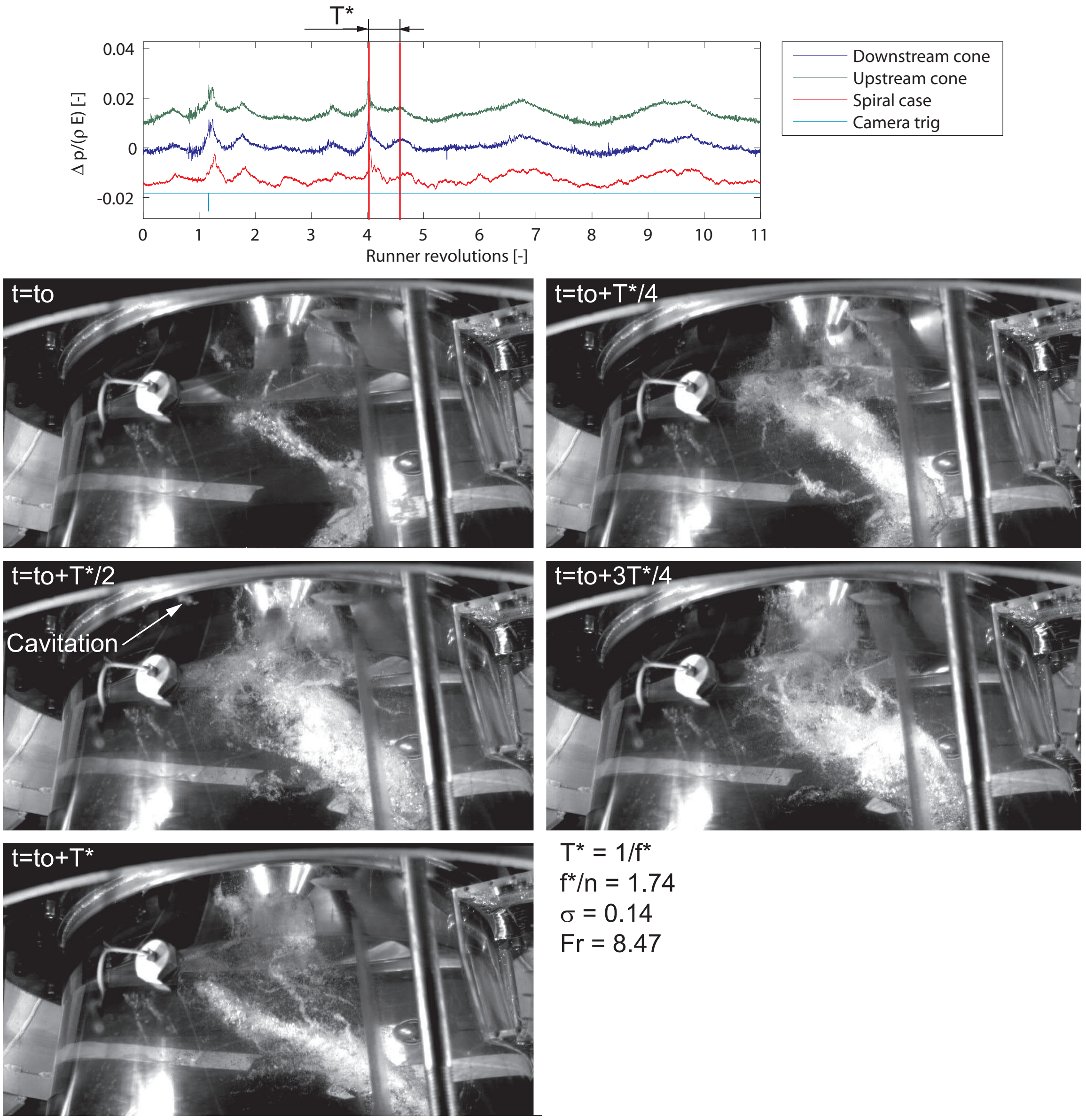

T* = 1/f*
f*/n = 1.74
σ = 0.14
Fr = 8.47

Figure 9.34: Vortex rope development for operating point N°5: $\sigma = 0.14, Fr = 8.47$.

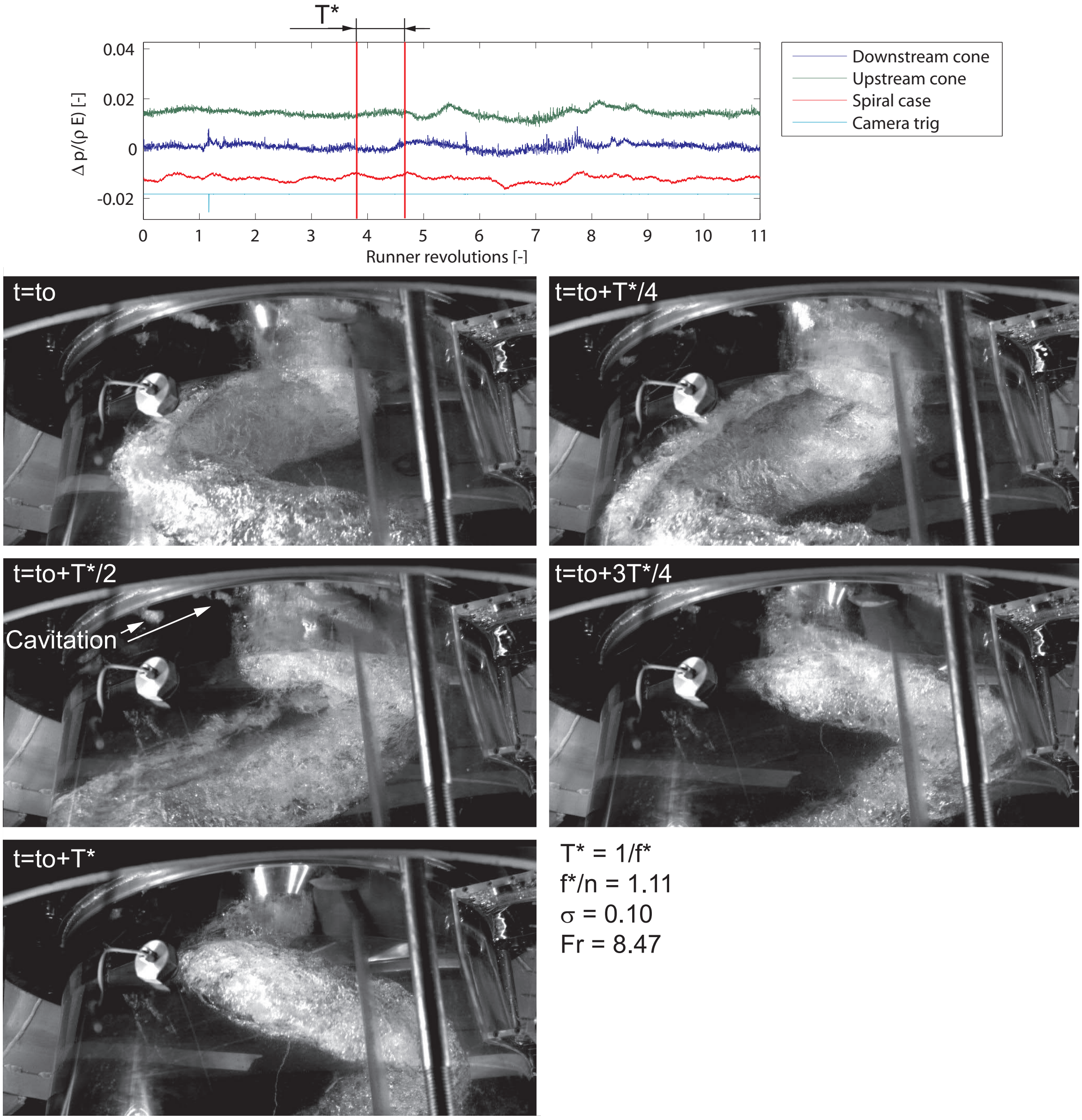

Figure 9.35: Vortex rope development for operating point N°6: $\sigma = 0.10, Fr = 8.47$.

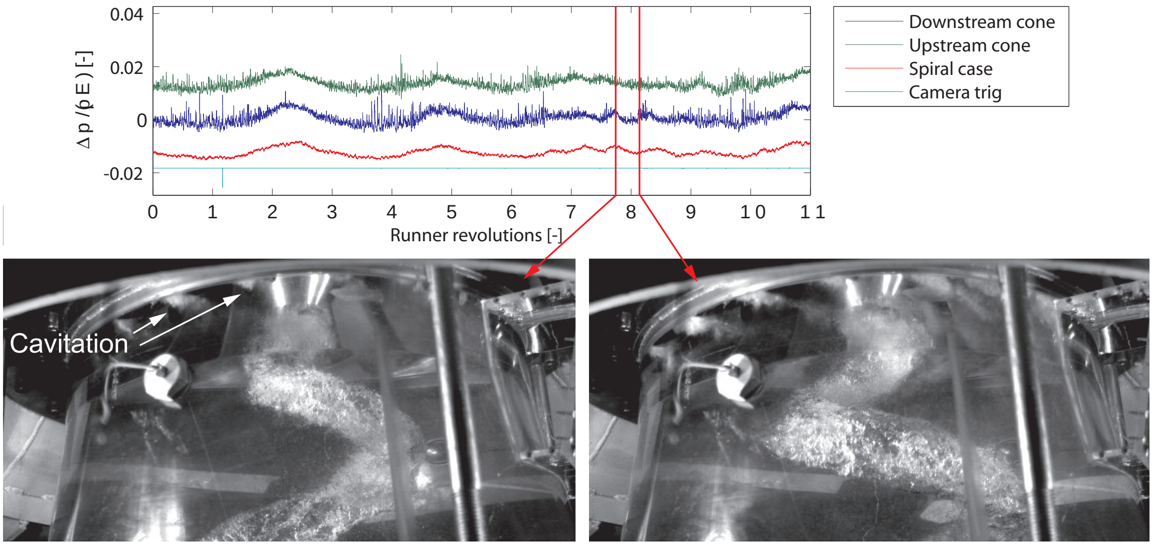

Figure 9.36: Vortex rope development for operating point N°4 **with air injection**: $\sigma = 0.18, Fr = 8.47$.

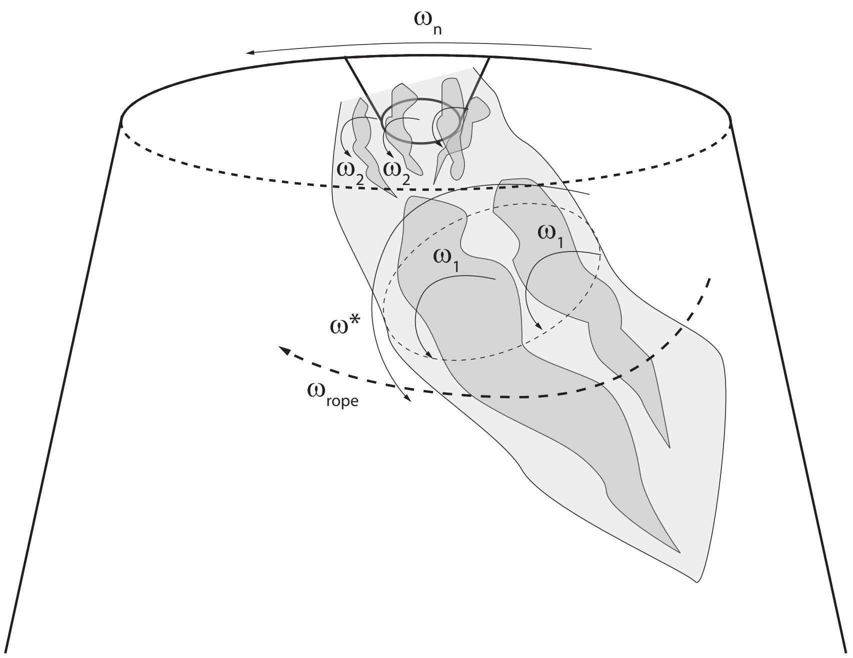

Figure 9.37: Vortex rope development for operating point N°5: $\sigma = 0.14, Fr = 8.47$.

Influence of the Froude Number

The operating conditions chosen for the investigation of the influence of the Froude number are identical as the previous point in terms of discharge coefficient and specific energy coefficient given in table 9.3, but the cavitation number is kept constant and equal to $\sigma = 0.30$ in order to focus on the conditions of resonance of the test rig. For these investigations 4 different values of the Froude number are taken into account and are obtained by varying the rotational speed of the turbine. The Froude number is given by $Fr = C_{ref}/\sqrt{g \cdot L_{ref}}$ that can be also be expressed, taking the reference velocity as $C_{ref} = \sqrt{E}$, as follows:

$$Fr = \sqrt{\frac{H}{L_{ref}}} \tag{9.11}$$

The Froude number affects the distribution of cavitation in the flow as it determines the pressure gradient relatively to the size of the machine. The relation between the position of the vapor pressure p_v can be expressed as a function of the Froude number, see [56], neglecting Reynolds effects, assuming the same cavitation number σ as a function of the reference position Z_{ref} as follows:

$$\frac{Z_{ref} - Z_1}{Z_{ref} - Z_2} = \frac{Fr_1^2}{Fr_2^2} \tag{9.12}$$

The Froude number being usually smaller on prototype than in the model, the elevation of the position of the cavitation is higher on prototype than in the model, [56], [80]. Due to the difference of Froude numbers, the vortex rope on scale model is more narrow and longer than on prototype [41], as illustrated in figure 9.38.

The selected values of operating conditions as well as observations remarks are given in the table 9.5. The waterfall diagram of the wall pressure pulsations measured at the downstream cone, upstream cone and spiral case are presented as function of the frequency and Froude number in figure 9.40.

Table 9.5: Operating conditions for the influence of the cavitation number.

N°	σ $[-]$	**Froude** $[-]$	**N** $[rpm]$	**Remarks**
1	0.30	8.47	700	Hydroacoustic resonance and mechanical vibrations
7	0.30	7.86	650	Hydroacoustic resonance and mechanical vibrations
8	0.30	7.26	600	Low hydroacoustic resonance and mechanical vibrations
9	0.30	6.64	550	Low hydroacoustic resonance and mechanical vibrations

First, it can be noticed from the observations of table 9.5 that hydroacoustic resonance and mechanical vibrations are observed for all tested conditions, even if the level

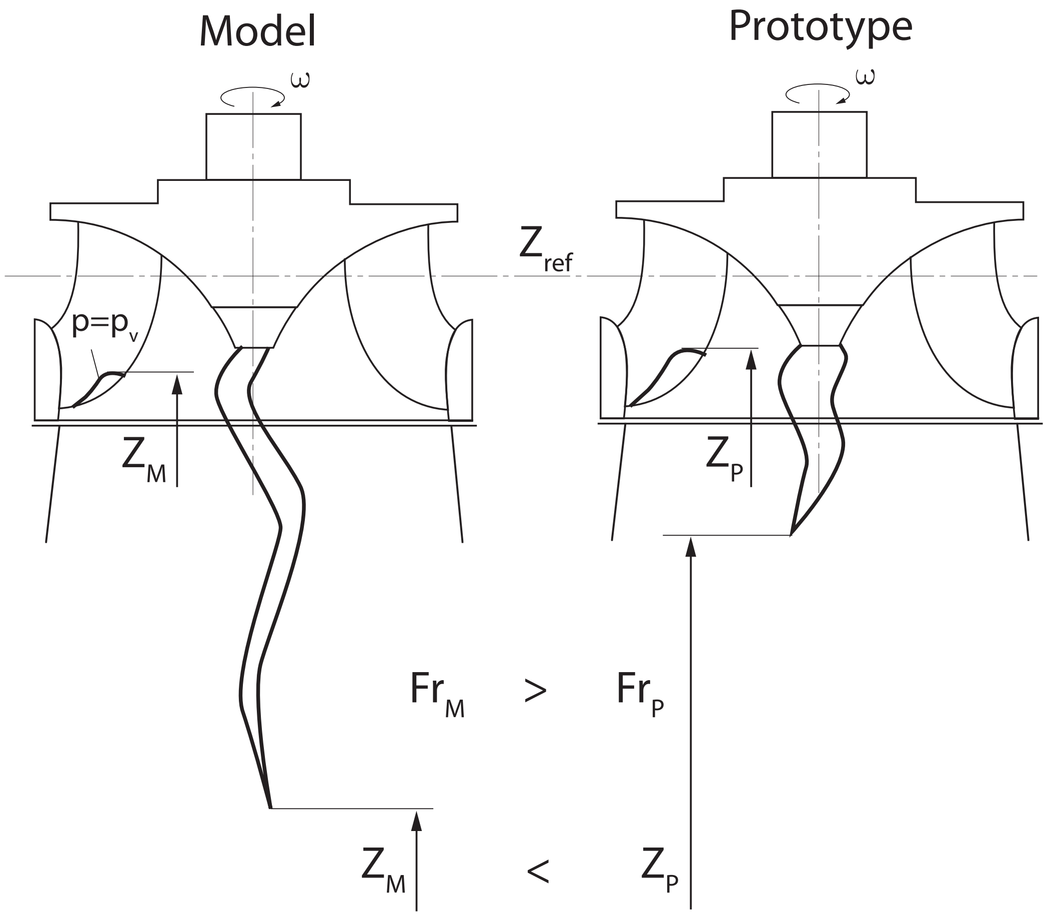

Figure 9.38: Difference of the cavitation development between model (M) and prototype (P) due to difference in Froude numbers.

of resonance and related vibration was lower for lower values of the Froude number. This is due to the fact that increasing the Froude number leads to a reduction of the specific energy and therefore of the absolute magnitude of the pressure fluctuations. However, as it is reported by the waterfall diagram of figure 9.40, the relative amplitudes of pressure fluctuations are not affected in the same way. The figure 9.41 represents the amplitude and frequency of the pressure pulsations of interest as function of the Froude number. It can be noticed that the frequency of the pressure pulsations are proportional to the runner rotational speed, in accordance with to Koutnik [94], and that the amplitudes are of the same order of magnitude for the values of Froude equal to $Fr = 8.47$ and 7.86, while they are divided at least by a factor 2 for $Fr = 7.26$ and 6.64. The reason for this difference is pointed out by the representation of one of the eight time histories used for the calculation of the amplitude spectrum for each Froude number value as presented in figure 9.42. It can be seen from the time history of the pressure, that the resonance phenomenon features more random behavior for $Fr = 7.26$ and 6.64 than for $Fr = 8.47$ and 7.86. Consequently the values obtained in the waterfall diagram are smaller for the higher values of Froude number.

No visualizations of the vortex rope are presented here as the shape of the vortex rope was not very much affected by the Froude number, at least in the range of tested Froude values, and therefore does not affect significantly the wave speed in the draft tube. It means that the eigen frequencies of the test rig, including the turbine and the draft tube, are not strongly affected by the change of the Froude number in the tested range. Then changing the rotational speed of the runner results in a mistuning between the excitation source, illustrated by the vortex rope self rotation, with the pulsation $\omega *$, and the eigen frequency of the test rig. It results in a situation where there is no more strict resonance but random resonance as it is the case for the same Froude but lower cavitation number; for example $\sigma = 0.18$. This means that the observed phenomenon is really of the resonance type and not of the self excited type. Similar conclusions have been found by Koutnik *et al.* [94] who found a small part of self excitation observing the pressure vs rope volume dependence.

Regarding the modulation process between the vortex rope precession and the self rotation of the vortex rope, f_{rope} and $f*$ respectively, is very well illustrated by the amplitude spectra measured for $Fr = 7.86$. Therefore, the time plots and related amplitude spectra are represented in figure 9.43 where it can be clearly seen that modulation between the two dominant pulsations leads to amplitudes in the spectrum for $f = f * \pm f_{rope}, f * \pm 2 \cdot f_{rope}, f * \pm 3 \cdot f_{rope}$,etc and also for $f = 2 \cdot f * \pm f_{rope}, f * \pm 2 \cdot f_{rope}, f * \pm 3 \cdot f_{rope}$,etc.

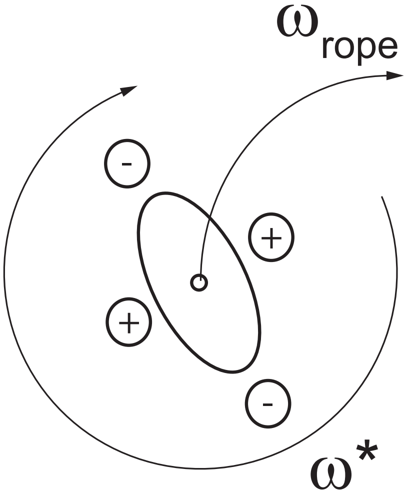

Figure 9.39: Elliptical vortex rope with related pressure distribution rotating with the pulsation $\omega *$.

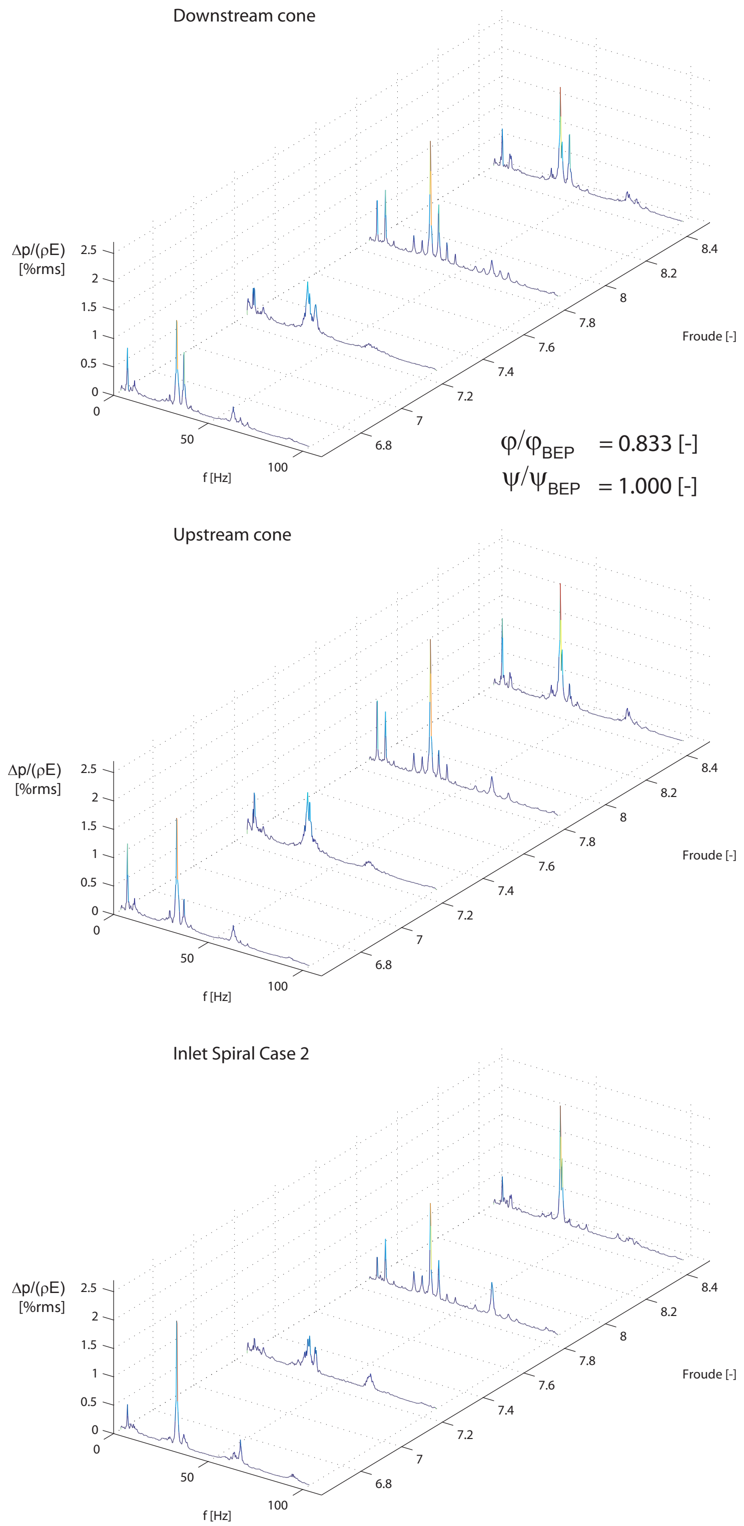

Figure 9.40: Waterfall diagram of the pressure fluctuations at the spiral case, upstream and downstream cone as function of the frequency and Froude number $\psi/\psi_{BEP} = 1$, $\varphi/\varphi_{BEP} = 0.833$ and $\sigma = 0.3$.

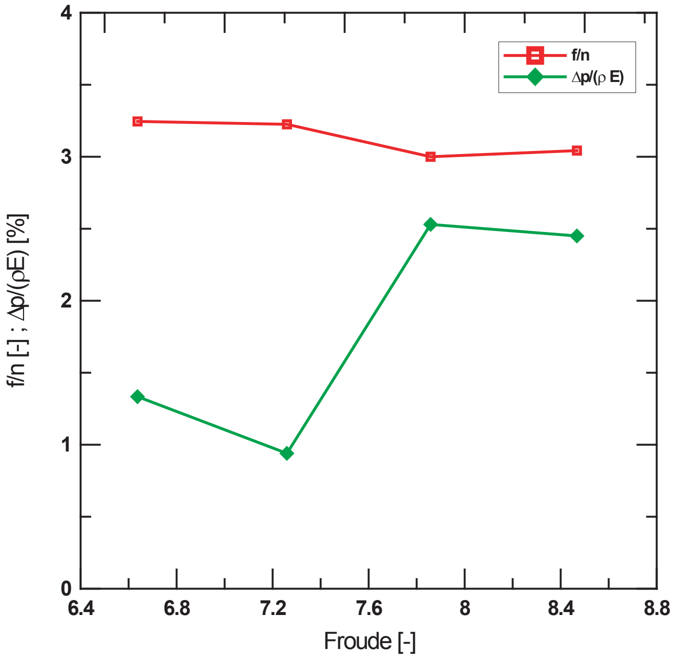

Figure 9.41: Evolution of the frequency and amplitude of the pressure pulsations as function of the Froude number for $\psi/\psi_{BEP} = 1$, $\varphi/\varphi_{BEP} = 0.833$ and $\sigma = 0.3$ at the downstream cone.

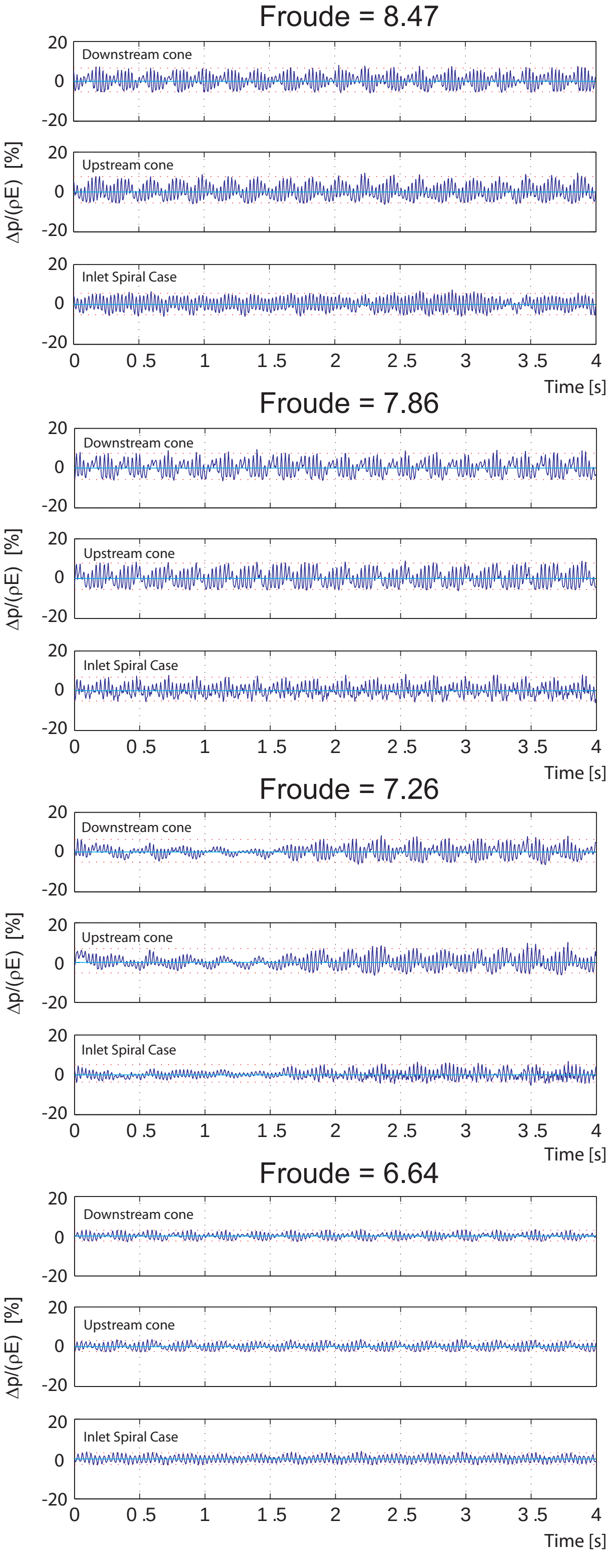
Froude = 8.47

Froude = 7.86

Froude = 7.26

Froude = 6.64

Figure 9.42: Time history of the pressure pulsations at the spiral case, upstream and downstream cone for different Froude values and for $\psi/\psi_{BEP} = 1$, $\varphi/\varphi_{BEP} = 0.833$ and $\sigma = 0.3$.

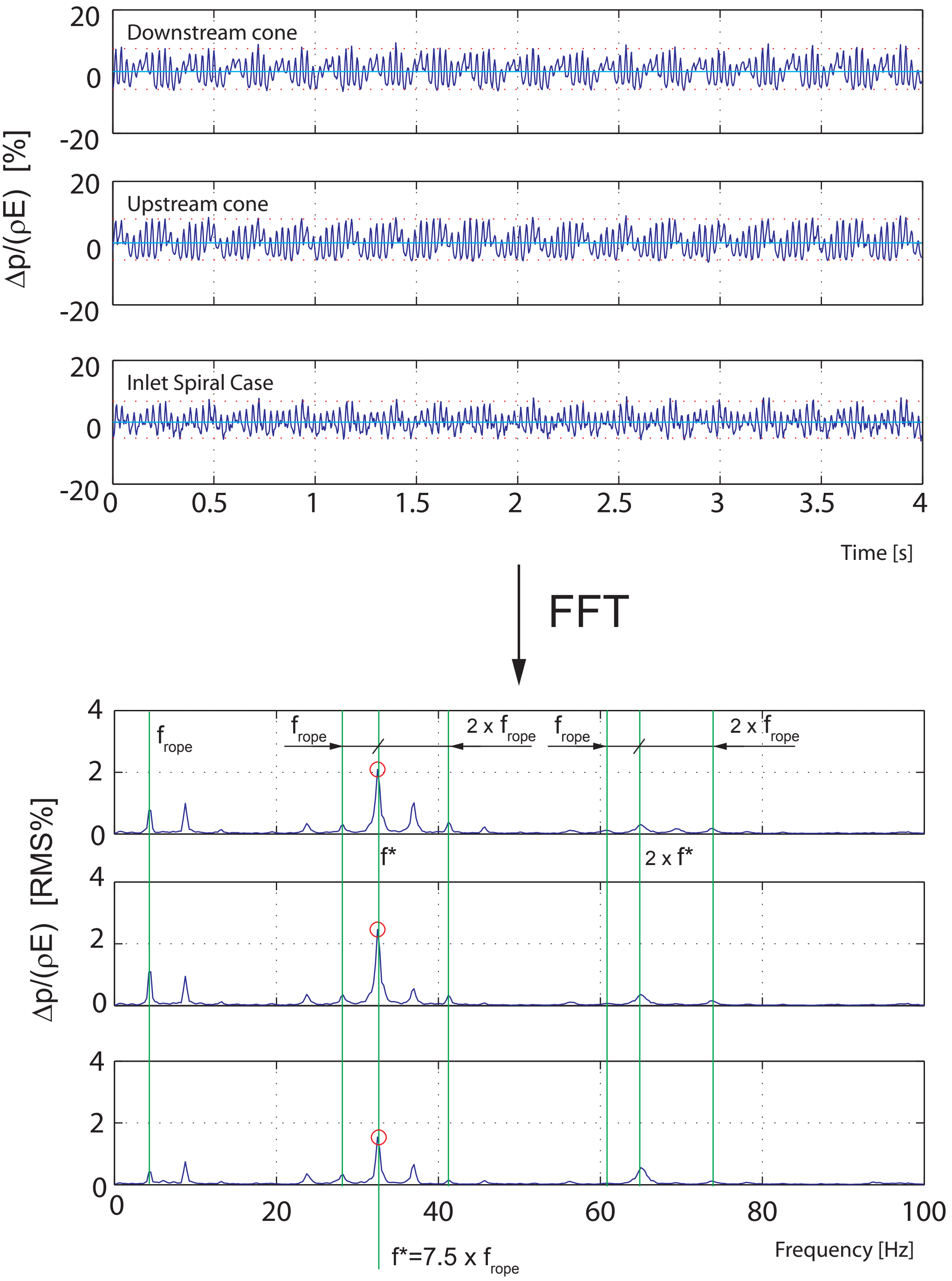

Figure 9.43: Modulation of the pressure pulsation at the vortex rope precession frequency f_{rope} and pressure pulsation f^* for $\psi/\psi_{BEP} = 1$, $\varphi/\varphi_{BEP} = 0.833$, $\sigma = 0.3$ and $Froude = 7.86$.

9.3.5 Concluding Remarks on the Visualization of the Vortex Rope at Upper Part Load

An experimental investigation on a reduced scale Francis turbine of specific speed $\nu = 0.5$ was performed using wall pressure measurements synchronized with movie recording. The upper part load is characterized by pressure pulsations in the range of $f/n = 1$ to 3. The flow visualizations with simultaneous pressure measurements demonstrate that the vortex rope features an elliptical cross section and that the vortex rope is self rotating at a frequency half of pressure fluctuations of interest. This particular structure of the flow leads to modulation of the pressure fluctuations related to the vortex rope precession and of the pressure fluctuations of interest.

The pressure fluctuations appear to be strongly linked to the cavitation number and therefore resonance conditions are commonly encountered during model tests when the excitation source of the vortex rope in the range of $f/n = 1$ to 3 matches the hydraulic system eigen frequencies. The Froude investigation shows that the pressure fluctuation frequency is proportional to the rotational speed, and therefore the draft tube flow behaves as an excitation source but with excitation frequencies above the rotational speed.

However, the elliptical shape of the vortex rope is only a consequence of the flow field and therefore results from the swirling flow leaving the runner, thus leading to such an unsteady pressure distribution. Therefore, it would be interesting to clarify the conditions of the onset of these flow instabilities similarly as it was done for the vortex breakdown phenomenon, see Flavey and Cassidy [33] and Benjamin [13], by both numerical and experimental approaches. From the experimental point of view, comparison of cavitating and non-cavitating flow examined with an unsteady PIV method might provide some key answers. But such an investigation must be correlated with an analytical stability analysis similar to Resiga *et al.* [139] in order to find qualitative criteria.

Chapter 10

Modelling of Over Load Pressure Pulsations on a Prototype

10.1 Over Load Surge Event at Pumped-Storage Power Plant

For higher-load operating conditions, Francis turbines can feature onset of a cavitating vortex rope in the draft tube cone which is generated by the incoming swirling flow [109]. At full or overload operating conditions, the cavitating rope may under certain conditions act as an energy source, which leads to self-excited pressure oscillations in the whole hydraulic system [79]. These pressure oscillations can jeopardize the mechanical and hydraulic system [85]. Depending on the turbine relative location in the circuit, the turbine head may oscillate and generate power swings.

These power and pressure oscillations have been experienced at over load during commissioning tests carried out with Unit 4 of a Pumped-Storage Plant, PS Plant, located in the southeastern United States featuring four 400 MW Francis pump-turbines. The pressure surge event was well monitored and the time histories of power and wall pressure in the spiral case and draft tube cone man-doors were simultaneously recorded, see figure 10.1. The event was apparently initiated by the shut down of Unit 2, with Unit 1 and Unit 3 at rest. The time sequence of the surge event onset is the following:

- Unit 4 and Unit 2 in approximately steady generating mode with Unit 1 and Unit 3 at rest;
- observation of low amplitude pressure pulsations at 2.9 Hz frequency for over load operating conditions;
- normal shut down of Unit 2;
- onset of high amplitude pressure pulsations at about 2.2 Hz frequency;
- generator power swing followed by pressure oscillations;
- standing pressure oscillations at about 2.2 Hz everywhere in the power plant piping.

The aim of this investigation is to present the hydroacoustic analysis of the PS Plant and to show the self induced oscillation nature of the observed pressure surge event. First

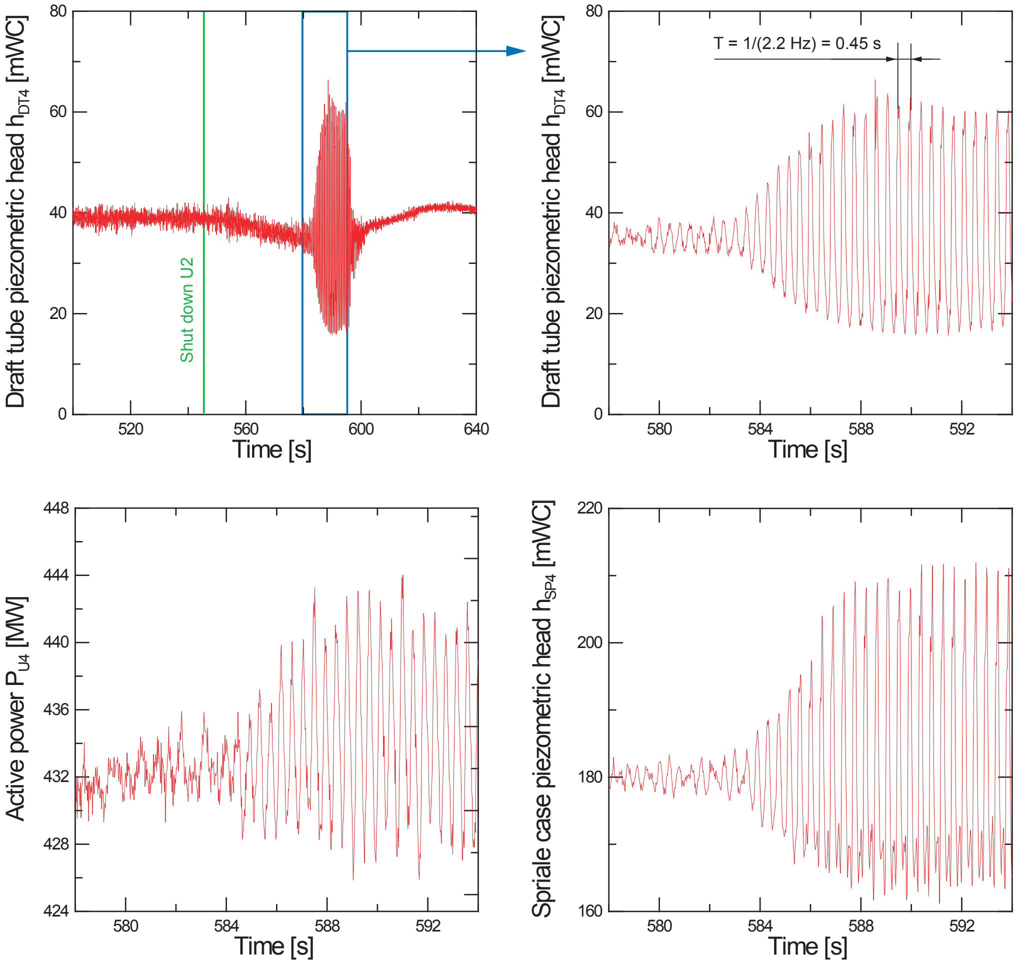

Figure 10.1: Recorded time history of pressure at the draft tube (top), pressure at spiral case inlet (bottom right) and power (bottom left) for Unit 4.

the main physical parameters of the system stability are introduced by using a simplified 1D mathematical model of the higher load vortex rope. Then, a free oscillation analysis of the full hydraulic circuit is performed to determine the stability domain of the PS Plant as a function of the vortex rope parameters. Following this, a hydroacoustic model of the PS Plant including the hydraulic circuit, the mechanical masses, the generators, the transformers, and the voltage regulators is developed and validated for the simulation and analysis of the above described time sequence of the pressure surge event onset, providing the cause of this pressure surge event.

10.2 Case Study: Pumped-Storage Plant

10.2.1 Modelling of the Power Plant

The investigated PS plant corresponds to the upgrade of the power plant of the SIMSEN validation presented in the section 7.2. The layout of the PS Plant is repeated below in figure 10.2 including the layout of the electrical installation. A 590 meters long penstock feeds four Francis pump-turbines with four downstream surge chambers of variable cross section all connected to a 304 meters long pressurized tailrace water tunnel. The design values of the upgraded pump-turbines are given in table 10.1.

The simulation model set up with SIMSEN-Hydro takes into account the full hydraulic system including pipes, spherical valves, downstream surge chambers, and pump-turbines. Moreover, the inertia of the rotating shaft line, the generators with saturation effects, the voltage regulators, the circuit breakers, and the transformers are included in the model. In this study, the electrical grid is considered as an infinite grid at 60 Hz fixed frequency.

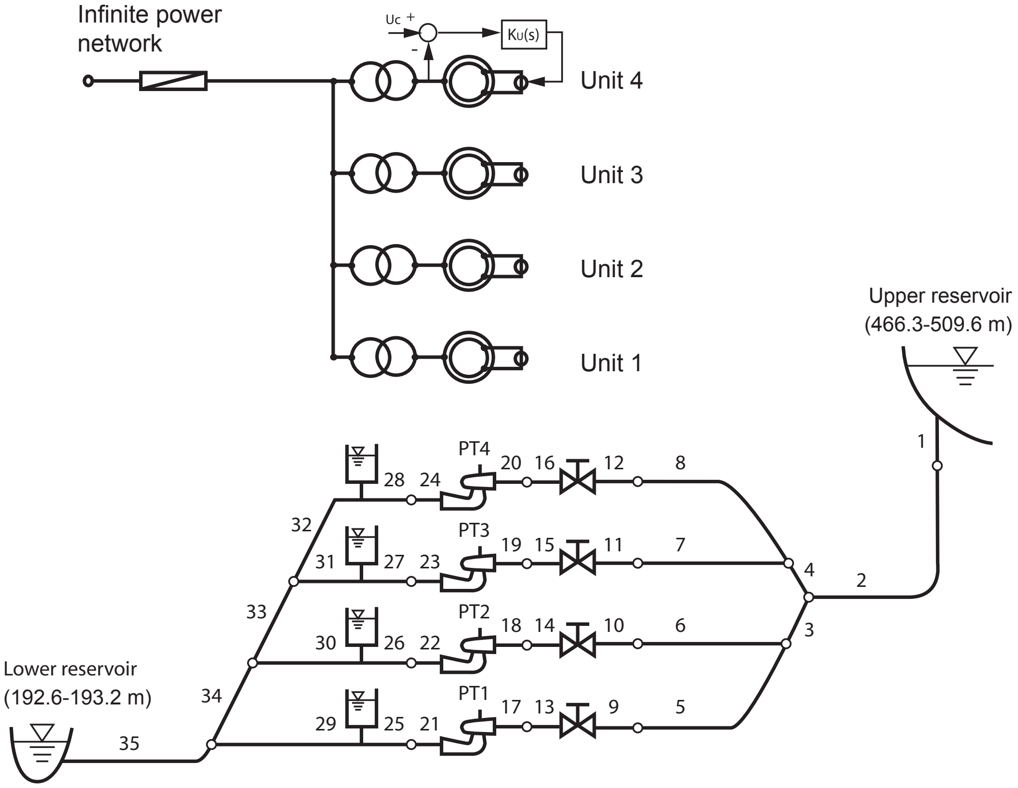

Figure 10.2: Layout of the Pumped-Storage Plant.

Table 10.1: Rated values of the pump-turbines of the validation test case.

H_n $[m]$	Q_n $[m^3/s]$	P_n $[MW]$	N_n $[rpm]$	D_{ref} $[m]$	J_{tot} $[kg \cdot m^2]$	ν $[-]$
305	138	390	300	5.08	$2.77 \cdot 10^6$	0.306

10.2.2 Full Load Vortex Rope Modelling

As the Francis turbine features blades with constant pitch, the outlet flow in the draft tube cone is optimal, almost purely axial, only for the best efficiency point. For off design operation, *i.e.* part load or full load, the circumferential components of the flow velocity are respectively positive or counter rotating, inducing a swirling flow [109]. For full load operation and a given setting level of the machine, the swirling flow results in the development of an axi-symmetric cavitation vortex rope below the runner, see figure 10.3 left.

As the frequency of the phenomenon of interest is very low, 2.2 Hz, the vortex rope is modelled by a lumped element using a cavitation flow model presented in section 5, located at the outlet of the pump-turbine of Unit 4. The lumped component modelling of the vortex rope gaseous volume is based on the assumption that the gaseous volume is a function of the two state variables H and Q, the net head and the discharge respectively, [27], [29] and [97]. As presented in section 5 the rate of change of the gaseous volume is given by the variation of discharge between the 2 fluid sections limiting the rope, see figure 10.3 right, and is therefore given by the equation repeated below:

$$Q_i - Q_{i+1} = Q_c = C \cdot \frac{dh_{i+1}}{dt} + \chi \cdot \frac{dQ_{i+1}}{dt} \tag{10.1}$$

Where the lumped parameters are defined as:

- the cavity compliance $C = -\frac{\partial V}{\partial h}$
- the mass flow gain factor $\chi = -\frac{\partial V}{\partial Q_{i+1}}$

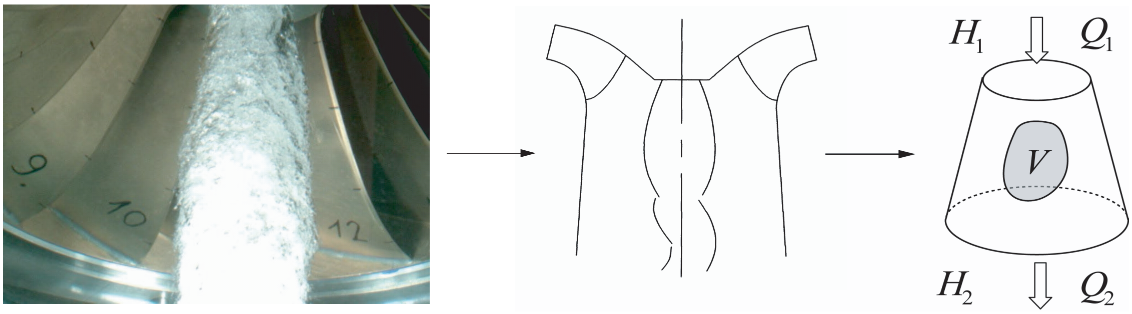

Figure 10.3: Modelling of the full load vortex rope.

10.2.3 Validation of the Simulation Model: First Commissioning in 1979

This investigation is related to the validation test case of section 7.2 for which load rejection in both generating and pumping mode are simulated with satisfactory agreement compared with available transient measurements carried out for Unit 1 during commissioning tests of the original runners in 1979. However, for the present investigation, the best efficiency point of the turbine characteristic is modified according to the new best efficiency point of the upgraded pump-turbines.

10.3 Event Modelling: New Commissioning in 2005

10.3.1 Free Oscillation Analysis of the Power Plant

The study of the stability of a dynamic system can be efficiently carried out performing modal analysis. This analysis is performed to determine the stability domain of the hydraulic installation with respect to the lumped parameters of the vortex rope, *i.e.* the rope compliance and mass flow gain factor. The Transfer Matrix Method described in [138] is used with advanced models of both friction losses and damping, [66]. The eigenvalues of the corresponding system global matrix have been computed to derive both the natural frequencies and the damping or amplification factors of the corresponding mode from, respectively, their imaginary and real parts [95]. The stability domain is defined as a function of both the vortex rope compliance and the mass flow gain factor in figure 10.4, where the blue dots indicate unstable areas.

Given that Unit 4 experienced pressure oscillations at 2.9 Hz just prior to the event and at 2.2 Hz after the event, and assuming that the event was caused by a hydroacoustic instability the corresponding values of the vortex rope compliance and the absolute value of the mass flow gain factor can be identified in figure 10.4. With these values for the lumped parameters of the cavitation vortex rope, for each calculated natural frequency, both the pressure and discharge mode shapes can be computed, as shown in figure 10.5 for 2.2 Hz. The modal analysis confirms that the maximum pressure oscillations occur close to Unit 4, which is in agreement with the field tests, and that both the spiral casing and the draft tube experience pressure oscillations in phase, see figure 10.1.

10.3.2 Time Domain Simulation of the Self-Excitation of the Power Plant

The time domain analysis is performed with the complete SIMSEN model featuring the vortex rope model for Unit 4, the inertia of the rotating shaft line, the generators with saturation effects, the voltage regulators, the circuit breakers, and the transformers. The event is simulated according to the sequence observed on site, *i.e.* Unit 2 operating normally, the modernized Unit 4 in operation at overload conditions, and Unit 1 and Unit 3 at rest with guide vanes closed, and then Unit 2 is shutdown according to the normal procedure. The normal shutdown consists of closing in 24 seconds the guide vanes following a two-slope closing law and tripping the generator when 10% of the generator power is reached.

For this analysis the vortex rope mass flow gain factor value is taken from the stability diagram, see figure 10.4, for the point corresponding to the stability limit at 2.9 Hz. To take into account the influence of the operating condition on the volume of the vortex rope, the rope compliance was determined using the results of the CFD simulations for the modernized units [95]. The draft tube flow is computed for different guide vane openings and the cavitation vortex rope volume is assumed to correspond to the volume limited by the vapor pressure iso-surface, enabling estimation of the "cavitation" volume as a function of σ, the Thoma number, and the guide vane opening, see figure 10.6 left. A power law is fitted with the corresponding 80% guide vane opening overload conditions:

$$V_{rope} = A \cdot \sigma^{B} \tag{10.2}$$

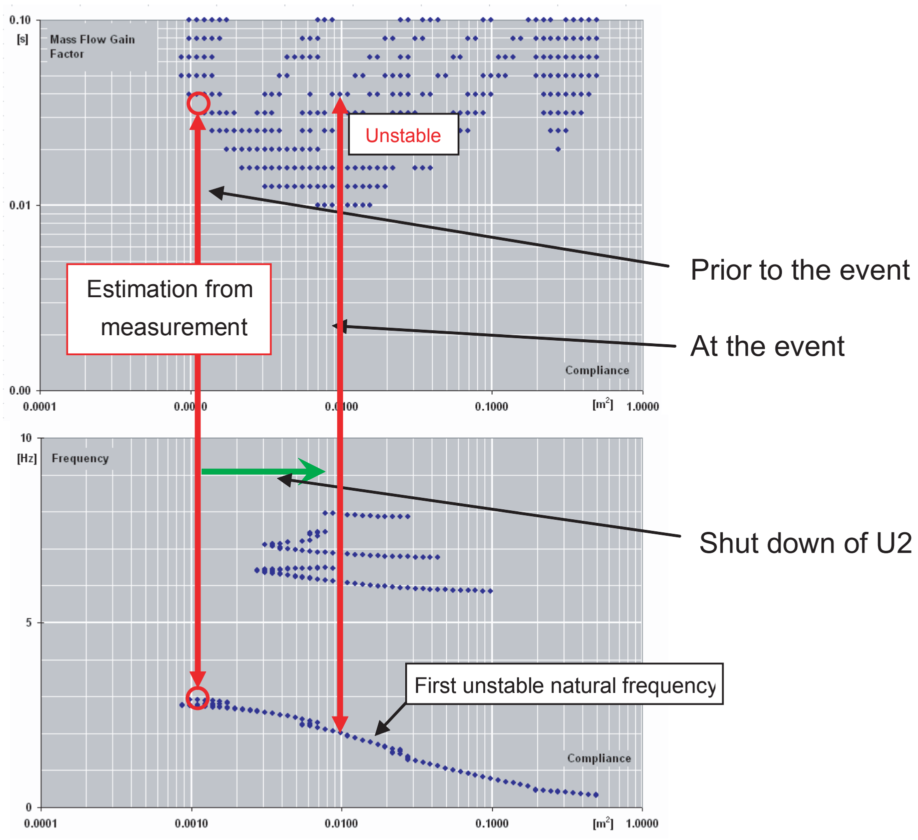

Figure 10.4: Stability diagram of the absolute value of the mass flow gain factor (top) and the unstable frequency (bottom) as function of Vortex rope compliance.

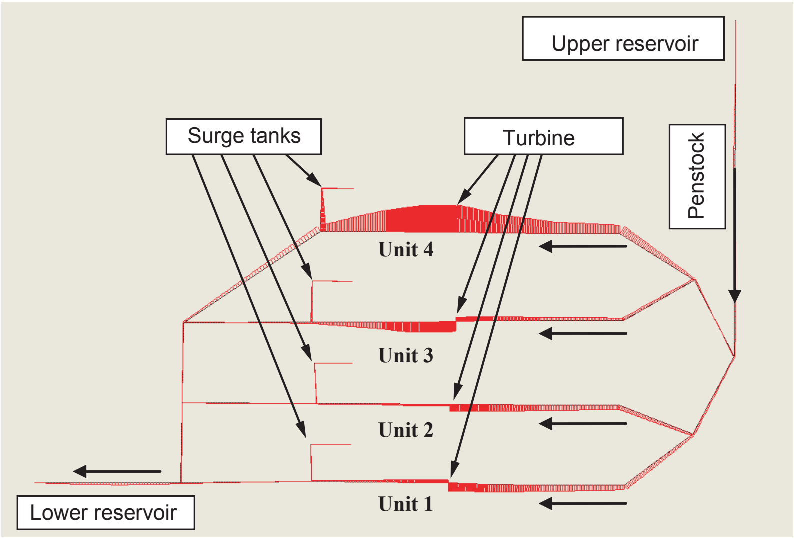

Figure 10.5: Pressure mode shape in the waterways, for natural frequency of 2.2 Hz.

where the Thoma number σ is defined as:

$$\sigma = \frac{NPSE}{E} \approx \frac{H_a - (Z_{\mathrm{Ref}} - Z_{\mathrm{Tail\ Water}}) - H_v}{H} \tag{10.3}$$

Therefore, the cavity compliance is derived according to equation 10.2:

$$C = \frac{\partial V}{\partial H_{\mathrm{Draft\ Tube}}} \approx \frac{\partial V}{\partial Z_{\mathrm{Tail\ Water}}} = -A \cdot B \cdot \frac{\sigma^{B-1}}{H} \tag{10.4}$$

The resulting estimated compliance is presented in figure 10.6 right. However, this approach is only applicable for full load operation where pressure iso-surfaces of the flow captured by CFD computation are close to the cavity limits observed in reduced-scale model tests. For part load operation, the iso-surfaces computed by current CFD models are not close to the cavity limits observed in model tests.

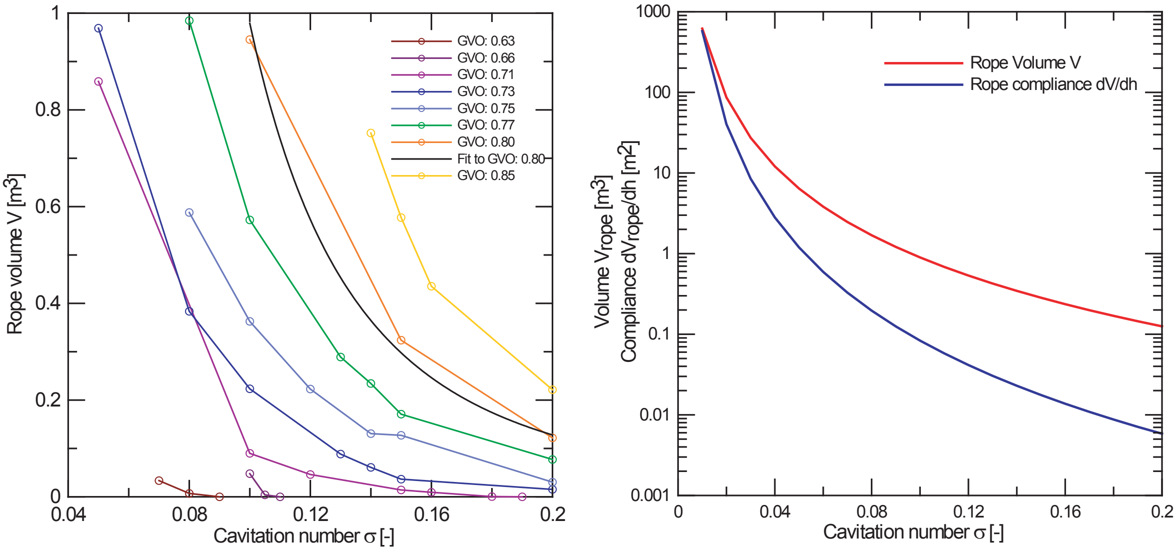

Figure 10.6: Vortex rope volume at full load computed with CFD (left), and deduced vortex rope compliance (right).

The results of the time-domain analysis are presented for Unit 2 and Unit 4 in figure 10.7 for the vortex rope parameters indicated as case C in table 10.2, which define the system stability limit. The transient resulting from the Unit 2 shutdown induces a slow downstream pressure drop due to downstream mass oscillation. As a result, the Thoma number value of Unit 4 decreases and the vortex rope compliance increases as the vortex rope volume increases. Then, considering a constant mass flow gain factor, the vortex rope compliance increases until the unstable domain of operation is reached; leading to the pressure oscillation onset in the draft tube; the system being in self-excited conditions. Then the system remains unstable as long as the sigma value, *i.e.* the vortex rope size, does not reach the same steady value as prior to the event. The calculated oscillation frequency corresponds well with the measured frequency value, whereas the agreement between the calculated and measured amplitudes is less good.

A parametric study of the influence of the vortex rope is carried out using the values given in table 10.2. For case A, the mass flow gain factor and compliance are both kept constant. For cases B, C and D, the cavity compliance is taken as a function of the Thoma number and the head, and the mass flow gain factor is still kept constant. The resulting draft tube piezometric heads are presented in figure 10.8. In case A, the amplitudes increase dramatically. Case B exhibits amplitudes that are strongly affected by the compliance dependence on the Thoma number value. Case C corresponds to the limit of stability with bounded amplitudes. In case D, the self-excitation is initiated but the oscillations are damped once the surge chamber level recovers its initial value. This sensitivity analysis shows clearly that the shutdown of Unit 2 initiates the self-excitation mode by decreasing the Unit 4 draft tube pressure and, consequently, the Thoma number value.

Table 10.2: Vortex rope parameters for 4 simulation cases.

Cases	**A**	**B**	**C**	**D**
Compliance C $[m^2]$	10^{-2}	$C = C(\sigma, H)$	$C = C(\sigma, H)$	$C = C(\sigma, H)$
Mass flow gain factor χ $[s]$	-0.005	-0.005	-0.004	-0.003

10.4 Concluding Remarks

An overload surge phenomenon was experienced at a pumped storage plant during over operating range tests. In order to have a better understanding of the onset condition of this phenomenon, a one-dimensional model of the power plant, including a model of the vortex rope, is carried out. The vortex rope at higher load conditions is modelled by defining a compliance parameter and a mass flow gain factor for the cavitation volume. Using this simplified model, the stability domain of the power plant with respect to the vortex rope parameters is determined through modal analysis and the vortex rope parameters for the power plant are estimated by locating the observed test conditions within the stability domain. Then, a time domain simulation of the dynamic behavior of the power plant according to the event time sequence observed on site is performed. The simulation model includes the hydraulic system with a non-linear vortex rope model, the rotating inertias, the electrical components, and the governors. In an original approach, the vortex rope cavitation compliance is modelled as a non-linear function of the Thoma number and the head, where the function is determined by comparison of results from scale-model experiments and CFD modelling. The simulation results show the role played in this case by the shutdown of a neighboring unit, which decreases the pressure downstream of the affected unit and, therefore, the cavitation number and eventually initiating the self-excited surge.

The comparison of calculated and measured results shows surprisingly good agreement considering the relatively simple model used for the complex flow - vortex rope structure within the pump-turbine. Moreover, this investigation provides a deeper insight into the physical phenomena underlying the onset of overload pressure surge. However, to be predictive, the hydroacoustic modelling requires a very accurate set of data provided from either reduced scale model measurements or advanced unsteady two-phase flow analysis.

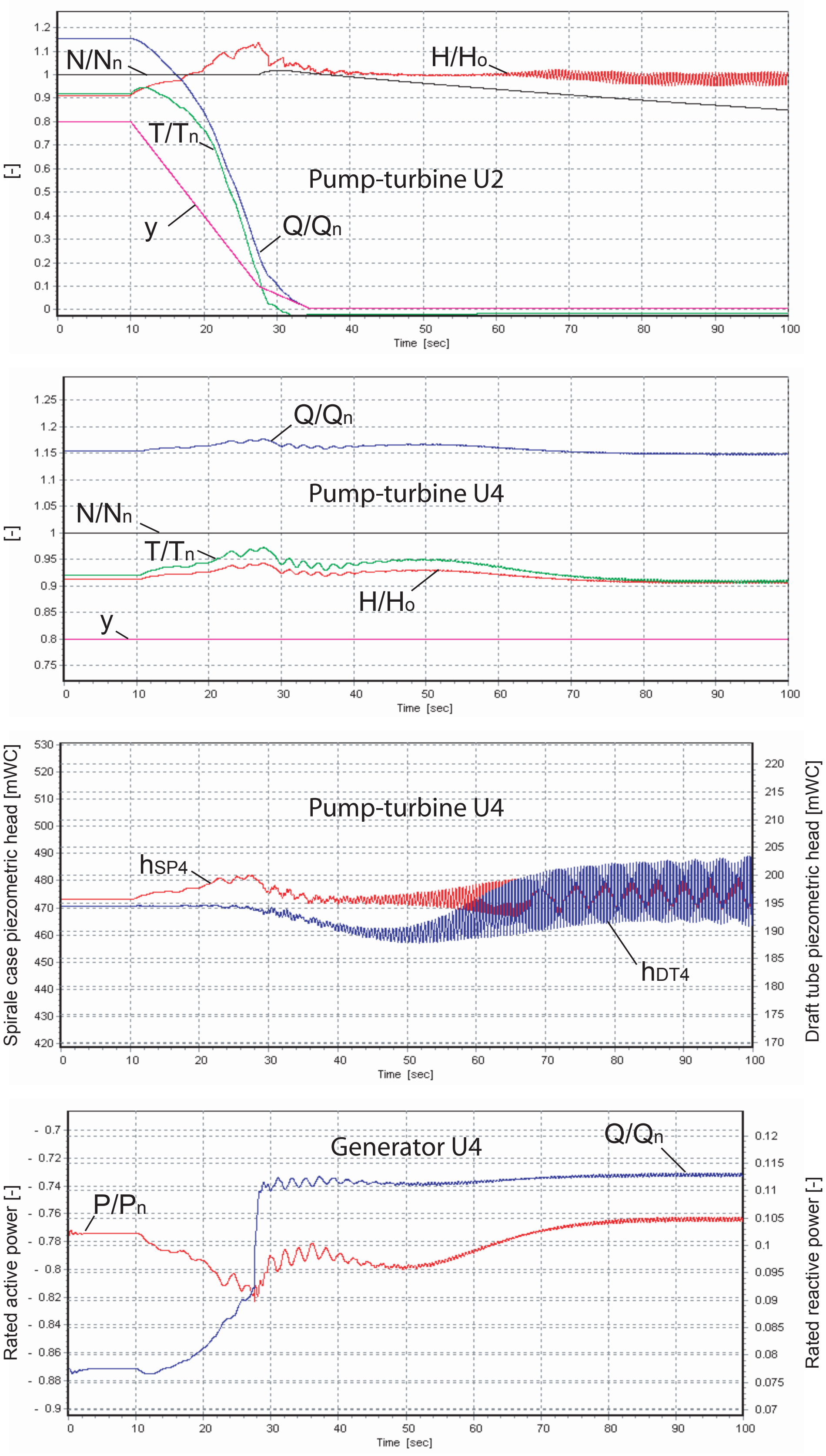

Figure 10.7: Simulation results of the transient of the pump-turbine of Unit 2 and Unit 4.

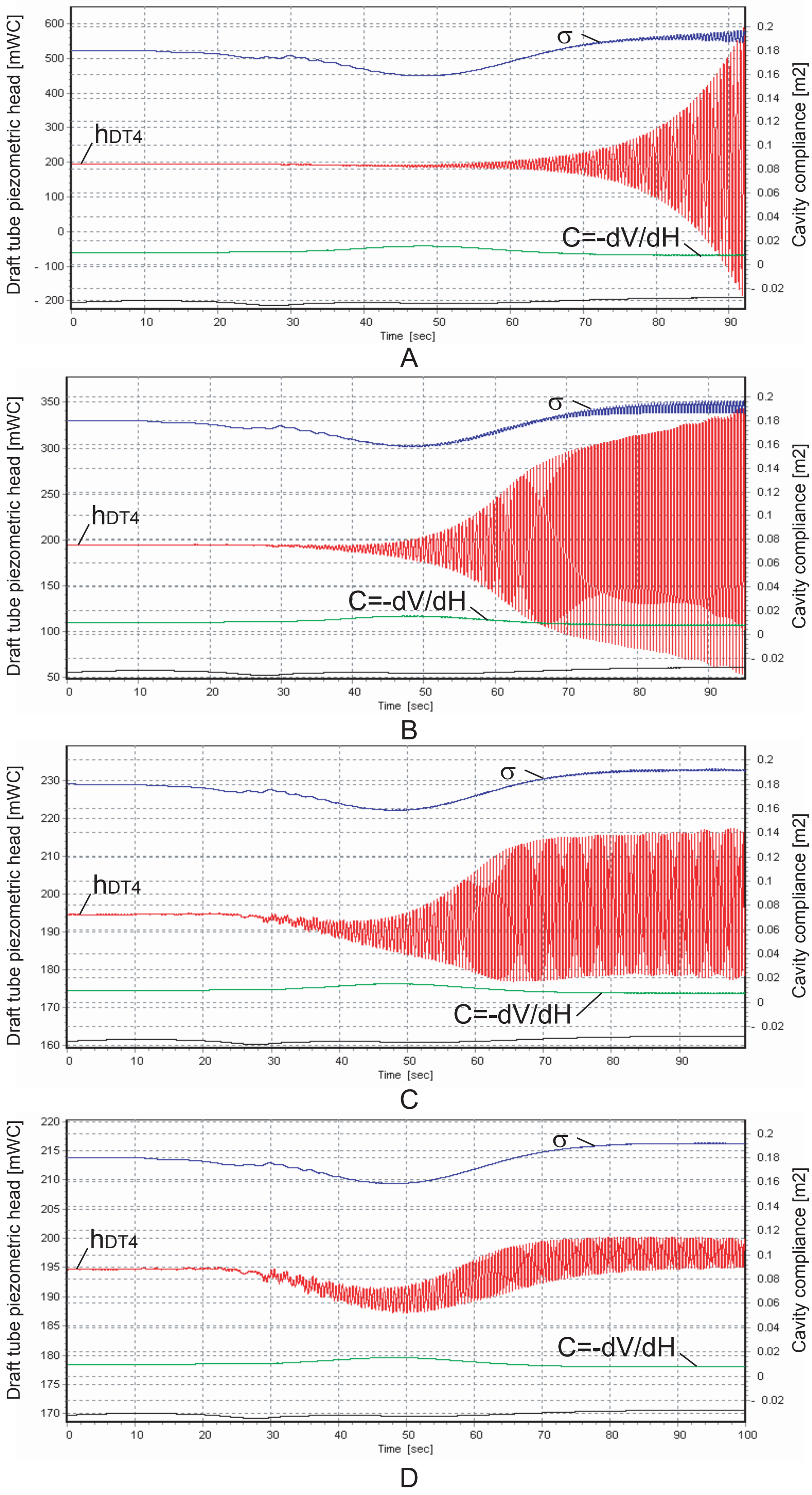

Figure 10.8: Simulation results of the draft tube pressure oscillations of Unit 4 for the rope parameters of table 10.2.

Chapter 11

Modelling of Rotor-Stator Interactions on a Scale Model

11.1 General Remarks

This section aims to present the numerical simulation of the hydroacoustic part of the RSI phenomenon based on a one-dimensional hydroacoustic model. Therefore the case of 20 guide vanes and 9 impeller blades high head Francis pump-turbine is investigated. First the RSI patterns of the pump-turbine are described. Then, the determination of the pump-turbine hydroacoustic parameters is described. The results obtained by the simulations in time domain indicates the RSI patterns of the pump-turbine of interest. A parametric study is presented and the influence of blade thickness, wave speed and rotational speed is investigated.

11.2 RSI Patterns in Francis Pump-Turbine

The flow field leaving the guide vane of a Francis pump-turbine in generating mode is characterized by the velocity defect caused by the guide vanes. The pressure field attached to the rotating impeller blade induces also incoming flow field distortions. No matter how complex these two periodic flow fields are they can be expressed as Fourier series. Then, both the stationary and rotating pressure fields can be expressed as:

$$p_s(\theta_r, t) = \sum_{n=1}^{\infty} B_n \cos\left(n \cdot z_0 \theta_r + \phi_n\right) \tag{11.1}$$

$$p_r(\theta_r, t) = \sum_{m=1}^{\infty} B_m \cos\left(m \cdot z_b \cdot \theta_r + \phi_m\right) \tag{11.2}$$

The resulting velocity field is characterized by a strong modulation process as illustrated in figure 11.1. The pressure in the area of the vaneless gap between the guide vanes and impeller blades can therefore be expressed as the product of both rotating and stationary fields of pressure leading to the summation of every p_{mn} component:

$$p_{mn}(\theta, t) = A_{mn} \cos\left(n \cdot z_o \cdot \theta_s + \phi_n\right) \cdot \cos\left(m \cdot z_b \cdot \theta_r + \phi_m\right) \tag{11.3}$$

For $n = 1, 2, ...\infty$ and $m = 1, 2, ...\infty$, and where A_{mn} is the combined pressure amplitude due to the interaction of each harmonics [113]. By using the well known identity for trigonometric functions, equation 11.3 can be expressed as:

$$\begin{aligned} p_{mn}(\theta_s, t) =& \frac{A_{mn}}{2} \cos\left(n \cdot z_o \cdot \theta_s - m \cdot z_b \cdot \theta_r + \phi_n - \phi_m\right) \\ &+ \frac{A_{mn}}{2} \cos\left(n \cdot z_o \cdot \theta_s + m \cdot z_b \cdot \theta_r + \phi_n + \phi_m\right) \end{aligned} \tag{11.4}$$

Moreover, the impeller angle coordinate is related to the stationary frame of reference as $\theta_r = \theta_s - \omega t$, then the pressure field in the stationary coordinates becomes:

$$\begin{aligned} p_{mn}(\theta_s, t) =& \frac{A_{mn}}{2} \cos\left(m \cdot z_b \cdot \omega \cdot t - (m \cdot z_b - n \cdot z_o)\, \theta_s + \phi_n - \phi_m\right) \\ &+ \frac{A_{mn}}{2} \cos\left(m \cdot z_b \cdot \omega \cdot t - (m \cdot z_b + n \cdot z_o)\, \theta_s - \phi_n - \phi_m\right) \end{aligned} \tag{11.5}$$

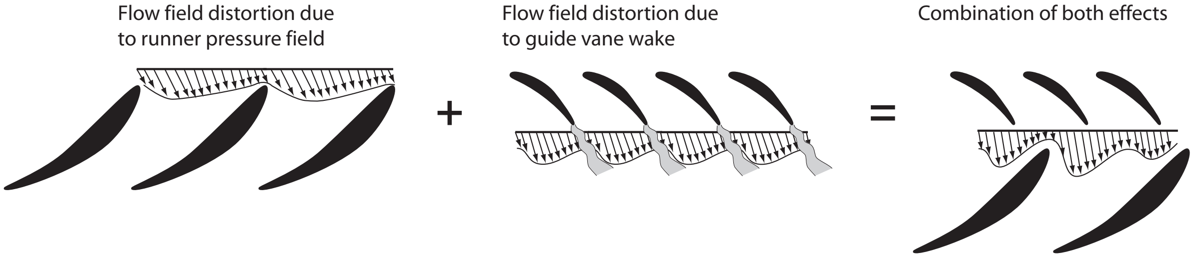

Figure 11.1: Modulation process between impeller blade flow field and guide vanes flow field.

This equation describes the RSI pressure field in the vaneless gap which is function of time and space [57]. This pressure field represents 2 diametrical pressure modes having the following numbers of minima and maxima :

$$k_1 = m \cdot z_b - n \cdot z_o \quad ; \quad k_2 = m \cdot z_b + n \cdot z_o \tag{11.6}$$

rotating with the respective spinning speed in the stationary frame of reference.

$$\omega_1 = m \cdot z_b \omega_b / k_1 \quad ; \quad \omega_2 = m \cdot z_b \omega_b / k_2 \tag{11.7}$$

Furthermore, the sign of the diametrical mode numbers k_1 and k_2 indicates that the diametrical mode is rotating in the same direction as the impeller when positive and counter-rotating when negative. It is also important to note that lower amplitudes are expected for higher k values, because of the high harmonic number. As a result, k_2 is usually not relevant. The figure 11.2 presents an illustration of the meaning of the k values.

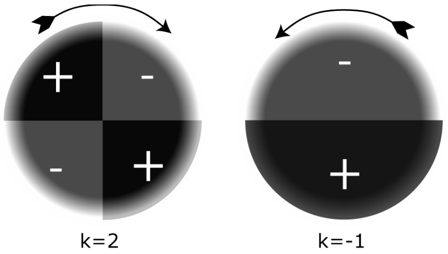

Figure 11.2: Diametrical modes shape patterns according to k values.

11.3 Case Study: Scale Model Pump-Turbine

The case investigated is a pump-turbine scale model installed on the PF3 test rig of the EPFL Laboratory for Hydraulic Machines in the framework of the research project "Hydrodyna". The scale model of this pump-turbine is presented in figure 11.3 and the rated efficiency hill chart is presented in figure 11.4. This pump-turbine features a 20 guide vane and 9 impeller blade rotor-stator arrangement. The main characteristics of this pump-turbine are summarized in table 11.1.

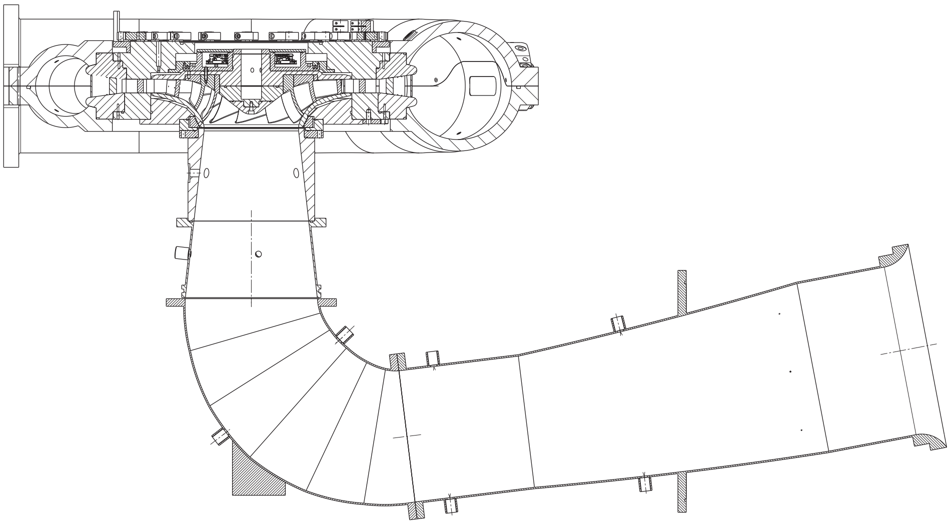

Figure 11.3: Scale model of the investigated pump-turbine.

Table 11.1: Scale mode pump-turbine main characteristics.

ν $[-]$	z_o $[-]$	z_b $[-]$	Q_n $[m^3/s]$	H_n $[m]$	N_n $[rpm]$
0.17	20	9	0.23	45	980

The pump-turbine has a specific speed of $\nu = 0.17$, 20 guide vanes, 9 impeller blades

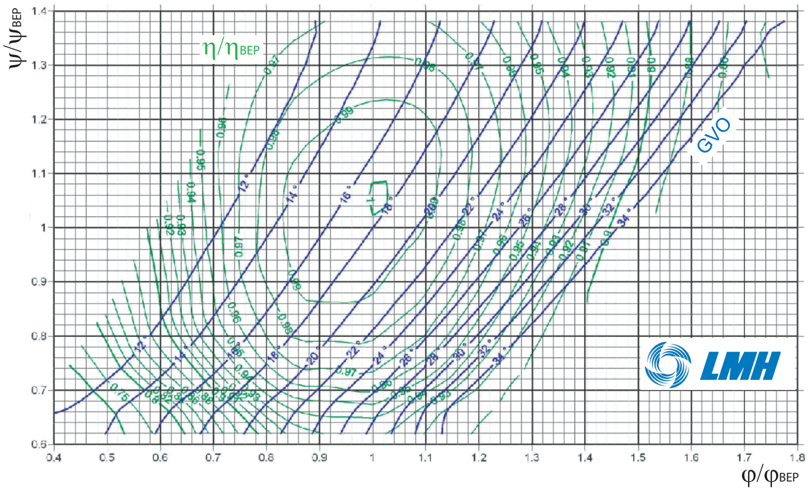

Figure 11.4: Rated efficiency hill chart $\eta/\eta_{BEP} = \eta/\eta_{BEP}(\varphi/\varphi_{BEP}, \psi/\psi_{BEP})$ of the pump-turbine.

and an outlet diameter, in turbine mode, of $D_{\bar{1}e} = 400\ mm$. According to this rotor-stator blade arrangement the RSI patterns of this pump-turbine are determined analytically using relations 11.5, 11.6 and 11.7, see table 11.2.

Table 11.2: RSI patterns of the pump-turbine ($z_o = 20; z_b = 9$).

				Stationary Frame			**Rotating frame**		
n	m	k_1	k_2	ω_1/ω_b	ω_2/ω_b	f/f_b	ω_1^*/ω_b	ω_2^*/ω_b	f^*/f_b
1	2	-2	38	-9.0	0.5	18	-10.0	-0.5	20
1	3	7	47	3.9	0.6	27	2.9	-0.4	20
2	4	-4	76	-9.0	0.5	36	-10.0	-0.5	40
2	5	5	85	9.0	0.5	45	8.0	-0.5	40

The table 11.2 points out the 4 diametrical rotating modes expected to present the most significant amplitudes. These diametrical modes are $k_1 = -2,\ 7,\ 5,\ -4$ with the related frequencies in the stationary frame $f/f_b = m \cdot z_b = 18,\ 27,\ 36$ and 45. In the rotating frame of reference these frequencies give $f/f_b = m \cdot z_o = 20$ for the first 2 modes and $f/f_{bo} = 40$ for the second 2 modes.

11.4 Hydroacoustic Modelling of RSI in Francis Pump-Turbine

11.4.1 Pump-Turbine Hydroacoustic Model

The plane view of the 20 guide vanes and 9 blades Francis pump-turbine scale model of interest is presented in figure 11.5 left. The related hydroacoustic model of this pump-turbine is made up out of a pipe network, see figure 11.5 right.

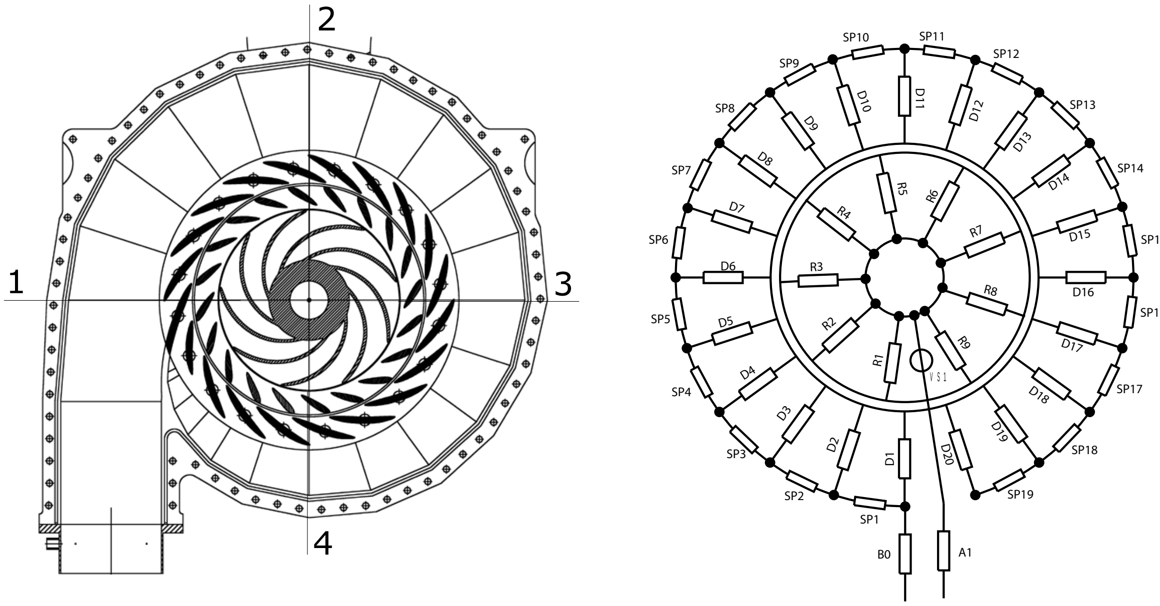

Figure 11.5: Plane view of the pump-turbine (left) and corresponding hydroacoustic model (right).

The hydroacoustic model is made of 20 pipes for the guide vanes (pipes D1 to D20), 9 pipes for the impeller (pipes R1 to R9) as well as 19 pipes for the spiral casing (pipes SP1 to SP19). The first part of the spiral casing between the turbine inlet and the guide vane N°1 is modelled by the pipe B0. The diffuser of the pump-turbine is modelled by the pipe A1. The energy transfer through the impeller is modelled by the pressure ”source” VS1 for which the head is a function of the discharge $H = H(Q)$ according to the slope of the pump-turbine characteristics linearized around the operating point of interest, see figure 9.9. The connection between the stationary part and the rotating part is achieved through 180 valves connecting each guide vane to each impeller vane. The 180 valves are controlled by the flow distribution between the stationary part and the rotating part according to the impeller angular position. The valve head loss is calculated to ensure the idealized discharge evolution presented in figure 11.6.

Assuming a constant impeller angular speed, the discharge evolution between one guide vane and one impeller vane is function of the connection area between them. During the rotation of the impeller 4 phases are identified:

- phase 1: the impeller blade starts passing in front of the first blade of a guide vane channel, the discharge between the guide vane channel and the impeller vane channel

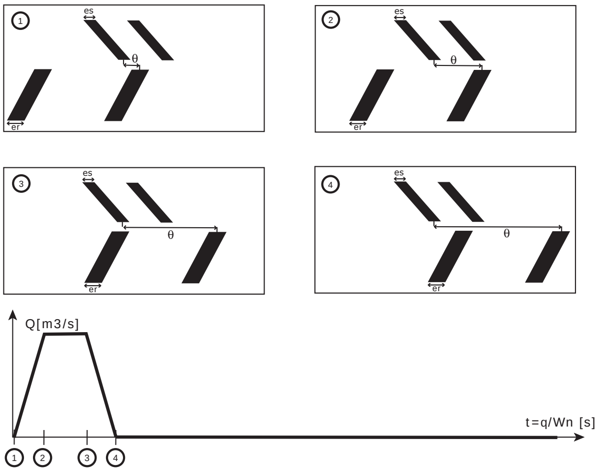

Figure 11.6: Idealized discharge evolution between an impeller vane and a guide vane as function of the spatial coordinate of the impeller θ.

increases linearly according to the connection area increase until the impeller blade reaches the second blade of the guide vane;

- phase 2: the discharge between the guide vane and the impeller vane channels remains constant until the second impeller blade reaches the first guide vane, the connection area being constant;
- phase 3: the discharge between the guide vane channel and the impeller vane channel decreases linearly according to the connection area decrease;
- phase 4: the discharge between the guide vane channel and the impeller vane channel is kept to zero as the connection area is zero until the phase 1 is reached again.

The discharge evolution described above acts like a sliding slot between the 20 guide vanes and one impeller vane. As a result there are 9 slots for the full pump-turbine, one for each impeller vane. Each slot angle being shifted by $2 \cdot \pi / z_b$. The discharge law can be modified in order to take into account the thickness of both the guide vanes and impeller blades, e_o and e_b respectively. The thickness can be expressed as equivalent angle measured in degrees at the vaneless gap radius. For the first part of the investigations, the thickness of the impeller blades is taken arbitrarily equal to 4°, the real one being 3°. The consideration of the blades thickness induces discontinuity in the overall discharge law. It means that the point 3 of the discharge law of an impeller blade does not correspond to the point 2 of the following impeller blade but is shifted of the value of $e_b + e_o$. The lack of discharge between two consecutive impeller blades is the source of the excitation mechanism of this RSI model.

11.4.2 Hydroacoustic Model Parameters Determination

For the determination of the RLC terms of the hydroacoutic model of a pipe, the following values must be determined for each pipe: (i) the length l; (ii) the cross section area A; (iii) the friction coefficient λ; (iv) the wave speed a.

The determination of the length and of the cross section is done using the structural characteristics of the pump-turbine scale model. The friction coefficient of the pipes are evaluated to be $\lambda = 0.02$ for all the pipes. The wave speed of a pipe is given by:

$$a^2 = \frac{1}{\rho\left(\frac{1}{E_{\text{fluid}}} + \frac{1}{A}\frac{\Delta A}{\Delta p}\right)} \tag{11.8}$$

Where E_{fluid} is the bulk modulus of the water and $\Delta A/(A \cdot \Delta p)$ is the rated area increase due to pressure increase. This term can be determined analytically for circular pipes but should be estimated for pipes having complex cross sections. In the case of the pump-turbine, the wave speed of the spiral casing and of the distributor are estimated using Finite Element Method, FEM, calculations. The determination of the wave speed of a given cross section of the spiral casing is carried out in two steps as presented in figure 11.7: (i) the distributor channel area increase due to a constant pressure in the distributor channel only is determined; (ii) the spiral casing area increase due to constant pressure in the spiral casing only is determined.

The FEM analysis is carried out with the commercial code ANSYS^{TM}. First, the stay vanes and the assembling bolts are considered individually to determine their stiffness. Then, by assuming that each spiral casing part of concern is axisymmetrical, the area increase is determined by including the stiffness of the stay vanes and of the bolts previously determined. The number of cells in the radial direction of the spiral casing section was set to 3 cells of mesh. This value was determined by comparison of circular pipe wave speed determined by both FEM and analytical calculation. The difference for such geometry was found to be 0.1%. The mechanical properties of the materials of the spiral casing and distributor channels are summarized table 11.3.

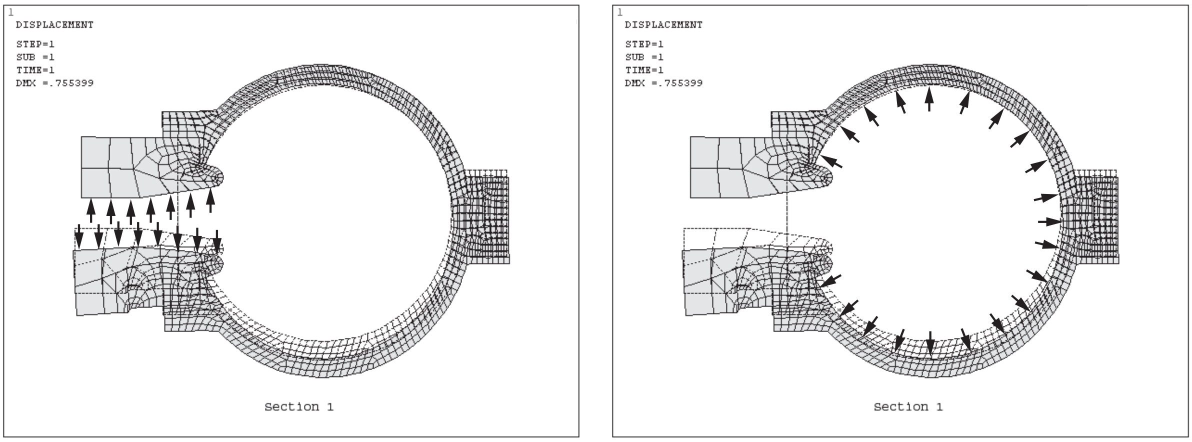

Figure 11.7: Determination of the wave speed in the distributor channel (left) and in the spiral casing (right).

The spiral casing material is a composite made of Epoxy resin matrix and fiberglass. The equivalent Young modulus is calculated according to the volume fraction of both components of the composite and by taking into account the main stress direction corresponding to the uniform loading of the hydrostatic pressure. Therefore, the fiberglass

Young modulus is calculated according to the fiber cross section area and density corresponding to the main stress direction of concern.

Table 11.3: Mechanical properties of spiral casing and distributor materials.

Material	**Young Modulus** $[MPa]$	**Poisson coeff.** $[-]$
Steel	210	0.27
Bronze	110	0.31
Composite: Epoxy Resin & Fiberglass	38	0.28

For the 4 cross sections presented in figure 11.8, the corresponding values of the wave speed are calculated, and reported in figure 11.9. As expected, due to a constant spiral casing wall thickness, the wave speed is increasing from the inlet up to the tongue as the cross section decreases. For the determination of the wave speed of the 19 elements of the spiral casing model a 2^{nd} order polynomial interpolation is used, see figure 11.9.

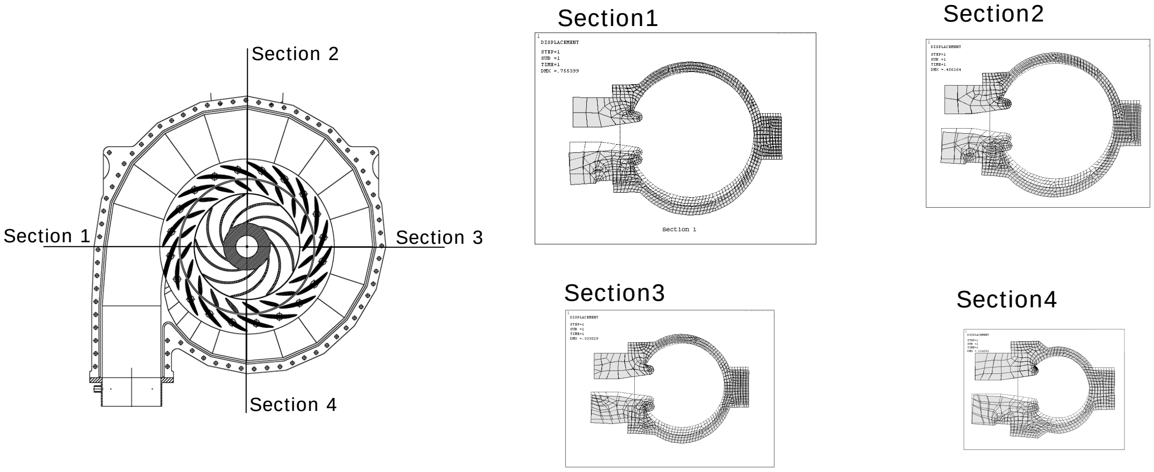

Figure 11.8: FEM model of 4 different cross sections of the spiral casing.

The wave speed of the distributor channels is found to be 800 m/s with small deviation between the 4 sections. The same value is chosen for the wave speed of the impeller blades.

11.5 Simulation of the Pump-Turbine RSI

The hydroacoustic model of the test rig includes the pump-turbine scale model, the 2 feeding pumps in series, the piping system and a downstream tank as presented in figure 11.10. The data related to the model of the test rig are given in table 9.2. The chosen operating condition for the simulation of the hydracoustic behavior of the test rig corresponds to the nominal operating point in turbine mode with no cavitation. Each pipe of the spiral casing is modelled with 1 element, and each guide vane and impeller vane is modelled with 3 elements. This spatial discretization ensures that the confidence

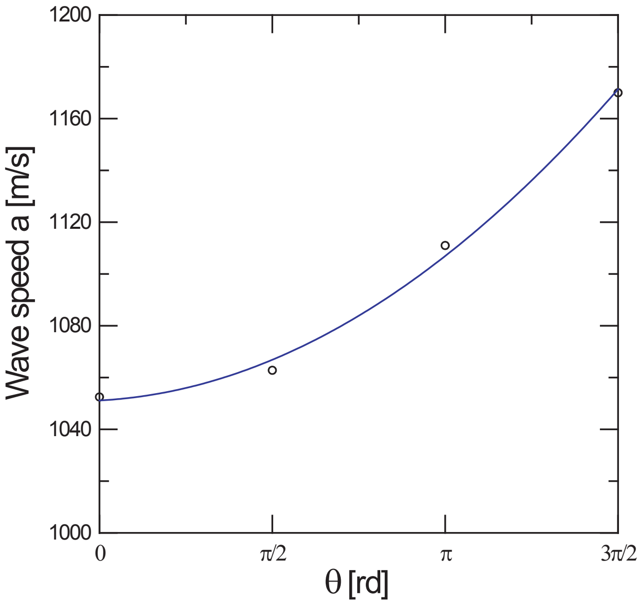

Figure 11.9: Wave speed evolution along the angular position of the spiral casing, calculated points (dot) and fitted line (solid line).

threshold of equation 3.91 is fulfilled with an error below 1%. In agreement with the CFL criteria, an integration time step corresponding to 0.5° of impeller rotation is selected. After convergence of the simulation to a periodic behavior, the simulation is continued for 10 impeller revolutions.

The resulting pressure fluctuations in the spiral casing and in the guide vanes close to the vaneless gap are properly non dimensionalized and presented in a waterfall diagram as a function of the dimensionless frequency f/f_b and the angular coordinate θ, see figure 11.11. In these diagrams the angular origin is taken at the spiral casing inlet and therefore $\theta = 360^{\circ}$ corresponds to the tongue.

The pressure fluctuation in the vaneless gap, figure 11.11 right, presents significant amplitudes (less than 0.5% of the nominal head) for the expected frequencies $f/f_b = 9, 18, 27, 36, 45$, etc. The analysis of the phase, not presented here, of these pressure fluctuations shows clearly the diametrical pattern of the pressure mode shapes with for example 2 minima and 2 maxima, *i.e.* 4π phase shift, for the frequency of $f/f_b = 18$. The pressure fluctuations in the spiral casing, of figure 11.11 left, indicates a standing wave for the frequency $f/f_b = 18$ with a wavelength of approximately 4/3 of the spiral casing length. A pressure node is located at $\theta = 150^{\circ}$ while amplitude maxima take place at $\theta = 20^{\circ}$ and $\theta = 230^{\circ}$. This standing wave influences the amplitude of the diametrical mode in the vaneless gap at the frequency $f/f_b = 18$, see figure 11.11 right.

The visualization of the different diametrical modes and related possible standing waves in the spiral casing is carried out by filtering the time signal of the pressure fluctuations of each spatial node in the pump-turbine using a pass band filter around the frequency of interest. For example, for $k_1 = -2$, in the stationary frame it corresponds to $f/f_b = 18$ while for the rotating frame it corresponds to $f/f_b = 20$. The figures 11.12 to 11.15 presents the resulting pressure fluctuation distributions in the entire machine

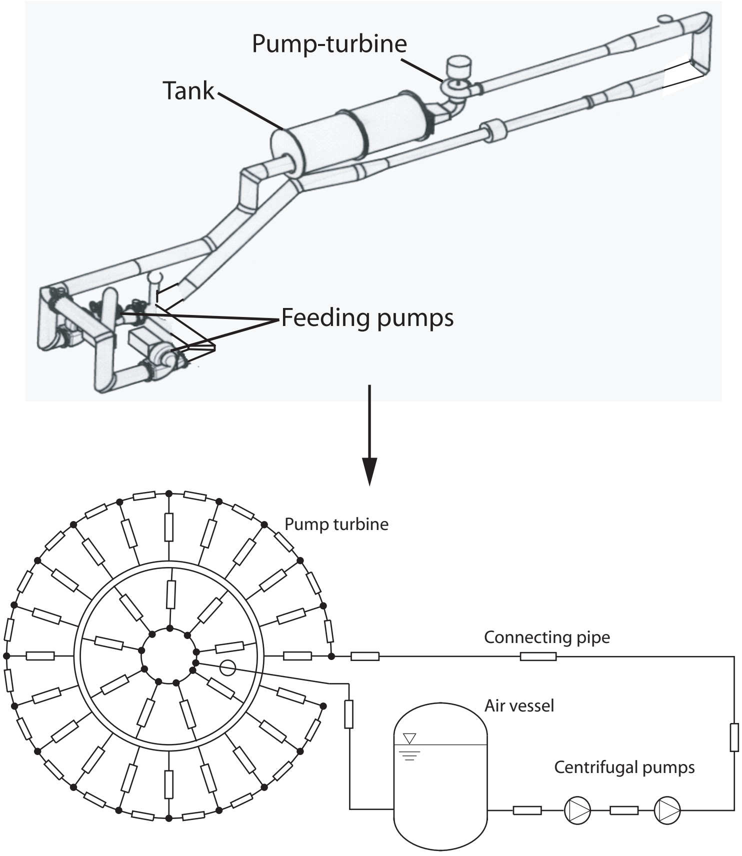

Figure 11.10: EPFL test rig PF3 including the pump-turbine scale model (top) and corresponding hydroacoustic model (bottom).

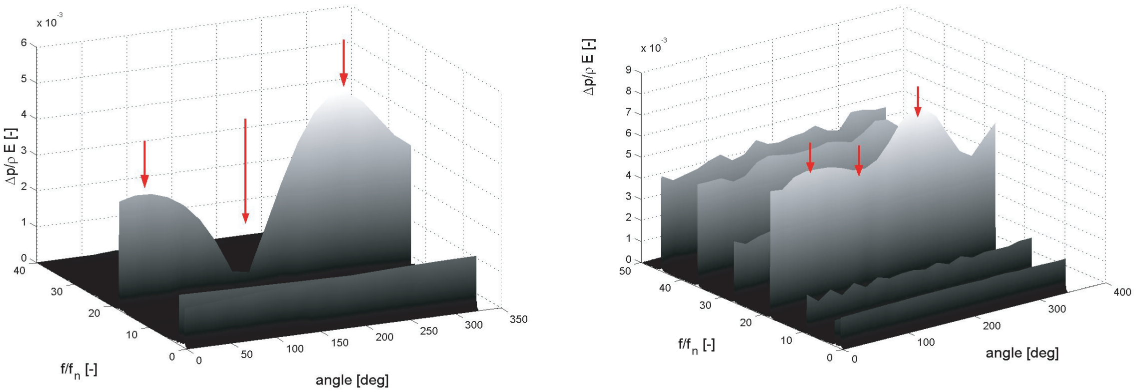

Figure 11.11: Waterfall diagram of the pressure fluctuations in the spiral casing (left) and in the guide vanes close to the vaneless gap (right).

respectively for $k_1 = -2, +7, -4$ and $+5$. The representation is done for the initial time, and for a 1/4 period later. The pressure amplitude of every node of the pump-turbine is represented on the z axis for the spatial position $[x, y]$ of the node. The bold solid line is the connection between each last node of the guide vane and points out the diametrical mode shape pattern expected with the related number of maxima/minima. The diametrical mode rotates in the opposite direction of the impeller rotation for $k_1 = -2$ and -4 and in the same direction as the impeller for $k_1 = +7$ and $+5$ as predicted by the analytical analysis above. For all the cases, the predicted number of minima and maxima also fits with the predictions. However, it can be noticed that the $k_1 = +7$ diametrical mode is the last resolvable mode with a resolution of 20 pressure signals. As already presented in figure 11.11 left, there is no standing wave in the spiral casing for the cases $k_1 = +7, -4$ and $+5$.

For $k_1 = -2$, the diametrical mode rotates with a spinning speed of $\omega_1/\omega_b = -9$ and features 2 maxima. It means that using a pressure transducer in the vaneless gap, the frequency of $f/f_b = 18$ is measured. The representation clearly points out the standing wave in the spiral case with the related positions of pressure nodes and maxima. The interaction between the standing wave and the diametrical mode are clearly pointed out through the pressure in the guide vanes where pressure fluctuations have similar amplitudes.

From these results it can be concluded that the hydroacoustic model of the pump-turbine enables to obtain and visualize the RSI pressure fluctuation patterns. Standing wave and diametrical modes are pointed out and corresponding spinning speeds are properly obtained too. The high amplitude of the standing wave in the spiral casing for $f/f_b = 18$ is probably related to a natural frequency of the hydraulic system which is close. However, it is important to notice that the rotating impeller corresponds to an unsteady boundary condition at the end of the guide vanes. This makes it difficult to do modal analysis using linearized approaches. One of the major advantages of simulating the dynamic behavior of such a system in the time domain is that it offers the possibility to take into account such non-linearities. The modelling based on a valve network driven according to the flow distribution between stationary and rotating parts appears to be efficient for the simulation of the hydroacoustic part of the RSI phenomenon. This approach has the advantage to provide also the pressure fluctuations due to RSI in the rotating impeller.

11.6 Parametric Study

As the hydroacoustic parameters determination is based on a simplified approach and some parameters are selected arbitrarily, a parametric study is performed in order to assess the sensitivity of the hydroacoustic model to these parameters. Therefore, the influence of the following parameters is investigated in this paragraph: (i) blade thickness; (ii) impeller vane wave speed; (iii) guide vane wave speed; (iv) impeller rotating frequency. The influence of these 4 parameters is investigated focusing on the frequency, $f/f_b = 18$, mode $k_1 = -2$.

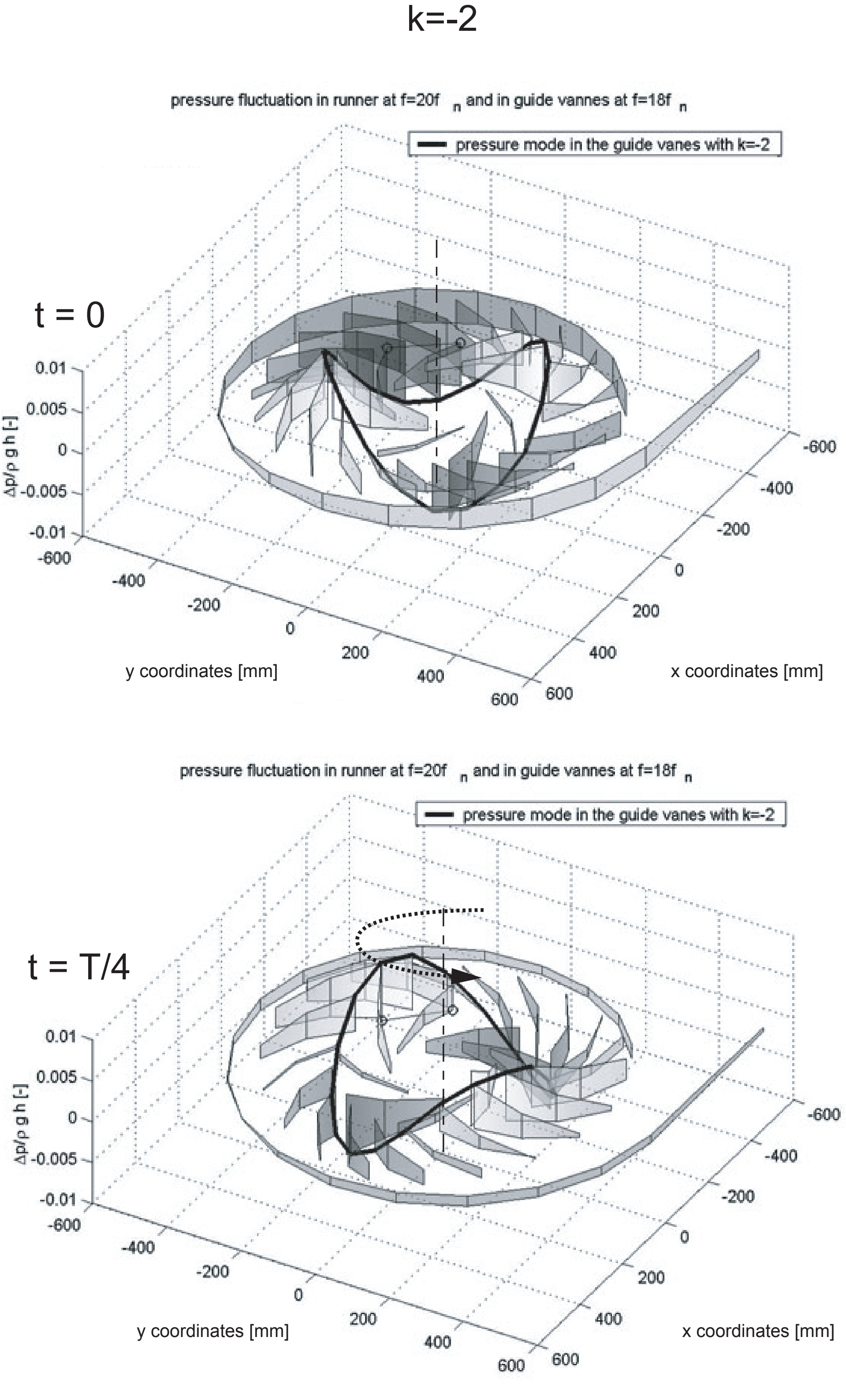

Figure 11.12: Pressure fluctuation patterns in the pump-turbine for $k_1 = -2$, $f/f_b = 18$, for $t = 0$ (top) and $t = T/4$ (bottom).

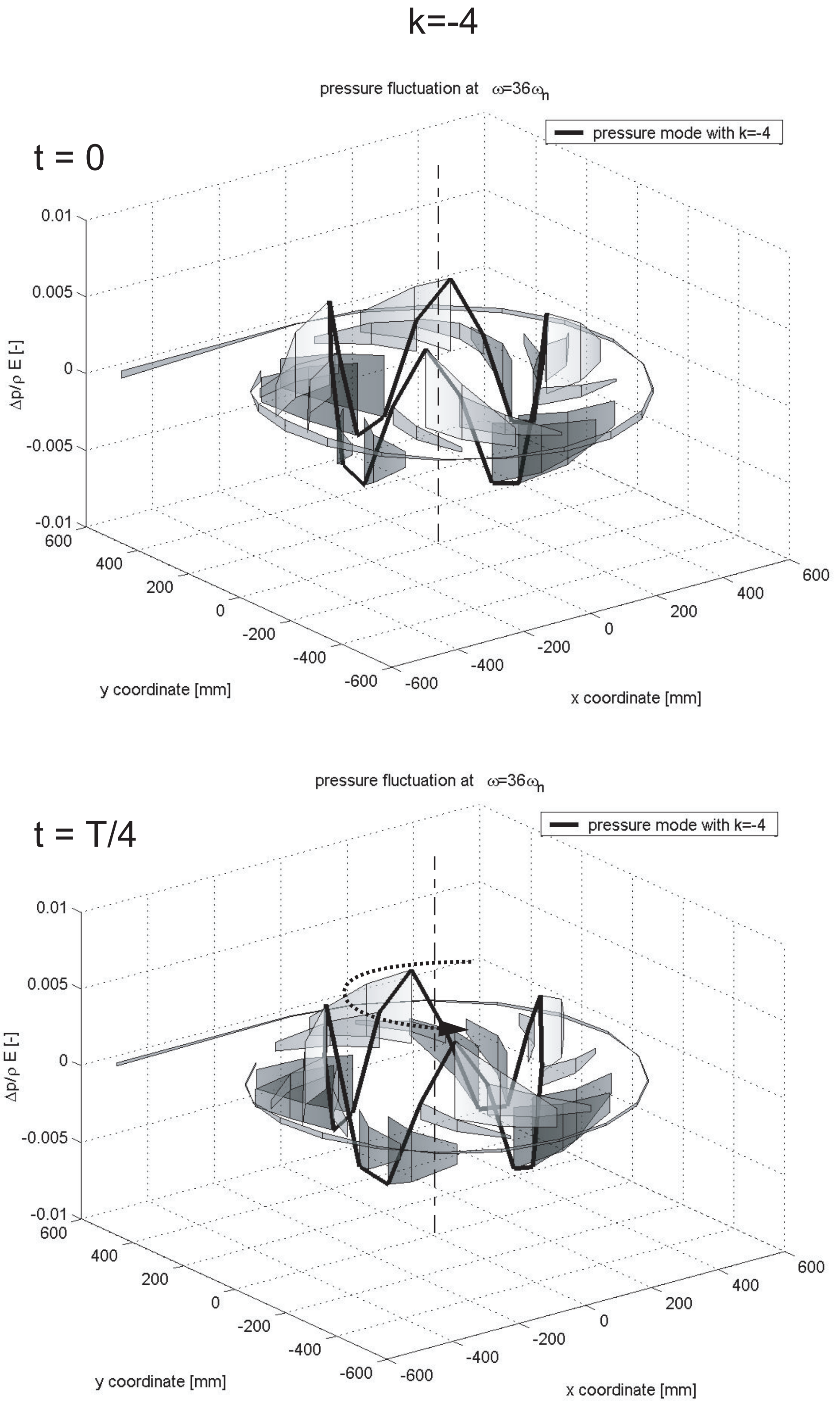

Figure 11.13: Pressure fluctuation patterns in the pump-turbine for $k_1 = -4$, $f/f_b = 36$, for $t = 0$ (top) and $t = T/4$ (bottom).

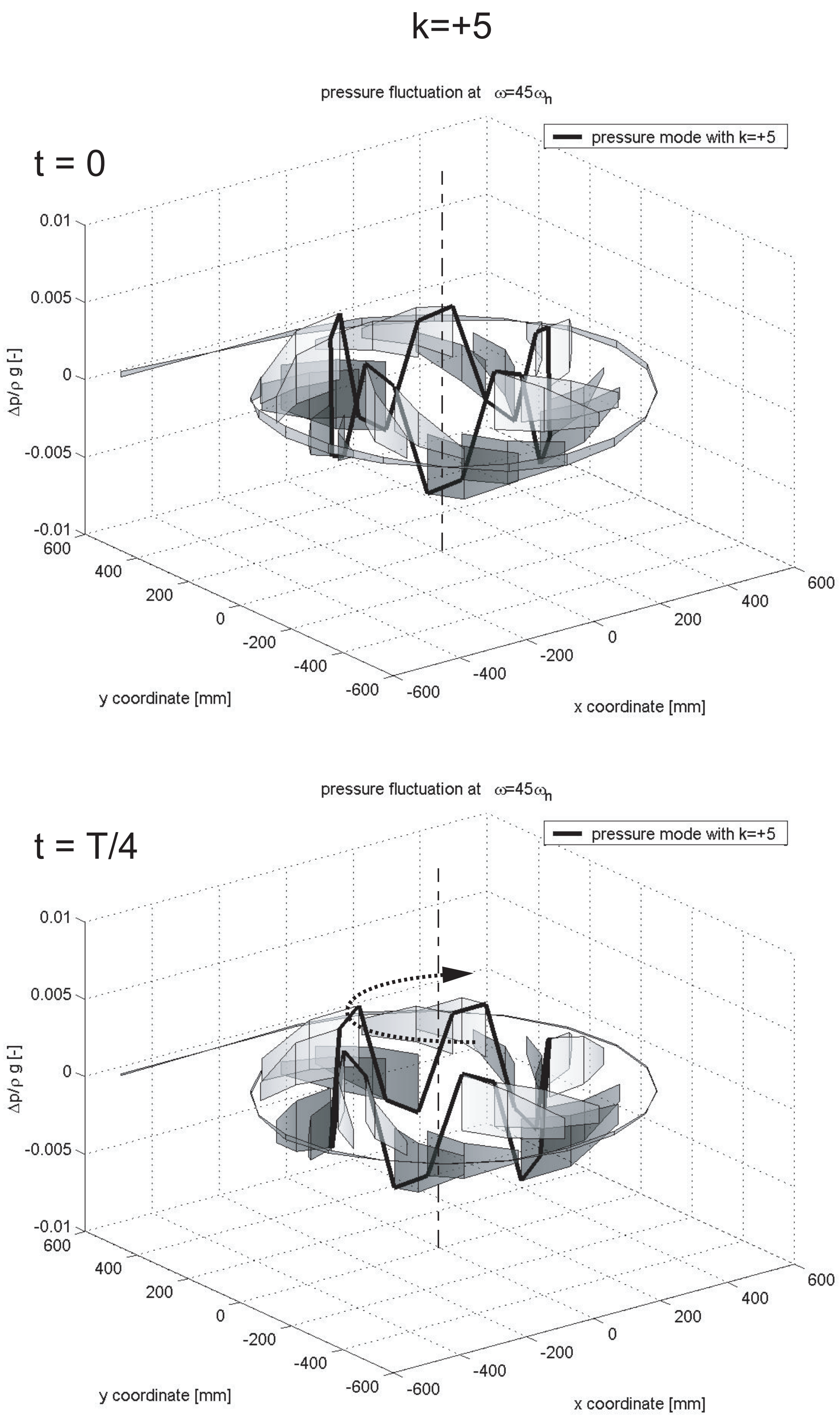

Figure 11.14: Pressure fluctuation patterns in the pump-turbine for $k_1 = +5$, $f/f_b = 45$, for $t = 0$ (top) and $t = T/4$ (bottom).

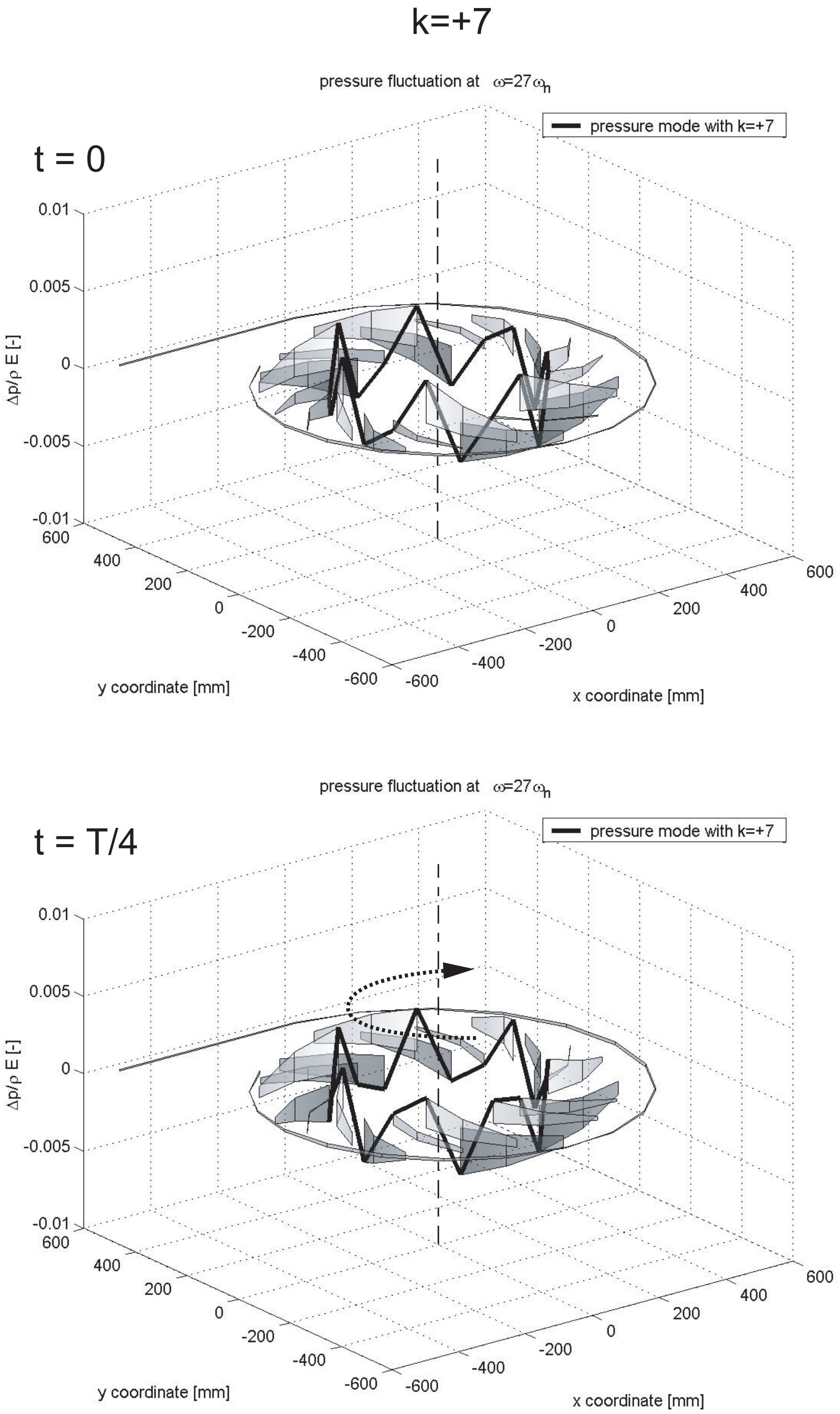

Figure 11.15: Pressure fluctuation patterns in the pump-turbine for $k_1 = +7$, $f/f_b = 27$, for $t = 0$ (top) and $t = T/4$ (bottom).

11.6.1 Blade Thickness Influence

The model of the excitation is based on the flow distribution between the stationary part and the rotating parts. The resulting discharge law between the 20 guide vanes and the 9 impeller blades can account for the guide vane and impeller blade thickness. The equivalent thickness of these blades affects the evolution of the connection area between a guide vane and an impeller vane. The figure 11.16 presents the 4 possible configurations which are : (A) no blade thickness, (B) consideration of the guide vane blade thickness only, (C) consideration of the impeller blade thickness only and (D) consideration of both guide vane and impeller blade thickness. The 4 different evolutions of the discharge law of the configurations (A), (B), (C) and (D) are represented on the right hand side of figure 11.16.

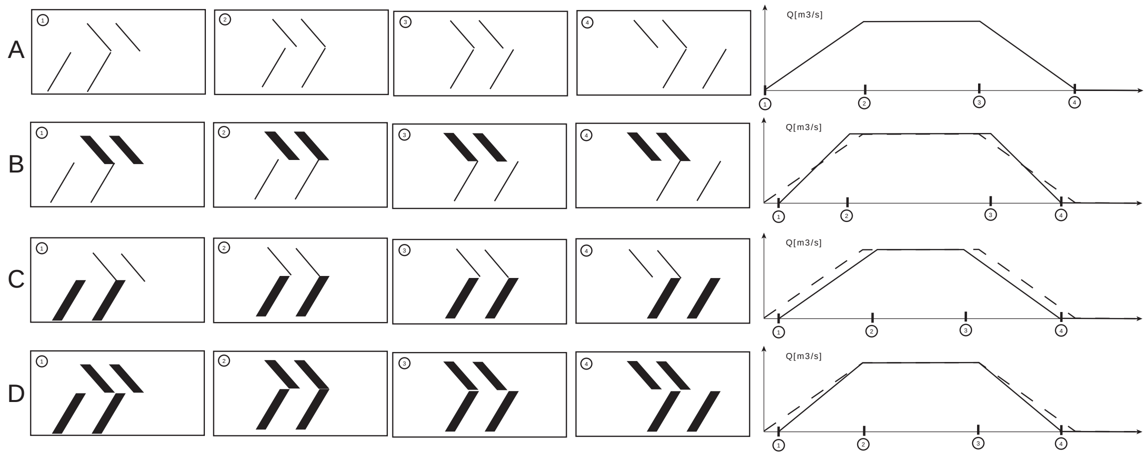

Figure 11.16: Discharge law resulting from the guide vane and impeller blade thicknesses consideration.

Considering the configurations (B), (C) and (D) 3 series of simulations are performed considering different blade thicknesses e_b. The resulting amplitudes of the pressure fluctuations in the vaneless gap are presented in figure 11.17. Configurations (B) and (C) provide similar pressure amplitudes in the vaneless gap for identical thicknesses. The combination of both thicknesses, configuration (D), induces much higher pressure amplitudes. These results show that the higher the blockage effects due to blade thickness, the higher the pressure amplitudes in the vaneless gap.

A dynamic pressure amplification factor is used to evaluate the influence between the vaneless gap pressure amplitudes and the amplitudes in the spiral casing. It enables separating the influence of any parameter on the RSI excitation and on the dynamic response of the system. The amplification factor is defined as the ratio between the pressure at any point in the spiral case and the average pressure in the vaneless gap and is expressed as:

$$DA = \frac{p_{\text{spiral}}}{\overline{p}_{\text{vaneless gap}}} \tag{11.9}$$

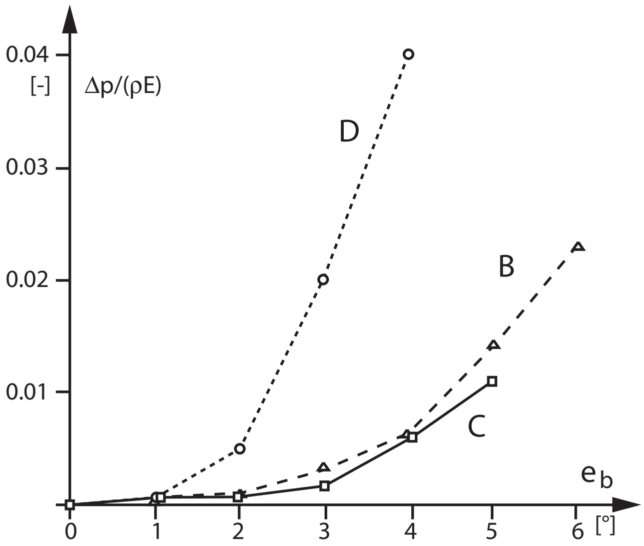

Figure 11.17: Pressure fluctuation amplitudes in the vaneless gap for the blade thickness arrangements of figure 11.16 for $f/f_b = 18$.

The figure 11.18 presents the dynamic amplification factor for 3 different guide vane thicknesses. It appears that even if the absolute amplitudes of the pressure fluctuations increase as the excitation in the vaneless gap increases, the dynamic amplification factor remains constant for the 3 tested thicknesses. One interesting consequence of this result is that even if the excitation parameters are arbitrary, the dynamic amplification will be meaningful. It also means that if the pressure fluctuations can be measured in the vaneless gap during the scale model tests, it would be possible to predict the amplitude of pressure fluctuations in the spiral case.

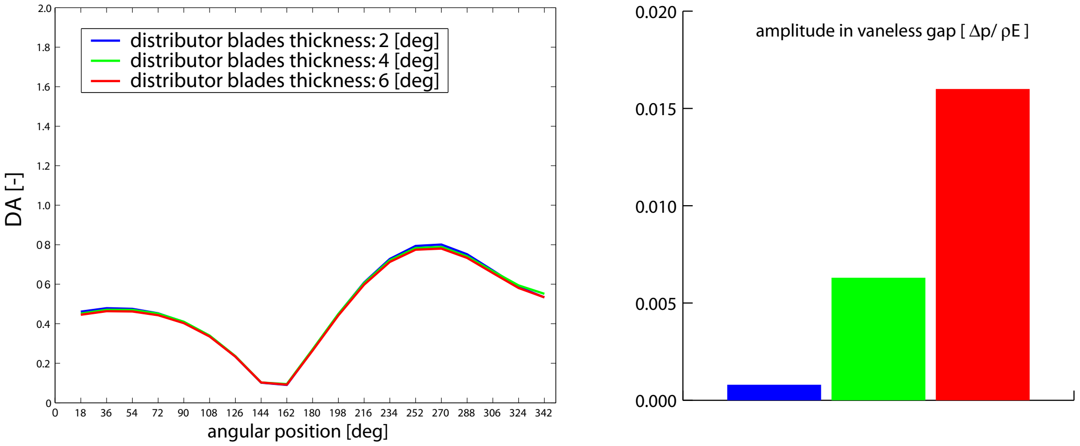

Figure 11.18: Influence of the distributor blade thickness on the dynamic amplification between spiral case and vaneless gap for $f/f_b = 18$.

11.6.2 Impeller Vane Wave Speed Influence

The influence of the impeller vane wave speed is investigated by simulating the dynamic behavior of the system considering three different values for this parameter. The chosen values for the impeller wave speed are 700 m/s, 800 m/s and 900 m/s. The figure 11.19 presents the dynamic amplification factor DA for the 3 different impeller vane wave speeds. It is clearly shown that the influence of the impeller vane wave speed is negligible. It means that for pump-turbines the combined effect of small vaneless gap and the impeller rotation acts like a dead end for such a frequency. However, this is right only as long as the diffuser remains short compared to the system dimensions.

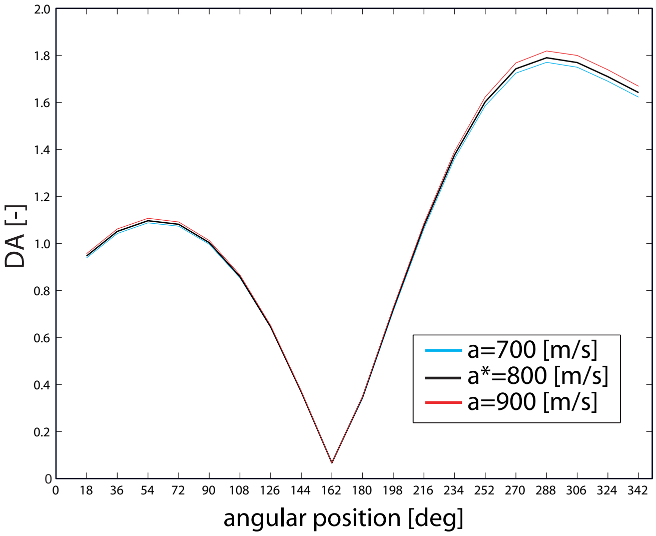

Figure 11.19: Influence of the impeller vane wave speed on the dynamic amplification between spiral case and vaneless gap for $f/f_b = 18$.

11.6.3 Guide Vane Wave Speed Influence

Four different values of the guide vane wave speed are chosen to investigate the influence of this parameter on the dynamic amplification between vaneless gap and spiral casing. The chosen values for the guide vane wave speed are 700 m/s, 800 m/s, 900 m/s and 1000 m/s. The resulting dynamic amplification DA and the mean value of the vaneless gap pressure fluctuation are presented in figure 11.20. The mean pressure fluctuation in the vaneless gap remains constant for the 4 cases. However, the dynamic amplification is strongly influenced by the guide vane wave speed. This is related to the fact that travelling time between vaneless gap and spiral casing affects strongly natural frequencies of the hydraulic system. It seems that, in this case, reducing the guide vane wave speed makes a natural frequency of the hydraulic system closer to $f/f_b = 18$.

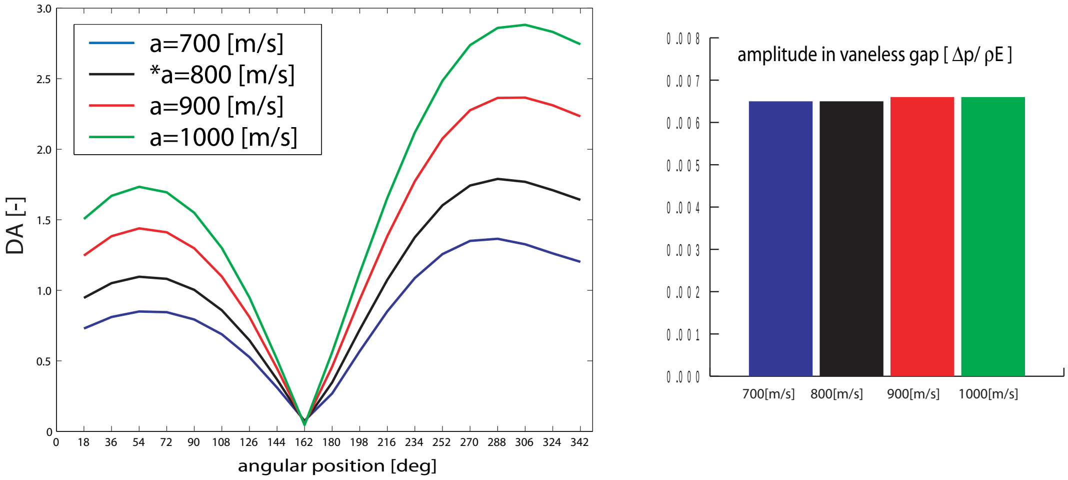

Figure 11.20: Influence of the guide vane wave speed on the dynamic amplification between spiral case and vaneless gap for $f/f_b = 18$.

11.6.4 Impeller Rotating Frequency Influence

Four different impeller rotation speeds are chosen to investigate the influence of this parameter. The chosen values corresponds to $f = 18 \cdot f_b = 292, 296, 300, 304\ Hz$. The resulting dynamic amplification DA and the mean value of the vaneless gap pressure fluctuations are presented in figure 11.21. The impeller rotating speed strongly influences the dynamic amplification between the vaneless gap and the spiral case. This is due to the change of excitation frequency, which seems to become closer to a natural frequency of the hydraulic system when the rotating frequency decreases. This result is coherent with the influence of the guide vane wave speed. In one case, the natural frequency of the hydraulic system increases with the increase of the guide vane wave speed, and in the second case the excitation frequency is reduced until it matches the hydraulic natural frequency. However, in both cases the amplitudes of the pressure fluctuations in the vaneless gap remain constant.

11.7 Concluding Remarks

Rotor-stator interaction in Francis pump-turbines may causes strong pressure fluctuations in the vaneless gap between the guide vanes and the impeller blades characterized by rotating diametrical mode shapes that can excite natural frequencies of the hydraulic system and resulting in standing waves in the spiral casing. These 2 effects can induce resonance with the mechanical or concrete structure jeopardizing the security of the power plant.

A new approach for the modelling of the hydroacoustic part of the phenomenon is proposed. A one-dimensional simulation model of a Francis pump-turbine is set up according to its topology featuring 20 guide vanes and 9 impeller vanes. The hydroacoustic parameters of the model are determined from the geometrical and structural characteristics of the machine and the test rig.

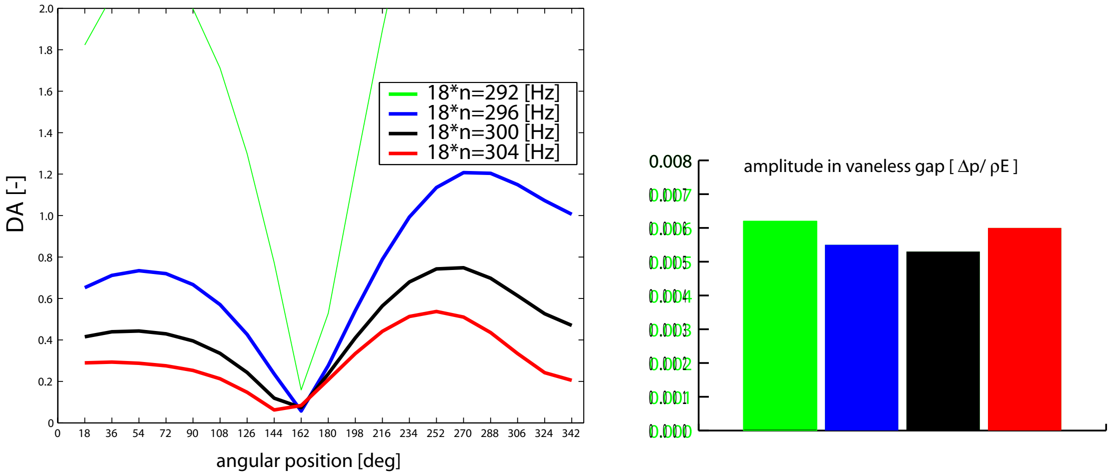

Figure 11.21: Influence of the impeller rotating speed on the dynamic amplification between spiral case and vaneless gap for $f/f_b = 18$.

The resulting RSI model comprises a network of 180 valves connecting each guide vane with each impeller vane. The valve opening functions are driven according to the flow distribution between the stationary and the rotating parts. The analysis of the pressure fluctuations resulting from the rotor-stator excitation shows that RSI patterns like rotating diametrical pressure modes and standing waves are properly simulated. The influence of the standing wave on the diametrical pressure mode is pointed out. The chosen excitation model appears to be realistic for the investigation of the hydroacoustic part of the RSI.

Moreover, a parametric study investigating the influence of blade thickness, impeller blades and guide vane wave speeds and impeller angular speed is carried out. It results that the wave speed in the impeller blades has not significant influence. The influence of the guide vane wave speed and of the impeller rotating frequency tends to show that the amplitude of the standing wave in the spiral casing for the frequency $f/f_b = 18$ is strongly affected by these parameters because of the closeness of a natural frequency of the hydraulic system.

Overall, this model gives satisfactory qualitative results and needs to be validated experimentally. However, if the dynamic amplification gives reliable trends, the determination of the absolute pressure fluctuation amplitudes is more challenging. The excitation model is based on the flow distribution between the stationary parts and the rotating parts of the machine. Its parameters are only related to connection area between guide vanes and impeller blades evolution due to impeller rotation. To obtain a more reliable quantitative result, the excitation model should be improved and be able to take into consideration all the parameters affecting RSI like the gap amplitude, the wake angle of the impeller blade, the blades thickness, etc. This could be achieved through the coupling of a one-dimensional code for the modeling of the hydraulic system with a CFD tool for the modeling of the RSI excitation. This approach seems realistic regarding the negligible influence of the impeller hydroacoustic parameters.

Chapter 12

Prediction of Pressure Fluctuations on Prototype

12.1 General

Direct computation of the prototype resonance due to vortex rope excitation using CFD computation requires taking into account fluid compressibility, wall deflections, cavitation modelling, and the geometry of the entire power plant. Such an approach is not yet feasible with current computation performance and models. Therefore, there is still a large place for prediction methods based either on scale models to prototype transposition or on identification based modelling.

12.2 Transposition from Scale Model to Prototype

12.2.1 Similitude Law in Hydraulic Turbomachines

The study of the flow in a prototype using scale model requires to ensure the same velocity distribution at both the inlet and the outlet of the turbine. Therefore, the geometries should be homologous and the velocity triangles should be identical. This condition is fulfilled if the discharge and energy coefficient are identical on both machines. Indeed, these coefficients define the ratio between the peripheral velocity U, the discharge velocity C_m and the absolute velocity taken here arbitrarily as $C = \sqrt{2 \cdot E}$ and can be expressed as follows:

$$\varphi = \frac{C_m}{U} = \frac{Q}{\pi \cdot R_{ref}^3 \cdot \omega} \quad ; \quad \psi = \frac{C^2}{U^2} = \frac{2 \cdot E}{R_{ref}^2 \cdot \omega^2} \tag{12.1}$$

Then the transposition of the internal and external forces acting on the fluid can be investigated through the Navier-Stokes equations which can be written in the compact derivative form as follows:

$$\underbrace{\frac{D\overrightarrow{C}}{Dt}}_{\text{inertia forces}} = \underbrace{-\frac{1}{\rho} \cdot \overrightarrow{\nabla} p}_{\text{pressure forces}} + \underbrace{\overrightarrow{f}}_{\text{body forces}} + \underbrace{\nu \cdot \overrightarrow{\nabla}^2 \cdot \overrightarrow{C}}_{\text{viscous forces}} \tag{12.2}$$

Expressing the particle derivative and rearranging the above equation gives:

$$\frac{\partial \overrightarrow{C}}{\partial t} + (\overrightarrow{C} \cdot \overrightarrow{\nabla}) \cdot \overrightarrow{C} = -\overrightarrow{\nabla}(\frac{p}{\rho} + g \cdot Z) + \nu \cdot \overrightarrow{\nabla}^2 \cdot \overrightarrow{C} \tag{12.3}$$

For expressing the Navier-Stokes equations in the dimensionless form, let introduce the dimensionless values:

$$\overrightarrow{\nabla}' = \overrightarrow{\nabla} \cdot L_{ref} \quad ; \quad t' = t \cdot \frac{C_{ref}}{L_{ref}} \quad ; \quad \overrightarrow{C}' = \frac{\overrightarrow{C}}{C_{ref}} \tag{12.4}$$

Introducing equations 12.4 in equation 12.3 and multiplying by $L_{ref}/(C_{ref}^2)$ yields:

$$\frac{\partial \overrightarrow{C}'}{\partial t'} + (\overrightarrow{C}' \cdot \overrightarrow{\nabla}') \cdot \overrightarrow{C}' = -\overrightarrow{\nabla}' \cdot \left(\underbrace{\frac{p - p_{ref}}{\rho \cdot C_{ref}^2}}_{Eu} + \underbrace{\frac{g \cdot L_{ref}}{C_{ref}^2}}_{1/Fr^2} \cdot (\frac{Z - Z_{ref}}{L_{ref}}) \right) + \underbrace{\frac{\nu}{L_{ref} \cdot C_{ref}}}_{1/Re} \cdot \overrightarrow{\nabla}'^2 \cdot \overrightarrow{C}' \tag{12.5}$$

From the dimensionless Navier-Stokes equation 12.5 the following dimensionless numbers are derived:

- Euler number: $Eu = \frac{p-p_{ref}}{\rho \cdot C_{ref}^2}$, ratio between pressure and inertia forces;
- Froude number: $Fr = \frac{C_{ref}}{\sqrt{g \cdot L_{ref}}}$, ratio between the inertia and gravity forces;
- Reynolds number: $Re = \frac{C_{ref} \cdot L_{ref}}{\nu}$, ratio between the inertia and viscous forces.

In addition, one can also express 2 others useful dimensionless numbers that are:

- the Mach number $Ma = \frac{C}{\sqrt{dp/d\rho}} = \frac{C}{a}$: another expression between the inertia and pressure forces;
- the Strouhal number $St = \frac{C_{ref} \cdot \Delta t}{L_{ref}}$: the ratio between the inertia and unsteady forces.

Fulfilling all the similitude laws leads to preform full scale experiments. Consequently only some of them can be satisfied during scale model tests and have to be chosen carefully according to the focus of the experiments.

12.2.2 Similitude of Cavitation

Cavitation problems require fulfilling the Thoma and Froude similitudes in addition to the kinematic similitude. The first similitude ensures having the same pressure at a given point with respect to a reference pressure, while the second ensures having the same pressure gradient $\partial p/\partial l$ along the curvilinear abscissa of the machine. In addition, the number of cavitation germs in the water, *i.e.* the number of nuclei by m^3 should be identical [73]. However, while the Thoma and the nuclei density similitudes can be achieved on the test rig, it is more problematic to achieve the Froude similitude. The Froude similitude leads to the following statement between model and prototype:

$$\left(\frac{E}{L_{ref}}\right)_M = \left(\frac{E}{L_{ref}}\right)_P \tag{12.6}$$

The smaller dimension of the scale model results in smaller test specific energy which combined with the Thoma similitude requires upstream pressure below atmospheric pressure. In addition, amplitudes of the pressure fluctuations become comparable to the pressure "noise" of the test rig. Consequently, the Froude similitude is very difficult to achieve for high specific speed Francis turbines.

12.2.3 Similitude of Pressure Fluctuations

The similitude of pressure pulsation requires satisfying both Strouhal and Euler similitudes [80]. These 2 statements provide the frequency and amplitudes of the pressure pulsation from the following equations:

$$\left(\frac{f_{puls}}{n}\right)_M = \left(\frac{f_{puls}}{n}\right)_P \quad \text{and} \quad \left(\frac{\Delta p}{\rho \cdot E}\right)_M = \left(\frac{\Delta p}{\rho \cdot E}\right)_P \tag{12.7}$$

However, the 2 above transposition rules are true only if interactions with the hydraulic system are small. If interactions occur, the impedance similitude should also be satisfied.

12.2.4 Similitude of Impedances

The similitude of impedances requires similitude of the characteristic impedance $Z_c = a/(g \cdot A) = Z_T = E/Q$ and the similitude of the number of waves $k = (\omega \cdot l)/a$ [80]. These two statements lead to the following equations:

$$\left(\frac{a}{n \cdot L_{ref}}\right)_M = \left(\frac{a}{n \cdot L_{ref}}\right)_P \quad \text{and} \quad \left(\frac{a}{n \cdot l_{ref}}\right)_M = \left(\frac{a}{n \cdot l_{ref}}\right)_P \tag{12.8}$$

Here L_{ref} is the reference dimension of the turbine, usually $R_{\bar{1}e}$, and l_{ref} is the longitudinal reference length of the hydraulic circuit. Combination of the 2 above equations leads to the similitude criteria:

$$\left(\frac{l_{ref}}{L_{ref}}\right)_M = \left(\frac{l_{ref}}{L_{ref}}\right)_P \quad \text{and} \quad \left(\frac{a^2}{E}\right)_M = \left(\frac{a^2}{E}\right)_P \quad \text{if } \psi_M = \psi_P \tag{12.9}$$

The 2 above similitude equations indicate that: (i) the adduction and tailrace tunnel systems must be homologous; (ii) the wave speed ratio is given by the ratio of the square root of the specific energies.

12.2.5 Limitation of the Transposition Method

The aim of the transposition method is to have direct similitude between pressure pulsations measured on scale model and those measured on prototype. The difficulty arises from the cavitation vortex rope similitude. The similitude of impedance shows that the wave speed must be in the ratio of the square root of the specific energies E. However, if this condition can be fulfilled for adduction and tailrace tunnel, it is more complex for the draft tube itself whose wave speed is strongly driven by the diameter distribution of the vortex rope, *i.e.* the Froude similitude, the wall deflection and also the dissolved air. Consequently it is not possible to adjust the wave speed on the model, and particularly because the wave speed on prototype is unknown.

Fischer *et al.* [52] also concluded from model tests, that model tests are representative as long as there is no interaction between the turbine and the hydraulic circuit on both sides: on the test rig and on the prototype. Nevertheless, the prediction of resonance on the prototype is precisely the goal.

Another approach for predicting the pressure pulsation on the prototype is to set up a hydroacoustic model of the prototype installation, and to use different identification methods, experimental or numerical, to determine the parameters of the model. Regarding the experimental approaches, Dörfler [40], Jacob [82] and also Fritsch and Maria [58] proposed solutions for the identification of vortex rope compliance and excitation source. A similar approach is proposed in the following section.

12.3 Proposition for Part Load Resonance Risk Assessment Methodology

12.3.1 General

In order to assess the resonance risks on prototypes, pressure fluctuation measurements are carried out during scale model tests to identify experimentally the pressure excitations sources and the vortex rope compliance [40]. Then, the pressure fluctuations due to a non uniform pressure field at the runner outlet [109], [114], can be decomposed into two parts as proposed by Angelico [5]; (i) the rotating part, due to vortex rotation, and (ii) the synchronous pulsating part resulting from the spatial perturbation of the rotating part. The pressure excitation source related to the synchronous pulsating part can be extracted using the procedure described by Dörfler, [40]. It is then possible to deduce the resulting mechanical torque pulsation in the frequency domain, using an appropriate one dimensional model of the full hydraulic system based on the impedance method, including the model of the vortex rope and the turbine itself, [45], [142], [58]. However, obtaining the induced electrical power pulsations, requires the inclusion of the linearized model of the synchronous machine, the voltage regulator, transformer, etc, which is very challenging.

Therefore a methodology using a time domain simulation for the determination of the part load resonance risk and its impact on the electrical power pulsations of a Francis turbine power plant is proposed. This risk is evaluated for the hydroelectric power plant with 4×250 MW Francis turbines of section 7.5. First, the model of the draft tube, taking into account the vortex rope volume and the pressure excitation source is described. Then a simplified model of the piping is derived for analyzing qualitatively the resonance risk of the power plant. Finally, a time domain simulation of the dynamic behavior of the whole hydroelectric power plant is performed in order to deduce the transfer function between the pressure excitation in the draft tube and the synchronous machine electrical active power. The influence of the draft tube wave speed, *i.e.* vortex rope volume, is presented.

12.3.2 Modelling of the Hydroelectric Power Plant

Hydraulic Power Plant Model

The layout of the hydroelectric power plant of interest is repeated in figure 12.1. This power plant corresponds to the hydroelectric power plant previously presented in section 7.5; the main parameters of the hydroelectric power plant being summarized in table 7.8. For this investigation the power plant is assumed to be connected to an infinite power network of $f = 50\ Hz$. The model of the power plant includes the hydraulic system, the synchronous generators with their voltage regulators and the transformers.

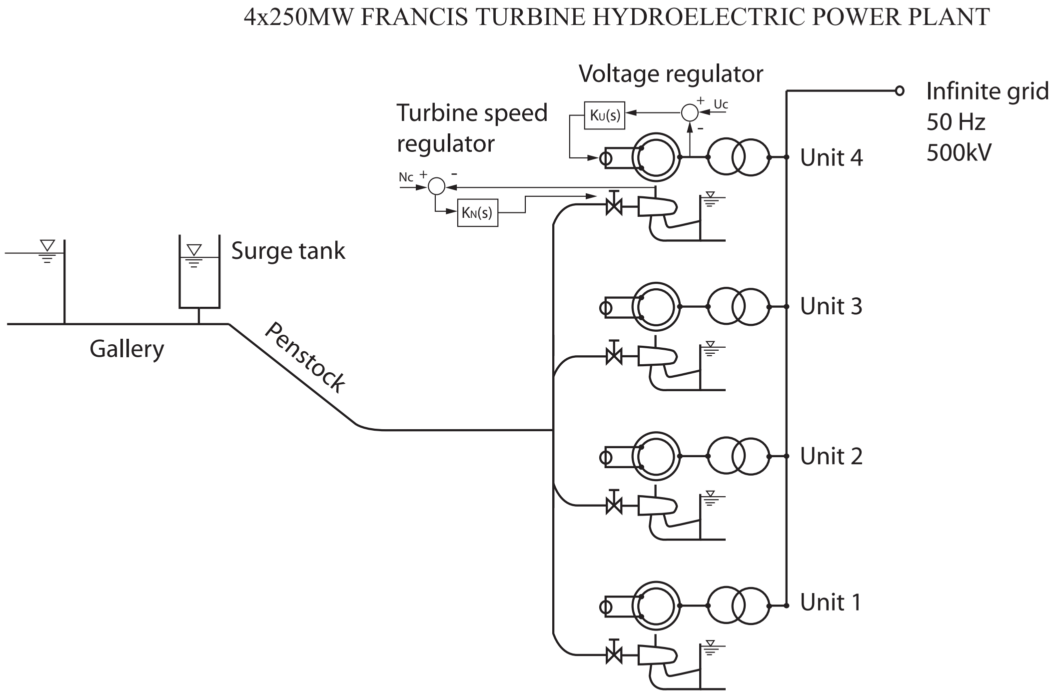

Figure 12.1: Layout of the hydroelectric power plant.

Draft Tube Modelling

For resonance risk assessment purposes, the Francis turbine draft tube can be properly modelled by a pressure source excitation in series with 2 pipes, as presented figure 12.2. In this model, the excitation source can be determined from scale model testing, [40], or CFD computation, [129], while the pipe is modelled using a one dimensional hydroacoustic model that requires knowing the following parameters: (i) the length of the pipe, obtained from the geometry; (ii) the cross section, determined also from the geometry; (iii) the wave speed, to be calculated or measured.

The geometrical parameters can be estimated by piecewise integration from draft tube inlet to outlet. However, the determination of the wave speed of the draft tube for all operating conditions is a very challenging task. Therefore, the draft tube wave speed is taken as a parameter in this investigation. Nevertheless, it is convenient to link the draft

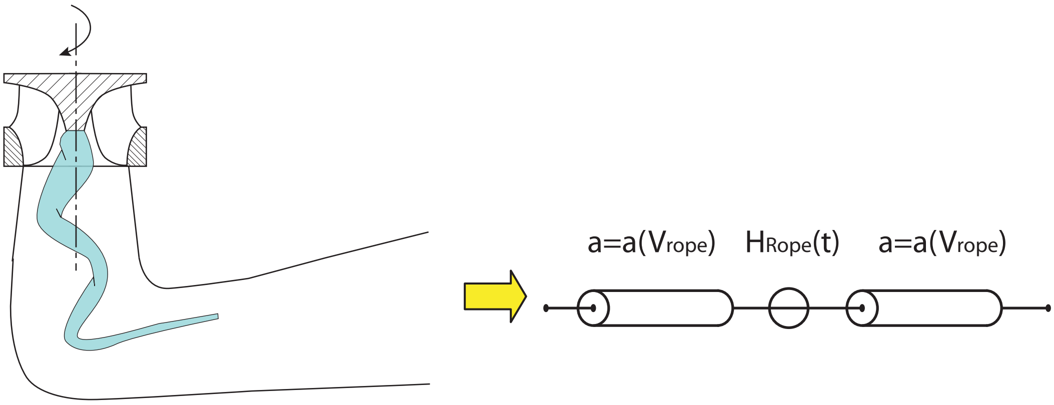

Figure 12.2: Model of the draft tube for resonance risk assessment.

tube wave speed to an equivalent rope diameter, resembling the approach developed by Philibert and Couston, [120], in order to link the wave speed to a physical dimension. Assuming a cross section of the draft tube with diameter D and with a rope diameter D_R, one can determine the gas volume fraction α of the cross section as follows:

$$\alpha = \frac{A_{Rope}}{A_{tot}} = \left(\frac{D_R}{D}\right)^2 \tag{12.10}$$

Where A_{rope} is the cross section of the rope and A is the total draft tube cross section for a given curvilinear abscissa. The wave speed in the liquid gas mixture is given by Wallis (1969) [152]:

$$a_m^2 = \frac{1}{\rho_m \cdot \left(\frac{\alpha}{\rho_g \cdot a_g^2} + \frac{(1-\alpha)}{\rho_L \cdot a_L^2}\right)} \tag{12.11}$$

The wave speed of the liquid gas mixture is represented as a function of the gas volume fraction, see figure 12.3 left, and as function of the cavitation rope rated diameter by combining equations 12.10 and 12.11, see figure 12.3 right. The wave speed of the mixture drops to very low values with increasing cavitation rope diameter. Cavitating rope diameters up to $D/D_R = 0.1$ are common in part load operation of Francis turbines, see Jacob [79]. For such rated diameters, the draft tube cross section wave speed would be below 100 m/s. However, it should be noticed that this model assumes a cylindrical vortex rope with constant diameter, from the draft tube inlet to outlet, whereas the real vortex rope is helicoidal and conical. Therefore, the presented approach is only useful to link the wave speed to a physical dimension. In addition, thermodynamic effects related to the cavitation phenomenon are neglected.

12.3.3 Resonance Risk Assessment Based on Simplified Model

The main natural frequencies of the piping system feeding the 4 turbines of the power plant can be estimated by means of the analysis of the natural frequencies of an equivalent pipe

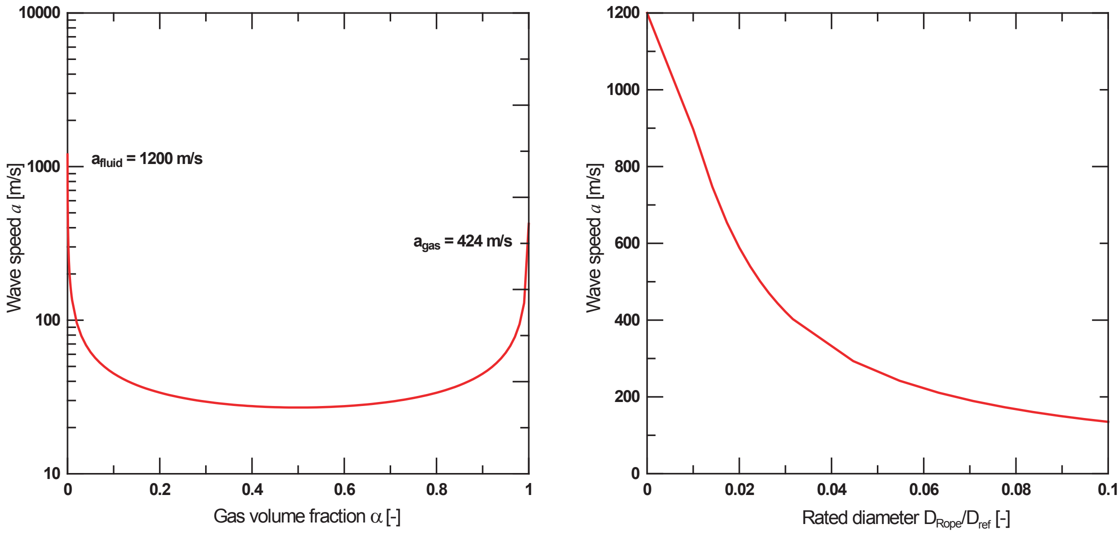

Figure 12.3: Wave speed in vapor/water mixture (left) and wave speed as function of rated diameter (right).

of the adduction system. Because of the longitudinal symmetry of the piping, a simplified model of the piping can be used. The simplified model, presented in figure 12.4, comprises 2 pipes: the adduction, and the draft tube. Thus the influence of the draft tube wave speed change on the natural frequencies can be qualitatively investigated.

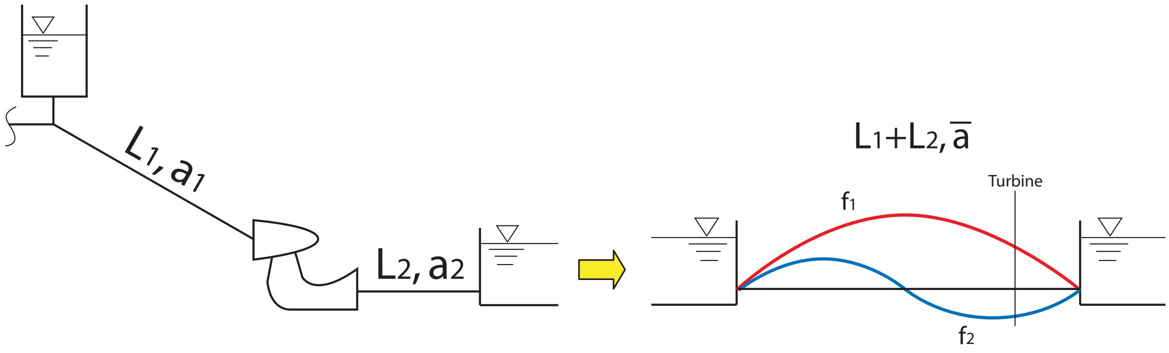

Figure 12.4: Simplified piping model.

The equivalent wave speed of the piping system is given by:

$$\bar{a} = \frac{L_1 + L_2}{\frac{L_1}{a_1} + \frac{L_2}{a_2}} \tag{12.12}$$

Considering both upstream and downstream free surface boundary conditions of the

Table 12.1: Main characteristics of the simplified model figure 12.4.

Description	**Length** $L[m]$	**Wave speed** $a[m/s]$
Adduction	1478	1146
Draft tube	30	1200, 200, 100, 50

piping, the equivalent wavelength of the eigen modes of the piping are given by:

$$\lambda_i = \frac{2}{i} \cdot (L_1 + L_2) \tag{12.13}$$

The corresponding natural frequencies are therefore given by [138]:

$$f_i = \frac{\overline{a}}{\lambda_i} = \frac{i}{2 \cdot \left(\frac{L_1}{a_1} + \frac{L_2}{a_2}\right)} \tag{12.14}$$

The 10 first natural frequencies of the simplified piping of figure 12.4 are computed for wave speeds in the draft tube ranging from $a = 1200\ m/s$ to $a = 50\ m/s$. The lengths and wave speeds of the simplified model are summarized in the table 12.1. The natural frequencies obtained for different rated cavitating rope diameters are presented in figure 12.5. As expected, the natural frequencies of the piping system decrease with decreasing the wave speed. The natural frequency of the generator $f_{generator} = 1.21\ Hz$ is also represented in figure 12.5. The graph indicates an intersection between the 4th piping natural frequency and the generator natural frequency for a draft tube wave speed of $a = 77\ m/s$. This intersection is in the range where pressure pulsations induced by the cavitating vortex rope extending from 0.2 to 0.4 times the turbine rotating frequency, n, are expected. This situation corresponds to one of the worst cases for the power plant, because there is a coincidence of the piping natural frequencies and the generator natural frequency. However, this requires that the pressure pulsation induced by the draft tube flow matches this frequency. In addition, the influence on the electrical power fluctuation is strongly dependant on the turbine position, relatively to the pressure mode shape corresponding to this 4^{th} natural frequency. Nevertheless, this simplified model shows the importance of investigating carefully the resonance risk for the power plant of interest.

12.3.4 Resonance Risk Assessment Based on a Complex Model

Generator Transfer Function

The transfer function of the synchronous machine between the mechanical and electromagnetic torques is calculated to deduce the generator natural frequency. Therefore, only the electrical part of the simulation model is taken into account. A PRBS signal is used to generate a mechanical torque white noise excitation, see figure 12.6 left. The transfer function between the mechanical and electromagnetic torques is calculated and represented in figure 12.6 right. This transfer function shows the generator natural frequency at 1.21 Hz, $0.217 \cdot n$, and mechanical masses natural frequency of 7.5 Hz, $1.35 \cdot n$ (described in chapter 7.5). The generator natural frequency is in the range of 0.2 to 0.4 n and represents thus a resonance risk.

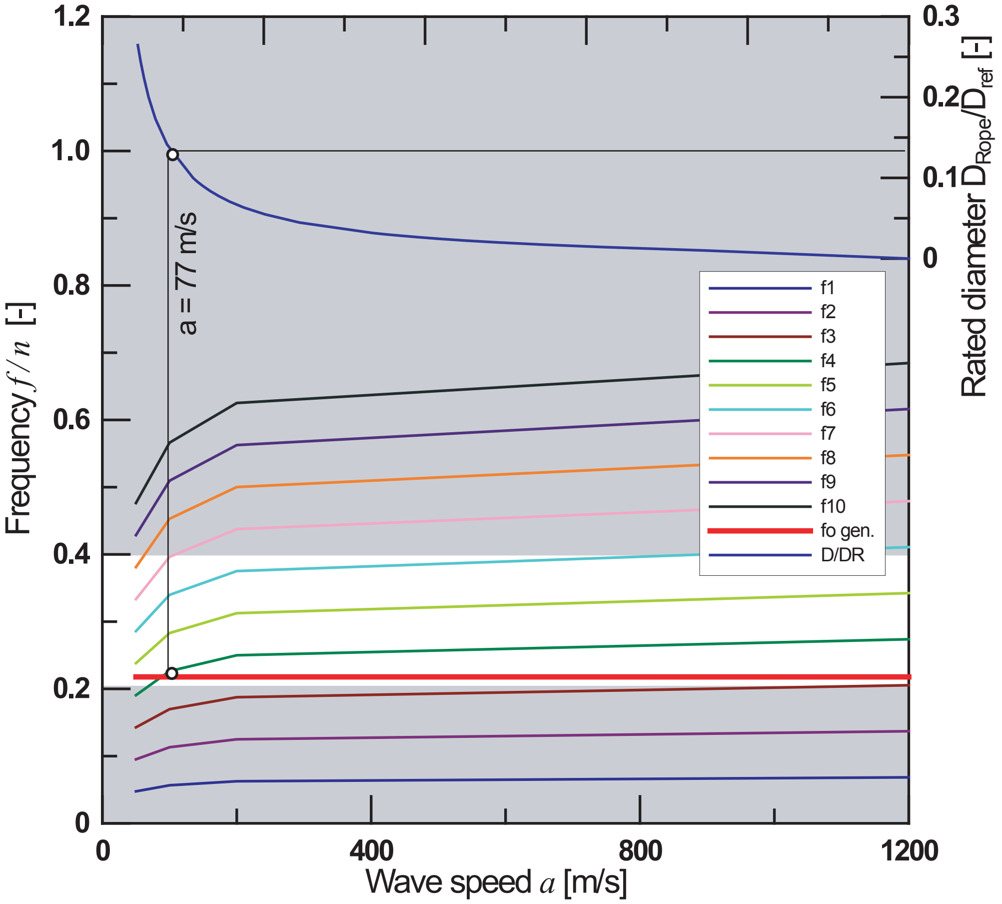

Figure 12.5: Power plant natural frequencies estimation with simplified model ($n = 5.555Hz$).

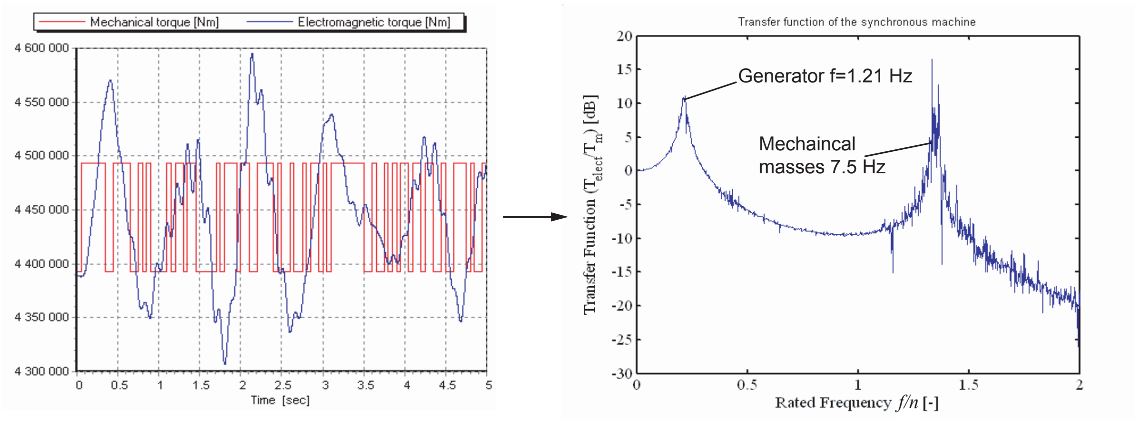

Figure 12.6: PRBS mechanical torque excitation of the generator (left) and resulting generator transfer function between mechanical and electromagnetic torque (right).

Piping Resonance

The full hydroelectric simulation model is taken into account to calculate the transfer function between the draft tube pressure source excitation and the electromagnetic torque. A PRBS draft tube pressure source excitation in the draft tube of the turbine of Unit 4 is considered for the time domain simulation. For this simulation the turbine speed governor is removed and the guide vanes are kept with constant opening of 40%, corresponding to 65% of the nominal discharge.

The resulting pressure oscillations in the piping system are represented as a waterfall diagram for draft tube wave speed values of: 200, 100, 77, and 50 m/s in figure 12.7. The pressure pulsations are represented as a function of the x coordinate starting from the surge tank, node 1, and extending along the piping until the Unit4 downstream tank, node 289, and the rated frequency f/n. It can be noticed that not all piping natural frequencies are excited; this is due to the draft tube excitation source relative position in the piping. It is pointed out that the value of natural frequencies drops with decreasing the draft tube wave speed. In addition, because the wave speed of the draft tube affects the pressure node and maxima location, these are not the same mode shapes that are excited for the different wave speeds. Regarding the frequency range of interest, 0.2 to 0.4 n, it can be seen that the lower the draft tube wave speed, the higher the number of natural frequencies in the frequency range of interest. Comparing these results with the simplified model it can be seen that the natural frequency at 77 m/s that was pointed out as critical is not excited by the draft tube pressure source and does not appear on the waterfall diagram, demonstrating the limitation of such simplified models.

Hydroelectric Resonance

The influence of the draft tube excitation on the mechanical and electromagnetic torques is evaluated by calculating the transfer function between the draft tube pressure excitation and both mechanical and electromagnetic torques. The 2 transfer functions are presented in figure 12.8 left and right respectively. Mechanical torque oscillations occur for all excited piping mode shapes. Moreover, the electromagnetic torque pulsations are strongly affected by the generator natural frequency. A clear amplification effect between the mechanical and the electromagnetic torque appears for a draft tube wave speed of 50 m/s, where there is coincidence of a piping natural frequency and generator natural frequency. Thus, the worst conditions for the power plant is when the draft tube excitation is at 0.217 n with a draft tube wave speed of 50 m/s. However, for this draft tube wave speed, electromagnetic torque pulsations are expected in almost the whole vortex rope frequency range due to the presence of 2 piping natural frequencies in this range, *i.e.* 0.217 n and 0.37 n.

Comparison with Experimental Data

Once the piping resonance frequency and mode shape as well as the generators resonance frequency are known for different wave speeds, these results have to be compared with measurements of draft tube pressure pulsations performed during scale model tests in order to evaluate the risk of resonance. The model tests, see figure 12.9, provide: (i) the vortex rope pressure pulsations frequencies and amplitudes [79]; (ii) the vortex rope

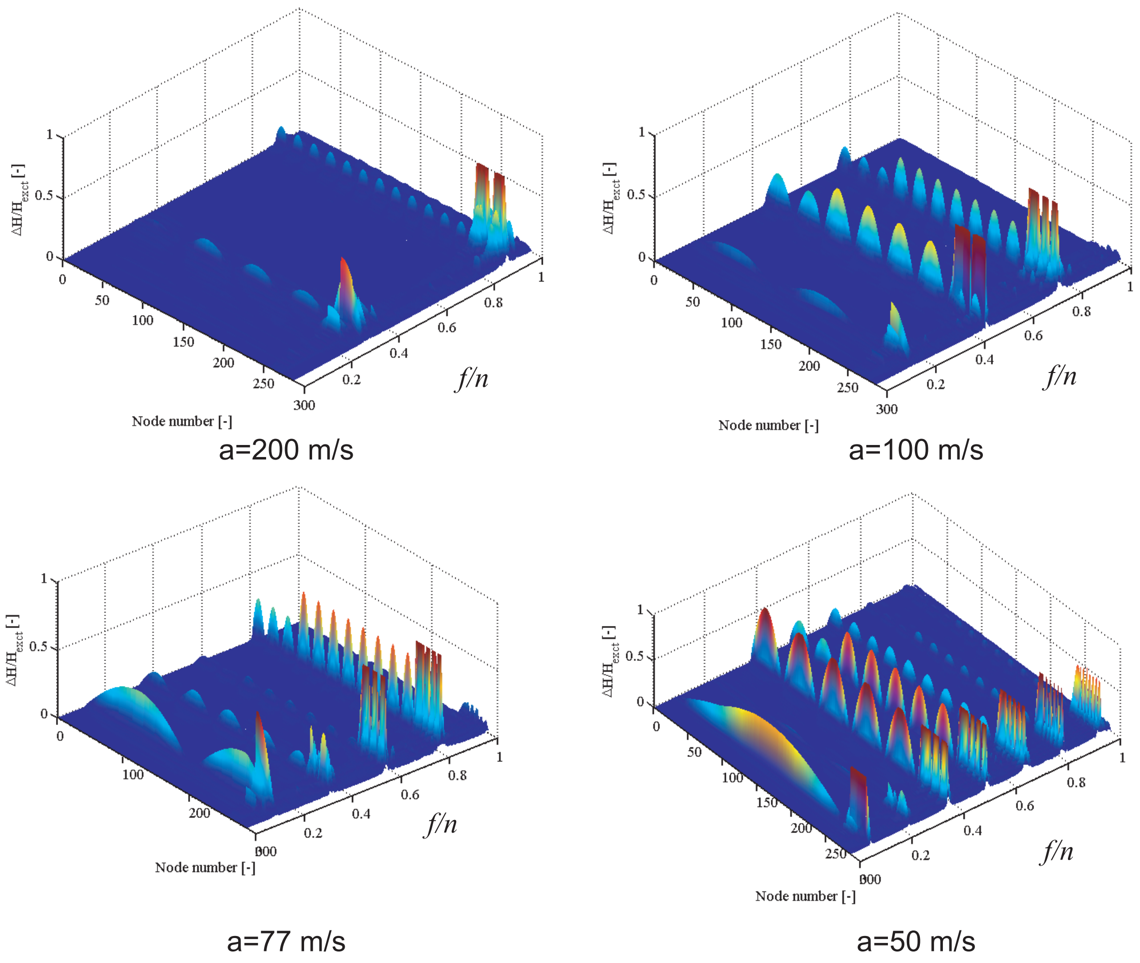

a=200 m/s

a=100 m/s

a=77 m/s

a=50 m/s

Figure 12.7: Piping pressure oscillations for different draft tube wave speed.

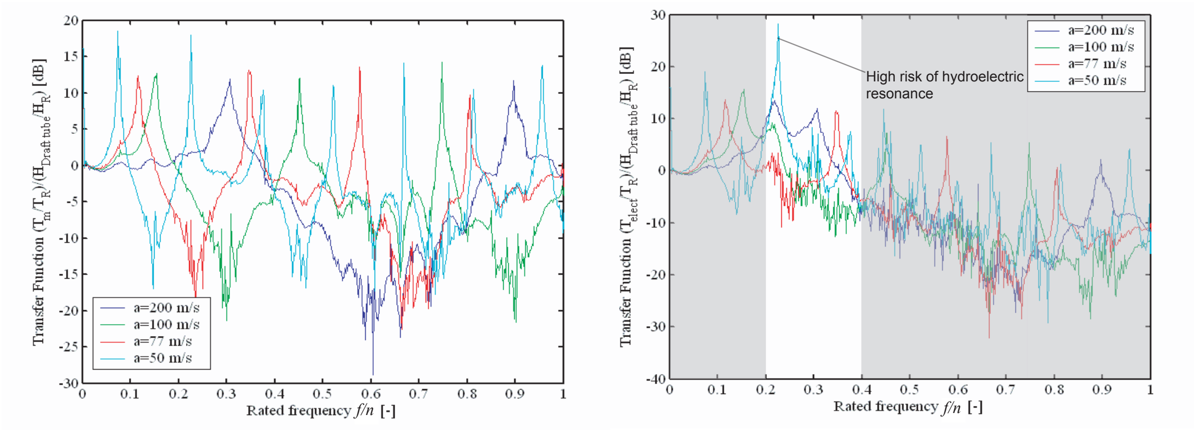

Figure 12.8: Transfer function between the draft tube pressure source and the turbine mechanical torque (left) and transfer function between the draft tube pressure source and the generator electromagnetic torque (right).

diameter by means of photography, or the vortex rope compliance by the method described by Dörfler [40].

Finally, the possible resonances with the piping system and with the generator are pointed out from cross checks between parametric simulations results and the model test data providing the set of resonant conditions. The amplitudes of pressure oscillations in the system and generator power swing can be estimated from the time domain simulation with the set of resonant parameters. The overall methodology is summarized in the synoptic scheme of figure 12.10.

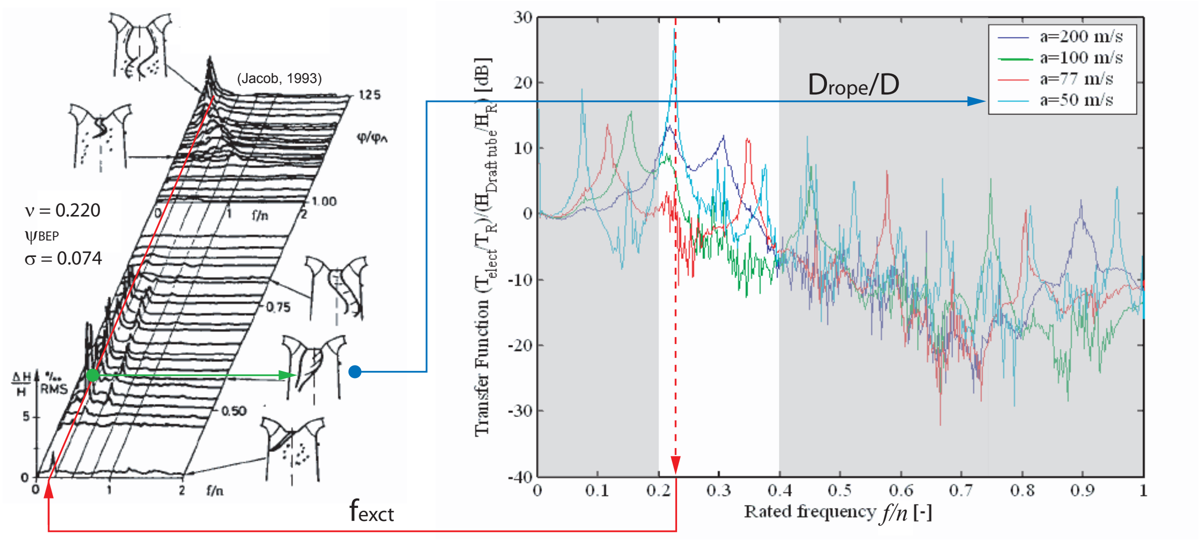

Figure 12.9: Assessment of hydroelectric resonance risk based on comparison of draft tube excitation vs electromagnetic torque transfer function from simulation with waterfall diagram of pressure fluctuations from experiments.

CFD Based Identification

It is also possible to deduce the required parameters from CFD computation. First, performing an unsteady single flow incompressible computation of the flow in the runner and draft tube, the volume of the vortex rope can be extracted for different cavitation number values by varying the downstream water level for the calculation of the iso-pressure p_v. Then, from the unsteady pressure wall, decomposition of the pressure provides the synchronous part of the pressure pulsation that corresponds only to the pressure source. Finally, the compliance of the vortex rope, calculated from the volume vs cavitation number evolution, and pressure source are injected into the hydroacoustic model for the prediction of the pressure and power fluctuations. This approach is summarized in figure 12.11. However, the CFD computation models are not yet able to predict the shape of the part load vortex rope well. Improvements are expected from new turbulence models, cavitation models or Large Eddy Simulation, LES, computations.

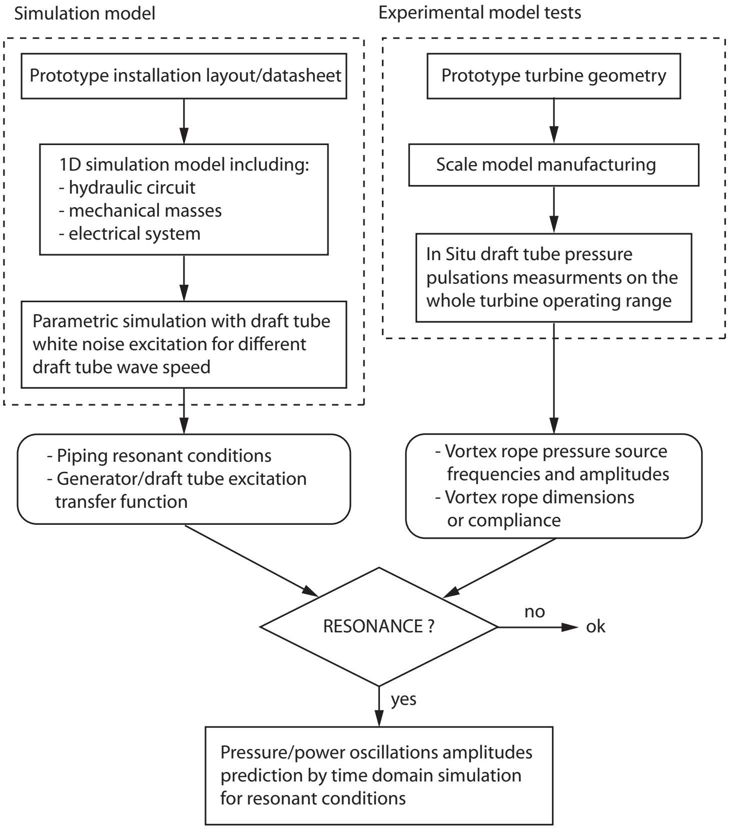

Figure 12.10: Synoptic scheme of the overall methodology.

Time domain analysis

In order to illustrate the consequence of a resonance in the hydroelectric power plant studied, a time domain simulation is performed with draft tube sinusoidal excitation at $f/n = 0.217$ with amplitude of $\Delta H = 10\ m$ and a draft tube wave speed of 50 m/s (the worst case for this power plant). For this simulation the turbine speed governor is neglected. The simulations results are respectively presented for the turbine variables, figure 12.12 a) and the generator variable figure 12.12 b). The time evolution of the head at the Unit 4 spiral casing and draft tube are presented in figure 12.12 c). The turbine head is strongly pulsating because of the difference of head between the inlet and the outlet of Unit 4 turbine. Consequently, the mechanical torque is pulsating at the vortex rope frequency. These mechanical torque pulsations are amplified by a factor 10 by the generator. Such situation would leads to catastrophic pressure and torque pulsations in the hydroelectric power plant. However, the amplitudes obtained with this simulation are not realistic, as they would be restricted by the non-linearities of the system such as the vortex rope cavitation number dependency, the damping of the fluid, the damping of the materials, etc.

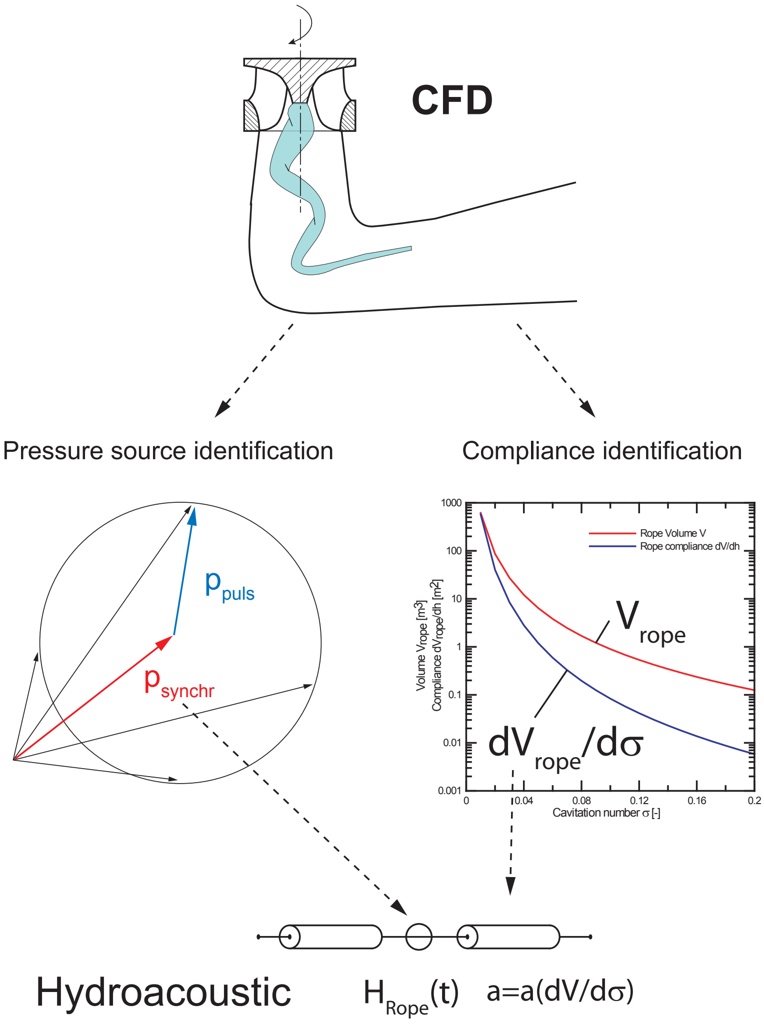

Figure 12.11: Synoptic scheme of the CFD prediction methodology.

12.3.5 Concluding Remarks

A methodology for the assessment of the risk of resonance of a hydroelectric power plant operating at part load and subject to draft tube pressure pulsations is presented. This method is based on a time domain simulation of the dynamic behavior of the whole hydroelectric power plant considering a white noise draft tube pressure excitation. This simulation is done for different draft tube wave speeds. The simulation results reveal the piping natural frequencies that are excited by the draft tube pressure source. In addition, the transfer function between the draft tube pressure source and the generator electromagnetic torque points out the risk of electrical power swing. However, the risk can be really evaluated only knowing the pressure excitations and the draft tube wave speed. If the former can be obtained from scaled model testing, the latter has to be estimated, either experimentally from vortex rope photography, or by CFD.

Nevertheless, the presented methodology is a helpful tool for predicting the risk of resonance at the early stages of pre-design or as a help for on site diagnostic purposes.

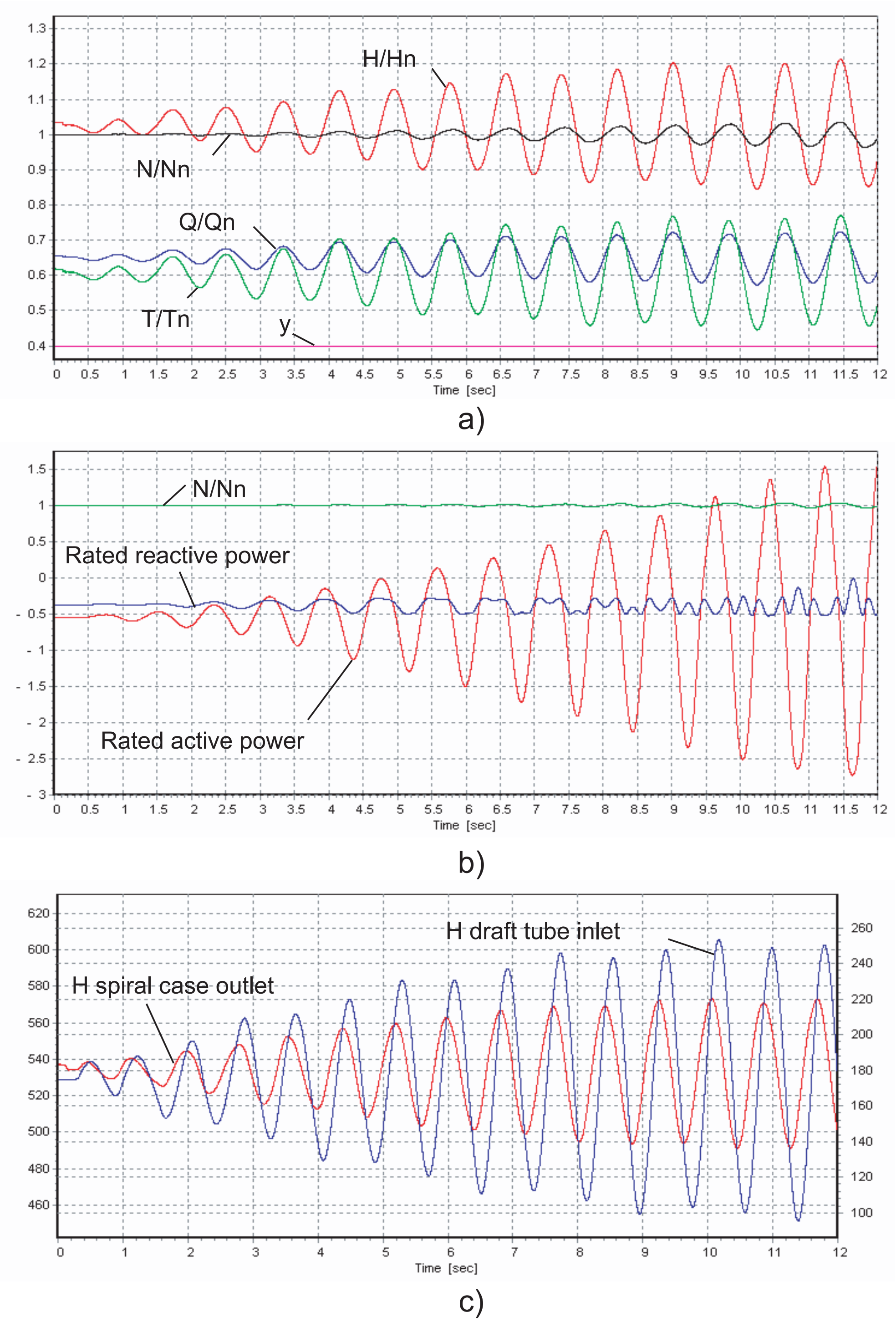

a)

b)

c)

Figure 12.12: Time evolution of the turbine variables a), generator variables b) and head at the turbine inlet/outlet c) of Unit 4 resulting from full hydroelectric resonance.

Conclusions

Chapter 13

Summary, Conclusions & Perspectives

13.1 Summary

This work is a contribution to the modelling of the dynamic behavior of Francis turbine hydroelectric power plants. An original modelling approach based on an electrical equivalent scheme of hydraulic conduits is generalized to hydraulic systems. The modelling is one-dimensional and takes into account compressibility effects in order to model propagation phenomena in hydraulic systems: the hydroacoustic modelling. The present work is composed of two parts, one dealing with the modelling methodology and application to transient phenomena, and the other one is devoted to the modelling of pressure fluctuation problems in Francis turbines.

13.1.1 Hydroacoustic Modelling of Hydraulic Circuits

Hydroacoustic Modelling by Electrical Equivalent

Fundamental continuity and momentum equations are treated with a finite difference scheme to establish an equivalent T-shaped circuit modelling an elementary pipe. The accuracy in the frequency domain of the derived discrete model of a pipe is deduced by comparison of the hydraulic impedance of an elementary pipe obtained from both the equivalent scheme and the exact solution. The comparison provides a frequency confidence threshold according to the spatial discretization and the element wave speed. Basically, this confidence threshold indicates that modelling of a wavelength with 10 nodes leads to an impedance error of 3% while the error drops to 1% with 20 nodes.

The modelling by equivalent scheme is then extended to classical hydraulic components such as valves, surge tanks, surge shafts, air vessels and cavity compliances. The quasi-static models of Francis, Pelton and Kaplan turbines are also presented and are based on the use of the turbines characteristic curves for transients analysis purposes. The models presented are validated on a test case of the emergency shutdown in generating and pumping mode of a 4 × 315 MW pumped-storage power plant. The comparison of the simulation results with experiments shows good agreement, validating the developed hydroacoustic models.

Hydroelectric transients

All these models are implemented in the EPFL software SIMSEN developed initially for the analysis of the dynamic behavior of electrical installations. This hydraulic extension offers the possibility to model an entire hydroelectric power plant comprising the hydraulic circuit, the electrical installations, the mechanical inertias and the control command systems enabling investigation of hydroelectric transients. Interactions between hydraulic circuit and electrical installation are shown to be of major concern for turbine speed governor parameters optimization.

The investigation of hydroelectric transients in islanded power networks also shows the restriction of speed governor performances regarding the hydraulic layout. Particularly, power plants featuring long penstocks and small diameter surge tanks require high order modelling to take properly into account waterhammer, mass oscillations and turbine characteristic non-linearity effects. A model of an islanded power network constituted of a thermal power plant and passive consumer load points out the positive stabilization effect up to 1 Hz of a large power network.

13.1.2 Modelling of Pressure Fluctuations in Francis Turbine

The review of pressure excitation sources associated with the operation of Francis turbines shows that the vortex rope and rotor-stator induced pressure fluctuations are the most likely to lead to resonance phenomena with the hydraulic circuit. Good modelling was already obtained in the past for part load vortex rope excitation on scale models [40], however, improvements have been made in the field of the modelling of the upper part load and the full load vortex rope as well as for the rotor-stator phenomenon.

Upper Part Load Analysis

Upper part load pressure fluctuations were recorded on a Francis turbine scale model in the framework of the FLINDT project. One-dimensional pressure fluctuations were shown by Arpe [6] but the origin of these pressure fluctuations was not identified. The modelling of the test rig based on the experimental determination of the wave speed in the draft tube shows that the pressure fluctuations measured in the whole draft tube by Arpe correspond to an eigen frequency of the test rig. As the pressure fluctuations are of a relatively high frequency, 32.5 Hz, a concentrated compliance model of the vortex rope is not sufficient. Therefore, the draft tube is modelled with distributed compliance in terms of variable wave speed along the diffuser. Regarding the modelling of the excitation source, during experiments, a shock phenomenon of the vortex rope on the wall of the draft tube occurring at the vortex rope frequency was noticed. The analysis of the frequency content at the location identified as the pressure source origin, in the inner elbow, revealed a signal with energy distributed in a wide frequency range especially for the vortex rope harmonics, up to the 10^{th} order. Therefore the excitation source is simulated with pressure pulse at the frequency of the vortex rope. The duration and amplitude of these pulses are determined by error minimization. The result of the time domain simulation shows very good agreement with the measurements.

However, the role of Froude similitude and cavitation number was not investigated deeply in the FLINDT project. Therefore, visualizations of the vortex rope with simultaneous pressure records were carried out on a Francis turbine with similar specific speed. The visualization indicates an elliptical shape of the vortex rope rotating with a frequency being the half of the resonance frequency. The volume of the cavitation rope appeared to change according to the pressure evolution. Low cavitation numbers show also the very complex structure of the rope constituted of multiple vortices. The Froude investigation demonstrated that the excitation frequency is proportional to the runner frequency and thus the rope can be associated with a one-dimensional excitation source. The additional study of the effect of Froude and cavitation number influence also shows that in the case of the FLINDT project, the operating point investigated was very particular point. For this operating point the shock phenomenon provides energy at harmonics of the vortex rope whose 7^{th} harmonic coincides with the half of the frequency of the self rotation of the rope and also with an eigen frequency of the test rig. For such a case, the ratio between the two excitation phenomena cannot be deduced from available experiments. However, additional work is necessary to separate the contribution of the influence of the shock phenomenon of the 1D pressure source in the excitation source model.

Full Load Investigation

The full load surge is investigated in the case of a pumped-storage plant where strong pressure fluctuations were recorded for over load conditions. This phenomenon is of the self excitation type. The stability of the whole system depends on the ratio of the 2 parameters of the vortex rope: the cavitation compliance and the mass flow gain factor. The stability diagram of the power plant represented as function of these 2 parameters is calibrated with the measurements and shows the self excited nature of the fluctuations. A simulation model of the entire power plant comprising the hydraulic circuit, with a model of the full load cavitation, the electrical installation, the mechanical inertias and the control system is set up for time domain simulation purposes. The vortex rope compliance is determined by CFD computation enabling the inclusion of the non-linear behavior of the vortex rope in the simulation. This approach, points out the role of the shutdown of a neighboring unit, decreasing the cavitation number and conducting the system in the unstable operation domain.

Rotor-Stator Interactions

The rotor-stator resonance is investigated for a scale model pump-turbine. The simulation model is set up on the basis of the flow distribution between stationary and rotating parts. The 20 guide vanes connected to the 9 runner vanes are all modelled by pipes and are connected all together throughout 180 valves driven according to the flow distribution during rotation. The induced pressure waves combine together and result in a standing wave in the spiral case at the frequency of twice the runner blade passing frequency. The simulation provides also all expected diametrical modes rotating in the vaneless gap with the predicted patterns. A parametrical study shows the important role of the closeness of eigen frequencies on dynamic amplification of the standing wave in the spiral case.

Resonance Risk Assessment

Finally, a methodology is proposed for the assessment of the risk of resonance due to part load vortex rope excitation. The method is based on a parametric study where the hydraulic resonance and power fluctuations are determined as function of the draft tube wave speed. A white noise excitation is used for the draft tube excitation in order to reveal all possible resonances. The possible resonances should be compared either with experimental data or with CFD computations of the excitation source and vortex rope compliance.

13.2 Conclusions

The one-dimensional modelling approach developed in the framework of the present work appears to be a powerful tool for the simulation, the analysis and the optimization of the dynamic behavior of hydroelectric power plants. This approach, based on equivalent schemes representation, enables qualitative and quantitative analysis of hydraulic system dynamics in an intuitive way. The proposed modelling can be used either for frequency or time domain analysis using the same model formulation and breaks the rupture between frequency and time domain investigations.

The implementation of these models in the simulation software SIMSEN opens the door to multi-physics modelling of hydroelectric power plants with high level of complexity for the entire system. Such a tool meets the requirement of improving the accuracy of solicitation prediction for increasing specific power of Francis turbines and reducing mistuning and troubleshooting on site during commissioning.

Using the same modelling, the focus can be put on either transient phenomena of hydroelectric power plants or on specific resonance or stability problems related to the operation of Francis turbines. The model of a Francis turbine can be set up for an investigation according to the topology of the machine taking advantage of the modularity of the one-dimensional modelling. This concept has been successfully applied for the modelling of upper part load pressure pulsation, requiring a high frequency model, for full load instabilities, requiring appropriate damping and cavitation model, and also for rotor-stator interaction where the model should take into account the guide vane and runner vane arrangement of the machine.

The one-dimensional approach has the advantage of providing simulation results in a short time for optimization and parametric studies, but requires a correct set of parameters. The amount of parameters increases with the complexity of the model and of the studied physics. Therefore, appropriate identification methodologies should be used. Propositions are made for the determination of wave speed in the draft tube with cavitation development based on either photography or on CFD computation. If the determination of the cavitation compliance at full load seems to be valid, the method should be validated for the mass flow gain factor and for part load problems.

13.3 Perspectives

13.3.1 Improving Models

There is always a need for developing and implementing new models in softwares like SIMSEN. Regarding the hydraulic side, the implementation of the following models would be interesting:

- improvement of damping models of the pipes by taking into account frequency dependant friction losses as proposed by Zielke [157] or Schohl [132] for laminar flow and [150], [133], for turbulent flow;
- pipe models with variable parameters along the abscissa [51];
- open channels [69];
- cavitating pipes having as parameters the nuclei density and initial diameter whose radius variation, *i.e.* the wave speed, is computed with the Rayleigh-Plesset equation [125], [122].

13.3.2 Towards More Dimensions

For high frequency problems like rotor-stator interactions, it is clear that the assumption of propagation of planar waves reaches its limits. For such a kind of problem, a generalization of the equivalent scheme representation from one to two or three dimensions as proposed by Bilbao [16] would be an interesting approach. The two dimensional approach was already successfully applied by Timouchev *et al.* [146], [147] to rotor-stator problems. The figure 13.1 shows the representation of the equivalent scheme for two dimensions.

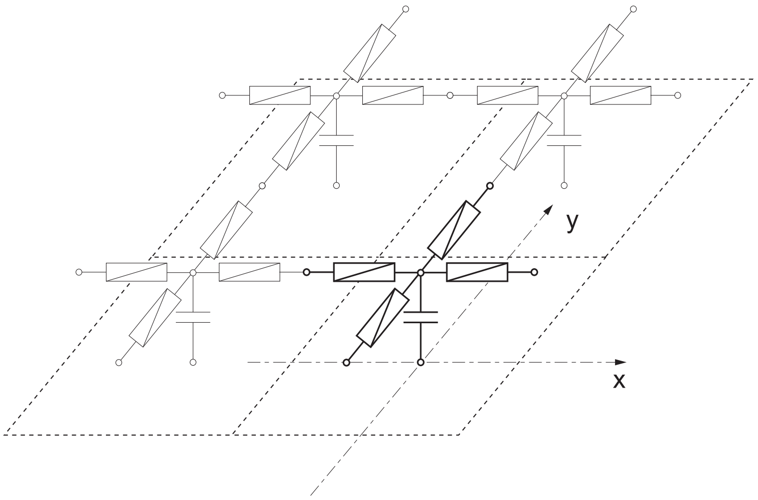

Figure 13.1: Two-dimensional modelling of a hydraulic system.

13.3.3 The CFD Solution

As mentioned above, the difficulty with problems involving complex physics is not only to have appropriate models but also to have reliable data for the parameter settings. Regarding the draft tube surge modelling, 2 key parameters are necessary: the wave speed along the draft tube and the excitation source amplitude and frequency. Recent improvements in the CFD computation of the part load vortex rope [104], [134] and [136], indicate that determination of missing parameters would be possible. The determination of these parameters can be done by a separate computation, as it is done for the full load vortex rope in chapter 10, or done concurrently. The concurrent methodology approach is illustrated in figure 13.2 where the CFD computation provides excitation sources and enables the determination of the cavitation volume for the wave speed determination, while the hydroacoustic computation provides realistic boundary conditions for the CFD computation [99], [129], [54] at each time step. However, direct coupling of CFD and hydroacoustic codes makes sense only if the CFD domain represents a short hydroacoustic domain, which is not the case for draft tube problems where wave speed can drop drastically.

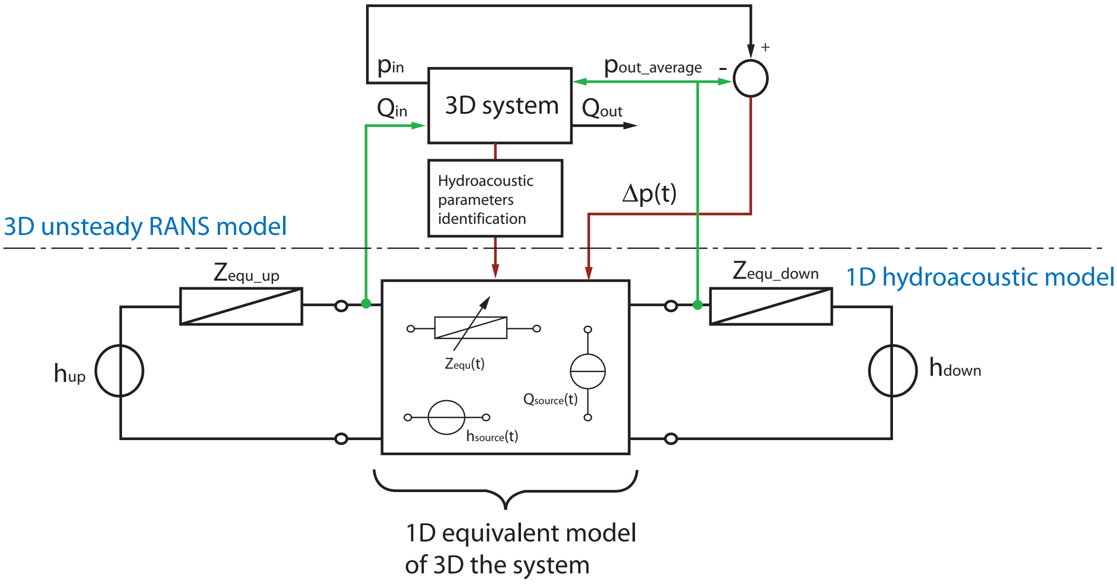

Figure 13.2: Coupling approach between CFD and hydroacoustic computation.

13.3.4 New Applications

The hydroacoustic modelling approach is applicable to other domains such as the bio-medical or engine applications. Regarding bio-medical applications, equivalent schemes have already been used for a long time for the modelling of the human cardiovascular systems [121], [54]. In the field of automotive engines, there is a large place for the optimization of the admission and exhaust systems as well as injection devices [138].

APPENDICES

Appendix A

Numerical Integration Methods

The set of ordinary differential equations (ODE) to be solved in SIMSEN is the following:

$$[A] \cdot \frac{d\overline{x}}{dt} + [B(t,x)] \cdot \overline{x} = \overline{c} \tag{A.1}$$

The integration method used in SIMSEN to solve the system of equation A.1 is the explicit 4^{th} order Runge-Kutta method (RK). This method might presents some restrictions in terms of stability for solving stiff problems. Stiff problems are characterized by:

- high stiffness in the problem resulting in very high eigen frequencies of the system to be solved;
- or, system presenting large differences of order of magnitudes leading to large differences between the smallest and the highest eigen values.

Stiff systems might be encountered in multi-physics systems such as hydroelectric power plants where electrical devices present time constants of $\tau = 0.001$ s and hydraulic mass oscillation periods of $T = 500$ s. In addition, the explicit RK method presents a stability domain covering the main part of the left hand complex plan that excludes system physically unstable. Therefore, a more robust method for checking the validity of simulation results is necessary. Implicit integration methods are usually used to overcome integration stability problems. Three test cases are considered for comparing the explicit and the implicit methods: (i) waterhammer effect in a pipe; (ii) surge effect due to physical instabilities; and (iii) van der Pol equation.

A.1 Integration Methods

The differential equation set of interest can be expressed in the following compact form:

$$\frac{dy}{dx} = f(x,y) \quad ; \quad y(x_o) = y_o \tag{A.2}$$

To solve this ordinary differential equation set, explicit an implicit RK methods are investigated.

A.1.1 Explicit Runge-Kutta Method

The explicit Runge-Kutta s^{th} order method applied to the system A.2 gives:

$$\begin{aligned}
&k_1 = f(x_o, y_o)\\
&k_2 = f(x_o + c_2 \cdot h, y_o + h \cdot a_{21} \cdot k_1)\\
&k_3 = f(x_o + c_3 \cdot h, y_o + h \cdot (a_{31} \cdot k_1 + a_{32} \cdot k_2))\\
&...\\
&k_s = f(x_o + c_s \cdot h, y_o + h \cdot (a_{s1} \cdot k_1 + ... + a_{s,s-1} \cdot k_{s-1}))\\
&y_1 = y_o + h \cdot (b_1 \cdot k_1 + ... + b_s \cdot k_s)
\end{aligned} \tag{A.3}$$

Where $h = x_1 - x_o$ and the parameters a_{ij}, b_i, c_i are given in the table A.1.

Table A.1: Parameters of the explicit Runge-Kutta method.

0					
c_2	a_{21}				
c_3	a_{31}	a_{32}			
$\vdots$	$\vdots$	$\vdots$	$\ddots$		
c_s	a_{s1}	a_{s2}	$\cdots$	$a_{s,s-1}$	
	b_1	b_1	$\cdots$	b_{s-1}	b_s

Using the simplified approach described by Butcher for a 4^{th} order method, the parameters of table A.1 gives the parameters table A.2:

Table A.2: Parameters of the Runge-Kutta explicit method 4^{th} order.

0				
1/2	1/2			
1/2	0	1/2		
1	0	0	1	
	1/6	2/6	2/6	1/6

The table A.2 gives the following set of equations:

$$\begin{aligned}
&k_1 = f(x_o, y_o)\\
&k_2 = f(x_o + h/2, y_o + h/2 \cdot k_1)\\
&k_3 = f(x_o + h/2, y_o + h/2 \cdot k_2)\\
&k_4 = f(x_o + h, y_o + h \cdot k_3)\\
&y_1 = y_o + h/6 \cdot (k_1 + 2 \cdot k_2 + 2 \cdot k_3 + k_4)
\end{aligned} \tag{A.4}$$

The triangular structure of the table indicates that a k_n can be calculated directly from the previous $k_{i<n}$. No iterations are necessary for the computation of y_1. The method is named ERK.

A.1.2 Implicit Runge-Kutta Method

The implicit s-stage Runge-Kutta method [67] leads to the following expression:

$$\begin{aligned} k_i &= f(x_o + c_i \cdot h, y_o + h \cdot \sum_{j=1}^{s} a_{ij} \cdot k_j) \quad ; \quad i = 1, ..., s \\ y_1 &= y_o + h \cdot \sum_{i=1}^{s} b_i \cdot k_i \end{aligned} \tag{A.5}$$

The table used for the explicit method is extended to the a_{ij} above the diagonal. The method is named IRK method. Then a given k_n is computed by iteration considering $k_{i>n}$. The k_i values converge if the Lipschitz condition (with the L is a constant) is fulfilled:

$$h < \frac{1}{L \cdot \max_i \sum_j |ai_j|} \tag{A.6}$$

Several set of a_{ij}, b_i, c_i parameters can be used and present different stability patterns and have to be chosen by experience depending on the nature of the system to be solved. Here 3 methods are tested, the Euler and Radau IIA 3^{rd} and 5^{th} order method.

Implicit Euler Method

The Euler implicit method provides the parameters of table A.3:

Table A.3: Parameters of the Euler implicit method.

1	1
	1

Implicit Radau IIA 3^{rd} Order Method

The Radau IIA 3rd order method provides the parameters of table A.4.

Table A.4: Parameters of the Runge-Kutta Radau IIA 3^{rd} order method.

1/3	5/12	−1/12
1	3/4	1/4
	3/4	1/4

The table A.4 gives the following set of equations:

$$\begin{aligned} k_1 &= f(x_o + 1/3 \cdot h, y_o + h/12 \cdot (5 \cdot k_1 - k_2)) \\ k_2 &= f(x_o + h, y_o + h/4 \cdot (3 \cdot k_1 + k_2)) \\ y_1 &= y_o + h/4 \cdot (3 \cdot k_1 + k_2) \end{aligned} \tag{A.7}$$

Implicit Radau IIA 5^{th} Order Method

The Radau IIA 5^{th} order method provides the parameters of table A.5.

Table A.5: Parameters of the Runge-Kutta Radau IIA 5^{th} order method.

$$\begin{array}{c|ccc}
\frac{4-\sqrt{6}}{10} & \frac{88-7\cdot\sqrt{6}}{360} & \frac{296-169\cdot\sqrt{6}}{1800} & \frac{-2+3\cdot\sqrt{6}}{225} \\
\frac{4+\sqrt{6}}{10} & \frac{296+169\cdot\sqrt{6}}{1800} & \frac{88+7\cdot\sqrt{6}}{360} & \frac{-2-3\cdot\sqrt{6}}{225} \\
1 & \frac{16-\sqrt{6}}{36} & \frac{16+\sqrt{6}}{36} & \frac{1}{9} \\
\hline
1 & \frac{16-\sqrt{6}}{36} & \frac{16+\sqrt{6}}{36} & \frac{1}{9}
\end{array}$$

A.2 Comparison of the Methods

Three test cases have been selected to compare performances and stability of the 3 integrations methods described above. The test cases are the following: (i) the waterhammer effect in a pipe due to a valve closure; (ii) the surge effects due to physical instabilities related to the mass flow gain factor; and (iii) the van der Pol equation.

For both hydraulic cases, the parameters of the piping system are the same. The test case piping layout is presented in figure A.1 and the related parameters are given in table A.6. The number of nodes used to model the pipe is 10. To solve the differential equation set with RK methods, the equation set A.1 is reordered as follows:

$$\frac{d\overline{x}}{dt} = \underbrace{[A]^{-1} \cdot \overline{c} - [A]^{-1} \cdot [B(x,t)] \cdot \overline{x}}_{f(t,x)} \tag{A.8}$$

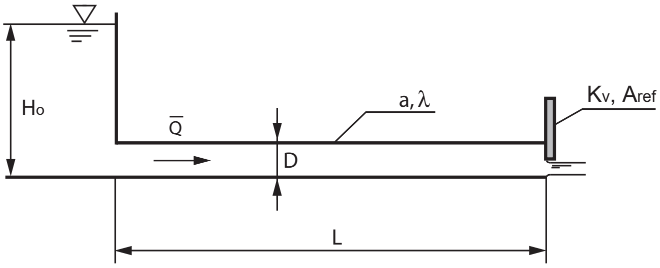

Figure A.1: Test case.

Table A.6: Test case parameters.

L $[m]$	D $[m]$	a $[m/s]$	λ $[-]$	Q_o $[m^3/s]$	fo = a/(4L) $[Hz]$
600	0.5	1200	0.02	0.5	0.5

A.2.1 Waterhammer Phenomenon

First, the waterhammer effect is simulated for 10 seconds for a partial closure law from fully opened valve to 10% valve opening within 2.1 seconds. The comparison of head and

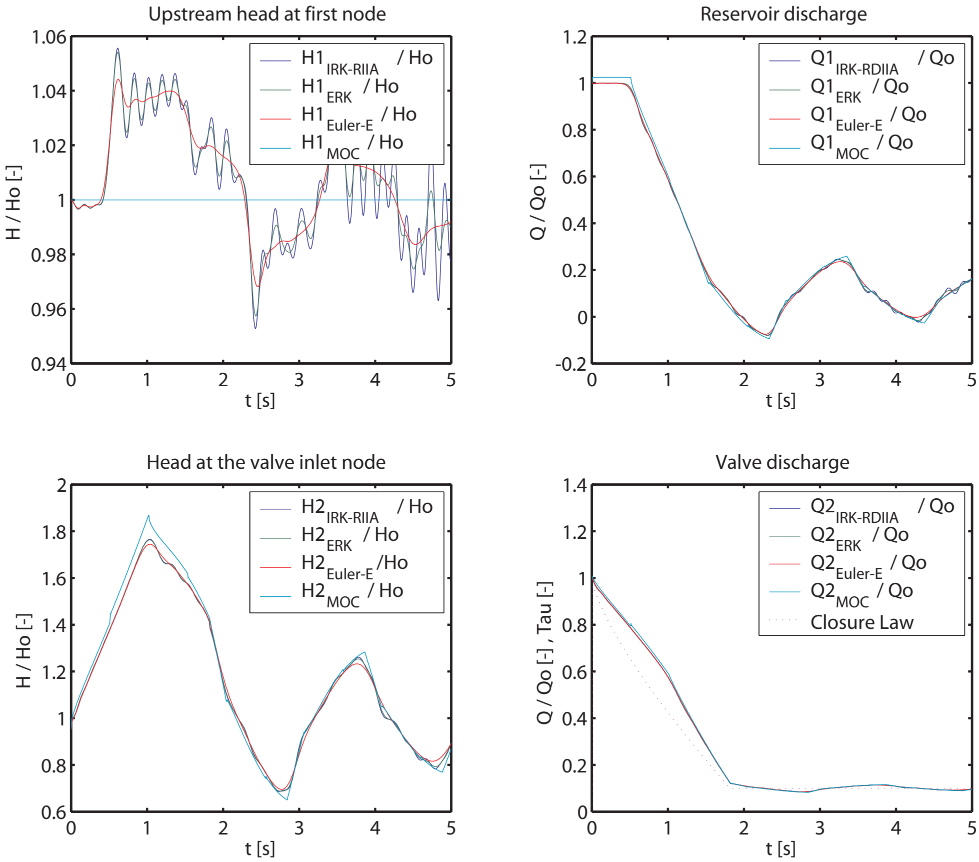

Figure A.2: Comparison of integration method for slow valve closure.

discharge at both end of the pipe are presented in figure A.2. The Method of Characteristic (MOC) is taken as reference.

Secondly, a fast valve closure of 0.2 seconds is simulated. The comparison of the simulation results is presented in figure A.3 and in figure A.4.

The comparison of the different integration method shows that there is only a little difference between all the integration methods. The number of iterations with the IRK-5^{th} method to reach an error of $\varepsilon = 10^{-5}$, is 4.71 if 10 nodes are used to model the pipe. Increasing the number of nodes to 20 implies 5.94 iterations to reach the same error limit. Thus, the computational time required for a simulation is 5 times greater. In addition, when the number of nodes increases, the integration time step has to be reduced in the same proportion to fulfil CFL criteria. The IRK methods can provide more accurate solutions than ERK methods but are detrimental with respect to the computational time.

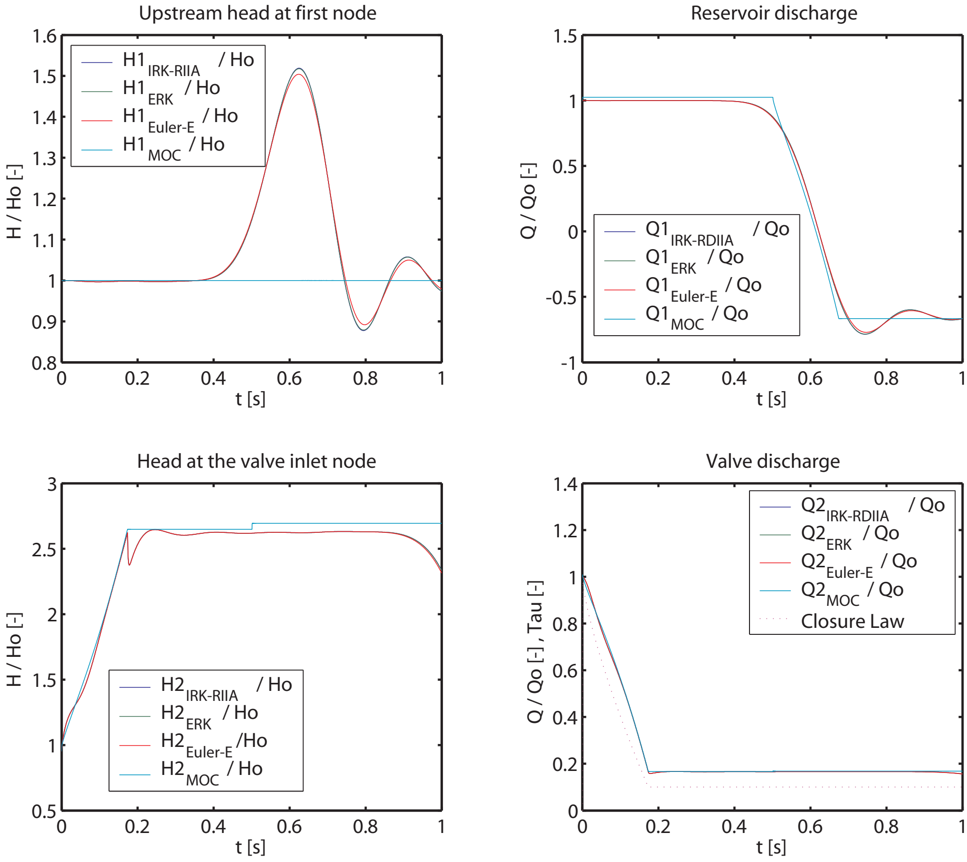

Figure A.3: Comparison of integration method for fast valve closure.

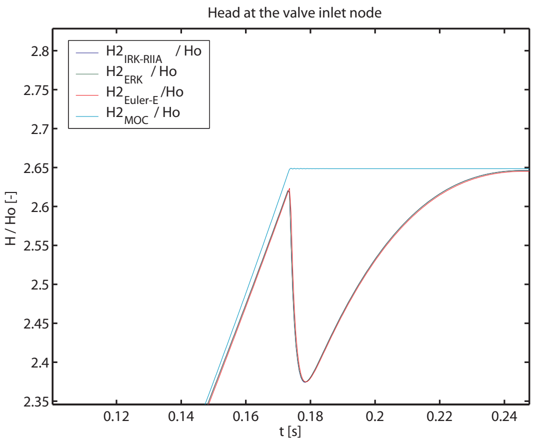

Figure A.4: Comparison of integration method for fast valve closure.

A.2.2 Surge Phenomenon

The surge phenomenon is simulated by considering a cavitation volume in the middle of the pipe. The cavitation volume is modelled as a compliant element featuring also a mass flow gain factor. Assuming that the cavitation volume is function of the head and the discharge yields to:

$$V(Q,H)_2 \Rightarrow dV = \frac{\partial V}{\partial H_2} \cdot dH_2 + \frac{\partial V}{\partial Q_2} \cdot dQ_2 \tag{A.9}$$

Time variation is given by:

$$\frac{dV}{dt} = \frac{\partial V}{\partial H_2} \cdot \frac{dH_2}{dt} + \frac{\partial V}{\partial Q_2} \cdot \frac{dQ_2}{dt} \tag{A.10}$$

Let's define:

- the cavity compliance $C = \frac{\partial V}{\partial H}$
- the mass flow gain factor $\chi = \frac{\partial V}{\partial Q}$

It yields to:

$$Q_2 - Q_1 = C \cdot \frac{dH_2}{dt} + \chi \cdot \frac{dQ_2}{dt} \tag{A.11}$$

When the mass flow gain factor is negative, the hydraulic system might become unstable. In this test case, the limit of the stability is reached for $\chi = -0.035$. The simulation of the unstable behavior of the pipe is initiated by a 50% valve closure is presented in figure A.5. This case features differences between the Euler method and the RK methods. However, again, no big differences between ERK and IRK are visible.

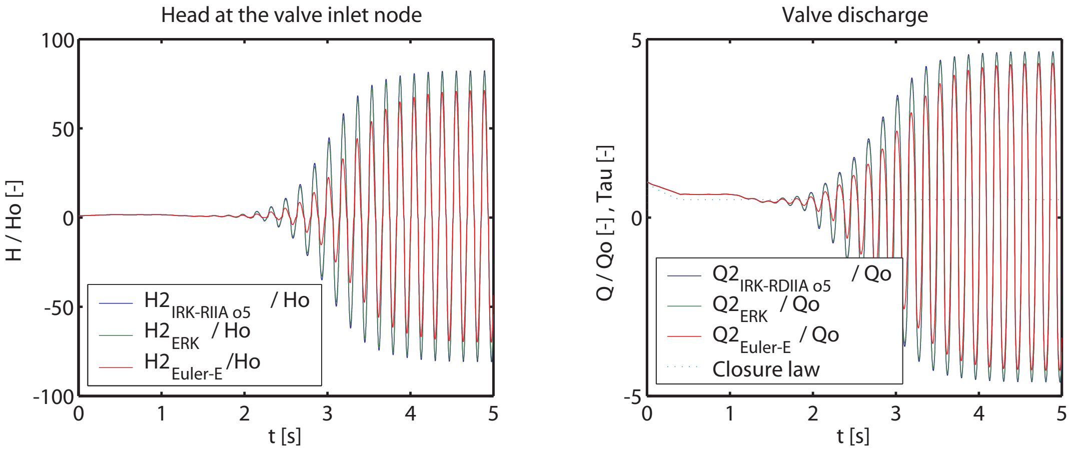

Figure A.5: Comparison of integration method for hydraulic surge.

A.2.3 Van der Pol Equation

The van der Pol equation is chosen as a test function to evaluate performances of the different integration methods. The van der Pol's equation is given by:

$$\frac{d^2y}{dt^2} + \varepsilon \cdot (y^2 - 1) \cdot \frac{dy}{dt} + y = 0 \tag{A.12}$$

In order to have a first order ODE, equation A.12 can be rearranged as follows:

$$\frac{dy_1}{dt} = y_2 \quad ; \quad \frac{dy_2}{dt} + \varepsilon \cdot (y_1^2 - 1) \cdot y_2 + y_1 = 0 \tag{A.13}$$

The matricial expression gives:

$$\begin{bmatrix} 1 & 0 \\ 0 & 1 \end{bmatrix} \cdot \frac{d}{dt} \begin{bmatrix} y_1 \\ y_2 \end{bmatrix} + \begin{bmatrix} 0 & -1 \\ 1 & \varepsilon \cdot (y_1^2 - 1) \end{bmatrix} \cdot \begin{bmatrix} y_1 \\ y_2 \end{bmatrix} = \begin{bmatrix} 0 \\ 0 \end{bmatrix} \tag{A.14}$$

The system is solved considering the following initial conditions:

$$y_1(0) = 2 \quad ; \quad y_2(0) = 0 \quad \rightarrow \quad y_o = \begin{bmatrix} 2 \\ 0 \end{bmatrix} \tag{A.15}$$

The van der Pol equation represents a dynamic system whose damping is negative for small amplitudes ($y < 1$) and is positive for high amplitudes ($y > 1$). The parameter ε enables emphasizing the instability of the system; the higher the ε, the more unstable is the system. The simulation results obtained for $\varepsilon = 10$ using 5 different integration methods are presented in table A.7 for different integration time steps and tolerances.

For high integration time steps, the Euler's methods, explicit or implicit, do not provide an accurate solution. The frequency of the oscillation is underestimated by the implicit method while it is overestimated by the explicit method. However, all RK methods, implicit or explicit, provide reasonable solution. The solution of ERK is almost identical to the IRK RADAU IIA order 3. The tolerance of the implicit method does not significantly influence the results but increases the number of loops per time step. Decreasing the integration time step strongly improves the simulation results of the Euler's methods. To reach the accuracy of RK method, the time step has to be divided by 100. So Euler's methods are not suitable for the simulation of unstable systems. Compared to the IRK methods, the ERK method provides good results in a reasonable computation time. Figure A.6 shows that all the methods provide the same results only for very small time step and tolerance. Between the IRK methods, the 3^{rd} order method is the most accurate method even for large tolerance and time steps as the solution is only slightly influence by the reduction of the integration time step. The solution of the 5^{th} order converges to the solution of the 3^{rd} order when the time step is reduced.

The ERK method is found to be the most suitable integration for the integration of hydraulic systems. IRK RADAU IIA o3 might be useful for the verification of the solution of the simulation results of hydraulic system physically unstable.

Table A.7: Comparison of simulation results for the van der Pol equation.

	$Tolerance = 0.01$	$Tolerance = 0.0001$
$dt = 0.01s$	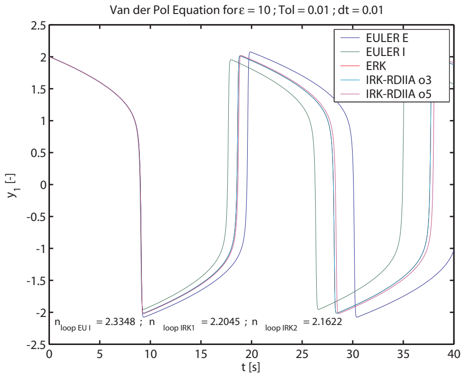	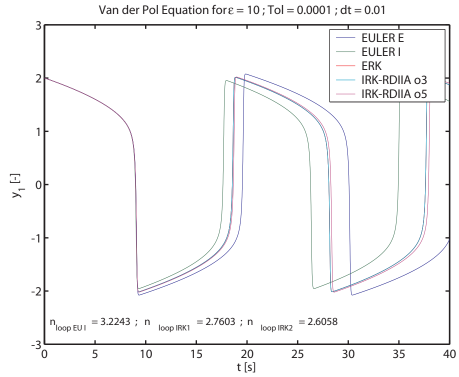
$dt = 0.001s$	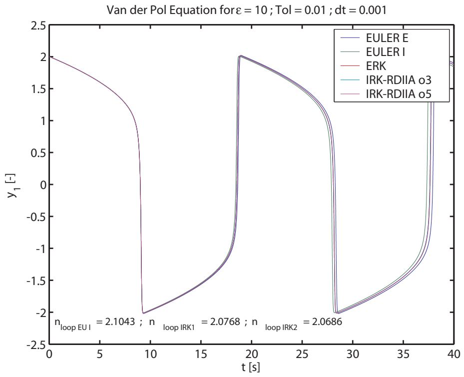	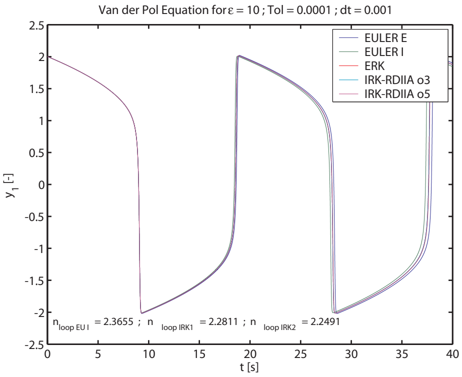

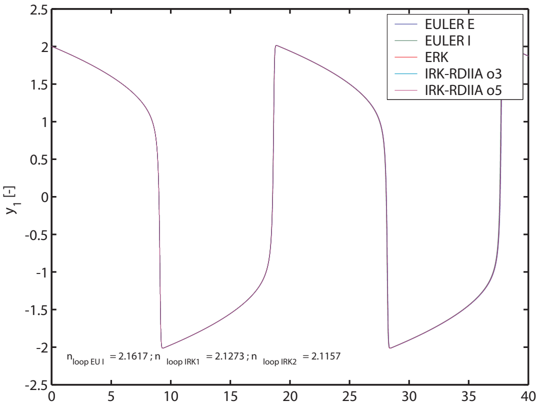

Figure A.6: Comparison of simulation results for the van der pol equation with small integration time step.

A.3 Stability Analysis of RK Methods

Let consider the smooth solution $\varphi(x)$ of equation A.1, $dy/dx = f(x,y)$. Linearizing $f(x,y)$ in its neighborhood as follows [68]:

$$\frac{dy(x)}{dx} = f(x,\varphi(x)) + \frac{\partial f}{\partial y}(x,\varphi(x)) \cdot (y(x) - \varphi(x)) + ... \tag{A.16}$$

Introducing $y(x) - \varphi(x) = \overline{y}(x)$ leads to:

$$\frac{d\overline{y}(x)}{dx} = \frac{\partial f}{\partial y}(x,\varphi(x)) \cdot \overline{y}(x) + ... = J(x) \cdot \overline{y}(x) + ... \tag{A.17}$$

As a first approximation, considering the Jacobian $J(x)$ constant and neglecting the errors terms yields to:

$$\frac{d\overline{y}(x)}{dx} = J \cdot \overline{y} \tag{A.18}$$

Using an explicit method to solve the equation above gives:

$$y_1 = R(h \cdot J) \cdot y_o \tag{A.19}$$

With the stability function $R(z)$:

$$R(z) = 1 + z + \frac{z^2}{2!} + ... + \frac{z^s}{s!} + O(z^{p+1}) \tag{A.20}$$

The stability function can be interpreted as the numerical solution of the Dalhquist test equation after one step for:

$$\frac{dy}{dx} = \delta \cdot y \quad ; \quad y_o = 1 \quad ; \quad z = h \cdot \delta \tag{A.21}$$

For an equations set of dimension k, y_m remains bounded for $m = 1 \rightarrow \infty$, if for all eigenvalues δ_k, the complex number $z = h \cdot \delta_k$ is contained in the domain S given by:

$$S = \{z \in C; |R(z) \leq 1\} \tag{A.22}$$

For implicit functions:

- Euler implicit:

$$R(z) = \frac{1}{1-z} \tag{A.23}$$

- IRK RADAU IIA order 5:

$$R(z) = \frac{1 + z \cdot 2/5 + z^2/20}{1 - z \cdot 3/5 + z^2 \cdot 3/20 - z^3/60} \tag{A.24}$$

The stability domains related to ERK methods of order 1 to 4 are presented in figure A.7 while stability domain of implicit Euler and IRK RADAU IIA order 5 are respectively presented in figure A.8 left and right.

So these integration methods are stable if $R(h \cdot \delta_k) \leq 1$.

This inequality shows the influence of between the integration step h. The explicit methods feature more stable behavior for higher order method that encloses region close to the origin and higher frequencies. Highly damped systems might also present instabilities. However, implicit method do cover the whole part of the left hand side an extended part of the right hand part of the complex plan. The Euler implicit method appears to be a very stable method. More than the IRK RADAU IIA 5^{th} order method.

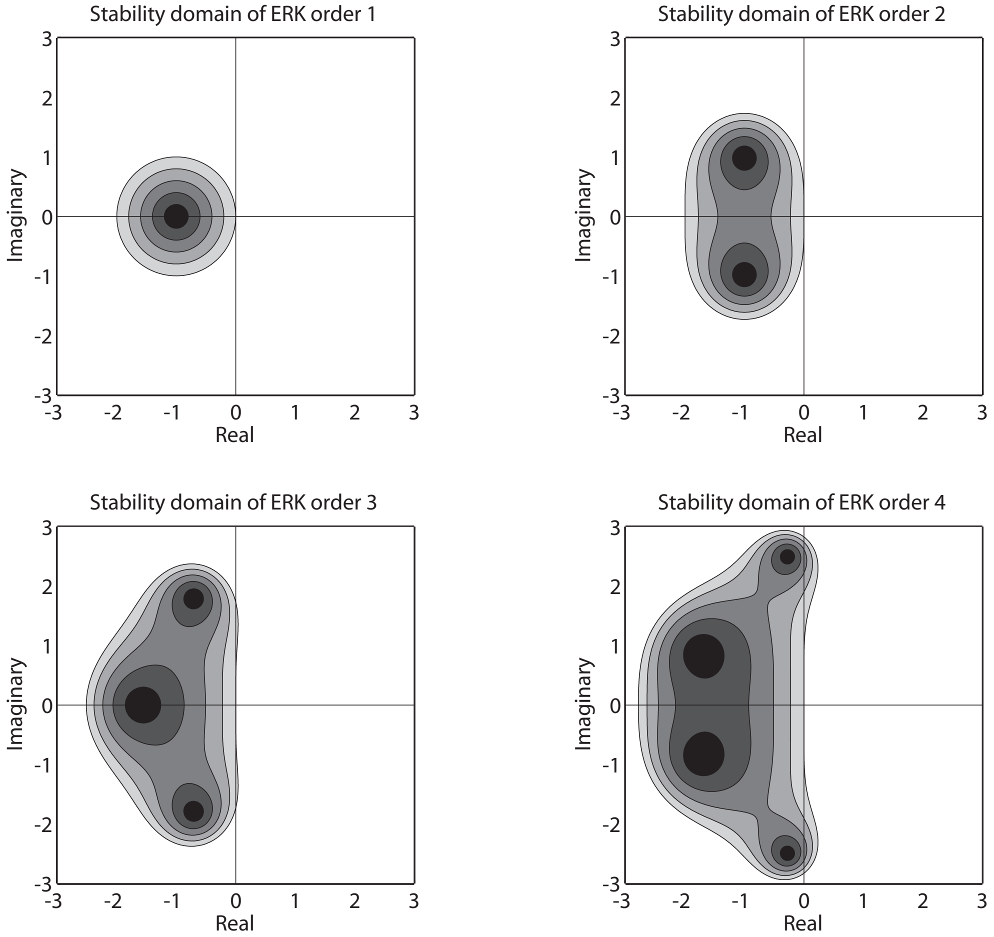

Figure A.7: Stability domain of ERK methods order 1 to 4.

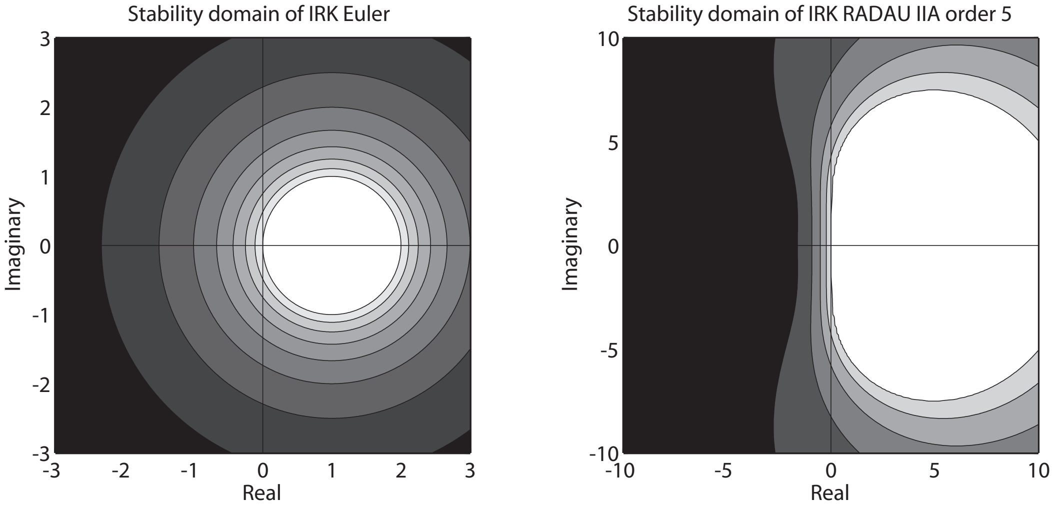

Figure A.8: Stability domain of the Euler implicit method (left), and stability domain of IRK RADAU method order 5 (right).

References

References

[1] Abbott, H. F., Gibson, W. L., and McCaig, I. W. Measurements of auto-oscillation in a hydroelectric supply tunnel and penstock system. *Trans. ASME, J. of basic Engineering 85* (December 1963), 625–630. Series D.

[2] Allievi, L. *Theory of Water Hammer.* Ricardo Garoni, Rome, 1925. Translated by E. E. Halmos.

[3] Anderson, A. Interaction of surge shafts and penstocks. In *Proceedings of the 4th Int- Conf. on Pressure Surges* (Bath, England, September 1983), pp. 297–312. paper G2.

[4] Angelico, F. M. G., Monaco, A. D., Fanelli, M., and Molinaro, P. A mechanical device for damping pressure oscillations in a hydroelectric power plant: a theoretical study through the transfer matrix method. In *Proceeding of the 17th IAHR Symposium on Hydraulic Machinery and Systems* (Beijing, September 1994), vol. 3, pp. 1221–1232.

[5] Angelico, F. M. G., Muciaccia, F. F., and Rossi, G. Part load behavior of a turbine: a study on a complete model of a hydraulic power plant. In *Proceeding of the 13th IAHR Symposium on Hydraulic Machinery and Systems* (Montréal, 1986). Paper 17.

[6] Arpe, J. *Analyse du champ de pression pariétale d'un diffuseur coudé de turbine Francis.* PhD thesis, EPFL, Lausanne, 2003. N°2779.

[7] Arpe, J., and Avellan, F. Pressure wall measurements in the whole draft tube : steady and unsteady analysis. In *Proceeding of the 21st IAHR Symposium on Hydraulic Machinery and Systems* (2002), pp. 593–602.

[8] Arzola, F., Azuaje, C., Zambrano, P., and Gulbrandsen, G. Undesired power oscillations at high load in large Francis turbines: experimental study and solution. In *Proceeding of the 23th IAHR Symposium on Hydraulic Machinery and Systems* (Yokohama, October 2006).

[9] Avellan, F. Flow investigation in a Francis draft tube: The flindt project. In *Proceeding of the 20th IAHR Symposium on Hydraulic Machinery and Systems* (Charlotte, USA, 2000). Paper 17.

[10] Avellan, F. *Cours de machines hydrauliques.* EPFL, IMHEF, 2001, ch. I: Introduction.

[11] Batchelor, G. K. *An Introduction to Fluid Dynamics.* Cambridge University Press., 1976.

[12] Benjamin, T. B. Theory of vortex breakdown phenomenon. *J. Fluid Mech. 14* (1962), 593–629.

[13] Benjamin, T. B. Some developments in the theory of vortex breakdown. *J. Fluid Mech. 28, part 1* (1967), 65–84.

[14] Bergeron, L. *Du coup de Bélier en hydraulique au coup de foudre en électricité.* Dunod, 1950.

[15] Biela, V., and Beltran, H. Draft tube fins. In *Proceeding of the 19th IAHR Symposium on Hydraulic Machinery and Systems* (Singapore, 1998), pp. 454–461.

[16] Bilbao, S. D. *Wave and scattering methods for the numerical integration of partial differential equations.* PhD thesis, Stanford, 2001.

[17] Bölcs, A. *Turbomachines thermiques*, vol. I. LTT/EPFL, 1993.

[18] Blevins, R. D. *Flow-induced vibrations.* Van Nostrand Reinhold, New York, 1990.

[19] Blommaert, G. *Etude du compretement dynamique des turbines Francis: contrôle actif de leur stabilité.* PhD thesis, EPFL, Lausanne, 2000. N°2222.

[20] Blommaert, G., Avellan, F., and Prénat, J.-E. Evaluation de la stabilité d'installations hydroélectriques à partir d'essais sur modèle réduit : étude expérimentale. In *Colloque SHF : machines hydrauliques, instationnarités et effets associés* (November 2000).

[21] Blommaert, G., Prénat, J.-E., Avellan, F., and Boyer, A. Active control of Francis turbine operation stability. In *Proceedings of the 3rd ASME/JSME Joint Fluids Engineering Conference* (San Francisco, California, July 1999).

[22] Bolleter, U. Blade passage tones of centrifugal pump. *Vibrations 4*, 3 (1988), 8–13.

[23] Bolleter, U. Hydraulic and mechanical interactions of feedpump systems. Tech. Rep. TR-100990, EPRI, Sept. 1992. TR-100990.

[24] Borel, L. *Thermodynamique et Energétique.* Presses polytechniques romandes, ISBN 2-88074-025-8, 1984.

[25] Bourdon, P. *Détection vibratoire de l'érosion de cavitation des turbines Francis.* PhD thesis, EPFL, Lausanne, 2000. n°2295.

[26] Bovet, T., and Henry, P. Le nouveau stand d'essai universel pour machines hydrauliques à réaction. Tech. Rep. 6, EPFL, Institut de Machines Hydrauliques, Lausanne, 1970. in french.

[27] Brennen, C., and Acosta, A. J. Theoretical, quasi-static analysis of cavitation compliance in turbopumps. *J. Space Craft 10*, 3 (March 1973), 175–180.

[28] Brennen, C., and Acosta, A. J. The dynamic transfer function for a cavitatin inducer. *Trans. ASME, J. of Fluids Eng. 98* (1976), 182–191.

[29] Brennen, C., and Braisted, D. Stability of hydraulic systems with focus on cavitating pumps. In *Proceeding of the 10th IAHR Symposium on Hydraulic Machinery and Systems* (Tokyo, 1980). Session V.

[30] Brennen, C. E. Theoretical, quasi-static analysis of cavitation compliance in turbopumps. *J. Fluid. Mech. 89*, 2 (1978), 223–240.

[31] Campmas, P. Stability of operating conditions for Francis turbines. In *Proceeding of the 1st IAHR Symposium on Hydraulic Machinery and Systems* (Nice, September 1960), pp. 1–14. Paper B4, in french.

[32] Canay, I. M. Extended synchronous machine model for calculation of transient processes and stability. *Electric machines and Electromechanics 1* (1977), 137–150.

[33] Cassidy, J. J., and Falvey, H. T. Observation of unsteady flow arising after vortex breakdown. *J. Fluid Mech. 41* (1970), 727–736.

[34] Chapman, A. D. R., and Robbie, J. F. Eigenvalue stability analysis of surge systems involving double vented shafts - theory and practice. In *Proceedings of the 4th Int. Conf. on Pressure Surges* (Bath, England, September 1983), pp. 353–377. paper H3.

[35] Chatelain, J. *Traité d'électricité: machines électriques*, georgi ed., vol. X. Presses polytechniques romandes, Lausanne, 1983.

[36] Chaudhry, M. H., and Mays, L. W. *Computer modeling of free-surface and pressurized flows.* Kluwer Academic Publisher, Dordrecht, Boston, London, 1994.

[37] Chen, Y. N. Water-pressure oscillations in the volute casings of storage pumps. *Sulzer Technical Review* (1961), 21–34. Research Number.

[38] Courant, R., Friedrichs, K., and Lewy, H. Über die partiellen differenzengleichungen der mathematischen physik. *Mathematische Annalen Volume 100*, number 1 (December 1928), 32–74.

[39] Delbe, C. *Modélisation comportementale et commande découplée d'un groupe turbo-alternateur connecté à un réseau fini de distribution d'énergie électrique.* PhD thesis, INSA, 1991. .91 ISAL (in french).

[40] Dörfler, P. K. System dynamics of the Francis turbine half load surge. In *Proceeding of the 11th IAHR Symposium on Hydraulic Machinery and Systems* (Amsterdam, 1982). paper 39.

[41] Dörfler, P. K. *System oscillations excited by the Francis turbine's part load vortex core: mathematical modeling and experimental verification.* PhD thesis, Techn. University Vienna, Vienna, 1982. (in german).

[42] Dörfler, P. K. On the role of phase resonance in vibrations caused by blade passage in radial hydraulic turbomachines. In *Proceeding of the 12th IAHR Symposium on Hydraulic Machinery and Systems* (Stirling, 1984), pp. 227–241. paper 3.3.

[43] Dörfler, P. K. Francis turbine surge prediction and prevention. *Proceedings of Waterpower' 85* (1985), 952–961.

[44] Dörfler, P. K. Observation of the pressure pulsation on Francis model turbine with high specific speed. *Hydropower & Dams* (January 1994), 21–26.

[45] Dörfler, P. K. Modèle mathémathique des oscillations excitées à charge partielle par la torche de cavitatiob dans les turbines Francis. *Bulletin Escher Wyss 1/2* (1980), 101–106. in french.

[46] Dörfler, P. K., Engineer, A. J., Pendse, R. N., Huvet, P., and Brahme, M. V. Stable operation achieved on single-stage reversible pump-turbine showing instability at no-load. In *Proceeding of the 19th IAHR Symposium on Hydraulic Machinery and Systems* (Singapore, 1998), pp. 430–440.

[47] Dériaz, P. A contribution to the understanding of flow in draft tubes of Francis turbines. In *Proceeding of the 1st IAHR Symposium on Hydraulic Machinery and Systems* (Nice, September 1960), pp. 1–13. Paper B1.

[48] Dube, B. *Optimisation des dispositifs de reglage primaire d'une installation hydroelectrique.* PhD thesis, EPFL, Lausanne, 1975. n°205.

[49] Duttweiler, M. E., and Brennen, C. Surge instability on a cavitating propeller. *J Fluid Mech. 458* (2002), 133–152.

[50] Energy Information Administration, Official Energy Statistics from the U.S. Government. International energy outlook 2006. Tech. rep., Official Energy Statistics from the U.S. Government, June 2006. Report N°:DOE/EIA-0484(2006).

[51] Fanelli, M. A. The pulsating regime in pressure conduits having lengthwise variations in cross-section and celerity. In *Proceedings of the Int. Conf. on Pressure Surges* (September 1972), pp. G6: 75–95. paper G6.

[52] Fischer, R. K., Palde, U., and Ulith, P. Comparison of draft tube surging of homologous scale models and prototype Francis turbines. In *Proceeding of the 10th IAHR Symposium on Hydraulic Machinery and Systems* (Tokyo, 1980), pp. 541–556.

[53] Fischer, R. K., Powell, C., Franke, G., Seidel, U., and Koutnik, J. Contributions to the improved understanding of the dynamic behaviour of pump turbines and uses thereof in dynamic design. In *Proceeding of the 22nd IAHR Symposium on Hydraulic Machinery and Systems* (Stockholm, 2004). paper B11-3.

[54] Formaggia, L., Gerbeau, J. F., Nobile, F., and Quarteroni, A. On the coupling of 3d and 1d navier-stockes equations for flow problems in compliance

vessels. *Computer methods in applied mechanics and engineering 191* (2001), 561–582.

[55] Fox, J. A. *Transient flow in pipes, open channels and sewers.* Ellis Horwood Limited, Chichester, 1989.

[56] Franc, J.-P., Avellan, F., Belhadji, B., Billard, J.-Y., Briançon-Marjolet, L., Fréchou, D., Fruman, D. H., Karimi, A., Kueny, J.-L., and Michel, J.-M. *La Cavitation: Mécanismes Physiques et Aspects Industriels.* Collection Grenoble Sciences. Presse Universitaires de Grenoble, Grenoble, 1995.

[57] Franke, G., Powell, C., Seidel, U., Koutnik, J., and Fischer, R. K. On pressure mode shapes arising from rotor/stator interactions. *Sound and Vibration* (March 2005), 14–18.

[58] Fritsch, A., and Maria, D. Comportement dynamique d'une turbine Francis à charge partielle: comparaison modèle-prototype. *La Houille Blanche*, 3/4 (1988), 273–280. in french.

[59] Ghahremani, F. G. Pump cavitation compliance. In *Caivtation forum* (New York, 1971), ASME, pp. 1–3.

[60] Godfrey, K. Design and application of multifrequency signals. *Computing and Control Engineering Journal 2*, Issue 4 (July 1991), 187–195.

[61] Gonzalez, J., Fernandez, J., Blanco, E., and Santolaria, C. Numerical simulation of the dynamic effects due to impeller-volute interaction in a centrifugal pump. *Trans. ASME, J. of Fluids Eng. 124* (June 2002), 348–355.

[62] Goosen, J., Simond, J.-J., Steigleder, K., Soenen, L., Steffens, J.-C., and Stubbe, J. Several aspects of the torsional fatigue damage of turbo-group shafts due to electrical disturbances. *A.I.M.* (1985). Liège, 63.1-10.

[63] Graeser, J.-E. *Régime transistoires en hydrauliques - Coup de Bélier.* EPFL-IMH, 1983.

[64] Grein, H. Vibration phenomena in Francis turbines: their causes and prevention. In *Proceeding of the 10th IAHR Symposium on Hydraulic Machinery and Systems* (Tokyo, 1980), pp. 527–539.

[65] Greitzer, E. M. The stability of pumping systems. *Trans. of ASME, J. of Fluids Eng. 103* (june 1981), 193–242.

[66] Haban, V., Koutnik, J., and Pochyly, F. 1-d mathematical model of high-frequency pressure oscillations induced by rsi inculding an influence of fluid second viscosity. In *Proceeding of the 21st IAHR Symposium on Hydraulic Machinery and Systems* (Lausanne, 2002), pp. 735–740.

[67] Hairer, E., Nørsett, S. P., and Wanner, G. *Solving ordinary differential equations 1, nonstiff problems.* Springer, 2000.

[68] Hairer, E., and Wanner, G. *Solving ordinary differential equations 2, stiff and differential algebraic problems.* Springer, 2002.

[69] Harbort, T. *Eintwicklung eines echtzeifähigen Simulationsprogramms zur Untersuchung instationärer Vorgänge in Wasserkraftwerken.* PhD thesis, Universität Stuttgart, 1999. in german.

[70] Hartog, J. P. D. *Mechanical vibrations*, 4th edition ed. McGraw-Hill, New York, 1956. pp. 7-9.

[71] Harvey, J. K. Some observations of the vortex breakdown phenomenon. *J. Fluid Mech. 14* (1962), 585–592.

[72] Henry, P., Graeser, J.-E., Prénat, J.-E., and Wegner, M. Scale effect concerning hydraulic quasi-stationary oscillations on a turbine model and test circuit. In *Proceeding of the 12th IAHR Symposium on Hydraulic Machinery and Systems* (Stirling, 1984), pp. 356–371.

[73] Henry, P., Lecoffre, Y., and Larroze, P. Y. Effets d'échelle en cavitation. In *Proceeding of the 10th IAHR Symposium on Hydraulic Machinery and Systems* (Tokyo, 1980), pp. 103–113.

[74] Henry, P., Wegner, M., and Greaser, J. E. Analyse expérimentale de la stabilité hydraulique de la turbine Francis a charge partielle. In *S.H.F.* (novembre 1981).

[75] Huvet, P. Steady oscillatory conditions between pump-turbine operating at partial flow and surge shaft. In *Proceeding of the 16th IAHR Symposium on Hydraulic Machinery and Systems* (Sao Paolo, 1992), pp. 349–358.

[76] Illiescu, M. S., Ciocan, G. D., and Avellan, F. 2 phase PIV measurements at the runner outlet in a Francis turbine. In *Proceedings of the 4th ASME/JSME Joint FLuid Engineering Conference* (Honolulu, Hawaii, July 2003), pp. 1–7. FEDSM2003-45756.

[77] International Electrotechnic Commission. IEC 60913 standard hydraulic turbines, storage pumps and pump-turbines-model acceptance tests. Tech. rep., IEC, Geneva, 1999.

[78] International Energy Agency. World energy outlook: 1999 insights. IEA.

[79] Jacob, T. *Evaluation sur modèle réduit et prediction de la stabilité de fonctionnement des turbines Francis.* PhD thesis, EPFL, Lausanne, 1993. N° 1146.

[80] Jacob, T. Similitude in stability of operation tests for Francis turbine. *Hydropower & Dams Volume I* (January 1994).

[81] Jacob, T., and Prenat, J.-E. Francis turbine surge : discussion and database. In *Proceeding of the 18th IAHR Symposium on Hydraulic Machinery and Systems* (Valencia, Spain, 1996), vol. 2, pp. 855–864.

[82] Jacob, T., and Prénat, J.-E. Identification of a hydraulic turbomachine's hydro-acoustic transmission parameters. In *Proceedings of the Working Group of the IAHR on the Dynamic Behaviour of Hydraulic Machinery under Steady Oscillatory Conditions* (Milan, Italy, September 1991).

[83] Jacob, T., Prénat, J.-E., Buffet, G., and Winkler, S. Improving the stability of operation of a 90 MW Francis turbine. In *Proceedings of the international Conference on Hydropower into the next Century* (Barcelona, Spain, June 1995).

[84] Jacob, T., Prénat, J.-E., and Maria, D. Comportement dynamique d'une turbine Francis à forte charge comparaison modèle-prototype. *La Houille Blanche*, 3/4 (1988), 293–300. in french.

[85] Jacob, T., Prénat, J.-E., Vullioud, G., and Araguas, B. L. Surging of 140 MW Francis turbines at high load, analysis and solution. In *Proceeding of the 16th IAHR Symposium on Hydraulic Machinery and Systems* (Sao Paolo, 1992).

[86] Jaeger, C. The theory of resonance in hydropower systems. discussion of incidents and accidents occuring in pressure systems. *Trans. ASME, J. of Basic Engineering* (December 1963), 631–640.

[87] Jaeger, C. *Fluid transients in hydro-electric engineering practice.* Blackie, Glasgow, 1977.

[88] Kamwa, I., Grondin, R., and Trudel, G. IEEE PSS2B versus PSS4B: the limits of performance of modern power system stabilizers. *IEEE Transactions on Power Systems 20* (May 2005), 903 – 915. Issue 2.

[89] Karimi, A., and Avellan, F. Comparison of erosion mechanisms in different types of cavitation. *Wear 113* (1986), 305–322.

[90] Knapp, R. T. Complete characteristics of centrifugal pumps and their use in the prediction of transient behavior. *Transaction of the ASME* (1937), 683–689. 59(3).

[91] Konidaris, D. N., and Tegopoulos, J. A. Investigation of oscillatory problems of hydraulic generating units equipped with Francis turbines. *IEEE Trans. on Energy Conversion 12* (1997). Issue 4.

[92] Kopf, E., Brausewetter, S., Giese, M., and Moser, F. Optimized control strategies for variable speed machines. In *Proceeding of the 22nd IAHR Symposium on Hydraulic Machinery and Systems* (Stockholm, June 2004), pp. 1–9. paper A 15-2.

[93] Koutnik, J. Analysis of pressure oscillations measured in the twin-penstock of pspp stechovice. In *Proceeding of the 20th IAHR Symposium on Hydraulic Machinery and Systems* (Charlotte, USA, 2000).

[94] Koutnik, J., Krüger, K., Pochyly, F., Rudolf, P., and Haban, V. On cavitating vortex rope form stability during Francis turbine part load operation. In *Proceedings of the first Meeting of the IAHR Int. Working Group on Cavitation and Dynamic Problems in Hydraulic Machinery and Systems* (Barcelona, June 2006).

[95] Koutnik, J., Nicolet, C., Schohl, G. A., and Avellan, F. Overload surge event in a pumped-storage power plant. In *Proceedings of the 23rd IAHR Symposium on Hydraulic Machinery and Systems* (Yokohama, Japan, October 18 - 21 2006).

[96] Koutnik, J., and Pochyly, F. Parametric excited pressure oscillations in hydraulic systems. In *Proceeding of the 21st IAHR Symposium on Hydraulic Machinery and Systems* (Lausanne, September 2002), pp. 653–658.

[97] Koutnik, J., and Pulpitel, L. Modeling of the Francis turbine full-load surge. In *Modeling, Testing and Monitoring for Hydro Power plants - II* (June 1996).

[98] Krueger, R. E. Selecting hydraulic reaction turbines. *Engineering Monograph 20* (1980).

[99] Longatte, F., and Kueny, J.-L. Analysis of rotor-stator-circuit interactions in a centrifugal pump. In *Proceedings of the 3rd ASME/JSME Joint Fluids Engineering Conf.* (San Francisco, California, July 1999).

[100] Lowys, P. Y., Paquet, F., Couston, M., Farhat, M., Natal, S., and Avellan, F. Onboard measurments of pressure and strain fluctuations in a model of low head Francis turbine - part 2: Measurments and preliminary analysis results. In *Proceeding of the 21st IAHR Symposium on Hydraulic Machinery and Systems* (Lausanne, September 2002), pp. 873–880.

[101] Marchal, M., Flesh, G., and Suter, P. The calculation of waterhammer problems by means of the digital computer. In *Proc. Int. Symp. Waterhammer Pumped Storage Projects* (Chicago, 1965), ASME.

[102] Martin, C. S. Stability of pump-turbines during transient operation. In *Proceedings of the 5th Int. Conf. on Pressure Surges* (Hannover, Germany, 1986), pp. 61–71. paper C3.

[103] Martin, C. S. Instability of pump-turbines with s-shaped characteristics. In *Proceeding of the 20th IAHR Symposium on Hydraulic Machinery and Systems* (Charlotte, USA, 2000).

[104] Mauri, S. *Numerical simulation and flow analysis of an elbow diffuser.* PhD thesis, EPFL, Lausanne, 2002. N°2527.

[105] Miller, D. S. *Internal flow system*, 2nd ed. BHRA, Cranfield, 1990.

[106] Moregenroth, M., and Weaver, D. S. Sound generation by a centrifugal pump at blade passing frequency. *Trans. ASME, J. of Fluids Eng. 120* (October 1998), 736–743.

[107] Muciaccia, F. F., Rossi, G., and Zanetti, V. Study on model of the dynamic behaviour of a hydraulic machine. In *Proceeding of the 12th IAHR Symposium on Hydraulic Machinery and Systems* (Stirling, 1984), pp. 340–355.

[108] Nishi, M. Study on swirl flow and surge in an elbow type draft tube. In *Proceeding of the 10th IAHR Symposium on Hydraulic Machinery and Systems* (Tokyo, 1980), pp. 557–565.

[109] NISHI, M. Surging characteristics of conical and elbow type draft tubes. In *Proceeding of the 12th IAHR Symposium on Hydraulic Machinery and Systems* (Stirling, 1984), pp. 272–283.

[110] NISHI, M., MATSUNAGA, S., KUBOTA, T., AND SENOO, Y. Flow regimes in as elbow-type draft tube. In *Proceeding of the 11th IAHR Symposium on Hydraulic Machinery and Systems* (Amsterdam, 1982), pp. 1–13. paper 38.

[111] NISHI, M., WANG, X., OKAMOTO, M., AND MATSUNAGA, S. Further investigation on the pressure fluctuations caused by cavitated vortex rope in an elbow draft tube. In *Cavitation and Gas Fluid Flow in Fluid Machinery and Devices* (1994), ASME, pp. 63–70.

[112] NISHIHARA, T., AKIMOTO, T., AND YAMAMOTO, K. Self-induced pressure pulsation in penstock caused by movable-seat seal using tapper water from penstock. In *Proceedings of Waterpower XIII* (Buffalo, USA, 2003), pp. 1–12.

[113] OHURA, Y., FUJII, M., SUGIMOTO, O., TANAKA, H., AND YAMAGATA, I. Vibration of the powerhouse structure of pumped storage power plant. In *Proceeding of the 15th IAHR Symposium on Hydraulic Machinery and Systems* (Belgrade, 1990). section U2.

[114] PALDE, U. J. Model and prototype turbine draft tube surge analysis by the swirl momentum method. In *Proceeding of the 7th IAHR Symposium on Hydraulic Machinery and Systems* (Vienna, 1974), no. paper III.

[115] PARRONDO-GAYO, J. L., GONZALEZ-PEREZ, J., AND FERNANDEZ-FRANCOS, J. The effect of the operating point on the pressure fluctuations at blade passage frequency in the volute of a centrifugal pump. *Trans. ASME, J. of Fluids Eng. 124* (September 2002), 348–355.

[116] PAYNTER, H. M. Surge and water hammer problems. *Transaction of ASCE 146* (1953), 962–1009.

[117] PEDRO, M. D., AND PAHUD, P. *Mécanique vibratoire - Système discret linéaires.* Presses Polytechniques et Universitaires Romandes, 1997.

[118] PEJOVIC, S. Troubleshooting of turbine vortex core resonance and air introduction into the draft tube. In *Proceeding of the 21st IAHR Symposium on Hydraulic Machinery and Systems* (Lausanne, 2002), pp. 511–516.

[119] PEJOVIC, S., OBRADOVIC, D., AND GAJIC, A. Field tests and calculations of the effects of air introduction into the draft tube upon hydraulic oscillations in a hydropower plant. In *Proceeding of the 13th IAHR Symposium on Hydraulic Machinery and Systems* (Montréal, 1986). paper 9.

[120] PHILIBERT, R., AND COUSTON, M. Francis turbine at part load : matrix simulating the gaseous rope. In *Proceeding of the 19th IAHR Symposium on Hydraulic Machinery and Systems* (Singapore, September 1998), vol. 1, pp. 441–453.

[121] Pillon, M. *Du modèle du coeur naturel au reglage du coeur artificiel.* PhD thesis, EPFL, Lausanne, 1990. N°889.

[122] Plesset, M. The dynamics of cavitation bubbles. *ASME J. Appl. Mech. 16* (1949), 228–231.

[123] Ramirez, C. *Plate-forme numérique d'essais pour machines électriques de puissance.* PhD thesis, EPFL, Lausanne, 2003. N°2821.

[124] Ratsaramody, J. *Programme de CAO-DAO d'installations hydroélectriques utilisable au stade d'un avant projet.* PhD thesis, EPFL, Lausanne, 1992. Thèse EES Polytechnique Antsiranana.

[125] Rayleigh, L. On the pressure developed in a liquid during the collapse of a spherical cavity. *Phil. Mag. 34* (1917), 94–98.

[126] Rheingans, W. J. Power swing in hydroelectric power plants. *Transaction ASME 62* (1940), 171–184.

[127] Ribaux, A. *Hydraulique appliquée III, Turbo-machines.* Editions de la Moraine, Genève, 1953.

[128] Rubin, S. Longitudinal instability of liquid rockets due to propulsion feedback (pogo). *J. Space Craft 3*, 8 (august 1966), 1188–1195.

[129] Ruprecht, A., and Helmrich, T. Simulation of the water hammer in hydro power plant caused by draft tube surge. In *Proc. Of 4th ASME JSME Conf.* (Honolulu, Hawaii, USA, 2003). paper FEDSM2003-45249.

[130] Sapin, A. *Logiciel modulaire pour la simulation et l'étude des systèmes d'entraînement et des réseaux électriques.* PhD thesis, EPFL, 1995. n° 1346.

[131] Sapin, A., Steimer, P. K., and Simond, J.-J. Modeling, simulation and test of a three-level voltage source inverter with output lf filter and direct torque control. In *IEEE, Conference Record of the 38th Industry Applications Conference Annual Meeting* (12-16 Oct. 2003), vol. 1, pp. 492–498.

[132] Schohl, G. A. Improved approximate method for simulatin frequency-dependent friction in transient laminar flow. *Trans. ASME, J. of Fluid Engineering 115* (September 1993), 420–424.

[133] Shu, J.-J. A finite element model and electronic analogue of pipeline pressure transients with frequency-dependent friction. *Trans. ASME J. of Fluids Engineering 125* (January 2003), 194–199.

[134] Sick, M., Dörfler, P. K., Michler, W., Sallaberger, M., and Lohmberg, A. Investigation of the draft tube vortex in a pump-turbine. In *Proceeding of the 22nd IAHR Symposium on Hydraulic Machinery and Systems* (Stockholm, July 2004), pp. 1–10. Paper B11-1.

[135] Souza, O. H. J., Barbieri, N., and Santos, A. H. M. Study of hydraulic transients in hydropower plants through simulation of nonlinear model of penstock and hydraulic turbine model. *IEEE Transactions on Power Systems 14* (1999), 1269 – 1272. Issue 4.

[136] Stein, P., Sick, M., Dörfler, P. K., White, P., and Braune, A. Investigation of the draft tube vortex in a pump-turbine. In *Proceeding of the 23rd IAHR Symposium on Hydraulic Machinery and Systems* (Yokohama, October 2006), pp. 1–10.

[137] Stirnemann, A., Eberl, J., Bolleter, U., and Pace, S. Experimental determination of the dynamic transfer matrix for a pump. *Trans. ASME, J. of Fluids Engineering 109* (1987), 218 – 225.

[138] Streeter, V. L., and Wylie, E. B. *Fluid transients in systems.* Prentice Hall, Englewood Cliffs, N.J., 1993.

[139] Susan-Resiga, R., Ciocan, G. D., Anton, I., and Avellan, F. Analysis of the swirling flow downstream a Francis turbine runner. *Trans. ASME, J. of Fluids Eng. 128* (January 2006), 177–189. Issue 1.

[140] Susan-Resiga, R., Vu, T. C., Muntean, S., Ciocan, G. D., and Nennemann, B. Jet control of the draft tube vortex rope in Francis turbines at partial discharge. In *Proceeding of the 23rd IAHR Symposium on Hydraulic Machinery and Systems* (Yokohama, October 2006). paper 192.

[141] Swaffield, J. A., and Boldy, A. P. *Pressure surge in pipe and duct systems.* Avebury Technical, Aldershot, 1993.

[142] Tadel, J., and Maria, D. Analysis of dynamic behavior of a hydroelectric installation with Francis turbine. In *Proc. 5th Int. Conf. on Pressure Surges* (Hannover, Germany, 1986), pp. 43–52.

[143] Tanaka, H. Special design considerations for ultra high head pump-turbines. *Hydropower & Dams* (November 1994), 107–112.

[144] The International Journal on Hydropower & Dams. Hydropower & dams world atlas 2001.

[145] Thoma, D. *Zur Theorie des Wasserschlosses bei selbsttätig geregelten Turbinenanlagen.* Munich (Oldenbourg), 1910. in german.

[146] Timouchev, S., and Pavic, G. Analysis of the influence of design and operating parameters on pressure pulsations in centrifugal pumps. *La Houille Blanche*, 3/4 (1998), 61–65.

[147] Timouchev, S., and Tourret, J. Numerical simulation of bpf pressure pulsation field in centrifugal pumps. In *Proceedings of the 19th International Pump Users Symposium* (2002).

[148] Tsujimoto, Y., Kamijo, K., and Yoshida, Y. Theoretical analysis of rotating cavitation in inducers. *Trans. of ASME, J. Fluids Eng. 115* (march 1993), 135–141.

[149] Ulith, P., Jaeger, E.-U., and Strscheletzky, M. Contribution to clarifying the inception of nonstationary flow phenomena in the draft tube of high specific speed Francis turbines operating at part load. In *Proceeding of the 7th IAHR Symposium on Hydraulic Machinery and Systems* (Vienna, 1974), pp. 1–18. paper III - 4.

[150] Vardy, A. E., and Brown, J. Efficient approximation of unsteady friction weighting functions. *ASCE Journal of Hydaulic engineering* (november 2004), 1097–1107.

[151] Vatcher, T. R., Hunter, M., Perreault, G., and Coulson, D. M. Hydraulic resonance in a 78 MW Francis turbine - field test results. In *Proceeding of the 12th IAHR Symposium on Hydraulic Machinery and Systems* (Stirling, 1984), pp. 371–391.

[152] Wallis, G. B. *One-dimensional two-phase flow.* Mc Graw-Hill, New York, 1969.

[153] Wang, D., and Johnson, C. D. A comparison study of some impulse-response identification methods. In *IEEE Proceedings. Twenty-First Southeastern Symposium* (March 1989), System Theory, pp. 52 – 56.

[154] Watanabe, S., and Brennen, C. E. Dynamics of a cavitating propeller in a water tunnel. *Trans. of ASME, J. Fluids Eng. 125* (march 2003), 283–292.

[155] Working group on Prime Mover and Energy Supply Models for System Dynamic Performance Studies. Hydraulic turbine control models for system dynamic studies. *Trans. Power Systems 7*, 1 (February 1992).

[156] World Energy Council. Survey of energy resources 2004. Tech. rep., WEC, London, 2004. online publication: http://www.worldenergy.org.

[157] Zielke, W. Frequency-dependent friction in transient pipe flow. *Trans. ASME, J. of Basic Engineering* (March 1968), 109–115.

[158] Zielke, W. Application of general computer programs for water hammer analysis. In *Lecture Series on Unsteady One Dimensional Flows in Complex Networks and Pressurized Vessels* (Sent-Genesius-Rode, Belgium, von Karman Inst. Fluid Dyn., Jan.14-18 1980). Lecture No.14, 14p.

[159] Zielke, W. Vibrations and resonance in hydraulic systems. In *Lecture Series on Unsteady One Dimensional Flows in Complex Networks and Pressurized Vessels* (Rhode Saint Genese, Belgium, von Karman Inst. Fluid Dyn., Jan.14-18 1980). Lecture No.13, 25p.

[160] Zielke, W., and Hack, H. P. Resonance frequencies and associated modes shapes of pressurized piping systems. In *Proceedings of the Int. Conf. on Pressure Surges* (September 1972), pp. G1: 1–13. paper G1.

Index

List of Publications

Papers

1. NICOLET, C., GREIVELDINGER, B., HEROU, J.-J., ALLENBACH, P., SIMOND, J.-J. and AVELLAN, F., *High Order Modeling of Hydraulic Power Plant in Islanded Power Network*, IEEE Transaction on Power Systems, Submitted for publication January 2007.

Conferences

1. KOUTNIK, J., NICOLET, C., SCHOHL, G. A. and AVELLAN, F., *Overload Surge Event in a Pumped-Storage Power Plant*, Proceedings of the 23rd IAHR Symposium on Hydraulic Machinery and Systems, Yokohama, Japan, October 18 - 21, 2006.

2. RUCHONNET, N., NICOLET, C. and AVELLAN, F., *One-Dimensional Modeling of Rotor Stator Interaction in Francis Pump-Turbine*, Proceedings of the 23rd IAHR Symposium on Hydraulic Machinery and Systems, Yokohama, Japan, October 18 - 21, 2006.

3. SIMOND, J.-J.,ALLENBACH, P., NICOLET, C. and AVELLAN, F., *Simulation tool linking hydroelectric production sites and electrical networks*, Proceedings of the 27th Int. Conf. on Electrical Machines, ICEM, Chania, Greece, September 2-5, 2006.

4. NICOLET, C., HEROU, J.-J., GREIVELDINGER, B., ALLENBACH, P., SIMOND, J.-J and AVELLAN, F., *Methodology for Risk Assessment of Part Load Resonance in Francis Turbine Power Plant*, Proceedings IAHR Int. Meeting of WG on Cavitation and Dynamic Problems in Hydraulic Machinery and Systems, Barcelona, 28-30 June 2006.

5. RUCHONNET, N., NICOLET, C. and AVELLAN, F., *Hydroacoustic Modeling of Rotor Stator Interaction in Francis Pump-Turbine*, Proceedings IAHR Int. Meeting of WG on Cavitation and Dynamic Problems in Hydraulic Machinery and Systems, Barcelona, 28-30 June 2006.

6. NICOLET, C., GREIVELDINGER, B., HEROU, J.-J., ALLENBACH, P., SIMOND, J.-J. and AVELLAN, F., *On the Hydroelectric Stability of an Islanded Power Network*, Proceedings IEEE Power Engineering Society General Meeting, 18-22 June 2006, Montréal, Canada, paper 623.

7. NICOLET, C., RUCHONNET, N., and AVELLAN, F., *One-Dimensional Modeling of Rotor Stator Interaction in Francis Pump-Turbine*, Proceedings of ISROMAC-11, ASME: International Symposium on Transport Phenomena and Dynamics of Rotating Machinery , Honolulu, Hawaii, USA, February 26-March 2, 2006.

8. NICOLET, C., ARPE, J. and AVELLAN, F., *Identification and Modeling of Pressure Fluctuations of a Francis Turbine Scale Model at Part Load Operation*, Proceedings of the 22nd IAHR Symposium on Hydraulic Machinery and Systems, Stockholm, Sweden, June 29 - July 2, 2004.

9. NICOLET, C., AVELLAN, F. and ROSSELL, J., *New Technology for high Disinfection Level of Flexible Endoscopes*, Fifth International Symposium on Cavitation (CAV2003) Osaka, Japan, November 1-4, 2003.

10. NICOLET, C., AVELLAN, F., ALLENBACH, P., SAPIN, A., SIMOND, J.-J. and HEROU, J.-J., *Transient Phenomena in Francis Turbine Power Plants: Interaction with the Power Network*, 11th International Meeting of the Work Group on the Behaviour of Hydraulic Machinery Under Steady Oscillatory Conditions, Stuttgart, Germany, October 8-10, 2003.

11. NICOLET, C., AVELLAN, F., ALLENBACH, P., SAPIN, A., SIMOND, J.-J., KVICINSKY, S. and CRAHAN, M., *Simulation of Transient Phenomena in Francis Turbine Power Plants: Hydroelectric Interaction*, Proceedings of Waterpower XIII, Advancing Technology for Sustainable Energy, Buffalo, New York, USA, July 29-31, 2003.

12. NICOLET, C., AVELLAN, F., ALLENBACH, P., SAPIN, A. and SIMOND, J.-J., *New Tools for the Simulation of Transient Phenomena in Francis Turbine Power Plants*, Proceedings of the 21st IAHR Symposium on Hydraulic Machinery and Systems, Lausanne, Switzerland, 9-12 September 2002, pp. 519-528.

13. NICOLET, C., SAPIN, A., SIMOND, J.-J., PRENAT, J.-E. and AVELLAN, F., *A new tool for the simulation of dynamic behaviour of hydroelectric power plants*, 10th International Meeting of the work group on the behaviour of hydraulic machinery under steady oscillatory conditions, IAHR, Trondheim, Norway, June, 26-28, 2001.

Curriculum Vitae

Christophe NICOLET

Av. de Mategnin 104
CH-1217 Meyrin

Né le 3 janvier 1977, célibataire
E-mail: christophe.nicolet@a3.epfl.ch

FORMATION

2001-2007: **Doctorat ès sciences techniques**
École Polytechnique Fédérale de Lausanne (EPFL)

1997-2001: **Diplôme Ingénieur en Génie Mécanique, EPF**
Ecole polytechnique fédérale de Lausanne (EPFL)
Prix Rhyming et diplôme d'honneur Génie Mécanique
Diplôme au Laboratoire de Machines Hydrauliques

1992-1997: **Diplôme d'Ingénieur en Génie Mécanique, HES**
Ecole d'Ingénieurs de Genève (EIG)
Mention: bien; Prix Institut Batelle
Diplôme au Laboratoire d'Energétique

EXPÉRIENCES PROFESSIONNELLES

2001-2007: **École Polytechnique Fédérale de Lausanne (EPFL), Suisse.**
Laboratoire de Machines Hydrauliques (LMH).

Activités de recherche et de développement:
Thèse de Doctorat: Modélisation des phénomènes hydroacoustiques, application aux turbines Francis:

- simulation comportement dynamique d'installations hydrauliques;
- dévelloppement de modèles hydrauliques pour implémentation dans SIMSEN;
- études transitoires/hydroacoustiques pour Sulzer Pumps, Meditecnic, les Forces Motrices de la Gougra et Colenco.

Activités d'enseignement:

- participation au cours d'Ecoulements Transitoires (Master; 5x2h/an);
- participation au cours de Spécialisation en Machines Hydrauliques (Postgrade; 2h/an);
- encadrement de 6 travaux pratiques de Master.

1999: 10 semaines chez **SIP (Société Genevoise d'Instruments de Physique)** à Meyrin, Genève; stage ingénieur au bureau de conception mécanique, approfondissement de l'étude d'une motobroche: dimensionnement d'un serrage d'outils et étude de différents systèmes de précharge de paliers. Utilisation d'Euclide, Excel et Maple.

1997-2000: 11 semaines cumulées en 3 stages chez **FAS (Fluid Automation Système SA)** à Versoix, Genève; stage ingénieur, câblage électrique et pneumatique d'automates d'assemblages pour électrovalves dans le département machines. Mise au point d'un calendrier de maintenance pour le parc de machines.

1998:	1 mois chez **Firmenich** à Meyrin, Genève; aide compositeur dans le département parfums.
1997:	1 mois chez **SOPAL (Société de Production d'Articles en Laiton)** à Sfax, Tunisie; stage ingénieur IAESTE, conception d'un banc d'essai d'étanchéité pour articles injectés.
1995-1996:	2 x 1 mois chez **Charmilles Technologies SA** à Meyrin, Genève; contrôleur en mécanique, département contrôle qualité / métrologie.

COMPÉTENCES INFORMATIQUES

Program.:	MATLAB, Delphi, FORTRAN, Maple.
Transitoires:	SIMSEN.
CFD:	Fluent, Gambit.
FEM:	ANSYS.
CAO:	Euclide (Dassault Systèmes), PRO-Engineer, Me10 (HP).
Acquisition:	HP-VEE.
Bureautique:	MS-Office, Latex, Adobe Illustrator et Photoshop, Grapher.

LANGUES

Francais	Langue maternelle.
Anglais	Parlé, lu et écrit: couramment, Cambridge First Certificat (2001, Perth).
Allemand	Parlé, lu et écrit: connaisances scolaires.

LOISIRS

Loisirs	Voyages, nature, excursions moto, plongée (PADI advanced), freesbee, gastronomie.